

Small Angle X-ray Scattering

edited by

O.GLATTER

Institut für Physikalische Chemie der Universität Graz, Austria

and

O.KRATKY

*Institut für Röntgenfeinstrukturforschung der Österreichischen Akademie der
Wissenschaften und des Forschungszentrums Graz, Austria*

1982



ACADEMIC PRESS

A Subsidiary of Harcourt Brace Jovanovich, Publishers

	London	New York
Paris	San Diego	San Francisco
São Paulo	Sydney	Tokyo
		Toronto

ACADEMIC PRESS INC. (LONDON) LTD.
24/28 Oval Road
London NW1

United States Edition published by
ACADEMIC PRESS INC.
111 Fifth Avenue
New York, New York 10003

Copyright © 1982 by
ACADEMIC PRESS INC. (LONDON) LTD.

All Rights Reserved

No part of this book may be reproduced in any form by photostat, microfilm, or any other means, without written permission from the publishers

British Library Cataloguing in Publication Data

Small angle X-ray scattering.

1. X-rays—Diffraction
I. Glatter, O. II. Kratky, O.
548'.83 QC482.D5

ISBN 0-12-286280-5

LCCN 81-68020

Printed in Great Britain by
The Alden Press

Contributors

- O. Glatter.** Institut für Physikalische Chemie der Universität Graz, Heinrichstrasse 28, A-8010 Graz, Austria
- K. C. Holmes.** Max-Planck-Institut für Medizinische Forschung, Jahnstrasse 29, D-6900 Heidelberg, Germany
- R. Kirste.** Johannes-Gutenberg-Universität, Fachbereich Chemie, Institut für Physikalische Chemie, D-6500 Mainz, Germany
- G. Kostorz.** Institut für Angewandte Physik, ETH-Hönggerberg, CH-8093 Zürich, Switzerland
- O. Kratky.** Institut für Röntgenfeinstrukturforschung der Österreichischen Akademie der Wissenschaften und des Forschungszentrums Graz, Steyrergasse 17, A-8010 Graz, Austria
- P. Laggner.** Institut für Röntgenfeinstrukturforschung der Österreichischen Akademie der Wissenschaften und des Forschungszentrums Graz, Steyrergasse 17, A-8010 Graz, Austria
- H. Leopold.** Institut für Physikalische Chemie der Universität Graz, Heinrichstrasse 28, A-8010 Graz, Austria
- K. Müller.** Institut für Röntgenfeinstrukturforschung der Österreichischen Akademie der Wissenschaften und des Forschungszentrums Graz, Steyrergasse 17, A-8010 Graz, Austria
- R. C. Oberthür.** Institut Max von Laue-Paul Langevin, 165X F-38042 Grenoble, Cedex, France
- I. Pilz.** Institut für Physikalische Chemie der Universität Graz, Heinrichstrasse 28, A-8010 Graz, Austria
- G. Porod.** Physikalisches Institut der Universität Graz, Universitätsplatz 5, A-8010 Graz, Austria
- H. Stuhrmann.** EMBL bei DESY, Notkestrasse 85, D-2000 Hamburg 52, Germany
- C. G. Vonk.** DSM Central Laboratory, PO Box 18, Geleen, Holland
- P. Zipper.** Institut für Physikalische Chemie der Universität Graz, Heinrichstrasse 28, A-8010 Graz, Austria

Preface

Most existing books on X-ray small angle scattering were published several years ago and recent reviews give detailed information only on special applications. We therefore felt that a book giving a compact presentation of the basic theory, techniques and applications at the present stage would fill a real gap in the literature. We accepted the kind invitation of Academic Press to edit and to contribute to such a book as we believe that the method of small angle X-ray scattering is now fully developed. The theory is complete, the experimental devices are well developed, laboratory systems are commercially available and dedicated X-ray facilities are available for special applications in several international research centres. Data analysis techniques have been improved substantially in the last two decades using numerical methods on computers. (Computer programs are available from the authors.) Although the development and the refinement of the technique will go on, X-ray small angle scattering is now a well established standard technique for the investigation of non-periodic structures with dimensions from about 10 Å up to several thousand Å.

The restriction to X-ray small angle scattering may appear arbitrary as neutron small angle scattering is based on the same physical principles, and investigations sometimes combine X-ray and neutron experiments. We confined ourselves to this topic because of space limitations and because a book on neutron scattering including a chapter on neutron small angle scattering was published recently.*

The book is divided into three sections: Introduction, Method and Applications. The Introduction gives a short basic description of the method and is directed to newcomers in the field. Detailed fundamental theoretical and experimental aspects are covered in the second section as well as methods for data evaluation and descriptions of special experimental techniques. Specific applications of the method to areas such as biological macromolecules, polymers and anorganic substances, are described in the third section.

The chapters are written by different authors, all of them experts in their

*Neutron scattering. In "Treatise on Materials Science and Technology", Vol. 15 (G. Kostorz, ed.). Academic Press, New York.

fields. We believe that the advantage of a clear presentation by specialists compensates for the drawback of a certain heterogeneity introduced by a large number of independent authors.

This book is aimed towards the level of graduate students, and a level of understanding which should appeal to biologically oriented as well as polymerically and physically oriented readers. So the book should offer an introduction for the newcomers as well as an integral review of the state of the art for the specialist. For this reason we have left out details in the theoretical and mathematical presentation and the chapters with applications are not necessarily to be considered as reviews of the current literature, but are written from a pedagogical point of view. The large number of references in all chapters allows the reader to follow up on the details.

We are grateful to the authors for their generous cooperation. We are also indebted to Ms. I. Ames and E. Lehner for their indefatigable and patient help in typing the manuscripts, Ms. B. Muller for the excellent preparation of many figures and to the staff of Academic Press for their continued help and co-operation.

*O. Glatter and O. Kratky
October 1981*

Contents

Part I. Introduction	1
1. A survey O. KRATKY	3
Part II. Method	15
2. General theory G. POROD	17
3.I. Instrumentation Experimental technique, slit collimation O. KRATKY	53
3.II. Instrumentation Point collimation and synchrotron radiation K. C. HOLMES	85
3.III. Instrumentation Data collection in X-ray small angle scattering H. LEOPOLD	105
4. Data treatment O. GLATTER	119
5. Interpretation O. GLATTER	167
6. Contrast variation H. B. STUHRMANN	197
7. Experimental practice K. MÜLLER	215
Part III. Applications	237
8. Proteins I. PILZ	239

x CONTENTS

9.	Nucleic acids and nucleoproteins P. ZIPPER	295
10.	Lipoproteins and membranes P. LAGGNER	329
11.	Natural high polymers in the dissolved and solid state O. KRATKY	361
12.	Synthetic polymers in solution R. G. KIRSTE and R. C. OBERTHUR	387
13.	Synthetic polymers in the solid state C. G. VONK	433
14.	Inorganic substances G. KOSTORZ	467
15.	Aggregations and micellar structures of small molecules in solution O. KRATKY and K. MÜLLER	499
	Subject index	511

Part I
Introduction

1

A Survey

O. KRATKY

*Institut für Röntgenfeinstrukturforschung der Österreichischen Akademie der
Wissenschaften und des Forschungszentrums Graz, Graz, Austria*

X-ray small angle analysis is a technique for studying structural features of colloidal size. Any scattering process is characterized by a reciprocity law, which gives an inverse relationship between particle size and scattering angle. Colloidal dimensions (between tens and several thousand Å) are enormously large compared to the X-ray wavelength (e.g. the most frequently used CuK_α-line of 1,54 Å) which makes the angular range of observable scattering correspondingly small. Since X-rays are primarily scattered by electrons, we can summarize the situation as follows: X-ray small angle scattering is always observed, and only observed, when electron density inhomogeneities of colloidal size exist in the sample. We are permitted to confine our considerations to coherent scattering, since incoherent scattering is negligibly weak at very small angles.

The scattering process can then be visualized as follows: the electrons resonate with the frequency of the X-rays passing through the objects and emit coherent secondary waves, which interfere with each other. We shall discuss this phenomenon in the context of a simple example.

Figure 1a shows a spherical particle. We assume that waves scattered from the two indicated points to an angle 2θ have a path difference of 1λ . It is easy to see that, if we include the scattering from all points (electrons), the superposition of waves with all possible phases will essentially lead to no scattering in the direction 2θ as a result of destructive interference. If we consider smaller scattering angles, the phase differences become smaller and the waves will begin to enforce one another. The scattering maximum will obviously be observed in the direction of zero scattering angle, where all waves are exactly in phase.

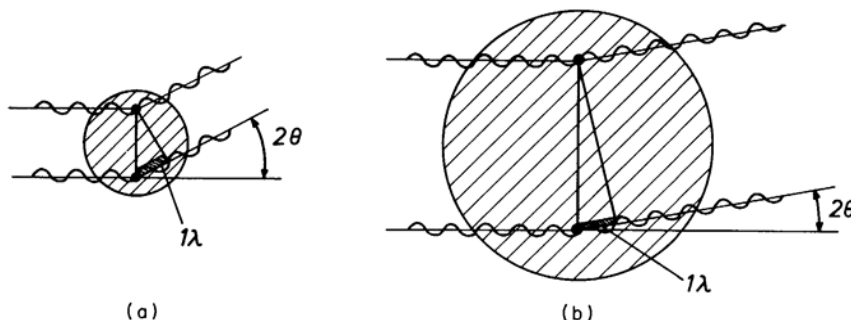


FIG. 1

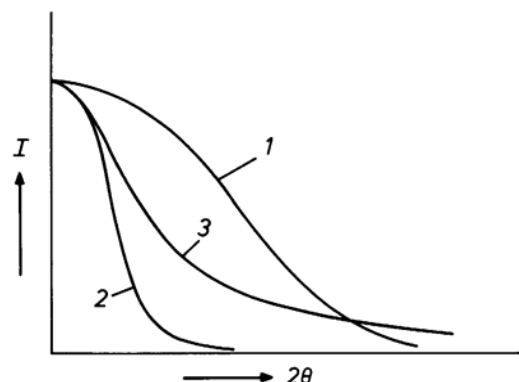


FIG. 2

Qualitatively, the observable scattering curve will be like curve 1, Fig. 2. Let us apply the above picture to a much larger sphere (for the same wavelength): here, path differences of 1λ will already occur at smaller scattering angles (Fig. 1b) resulting in a narrower scattering curve (curve 2, Fig. 2). Finally for particles that are huge compared to the wavelength, X-ray small angle scattering occurs.

Following the above train of thought, it is possible to compute the expected scattering curve for any particle shape (Chapters 2, 4, 5). For anisotropic particles, one has to calculate the scattering for every orientation and average the results. One of the different techniques for calculating scattering curves involves the distance distribution function of the electrons $p(r)$, which is obtained from geometrical considerations. The scattering curve I is obtained from $p(r)$ by Fourier inversion

$$I(h) = 4\pi \int_0^\infty p(r) \frac{\sin hr}{hr} \cdot dr, h = \frac{4\pi \sin \theta}{\lambda} \quad (1)$$

One understands that the small angle scattering curve will remain essentially unaffected if we shift electrons within a particle by distances which are small compared to the overall particle dimension. Thus, particles with relatively small inhomogeneities can be treated as if they had a uniform electron density distribution.

So far, we have implicitly assumed that particles are surrounded by a vacuum, in which case the scattered amplitude is proportional to the number of moles of electrons per unit volume, the electron density ρ . For dissolved particles, only the electron density difference $\rho_2 - \rho_1$ (ρ_2 = electron density of solute, ρ_1 = electron density of solvent) is effective. The scattered amplitude is thus proportional to $\rho_2 - \rho_1$, the scattered intensity to $(\rho_2 - \rho_1)^2$. If ρ_2 and ρ_1 are equal, the X-ray beam does not "see" the particles, since the solution represents a homogeneous electron density continuum, and waves scattered into any direction will be extinguished. The term "electron density" is frequently used for the electron density difference, the "contrast".

So far, we have talked about X-ray small angle scattering of an isolated particle, the "particulate scattering", postulated by Guinier in 1938. For homodisperse, sufficiently dilute solutions, the scattered intensities of the individual particles simply add up. The problem of the small angle analysis consists in deducing size, shape, mass and possibly even the electron density distribution from the scattering curve. One has to find a model particle, which is "equivalent in scattering" with the particle in solution, i.e. whose scattering curve agrees within experimental error with the experimental curve. The more accurate the latter was determined and the larger its angular range, the more challenging and the more rewarding is the problem of the analysis. This is particularly true if not only the main maximum of the scattering curve, but also subsidiary maxima, were observed. These subsidiary maxima are frequently very weak, but their position, height and shape are sensitive to rather small changes in the model. A complete solution to the problem of finding a model equivalent in scattering frequently requires several cycles of approximation, sometimes even mere trial and error.

It is, however, possible to obtain a number of parameters directly from the scattering curve, without the ambiguity of trial and error. These parameters form themselves an important body of information, and they are the basis for any overall analysis.

The first of these parameters is the *radius of gyration*, R . Formally, it corresponds to the radius of inertia in mechanics; it is the root-mean square of the distances of all electrons from their centre of gravity. Therefore, R is an intuitive measure for the spacial extension of the particle. In a plot of $\ln I$ vs $(2\theta)^2$ (Guinier plot), R is proportional to the square root of the slope of the tangent in the limit $2\theta \rightarrow 0$.

If the particles are rod-like, multiplication of the scattering curve by 2θ

yields the so-called cross-section factor, i.e. a curve, which depends only on size, shape and electron density distribution within the cross-section. A Guinier plot of this curve yields the radius of gyration of the cross-section R_c .

For plate-like particles, multiplication by $(2\theta)^2$ yields the thickness factor, which depends only on the particle thickness and on the electron density distribution perpendicular to the particle plane. The radius of gyration of the thickness R_t is obtained analogous to R and R_c . For particles with uniform electron density distribution, the thickness t follows from R_t according to $t = R_t \sqrt{12}$.

The *volume* V , another directly obtainable parameter, can be calculated for particles with sufficiently homogeneous electron density distribution according to

$$V = K \frac{I_0}{\int_0^\infty I(2\theta) \cdot (2\theta)^2 \cdot d(2\theta)} ; K = \frac{\lambda^3 a^2}{4\pi} \quad (2)$$

(a = distance sample – detector).

The integral in the denominator is known as “invariant”: for a given concentration, its value does not depend on the degree of dispersion. Since the zero intensity increases with the particle weight – and hence also with the volume – it is plausible that the formula for the volume involves the quotient of I_0 and the invariant.

If one knows the “absolute intensity”, i.e. the quotient of scattering intensity and primary intensity, one can obtain the *particle molecular weight*, or – for polydisperse solutions – its weight average.

The small angle technique can thus be used to “weigh” particles. The derivation of the underlying quantitative relationship is based on the fact that the scattering of one electron amounts to 7.9×10^{-26} times the primary intensity per square centimetre, when measured at a distance of 1 cm from the scattering electron. A unique feature of the small angle method is the fact that it also allows a determination of the mass per unit length for rod-like particles and the mass per unit area for plate-like particles.

Finally, one might also quote the *distance distribution function* $p(r)$ among the directly obtainable parameters. It is obtained by Fourier inversion of the scattering curve

$$p(r) = \frac{1}{2\pi^2} \int_0^\infty I(h) \cdot hr \cdot \sin hr \cdot dh \quad (3)$$

We return to the problem of the particle-shape determination. We have outlined how theoretical scattering curves can be computed for a model of given shape. In fact, there exists an “atlas” of scattering curves for numerous three-axial bodies, such as ellipsoids, parallelepipeds, elliptic cylinders, hollow cylinders, hollow spheres etc. Using this atlas and the above parameters, it was possible to obtain reasonable approximations of size and shape especially of

biological macromolecules. A large number of proteins (Chapter 8), nucleic acids, viruses and ribosomes (Chapter 9) have been investigated with great success.

A particularly nice example is hemocyanine. Good agreement between the theoretical and the experimental curve was obtained up to the third subsidiary maximum for a hollow cylinder model. The relative intensities of the main maximum and the first subsidiary maximum were found to depend strongly on the ratio of inner and outer radii, which offered a sensitive criterion for the determination of this radial ratio.

For more complex particle shapes, it is occasionally convenient to approximate the particle with a large number of small, closely packed spheres. These spheres do not in any way correspond to molecular subunits; they are just a remedy to approximate any complicated particle shape.

The availability of electronic computers also permits the computation of models consisting of several three-axial bodies; i.e. for the IgG-globuline a model consisting of three elliptic cylinders was found to be equivalent in scattering with the real molecule.

Instead of comparing experimental and theoretical scattering curves, one can also compare theoretical and experimental (using equation 3) $p(r)$ functions. Though both approaches are completely equivalent, the latter has the advantage of being closer to human intuition. The new “indirect Fourier transformation method” allows the computation of $p(r)$ functions even for non-ideal experimental situations. In fact, in recent years it has become more and more common to publish the distance distribution function together with the scattering curve. Among other advantages, the $p(r)$ function allows the immediate deduction of one important particle parameter: the r -value at which $p(r)$ drops to zero indicates the *largest particle dimension*.

The relative arrangement of subunits can be deduced from labelling experiments: heavy atoms or groups of heavy atoms are attached to each subunit and the scattering curves of labelled and unlabelled material are determined. The distances between the labels can then be deduced from certain difference curves. The power of this technique is greatly increased when neutrons are used instead of X-rays, since, for neutron scattering, labelling simply consists of exchanging hydrogen by deuterium.

The next step of refinement of the small angle model consists of including pronounced electron density inhomogeneity within the particle. This is particularly desirable when a particle consists of several chemical constituents. Two different approaches to that problem have so far been used. If the particles are, to a good approximation, spherically symmetrical (like, for example, many lipoproteins; Chapter 10), the radial electron density distribution is obtained directly by Fourier inversion of the scattering amplitude. The amplitude is the square root of the intensity, which immediately leads to the problem of assigning

the correct sign. This phase problem, which can be a major obstacle in X-ray crystallography, is usually of minor significance in small angle research: since the sign can only change when the scattering curve drops to zero, the number of possible sign combinations is limited. The problem can be avoided totally in small angle scattering with the recently developed convolution square root technique which allows the computation of the radial electron density from the distance distribution function (see Chapter 4). Knowing the electron density of the chemical constituents, the radial electron density permits a deduction of the relative arrangement of the different constituents.

Analogous possibilities exist for a deduction of the radial electron density distribution of long, cylindrically symmetric particles as well as for the electron density perpendicular to the plane of lamellar shaped molecules, provided the lamella is known to have mirror symmetry.

A second technique for determining electron density inhomogeneities is called the "phase-contrast technique". Its applicability is independent of the presence of any particle symmetry. The basic idea is as follows: if one modifies the electron density of the solvent, the contrast between particle and solvent is altered and hence the scattering changes. If one succeeds in finding a solvent whose electron density is identical to the electron density of one of the particle constituents, the scattering from this constituent vanishes and one obtains information about the rest of the molecule. Thus, if a virus particle consisting of protein shell and nucleic acid core is under investigation and the solvent electron density is adjusted to the protein, the X-ray beam "sees" only the nucleic acid. Although it is not possible to "blank out" completely the electron density of a constituent, contrast variation yields valuable information: if the scattering curve is known from at least three solvents with different electron densities, the scattering curve can be split into three terms (Chapter 6). One term corresponds to the scattering function of a hypothetical particle with the overall shape of the physical molecule, but with uniform electron density. It can thus be compared to theoretical scattering functions of homogeneous bodies and yields the shape of the particle envelope. The second term corresponds to the scattering which one would observe if the particle were investigated in a solvent whose electron density equals the mean particle density. This term yields, thus, information about the inhomogeneities of the electron density distribution within the particle. The third term is a mixed function, which will not be discussed here.

The main problem with the phase contrast consists of finding suitable solvents with sufficiently different electron densities, which do not alter the structure of the dissolved molecules. Neutron scattering, however, is superior in this respect, because it allows large variations of the contrast by simple exchange of H_2O by H_2O-D_2O mixtures.

The study of changes in the particle structure upon external influences

(change of temperature, change of solvents, reactions with other molecules, irradiation with high-energy radiation etc.) is an important field of application of small angle scattering (Chapter 8). We mention a characteristic example: second-order phase transitions occur in the lipid core of human high-density lipoproteins upon raising the temperature. The critical temperature is different for samples of different human beings and appears to correlate with a disposition for atherosclerosis. Many studies exist about conformational changes, e.g. reaction of apoenzyme with coenzyme to form the holoenzyme, reactions between antibodies and haptens, etc.

In the field of biological macromolecules, one is usually concerned with homodisperse solutions of molecules with identical shape, whose structures do not change with time. A completely different situation exists with natural and synthetic chain molecules in solution (Chapters 11, Section I, and 12), which have a rapidly changing coil structure. Apart from the molecular weight (or, for polydisperse systems, its weight average), application of the small angle technique yields a useful parameter characteristic for the degree of coiling: the "persistence length". Its value follows directly from a characteristic bend in an $I(2\theta) \cdot (2\theta)^2$ vs 2θ plot. The determination of the persistence length by small angle scattering is superior to other methods, which all involve indirect deductions from the hydrodynamic length and the radius of gyration, assuming a Gaussian coil. This assumption is not inherent in the small angle determination; the X-ray beam acts as a fine probe which averages the degree of coiling over the whole of the chain molecule. Even branched molecules can be analysed with the small angle scattering technique, especially if "comb-like" branching exists (i.e. many short branches along the main chain).

The small angle scattering method has also proven useful for the characterization of dissolved particles, which are not biological macromolecules. Examples are oligomers of dyes (Chapter 15, Section V), where a knowledge of degree and geometry of association is important for an understanding of the process of textile dyeing. From the experimental point of view, it is noteworthy that for low concentrations monomers, with molecular weights often of only a few hundred, exist in solution, which still yield an interpretable small angle scattering curve. Bearing in mind that, on the other hand, particles with molecular weights of many millions are frequently studied with small angle scattering, one appreciates the enormous range of applicability of this technique. This flexibility is simply achieved by adjusting the width of the X-ray beam entering into the small angle camera and by modifying the registration time for the scattered radiation (Chapters 3 and 7). Other examples for organic molecules in solution, which were extensively studied with small angle scattering, are soap micelles and micelles in the gall fluid (Chapter 15, Sections I-IV).

So far, we have discussed exclusively the study of colloidal particles in solution. However, there exist numerous successful applications of the small

angle scattering technique for the characterization of solids, e.g. natural and synthetic high polymers, metals, alloys, glasses and colloidal powders.

It should be remembered that natural fibres, in particular cellulose, as well as colloidal coal, were at the cradle of X-ray small angle scattering research. They were the first substances whose small angle scattering was observed in the late 1920s and early 1930s. Already then, this phenomenon was recognized as originating from the colloidal structure of these substances.

In 1938, Guinier proposed his concept of particulate scattering. At the same time it was recognized, that for densely packed colloidal particles (like the micelles of solid highpolymers) interparticle interference effects are dominating and that the scattering is, therefore, similar to what one expects from a distorted crystal lattice. This analogy is suggested by the fact that the ribbon-shaped micelles are stacked to form closely-packed parcels (Chapter 11, Section II). This lamellar-stack model has since found widespread acceptance, not only for the solid cellulose, but also for synthetic high-polymers (Chapter 13). It did, however, take some time before it was generally accepted that there is a qualitative and principal difference between diluted and dense systems. In fact, it took several unsuccessful attempts to apply the idea of particle scattering (with full neglect of interparticle interference effects) to densely packed systems, whose volume of hollow spaces is only about 1% of the total volume, i.e. whose state is infinitely far removed from that of a dilute solution.

In fact, a number of years later, the technique of "air-swelling" was invented, which involved a loosening-up of densely packed fibres by several times their original volume, with concomitant destruction of the parallel ordering of adjacent micelles. This technique permitted the application of the particle-scattering concept to cellulose and silk since, as it was generally recognized, the interparticle interference effects became progressively less severe the more anisotropic the particles are. It is gratifying that the dimensions obtained from the dense system (using the lamellar stack model) show good agreement with the ones obtained from the air-swollen samples (using the particle scattering concept). Differences between the results of the two approaches can be interpreted in terms of changes in the structure of the micellae upon transition between the two states.

Different approaches have been successful for the application of small angle scattering to the study of metals, alloys, glasses and ceramics (Chapter 14). If one phase occurs finely dispersed and dilute among the rest of the substance – in this sense hollow spaces can also be considered a phase – the concept of particle scattering can be applied, provided the electron contrast between this phase and the surrounding matrix is sufficiently stronger than electron density variations within the matrix. Compared to monodisperse solutions, however, the situation is usually complicated by the fact that the influences of particle anisotropy and of polydispersity on the scattering curve cannot be unequivocally separated.

Both deviations from a monodisperse system of spheres have the effect of flattening-out the scattering curve, as indicated in Fig. 2, curve 3. This constitutes a fundamental problem in small angle research. Thus, the scattering of a homodisperse system of ellipsoids of a given axial ratio can always be approximated in terms of a distribution of spheres of different radii. Fortunately, this ambiguity is not always as severe as it could be. Just for inorganic systems practically only spherical particles need to be considered.

High concentrations of inhomogeneities reduce the intensity at low scattering angles. We mention the case of silica spheres dispersed in water ("Ludox"): for volume fractions between 1% and 16%, the diameter determined using the Guinier-plot for single particle scattering changed from 210 Å to 148 Å. However, even small contributions of interparticle interferences can be easily recognized from the $p(r)$ function.

There exists a fundamentally different approach, which is not based on any model assumption, and which is, therefore, always applicable: the direct determination of parameters following the general scattering theory (Chapters 2, 4, 5).

The first of these parameters is the *mean square fluctuation of electron density*, which is obtained from

$$\overline{(\Delta\rho)^2} = \frac{a^2 \int_0^\infty I(2\theta) \cdot (2\theta)^2 d(2\theta)}{k \cdot t \cdot P_0}; k = \frac{\lambda^3}{4\pi} i \cdot N^2 = 8,34 \times 10^{-3} \quad (4)$$

For a two-phase system with known electron density difference $(\Delta\rho)_{1,2}$ between the two phases, the volume fractions w_1 and $w_2 = 1 - w_1$ of the two phases follow from

$$\overline{(\Delta\rho)^2} = w_1 \cdot w_2 (\Delta\rho)_{1,2}^2 \quad (5)$$

Porod's law (Chapter 2) states that the tail-end of the scattering curve follows the course

$$I = \frac{K}{(2\theta)^4} \quad (6)$$

where K is related to the *inner surface* (in Å² per Å³ of the sample) by the equation

$$O/V = \frac{2\pi^2}{a\lambda} \cdot w_1 w_2 \frac{K}{Q} \quad (7)$$

The quantities $\overline{(\Delta\rho)^2}$ and O/V are powerful aids for the analysis. They constitute an invaluable check for any proposed model. It might be appended that equations 4–7 were also frequently used for the analysis of natural and synthetic highpolymers in the solid state.

Naturally, a basic requirement for the significance of any analysis is a sound scattering experiment. Today, the small angle scattering technique can be regarded as a precision method with a high experimental standard (Chapter 3).

Available well developed instruments are reliable and, to a large extent, automatic, which also makes the small angle scattering technique a useful tool for routine work, for which any laboratory can be equipped with commercially available instruments at reasonable costs.

For extreme demands, on the other hand, there exist highly specialized and powerful instruments in some laboratories around the world. Here, especially, those laboratories must be mentioned which make use of the radiation of synchrotrons and storage rings (e.g. DESY Hamburg, Lure Orsay, Stanford, Novosibirsk), where the radiation intensity exceeds that of a conventional X-ray generator by about three orders of magnitude. Obviously, only technologically very advanced countries or communities are in a position to offer such facilities for the purpose of diffraction experiments. With these tools the possibility of performing time-resolving studies can be realized, i.e. the observation of transient states in macromolecular assemblies as, for example, in the contraction-relaxation cycle of muscle.

As already mentioned above, many problems, particularly the determination of density inhomogeneities within a particle can only be solved by neutron diffraction. Also, only a few centres exist around the world, for this purpose, which are equipped for such studies. At present the Institut Max von Laue – Paul Langevin in Grenoble, France, and the Brookhaven National Laboratory, Upton, USA, for example, have sufficiently powerful high neutron flux reactors.

With regard to special registration devices the two-dimensional position sensitive detector should be mentioned. Such instruments exist at the above mentioned centres as well as at the National Center for Small Angle Scattering Research at the Oak Ridge National Laboratory, USA, and allow, in combination with cameras that are several metres long, the measurement of small angle scattering patterns from oriented systems in very short times. Research centres having such equipment at their disposal generally offer the possibility for visiting scientists to use their facilities during short periods for specific problems where preliminary studies by conventional techniques have prepared the ground.

In the following section books and review papers concerning small angle scattering are listed.

References

- Alexander, L. E. (1969). In "X-Ray Diffraction Methods in Polymer Science", pp. 280–256. Wiley, New York.
 Beeman, W., Kaesberg, P., Anderegg, J. W. and Webb, M. B. (1957). Size of particles and lattice defects. In "Handbuch der Physik", Vol. 32. Springer Verlag.
 Brumberger, H. (1967). Proceedings of the Conference held at Syracuse University, June 1965, on "Small-Angle X-ray Scattering". Gordon and Breach, New York.
 Guinier, A. and Fournet, G. (1955). "Small Angle Scattering of X-rays". Wiley, New York and Chapman and Hall, London.
 Jacrot, B. (1976). The study of biological structures by neutron scattering from solution. In "Rep. Prog. Phys.", Vol. 39, pp. 911–953.
 Kratky, O. (1963). X-ray small angle scattering with substances of biological interest in diluted solution. In "Progress in Biophysics", Vol. 13, pp. 105–173. Pergamon Press, Oxford.
 Kratky, O. and Pilz, I. (1972). Recent advances and applications of diffuse X-ray small-angle scattering on biopolymers in dilute solutions. In "Quarterly Reviews of Biophysics", Vol. 5, pp. 481–537.
 Pessen, H., Kumosinsky, T. F. and Timasheff, S. N. (1973). Small-angle X-ray scattering. In "Methods of Enzymology", Vol. 27, pp. 151–209. Academic Press, New York and London.
 Pilz, I. (1973). Small-angle X-ray scattering. In "Physical Principles and Techniques of Protein Chemistry". Part C, pp. 141–243. Academic Press, New York and London.
 Pilz, I., Glatter, O. and Kratky, O. (1979). Small-angle X-ray scattering. In "Methods of Enzymology", Vol. 61, pp. 148–249. Academic Press, New York and London.
 Reviews, Papers and Abstracts from the 4th International Conference on "Small Angle Scattering" in Gatlinburg, USA (1978). In *J. Appl. Cryst.* **11**, 295–674.

2

General Theory

G. POROD

Physikalisches Institut der Universität Graz, Graz, Austria

I.	Principles of diffraction	18
	A. Scattering	18
	B. Interference	18
	C. Small angle scattering	20
	D. Correlation function	21
II.	Particle scattering. Special cases	22
	A. Single particles	22
	B. Guinier approximation	25
III.	Particle scattering. General treatment	26
	A. Correlation function and chord distribution	26
	B. Central part	27
	C. Final slope	29
IV.	Extremely anisometric and composite particles	32
	A. Rod-like particles	32
	B. Flat particles	35
	C. Composite particles	36
V.	The influence of dense packing	38
	A. The radial distribution function	38
	B. The surrounding function	39
	C. Statistical fluctuations	41
VI.	Non-particulate systems	42
	A. Babinet principle	42
	B. Correlation function	44
	C. Intensity function; integral parameters	45
	D. Final slope; internal surface	46
VII.	Non-uniform electron density	48
	A. General remarks	48
	B. Heterogeneous particles	48
	C. Correlation function and final slope	49
	References	50

I. Principles of Diffraction

A. Scattering

Structure analysis may be based on the diffraction of X-rays, electrons and neutrons. Although in the following treatment we will be concerned with X-rays only, all the results may be applied to electron and neutron diffraction as well, with only slight modifications.

Diffraction is produced by the interference of waves scattered by an object. In the case of X-rays striking the object, every electron becomes the source of a scattered wave. As the energy of an X-ray photon is very large compared with the binding energy of an atom, all electrons will behave as if they were free (except for very heavy atoms, which play no role in small angle scattering). Accordingly, all secondary waves are of the same intensity, by the well known Thomson formula

$$I_e(\theta) = I_p \cdot 7.90 \cdot 10^{-26} \cdot \frac{1}{a^2} \cdot \frac{1 + \cos^2 2\theta}{2} \quad (1)$$

where I_p is the primary intensity, a the distance from the object to the point of registration. The numerical factor is the square of the so-called classical electron radius (e^2/mc^2). The intensity depends only slightly on the scattering angle 2θ by the polarization factor, which is practically equal to 1 for the small angles in all problems of interest here. As the electron scattering intensity I_e applies to all formulae to follow, it will be omitted for brevity: this means that the amplitude and the intensity of a secondary wave scattered by a single electron will be taken of magnitude 1. In case the absolute intensity is needed, I_e should be calculated again.

B. Interference

The scattered waves are coherent. Though incoherent (Compton-) scattering will occur too, it can be neglected as only small angles are involved in our problems. Coherence means that the amplitudes are added, and the intensity is then given by the absolute square of the resulting amplitude. The amplitudes are of equal magnitude (= 1 by our convention), and differ only by their phase φ , which depends on the position of the electron in space. It is convenient to represent a single secondary wave by the complex form: $e^{i\varphi}$. The phase φ is $2\pi/\lambda$ times the difference between the optical path and some arbitrary reference point.

The calculation of φ is illustrated by Fig. 1. Let us denote the direction of the incident beam by the unit vector s_0 , and of the scattered beam by s . The path difference of a point P , specified by the vector r , against the origin 0 is then

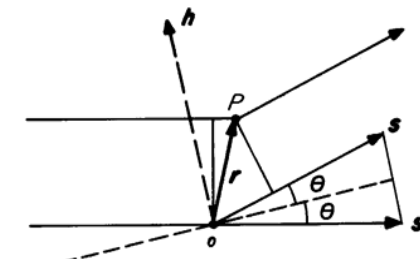


FIG. 1. Scattering by two point centres.

directly seen to be $-r(s - s_0)$. The phase is therefore $\varphi = -(2\pi/\lambda)r(s - s_0)$. This takes the form $\varphi = -hr$. From Fig. 1 it is seen that $(s - s_0)$ lies symmetrically with respect to the incident and the scattered beam, and that its magnitude is $2\sin \theta$. Here θ means half the scattering angle, according to the glancing angle used in crystallography. Consequently, the vector h has the same direction and the magnitude: $h = (4\pi/\lambda)\sin \theta$ (where $\sin \theta$ may be replaced by θ in small angle scattering).

The vector product hr means that only the component of r in h is relevant for the phase. So all points in a plane perpendicular to h will have the same phase. Diffraction might, therefore, be regarded as a "reflection" by a set of planes (dashed lines in Fig. 1). This concept, though of great importance in crystallography, will not be used much here.

It could now be possible to obtain the resulting amplitude by summing up all secondary waves, represented by a term e^{-ihr} each. But, considering the enormous number of electrons and the fact that a single electron cannot be exactly localized, it will be convenient to introduce the concept of electron density first. This may be defined as the number of electrons per unit volume (cm^3), and then be denoted by $\rho(r)$. A volume element dV at position r will then contain $\rho(r)dV$ electrons. So summation can be replaced by integration over the whole volume V irradiated by the incident beam:

$$F(h) = \iiint dV \cdot \rho(r) e^{-ihr} \quad (2)$$

Mathematically speaking, the amplitude F of diffraction in a certain direction (specified by h) is the Fourier transform of the electron density distribution within the object. From Eqn (2) the best way of deriving the intensity $I(h)$ as the absolute square is by using the conjugate complex F^* :

$$I(h) = FF^* = \iiint dV_1 \cdot dV_2 \cdot \rho(r_1)\rho(r_2) e^{-ih(r_1 - r_2)} \quad (3)$$

This is a Fourier integral again, involving only the relative distance $(r_1 - r_2)$ for

every pair of points. It is convenient, therefore, to carry out the double integration in (3) in two different steps: first to summarize all pairs with equal relative distance, and then to integrate over all relative distances, including the phase factor.

The first step is the mathematical operation of convolution square or auto-correlation, and is defined by

$$\text{auto-correlation } \tilde{\rho}^2(r) \equiv \iiint dV_1 \rho(r_1) \rho(r_2) \\ \text{with: } r = (r_1 - r_2) = \text{constant} \quad (4)$$

The resulting function, well known as the Patterson function and widely used in crystallography, has the following properties: every electron pair with relative distance r can be represented by a point in a fictitious C -space, say. The density of these points is then given by $\tilde{\rho}^2(r)$. As every pair is counted twice with r and $-r$, it follows that the distribution in the C -space must show a centre of symmetry, whether this be the case in ordinary space or not.

The second step consists of an integration over the C -space:

$$I(h) = \iiint dV \cdot \tilde{\rho}^2(r) \cdot e^{-ihr} \quad (5)$$

This is a Fourier transform again. So the intensity distribution in h or reciprocal space is uniquely determined by the structure of the object, as expressed by $\tilde{\rho}^2(r)$. Conversely, the latter can be obtained from $I(h)$ by the inverse Fourier transform:

$$\tilde{\rho}^2(r) = \left(\frac{1}{2\pi}\right)^3 \iiint dh_x dh_y dh_z \cdot I(h) \cdot e^{ihr} \quad (6)$$

One quite general conclusion can be drawn from (5) and (6): there is a reciprocity between ordinary and reciprocal space. As they are connected by the phase hr only, the result will be the same, when r is enlarged and h is diminished by the same factor. So large particles will give a diffraction pattern concentrated at small angles.

C. Small Angle Scattering

Especially with particles or inhomogeneities of colloidal dimensions, and with a usual wavelength of about 1 Å, the pattern is limited to a range of one or two degrees. This is the typical domain of small angle scattering, which will now be discussed in more detail. Furthermore, let us introduce two restrictions which are met by the majority of cases, and will greatly simplify the problem:

- (1) The system is statistically isotropic. It makes no difference here whether

this is a property of the structure itself or a consequence of some change in time (rotation of particles or the like).

- (2) There exists no long range order. This means that there is no correlation between two points separated widely enough.

From Restriction (1) it follows that the distribution $\tilde{\rho}^2$ in C -space depends only on the magnitude r of the distance, though this will not be true for $\rho(r)$ in ordinary space. Likewise, the phase factor e^{-ihr} can be replaced by its average, taken over all directions of r . This is expressed by the fundamental formula of Debye (1915):

$$\langle e^{-ihr} \rangle = \frac{\sin hr}{hr} \quad (7)$$

by means of which (5) is reduced to the form

$$I(h) = \int 4\pi r^2 dr \cdot \tilde{\rho}^2(r) \frac{\sin hr}{hr} \quad (8)$$

According to Restriction (2), at large r the respective electron densities should become independent, and might be replaced by the mean value $\bar{\rho}$. The auto-correlation, as defined by (4), must so tend towards a constant value $V\bar{\rho}^2$, while the initial value $\tilde{\rho}^2(0)$ is $V\bar{\rho}^2$ (the maximum, of course). So the structure is represented by the finite region only, where $\tilde{\rho}^2$ deviates from the final value, as the latter obviously contains no information. This is in accordance with the fact that a constant value throughout the total volume (always assumed to be very large) acts like a blank object and cannot make any contribution to the diffraction pattern (but for extremely small angles not accessible to experiments). It is convenient, therefore, to drop this "background" from the beginning, and to use the electron density fluctuation $\eta = \rho - \bar{\rho}$ instead of the density ρ itself. The auto-correlation (4) is then redefined as

$$\tilde{\eta}^2 = (\widetilde{\rho - \bar{\rho}})^2 = \tilde{\rho}^2 - V\bar{\rho}^2 = V \cdot \gamma(r) \quad (9)$$

D. Correlation Function

By a slight change of notation we have introduced in (9) the so-called correlation function $\gamma(r)$ (Debye and Bueche, 1949). Comparing (4) and (9) we can interpret $\gamma(r)$ as the average of the product of two fluctuations at a distance r :

$$\gamma(r) = \langle \eta(r_1) \eta(r_2) \rangle \quad \text{with } r = |r_1 - r_2| = \text{constant} \quad (10)$$

also with the property $\gamma(0) = \overline{\eta^2}$, and $\gamma \rightarrow 0$ for larger r . According to Restriction (2) we assume that the final value of 0 is reached within a finite range (of colloidal dimension). Equation (8) now takes the form (Debye and Bueche, 1949)

$$I(h) = V \int_0^\infty 4\pi r^2 dr \cdot \gamma(r) \frac{\sin hr}{hr} \quad (11)$$

This is the most general formula for the diffraction of systems obeying Restrictions (1) and (2). $\gamma(r)$ is found by the inverse Fourier transform

$$V\gamma(r) = \frac{1}{2\pi^2} \int_0^\infty h^2 dh \cdot I(h) \frac{\sin hr}{hr} \quad (12)$$

Both formulae are of outstanding importance for all problems to follow. But let us first draw some general conclusions: obviously (11) and (12) take a particularly simple form for $h = 0$ and $r = 0$, as then the Debye factor has the value 1. So we have

$$I(0) = V \int_0^\infty 4\pi r^2 dr \cdot \gamma(r) \quad (13)$$

$$V\gamma(0) = \frac{1}{2\pi^2} \int_0^\infty h^2 dh \cdot I(h) = V\eta^2 \quad (14)$$

The meaning of Eqn (13) requires some consideration. For, at $h = 0$ exactly, all secondary waves are in phase, so that we might expect $I(0)$ to be equal to the square of the total number of electrons in the irradiated volume V . This cannot be observed, however. Equation (13) may be interpreted in the sense that each electron of the volume V acts in coherence only with a surrounding region, as defined by $\gamma(r)$. So $I(0)$ should be regarded as an extrapolated value, rather than as a measurable quantity.

Formula (14) shows that the integral of the intensity over the reciprocal space is directly related to the mean square fluctuation of electron density, irrespective of special features of the structure. If, for example, parts of the system were shifted or deformed, the diffraction pattern might be altered considerably, but the integral in Eqn (14) must remain invariant.

$$\text{"invariant" } Q = \int_0^\infty h^2 dh \cdot I(h) \quad (15)$$

By virtue of this property it will play an important role later.

II. Particle Scattering. Special Cases

A. Single Particles

Let us now consider a dilute solution of identical particles of constant electron density ρ , embedded in a medium of constant ρ_0 (solvent). So only the difference

$\Delta\rho = (\rho - \rho_0)$ will be relevant for diffraction. If the particles are separated from each other widely enough, it is plausible to assume that they will make independent contributions to the diffracted intensity, so that only one single particle (denoted by the index 1) needs to be considered. This will be discussed in more detail later in Section 5, and will be found to be true.

The simplest case is that of particles showing spherical symmetry. As all orientations in space are equivalent, then it suffices to calculate the amplitude, and then to square it to get the intensity. This procedure is well known for the calculations of atomic structure factors. For the special case of a sphere (radius R_0 , volume V) of uniform density the result has been given by Rayleigh (1911):

$$\text{sphere } I_1(h) = (\Delta\rho)^2 V^2 \left[3 \frac{\sin hR_0 - hR_0 \cos hR_0}{(hR_0)^3} \right]^2 \quad (16)$$

Though derived for a very special case only, Eqn (16) shows (Fig. 2) all the typical features common to the diffraction patterns produced by not too anisometric particles. The central peak is easily understood: all secondary waves are in phase at $h = 0$, and are simply added. The amplitude must, therefore, be equal to the number (Δn_e) of excess electrons, as only the contrast to the surrounding is effective. This must be true for any particle, irrespective of size and shape:

$$\text{single particle } I_1(0) = (\Delta\rho)^2 V^2 = (\Delta n_e)^2 \quad (17)$$

For particles of non-spherical shape the intensity can only be calculated by numerical methods. This is greatly facilitated by some special symmetry of the particle. We shall consider such cases first. A centre of symmetry, which we will assume for the following examples, simplifies the calculation of the amplitude, as this becomes real for any orientation. The phase factor e^{-ihr} can then be replaced by $\cos hr$:

$$\text{orientated particle } F_1(h) = (\Delta\rho) \int dV \cdot \cos hr; \quad I_1(h) = F^2 \quad (18)$$

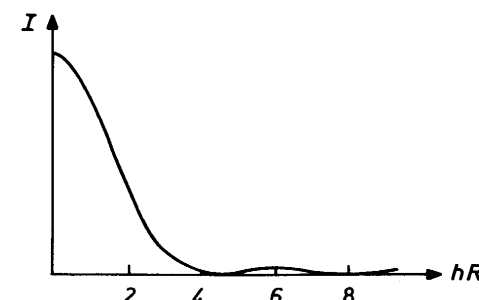


FIG. 2. Scattering intensity of a sphere.

where the integral should be extended over the volume of the particle. The observable intensity is then found by taking the average of F^2 over all orientations. Incidentally, that amounts to the same as keeping the particle fixed and rotating \mathbf{h} with respect to it.

It should be noted, in this context, that a Fourier integral like Eqn (18) always results in an oscillating function, alternating between positive and negative values, which must, therefore, become zero at certain points. (This could not be so if there were no centre of symmetry.) But this characteristic feature will be more or less blurred by taking the average, so only for spherical particles, or nearly spherical, the oscillating slope is to be expected to play a marked role.

Ellipsoids provide a particularly simple case. As was pointed out by Hosemann (1939), for every orientation of an ellipsoid the amplitude will be the same as for a sphere with a certain radius. This follows from the fact that only the component of \mathbf{r} in \mathbf{h} is relevant for the phase, so the shifting of a plane perpendicular to \mathbf{h} will not alter the amplitude. Now, it is well known that in this way an affine relation between an ellipsoid and a sphere can be established. If we define the orientation by the angles α, β, γ between the half-axes a, b, c and \mathbf{h} , respectively, the equivalent radius R_e is found to be

$$\text{ellipsoid } R_e^2 = a^2 \cos^2 \alpha + b^2 \cos^2 \beta + c^2 \cos^2 \gamma \quad (19)$$

This should be substituted into Eqn (16), leaving V constant, and then the average formed, which can only be done by numerical integration.

Another simple type is provided by rectangular parallelepipeds. The amplitude for an oriented particle can then be split into three factors, corresponding to one axis each. Let us designate the axes by $2a, 2b, 2c$; the respective Cartesian coordinates by x, y, z ; the direction of \mathbf{h} relative to these axes by the unit vector (α, β, γ) , where α, β, γ stand for the cosines of the respective angles. The phase $h\mathbf{r}$ is then expressed by $h(x\alpha + y\beta + z\gamma)$, so that the exponential phase factor can be separated into three factors of the form $e^{-ihx\alpha}, \dots$. The decisive point here is that the volume integral can also be split into three single integrals along the axes. This is made possible by the fact that the boundary conditions for x, y, z are independent of each other. (It was not possible for ellipsoids, for example.) For one axis we have

$$\int_{-a}^{+a} dx \cdot e^{-ihx\alpha} = \int_{-a}^{+a} dx \cdot \cos(hx\alpha) = 2a \cdot \left(\frac{\sin haa}{\sin ha\alpha} \right) \quad (20)$$

The total amplitude for a fixed orientation is then

$$\text{parallelepipedon } F_1(\mathbf{h}) = (\Delta n_e) \frac{\sin(ha\alpha)}{ha\alpha} \frac{\sin(hb\beta)}{hb\beta} \frac{\sin(hc\gamma)}{hc\gamma} \quad (21)$$

The oscillating character, as mentioned before, is shown clearly here.

To obtain the intensity, the square F^2 must be averaged again over all orientations. It should be borne in mind, however, that this cannot be done for the three factors separately, for α, β and γ are not independent variables.

Cylinders can be treated in a similar way by separating the axis and the cross-section. This will be of importance in the discussion of very unisometric particles, and will be considered in more detail later in Section IV.

Many intensity functions have been calculated by these or similar methods, e.g. for ellipsoids (Guinier, 1939; Shull and Roess, 1947; Porod, 1948; Schmidt and Hight, 1959; Mittelbach and Porod, 1962), for parallelepipeds (Porod, 1948; Mittelbach and Porod, 1951a) and for cylinders (Porod, 1948; Fournet, 1951; Mittelbach and Porod, 1951b). The results are all similar to the function in Eqn (16) for a sphere, particularly in the central range, showing marked differences only in the final slope at larger angles, as is to be expected.

B. Guinier Approximation

From the above it might be concluded that for the central part a universal approximation for all particles must exist. This was first given by Guinier (1939)

$$I_1(\mathbf{h}) = (\Delta n_e)^2 e^{-h^2 R^2/3} \quad (22)$$

with the "radius of gyration" R as the only parameter. It is defined as the mean square distance from the centre of gravity: $R = \sqrt{\bar{r}^2}$, where the role of "mass" is played by the electrons, of course.

The Guinier formula can be derived as follows: let us consider the amplitude of an orientated particle (18). For the central part it will suffice to expand $\cos h\mathbf{r}$ into a power series: $1 - (h\mathbf{r})^2/2 + \dots$. The volume integral then turns into $V(1 - (h\mathbf{r})^2/2 + \dots)$, where the average is taken with \mathbf{h} fixed and \mathbf{r} varying over the volume. In Cartesian coordinates we have (just as before for parallelepipeds) $h\mathbf{r} = h(x\alpha + y\beta + z\gamma)$. In squaring and averaging, the mixed products like \bar{xy} cancel, if the centre of mass is taken as the origin. So we have at last $\langle (h\mathbf{r})^2 \rangle = h^2(\bar{x^2}\alpha^2 + \bar{y^2}\beta^2 + \bar{z^2}\gamma^2)$.

This should be substituted into the power series, the amplitude then squared to give the intensity and finally the average taken over all orientations

$$\begin{aligned} I_1(\mathbf{h}) &= (\Delta n_e)^2 V^2 \langle 1 - h^2(\bar{x^2}\alpha^2 + \bar{y^2}\beta^2 + \bar{z^2}\gamma^2) + \dots \rangle \\ &= (\Delta n_e)^2 \cdot \left(1 - h^2 \frac{\bar{r}^2}{3} + \dots \right) \end{aligned}$$

making use of $\langle \alpha^2 \rangle = \langle \beta^2 \rangle = \langle \gamma^2 \rangle = 1/3$, and of: $\bar{r}^2 = (\bar{x^2} + \bar{y^2} + \bar{z^2})$.

The power series (23) is in accordance with the Guinier approximation up to the h^2 -term, irrespective of particle shape and symmetry. The higher terms with then involve higher "moments", $\bar{r^4}, \bar{r^6}, \dots$, which must depend on the

special features of the particle and cannot, therefore, in general agree with the Guinier function. With a sphere, for example, expansion of Eqn (16) shows that the h^4 -term of the rigorous function is less than that of the approximation (22), with $R = \sqrt{3/5} \cdot R_0$, but a sphere is an extreme case in this respect. Any deviation from spherical shape, keeping R constant, must involve larger distances, and so increase the higher terms. There are many shapes, consequently, which fit Eqn (22) up to the h^4 -term. With still greater anisometry the rigorous function will exceed the approximation. A size distribution must work in the same sense.

On the whole, the Guinier formula holds surprisingly well in the majority of cases. Only for very anisometric particles it should be replaced by another approximation, which will be discussed later in Section IV.

III. Particle Scattering. General Treatment

A. Correlation Function and Chord Distribution

The general case is best treated by the use of the correlation function (c.f.) $\gamma(r)$, as defined in Eqn (10). As the electron density difference ($\Delta\rho$) is always assumed to be constant here, it is convenient to separate it in the form

$$\gamma(r) = (\Delta\rho)^2 \cdot \gamma_0(r); \quad \gamma_0(0) = 1; \quad \gamma_0(r \geq D) = 0 \quad (24)$$

where $\gamma_0(r)$ is only related to the geometry of the particle. As always a largest diameter D , say, must exist; γ_0 will vanish for $r \geq D$. The normalized c.f. γ_0 (formerly termed "characteristic function", Porod, 1951) can be given a more intuitive meaning (Porod, 1948). Let us imagine the particle shifted by a vector r , as shown in Fig. 3. It is clearly seen, then, that the volume \hat{V} in common with the particle and its "ghost" just contains all points that give a contribution to $\gamma_0(r)$. Accordingly, we need only average over all directions of r , with $r = |r|$ being kept constant

$$\gamma_0(r) = \langle \hat{V}(r) \rangle / V \quad (25)$$

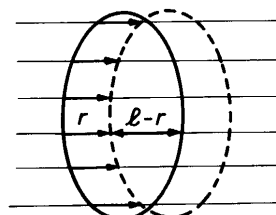


FIG. 3. Particle and "Ghost".

The argument can be further enhanced. If we draw lines with narrow and equal spacing (Fig. 3), the particle is cut into rods of varying length l , which might be termed "chord" (or formerly "intersection length"). The group of chords for all directions may be considered using a distribution function $G(l)$ (Guinier and Fournet, 1955; Porod, 1965), such that $G(l) dl$ is the probability that a chord chosen at random is of length between l and $(l + dl)$. Now it is seen from Fig. 3 that for each chord with $l > r$ a piece $(l - r)$ is contained in $\hat{V}(r)$. Therefore, this can be replaced in (25) by an integral extended over the chord distribution

$$\gamma_0(r) = \frac{1}{\bar{l}} \int_r^D (l - r) G(l) dl; \quad \text{with } \bar{l} = \int_0^D l G(l) dl \quad (26)$$

By differentiation we find

$$\frac{d\gamma_0(r)}{dr} = -\frac{1}{\bar{l}} \int_r^D G(l) dl; \quad \frac{d^2\gamma_0(r)}{dr^2} = \frac{1}{\bar{l}} G(r) \quad (27)$$

Thus the chord distribution $G(l)$ is, in a mathematical sense, equivalent to the correlation function $\gamma_0(r)$ and is, therefore, equally well suited to represent a particle with respect to its diffraction pattern. Many attempts have been made to develop this concept further (Porod, 1965; Mering and Tchoubar, 1968; Tchoubar and Mering, 1969; Luzzati *et al.*, 1976; Schmidt, 1967; Porod, 1965b). There are serious difficulties, however, in treating more complicated cases, such as hollow or composite particles, or densely packed systems. Here it may suffice to cite only one very simple example, which follows from clear geometry

$$\text{sphere } G(l) = \frac{1}{2R_0^2}; \quad \bar{l} = \frac{4}{3}R_0; \quad \gamma_0(r) = 1 - \frac{3}{2}\left(\frac{r}{D}\right) + \frac{1}{2}\left(\frac{r}{D}\right)^3 \quad (28)$$

The intensity $I_1(h)$ is, according to Eqn (11),

$$I_1(h) = (\Delta\rho)^2 \cdot V \cdot \int_0^D 4\pi r^2 dr \cdot \gamma_0(r) \frac{\sin hr}{hr} \quad (29)$$

where $\gamma_0(r)$ can be obtained by the inverse Fourier transform

$$(\Delta\rho)^2 \cdot V \cdot \gamma_0(r) = \frac{1}{2\pi^2} \int_0^\infty h^2 dh \cdot I_1(h) \frac{\sin hr}{hr} \quad (30)$$

B. Central Part

Instead of calculating for special types of particles, let us instead consider what general conclusions can be drawn from the above formulae. It is reasonable to treat the central part and the final slope of $I_1(h)$ separately.

First, it is obvious that $I_1(0)$ must be equal to the square of the number of excess electrons again, as already stated before. This result is now directly seen from Eqn (29), as the integral over the normalized c.f. $\gamma_0(r)$ must, from its definition, equal the volume

$$I_1(0) = (\Delta\rho)^2 V^2 = (\Delta n_e)^2$$

because

$$\int_0^D 4\pi r^2 dr \cdot \gamma_0(r) = V \quad (31)$$

For practical applications, it must be borne in mind that the intensity, as measured in experiments, still involves the number of particles and the electron scattering factor (1). These factors can be accounted for, however, by the use of the "invariant", already mentioned in connection with Eqn (14). Here it takes the form

$$Q_1 = \int_0^\infty h^2 dh \cdot I_1(h) = 2\pi^2 \cdot (\Delta\rho)^2 \cdot V \quad (32)$$

which in combination with Eqn (31) gives

$$2\pi^2 \cdot I_1(0)/Q_1 = V \quad (33)$$

As the intensity is present here in the numerator as well as in the denominator, all additional factors will cancel, and the arbitrary unit of intensity as well. So the volume can be determined from the diffraction pattern alone, no other data being required. In the case of a mixture of different particles being present, some mean value is obtained, of course. It is a weighted average rather than a number average, with a statistical weight of $V(\Delta\rho)^2$ for each particle, as is evident from the additive form of the invariant.

Next the central part of $I(h)$ will be examined. This is best done by developing the Debye factor into a power series: $1 - h^2 r^2/3! + h^4 r^4/5! \dots$, and then integrating the terms separately. It is convenient to split the factor V , whereby the integrals become averages $\bar{r}^2, \bar{r}^4, \dots$ with $\gamma_0(r)$ as a weight function. So we have

$$I_1(h) = (\Delta n_e)^2 \left\{ 1 - \frac{h^2 \bar{r}^2}{3!} + \frac{h^4 \bar{r}^4}{5!} - \dots \right\}$$

with

$$\bar{r}^n = \frac{1}{V} \int_0^D 4\pi r^2 dr \gamma_0(r) r^n \quad (34)$$

The abstract definition of the coefficients of the norm \bar{r}^n can be given a more intuitive meaning: if we choose at random two points, r_1 and r_2 , within the particle, their difference $(r_1 - r_2)$ is by definition equal to r , as used in the correlation function and in Eqn (34). The averages can now be formed without the use of $\gamma_0(r)$, by varying the two points independently of each other within the particle volume:

$$\bar{r}^n = (\bar{r}_1 - \bar{r}_2)^n; \text{ and especially } \bar{r}^2 = (\bar{r}_1 - \bar{r}_2)^2 = \bar{r}_1^2 + \bar{r}_2^2 = 2R^2 \quad (35)$$

Here it was assumed that the centre of mass was taken as a reference point for r_1 and r_2 , so that the linear averages must vanish. Further, the relation $\bar{r}_1^2 + \bar{r}_2^2 = R^2$ with the radius of gyration is then obvious. Substituting in Eqn (34) shows that there is agreement with the Guinier approximation again up to the h^2 -term. This is, therefore, always valid for a certain range.

The argument can be refined by the direct calculation of the higher terms, using Eqn (35) (Porod, 1948). This is more convenient than the method mentioned before using the amplitude. But, as the special cases are well known and so can be treated with some ease, we shall not go further into the matter.

The radius of gyration and the volume are not the only parameters characterizing size that can be obtained from the diffraction pattern. To see this, let us first define a "correlation length" l_c as the mean width of the correlation function.

Its meaning becomes more intuitive, when it is expressed in terms of the chord distribution. This can be done by the use of relations (26) and (27). After a short calculation (integration by parts) we have

$$\text{correlation length } l_c \equiv 2 \int_0^D \gamma_0(r) dr = \bar{l}^2/\bar{l} \quad (36)$$

in other words, l_c is the weight average of \bar{l} . This is equivalent to the following description: if lines are drawn through all points in all directions, the number average of the chords so obtained is equal to l_c .

To find l_c from the intensity function let us first form the integral $\int I_1(h) h dh$ which, by the way, corresponds to the total scattered intensity. Using (29) this gives

$$\int_0^\infty I_1(h) h dh = (\Delta\rho)^2 V \cdot 4\pi \int_0^D \gamma_0(r) dr = (\Delta\rho)^2 V \cdot 2\pi l_c \quad (37)$$

Again the invariant Q can be used to eliminate $(\Delta\rho)^2 V$ as well as all additional factors:

$$l_c = \pi \cdot \int_0^\infty I_1(h) h dh / Q_1 \quad (38)$$

C. Final Slope

V, R and l_c may be termed "integral" parameters (Porod, 1965a), as they are characteristic of the overall dimensions of the particle. Correspondingly, they are mainly related to the central part of $I(h)$. If we now proceed to discuss the final slope, we may expect this to depend chiefly on the fine structure of the particle, which is expressed by the behaviour of $\gamma_0(r)$ at small r . It is convenient, therefore, to expand $\gamma_0(r)$ into a power series

$$\gamma_0(r) = 1 - ar + br^2 + cr^3 \dots \quad \text{with } a = 1/\bar{l} \quad (39)$$

where the coefficients a, b, c, \dots may be termed "differential" parameters (Porod, 1965a). The first of these is immediately related to the chord distribution by Eqn (27). On the other hand, it seems plausible that it must depend on the surface S of the particle in some way. For, only a shell of thickness r can make a negative contribution to $\gamma_0(r)$, since it is only here that part of the neighbouring points, at a distance r , are outside.

To put the argument in a quantitative form, let us resume the derivation of γ_0 , as expressed in Eqn (25) and illustrated by Fig. 3. For small r the common volume \hat{V} differs from V itself only by the shift of the surface. The contribution of a surface element dS to this shell is $dS \cdot r \cos \vartheta$, if we specify the angle between r and the surface normal by ϑ . Now, instead of integrating over the surface, let us first take the average of this infinitesimal contribution for all directions of r . This means only averaging $|\cos \vartheta| = 1/2$. Further it must be considered that only the part of r directed inwards makes a contribution, which results in a second factor $1/2$. Each surface element will, therefore, diminish by $1/4 dS \cdot r$ in the average, which gives $1/4 Sr$ for the total surface. So we have

$$\langle \hat{V}(r) \rangle \doteq V - \frac{1}{4}Sr; \quad \gamma_0(r) \doteq 1 - \frac{S}{4V}r; \quad a = \frac{S}{4V} = \frac{1}{\bar{l}} \quad (40)$$

We can now substitute into (29) to obtain approximately

$$I_1(h) \doteq (\Delta\rho)^2 V \int_0^D 4\pi r^2 dr \cdot \left(1 - \frac{r}{\bar{l}} + \dots\right) \frac{\sin hr}{hr} \quad (41)$$

This may be integrated by parts, which will not be done here in full detail. Let us remark only that a series of negative powers in h is obtained and, due to the upper limit, also pseudo-periodic terms, which fall off very rapidly and can only be of importance with nearly spherical particles, as explained before. Bearing in mind that only an approximation to the final slope is intended here, we shall retain only the most important term.

$$I_1(h) \rightarrow (\Delta\rho)^2 V \cdot \frac{8\pi}{\bar{l}} \cdot \frac{1}{h^4} = (\Delta\rho)^2 \cdot \frac{2\pi}{h^4} \cdot S \quad (42)$$

This fourth power law, derived independently by Debye *et al.*, (1957), and by Porod (1951), has proved to hold much better than might be assumed from the rather involved derivation. In fact, it is valid not only for single particles, but also for densely packed systems and for non-particulate structures (with a slight modification of the factor only), provided that there exists a well defined internal surface. This seems plausible, for as only the structure near the surface is responsible for the final slope of $I(h)$, it should not be influenced by the large-scale properties of the particles or their mutual arrangement. Further, it

is obvious from Eqn (42) that the contributions of different particles will simply be added, so that the asymptotic value of $I(h)$ must be proportional to the total interface S .

The practical application requires the measurements of absolute intensity. To avoid this, the invariant Q may be used:

$$I(h)/Q \rightarrow \frac{1}{\pi} \cdot \frac{S}{V} \cdot \frac{1}{h^4}; \quad \frac{S}{V} = \pi \cdot \lim I(h) h^4/Q \quad (43)$$

So the specific surface can be determined from the diffraction pattern alone, without using additional data.

The discussion of the final slope of $I(h)$ may be further refined by taking into account higher terms in the series (39). As the problem is rather involved, and as only in special cases with extreme experimental precision does it seem possible to make practical use of it, the question may be outlined here only qualitatively.

First, it can be shown that the parameter b must vanish in most cases. This is best seen from relation (27), which implies $b = G(0)/2\bar{l}$. So b is closely related to the initial value of the chord distribution. Now it can be understood, without much mathematics, that the latter will be zero in general. For, a chord of $l=0$ can only be obtained by a line cutting the particle nearly tangentially. Then, at a curved surface, l must increase with the second power of the distance from the surface. Consequently, an interval dl corresponds to a bundle of lines which are small to the second order. This implies that $G(0) = 0$. The argument breaks down, however, in case of the particle having edges or corners, for then the bundle width varies linearly with l , and a finite value of $G(0)$ and of b is obtained. So it might be said that the parameter b is, in a certain sense, a measure of "angularity" (Porod, 1965a). Unfortunately, there is no satisfactory way of determining it from the intensity function, although suggestions could be made (Porod, 1965a). The reason is that in the integral of Eqn (41) monotonous terms are only produced by odd powers of r , while the even powers only give rise to oscillating terms.

The third parameter c could be shown to be positive for smooth particles (Kirste, 1962). It is related to the curvature of the surface, as was to be expected. If edges or corners are present in the particle, these cause a negative contribution to c . For purely angular bodies like a cube, for example, c should be negative, therefore.

The preceding statements will best be illustrated by three typical examples. Let us first consider a sphere as representative of a smooth particle. The correlation function is already known Eqn (28). The lack of b and the positive sign of c are seen directly. Further, it is a special property of a sphere that no higher terms occur in $\gamma_0(r)$. This may be interpreted as a sign that, beyond a constant curvature, no other structural details of the surface exist.

Our second example could be a rectangular parallelepipedon with axes $A < B < C$, say. Using Eqn (25) $\gamma_0(r)$ is easily obtained considering that the common volume V is a rectangular parallelepipedon again. The average over all directions is easily performed

$$\text{parallelepipedon } \gamma_0(r) = 1 - \frac{r}{2} \left(\frac{1}{A} + \frac{1}{B} + \frac{1}{C} \right) + \frac{2}{3\pi} r^2 \left(\frac{1}{AB} + \frac{1}{BC} + \frac{1}{CA} \right) - \frac{r^3}{4\pi} \cdot \frac{1}{ABC}; \quad \text{valid only for } r < A \quad (44)$$

Here the typical features are the occurrence of the r^2 -term and the negative sign of the r^3 -term. The lack of higher terms may be attributed again to the especially simple shape of the body.

Thirdly, let us consider the Guinier approximation under the assumption that it is the *exact* intensity function of some system. It is evident that it cannot be produced by particles in a proper sense, because the h^{-4} -law is not valid here. Further, it is a well known result of Fourier theory that the transform of a Gauss-function is a Gauss-function again. So must be $\gamma_0(r)$, therefore. Being an even function, all odd parameters a, c, \dots are zero, which is in agreement with the lack of a surface. On the other hand, the even parameter b , though present, is negative and cannot, therefore, represent the "angularity" of a particle. Rather it indicates an overall fluctuation of electron density without a sharp boundary.

The above examples show that the correlation function is very sensitive to structural details and could give valuable information, if it were *exactly* known. Now, it is possible, in principle at least, to calculate $\gamma_0(r)$ from $I(h)$ by the Fourier transform of Eqn (30) or, more generally, Eqn (12). But this requires an exact knowledge of the intensity, and especially of its final slope. So the practical application of the preceding relations will depend on the experimental accuracy available.

IV. Extremely Anisometric and Composite Particles

A. Rod-like Particles

Very long-stretched or very flat particles show some peculiar features in their diffraction patterns (Shull and Roess, 1947; Debye *et al.*, 1957), which need special consideration. Let us first regard a rod of length L and of cross-section A . In this case, as was already shown in Section II, the amplitude can be separated into two factors belonging to L and A , respectively. This is done by

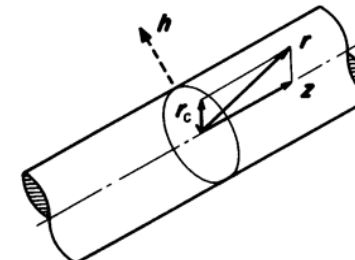


FIG. 4. Vectors in a rod-like particle.

introducing the corresponding components: $r = z + r_c$, as shown in Fig. 4. The axial factor is already known from Eqn (20). So we have for the rod

$$F_1(h) = (\Delta\rho) \cdot L \frac{\sin hL\gamma/2}{hL\gamma/2} \cdot \iint dA \cdot e^{-ihr_c} \quad (45)$$

where γ means the cosine of the angle between h and the axis. Now let us assume that L is very much larger than the diameter D of the cross-section. The consequence is that the axial factor drops to zero very rapidly. It will be negligible, except for those orientations where γ is very small, to compensate for the largeness of L . This is equivalent to saying that the rod makes a contribution to the diffraction only when it lies nearly perpendicular to h . The essential point is that in these positions the cross-sectional factor remains nearly unaltered with a slight skipping of the axis. So the two factors can be regarded as nearly independent, and the averages of their square can be formed separately. The axial factor gives

$$\langle F_L^2 \rangle = L^2 \int_0^\infty \left(\frac{\sin hL\gamma/2}{hL\gamma/2} \right)^2 d\gamma = L \cdot \frac{\pi}{h} \quad (46)$$

where the upper limit of the integral is put at ∞ instead of correctly at 1, which makes no serious fault. The remaining factor, when squared and averaged, gives a function $I_c(h)$, which is related only to the cross-section. For the rod:

$$I_1(h) \doteq L \cdot \frac{\pi}{h} \cdot I_c(h) \quad (47)$$

The factor $1/h$ is characteristic of rod-like particles (Kratky and Porod, 1962; Porod, 1948). It is easily accounted for by multiplying the intensity by h to give the cross-section function I_c . Equation (47) can only be an approximation, which becomes invalid at very small angles. But, with L very large, Eqn (47) breaks down, where the region becomes so small that it is no longer accessible to experiment. This will be assumed for the following.

For the calculation of $I_c(h)$ it must be borne in mind that h should be

regarded as lying in the plane of the cross-section. So the problem is two-dimensional only but otherwise quite similar to the calculation of $I_1(h)$ for a whole particle. This means simply that

$$I_c(h) = (\Delta\rho)^2 \cdot \iiint dA_1 dA_2 e^{-ih(r_{c1}-r_{c2})} \quad (48)$$

where $(\Delta\rho)$ may be regarded as the number of excess electrons per unit area and unit length. Let us further introduce the distance vector $r_c = (r_{c1} - r_{c2})$ and a corresponding correlation function $\gamma_c(r_c) = (\Delta\rho)^2 \gamma_{co}(r_c)$. The average of the phase factor, however, must be altered against Eqn (7), since the variation is in two dimensions now, instead of three

$$\langle e^{-ihr_c} \rangle = J_0(hr_c) \quad (49)$$

where J_0 means the Bessel-function of the zero order, which shows qualitatively a behaviour similar to the Debye function of Eqn (7). So we have

$$I_c(h) = (\Delta\rho)^2 \cdot A \int_0^D 2\pi r dr \cdot \gamma_{co}(r) J_0(hr) \quad (50)$$

The index c has here been dropped at r , as the meaning is clear by the context.

The calculation is greatly simplified, of course, in case of a circular cross-section. For then the amplitude is not dependent on rotation and needs only to be squared

$$F_c = (\Delta\rho) \int_0^R 2\pi r dr \cdot J_0(hr) = (\Delta\rho) \cdot A \cdot \left(2 \frac{J_1(hR_0)}{hR_0} \right); \quad (51)$$

$$I_c(h) = F_c^2(h)$$

The expression in brackets, containing the Bessel function of the first order, has the value 1 for $h = 0$ and exhibits a slope similar to an ordinary intensity function. This similarity holds for other shapes of the cross-section, too.

It is convenient, and in most cases also sufficient, to have an approximate formula, for the central part at least, like that of Guinier for particles. This can be obtained easily. Since the argument is essentially the same as that used before, we can be brief. The only difference from Eqn (34) is that the power series $J_0(hr) = 1 - h^2 r^2 / 4 \dots$ has the coefficient 1/4 instead of 1/6 at the second term. With this slight modification we get

$$I_c(h) = (\Delta\rho)^2 A^2 \cdot e^{-h^2 R_c^2/2}; \quad R_c^2 = \bar{r}_c^2 \quad (52)$$

The radius of gyration R_c is defined in the same way as R , but for the cross-section only. For a circle, for example, $R_c = R_0/\sqrt{2}$.

The approximation of Eqn (52) cannot hold for the final slope, of course. There the h^{-4} -law is valid for the whole particle. Since now a factor $\approx h^{-1}$ has

been split off, it follows that the final slope of $I_c(h)$ must be $\approx h^{-3}$. The determination of the specific surface according to Eqns (42) and (43) remains valid as well; only the meaning of S/V can here be replaced by the circumference per area, as the length L cancels out.

Incidentally, the assumption of a rigid rod with a straight axis was not essential for the preceding considerations. Quite similar results hold also for a flexible thread with sufficiently soft bending. This can be qualitatively understood as follows. Any part of the thread that happens to lie fairly perpendicular to h , i.e. in a "plane of reflection", will contribute to diffraction like a rod, while other strongly tilted parts are negligible in this respect. In fact, a continuously bending thread behaves very much like a chain of rods linked together. As this topic is of particular interest for macromolecules in solution, it will be dealt with in a separate chapter (by Kirste).

B. Flat Particles

Let us now consider a flat particle, whether stiff or slightly bending, with a finite thickness T and extremely large in two dimensions. By analogy to the case of a rod, we might expect that $I(h)$ can now be separated into a factor $\sim h^{-2}$ (Kratky and Porod, 1948; Porod, 1948) and a "thickness-factor" $I_t(h)$. That this is true can be seen by the same argument as was used for a rod. For a certain orientation (cf. Fig. 4) the amplitude can again be written in the form of Eqn (45). It must be borne in mind, however, that now T (instead of L) is small; and the corresponding factor, therefore, is relevant for diffraction. The second factor, on the contrary, contains now the extreme dimensions. Consequently, it is negligible for nearly all orientations, except those where h is nearly perpendicular to the plane, and its component in the plane, therefore, is small enough to compensate for the largeness of r_c . In this case the component of h in z is practically equal to h , and the thickness-factor remains unaltered. The square of the planar factor can therefore be averaged independently. In the limiting case of a very large plane, all shapes give the same results: $A \cdot 2\pi/h^2$.

So we have finally

$$\text{flat } I_1(h) = A \cdot \frac{2\pi}{h^2} \cdot I_t(h)$$

$$\text{special } I_t(h) = (\Delta\rho)^2 \cdot T^2 \cdot \left(\frac{\sin hT/2}{hT/2} \right)^2 \quad (53)$$

where the special case means constant thickness T and constant $(\Delta\rho)$. For general cases it may be convenient to replace Eqn (53) by a Guinier type approximation. This follows directly from the power series of the special $I_t(h)$, with $R_t = \sqrt{z^2} = T/\sqrt{12}$

$$\text{flat } I_t(h) = A \cdot \frac{2\pi}{h^2} (\Delta\rho)^2 T^2 e^{-h^2 R_t^2} \quad (54)$$

The final slope of I_t , however, must drop $\approx h^{-2}$, in order to obey the h^{-4} -law for the whole particle. The specific surface, as obtained from this law, reduces here simply to $1/T$. So the one parameter T can be determined by three quite different ways: from $I_t(0) \approx T^2$, from the slope of the central part (Eqn (54)) and from the final slope, as explained above. Since, further, the planar factor $\approx h^{-2}$ is a very characteristic feature, it is clear that a homogeneous platelet is particularly well characterized by its diffraction pattern.

There is yet another interesting point about platelets: $I_t(h)$ corresponds to a one-dimensional Fourier transform. That means a great simplification in so far as symmetry along T alone suffices to make the amplitude real. As comparison: in two or three dimensions circular or spherical symmetry is required for that purpose. Now, a real amplitude can be obtained by simply taking the square root of the intensity, and so a direct calculation of the structure along T is possible.

To make this clear, let us assume some symmetrical electron density distribution $\eta(z)$ along T (difference to the surrounding). The amplitude F_t is then

$$F_t(h) = \int_{-T/2}^{+T/2} \eta(z) \cos hz \cdot dz; \quad I_t = F_t^2 \quad (55)$$

and we have by the inverse Fourier transform

$$\eta(z) = \frac{1}{\pi} \int_0^\infty F_t(h) \cos hz \cdot dh; \quad F_t = \sqrt{I_t} \quad (56)$$

This procedure breaks down in the most general case, whether there is some grouping of different platelets or whether $\eta(z)$ lacks symmetry. A correlation function should then be used. As this treatment seems sufficiently clear now, it need not be further discussed.

C. Composite Particles

Finally we will consider another type that differs markedly from ordinary particles: the question of composition particles, which are built up of simple subparticles in a definite array. Let us first consider a fixed orientation of such a composite particle. The positioning of the centres of mass of the subparticles may be designated by $r_1, r_2, \dots, r_j, \dots, r_N$, and their amplitudes (with respect to each centre) by $F_1, F_2, \dots, F_j, \dots, F_N$. The position of the subparticles

are each accounted for by an additional phase factor e^{-ihr_j} . The total amplitude then takes the form

$$\text{composite } F(h) = \sum_1^N F_j(h) \cdot e^{-ihr_j} \quad (57)$$

and the intensity is again the absolute square of the amplitude, averaged over all orientations:

$$I(h) = FF^* = \left\langle \sum \sum F_j F_k^* \cdot e^{-ih(r_j - r_k)} \right\rangle \quad (58)$$

The double sum contains N terms with $j = k$, the phase factor consequently vanishing. They represent, therefore, the intensity diffracted by the subparticles alone. The remaining terms with $j \neq k$ obviously represent the interference between the subparticles, according to the relative distance $r_{jk} = (r_j - r_k)$. As each pair is counted twice with $r_{jk} = -r_{kj}$, only the real part remains. It must be borne in mind here that in general each amplitude will have a phase too: $F_j = |F_j| \cdot e^{i\varphi_j}$. This is only zero for centrosymmetric particles. So we have, for the general case,

$$I(h) = \sum_1^N I_j(h) + 2 \cdot \left\langle \sum_{j \neq k} |F_j| |F_k| \cos (hr_{jk} + \varphi_k - \varphi_j) \right\rangle \quad (59)$$

This expression is rather involved as, in general, each $|F_j|$ and φ_j is dependent on orientation. We will restrict ourselves, therefore, to the special case of spherical subparticles. All φ_j vanish then, and the F_j become independent of their orientation. Only the cosine needs to be averaged with the result of Eqn (7), already known:

$$I(h) = \sum_1^N I_j(h) + 2 \cdot \sum_{j \neq k} \sum F_j(h) F_k(h) \frac{\sin hr_{jk}}{hr_{jk}} \quad (60)$$

This formula was first derived by Debye (1930) especially for molecules, the F_j then meaning the atomic structure factors. In fact, no restriction other than centrosymmetry is necessary for subparticles. There is no need for constant electron density or a defined boundary, for example. Even a hole could be treated like a subparticle with negative F_j .

With N very large, the interference terms must become predominant over the single terms. At the same time the amplitudes become less critical, as the subparticles then must necessarily be much smaller than the whole composite, and so only the central part is involved. Equation (60) may be used, therefore, to get a rough approximation for $I(h)$ of some complicated particle by treating it as a similar cluster of spheres, say. This works quite well, as was first shown by Kratky (Kratky and Sekora, 1943; Kratky, 1947).

V. The Influence of Dense Packing

A. The Radial Distribution Function

Only the scattering of single particles has been treated so far, though, of course, a great number of them are always present. It was assumed that the intensities are simply added to give the total diffraction pattern. This is true for a very dilute solution, but with increasing concentration some interference effects should be expected. This will be discussed now, in principle at least.

First, it is clear that the interference might even be very strong, if forces, attractive or repulsive, are acting between the particles; this must lead to some ordered mutual arrangement, and diffraction is very sensitive to order. But let us exclude such forces and consider only the influence of pure geometry (impenetrability of the particles). So it is the question of minimum interference only, which must occur.

At first the simplest possible case will be considered, a system of volume V , containing N identical particles of spherical shape (diameter D). The whole system can then be treated as one huge composite particle, the spheres representing the subparticles. Equation (60) may then be applied, with two modifications: first, because of the identity, $I_1(h)$ of the single sphere can be taken as a common factor; secondly, as the mutual distances r_{jk} are now varying in time, another average must be formed to cover all possible arrangements. For this special system

$$I(h) = I_1(h) \left[N + 2 \left\langle \sum_{j \neq k} \frac{\sin hr_{jk}}{hr_{jk}} \right\rangle \right] \quad (61)$$

For large distances r_{jk} the interference terms will cancel, if there is no long range order; but in the short range some effect is to be expected, for there the spheres cannot be arranged totally independently of each other. At least a minimum distance equal to the diameter D must be kept.

The situation is best described by introducing a radial distribution function $P(r)$ as follows (Zernicke and Prins, 1927; Debye and Menke, 1930). On average each sphere has the same surrounding (statistically speaking), which is also isotropic. So it will suffice to regard only one central particle, and to ask that the probability that another particle will be found in the volume element dV at a distance r apart. The mean value of this probability is obviously $(N/V)dV$; any deviation from this may be accounted for by a factor $P(r)$. From the above it follows that in the range of impenetrability ($r < D$) $P(r) = 0$, and in the long range (r large) $P(r) = 1$. If the latter were valid everywhere, the interference terms would exactly cancel. So only the difference $(P(r) - 1)$ is relevant for diffraction. Equation (61) then takes the form

$$I(h) = NI_1(h) \left[1 + \frac{N}{V} \int_0^\infty 4\pi r^2 dr (P(r) - 1) \frac{\sin hr}{hr} \right] \quad (62)$$

The second term contains all interparticle interference. Its predominant part is the "hole" of radius D , where $(P(r) - 1) = -1$. The whole term should, therefore, be mainly negative and exhibit a steeper slope than the particle scattering, the "hole" necessarily being larger than the sphere. The effect must be to decrease the intensity in the central part mainly, which results in a liquid-type pattern. This was first shown by Debye (1915) by using the simplest possible assumption that $P(r) = 1$ for $r > D$, so that the impenetrability alone is accounted for. The effect is essentially the same, even if some size distribution for the spheres is assumed (Porod, 1952). Contrary to what is sometimes suggested, with this model the interference cannot be destroyed by mere variation of size. For all terms work in the same sense at small angles.

It should be noted that the model of Debye, though quite plausible, cannot be correct in a strict sense. This is seen from the fact that for high concentrations (volume fraction $> 1/8$) Eqn (62) leads to negative "intensities", which is impossible, of course. Many attempts have been made to derive some self-consistent radial distribution function, either by geometry (Porod, 1952) or by statistical thermodynamics (Guinier and Fournet, 1955); but no rigorous solution can be given so far. Also it seems hopeless to extend Eqn (62) so as to cover the case of non-spherical particles, too. The difficulty is that then $P(r)$ should be a function not only of r , but also of orientation. On the other hand, the problem of other shapes must be considered somehow. There is strong reason to believe that the role of interparticle interference is over-emphasized by the assumption of spheres, since these can only contact at one point and show a tendency to keep each other apart: any other shape would allow closer packing. It is simply the relationship between neighbouring particles that matters most in our problems. So we will try another line of attack as follows.

B. The Surrounding Function

Let us again assume a system of N particles, which now may be of any size and shape, in a volume V . The amplitude and the intensity of the whole grouping are then described by Eqns (57) and (58). The latter summation can be written as a sum of "shares" $[I(h)]_j$ in the following way:

$$I(h) = \sum_1^N [I(h)]_j; \quad [I(h)]_j = \left\langle F_j \cdot \sum_1^N F_k^* \cdot e^{-ih(r_j - r_k)} \right\rangle \quad (63)$$

Each share can be regarded as the contribution of a certain particle, including its interference with all other particles. Since all shares are defined in an

analogous way, it suffices to consider in detail only one of them, arbitrarily specified by the index 1. It entails no loss of generality if we regard the centre of particle 1 as the reference point, i.e. if we put $r_1 = 0$. Furthermore, it is convenient to separate I_1 from the remaining sum, which then represents the surrounding only:

$$[I(h)]_1 = I_1(h) + \left\langle F_1 \cdot \sum_{k \neq 1} F_k^* e^{ihr_k} \right\rangle \quad (64)$$

The second term can be given a more intuitive meaning: with particle one kept fixed in space, the other ones will take all possible configurations in time. The amplitude, averaged over these configurations, can then be interpreted as the Fourier transform of a "smeared out" surrounding, defined by an averaged electron density difference $\bar{\Delta}\rho(r)$, which would be equal to $(\Delta\rho)$, if some point were always covered by a particle, and equal to 0, if this were never the case. Of course, some intermediate value must result at every point, according to the probability of covering. In the region far outside, especially, because of the assumed lacking of long-range order, the final mean value $\varphi(\Delta\rho)$ must be reached. Here φ means the volume fraction of the particles. For diffraction only the deviation from that mean value matters. This may be expressed by a "surrounding function" $U_1(r)$ (Porod, 1972), defined in the following way

$$(\Delta\rho)_1(r) \equiv (\Delta\rho)[\varphi + (1 - \varphi)U_1(r)] \quad (65)$$

$U_1 = 1$ represents certainty, and $U_1 = 0$ indifference of covering. So U_1 marks that finite region outside particle one, where some ordering influence is felt. When subtracting the constant value φ , as explained above, care must be taken to do this over the *whole* volume, that means inside particle one, too. Omitting details, the final result is

$$\text{share } [I(h)]_1 = (1 - \varphi)I_1(h) + (1 - \varphi)(\Delta\rho) \left\langle F_1(h) \iiint dV \cdot U_1(r) e^{ihr} \right\rangle \quad (66)$$

where the integral is to be extended over the volume *outside* only. The average should be taken over all orientations of particle one, while the surrounding remains fixed relative to the central particle.

Though $U(r)$, like $P(r)$, cannot be calculated in a rigorous way, some qualitative conclusions can be drawn from Eqn (66). First, it is obvious that the interference term can vanish, only if $U(r)$ is zero everywhere. With spheres, for example, this is clearly impossible, as there is only a point to point contact at the boundary and, therefore, each sphere must be surrounded by a region of negative U , but it would be possible for particles with a plane boundary,

cubes for example. The argument shows that for interparticle interference *shape* must play a much more important role than for particle scattering.

This is purely geometrical reasoning so far. For rather concentrated systems the contact between particles should be regarded from a more physical point of view, too. There may be some tendency for aggregation or separation, as is assumed for irreversible and reversible colloids. An attempt at discussing this problem may be outlined here only qualitatively (Porod, 1972). The physical aspect can be described by a probability of contact, either higher or lower than expected from pure geometry. The essential point is that such a probability must be propagated from one particle to its neighbour and so forth. So the first case (positive sequence) leads to a range of increased $U(r)$ over several particles and, consequently, to an increased intensity in the central part (gas-type). The latter case (negative sequence), however, produces an oscillating slope for $U(r)$, beginning with negative values. On the whole the intensity is decreased at small angles (liquid-type), as shown in Fig. 5. This was to be expected anyway from pure geometry (impenetrability), and the effect is only increased by an additional tendency for separation. On this occasion, it should be stressed that the intensity due to interference cannot be attributed to some real or fictitious "particle", though, for a gas-type pattern this might well be suggested. But in any case, the second term in Eqn (66) is such that an interpretation in terms of particle scattering must fail.

C. Statistical Fluctuations

In the theory of diffraction it has been known for a long time, and has been established for X-rays also by Zernicke and Prins (1927), that the intensity at zero-angle is closely related to the statistical fluctuations of the system.

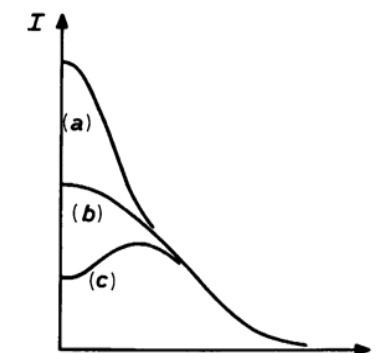


FIG. 5. Characteristic types of scattering functions. (a) gas-type; (b) particle scattering; (c) liquid-type.

In fact, if the system were ideally ordered, i.e. all particles placed on the sites of a lattice, there would be no small angle scattering at all, as is well known from the X-ray analysis of crystals. The assumption, made at the beginning, that there is no long-range order, is therefore an essential one. It implies that the system is governed by statistical laws only and must, therefore, show fluctuations.

We might argue as follows. Let us imagine the total volume V as being subdivided by a regular lattice of n domains of equal size V/n each. In the average, such a domain then contains N/n particles (all assumed to be equal for simplicity). In fact, the number may be slightly different, N_α say in the α -th domain. As the uniform distribution is ineffective for diffraction, it is only the difference $(N_\alpha - \bar{N}_\alpha)$ that matters. Now let us regard scattering at an angle as almost zero. It should be small enough so that all secondary waves within a domain are in phase, and still large enough so that interference between the domains is cancelled out. The amplitude of a single domain is then equal to the number of excess electrons $(N_\alpha - \bar{N}_\alpha)(\Delta n_e)$, and the total intensity is the sum of the squares. All domains being equivalent in the average, this may be written as

$$I(0) = n \cdot \overline{(N_\alpha - \bar{N}_\alpha)^2} \cdot (\Delta n_e)^2 \quad (67)$$

The result cannot depend, of course, on the arbitrary choice of the domains. This is best seen in the case of a stochastic system. The mean square fluctuation is then equal to N_α , and $n \cdot \bar{N}_\alpha = N$, the total number of particles. Upon substitution in Eqn (67), this is equivalent to pure particle scattering without interference. Any deviation from it, as expressed by $P(r)$ or $U(r)$, indicates consequently some tendency for ordered arrangement. The fluctuation can then be smaller (liquid-type) or larger (gas-type) than with "normal" statistics.

While the relationship between the diffraction pattern and the typical particle parameters, such as volume and Guinier radius, then breaks down as a consequence of interparticle interference, the final slope should still be related to the specific surface. To examine this question it will be convenient to drop the particle concept completely, and to regard the problem from a more general point of view.

VI. Non-particulate Systems

A. Babinet Principle

Small-angle scattering is not bound to the presence of well defined particles. The only condition is that there are heterogeneities of any kind in the colloidal range. To show this in general, let us consider a model like that of Fig. 6. It

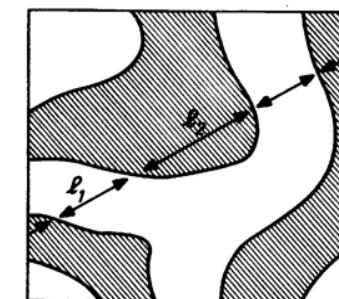


FIG. 6. Non-particulate two-phase system (schematic).

consists of two different substances (distinguished by indices 1 and 2) of constant electron density each, and filling the fractions φ_1 and φ_2 of the total volume V . Such a model should not be too far-fetched. It might represent either some precipitate, where the individuality of particles is lost by close contact, or some material containing many holes and pores, or other similar structures.

First, we note that there is a well defined average electron density $\bar{\rho}$ and a mean square fluctuation

$$\bar{\rho} = \varphi_1 \rho_1 + \varphi_2 \rho_2; \quad \overline{\eta^2} \equiv \langle (\rho - \bar{\rho})^2 \rangle = (\rho_1 - \rho_2)^2 \cdot \varphi_1 \varphi_2 \quad (68)$$

The latter is directly related to the known "invariant" of the system:

$$\text{invariant } Q \equiv \int_0^\infty h^2 dh \cdot I(h) = V \overline{\eta^2} \cdot 2\pi^2 = V(\rho_1 - \rho_2)^2 \cdot \varphi_1 \varphi_2 \cdot 2\pi^2 \quad (69)$$

Furthermore, it is always true that a constant $\bar{\rho}$ throughout the whole volume is of no consequence and may, therefore, be subtracted. So the system is fully equivalent to another one, where only region one is filled with matter of uniform electron density $\Delta\rho = (\rho_1 - \rho_2)$, region two being void, or vice versa. Both cases must yield exactly the same diffraction pattern. This corresponds to the well known principle of reciprocity of Babinet in optics. In the present case it can be directly understood without using much mathematics. To that purpose, let us imagine both regions to be of the same ρ , though materially distinguishable. The amplitude of the whole system is then zero for any finite angle, provided only that V is large enough. On the other hand, the amplitude is the sum of the two amplitudes, produced by regions one and two. These must, therefore, be equal but for the sign. If only one region is filled with matter, its amplitude remains the same as before, while the other is zero. Obviously the resulting intensity is the same in both cases.

From the Babinet principle, thus established, the cogent conclusion may be drawn that all formulae for such a two-phase system must be symmetrical

with respect to both regions as, for example, Eqns (68) and (69). At first sight, this might seem to be in contradiction to all that has been said about particle scattering so far. But a very dilute system is an extreme case, where some simplifications are allowed. φ_2 may be put equal to 1, and so it need not be necessary to distinguish between $\bar{\rho}$ and ρ_2 and so on. In a rigorous treatment there is not contradiction at all.

B. Correlation Function

The concept of the correlation function, as introduced in Section III for single particles, must now be generalized for two-phase systems (Porod, 1951). Let us again pick at random two points separated by a distance r . There are four combinations possible, as each point may be found in "1" or in "2". The respective probabilities may be designated by $P_{11}, P_{12}, P_{21}, P_{22}$, with $P_{12} = P_{21}$ because of the statistical isotropy. For a single point the probability of lying in "1" or "2" is obviously φ_1 or φ_2 . But if the first point is known to be in "1", say, the probabilities for the second point are thereby altered. This can be expressed as follows

$$P_{11} = \varphi_1 P_{11}; \quad P_{12} = \varphi_1 P_{12} = \varphi_2 P_{21}; \quad P_{22} = \varphi_2 P_{22} \quad (70)$$

These probabilities cannot be independent. The sum $P_{11} + P_{21}$, for example, means the probability of finding the second point in "1", irrespective of whether the first one lies in "1" or "2". Obviously this must be φ_1 ; and the analogous result must hold for $P_{12} + P_{22} = \varphi_2$. So we have

$$P_{11} + P_{12} = 1; \quad P_{21} + P_{22} = 1 \quad (71)$$

As P_{12} and P_{21} are already related by Eqn (70), there remains only one unknown function. To account for the mathematical symmetry, the result can be given the following form

$$P_{11}(r) = \varphi_1 + \varphi_2 \gamma_0(r); \quad P_{12}(r) = \varphi_2 - \varphi_2 \gamma_0(r);$$

$$P_{21}(r) = \varphi_1 - \varphi_1 \gamma_0(r); \quad P_{22}(r) = \varphi_2 + \varphi_1 \gamma_0(r);$$

with

$$P_{11}(0) = P_{22}(0) = 1; \quad P_{12}(0) = P_{21}(0) = 0; \quad \gamma_0(0) = 1; \quad (72)$$

It is now easy to see that the function $\gamma_0(r)$, as introduced in Eqn (72) is identical to the normalized correlation function of Eqn (24). To that purpose let us go back to the original definition by Eqn (10) of $\gamma(r)$. In the present case only two values of the fluctuation η are possible: $\eta_1 = \varphi_2(\Delta\rho)$, and $\eta_2 = -\varphi_1(\Delta\rho)$. Furthermore, only the four combination with the respective probabilities, as specified by Eqns (70) and (72), need to be considered in forming the average. So we have by elementary calculation

$$\gamma(r) \equiv \langle \eta(x)\eta(x+r) \rangle = P_{11}\eta_1^2 + 2P_{12}\eta_1\eta_2 + P_{22}\eta_2^2 = \varphi_1\varphi_2(\Delta\rho)^2\gamma_0(r) \quad (73)$$

where $\varphi_1\varphi_2(\Delta\rho)^2 = \bar{\eta}^2$ as shown in Eqn (68). The meaning of $\gamma_0(r)$ is thus established.

C. Intensity Function; Integral Parameters

The intensity for the whole system is now expressed by

$$I(h) = V \cdot \varphi_1\varphi_2(\Delta\rho)^2 \int_0^\infty 4\pi r^2 dr \cdot \gamma_0(r) \frac{\sin hr}{hr} \quad (74)$$

In a mathematical sense, it only differs from particle scattering by one factor. So we can expect the resulting function $I(h)$ to show the same general features: bell-shaped central part and final slope. In fact, no criterion can be given for a diffraction pattern for deciding whether the system is particulate or non-particulate.

The most general information that can be gained from the pattern is the correlation function. By the inverse Fourier transform and using the invariant Q to eliminate the factors we have

$$\gamma(r) = \frac{1}{Q} \int_0^\infty h^2 dh \cdot I(h) \frac{\sin hr}{hr} \quad (75)$$

But the meaning of $\gamma_0(r)$, as discussed above, is now even less intuitive than for a particle. In a certain sense it describes the averaged surrounding, as seen from one arbitrary point, and marks the region with an excess probability of finding the same matter as in the reference point. So the concepts of size and shape may still be applied, though in a different sense than for particles.

At first a correlation volume v_c can be defined by analogy to the particle case. The relation to the intensity at zero-angle must obviously then be maintained

$$I(0) = V\varphi_1\varphi_2(\Delta\rho)^2 \cdot v_c; \quad v_c \equiv \int_0^\infty 4\pi r^2 dr \cdot \gamma_0(r) \quad (76)$$

or, by the use of the invariant Q

$$v_c = \frac{2\pi^2}{Q} \cdot I(0) \quad (77)$$

The latter formula is mathematically identical to Eqn (33), as given for a single particle, but now it has a more general meaning, referring to any heterogeneity, in whatever case. It might seem plausible to regard v_c as a measure of the size of the heterogeneities; but that would not make sense in every case. As an

example, for a densely packed system, as discussed in Section V, v_c might become very small and even zero ("liquid-type"), though large particles are present. The reason for this apparent discrepancy is that $\gamma_0(r)$ can take negative values in the general case whilst this is impossible with single particles, of course. The "volume" v_c and $I(0)$ should be better interpreted in terms of statistical fluctuations (cf. Section V.C) rather than as a measure of "size".

The loss of intuitiveness, as discussed above for v_c , is valid for other integral parameters, too, in non-particulate systems. The correlation length l_c , for example, as defined in Eqn (36) and related to the intensity function by Eqns (37) and (38) (the latter formula holds in full generality), is also affected by negative values of $\gamma_0(r)$. The influence is not too serious, though, since large distances are not over-estimated, as they are in v_c . So l_c might in most cases still represent a fairly good measure of "size".

The radius of gyration, on the contrary, is the most sensitive parameter of all. By its definition, it is bound to the particle concept, and should be used best for particle scattering only. With non-particulate systems it is liable to become obsolete. This is obvious, for example, in a liquid-type pattern, and can lead to misunderstanding in other cases, where the reasoning is not so clearly seen.

Finally, it should be noted that the concept of "shape" is still applicable to non-particulate systems. It makes sense to distinguish (Porod, 1965) – in a rough way at least – between globular, fibrillar and lamellar systems. The criterion given for particles in Section IV, factor $\approx h^{-1}$ for fibrils and $\approx h^{-2}$ for lamellae, remains valid. The reason is that the derivation given in Section IV, though developed for particles, makes no direct use of the particle concept. If the length of the fibrils, for example, can be regarded as infinite, it will make no difference whether the ends are free or connected. The same is clearly true for lamellae.

D. Final Slope; Internal Surface

The relationship between the final slope of the intensity function, the surface of a particle and the mean chord was established in Section III. With a non-particulate system the argument remains essentially valid still, as only the surface structure is of importance in this context, independent of large scale features. But a modification is needed in so far as the surface now belongs equally well to region one and two. In other words, Babinet's principle must be obeyed.

To discuss this point, let us first consider the chord distribution. A line crossing through the system (Fig. 6) will cut out alternating chords l_1 and l_2 from the two regions. It is evident that the mean lengths must be in the proportion of the respective volume fraction: $\bar{l}_1 : \bar{l}_2 = \varphi_1 : \varphi_2$. From pure geometry,

the relationship of Eqn (40) must apply to either of them, using $V\varphi_1$ and $V\varphi_2$ for the regions:

$$l_1 = 4 \frac{V}{S} \varphi_1; \quad l_2 = 4 \frac{V}{S} \varphi_2$$

The connection with the first differential parameter, as shown in Eqn (40), has to be modified, however, so that it becomes related to both regions in a symmetrical way. Formally, this can be done by introducing a certain average \bar{l} of the mean chords \bar{l}_1 and \bar{l}_2 such that $a = 1/\bar{l}$. The correct relationship between these parameters must fulfill the condition that $\gamma_0(r)$ is connected with l in the same way as the probability P_{11} of Eqn (72) is with l_1 , and P_{22} with l_2 :

$$\gamma_0(r) = 1 - r/\bar{l} \dots; \quad P_{11}(r) = 1 - \varphi_2 \cdot r/\bar{l} \dots; \quad P_{22}(r) = 1 - \varphi_1 \cdot r/\bar{l} \dots \quad (79)$$

from which follows

$$\bar{l} = \bar{l}_1 \varphi_2 = \bar{l}_2 \varphi_1 = 4 \varphi_1 \varphi_2 \frac{V}{S}; \quad \text{or: } \frac{1}{\bar{l}} = \frac{1}{\bar{l}_1} + \frac{1}{\bar{l}_2} \quad (80)$$

It is clear that in the limiting case of a dilute system \bar{l} becomes equal to \bar{l}_1 . It then entails no contradiction with Babinet's principle, if the particles alone are taken into account.

The connection with the final slope is essentially the same as derived in Eqn (42) for particles.

$$I(h) \rightarrow V\varphi_1 \varphi_2 (\Delta\rho)^2 \cdot \frac{8\pi}{\bar{l}} \cdot \frac{1}{h^4} = (\Delta\rho)^2 \cdot \frac{2\pi}{h^4} \cdot S \quad (81)$$

To get rid of the problem of absolute intensity it is again convenient to divide by the invariant Q

$$\lim h^4 I(h)/Q = \frac{1}{\pi \varphi_1 \varphi_2} \cdot \frac{S}{V} \quad (82)$$

So while the formula is practically the same for particles and non-particulate systems, a serious difficulty might arise in the latter case from the definition of the surface S . In fact, we might imagine particles packed together so closely, or a substance containing holes, pores or cleavages of so small a diameter, that it seems doubtful whether they will make a contribution to the surface S or not. If such a fine structure is present, we must expect the limiting value of Eqn (82), instead of being constant, to increase with increasing angle.

Another point which makes a difference compared with particle scattering should be mentioned. It seems obvious that in a non-particulate system no largest distance D can be defined. The correlation function should drop to zero asymptotically without a sharp end-point. Consequently, no oscillating terms can appear in the final slope, these being a typical cutting-off effect of a

Fourier integral. But this negative result cannot be regarded as a strict criterion, since with particles of irregular shape or with a broad size distribution the oscillations become negligible too.

VII. Non-uniform Electron Density

A. General Remarks

The assumption made throughout in the preceding sections of uniform electron density will certainly hold, as a good approximation at least, in most cases. Its importance lies in the fact that the structure can be treated as a geometrical problem only. But there may be systems of such a marked heterogeneity that the concept of uniform regions breaks down. The question is, first, when this is the case and, secondly, what can then be done regarding the diffraction pattern.

First, the natural heterogeneity due to the atomic structure is of no consequence for small angle scattering. It can be replaced by a continuous electron density, but this must be regarded as a function $\rho(r)$ now, rather than a constant as assumed so far. There remains a certain vagueness, it is true, as to the size of region to be "smoothed", but no general answer can be given in this respect. The problem must be considered individually for special cases.

At any rate, if smoothing is allowed for $\rho(r)$ the same is true for $\gamma(r)$ so that the general formulae of Eqns (11) and (12) can be applied.

The evaluation of the diffraction pattern can then be made in two different ways. First, one might choose a plausible model and try to approach the experimental intensity function by successive alterations; or secondly, one can calculate the correlation function by Eqn (12), and then try to interpret it by some structure. Which method is best suited in a certain case is a question of practical application and will be treated in later chapters. Here only two problems of general importance will be considered in detail.

B. Heterogeneous Particles

The difference compared with homogeneous particles, as treated in Sections II and III, can be caused by the internal structure and by solvation. Both effects should, in general, not invalidate the qualitative features of particle scattering; but the quantitative relations need special consideration.

So the concepts of a particle volume and of a constant electron density difference are no longer well defined and cannot, therefore, be used in the formula of Eqn (17), but the alternative expression: $I_1(0) = (\Delta n_e)^2$ still remains valid if the excess number of electrons (Δn_e) is redefined in a correct way. This

is necessary, since only the electron number n_e of the *free* particle and the electron density ρ_0 of the solvent are exactly defined. As, on the other hand, the volume is uncertain, and there may be some additional change of electron number by solvation, it seems not clear *a priori* how many electrons should be subtracted. The question is settled by the following argument. Let us imagine a certain volume V of the solvent and separately a particle of electron number n_e . If we now put the particle into the solvent, the whole volume will be increased by a certain amount, v'_1 say, (identical with the partial molecular volume in thermodynamics). Now it is clear that the change of the total volume by itself is irrelevant for diffraction, but near the particle the volume v'_1 has been displaced and with it the number $v'_1 \rho_0$ of electrons. So we have

$$(\Delta n_e) = n_e - v'_1 \rho_0; \quad I_1(0) = (\Delta n_e)^2 \quad (83)$$

Another characteristic feature of heterogeneous particles is the way diffraction depends on the electron density ρ_0 of the solvent. If the density ρ of the particle were constant, a variation in ρ_0 would produce only a change of absolute intensity, the function $I(h)$ remaining unaltered; but if $\rho(r)$ itself varies within the particle, the difference $[\rho(r) - \rho_0]$ is a function where the relative values are markedly altered by a variation of ρ_0 , and so is the intensity function $I(h)$. This is a complication which, on the other hand, can be used to obtain additional information by investigating the same particles in different solvents. (This will be treated in more detail in Chapter 7).

C. Correlation Function and Final Slope

Let us now consider a non-particulate system containing fluctuations η of electron density about a mean value $\bar{\rho}$, which is, of course, irrelevant for scattering. Under the assumption of statistical isotropy, it suffices to regard the fluctuations along a line, $\eta(x)$ say. According to what was said in Section A, this function can be supposed to be "smooth", though it may be of a quite irregular nature. So it can be developed in a power series in order to calculate the correlation function for short distances r

$$\gamma(r) \equiv \langle \eta(x) \cdot \eta(x+r) \rangle = \left\langle \eta(x) \left[\eta(x) + \left(\frac{\partial \eta}{\partial x} \right) r + \frac{1}{2} \left(\frac{\partial^2 \eta}{\partial x^2} \right) r^2 \dots \right] \right\rangle \quad (84)$$

In forming the average the second term must vanish, as positive and negative values will necessarily cancel in the long run. The third term must be negative, as near a maximum the second derivative is negative, and positive near a minimum. Applying integration by parts we finally have

$$\gamma(r) = \bar{\eta}^2 - \frac{1}{2} \left(\frac{\partial \eta}{\partial x} \right)^2 r^2 \dots \quad (85)$$

The behaviour of $\gamma(r)$ is distinctly different from that which was found for particles in Section III. The lack of the linear term is obviously due to the fact that in the present case there is no sharp boundary. Consequently, also the characteristic h^{-4} -slope cannot appear. On the other hand, the r^2 -term in Eqn (85) seems to be typical of fluctuating systems. For smooth particles it was found to be zero, and to have a positive value for angular bodies.

The above calculation cannot account for a sharp boundary between two regions, which would mean a sudden jump of $\eta(x)$. This can be treated, however, as an additional effect, causing a linear term in $\gamma(r)$ and the normal h^{-4} -slope due to the interface. The arguments remains valid also for the case of several interfaces S_j with different "jumps" $(\Delta\rho)_j$. So Eqn (81) is easily generalized to

$$I(h) \rightarrow \frac{2\pi}{h^4} \cdot \sum S_j (\Delta\rho)_j^2 \quad (86)$$

It should be stressed that only the differences $(\Delta\rho)_j$ at each boundary play a role for the final slope, while the fluctuations within the region are ineffective.

- Porod, G. (1965b). In "Electromagnetic Scattering" (R. L. Rowell and R. S. Stein, eds), p. 319. Proceedings of the Second Interdisciplinary Conference on Electromagnetic Scattering.
 Porod, G. (1972). *Monatsh. Chem.* **103**, 395.
 Rayleigh, Lord (1911). *Proc. Roy. Soc. (London)* A-84, 25.
 Schmidt, P. W. (1967). *J. Math. Phys.* **8**, 475.
 Schmidt, P. W. and Hight, R. Jr. (1959). *J. Appl. Phys.* **30**, 866.
 Shull, C. G. and Roess, L. C. (1947). *J. Appl. Phys.* **18**, 295.
 Tchoubar, D. and Mérинг, J. (1969). *J. Appl. Cryst.* **2**, 128.

References

- Debye, P. (1915). *Ann. Physik* **46**, 809.
 Debye, P. (1930). *Physik Z.* **31**, 419.
 Debye, P. and Bueche, A. M. J. (1949). *Appl. Phys.* **20**, 518.
 Debye, P and Menke, H. (1930). *Physik Z.* **31**, 797.
 Fournet, G. (1951). *Bull. soc. franc. mineral. crist.* **74**, 39.
 Guinier, A. (1939). *Ann. Phys.* **12**, 161.
 Guinier, A. and Fournet, G. (1955). In "Small-angle Scattering of X-rays", Wiley, New York.
 Hosemann, R. (1939a). *Z. Physik* **113**, 751.
 Hosemann, R. (1939b). *Z. Physik* **114**, 113.
 Kirste, R. and Porod, G. (1962). *Kolloid-Z.* **184**, 1.
 Kratky, O. (1947). *Monatsh. Chem.* **76**, 325.
 Kratky, O. and Porod, G. (1948). *Acta Physica Austriaca* **2**, 133.
 Kratky, O. and Sekora, A. (1943). *Naturwiss.* **31**, 46.
 Luzzati, V., Tardieu, A., Mateu, L. and Stuhrmann, H. B. (1976). *J. Mol. Biol.* **101**, 115.
 Mérинг, J. and Tchoubar, D. (1968). *J. Appl. Cryst.* **1**, 153.
 Mittelbach, P. and Porod, G. (1951a). *Acta Physica Austriaca* **14**, 405.
 Mittelbach, P. and Porod, G. (1951b). *Acta Physica Austriaca* **74**, 39.
 Mittelbach, P. and Porod, G. (1962). *Acta Physica Austriaca* **15**, 122.
 Porod, G. (1948). *Acta Physica Austriaca* **2**, 133.
 Porod, G. (1951). *Kolloid-Z.* **124**, 83.
 Porod, G. (1952a). *Kolloid-Z.* **125**, 51.
 Porod, G. (1952b). *Kolloid-Z.* **125**, 109.
 Porod, G. (1965a). In "Small-angle X-ray Scattering" (H. Brumberger, ed.), p. 1. Proceedings of the Conference held at Syracuse University.

3.I

Instrumentation, Experimental Technique, Slit Collimation

O. KRATKY

*Institut für Röntgenfeinstrukturforschung der Österreichischen Akademie der
Wissenschaften und des Forschungszentrums Graz, Graz, Austria*

I.	X-ray laboratory	54
II.	X-ray source and camera set-up	54
	A. Choice of Anode Material	54
	B. Installation of X-ray tube and camera	57
	C. X-ray tubes with rotating anode	58
III.	Small angle cameras	59
	A. General	59
	B. Slit cameras	59
	C. The block camera	62
	D. The Bonse-Hart camera	69
	E. The glass camera of Schnabel, Hosemann and Rode	72
	F. The cone camera	73
IV.	Monochromatization	74
	A. Pulse height discriminator, alone or combined with a K_{β} -filter	74
	B. Pulse height discriminator combined with numerical elimination of the K_{β} -contribution	75
	C. Balanced filters	75
	D. Crystal monochromator, in the incident or diffracted beam	76
	E. Totally reflecting mirrors	77
	F. Numerical elimination of polychromatic effects	77
V.	Absolute intensity	77
VI.	Experimental elimination of the effect of intensity fluctuations, monitor	80
	References	81

In the current section we assume that the reader is roughly familiar with the function of commercially available equipment (e.g. X-ray generators, X-ray tubes, cameras etc.), necessary for scattering experiments. Details will be discussed in the current section and in Chapters 3.II and 3.III, as well as in Chapter 7.

I. X-ray Laboratory

The X-ray laboratory has to conform to the following requirements:

- (1) Provision for complete darkness: some of the adjustment operations of the small angle camera require darkness and good adaption of the eye.
- (2) No strong vibrations, caused for example by road traffic, since vibrations may affect the alignment of the camera.
- (3) Air conditioning: if the camera is not mechanically connected to the X-ray tube, thermal effects may cause a movement of the focus relative to the camera, leading to intensity instabilities. In this case, the ambient temperature should be kept constant within $\pm 2^\circ\text{C}$. If, however, the front end of the camera is suspended at the top of the X-ray tube (see Section III.C2), no special measures for the control of the room temperature are required.

Humidity should neither be extremely high nor extremely low; very low humidity causes electrostatic charging, high humidity may lead to electric flashovers.

- (4) Sufficient water supply: direct use of tap water is permissible, if its temperature fluctuates less than $\pm 2^\circ\text{C}$. Larger temperature fluctuations cause intolerable intensity fluctuations. A closed cooling water cycle is advantageous: it maintains constant water temperatures and avoids calcification of the anode. Calcerous deposits at the anode reduce its thermal conductivity and decrease the cooling effect. Obviously, one *has* to use a closed cooling water system if the public water supply cannot provide enough water.

II. X-ray Source and Camera Set-up

A. Choice of Anode Material

For the vast majority of applications, an X-ray tube with a copper anode has been used in the past; the wavelength of its characteristic radiation (CuK_α -line) is 1.54 Å.

The use of longer wavelength radiation would obviously spread the scattering curve over a larger angle, therefore permitting higher resolution. This possibility

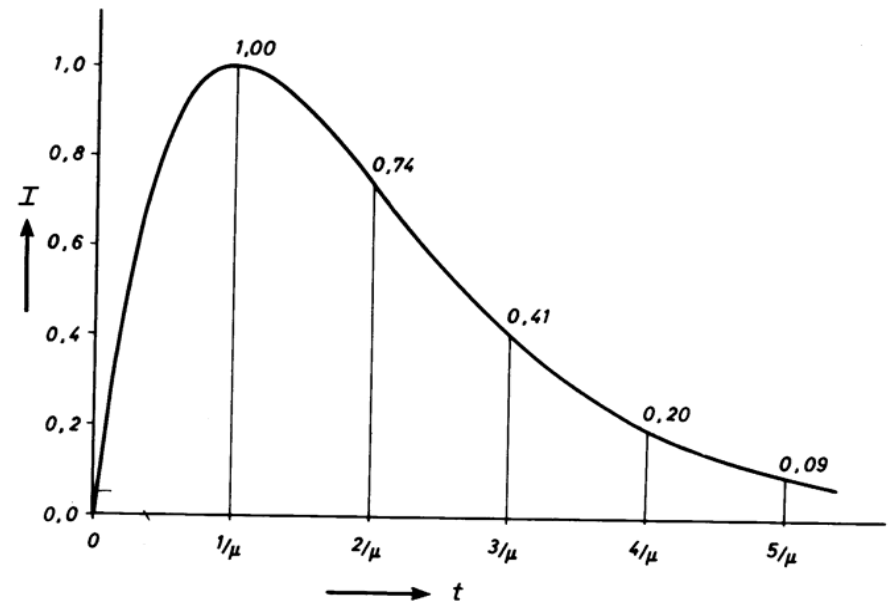


FIG. 1. Dependence of scattered intensity I on the sample thickness t .

however, is only very rarely used due to the sharp increase in absorption with increasing wavelength: increased absorption decreases the optimum sample thickness and the maximum scattered intensity. The intensity I scattered at small angles is proportional to $t e^{-\mu t}$ (t being thickness of the sample; μ , absorption coefficient); this expression has its maximum at $t_{\text{opt}} = 1/\mu$. If the material to be investigated has a very high absorption coefficient, it is often difficult to obtain sufficiently thin samples. Figure 1, which shows the dependence of the scattered intensity I on the sample thickness t (expressed as a multiple of the optimum thickness $1/\mu$), demonstrates the decrease in intensity for a thickness exceeding $1/\mu$. In favourable cases the absorption may permit the use of chromium K_α -radiation ($\lambda = 2.29 \text{ \AA}$) but they will usually disqualify longer wavelengths.

At this point, however, the work of Herglotz^{(1),(2)} has to be mentioned: he describes an open X-ray tube combined with a pinhole camera to overcome some of the difficulties of Al-radiation ($\lambda = 8.34 \text{ \AA}$). The interior of the X-ray tube (which is permanently connected to a vacuum pump) is separated from the interior of the camera only by a $6 \mu\text{m}$ thick Al-foil. Since the tube is essentially "open", frequent removal of the tungsten deposit at the anode is easy. Excellent measurements on 0.01 mm thick polymer foils were performed on this instrument.

TABLE 1
 $t_{\text{opt}} [\mu\text{m}]$

	CuK_α	MoK_α
Be	3584	18 041
C (Graphite)	966	7111
Mg	149	1398
Al	76,2	718
Fe	4,1	33,0
Ni	24,6	24,1
Cu	21,2	22,0
Zn	23,2	25,3
Pb	3,8	7,4
H_2O	976	8307
C_2H_5OH	1964	15 249
SiO_2 (Quartz)	109,5	1018
Laboratory glass	76,7	647
$(CH=CH)_n$ (Lupolen R)	2547	17 975

We do not know of any other work using such long wavelength radiation for small angle scattering, but the possibility should be kept in mind. Although the Herglotz camera employs pinhole collimation, there is no obvious reason why the same set-up should not work with slit collimation, too.

Usually it is not necessary to cope with the above problems, since the resolution obtainable with copper radiation (see Chapter 11, Section II) is sufficient. In fact, there are several cases, to be discussed in the following, where it can be favourable to use shorter wavelengths.

(1) Table 1 shows that inorganic materials often have a prohibitively small optimum sample thickness for copper radiation. Occasionally, for samples containing light metals, molybdenum radiation ($\lambda K_\alpha = 0,71 \text{ \AA}$) may be suitable. With its excitation voltage of 20 kV, molybdenum tubes can be conveniently run under usual operating conditions (50–60 kV). However, samples containing high concentrations of heavy metals have an optimum thickness which is prohibitively small, even for molybdenum radiation. Tungsten radiation ($\lambda K_\alpha = 0,21 \text{ \AA}$) would be suitable, but for sufficient intensity the tube voltage has to be at least 100 kV, which requires special equipment. It should be feasible, however, to run a tungsten tube with "normal" voltages (e.g. 60 kV) and use a fraction of the white radiation for the scattering experiment. Sufficient monochromatization could be achieved with any of the standard techniques (balanced filters, monochromator, pulse height discriminator). The resolution of available small angle cameras is in most cases sufficient to cope with the decrease in scattering angles. Little practical experience is so far available, especially with

tungsten radiation, but experiments would be very desirable, as they could extend the small angle technique to the study of strongly absorbing metals, which were so far practically excluded.

(2) Shorter wavelengths "compress" the scattering curve in a correspondingly smaller angular range. This can be useful when the maximum attainable angle of a given goniometer is too small to record enough of the scattering curve with copper radiation. In such a case, the use of a shorter wavelength has the added advantage that a correction for the angle-dependence of the absorption (as a result of different pathlengths in the sample) becomes small or even negligible.

(3) The advantage of weaker absorption results is an increase in maximum intensity with the optimum thickness (i.e. with $1/\mu$). However, to obtain the same resolution with shorter wavelengths would require correspondingly narrower entrance slits and counter slits, which in turn decreases the intensity. It is, however, not possible to give a general rule as to which radiation yields highest scattered intensity, because the X-ray flux obtainable from tubes with different anode materials is difficult to predict.

(4) The optimum thickness of macromolecular solutions in water or organic solvents is about 10 mm for molybdenum radiation (Table 1). Sample cuvettes can therefore be equipped with flat glass windows of 0,12 mm thickness. Such cuvettes have a uniform and precisely measurable thickness. On the other hand, the same samples have an optimum thickness around 1 mm for copper radiation, which dictates the use of Mark capillaries, which usually are of rather irregular shape with a poorly defined average thickness. This advantage of molybdenum radiation, however, does not come into effect if there is not enough sample available to fill the 10 mm cuvettes, which is frequently the case when biological macromolecules are of interest.

(5) Tungsten deposits at the anode, which accumulate with time, have a smaller effect on the primary intensity for short wavelength radiation than for longer wavelength.

B. Installation of X-ray Tube and Camera

We assume that an X-ray tube with line focus and four windows is used. First, one has to decide whether the tube should be mounted vertically or horizontally. Better mechanical stability and access to all four windows favour the vertical position, but several types of small angle cameras (e.g. the Rigaku Denki goniometer) require a horizontal tube. In the following discussion we assume that the X-ray tube is mounted vertically, as this appears to be preferred by most workers.

Another basic decision concerns the type of window which is to be used for

the camera. Let us assume the size of the focus is 10×1 mm and the X-ray path has the usual 6° inclination against the horizontal plane of the focus. In this case the projection of the focus into the plane perpendicular to this X-ray path is a line with dimensions 10×0.1 mm on the "long" side of the focus. On its "narrow" side, the focus appears as a radiating square of dimensions 1×1 mm. One frequently talks about working "at the line focus" or "at the square focus", respectively.

Naturally, a "slit camera" (i.e. a camera whose collimation system is designed for a primary beam whose cross-section has the shape of a long and narrow rectangle) should be placed in front of the line focus, whereas a "pinhole" camera (i.e. one which utilizes a circular primary beam cross-section) should be placed at the square focus. If the tube is mounted vertically, the longer dimension of the slit is referred to as its "length", the smaller dimension is called "width". It should be noted that, in the case of the X-ray tube being mounted horizontally and working at the line focus the larger dimension of the slit runs vertically, and is correspondingly called "slit height" instead of "slit length". In both cases (i.e. vertical and horizontal X-ray tube), the smaller dimension of the slit is referred to as the "slit width".

C. X-ray Tubes with Rotating Anode

Several manufacturers offer high-power generators whose X-ray tubes could not be cooled in the conventional way without local over-heating at the focus due to the high electron flux. To circumvent this difficulty, the focus is generated at the surface of a water-cooled cylinder, which rotates at high angular velocity to dissipate the heat over the whole of its circumference. Such X-ray sources have a very high water consumption, which is roughly proportional to their power.

The power of commercially available instruments of this type ranges from 6 kW to 60 kW, which is about 3–30 times larger than for sealed tubes. The high primary intensity allows correspondingly shorter exposures, which is particularly useful for the study of time-resolved processes or of unstable materials. Moreover, many investigations involving low electron density contrast, or high dilutions, demand high power sources.

High power X-ray generators run with the usual voltages (40–50 kV) and produce the same radiation as conventional sources with a higher primary intensity. This requires exceptional care in the design of radiation shields, i.e. sufficient thickness of the absorption material and absolute avoidance of small leaks.

III. Small Angle Cameras

A. General

Pinhole cameras, i.e. cameras which use a primary beam with more or less point-shaped cross-section, are rarely used for small angle experiments due to their poor intensity. Only in combination with high-intensity synchrotron sources, pinhole systems are in current use. They will be discussed in Chapter 3.II.

The current chapter will be confined to a discussion of cameras with slit collimation, which utilize a primary beam with line-shaped cross-section. In general, these cameras yield sufficiently high scattered intensity also with conventional X-ray sources.

In the following, several cameras of this type will be described.

B. Slit Cameras

The simplest collimation system consists of two parallel slits. The narrower these slits are and the larger the distance between them, the higher is the attainable resolution. This simple design has the disadvantage that the slits emit secondary scattering (parasitic scattering) into the small angle region, which makes it impossible to use this camera for high resolution work. The design, however, can be considerably improved by a third slit (Fig. 2, slit S_3) which is adjusted in such a way that it is just not hit by the direct beams 1 and 2, but absorbs as much as possible from the parasitic scattering originating from slit S_2 . Consequently, the parasitic scattering is intense between lines 3 and 4, while the "diagonal scattering" (limited by lines 5 and 6) is much less intense. Naturally, it depends on the mechanical precision of the instrument by how much the region between lines 3 and 4 exceeds the one between 1 and 2. If the sample to be investigated is a good scatterer, it may be possible to record its scattering already between lines 3 and 5 (or 4 and 6, respectively) while for weakly scattering samples one will be confined to the range beyond lines 5 and 6, where the parasitic scattering is negligible. In the plane of registration PR the zones s correspond to regions of strong, the zones w to regions of weak, parasitic scattering.

Guinier and Fournet⁽³⁾ give a very detailed discussion of the problems and limitations of slit cameras. We also refer to an original publication, where the optimum dimensions of slit collimation systems are discussed.^{(4)*}

A slit camera which was used very successfully is the one of Beeman and

* Slit cameras of this type are offered by several companies. We mention especially: Rigaku Corp. Tokyo, Japan.

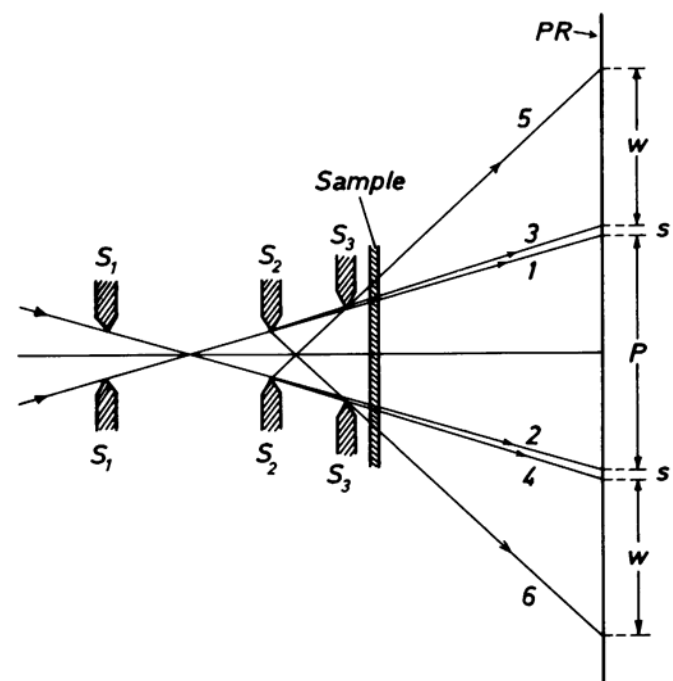


FIG. 2. Slit camera with three slits S_1 , S_2 and S_3 , each consisting of a pair of edges running perpendicular to the plane of paper. The dimensions in the vertical direction are greatly enlarged.

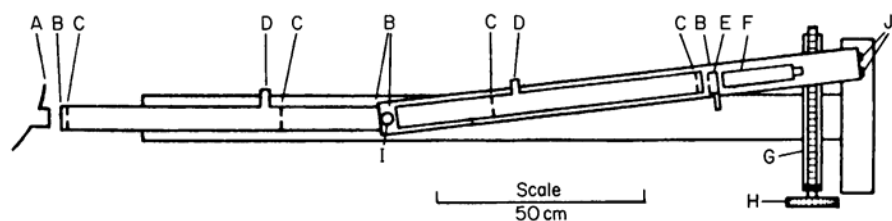


FIG. 3. Diagram of slit collimating system^{(5),(6)}. (A) X-ray tube exit window; (B) mica window; (C) tantalum slits; (D) vacuum connections; (E) Ross filters on slide; (F) GEIGER counter; (G) high precision screw; (H) calibrated wheel; (I) pivot and sample holder; (J) rollers.

co-workers^{(5),(6)} (Fig. 3). Two stationary tantalum slits C collimate the beam incident upon the scatterer. Two additional slits C analyse the angular distribution of the radiation leaving the sample. The second pair of slits, together with specimen holder and Geiger counter, are attached to an arm which may be rotated, by means of a calibrated screw, about an axis through the centre of the specimen.

A rather unusual design is adopted in the slit camera of Stasiecki and Stuhrmann,⁽⁷⁾ whose overall length is 50 m! Half of this length is taken up by the collimation system, the other half by the distance sample plane of registration. The authors used this camera to demonstrate that particle scattering can be recorded even for particles of microscopic dimensions. They studied erythrocytes and found a largest diameter of $6 \pm 0.5 \mu\text{m}$ and a molecular weight of $M = (4.7 \pm 1.2) \times 10^{13}$ daltons, which exceed the respective one for smaller protein molecules by 3 and 9 orders of magnitude. To make this scattering experiment with erythrocytes on a camera with 20 cm distance between sample and plane of registration would require an entrance slit of less than $0.5 \mu\text{m}$ and the whole scattering range would be compressed into a few μm . The proportionality

$$M \sim \frac{I_0}{P_0} a^2$$

(I_0 , zero-angle scattered intensity; P_0 , primary intensity) illustrates that an increase in M by a factor 10^9 and in a by a factor 10^2 results in an increase in the ratio I_0/P by 5 orders of magnitude. This has the consequence that the scattered intensity can be recorded together with the primary intensity. In fact, the scattered intensity could be obtained (by subtraction of a blind curve) directly from the tail of the primary peak profile.

The success in this interesting experiment suggests that an optimization of the camera dimensions could be a viable tool for investigations on particles whose size is intermediate between the classically studied macromolecules and Stuhrmann's erythrocytes. It is quite possible, that occasionally a 4–5 m long camera could improve the results obtainable with conventional instruments. This is particularly true when a position sensitive detector is being used, whose space resolution becomes insufficient for large particle dimensions. Even today, one often uses the position sensitive detector for conventional measurements in combination with an adaptor to increase the distance sample-detector to 0.5 m.

An auxiliary device capable of considerably reducing the slit-length smearing is occasionally used in combination with slit cameras: the Soller slit. It consists of a set of parallel, thin lamellae, whose planes are arranged parallel to the primary beam axis and perpendicular to the plane of the beam. It is inserted into the camera behind the primary beam stop. Recently, Todo *et al.*⁽⁸⁾ have described such a device with 0.06 mm thick lamellae spaced at 0.6 mm. The authors conclude that this device yields better results than the *bloc* collimation system. It is certainly true that a curve recorded with a Soller slit is more similar to a desmeared scattering curve than a curve afflicted with the usual slit-length smearing effect; consequently, some of the errors introduced by the (numerical) desmearing process are smaller. However, this advantage is accompanied by a severe loss in intensity. Without a Soller slit one yields, under otherwise identical conditions, a much higher intensity, smaller statistical errors and hence a better

starting point for the desmearing process. Whether this outbalances or even overcompensates the advantage of the Soller slit could only be decided after extensive test measurements.

The above authors used the Soller slit on a high-power rotating-anode X-ray source (200 mA, 40 kV), and compared the results to data obtained from a block camera in front of a conventional sealed tube (35 mA, 45 kV). Moreover, they did not report counting times. The reported data, therefore, do not offer a sound basis for a comparative evaluation.

It is certainly conceivable that the intensity loss is tolerable under certain circumstances, e.g. use of a high-power X-ray source, strongly scattering and radiation-insensitive samples (Todo *et al.* used solid high polymers). It remains questionable, on the other hand, whether a Soller slit used with a *weakly* scattering sample (e.g. a diluted solution of biological molecules) and a normal X-ray source would not require counting times which are intolerably long in view of the limited stability of biological samples.

All in all, the work of Todo *et al.* has drawn attention to a long known but rarely used device, which may well be useful for a number of applications. A final appraisal of its range of applicability, however, has to await additional studies.

C. The Block Camera

1. THE COLLIMATION SYSTEM

The problem of parasitic scattering can be largely removed with the arrangement depicted in Fig. 4a: it shows a section parallel to the propagation direction of the beam and perpendicular to the length direction of the focus. The radiation source is represented by the projection *f* of the focal spot into a plane perpendicular to the beam axis. Collimation of the beam is achieved by three construction elements, the two blocks B_1 and B_2 and the edge *E*, which all run perpendicular to the plane of the paper.^{(9),(10)} It is essential that the plane defined by the polished upward directed surface F_1 of B_1 coincides exactly with the downward directed surface F_2 of B_2 . This plane is called the main section *H*. The width of the entering beam is defined by the distance *d* between the edge *E* and the main section *H*. It is easy to see that there should be no parasitic scattering at all above the main section. In fact, there is a very small amount of parasitic scattering above *H* which is due to mechanical imperfections. Figure 5 shows schematically how the instrument is designed to ensure that planes F_1 and F_2 coincide: block B_1 is the centre piece of a *U*-shaped body, while block B_2 , called the bridge, is pressed on to its side-pieces from above.

With respect to the ideas discussed in Sections 3 and 4 of this chapter it may

be mentioned that it is sufficient to make the block B_1 quite small, as shown in Fig. 4b. Essential for the collimating effect is the position of the "middle edge" *M*.

2. OVERALL CONSTRUCTION OF THE CAMERA

Figure 6 shows a recent version of the camera mounted in front of the X-ray tube *R*,⁽¹¹⁾ and Fig. 7 gives a vertical section through the camera in the direction of the X-ray beam. The collimation system *C*, the sample holder *SH* and the primary beam stop *PS* are all mounted inside an evacuated housing *V*, with front window *W*₁ and end window *W*₂. This design is a modification of an older version, which had the sample outside the evacuated region – with the obvious disadvantage of a higher background due to the scattering from two additional windows and from the air around the sample. The use of continuous vacuum follows a suggestion by Hendricks.⁽¹²⁾

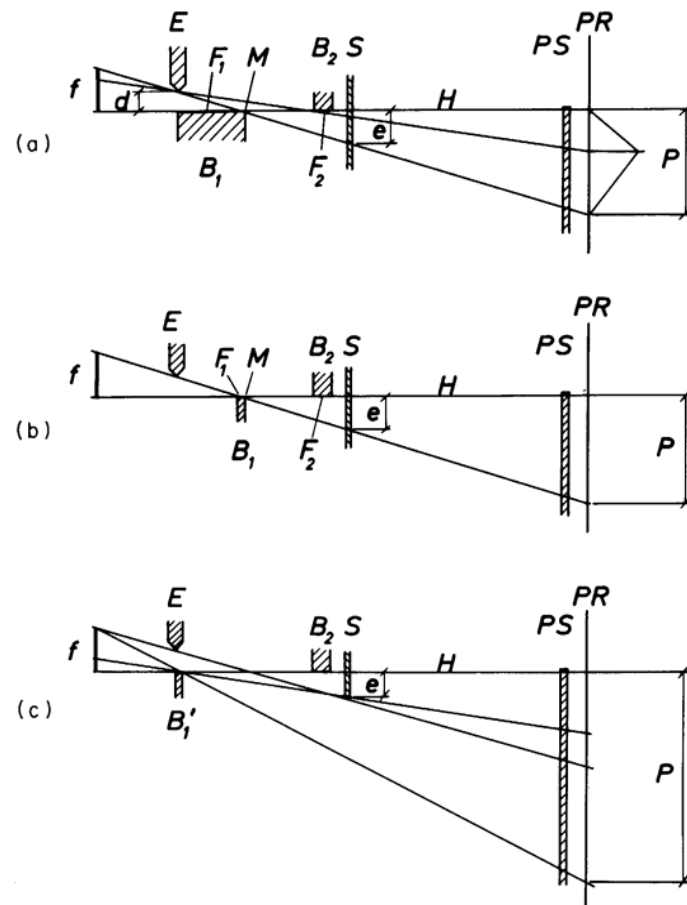
The radiation is recorded outside the vacuum tube. If a film or a position sensitive detector is used, a stable suspension at the camera housing is sufficient. For the pointwise recording of the scattering curve the simultaneous movement of detector slit *DS* and of the detector *D* is guided by the slits *S*₁ and *S*₂.

Since the focus is an inhomogeneous emitter of radiation, intensity fluctuations can occur if the relative position of focus and collimation system changes. Suspension of the front end of the camera at the top of the X-ray tube has turned out to avoid such relative movements between focus and collimation system and to eliminate most thermal and mechanical influences. The two adjustment screws *F*₁ and *F*₂ (Fig. 6) are sufficient for an optimum positioning of the camera.

3. ADVANTAGES AND DIFFICULTIES OF THE BLOCK COLLIMATION SYSTEM

The above design attempts to reduce parasitic scattering at small scattering angles in order to permit an extension of the accessible part of the scattering curve to angles corresponding to Bragg's values of several thousand Ångstrom. At the same time, the design should reduce the background for the whole of the scattering curve in order to permit experiments with very weakly scattering samples. Figure 8 demonstrates that these demands are indeed fulfilled. The parasitic scattering does not extend beyond 1.5×10^{-3} radians ($\approx 1000 \text{ \AA}$), and the effect of parasitic scattering can easily be corrected for by appropriate subtractions for angles down to 0.65×10^{-3} radians ($\approx 2400 \text{ \AA}$).

Figure 9 gives another relevant comparison. It shows the scattering curve of polyethylene, which is frequently used as a secondary standard for absolute intensity measurements (Section V). Since its scattering curve is known with



high accuracy,⁽⁴⁷⁾ polyethylene is also useful as a test substance for camera checks. It is apparent that the blank scattering of the camera alone, which is exaggerated in Fig. 9 by a factor of 10, is negligible compared to the Lupolene curve for the whole given angular range.

Figure 10 shows the scattering curve of a solution of high density Lipoprotein. Again, one can see that, in spite of the relatively large entrance slit of 100 μm , the camera scattering is negligible down to 500 \AA , Bragg's value, even compared to the blank scattering of the solvent-filled capillary.*

It is this asymmetric design which is the main difference to other systems,

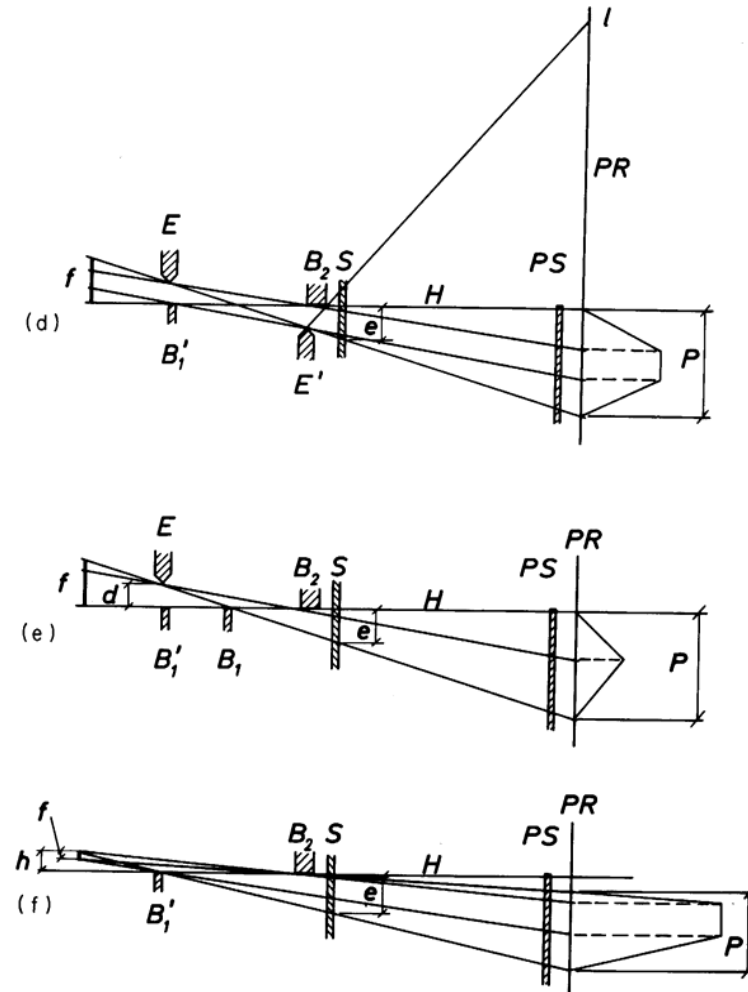


FIG. 4. Section through block collimation systems.⁽⁹⁾⁻⁽¹¹⁾ The dimensions in the vertical direction are greatly enlarged. (S) sample; (P) primary beam profile; (PS) primary beam stop; (PR) plane of registration.

which have (compare with Section III.B and Fig. 2) a region of parasitic scattering on both sides of the primary beam. Of course, it is possible to measure down to any small angle with a slit camera too, by simply using sufficiently narrow slits, but the intensity will be smaller by a factor 4-6 compared to a block camera adjusted for the same resolution.⁽⁹⁾ This advantage of the block collimation has to be payed for by two difficulties.

* The camera of this design is offered by A. Paar KG., Graz-Strassgang, Austria.

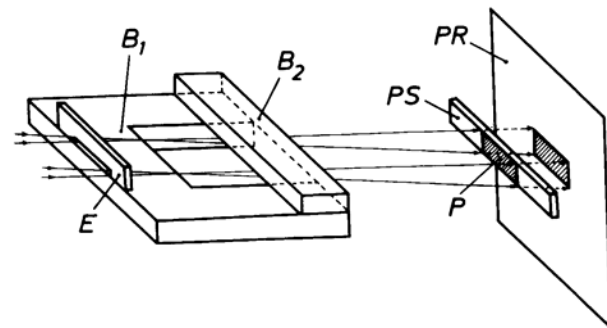


FIG. 5. Schematic drawing of the collimation system.^{(9),(10)} (P) primary beam. Explanation of the other symbols – see legend to Fig. 4.

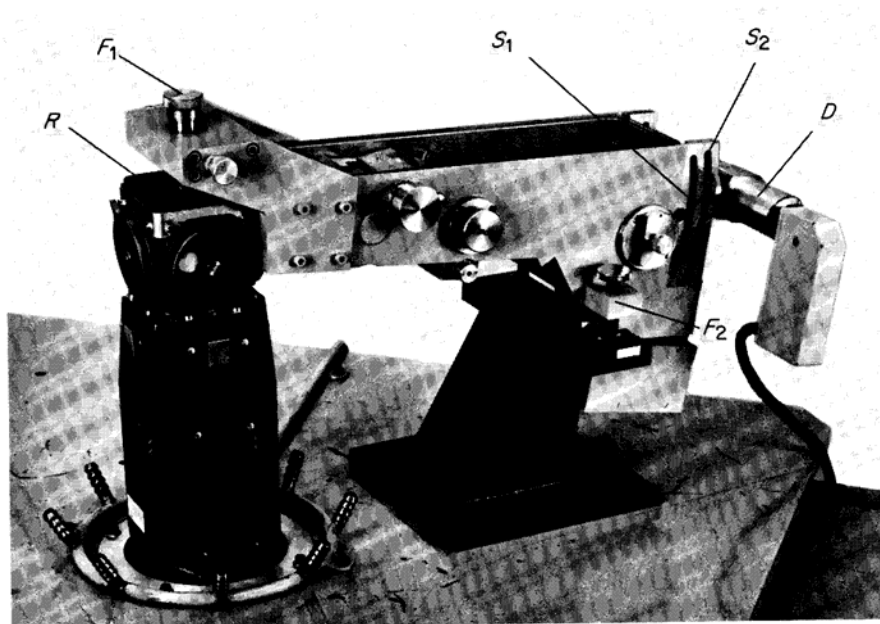


FIG. 6. Small angle camera.⁽¹¹⁾

(1) As a consequence of the asymmetric design, the scattered radiation can only be recorded at one side of the primary beam; below the main section H , the parasitic scattering is very strong. The zero-point of the scattering curve must therefore be determined by measuring the primary beam intensity profile.

(2) At large angles, where parasitic scattering is negligible anyway, the block

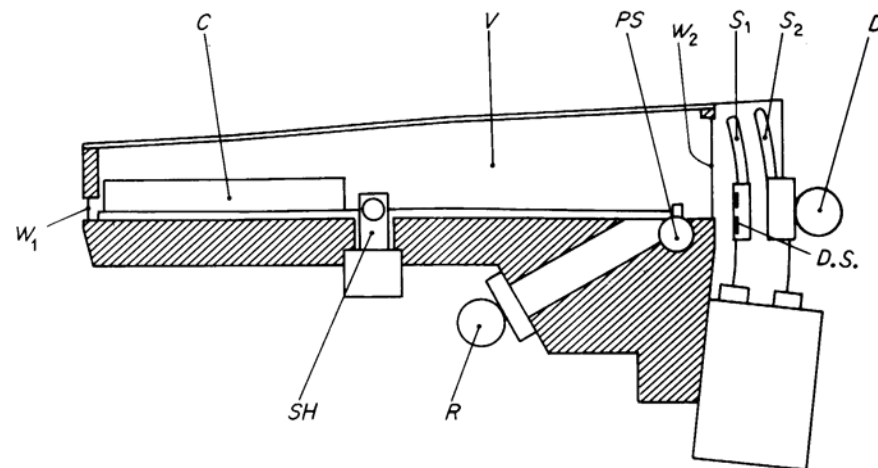


FIG. 7. Section through the small angle camera.⁽¹¹⁾

collimation system yields less intensity than systems with two or three slits. This is so because block B_1 (Fig. 4b) partially screens the primary beam entering through entrance slit d and hitting the sample S in the zone e . According to an old suggestion by Henke⁽¹³⁾ and Schulze,⁽¹⁴⁾ this disadvantage can be removed by shifting the block B_1 below edge E (now designed by B'_1) (Fig. 4c). This modification results in a very broad primary beam profile P , which could not allow high resolution. To improve the resolution, Henke and Schulze use a sample with a very sharp lower edge which is only partially immersed into the beam as shown in Fig. 4c. In spite of its advantages, this modification has hardly been used, mainly due to difficulties in determining the zero point of the scattering curve, in measuring the absolute intensity and in obtaining the sample in a form which fulfills the very stringent geometrical constraints. The arrangement in Fig. 4d has the gain in intensity of Henke and Schulze's set-up, without its just mentioned disadvantages. Since the newly inserted edge E' which defines a lower limit for the primary beam emits parasitic scattering up to the limit l , one can only measure, with complete absence of parasitic scattering, above l . It is therefore advantageous to use the arrangement in Fig. 4e for measurements at very small angles (which is for this purpose equivalent to Figs 4a and b) and to switch to the arrangement in Fig. 4d at larger angles by removing B_1 and inserting E' .

4. A MODIFICATION OF THE BLOCK COLLIMATION SYSTEM: INTEGRATION OF THE X-RAY TUBE INTO THE CAMERA

A recently proposed and tested arrangement incorporates some of the above ideas⁽¹⁵⁾ (Fig. 4f): the collimation system consists only of the blocks B'_1 and B_2 ;

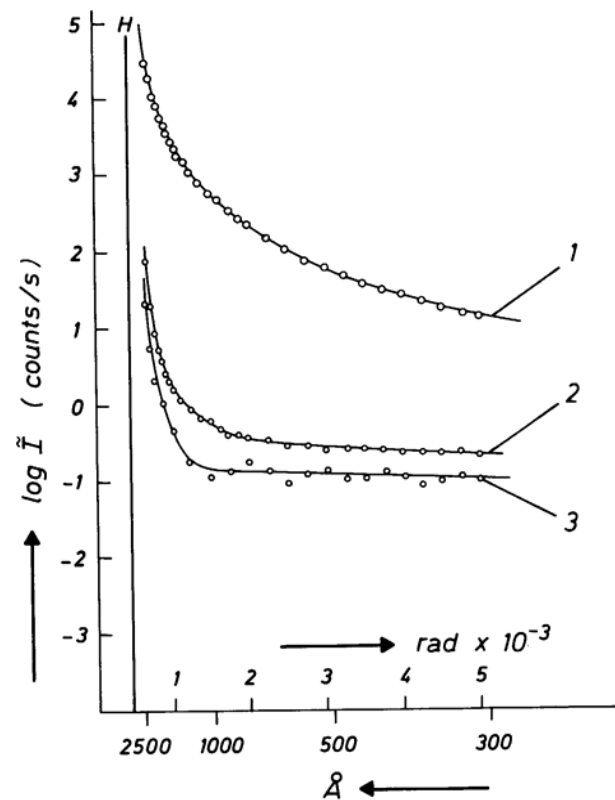


FIG. 8. Measurements with the block camera. (1) Scattering of polyvinylchloride powder in 1 mm Mark capillary; (2) blank scattering of the capillary; (3) blank scattering of the empty camera. Curves 2 and 3 are corrected for absorption. (H) Main section, entrance slit 43 μm , counter tube slit 15 μm .

in addition, the anode plays an integral role for the collimation. With the focus f well above the main section, the anode takes the function of the edge E in the conventional design. The integration of the focus into the collimation system requires that position and orientation of the anode plane with respect to the rest of the collimation system is extremely well defined (positional errors must not exceed 1–2 μm). The X-ray tube is therefore mounted into a holder which is part of the camera housing.

While the conventional block collimation system produces a primary beam with triangular intensity profile in the plane of registration (Fig. 4a), the integrated camera yields a trapezoidal primary beam. The dimensions of this trapezoid are determined by the distance h between the upper end of the focus and the main section H , and by the width of the projection of the focus. The highest

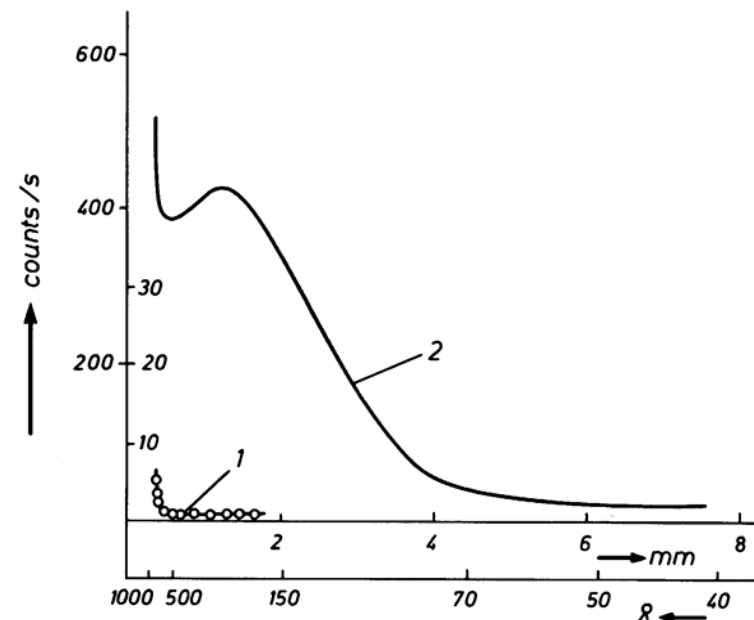


FIG. 9. Measurements with the block camera. (1) Blank scattering of the empty camera exaggerated by a factor 10; (2) scattering of lupolen. Entrance slit 80 μm .

intensity is obtained if the beam profile is rectangular. Since the steepness of the sides of the trapezoid increases with decreasing focal width, it is advantageous to use a narrow focus of high brilliance. Since the anode is a surface radiator, a decrease in the take-off angle increases the brilliance of the focus (while the total energy remains constant). There is in practice a lower limit in the take-off angle due to imperfection in the planarity of the anode surface, which deteriorates with increasing age of the tube. Thus, it is unsafe to decrease the take-off angle beyond 3°. However, if one also uses a fine focus tube (with only 0.4 mm focal width), the increase in brilliance, compared to a normal tube with the usual 6° take-off, is considerable: both theoretical considerations and measurements show that this arrangement yields at medium scattering angles an intensity about two times higher (for the same resolution) than the arrangement in Fig. 4a or b. At very high resolution, when the focus "touches" the main section, the gain in intensity is even as high as a factor of three to four.

D. The Bonse-Hart Camera^{(16),(17)}

This instrument is based on multiple reflections of the primary beam from opposite sides of a groove in an ideal germanium crystal (2 in Fig. 11). The

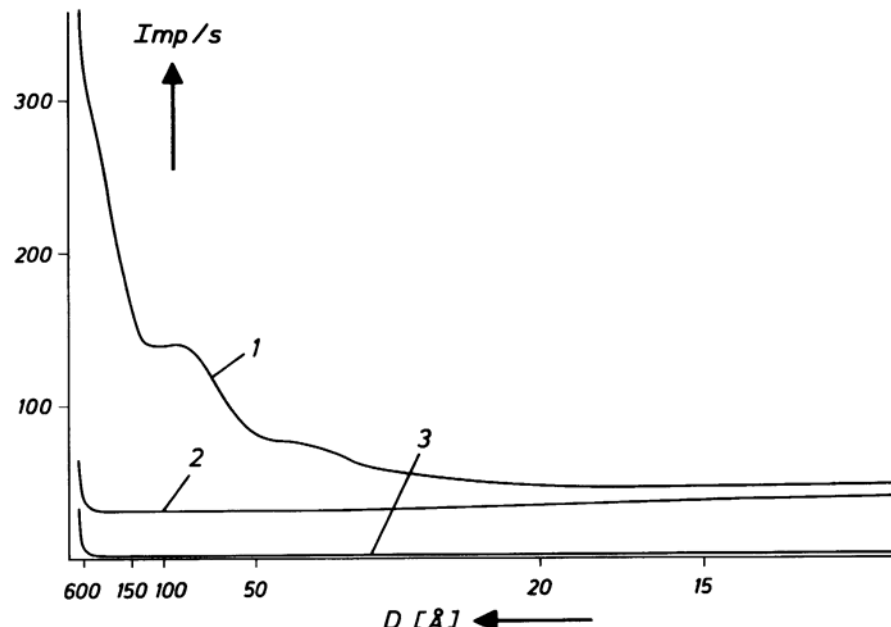


FIG. 10. Measurements with the block camera. (1) Scattering of a HDL₃ solution, 5.1%; (2) blank scattering of the Mark capillary with solvent; (3) blank scattering of the empty camera; corrected for absorption. Exaggerated by a factor of 10.

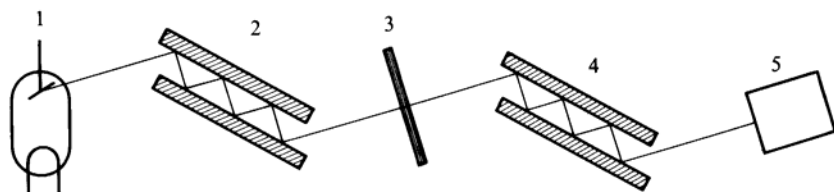


FIG. 11. Schematic drawing of the Bonse-Hart camera.

divergence of the beam decreases every time it is reflected from one of the walls, leading to a strictly monochromatic beam with a divergence of only several arc seconds. After penetrating the sample 3, the beam is again reflected several times from the inner walls of a second crystal 4 and finally enters the detector 5. Crystal 4 can be turned about an axis perpendicular to the plane of the paper with a precision spindle. This rotation of crystal 4 about its centre allows the recording of the small angle scattering originating from the sample: it is easy to see that if crystal 4 is turned by an angle, α say, from its position parallel to crystal 2, only the radiation scattered by the sample to the same angle can reach the detector. The appealing feature of this ingenious design is the fact that one can measure

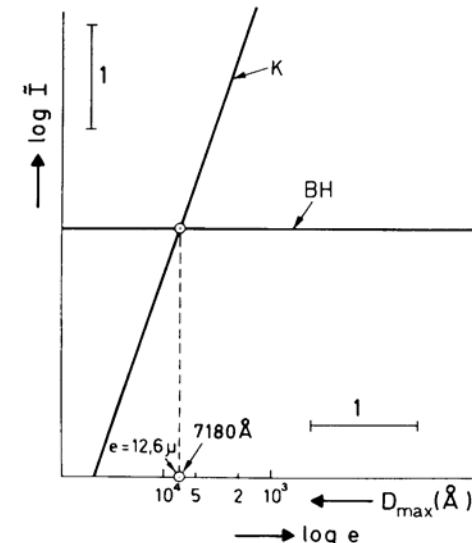


FIG. 12. Comparison of intensities as a function of resolution between the Bonse-Hart system and the block collimation system.

down to the smallest angles without using a narrow entrance slit: all other techniques have to deal with the fact that the primary intensity drops rapidly due to the narrow entrance slits required to measure down to very small angles, while the Bonse-Hart system uses the same primary intensity for all angles. On the other hand, with decreasing resolution, the other methods offer the option of increasing the size of the entrance slit with concomitant increase in primary intensity, while the Bonse-Hart system does not offer such an option.

A quantitative experimental comparison with the block collimation system has yielded the result presented in Fig. 12.⁽¹⁸⁾ While the Bonse-Hart system BH yields constant intensity, the primary intensity of the block collimation system K increases with the third power of the width of the entrance slit e (which, in turn, is inversely proportional to the highest attainable Bragg's value). The two curves intersect at an angle corresponding to a Bragg's spacing of about 7000 Å. If, say, it is sufficient to obtain a resolution of 1000 Å, the block camera yields a 7^3 (= 343) times higher intensity than the Bonse-Hart camera. Alternatively, if one aims at a resolution of, say, 3×7000 Å (= 21 000 Å), the Bonse-Hart system is more sensitive by a factor of 3^3 (= 27). Since the majority of applications of the small angle technique require resolutions far below 7000 Å, the Bonse-Hart technique has up to now only been used in a few special problems, in spite of its truly ingenious design. We refer to measurements on polystyrene latex spheres of 5570 Å diameter⁽¹⁶⁾ and materials of interest to petroleum production (Dwiggins)^(17a) with radii of gyration up to 35 000 Å.

Recently, M. Deutsch⁽¹⁹⁾ has reported remarkable improvements in the Bonse-Hart camera. It is clear from the above, that the Bonse-Hart camera in its original version yields an enormously high resolution, which is unnecessary for the majority of applications. The price for high resolution is low intensity: "The usual trade-off of lower resolution for higher intensity, so easily accomplished in its slit collimating system by opening up the slits, is impossible, here" (Deutsch).⁽¹⁹⁾ Deutsch suggests two modifications of the Bonse-Hart camera, which reduce resolution but increase intensity: reduction in the number of reflections from 5 to 4,2 or 1 and grinding the crystal in such a way, that the grooves do not run parallel to the reflection plane; thus, the angle α between crystal surface and reflected X-ray beam can be adjusted to any value between θ and close to zero.

The two above parameters can be chosen such that the result is similar to opening the slits in a slit camera. There exists a crossing point for each number of reflections, where resolution and primary intensity are the same for the block collimation and the modified Bonse-Hart system. Deutsch finds, that 4, 2 and 1 reflections correspond to slit width of 30, 54 and 125 μm , respectively. However, Deutsch has based this consideration on the block collimation system as it was in 1970. More recent improvements (integrated camera, c.f. Fig. 3f) have yielded a considerable increase in intensity at least by a factor of 2, at smallest angles at least a factor of 3. This shifts the cross-over points to 23, 41 and 94 μm for 4,2 and 1 reflections, respectively. These slit widths correspond to largest measurable Bragg's values of 3900, 2200 and 960 \AA . In summary the Bonse-Hart-Deutsch system is superior at Bragg's values larger than 960 \AA ; the block system is superior at smaller Bragg's values. The whole of the above discussion assumes, however, that the background radiation, which was (according to Kratky and Leopold⁽¹⁸⁾) much stronger for the Bonse-Hart collimation, can indeed be drastically reduced with the measures suggested by Deutsch.⁽¹⁹⁾ So far, no real measurements have been carried out with the new system, but its potentials for high-resolution investigations need serious consideration.

E. The Glass Camera of Schnabel, Hosemann and Rode⁽²⁰⁾

These authors have described a new type of small angle camera. Following an older suggestion by Damaschun *et al.*⁽²¹⁾ they use a polished, totally reflecting glass plate as a monochromator; a second glass plate shields the plane of observation from background radiation. The primary beam is limited only by the width of the microfocus and by the slit between the two glass blocks.

The authors report comparative tests between their instrument and the block camera described above, using 20 μm and 60 μm entrance slits on both instruments. They find that the glass camera yields a 4,2 times more intense

primary beam with a 20 μm entrance slit, while the block camera is better by a factor of 2 when a 60 μm entrance slit is used.*

F. The Cone Camera

Many proteins have very weak subsidiary maxima in the tail end of their scattering curve. Exact knowledge of position and height of these maxima is very important for a reliable determination of particle shape (in the case of non-spherical molecules) or radial electron distribution (for spherical particles). The collimation effect introduced by slit cameras ("slit length smearing") levels such weak maxima and it is difficult to obtain them quantitatively correct from the desmearing procedure.

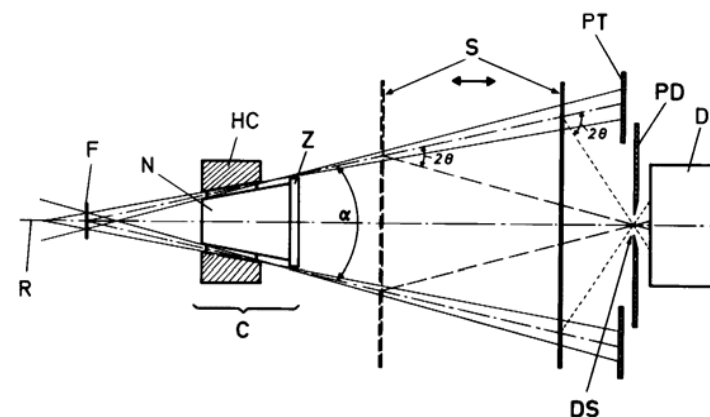


FIG. 13. Schematic drawing of the "cone camera". Dimensions in the vertical direction are greatly enlarged.

For such problems the "cone camera"⁽²²⁾⁽²³⁾ can be useful: its rotationally symmetric collimation system (Fig. 13) collimates a primary beam that has the form of a cone shaped shell. The camera consists of a hollow, truncated cone *HC* and a conical needle *N*, which are both concentric with the rotation axis *R*. The needle is held inside the hollow cone by very small pins. It extends into the cylindrical body *Z*, which serves for the elimination of parasitic scattering. The primary beam penetrates the flat sample *S* adjusted perpendicular to the cone axis and hits the primary beam trap *PT* consisting of a circular screen. Radiation scattered to the angle 2θ enters into the pinhole diaphragm *PD* and is recorded by the detector *D*. The angle 2θ is changed by a shift of the sample along the

* This camera is obtainable from Robert Huber, D-8211 Rimsting, West-Germany.

camera axis to any point between collimation system and pinhole diaphragm. Two possible positions of the sample and the corresponding scattering angle 2θ are indicated in the figure.

The observed intensity is affected by a moderate collimation effect of the kind known as slit width smearing in the case of line shaped primary beams. For its mathematical elimination we refer to Kratky *et al.*⁽²³⁾

At present, this camera is only suitable for measurements in the tail end of the scattering curve, since very small opening angles of the collimation system are mechanically not feasible. The present version allows a variation of the Bragg spacing between 7.7 and 65 Å.

Encouraging results have so far been obtained in the application of this camera to the study of high polymers⁽²⁴⁾ and biological macromolecules in solution.⁽²⁵⁾

IV. Monochromatization

Quantitatively correct interpretation of diffuse small angle X-ray experiments requires the knowledge of the scattering curve corresponding to monochromatic radiation. Polychromatic effects have to be eliminated, either experimentally or numerically. The following methods are in use:

- (1) Pulse height discriminator alone or combined with a K_β -filter.
- (2) Pulse height discriminator combined with numerical elimination of the K_β -contribution.
- (3) Balanced filters.
- (4) Crystal monochromator (Bragg reflection), either in the incident or in the diffracted beam.
- (5) Totally reflecting mirror, usually consisting of a carefully polished glass plate.
- (6) Numerical elimination of polychromatic effects.

In the following, each method will be briefly discussed.

A. Pulse height discriminator, alone or combined with a K_β -filter

So far, this seems to be the most widely used method. The pulse height discriminator (Chapter 3. III), which is tuned to the K_α -line, is connected to a proportional or scintillation counter. The efficiency in suppressing white radiation is inversely related to the channel width. The wavelength of the K_β -line is too close to the K_α -wavelength to be sufficiently attenuated by the pulse height discriminator alone (for example: $\lambda(\text{Cu}K_\alpha) = 1,54 \text{ \AA}$; $\lambda(\text{Cu}K_\beta) = 1,39 \text{ \AA}$). This necessitates the use of a K_β -filter. In the following, the discussion will be

limited to copper radiation, for which the K_β -filter consists of a nickel foil. The absorption edge of nickel lies between the $\text{Cu}K_\alpha$ and the $\text{Cu}K_\beta$ wavelengths; thus nickel absorbs K_β much stronger than K_α . Usually, a $10 \mu\text{m}$ thick nickel foil is quite suitable. Since such a filter attenuates the K_α -radiation by a factor of 0.67, many workers refrain from the use of a Ni-filter. In fact, this introduces only a small error in the scattering curve: the influence of the K_β -radiation is, at least partially, compensated by wavelengths longer than K_α which, due to their higher absorption, are counted more efficiently than shorter waves.

B. Pulse Height Discriminator Combined with Numerical Elimination of the K_β -contribution

Zipper⁽²⁶⁾ has shown how the influence of the β -line can be eliminated numerically. This method avoids intensity losses through absorption by the β -filter. It requires knowledge of the intensity ratio γ between K_β and K_α , which is determined from several intensity measurements.

If γ is known, the numerical monochromatization can be performed simultaneously with the desmearing procedure. (Glatter⁽²⁷⁾).

C. Balanced Filters

This monochromatization technique by Ross⁽²⁸⁾ requires two exposures with different filters in front of the collimation system, under otherwise identical conditions. For copper radiation, the two filters consist of nickel and cobalt, respectively. The wavelength of the absorption edge of cobalt ($\lambda = 1,604 \text{ \AA}$) is slightly above the $\text{Cu}K_\alpha$ wavelength, the one of nickel ($\lambda = 1,483 \text{ \AA}$) just below. Let T_{Ni} be the thickness of the nickel filter and T_{Co} the one of the cobalt filter; we call the two filters "balanced" if $T_{\text{Ni}}/T_{\text{Co}} = 1/1,0711$. Under this condition, subtraction of the two scattering curves leaves only the contribution from radiation whose wavelength lies between the two absorption edges. Contributions from radiation with $\lambda < 1,483 \text{ \AA}$ and with $\lambda > 1,604 \text{ \AA}$ cancel. Since the total intensity of continuous radiation in this narrow range is negligible compared to the $\text{Cu}K_\alpha$ intensity, the difference curve can be regarded as monochromatic. The maximum intensity is obtained with $T_{\text{Ni}} = 6,99 \mu\text{m}$ and $T_{\text{Co}} = 7,48 \mu\text{m}$.

In spite of its conceptual ingenuity, this technique is used relatively seldom due to experimental difficulties: two measurements must be performed under strictly identical conditions. In particular, the time-integral over the primary intensity (i.e. the total energy) has to be identical for both measurements. Methods for the preparation of suitable metal foils for copper radiation have been described.⁽²⁹⁾ For molybdenum radiation, the pair consists of one Zr and

one Y (or Sr) filter. Practicable methods for the preparation of filters of correct thickness were described for Zr⁽²⁹⁾ and Sr⁽³⁰⁾.

D. Crystal Monochromator, in the Incident or Diffracted Beam

In the majority of applications, the monochromator crystal is positioned in front of the collimation system, so that the sample is hit only by the purely monochromatic radiation. We refer to the exhaustive description of several types of monochromators,^{(31),(32),(33)} including the flat quartz monochromator, the bent quartz plate (Johann) and the monochromator consisting of a bent quartz plate whose surface is ground to twice the bending curvature (Johannson).

Several arrangements for the use of monochromators have been described in the literature, viz. by Damaschun *et al.*,⁽²¹⁾ Guinier,⁽³⁴⁾ Fankuchen,⁽³⁵⁾ Luzzati *et al.*^{(36),(37)} and by Pessen *et al.*⁽³⁸⁾. An interesting combination of a Johannson monochromator with a Cauchois-transmission monochromator was described by Jagodzinski and Wohlleben⁽³⁹⁾ in their camera for film detection.

The biggest disadvantage accompanying the use of most crystal monochromators (e.g. quartz) is the considerable loss in intensity. Sparks⁽⁴⁰⁾ was able to demonstrate that hot-pressed pyrolytic graphite is a highly efficient X-ray monochromator, which largely overcomes this drawback. Hendricks⁽⁴¹⁾ was the first who introduced this monochromator into the field of small angle scattering and who extensively tested its suitability. Graphite is favourable for small angle scattering because its mosaic spread roughly equals the divergence desired for the primary beam in the plane perpendicular to the longitudinal direction of the entrance slit.

Contrary to previously used set-ups, Hendricks⁽⁴¹⁾ recommends mounting the monochromator behind the detector slit. A completely polychromatic primary beam thus penetrates the sample; only the scattered radiation hits the monochromator, which reflects the monochromatic component into the detector. The detector slit moves as usual on the perimeter of a circle whose centre is the sample axis. Monochromator crystal and detector are rigidly attached to the detector slit.

Whenever radiation-sensitive samples are under investigation, it is more favourable to mount the monochromator in front of the camera. Hendricks' technique, on the other hand, is preferable if the sample emits fluorescent radiation, e.g. if copper radiation is used and the sample contains iron. This fluorescent radiation will be completely eliminated by the monochromator behind the detector slit, while it would be registered if the monochromator is in front of the sample. Another advantage of Hendricks' arrangement is, in any case, the simpler alignment of camera and monochromator.

E. Totally Reflecting Mirrors

Damaschun *et al.*⁽²¹⁾ have demonstrated, that reflection from a carefully polished glass surface is a practicable monochromatization technique for small angle investigations. Figure 14 shows the arrangement of the reflector, combined with the collimation system described by Kratky, and Kratky and Skala.^{(9),(10)} The characteristic radiation retains 90% of its intensity, but reflection does not yield completely monochromatic radiation. For many applications, however, the degree of monochromatization is sufficient.

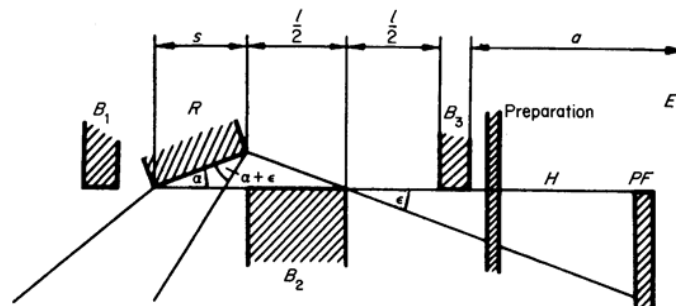


FIG. 14. Monochromatization according to Damaschun *et al.* by total reflection at a glass plate R.

F. Numerical Elimination of Polychromatic Effects

It is convenient to determine the spectral composition in the primary beam with the help of a small X-ray spectrograph, which is inserted in front of the counter tube. The monochromatic scattering curve free of polychromatic and convolutional distortions can be obtained numerically (Glatter⁽²⁷⁾) from the primary beam profile (in length and width directions) and from the spectral composition. This procedure combines the advantage of the full direct beam with complete monochromatization. In view of this advantage, the time required for the determination of the spectral composition should be negligible.

V. Absolute Intensity

Experimental determination of the molecular weight, the mass per unit length of elongated particles, the mass per unit area of flat particles and the volume fractions in multi-phase systems requires knowledge of the absolute intensity, i.e. the ratio of scattered intensity to primary intensity (see Chapter 4, eqns 49, 54, 58, 77). While the scattered intensity can be directly determined with

commercially available instruments (see Chapter 3.III), direct determination of the primary intensity is not possible due to the rapid succession of quanta in the primary beam which cannot be resolved even with the most advanced detectors.

Several methods have been described to overcome this difficulty. First, we mention Luzzati's method,^{(42),(43),(44)} which was developed mainly for copper radiation. It involves the determination of the absorption of several thin nickel foils, which are then stacked to yield sufficiently strong attenuation of the primary beam by several orders of magnitude. The individual filters of such a stack have to be calibrated very carefully, since errors in the absorption of individual filters may add up. The method requires strictly monochromatic radiation, since even a small contamination with short-wavelength radiation will lead to large errors due to the strong inverse dependence of absorption and wavelength. Thus, Luzzati's filter method can be used only in combination with crystal monochromatization of the primary beam.

At the same time, a method was introduced which involves a defined mechanical attenuation of the primary beam.^{(45),(46)} The instrument, which was called the "rotator", uses the principle of a sector diaphragm. Although the method was only used in few laboratories, it has served as a convenient instrument to calibrate *secondary standards*,⁽⁴⁷⁾ which are today in wide use.

Such a secondary standard consist of a platelet of polyethylene ("Lupolen" 1811M of the Badische Anilin & Soda-fabrik), whose absolute intensity, i.e. the quotient of scattered and primary intensity, is determined for an angle of 0,01603 radians (corresponding to a Bragg spacing of 150 Å). Rapid and simple determinations of the primary intensity are then possible in every laboratory with access to such a calibrated Lupolen. It should be noted at this point, however, that the quotient in absorption between secondary standard and sample under investigation has to be allowed for, i.e. the user has to measure the absorption of his sample, while the determination of the absorption of the Lupolen standard is part of the calibration procedure.

The question was raised whether radiation effects and varying temperature might change the scattering behaviour of Lupolen. A systematic investigation⁽⁴⁸⁾ showed that, between 4°C and 30°C, the temperature effect is strictly reversible and the scattering power increases 1% per 1°C. In the course of another study, it could be shown that a very high dose of X-rays (a high multiple of the dose applied in the course of many years' normal use) did not lead to any detectable change in scattered intensity.⁽⁴⁹⁾

These positive results are confirmed and supplemented by an interesting study by Schaffer and Hendricks.⁽⁵⁰⁾ They demonstrated how one can determine a calibration constant for Lupolen which is independent of collimation condition and wavelength.

The recently developed "Moving Slit Method"⁽⁵¹⁾ offers another alternative

method for the direct determination of the primary energy. Like the "Rotator Method" it is based on a defined mechanical attenuation of the primary beam. Two slits are installed perpendicular to the plane of the primary beam; the one with width L_r is located in the plane of registration, the other one (width L_f) is located near the focus. The second slit can be moved with velocity v across the length of the beam. The primary intensity P_0 (energy $\text{cm}^{-1} \text{s}^{-1}$ of the primary beam) can then be calculated from

$$P_0 = \frac{N \cdot v}{L_f \cdot L_r} \quad (1)$$

where N is the number of quanta reaching the counter during one passage of slit L_f . This determination is usually carried out with the sample inserted at its usual position, in which case P_0 already contains the sample absorption.

With L_r and L_f in the order of 10^{-2} cm (which can be determined with sufficient accuracy under a microscope) and the velocity v around $0,1 \text{ cm s}^{-1}$ (controlled by a step motor), one typically obtains a count N between 10 000 and 100 000 in the 10s required for one passage of slit L_f . Thus, the corresponding count rate is well within the time resolution of a proportional counter and the determination is unaffected by coincidence errors. The determination can be repeated to reduce the error from counting statistics. In any case, the time required for one determination of the primary intensity is in the order of 60s. It is, therefore, straight forward to determine the primary intensity before and after each scan through the region of scattered intensity, which not only yields the absolute intensity but may also indicate primary intensity fluctuations.

Several authors have also developed *primary standards*.⁽⁵²⁾ They consist of well defined samples for which the ratio of primary intensity and scattered intensity can be evaluated theoretically. A particularly carefully developed method is the one of Beeman,^{(53),(54)} Schaffer⁽⁵⁵⁾ and Katz,⁽⁵⁶⁾ which uses the scattering of various gases (C_4F_8 , SF_6 and CCl_2F_2). Another method by Patel and P. Schmidt⁽⁵⁷⁾ is based on Silica Gel as scatterer, and still another one (P. H. Hermans *et al.*) uses Goldsol.⁽⁵⁸⁾ The latter method is based on the experimental determination of the invariant, which is related to the primary intensity through the mean square fluctuation of the electron density which, in turn, can be calculated from the known composition of the sample (Eqn 77 in Chapter 4). Although the method is conceptually appealing, it is not very accurate due to difficulties in performing a precise experimental determination of the invariant.

None of the techniques using primary standards is used frequently in routine small angle work, mainly because the preparation of the standards is difficult and the measurements are time-consuming. So far, only Luzzati's filter method and the Lupolene method (which, of course, requires the "rotator" for calibration) are in routine use. The moving slit method is still too new to have found widespread application.

When films are used for the recording of radiation (compare Chapters 3.III and 7), the determination of the primary intensity is comparatively simple. A convenient method^{(45),(59)} is to move the film perpendicular to the primary beam's length direction during the exposure of the (unattenuated) beam, thus producing a broad band. The total time of exposition is around 60 s, and the blackening of the resulting image can be conveniently densitometered. Exposition of a stationary film to the direct beam would require very short exposure times (fractions of a second, which is hard to achieve) and has the additional disadvantage of producing an image with very steep flanks, which is difficult to densitometer.

A recently described method for absolute intensity determination by Sassouï, Hosemann and Čačković⁽⁶⁰⁾ also uses a film as a radiation detector: here, the primary beam stopper emits fluorescent radiation, a defined fraction of which hits the film. The method, however, has to be calibrated with a constant radiation source, so that it corresponds to a secondary-standard technique. In the present form, it can only be used in combination with a pinhole camera.

VI. Experimental Elimination of the Effect of Intensity Fluctuations, Monitor

No other type of X-ray scattering experiments requires as stable X-ray sources as small angle investigations: SAXS measurements frequently take many hours, in the course of which the scattered intensity is recorded at many different angles; intensity fluctuations during that time, therefore, lead to a deformation of the observed curve. The stringent requirement for maximum stability in the primary intensity can only be relaxed if a position-sensitive detector (Chapter 3.III) is used, since it records the whole of the scattering curve simultaneously.

The most important reason for intensity fluctuations seems to be the relative movement of the camera with respect to the anode; such a movement may either be caused by mechanical or by temperature effects, which cannot be avoided even by careful stabilization of the room temperature: the X-ray tube, which is heated and cooled at the same time, never allows a constant temperature of the entire system. The suspension of the camera at the top of the X-ray tube near the anode is capable of reducing these effects, as discussed above.

A monitor, however, would be a very useful and important tool if a camera of this type were not at one's disposal, or some other recommended precautions (compare Chapter 3.I, Section I) could not be observed because the necessary equipment was unavailable, or if one is aiming at the very highest precision.

The basic idea of the monitor is to divide the scattered intensity by the (simultaneously recorded) primary intensity or a quantity proportional to it.

This obviously eliminates errors in the scattering curve caused by fluctuations in the primary intensity. Several ways have been suggested and tried for the experimental implementation of this idea.

Chipman and Jennings,⁽⁶¹⁾ and Jennings *et al.*⁽⁶²⁾ use the scattering of a mylar foil in the primary beam as a reference.

Recently, Hendricks *et al.*⁽⁶³⁾ have suggested an arrangement with an ionization chamber within the collimation system.

Another suggestion⁽⁶⁴⁾ involves the use of a Bragg reflection originating from the primary beam stop made from platinum. Becherer *et al.*⁽⁶⁵⁾ record the fluorescence induced by the copper radiation on the iron beam stop. In a modification of this method, cobalt is used instead of iron, since it appears to be more suitable for this purpose:⁽⁶⁶⁾ its absorption edge ($\lambda = 1,608 \text{ \AA}$) lies closest to the wavelength of the CuK_α radiation ($\lambda = 1,54 \text{ \AA}$), and the most intensive fluorescence is obtained.

References

- (1) Herglotz, H. K. (1976). In "Characterization of Materials in Research, Ceramics and Polymers", Chapter 5. Syracuse University Press, Syracuse.
- (2) Herglotz, H. K. (1971). "Advances in X-Ray Analysis" (C. S. Barrett, J. B. Newkirk and C. O. Rund, eds), Vol. 14, 275 pp., Plenum Press, New York.
- (3) Guinier, A. and Fournet, G. (1955). "Small-Angle Scattering of X-Rays", 86 pp. Wiley, New York, and Chapman and Hall, London.
- (4) Bolduan, O. E. A. and Bear, R. S. (1949). *J. Appl. Phys.* **20**, 283.
- (5) Ritland, H. N., Kaesberg, P. and Beeman, W. W. (1950). *J. Appl. Phys.* **21**, 838.
- (6) Anderegg, J. W., Beeman, W. W., Shulman, S. and Kaesberg, P. J. (1955). *J. Amer. Chem. Soc.* **77**, 2927.
- (7) Stasiecki, P. and Stuhrmann, H. B. (1978). *J. Appl. Cryst.* **11**, 1.
- (8) Todo, A., Hashimoto, T. and Kawai, H. (1978). *J. Appl. Cryst.* **11**, 558.
- (9) Kratky, O. (1954 and 1958). *Z. Elektrochem.* **58**, (1954) 49; **62**, (1958) 66.
- (10) Kratky, O. and Skala, Z. (1958). *Z. Elektrochem.* **62**, 73.
- (11) Kratky, O. and Stabinger, H. (in preparation).
- (12) Hendricks, R. W. (1970). *J. Appl. Cryst.* **3**, 348.
- (13) Henke, J. and Schulze, G. E. R. (1957). *Z. Naturforschg.* **12a**, 346.
- (14) Henke, J. and Schulze, G. E. R. (1958). *Exp. Techn. Phys.* **5**, 180.
- (15) Stabinger, H. and Kratky, O. (1979). *Makrom. Chem.* **180**, 2995.
- (16) Bonse, U. and Hart, M. (1967). In "Small-Angle X-Ray Scattering" (H. Brumberger, ed.), 121 pp. Gordon & Breach, New York.
- (17) Bonse, U. and Hart, M. (1965). *Appl. Phys. Lett.* **6**, 155.
- (17a) Dwiggins, C. W. (1980). *J. Appl. Cryst.* **13**, 572.
- (18) Kratky, O. and Leopold, H. (1970). *Makrom. Chem.* **133**, 181.
- (19) Deutsch, M. (1980). *J. Appl. Cryst.* **13**, 252, 256.
- (20) Schnabel, E., Hosemann, R. and Rode, B. (1972). *J. Appl. Phys.* **43**, 3237.

- (21) Damaschun, G. (1964 and 1965). *Naturwiss.* **51**, (1964) 378; *Exp. Technik der Physik III* (1965), 224.
Damaschun, G., Kley, G. and Miller, J. J. (1968). *Acta Physica Austriaca* **28**, 223.
- (22) Kratky, O. *Mh. Chem.* **100**, (1969) 376; **100**, (1969) 1788.
- (23) Kratky, O., Stabinger, H., Wrentschur, E. and Zipper, R. (1976). *Acta Phys. Austriaca* **44**, 173.
- (24) Lederer, K., Klapp, H., Zipper, P., Wrentschur, E. and Schurz, J. (1979). *J. Polymer Sci., Polymer Chem. Ed.* **17**, 639.
- (25) Zipper, P. and Durchschlag, H. (1978). *Eur. J. Biochem.* **87**, 85.
- (26) Zipper, P. (1969). *Acta Phys. Austriaca* **30**, 143.
- (27) Glatter, O. (1977). *J. Appl. Cryst.* **10**, 415.
- (28) Ross, P. A. (1928). *J. Opt. Soc. Amer.* **16**, 433.
- (29) Phelps, C. G. and Craig, B. G. (1963). *Rev. Sci. Instr.* **34**, 812.
- (30) Becherer, G., Herms, G. and Motzfeld, V. (1965). *J. Scient. Instr.* **42**, 754.
- (31) Guinier, A. and Fournet, G. (1955). "Small-Angle Scattering of X-Rays", 96 pp. Wiley, New York and Chapman and Hall, London.
- (32) Beeman, W. W., Kaesberg, P., Anderegg, J. W. and Webb, M. B. (1957). In "Handbuch der Physik" (S. Flügge, ed.) Vol. 32, 365 pp. Springer-Verlag.
- (33) Witz, J. (1969). *Acta Cryst.* **A25**, 30.
- (34) Guinier, A. (1946). *C.R. Acad. Sci.* **223**, 31.
- (35) Fankuchen, I. (1937). *Nature (London)* **139**, 193.
- (36) Luzzati, V. (1960). *Acta Cryst.* **13**, 939.
- (37) Luzzati, V., Witz, J. and Baro, R. (1963). *J. Phys. (Paris) Suppl.* **24**, 141.
- (38) Pessen, H., Kumosinski, T. F. and Timasheff, S. N. (1971). *J. Agr. Food. Chem.* **19**, 698.
- (39) Jagodzinski, H. and Wohlleben, K. (1960). *Z. Elektrochem. Ber. d. Bunsenges. f. phys. Chem.* **64**, 212.
- (40) Sparks, C. J. (1966). Metals and ceramics. *Div. Ann. Progr. Rept. RNL-3970*, 57.
- (41) Hendricks, R. W. (1970). *J. Appl. Cryst.* **3**, 348.
- (42) Luzzati, V. (1960). *Acta Cryst.* **13**, 939.
- (43) Luzzati, V., Witz, J. and Baro, R. (1963). *J. Phys. (Paris) Suppl.* **24**, 141A.
- (44) Pessen, H., Kumosinsky, T. F., Timasheff, S. N., Calhoun, R. R. Jr. and Connelly, J. A. (1970). *Advan. X-ray Anal.* **13**, 622, 626.
- (45) Kratky, O. *Makrom. Chem.* **35A** (1960), 12. *Z. analyt. Chem.* **201** (1964), 161.
- (46) Kratky, O. and Wawra, H. (1963). *Mh. Chem.* **94**, 981.
- (47) Kratky, O., Pilz, I. and Schmidt, P. J. (1966). *J. Colloid Interface Sci.* **21**, 24.
- (48) Pilz, I. (1969). *J. Colloid Interface Sci.* **30**, 140.
- (49) Pilz, I. and Kratky, O. (1967). *J. Colloid Interface Sci.* **24**, 211.
- (50) Schaffer, L. B. and Hendricks, R. W. (1974). *J. Appl. Cryst.* **7**, 156.
- (51) Stabinger, H. and Kratky, O. (1978). *Makrom. Chem.* **179**, 1655.
- (52) Weinberg, D. L. (1963). *Rev. Sci. Instr.* **34**, 691.
- (53) Beeman, W. W. (1965). In "Small-Angle X-Ray Scattering" (H. Brumberger, ed.), 197 pp. Gordon and Breach, New York.
- (54) Shaffer, L. B. and Beeman, W. W. (1970). *J. Appl. Cryst.* **3**, 379.
- (55) Shaffer, L. B. (1964). Ph. D. Thesis, University of Wisconsin.
- (56) Katz, L. (1959). Ph. D. Thesis, University of Wisconsin.
- (57) Patel, I. S. and Schmidt, P. W. (1971). *J. Appl. Cryst.* **4**, 50.
- (58) Hermans, P. H., Heikens, D. and Weidinger, A. (1959). *J. Polym. Sci.* **35**, 145.
- (59) Kratky, O. (1963). *Progress In Biophysics* **13**, 105.
- (60) Sassou, M., Hosemann, R. and Čačković, H. (1979). *Z. f. Krist.* **150**, 199.
- (61) Chipman, D. R. and Jennings, L. D. (1963). *Phys. Rev.* **132**, 728.
- (62) Jennings, L. D., Chipman, D. R. and De Marco, J. J. (1964). *Phys. Rev. A* **135**, 1612.
- (63) Hendricks, R. W., De Lorenzo, J. T., Glass, F. M. and Zedler, R. E. (1972). *J. Appl. Cryst.* **6**, 129.
- (64) Kratky, O., Leopold, H., Pilz, I. and Seidler, H. P. (1971). *Z. angew. Physik* **31**, 49.
- (65) Becherer, G., Zicker, K. and Kranold, R. (1972). *Experimentelle Technik der Physik* **20**, 259.
- (66) Kratky, Ch., Kratky, O. and Wrentschur, E. (1975). *Acta Phys. Austriaca* **41**, 105.

3.II

Instrumentation. Point Collimation and Synchrotron Radiation

K. C. HOLMES

Max-Planck-Institut für Medizinische Forschung, Heidelberg, W. Germany

I.	Experimental design	85
A.	Point collimation	85
B.	Synchrotron radiation	87
C.	X-ray optics	90
D.	Detectors	92
II.	Small angle cameras for synchrotron radiation	93
A.	Remote control	93
B.	Curved mirrors	94
C.	Curved crystal monochromators	95
D.	Mirror-monochromator camera at DESY	96
E.	Mirror-monochromator camera at NINA	98
F.	Mirror-monochromator camera at SPEAR	98
G.	Monochromator-mirror camera at V'EPP-3	99
H.	Mirror-monochromator cameras at DORIS	99
I.	Separated function focusing monochromator at SPEAR	99
III.	Extension of the methodology	100
A.	The possibility of using a wider band-pass	100
B.	Towards an optimum design	101
	References	102

I. Experimental Design

A. Point Collimation

As has been discussed in Chapter 3.I, in the majority of small angle scattering studies of solutions it is advantageous to use slit collimation as compared with

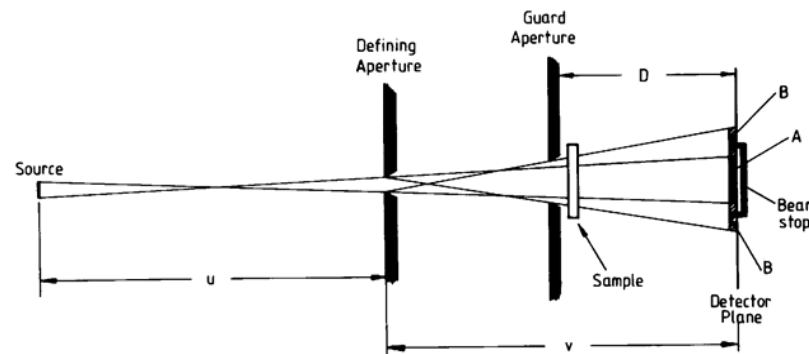


FIG. 1. Diagram showing the geometry of a point collimation camera. The angular resolving power is given by the diameter (A) of the collimated beam at the detector plane. The smallest angle of observation is determined by the diameter (B) of the penumbra produced by the guard aperture immediately in front of the specimen. The parameters u , v and D will be chosen to optimize the intensity for a given case (see, for example, Hendricks, 1978).

point collimation because of the considerable gain in X-ray flux. Slit collimation, however, leads to difficulties at small angles, where the form of the aperture is convoluted with the profile of the required scattering curve. If the accurate form of the scattering curve is required for detailed analysis it is advantageous to use point collimation. Point collimation is most easily achieved by the use of a point source and two round apertures. The first aperture defines the beam and the second limits the scatter from the first aperture (Fig. 1). Two criteria define the resolution of the system:

- (1) the smallest angular approach to the main beam which can be achieved before encountering scatter from the defining apertures;
- (2) the angular resolution of the instrument.

In low angle scattering applications the second criterion is, on the whole, less critical than the first. Optimum performance is usually achieved with the guard aperture about mid-way between the defining aperture and the detector. To achieve reasonable speed of data collection it is necessary to integrate over circles in the detector plane. In practice this is conveniently done by means of a two-dimensional gas counter.

The nature of the apertures deserves comment: in the simplest case these would be pinholes in an appropriately dense material, electron microscope apertures turn out to be very good for the purpose. In the case of normal X-ray diffraction cameras intended for crystal diffraction, such apertures are mounted colinearly in a brass tube about 10 cm long. However, the angle of closest approach to the direct beam for such systems is usually about 2° making such collimators unsuitable for low angle scattering. Better low angle performance is achieved by making the system longer, however longer systems are difficult

to align so that such systems are often based on mutually perpendicular slits rather than round apertures. The apertures should be made out of a suitable hard dense material (e.g. dental gold) which does not fluoresce in the radiation being used. The apertures must be carefully aligned with each other and must be shaped so as to avoid reflection from the surfaces in the beam. Normally, the required accuracy of alignment is achieved by mounting the apertures on an optical bench. Provision for evacuating the beam path (or for using helium filled tubes) must be made. This requirement can complicate the design considerably because it is not desirable to have X-ray windows close to the sample. A vacuum camera incorporating carefully made round (pinhole) apertures is marketed by Anton Paar K.G. (Graz).

The use of the characteristic scattering from an X-ray tube without a monochromator exacerbates the problem of parasitic scattering. To reduce scattering one can use a graphite monochromator or one can employ focusing monochromators.

A further consideration in the design of point collimation cameras is scale. If the size of the sample is not limiting then it is usually advantageous to make the system as big as possible (this would not be true if one were employing film as a detector, but film is not very suitable for low angle scattering on account of its limited dynamic range). A consideration working against this strategy is the fact that X-ray tubes become more brilliant the smaller the source. In practice the small brilliant source is better suited to use with focusing optics. Analyses of the optimum strategies have been given by Hendricks (1978) and by Rosenbaum and Holmes (1980). A highly developed system making use of conventional sources (high power rotating anode tubes) is the ORNL 10 meter camera at Oak Ridge (Hendricks, 1978).

With the use of focusing elements such as curved mirrors and curved monochromators it is possible to achieve much higher fluxes than can be achieved with simple collimation but often at the cost of high parasitic scatter from the unguarded surfaces of the optical elements. The guarding can be achieved by making the apertures small, but with a concomitant loss of flux. However, the introduction of synchrotron radiation sources has dramatically altered the design possibilities for point focus cameras. The excellent optical properties and the high intensity lend themselves to the production of point focused beams with small numerical aperture so that the construction of long well-guarded cameras is possible. This has led to a renewed interest in X-ray optics and X-ray optical elements. A review of current small angle scattering using synchrotron radiation has been given by Stuhrmann (1978).

B. Synchrotron Radiation

The special properties of a synchrotron radiation source are:

- (a) very high intensity; (b) very good intrinsic collimation; (c) the source is white;

(d) the radiation is emitted in pulses a few tenths of a nanosecond long with a repetition frequency of a megahertz.

A general description of synchrotron radiation has been given in a number of texts (e.g. Godwin, 1969). The most pertinent properties are summarized below.

In an electron synchrotron or storage ring the electrons (or positrons) travelling at very high speeds are constrained in a circular trajectory by means of electromagnets. Accelerated charges radiate energy. The electrons are subjected to a strong centripetal acceleration in each bending magnet. The strength of the radiated field is proportional and parallel to the second derivative of the vector joining the observer to the moving charge. Since the electrons are travelling at essentially the speed of light, in evaluating the radiated field one must take account of the time it takes a signal (potential) leaving the electron and travelling with the speed of light to reach the observer. A diagram of the situation is given in Fig. 2a. The points A, B, C and D represent the position of an electron on a circular trajectory at equal time intervals.

The circles a, b, c and d are the boundaries of propagation of information about events A, B, C and D (retarded potentials). The boundaries bunch together along lines which are tangent to the electron trajectory. A graph of the apparent lateral displacement as a function of time is a hypercycloid (Fig. 2b). The amplitude of the radiated wave is proportional to the second derivative of this curve. At the cusp of the hypercycloid the second derivative reaches a high value for a very short time (in more pictorial terms the electron appears and disappears very suddenly). Typically, the pulse of radiation has a duration of 10^{-18} s. From the length of the pulse one can evaluate the spectral distribution and one finds that the maximum is in the X-ray region. The first full theoretical treatment was given by Schwinger (1949). Using Schwinger's formula one may evaluate the spectral distribution and intensity for mono-energetic electrons at various energies. A useful parameter of synchrotron radiation is the critical wavelength λ_c . The dependence of λ_c on the radius of curvature (R) and energy (E) is

$$\lambda_c = 5.59RE^{-3} \quad (1)$$

(These and the following formula are taken from the review article by Godwin (1969).) The maximum power is found at

$$\lambda_{\max} = 0.42\lambda_c \quad (2)$$

Near λ_{\max} we have the approximate relationship for the intensity

$$I = 9 \times 10^{-24} \gamma^2 R^{-3} \quad (3)$$

The parameter γ (the ratio of the relativistic to rest mass of the electron) is given by

$$\gamma = 1890E \quad (4)$$

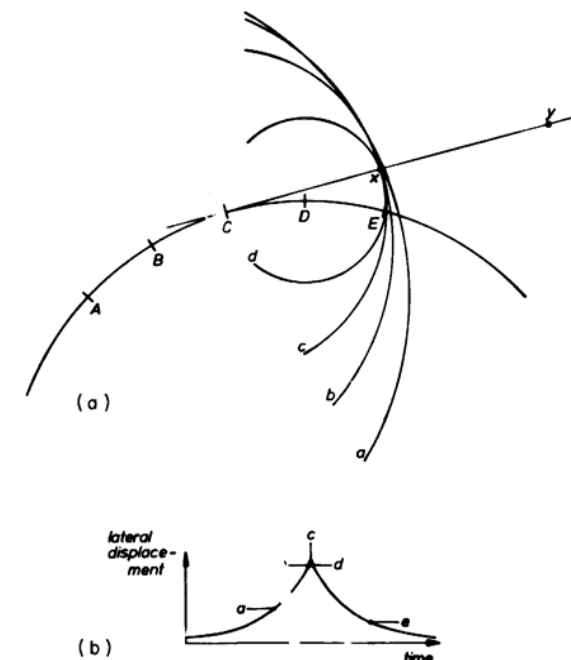


FIG. 2. (a) $ABCDE$ represents the curved trajectory of an electron travelling with a speed very close to the velocity of light. The circles a, b, c, d are the boundaries of propagation of information about the events $ABCD$. They spread out with the velocity of light and because of the very high speed of the electron they bunch together along tangents to the electron trajectory (e.g. XY). (b) A graph of the lateral position of the electron as a function of time as it appears to the observer at the point X . The information that the electron was at A is available only a short while before the information that the electron is at B, C or D . To the observer these three events apparently occur at about the same time. The information that the electron is at E arrives later. Therefore the electron appears and disappears very suddenly. The radiated electromagnetic field is proportional to the second derivative of the apparent displacement so that the electron gives rise to a very short pulse of radiation as it comes into the tangent position with respect to the observer.

(Note that for these equations, the units of measurement are $R(\text{m})$, $E(\text{GeV})$, $I(\text{erg s}^{-1} \text{\AA}^{-1} \text{electron}^{-1})$.)

Equation (3) demonstrates the great sensitivity of the emitted intensity to the electron energy. The angular spread of the beam is approximately $\pm 1/\gamma$ [i.e. about ± 0.12 mrad at 5 GeV]. Thus the beam travels along a line which is tangent to the instantaneous electron path. The vertical divergence of the beam ($1/\gamma$) is very small.

A special property of the synchrotron source is the correlation between the direction of emission and position in the plane of the source. This is due to the fact that the trajectories of the electrons in the ring are themselves part of an optical system. Moreover, because of the collinearity of the electron and the

emitted radiation the electron trajectories are essentially part of the external optical system. Therefore, the electron paths must be included in a consideration of the optical properties of the source (Hastings, 1977). This is done by considering the luminosity (B) as a function of position and angle in an optical phase space (Green, 1976; Hastings, 1977). Compared with conventional sources the unusual property of synchrotron radiation is that the source is virtual and astigmatic. The apparent dimensions of the X-ray source (S_x, S_y) are the widths of the luminosity functions at some virtual source points. In practice one has to establish empirically where the source points are. The use of a pair of cylindrical lenses for the X-ray optical system allows the correction of the astigmatism of the source.

The average luminosity (\bar{B} photons per unit solid angle per unit area per wavelength interval) is an invariant of the system: all non-lossy optical elements leave this quantity unaltered – it can only be degraded. This result can be obtained by applying Liouville's theorem to the function B in the optical phase space. The average luminosity is calculated by taking the total number of photons emitted per unit wavelength interval per radian in the $x-y$ plane and by dividing this number by the area of the *virtual* source (S_x, S_y) and by the apparent angle of vertical divergence.

C. X-ray Optics

1. THE OPTICAL ELEMENTS

The most readily obtainable X-ray focusing elements of sufficient perfection to be used with synchrotron radiation are cylindrical lenses: curved mirrors used at grazing incidence and curved crystal monochromators used at small Bragg angles. A review of curved mirrors and curved crystal monochromators for conventional sources has been given by Witz (1969). Curved crystal monochromators behave as mirrors when used with white radiation so that the two classes of focusing elements can be treated in a unified way. Monochromators have the extra property that a variation in the glancing angle θ (the Bragg angle) leads to a variation in the reflected wavelength.

The combination of a curved mirror at right angles to a curved monochromator was introduced for conventional X-ray sources by Huxley and Holmes (see Huxley and Brown, 1967) in their investigations of scattering from muscle fibres and was introduced for synchrotron radiation by Barrington Leigh and Rosenbaum (1974). For many applications this turns out to be the best combination.

Most of the electrons in atoms behave as if they were free when illuminated with X-radiation. As a result the refractive index of solids for X-rays is slightly less than unity and total external reflection can be observed from polished

surfaces at grazing angles of incidence. Typically the critical grazing angle for total external reflection (θ_c) lies between 3 mrad and 10 mrad. Electron dense materials have a larger θ_c but have also higher absorption, which leads to the critical reflection phenomenon becoming unsharp. The surface of the mirror must be very well polished (Franks and Breakwell, 1974). A very good optical finish on fused quartz or glass is necessary. Polished metals are not sufficiently flat. However, metal surfaces can be prepared by vacuum deposition on polished quartz or glass.

Perfect single crystals which show total primary extinction are used as monochromators. The importance of using perfect single crystals rather than mosaic crystals is that they give *specular* reflection essentially without dispersion within the narrow range of wavelengths allowed by dynamical theory. Mosaic crystals degrade the luminosity of synchrotron radiation because they are dispersive and only in special circumstances can a mosaic monochromator such as graphite be successfully employed.

2. THE FOCUSING CONDITION

Rays emanating from a source S are focused by a curved mirror or monochromator $MO'M$ (Fig. 3) to a focus I . For a mirror the glancing angle of incidence (θ) must be equal to the glancing angle of reflection. For a monochromator it is usual to cut the surface of the crystal at an angle σ to the Bragg planes (Guinier, 1946) so that the glancing angle of incidence is $\theta + \sigma$ and the glancing angle of reflection is $\theta - \sigma$. One obtains

$$2/R = \sin(\theta - \sigma)/v + \sin(\theta + \sigma)/u \quad (5)$$

and

$$\theta = z/2 \{\sin(\theta - \sigma)/v + \sin(\theta + \sigma)/u\}, \quad (6)$$

If $\sigma = 0$ (mirror or symmetrical monochromator) (5) becomes

$$2/R \sin \theta = 1/u + 1/v \quad (7)$$

For symmetrical curved crystal monochromators used with monochromatic radiation the Bragg law imposes the additional constraint $u = v$, whereupon (7) becomes

$$u = v = R \sin \theta \quad (8)$$

Equation (8) is the Johann focusing condition (Johann, 1931).

For a long mirror u and v are different for the two ends of the mirror so that the mirror should be appropriately shaped in order to bring the ray bundle to a focus at I . For exact on-axis focusing we require the general point A to lie on an ellipse (with foci S and I) generated by

$$u + v = u_0 + v_0 \quad (9)$$

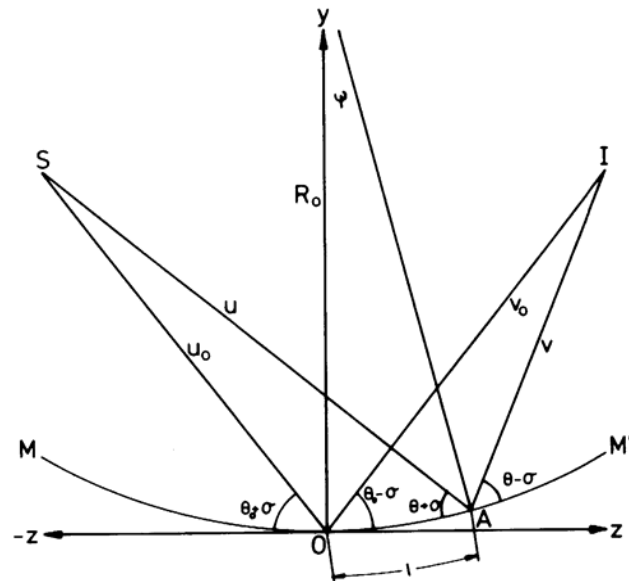


FIG. 3. Focusing geometry: rays emanating from S are focused to I by the mirror or monochromator $M'M'$. The radius of curvature of the mirror (monochromator) is R_0 . The angle of incidence on the mirror is $\theta + \sigma$, the angle of reflection is $\theta - \sigma$. For a mirror $\sigma = 0$.

For any curve not satisfying Eqn (9) the elements of the mirror will not focus to the same point but will produce a caustic image (spherical aberration).

D. Detectors

Four kinds of detectors have been used with synchrotron radiation: X-ray film, T.V. detectors, one-dimensional position-sensitive proportional counters (PSDs), and multi-wire proportional chambers (MWPCs) as area detectors. The characteristics of the detector are important in determining experimental design. In all cases where the detector or the environment of the detector imposes a high background it is necessary to maximize intensity rather than flux. Detectors have typically between 250 and 1000 resolution elements along an axis.

X-ray film is the simplest detector to use: it has very good spatial resolution; quantum efficiency is high; data storage is easy. Measuring the optical density (O.D.) is relatively simple and straightforward. The O.D. has virtually the same statistics as grain counting (Arndt, 1977). Unfortunately, the dynamic range of film is limited which makes it difficult to use for low angle scattering. Other disadvantages of film include the fact that it is difficult to use for time resolved studies and that it has an intrinsic fog level equivalent to about 200 000 counts mm^{-2} .

X-ray phosphors ($\text{ZnS}(\text{Ag})$) in conjunction with high sensitivity television tubes have been employed for the registration of X-ray scattering diagrams (Arndt and Gilmore, 1979; Reynolds *et al.*, 1978). Milch (1979) has used a silicon intensified target vidicon (SIT-vidicon) coupled to the phosphor by a fibre optics face plate to study the scattering from muscle. A raster of 256×256 picture elements (pixels) may be read out from an area of $25 \times 25 \text{ mm}$. On account of the small size of the detector and the relatively high spatial resolution of the system one is required to use a small focal spot. Moreover, on account of the relatively high dark current of this device one is forced to work with a high intensity at the focal plane, which sets limits to the length of the camera.

A number of authors have used PSDs for measurements on muscle or muscle fibres (Vasina *et al.*, 1975; Vasina, 1976; Goody *et al.*, 1976; Podolsky *et al.*, 1976; Baru *et al.*, 1978; Faruqui and Huxley, 1978; Gabriel *et al.*, 1978). Generally, such counters have a low background and good spatial resolution. Moreover, the size of the counter is not critical, making such counters easy to employ. One major drawback has been the saturation count rate. If the counter is employed with an analogue readout system (time-voltage converter + voltage-digital converter) the data rate, which is determined by the electronics, cannot exceed about 50 000 per second *over the whole length* of the counter.

Multi-wire proportional chambers are just beginning to find application in small angle scattering (Baru *et al.*, 1978b; Gabriel *et al.*, 1978). At present the total count rate is limited to 50 000 (or with improved electronics to 10^6) over the whole area of the counter. To use such counters it is necessary to use a relatively large specimen-detector distance ($D > 2 \text{ m}$) and to screen out the centre of the scattering pattern when measuring the weaker parts.

II. Small Angle Cameras for Synchrotron Radiation

A. Remote Control

In the case of synchrotrons the high background radiation levels make it impossible to work in the neighbourhood of the direct or reflected beam. The apparatus must stand in a shielded area which is not available to the experimenter when the beam shutter is open. Thus all normal manipulations such as aligning cameras must be performed by remote control. For storage rings the situation is somewhat better and it is possible to work within the shielding walls. Even so the direct beam is never available to the experimenter so that the primary optical elements which sit in the direct beam must be remotely controlled.

B. Curved Mirrors

In a number of experiments fused quartz (Spectrosil) has been employed as a mirror (Franks and Breakwell, 1974). The general experience with synchrotrons and storage rings has been that deposited metals are unstable when exposed to the primary beam and they have not been widely used. However, Hastings *et al.* (1978) have successfully employed platinum deposited on a fused quartz substrate.

The relationship between the critical grazing angle (θ_c) and wavelength for fused quartz is (Hendrix *et al.*, 1979)

$$\theta_c(\text{mrad}) = 26.3\lambda(\text{nm}) \quad (10)$$

so that θ_c is typically 3–4 mrad. Only wavelengths longer than those given by Eqn (10) can be reflected. In this way the mirror acts as a high frequency filter, which is particularly valuable for eliminating higher harmonics.

To accept the full vertical divergence of the synchrotron radiation at 20 m using a grazing angle of 3 mrad one needs a mirror of length 1.5 m. Typically the radius of curvature of the mirror is 2–4 km. Maintaining such a radius of curvature over such a mirror length presents problems: if the mirror is thick enough to be stable it is too thick to bend. Horowitz and Howell (1972) allowed their mirror to bend under gravity. However, leaving a glass under strain, even its own weight, leads to flow. Webb *et al.* (1977) used a relatively thin mirror and provided frequent adjustable supports. The European schools (Barrington Leigh and Rosenbaum, 1974; Franks and Breakwell, 1974; Hendrix *et al.*, 1979; Haselgrave *et al.*, 1977) have favoured segmented mirrors, each segment being thick enough to be stable against flow but thin enough to be bent. For Spectrosil a thickness of 15–20 mm seems to be the right compromise between stability and flexibility for a 20 cm mirror segment. Longer segments would need to be thicker to retain enough stability against flow and would thereby become too inflexible to be bent. Mirror lengths of 20 cm can be relatively easily manufactured and polished: longer mirrors are very expensive.

Segmented mirrors need well machined mechanical holders to allow their bending and mutual alignment. The bending of each segment is traditionally achieved by pressure on pairs of steel pins separated by 15–20 mm sitting on the back and front surfaces at each end of the mirror (Franks and Breakwell, 1974). The pins on the front face are cut away in the middle to allow the X-ray beam through. This method is not well suited for application to synchrotron radiation since it necessitates placing a steel pin in the direct beam where it fluoresces brightly. Harmsen and Rosenbaum (1979) have used metal plates glued to the ends of the mirror segments to apply the couple. This method of bending has the advantage that both concave and convex bending is possible. In this way possible permanent distortions of the mirrors caused by flow can be compensated.

The radius of curvature of each segment is so small that the detailed nature of the bending achieved (e.g. circle or ellipse) is not important. The heights of the mirrors must be adjustable to allow for their mutual alignment. The precision of this alignment needs to be about 3 μm (Rosenbaum, 1979) in order to overlap the images produced by each mirror segment with a precision of one third of the image diameter. The heights are adjusted to bring the images of the segments into coincidence at the focus. The overall form of the segmented mirror is, therefore, operationally defined and will be elliptical.

C. Curved Crystal Monochromators

The following crystals have been used as monochromators for synchrotron radiation: quartz (10,1 planes); silicon (111 planes); germanium (111 planes); graphite (001 planes). The first three are perfect single crystals with very narrow rocking curves which give specular reflection without appreciable dispersion. Of the three germanium has the widest band-pass and has zero reflectivity for second order components. Germanium is at present the most widely used material. Graphite is a mosaic monochromator with a mosaic spread of *c.* 1/2°. A mosaic monochromator can only be used if the distance between the monochromator and the detector is very short so that the dispersion introduced by the monochromator does not lead to a spreading out of the beam. Bending is often achieved by applying couples to both ends of the crystal slab. When used with synchrotron radiation it is important that no material should be present on the front surface of the monochromator on account of fluorescence. In the DESY camera (Barrington Leigh and Rosenbaum, 1974), steel pins were glued to the back surface of the monochromator. Symmetrical couples at both ends of the crystal were generated by pressure on these pins. A novel method of achieving a cylindrical form has been used by Lemonnier *et al.* (1978). Lemonnier and collaborators make use of the fact that if a plate with the shape of an isosceles triangle is held firmly at the base and a force is applied to the apex, the plate takes up the form of a cylinder.

In the classical form introduced by Johann (1931) curved crystal monochromators have a cylindrical shape and the source, crystal, and focus are symmetrically arranged on the circumference of a circle. The crystal is bent elastically to a radius of curvature equal to twice that of the focusing circle. The simple Johann geometry has the restriction, for a monochromatic source, that the object and image distance must be equal. This condition can be relaxed by cutting the crystal at an angle σ to the Bragg planes. The focusing conditions are now the Guinier conditions. With synchrotron radiation, because it is polychromatic, the Guinier conditions do not have to be obeyed – the penalty incurred in departing from the Guinier conditions is an increase in the wavelength inhomogeneity – but it is always necessary to obey Eqn (5) since this is

an expression of specular reflection. For synchrotron radiation the monochromator is employed near the Guinier conditions but usually far enough away to produce some wavelength inhomogeneity.

On account of the asymmetric cut (σ) the beam leaving the monochromator will be narrower or wider than the beam entering the monochromator in the ratio

$$N_u/N_v = \sin(\theta + \sigma)/\sin(\theta - \sigma) \quad (11)$$

where N_u and N_v are the widths of the beam on the input and output sides of the monochromator. For a monochromatic source the Guinier conditions mean that the condition

$$N_u/N_v = u/v \quad (12)$$

must hold. Equation (12) shows that the angle of divergence before the monochromator is equal to the angle of convergence after the monochromator, a necessary condition for monochromatic radiation, but a condition which no longer holds for a polychromatic source.

A further effect of the asymmetric cut is to alter the band-pass of the monochromator. Dynamical theory (see Zachariasen, 1967, pp. 123–126) shows that the integrated reflectivity (P_h/P_o), for Laue scattering (white source) from a perfect crystal without absorption, is

$$P_h/P_o \propto (N_v/N_u)^{1/2} \quad (13)$$

(P_h/P_o is the effective bandwidth of the monochromator).

Using synchrotron radiation, Eqn (12) can be disregarded and we may choose a convenient value for σ . In practice a value of four for N_u/N_v can be achieved without incurring significant absorption losses. The bandwidth is thereby decreased by a factor of two but this is more than compensated for by the increase in intensity resulting from the compression of the beam. Since a passive optical element cannot raise the luminosity, some compensating effect must occur: the outgoing beam has more cross-fire than the incoming beam so that the size of the image is enlarged towards the value it would have from a consideration of the ratio v/u , thereby maintaining a constant luminosity.

A further effect is that the width of illuminated monochromator crystal as seen by the detector through the guard slits is reduced. This is important when considering the effects of parasitic scattering on the small angle resolution about the direct beam.

D. Mirror-monochromator Camera at DESY

Barrington Leigh and Rosenbaum (1974, 1976) employed a grazing incidence curved mirror to reflect and focus the beam in the vertical plane and a curved monochromator to focus and monochromatize the beam reflecting in the

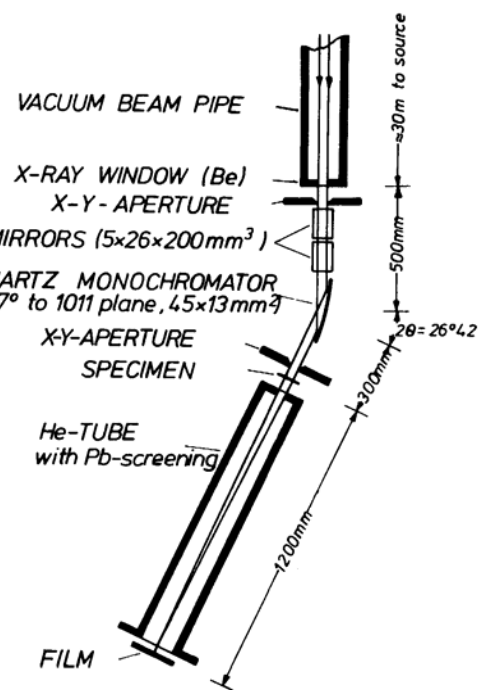


FIG. 4. Diagram of the X-ray optical arrangement used by Barrington Leigh and Rosenbaum (1974). The synchrotron radiation came through a vacuum pipe connected to the synchrotron ending in a beryllium window. The beam passed through two pairs of defining slits set at right-angles and was reflected at glancing incidence by two 20 cm long fused quartz mirrors. A bent quartz crystal monochromator (or later a germanium crystal) was used to focus the beam in the horizontal plane. The guard aperture, specimen holder, backstop and detector holder were mounted on an optical bench aligned with the reflected beam. All the optical elements were mounted in helium-filled boxes to avoid air-scatter. All adjustments could be remotely controlled. Optical settings were made with the help of three television cameras.

horizontal plane. Typically specimen-film or specimen-detector distances between 40 cm and 120 cm were employed. The X-ray mirror consisted of two 20 cm sections 10 mm thick each which might be bent to focus the beam so that movements for mutual alignment of the two mirrors were provided.

A bent quartz monochromator cut at 7° to the 10,1 planes focused the beam in the horizontal plane. The beam was also compressed fourfold by the asymmetric cut of the crystal. Subsequently, a germanium crystal cut at 7° to the 111 planes was substituted for quartz. The beam after the monochromator was about 6 mm × 1.5 mm and focused to a point less than 200 μm diameter. The distance between the monochromator and the focus could be varied between 1 m and 3 m. A diagram of the small angle scattering camera is given in Fig. 4.

The mirrors and monochromator were mounted on the end of a optical bench along which the reflected beam travelled. All the components of the X-ray camera (slits, specimen-holder, film-holder, counter-holder) were mounted on the optical bench. The angle between the bench and the direct beam (2θ) was fixed at 26° ($\lambda = 0.15$ nm for quartz or germanium). Two sets of slits were used: a set of primary slits in front of the mirror box and a set of guard slits in front of the specimen. The apparatus was located in an experiment hall which could not be entered when the beam shutter was open. Remote control was achieved by the use of small d.c. motors fitted with reduction gears. Forty movements could be controlled.

The mirrors were mounted in a helium-filled plexiglass case fitted with thin mylar windows. The monochromator housing was also filled with helium. During experiments all other X-ray paths were enclosed in evacuated plexiglass tubes fitted with mylar windows. Using a germanium monochromator a flux of 7×10^8 photons s $^{-1}$ ($\lambda = 0.15$ nm) was routinely obtained from this camera when the synchrotron was operating at 7.2 GeV and 10 mA. The gain in speed over a small angle camera of similar performance used with a fine focus rotating anode tube (Elliott G \times 13) was about 40.

E. Mirror-monochromator Camera at NINA

Haselgrave *et al.* (1977) used a heavier construction method and the remote control was carried out with stepping motors. A 2×20 cm segmented cylindrically bent mirror (Franks and Breakwell, 1974) was used with a cylindrically bent germanium monochromator cut at 7° to the 111 planes. The mirrors and monochromator were housed in a helium-filled enclosure.

F. Mirror-monochromator Camera at SPEAR

Instead of the segmented mirrors favoured by the DESY and NINA groups, Webb *et al.* (1977) used a single 1.2 m length of float glass. They used a silicon monochromator cut at 8.5° to the 111 planes. A flux of 6×10^8 photons s $^{-1}$ was recorded at the focus with SPEAR running at 3.7 GeV and 20 mA. The focus was about 0.5×0.5 mm 2 . The wavelength could be varied. The radiation safety system at SPEAR deserves attention. A number of experiments are arranged along each beam-line each taking a fraction of the beam. Each experiment is situated inside a radiation hutch which has its own beam shutter and its own set of radiation interlocks. Adjustments within a hutch must be carried out by remote control when the beam shutter is open.

G. Monochromator-mirror Camera at V'EPP-3

A variation on the mirror-monochromator theme has been used on the storage ring V'EPP-3 for studies on muscle (Vasina *et al.*, 1975). In this camera the monochromator (quartz) was before the mirror and sat in the direct beam of the storage ring. This appeared to give less scattering around the direct beam than was experienced with the alternative arrangement. Since the source dimensions were small Vasina and her collaborators were able to work close to the source point and were able to achieve a high intensity with relatively small optical elements.

H. Mirror-monochromator Cameras at DORIS

The first camera on the storage ring DORIS (Harmsen and Rosenbaum, 1979) employs 8×20 cm mirror segments and a cylindrically bent germanium monochromator (Fig. 5). Focusing is achieved by overlapping the reflected strips of radiation from each of the mirrors giving a focus of 500–600 μ m in height (the value depends upon the wavelength used since this affects the grazing angle on the mirror). The whole optical bench, which is 4.2 m long, may be rotated about an axis through the monochromator.

The optical elements are designed so that the direct beam, which is 250 mm wide, may be divided into sections without the optics of the first section casting a shadow on the following sections. This requirement imposes strong constraints on the design of the mirror bender and mirror supports. The optical system (8 mirrors and germanium monochromator) are housed in an evacuated chamber which contains another mirror-monochromator system and also provides the beam path for the direct beam. In a typical experiment on this camera 10^{10} photons s $^{-1}$ have been obtained at 3.7 GeV and 10 mA.

A second camera of a similar kind has been set up on DORIS by Hendrix *et al.* (1979). Hendrix *et al.* have used the same design of mirror-block as Harmsen and Rosenbaum but have used a triangular monochromator. The optical bench is constructed for a fixed wavelength. The flux measured with a calibrated ionization chamber was 5×10^{11} photons s $^{-1}$ at 0.15 nm (4.6 GeV; 20 mA).

I. Separated Function Focusing Monochromator at SPEAR

Hastings, Kinkaid, and Eisenberger (1978) have used a 60 cm long platinum-coated toroidal mirror in the symmetrical mode ($u = v$) to collect 6 millirad of synchrotron radiation and focus it to a point. Shortly before the focus a double crystal monochromator (germanium 111) is interspersed. The main advantage of the system is that the wavelength may be altered without disturbing the focus.

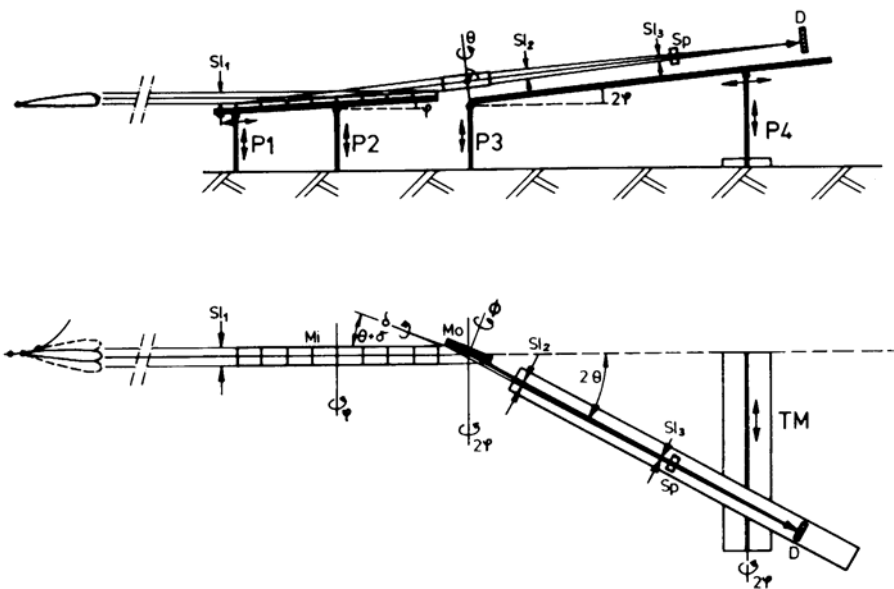


FIG. 5. Plan and elevation of the mirror-monochromator camera X11 at the electron-positron storage ring DORIS (Hamburg). The beam comes from the left, the tangent point is about 15 m from the camera. Each of the posts P1, P2, P3 and P4 may be adjusted in height to allow for alterations in the height of the positron beam. In addition P4 may traverse to allow alteration of the wavelength. An Eulerian cradle allows the monochromator (Mo) to be positioned at right angles to the mirrors (Mi) so that its axis of bending is exactly at right angles to the beam direction. The monochromator can be focused. The eight segments of the mirror can be separately aligned so as to lie along an ellipse. The fused quartz mirrors and germanium monochromator are housed in a vacuum enclosure. There are three slits systems: one before the mirrors (S1 1), one after the mirrors and the monochromator (S1 2), and one (guard S1 3) in front of the specimen (sp). S1 1 is the first defining aperture, but on account of the considerable length of the camera (c. 6 m) and the size of the source, the beam must be redefined by S1 2 at the beginning of the optical bench. All movements connected with the monochromators and mirrors are remotely controllable. The part of the optical bench behind slit S1 2 is outside the shielding wall and may be observed directly.

The disadvantage of the present set-up is the equality of v and u which produces an image the same size as the source.

-

III. Extension of the Methodology

A. The Possibility of Using a Wider Band-pass

The band-width ($\Delta\lambda$) of a perfect single crystal monochromator is about 0.0004 at wavelengths around 0.15 nm (see Boeff *et al.*, 1978). In order to record a

scattering pattern with adequate angular resolution we require the contribution of the intrinsic broadening to be small. In a practical situation a band-width of 0.01 would be quite adequate, so that existing monochromators appear to have an unnecessarily small band-width. In theory it is possible to increase the band-width by distorting the crystal so that the distance between Bragg planes varies as the X-ray beam penetrates the crystal. This may be done either by mechanical stress (i.e. bending) or by diffusing in foreign atoms. In a detailed theoretical study Boeff *et al.* have shown that, for X-rays, not more than a factor of four could be obtained by such methods. The bending radii normally used for monochromators (10–20 m) are not sufficient to cause any appreciable increase in the band-width. In an unpublished study Rek and Harmsen have investigated the effect of implanting foreign ions. By implanting boron in a perfect single crystal of silicon they have increased the integrated reflectivity by a factor of three. The topographic studies necessary to determine the extent of the damage to the surface are in hand but the results are not yet available.

An alternative approach is the use of specially fabricated multi-layer monochromators. This approach has been successfully used for soft X-rays (Haelbich *et al.*, 1979). For 0.15 nm X-rays the thickness of the layers may not be greater than 5 nm. With such small distances, diffusion across the layers becomes a major problem.

A completely different kind of approach has been suggested by Stuhrmann (1978) based on the use of mirrors and filters to define a wavelength interval. The difficulty with this method for low angle scattering is that, although the short wavelength cut-off can be well defined by critical external reflection from a suitable mirror, the long wavelength cut-off can only be defined by absorption, which is not sharp. Such an arrangement has the advantage of being non-dispersive.

B. Towards an Optimum Design

The pioneer experiments on the use of synchrotron radiation as a source for X-ray scattering are now eight years old. A considerable mass of experience, some of it obtained under very difficult conditions, has been accumulated. The X-ray optical systems must be simplified since, at present, they are too difficult to set up and maintain and take too long to alter between experiments. Furthermore, the dictates of the experiment itself may well be such that the experimental group does not have the resources to cope with a complex optical system.

The new dedicated sources (Brookhaven, Daresbury) have a high luminosity and small beam size. It should, therefore, be possible to operate without a mirror, as has been done successfully at Novosibirsk (V'EPP-3) and at Orsay (DCI). One relies on the small vertical divergence of the beam and its small size

to produce adequate collimation in the vertical plane. This may be augmented, as was done by Vasina *et al.* (1976) by a single segment mirror after the monochromator.

An alternative approach is to use a toroidal mirror (see Section B9). A symmetrical mirror can certainly be employed for low angle scattering if the source is small enough and the luminosity is high.

References

- Arndt, U. W. (1977). X-ray film, In "The Rotation Method" (U. W. Arndt and A. J. Wonocott, eds), pp. 207–218. North-Holland, Amsterdam.
- Arndt, U. W. and Gilmore, D. J. (1979). X-ray television area detectors for macromolecular structural studies with synchrotron radiation sources. *J. Appl. Cryst.* **12**, 1–9.
- Barrington Leigh, J. and Rosenbaum, G. (1974). A report on the application of synchrotron radiation to low-angle scattering. *J. Appl. Cryst.* **7**, 117–121.
- Barrington Leigh, J. and Rosenbaum, G. (1976). Synchrotron x-ray sources: a new tool in biological structural and kinetic analysis. *Ann. Rev. Biophys. Bioeng.* **5**, 239–270.
- Baru, S. E., Provitz, G. I., Savinov, G. A., Sidorov, V. A., Feldman, I. G. and Khabakhpashev, A. G. (1978). One-coordinate detector for rapid multisnap recording of x-ray pictures. *Nucl. Instr. Meth.* **152**, 195–197.
- Baru, S. E., Provitz, G. I., Savinov, G. A., Sidorov, V. A., Khabakhpashev, A. G., Shuvalov, B. N. and Yakovlev, V. A. (1978). Two-coordinate x-ray detector. *Nucl. Instr. Meth.* **152**, 209–212.
- Boeff, A., Lagomarsino, S., Mazkedian, S., Melone, S., Puliti, P. and Rustichelli, F. (1978). X-ray diffraction characteristics of curved monochromators for synchrotron radiation. *J. Appl. Cryst.* **11**, 442–449.
- Faruqui, A. R. and Huxley, H. E. (1978). Time-resolved studies on contracting muscle using small-angle x-ray diffraction. 1. Design of data collection system. *J. Appl. Cryst.* **11**, 449–454.
- Franks, A. and Breakwell, P. R. (1974). Developments in optically focusing reflectors for small-angle x-ray scattering cameras. *J. Appl. Cryst.* **7**, 122–125.
- Gabriel, A., Dauvergne, F. and Rosenbaum, G. (1978). Linear, circular, and two dimensional position sensitive detectors. *Nucl. Instr. Meth.* **152**, 191–194.
- Godwin, R. P. (1969). In "Springer Tracts in Modern Physics" (G. Hoehler, ed.), Vol. 51, pp. 2–73. Springer-Verlag, Heidelberg.
- Goody, R. S., Barrington Leigh, J., Mannherz, H. G., Tregebar, R. T. and Rosenbaum, G. (1976). *Nature (Lond.)* **262**, 613–615.
- Green, G. K. (1976). "Spectra and Optics in Synchrotron Radiation", B.N.L. Report 50522. Brookhaven National Laboratory, Upton, N.Y.
- Guinier, A. (1946). Rayon X – sur les monochromateurs à cristal courbe. *C. R. Acad. Sci., Paris* **223**, 31–32.
- Haelbich, R. P., Segmueller, A. and Spiller, E. (1979). Smooth multilayer films suitable for x-ray mirrors. *Appl. Phys. Lett.* **34**, 184–187.
- Haselgrave, J. C., Faruqui, A. R., Huxley, H. E. and Arndt, U. W. (1977). The design and use of a camera for low-angle x-ray diffraction experiments with synchrotron radiation. *J. Phys. E. Sci. Instrum.* **10**, 1035–1044.
- Hastings, J. B. (1977). X-ray optics and monochromators for synchrotron radiation. *J. Appl. Phys.* **48**, 1576–1584.
- Hastings, J. B., Kincaid, B. M. and Eisenberger, P. (1978). A separated function focusing monochromator system for use with synchrotron radiation. *Nucl. Instr. Meth.* **152**, 167–171.
- Hendricks, R. W. (1978). The ORNL 10-meter small-angle x-ray scattering camera. *J. Appl. Cryst.* **11**, 15–30.
- Hendrix, J., Koch, M. H. J. and Bordas, J. (1979). A double focusing x-ray camera for use with synchrotron radiation. *J. Appl. Cryst.* **12**, 467–472.
- Horowitz, P. and Howell, J. A. (1972). A scanning x-ray microscope using synchrotron radiation. *Science* **178**, 608–611.
- Huxley, H. E. and Brown, W. (1967). The low angle x-ray diagram of vertebrate striated muscle and its behaviour during contraction and rigor. *J. Mol. Biol.* **30**, 383–434.
- Johann, H. H. (1931). Die Erzeugung lichtstarker Roentgenspektren mit Hilfe von Konkavkristallen. *Z. Phys.* **69**, 185–206.
- Lemonnier, M., Fourme, R., Rousseaux, F. and Kahn, R. (1978). X-ray curved-crystal monochromator system at the storage ring DCI. *Nucl. Instr. Meth.* **152**, 173–177.
- Milch, J. R. (1979). Slow scan SIT detector for x-ray diffraction studies using synchrotron radiation, I.E.E.E. *Trans Nucl. Sci.* **NS-26**, 338–345.
- Podolsky, R. J., Onge, R. St., Yu, L. and Lynn, R. W. (1976). X-ray diffraction of actively shortening muscle. *Proc. Nat. Acad. Sci. USA* **73**, 813–817.
- Reynolds, Geo. T., Milch, J. R. and Gruner, S. M. (1978). High sensitivity image intensifier-TV detector for x-ray diffraction studies. *Rev. Sci. Instrum.* **49**, 1241–1249.
- Rosenbaum, G. (1979). "Die Anwendung von Synchrotron Strahlung in der Biologie". Ph. D. Thesis, University of Heidelberg.
- Rosenbaum, G. and Holmes, K. C. (1980). In "Synchrotron Radiation Research" (H. Winick and S. Doniach, eds), pp. 533–564. Plenum Press, New York.
- Schwinger, J. (1949). On the classical radiation of accelerated electrons. *Phys. Rev.* **75**, 1912–1925.
- Stuhrmann, H. B. (1978). The use of x-ray synchrotron radiation for structural research in biology. *Quart. Rev. Biophys.* **11**, 71–98.
- Vasina, A. A. (1976). The use of synchrotron radiation for structure research on biopolymers (in Russian). *Molec. Biol. (Moscow)* **8**, 242–307.
- Vasina, A. A., Gerasimov, V. S., Zheleznyaya, L. A., Matyushin, A. M., Sorikin, B., Skrebnitskaya, L. N., Shelestov, V. N., Frank, G. M., Avakyan, Sh. M. and Alikhanyan, A. I. (1975). Experience with the use of synchrotron radiation for x-ray diffraction studies of biopolymers. *Biophysics (Moscow)* **20**, 813–820.
- Webb, N. G., Samson, S., Stroud, R. M., Gamble, R. C. and Baldeschwieler, J. D. (1977). A focusing monochromator for small angle diffraction studies with synchrotron radiation. *J. Appl. Cryst.* **10**, 104–110.
- Witz, J. (1969). Focusing monochromators. *Acta Cryst.* **A25**, 30–41.
- de Wolff, P. M. (1951). In "Selected Topics on Crystallography" (J. Bouman, ed.). North Holland, Amsterdam.
- Zachariasen, W. H. (1967). "Theory of X-ray Diffraction in Crystals". Dover Publications, New York.

3.III

Instrumentation. Data Collection in X-ray Small Angle Scattering

H. LEOPOLD

Institut für Physikalische Chemie der Universität Graz, Graz, Austria

I. Introduction	105
II. Radiation detectors	107
III. Detector electronics	110
IV. Positioning	111
V. Programmed operation	112
VI. Photographic methods	113
VII. Position-sensitive detectors	114
References	117

I. Introduction

In general, the desired output of a small angle X-ray scattering (SAXS) experiment is the scattering curve (scattered intensity as function of the scattering angle), represented in a digital data format, thus facilitating further data treatment by means of a digital computer. This chapter will give basic information on established techniques which are, at present, available to the majority of the experimenters wishing to recover the latent information of the scattering pattern. As there are many implementations of one principle in actual use, this review cannot claim to be complete.

Two physical magnitudes have to be translated into electrical signals: the scattered intensity must be sensed by some radiation detector and the scattering angle measured by some position-sensitive device as in SAXS, the angle is usually represented by linear displacement (tangent of scattering angle) on account of

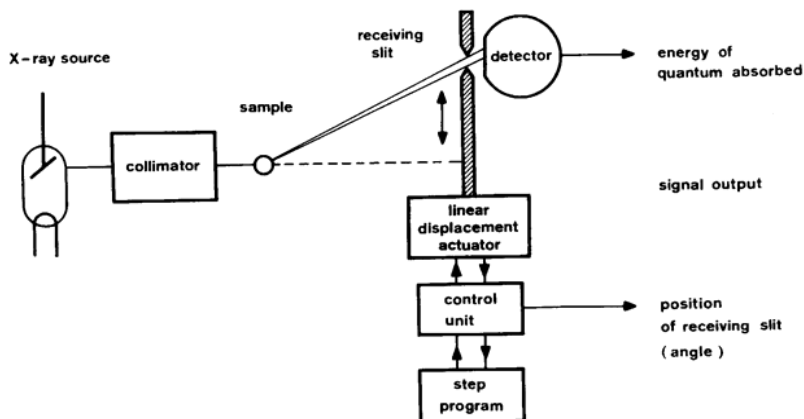


FIG. 1. Implementation of the sequential mode of data collection.

the small angular range. Two different modes of data collection are in common practice: the sequential and the parallel mode.

In the sequential mode (Fig. 1), a positioning device moves a receiving slit into the desired angular position and the radiation detector senses the scattered intensity at that position. In order to obtain the whole scattering curve, a series of different angles must be positioned sequentially and the intensity readings at every position must be recorded. The sequential positioning may be performed manually, or automatically by a programmed device which also encodes the actual position of the receiving slit into a digital word. Angular accuracy with respect to resolution is high, as it depends only on the mechanical precision of the positioner (goniometer). A very high dynamic range in intensity, i.e. the ratio of the highest and the lowest intensity to be detected within one scattering curve, can be covered, as the detector receives only the scattered beam at one point of the scattering curve. In addition, the width of the receiving slit can be altered in accordance with the intensity received at that position, thereby enhancing the intrinsic dynamic range of the detector. Data collection time may become long with this well established mode of operation, and sometimes prohibitive with samples of fast changing properties. As in the sequential mode, the intensities at different angles are measured at different times — the stability of the primary intensity is of importance. Therefore, the X-ray generator should show a very good long-term stability. Errors due to fluctuations can be reduced by monitoring⁽¹⁾ the primary intensity.

In the parallel mode (Fig. 2), a position-sensitive device senses the intensity of the scattering pattern within the whole scattering range simultaneously. This way, measuring time drops down dramatically and the primary stability is of little importance. The angular accuracy and dynamic range of the scattered

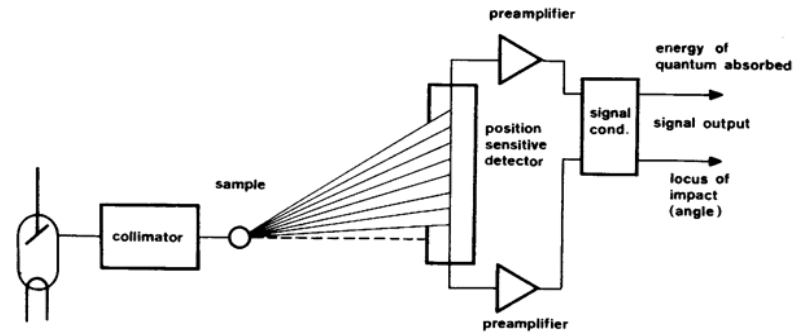


FIG. 2. Implementation of the parallel mode of data collection.

intensity is, in general, limited by internal features of the sensor. Examples for such a sensor are the photographic film and various kinds of position-sensitive proportional counters (PSPC). The film offers the advantage of economy and of being a hard (non-volatile) copy of the scattering curve, but cannot deliver electrical signals for further data treatment by simple means. On the other hand, the output signals of the PSPC can be converted into digital words representing the scattering curve. Cutting the scattering curve into several sections of different integral intensity and measuring these sections separately by means of the PSPC mounted on a goniometer arm positioned for the corresponding section can increase the angular accuracy and dynamic range of the PSPC to almost any desired level.

Both modes of operation can be combined advantageously by using an array of monolithic solid-state detectors or photodiodes,⁽²⁾ one for each point of the scattering curve. This results in accurate digital encoding of the position, independent of the scattered intensity handled by the individual detector.

II. Radiation Detectors

In SAXS, soft X-rays (photon energies between 5 keV and 20 keV) are used as primary radiation. A suitable detector should respond to this range of energy, should show up a good detection efficiency, low background and should be capable of a high count rate. In the case of strongly scattering samples, especially in close vicinity of the primary beam, rates in the order of 10^5 c.p.s. can be observed even when using a narrow receiving slit. If there is no monochromator in the path of radiation, the detector itself should allow a certain degree of monochromatism by electronic pulse height analysis.

In gas-filled and solid-state detectors, the ionizing property of radiation is

used to produce a certain amount of electric charge per event. The mean energy absorbed per one electron released amounts to approximately 30 eV in gases and approximately 3 eV in silicon. Therefore, as response to one 8 keV photon, one can expect approximately 4×10^{-16} coulombs per photon in silicon, or 4×10^{-17} in a gas. By proper selection of the absorbing material and its dimensions, almost all photons will be absorbed within the detector (counting efficiency).

In the Si solid-state detector, the absorption takes place in a reversed biased silicon diode. The charge is collected by the detector bias voltage. This kind of detector is perfectly suited for SAXS, offering the best energy resolution available at present. In general, a cooling system (liquid nitrogen) is necessary to obtain an adequate thermal noise level on account of the low amount of charge available per event.

The proportional counter (PC) is, in principle, a gas-filled absorption chamber with two collecting electrodes. One is formed by the outer metal wall, the other by the insulated inner wire. With a low bias voltage between the electrodes, such a device will operate as an ionization chamber with no gas amplification. The charge released by the absorption of a single low energy photon is too small to be processed separately, but the average ionization current at high photon flux can be used to monitor the primary beam.⁽³⁾ If the electric field strength in the chamber is raised by increasing the detector bias voltage (1000–2000 V), the electrons released by the absorption gain sufficient energy to cause ionization of the gas molecules. An avalanche of secondary electrons results in increasing the primary charge by the factor A , called the gas amplification, selecting the correct bias A amounts from 10^3 to 10^5 . Due to the radial field geometry, the avalanche is limited to a very small volume in close vicinity of the inner wire, so that A is the same for every photon. This fact preserves the proportionality between photon energy and charge collected, but the amplified charge can be processed comfortably without the need of cooling.

A proper selection of the filling gas and the window material (for example Xenon; mica) results in a perfect response of the detector to Cu, Co, Fe and Cr radiation. Due to the absorption behaviour of the gas, the counter is insensitive to photons of higher energy. Photons of lower energy are absorbed in the window. This intrinsic selectivity facilitates the signal processing by avoiding an overload to the amplifier caused by the higher energy components of the spectrum of the X-ray tube operated with high anode voltage. Therefore, the PC should be the first choice for detecting soft X-rays. A background of 1 c.p.m. and a resolution time of $1\mu s$ can be obtained. The energy resolution of the PC is not as good as with the solid-state detector, due to the lower number of primary electrons per photon and the statistic behaviour of the avalanche, but it is definitely sufficient for SAXS.

Increasing the bias voltage above the proportional region destroys the

relation between charge collected and photon energy. The detector is then operated in the Geiger-Müller region. The output pulses become uniform, but independent of the photon energy, the recovery time will be in the order of 1 ms. Neither fact is desirable for SAXS.

In the scintillation detector, the scintillations emitted from atoms excited by the passage of radiation are converted into electrical charge by means of a photomultiplier. Using a sodium iodide crystal as scintillator, one photo electron is released from the photocathode for each 300 eV of energy dissipated in the crystal. The electron multiplication in the photomultiplier compensates for this low sensitivity, but adds to the broadening of the energy resolution still sufficient for SAXS. The scintillation detector shows up a uniform response to a wide range of photon energies. It is able to detect soft X-rays with high efficiency, but does not reject the high energy components of the continuous spectrum of the X-ray source. This has to be done entirely by pulse height analysis. A background of 3 c.p.m. and a resolution time of less than $0.3\mu s$ will be obtained.

In Fig. 3, typical energy resolutions of a solid-state, a proportional and a scintillation detector are given. On an arbitrary scale, the curves show the distribution of the pulse height corresponding to the charge received from the detectors if irradiated by a monochromatic CuK_α radiation. Note that the counting efficiency is given by the integral over the curves, which is quite comparable for the three types of detectors.

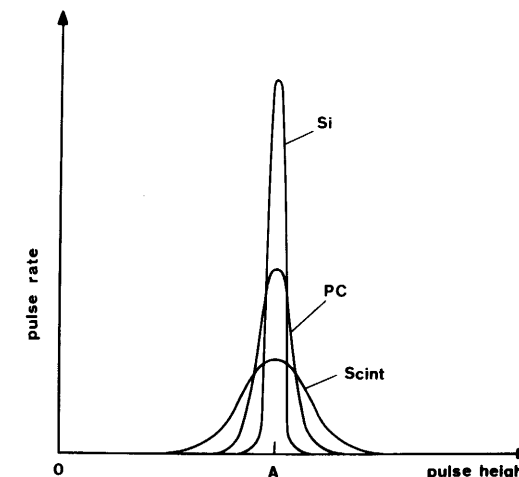


FIG. 3. Response of a silicon solid-state detector (Si), a proportional counter (PC) and a scintillation counter (Scint) with respect to quantum energy. Pulse height A corresponds to the monochromatic radiation.

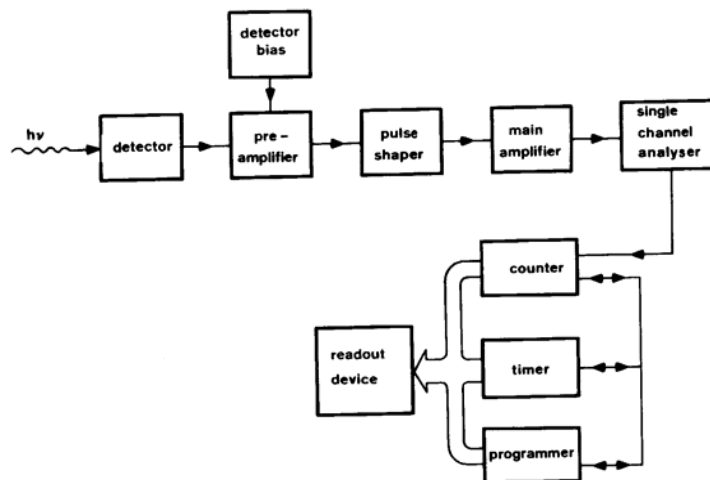


FIG. 4. Signal processing with conventional (not position-sensitive) radiation detectors.

III. Detector Electronics

The electronic instrumentation around the radiation detector provides for a correct detector bias, amplifies the detector's signal, shapes it into energy proportional voltage pulses and selects those corresponding to the desired photon energy, thereby suppressing noise and polychromatic radiation. In addition, a digital counter counts the selected events during a finite counting time. The content of this counter divided by the counting time is the scattered intensity in digital representation.

In Fig. 4, a schematic diagram of a typical instrumentation suitable for the three preferred types of detectors is shown. The preamplifier, in close vicinity of the detector to avoid electrical interference, converts the charge pulses into voltage steps superimposed on a d.c. level depending on the average count rate. The pulse shaper is necessary to produce pulses of definite length (approximately $1\mu\text{s}$) with a pulse height (referred to zero d.c. level) corresponding to the height of the steps. In the main amplifier, often called the linear amplifier, the pulses are amplified to the correct level needed by the single channel analyser (pulse height discriminator). This unit responds only to pulses ranging in pulse height between two preset levels. The difference between the upper and the lower level is called the window width. Electronic monochromatization is accomplished by setting the window in such a way that it covers the pulse height distribution generated by the desired photon energy (refer to Fig. 3). Pulses of lower height, i.e. originated by noise and electrical interference, are

rejected, as well as pulses higher than the upper level generated by the high energy components of the X-ray spectrum.

Care should be taken not to saturate the main amplifier by too large a rate of these high energy pulses, especially when operating a scintillation or solid-state detector. The bias of amplifying detectors (PC and scintillation) should be kept as low as possible for long life time, stable amplification in the detector, good energy resolution and high permissible count rate. The bias (high voltage) is adjusted in such a way that the desired pulses just override the noise level. Then the amplification factor of the main amplifier is selected, so that the centre of the distribution is situated somewhere below the middle of the range of the single channel analyser. The pulse height distribution should now be measured by scanning over the range, beginning at zero with a low window width. The settings of the lower and upper levels can now be made where the tail-ends of the distribution become horizontal. When in the course of normal operation unstable intensity readings are encountered, the distribution curve should be checked. A shift indicates an unstable bias, a broadening of the end of the PC's lifetime. In order to avoid a ground loop introducing unwanted electrical signals, the detector's ground should be electrically isolated from the housing of the X-ray generator.

IV. Positioning

In the sequential mode of data collection, a positioning device is responsible for the correct placement of the receiving slit, thereby defining the scattering angle. In addition, the positioning device must provide information on the actual position of the slit. A precision micrometer screw operated by hand, or motor-driven, is commonly used as positioner. Operated in an open loop mode, the accuracy of the micrometer defines the accuracy of positioning. In this case, the angle of rotation of the screw is taken as a measure for the scattering angle. For general SAXS work, a good micrometer fulfills the demands. A higher accuracy and long-term stability can be obtained by forming a closed-loop system in which the actual position is sensed by an accurate displacement sensor (optical shaft encoder) and the operation of the screw is controlled accordingly.⁽⁴⁾

For automatic positioning, the micrometer screw is operated via a reduction gear, either by a stepping motor or by any kind of motor and additional position sensing. With the stepping motor, the number of stepping pulses to the motor is the measure of the position. A lost pulse will shift the abscissa of the scattering curve. To avoid this risk, positioning speed must be kept safely in a range where the stepping motor responds to every pulse. With a free running motor, a photoelectric or magnetic sensor produces a pulse for a certain incremental

displacement of the receiving slit, usually for the smallest step size of an abscissa program. The pulses can be counted and, after completion of a desired displacement, the motor will be switched off and an additional brake can be activated, thereby avoiding an overshoot. This mode of operating the screw releases the stress on the motor and allows a high positioning speed.

V. Programmed Operation

Measuring a SAXS curve by hand in the sequential mode is a time-consuming work, as the operator has to set a new position and wait for the completion of the radiation counting at that position. Therefore, almost all SAXS goniometers in use, at present, are operated automatically.

In this mode of operation, the scattering curve is scanned step-wise, according to a program stored in a programmer. The step-program has to be selected carefully, in accordance with the shape of the sample's scattering curve and the setting of the entrance and receiving slit, in order to optimize the accuracy of measurement and the time invested. It is good practice to cut the total angular range of the scattering curve into different sections (according to regions of different slope) and to keep the step size (width of one step) constant within one section. Then the total step-program can simply be worked out by defining the individual number and size of steps in each section (step group), instead of stating the abscissa of each measuring point. This mode of incremental programming keeps the amount of data to be stored as small as possible. The programmer itself can add up number and size of the steps and this way provide a digital representation of the actual abscissa value.

The zero point of the abscissa of the scattering curve is situated at the centre of gravity of the primary beam profile. The distance between this point and the first measuring point must also be stored in the program in order to allow correct evaluation of the abscissa.

In addition to this positioning, the programmer also has to control the operation of the counter and the timer of Fig. 4. If a programmed position is reached, the programmer starts the counter and the timer and has to wait until it receives a signal indicating that the counting and data transfer cycle is completed. During data transfer, the programmer also transmits the actual abscissa to the readout device.

A motor-operated micrometer can be relatively easily interfaced to an on-line minicomputer or microprocessor system, thereby providing for the necessary hardware. This computer can also take over the counter, timer and readout function. In fact, one can see various "home-made" minicomputer installations operating quite well in different laboratories.

A SAXS programmer based on the outlines given above is described in

reference (5). Step widths of 5, 10, 20, 50, 100, 200, 500, 1000, 2000 or 4000 microns ($1\mu\text{m}$ corresponds to approximately 4.5×10^{-6} radians with the Kratky camera) and step numbers of 1, 2, 4, 5, 8, 10, 15, 20, 30 or 50 can be selected in up to 7 groups. The first measuring point can be offset up to $9999\mu\text{m}$ with respect to the centre of the primary beam, and a definite number of runs of the whole curve may be programmed. The restriction to ten different step widths and step sizes allows the use of numerical switches to store the whole program in a non-volatile manner and, therefore, makes programming very comfortable without any effort in software. The experience on more than 100 such instruments* shows that the variety of step sequence fulfills the needs in the different fields of SAXS.

The readout device of Fig. 4 may be a printer, a punch tape unit, or magnetic data storage device (magnetic tape, floppy disk). It finally collects and stores the digital data generated by the measuring system in the course of one or more exposures. Of course, the measuring system may also be directly connected to a large-scale computer for further data treatment without intermediate storage of the experimental data, but there is no stringent reason to do so, as the data rate generated by a sequentially scanning SAXS installation is low. A decision should be based on the local conditions.

The instrumentation necessary to implement a complete detector system operating in the sequential mode (detectors, signal processing units, digital counters and timers, control instrumentation, data storage devices) are manufactured by a considerable number of companies operating in the field of analytical or nuclear instrumentation, therefore no recommendation is given. If a measuring chain should consist of parts of equipment originating from different manufacturers, the problem of interfacing should be cleared up before purchase.

VI. Photographic Methods

The parallel mode of collecting SAXS data can be implemented by using the photographic film as a position-sensitive radiation detector. This method was common practice in the early days of SAXS, but became obsolete, due to the competition of pulse counting detectors operated in the sequential mode. The inherent advantages of the parallel mode were deliberately exchanged against higher dynamic range, better reproducible response of the counting detector and the ease of obtaining an electrical representation of the scattered intensity without the need for measuring optical density.

* Manufactured by A. Paar KG., Graz, Austria.

Nowadays, changes seem to have occurred again. The film material is definitely better than that of 1950, the effect of X-ray on photographic material is well understood and measurements have been made comparing photographic methods to step scanning and position-sensitive pulse counting detectors.⁽⁶⁾ The dynamic range of the film is limited on the high intensity side by the saturation of the AgBr layers and the fog on the low intensity side. While this ratio (20:100 dependent on the speed of the film) will be sufficient for a number of SAXS problems, the fog forms an absolute limit when sensing low intensities which could be detected with good signal to noise ratio, by means of a pulse counting detector. Due to the fog density, present day X-ray films can be used with exposure levels larger than approximately one quantum per ten micrometers squared of Cu-radiation. Within the dynamic range, the linearity of the response of the recorded intensities (including errors in densitometry) is obtained in the order of 1%. This suggests that measurements of the absolute intensity also can be made if on each film a standard exposure is included. The spatial resolution of the film amounts to a few micrometers. Measuring the optical density, the total information stored on the film must be recovered. With slit geometry, the height of the receiving slit of the densitometer perpendicular to the direction of the scan must correspond to the height of the exposure on the film in order to average over the contributions of each elemental length of the focal line. If this height of the receiving slit cannot be obtained, due to experimental limitations in the densitometer, multiple scanning⁽⁷⁾ (the receiving slit shifted in lateral direction after each scan) will give good results.

An actual decision can be made by comparing the background scattering intensity of the sample (solvent) to the exposure corresponding to the fog density. If the background times the exposure time is in the order of the fog exposure (as with organic solvents and slit geometry), the film will be comparable to a position-sensitive pulse counting detector. For pinhole collimation, however, with its low primary irradiation, the reduction of the pattern's intrinsic signal to noise ratio due to the fog will be, in many cases, prohibitive.

VII. Position-sensitive Detectors

Like the photographic film, a position-sensitive detector receives the integral distribution of the scattered radiation over its total range, but provides, for a two-dimensional electrical signal representing the scattered intensity, a function of the scattering angle.

At present, the position-sensitive proportional counter (PSPC) is favourable with position encoding, according either to the RC-line method⁽⁸⁾ or the charge division method.⁽⁹⁾ In the RC-line method, a gas-filled proportional counter is used with a resistive inner wire (mostly carbon coated quartz fibre). The

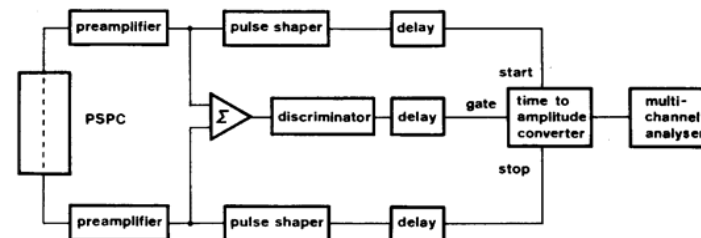


FIG. 5. Signal processing with position-sensitive proportional counter. The RC-line method of positional encoding is shown.

wire and the detector's distributed intrinsic capacitance form a resistance-capacitance delay line which makes the rise time of the voltage pulses sensed at the ends of the detector dependent on the location of the primary ionization. As shown in Fig. 5, two preamplifiers and pulse shapers convert the difference in rise time into a time-lapse translated into a voltage by means of a time-to-amplitude converter. In addition, a sum channel, fed by a signal representing the quantum energy of the absorbed photon, enables the gate of the time-to-amplitude converter in case of the advent of a photon of the desired quantum energy. Thus, the rate of the output pulses of the converter represents the intensity at a position indicated by the height of the pulse. The frequency distribution of these pulses plotted against the pulse height, therefore, is identical to the scattering pattern. It can be visualized on the scope of a multichannel analyser and stored on magnetic tape or disk.

In the charge division method of positional encoding, the resistive inner wire is terminated by two charge-sensitive amplifiers, forming a virtual ground at the detector's ends. The total charge resulting from one absorption of a photon is divided into two fractions, according to the ratio in distance given by the position of the impact. These fractions appear as output signals of the two amplifiers. The sum of the amplitudes of the two signals represents the quantum energy of the photon (as in ordinary proportional counters). The ratio between either fraction and the sum denotes the position of the impact. As the fractional signal and the sum originate from the same ionizing event, the accuracy of positional encoding is not limited by the statistical behaviour of the gas amplification within the counter. At present, it seems that there is a preference for the RC-line method, as the electronic signal processing can be performed more easily. The advent of fast dividing analog-to-digital converters of high resolution may introduce a change in the future.

A weak point in the PSPC is the carbon fibre, sensitive to overload. An unfiltered primary beam in the Kratky camera can burn the coating of the fibre, making a replacement necessary. A metal inner wire,⁽¹⁰⁾ instead of the carbon fibre, overcomes this drawback. Another type of PSPC, the so-called

"back gammon detector",⁽¹¹⁾ divides the charge into fractions dependent on the position of the impact by means of two adequately shaped cathodes and, therefore, dispenses with the resistive wire.

In comparison to a goniometer-operated SAXS system, the application of a position-sensitive detector shortens the time of exposure by up to two orders of magnitude in cases of samples showing a scattering curve of moderate dynamic range (small particles in solution, partially oriented samples) and lowers the radiation dose imposed on the specimen accordingly. Samples with time-dependent properties can be investigated within the necessary short time. On the other hand, new problems arise when operating a PSPC, not encountered in the sequential mode: spatial resolution of the detector, error in positional encoding, deviation from uniform response at different positions and count rate capability. As an example of the performance of position-sensitive proportional counters using the RC-line method, Table 1 shows the specifications of two

TABLE 1

	PSPC 1	PSPC 2
Active volume	50 mm 10 mm 3 mm	100 mm long 8 mm wide 5 mm deep
Spatial resolution (FWHM)	70 μm	250 μm
Detection efficiency including window	90%	80%
Processing time including electronics	10 μs	2 μs
Positional error as percentage of length	0,5%	1%
Uniformity of response	2%	3%

commercially available detectors sensing Cu-radiation (8,04 keV). Position-sensitive proportional counter 1,⁽¹²⁾ distributed by Siemens AG, W. Germany, is an open device using slowly flowing (10 ml min^{-1}) Xenon at high pressure (approximately $1,5 \times 10^6 \text{ Pa}$) as detection gas and a carbon coated quartz fibre as anode. Position-sensitive proportional counter 2,⁽¹³⁾ made by Technology for Energy Corporation, U.S.A., is a sealed device with a stainless steel anode. This PSPC uses a gas mixture of 97% Xe and 3% CH₄ at $2,2 \times 10^5 \text{ Pa}$. The count rate capability can be estimated from the processing time. With respect to coincidence loss, the reciprocal of the tenfold processing time may be regarded as the maximum count rate of randomly occurring photons uniformly distributed over the PSPC length. This results in 10^4 c.p.s. for PSPC 1 and 5×10^4 for PSPC 2. The count rate capability of the PSPC limits its applicability in SAXS

installations with high intensity primary sources compared to ordinary proportional counters which tolerate at least the same count rate at one single point of the scattering curve. Some other manufacturers of RC-line encoding PSPCs are: Ortec Inc., U.S.A., Tennelec Inc., U.S.A., Rigaku Corp., Japan and Marconi-Elliott, Great Britain.

As an example of a PSPC using the charge division method of positional encoding, the specifications of a detector according to reference (11) called LETI, model A, made by Instruments SA, Division Jobin-Yvon, France, will be presented. With an effective length of 55 mm, the spatial resolution (FWHM) amounts of 125 μm . The uniformity of the detector's sensitivity is within 2%, the error in position encoding 0,5%. The filling gas is a mixture of 90% Xe and 10% CH₄ at atmospheric pressure in a sealed housing. The quantum efficiency to Cu-radiation amounts to 50%. The total processing time of 30 μs results in a count rate capability of 3000 c.p.s. A test-report on this counter,⁽¹⁴⁾ operating in a Kratky system shows that even this low rate capability yields a considerable reduction in experiment time.

References

- (1) Kratky, O., Leopold, H. and Seidler, H. P. (1970). *Z. Angew. Phys.* **31**, 49–50.
Kratky, Ch., Kratky, O. and Wrentschur, E. (1975). *Acta Physica Austriaca* **41**, 105–123.
- (2) Borso, C. S. and Danyluk, S. S. (1980). *Rev. Sci. Instrum.* **51**, 1669–1675.
- (3) Hendricks, R. W., de Lorenzo, J. T., Glass, F. M. and Zedler, R. E. (1972). *J. Appl. Cryst.* **6**, 129–132.
- (4) Leopold, H. and Jensen, B. T. (1974). *J. Appl. Cryst.* **7**, 130.
- (5) Leopold, H. (1968). *Z. Angew. Phys.* **25**, 81–85. English translation in *Siemens Review* **36**, (1969) 51–55.
- (6) Vonk, C. G. and Pijpers, A. P. (1981). *J. Appl. Cryst.* **14**, 8–16.
- (7) Kratky, O., Kahovec, L. and Werner, H. (1959). *Z. Elektrochem.* **63**, 63–70.
- (8) Borkowski, C. J. and Kopp, M. K. (1968). *Rev. Sci. Instrum.* **39**, 1515–1522.
- (9) Kuhlmann, W. R., Lanterjung, K. H., Schimmer, B. and Sistemich, K. (1966). *Nucl. Instr. Methods* **40**, 118–120.
- (10) "The Application of a One-dimensional Position-sensitive Detector to a Kratky Small Angle X-ray Camera" by T. P. Russell, R. S. Stein, M. K. Kopp, R. E. Zedler, R. W. Hendricks and J. S. Lin. ORNL/TM-6678, Oak Ridge National Laboratory, USA (1979).
- (11) Allemand, R. and Thomas, G. (1976). *Nucl. Instr. Methods* **137**, 141–149.

* Manufactured by A. Paar KG, Graz, Austria.

- (12) "The Position Sensitive Proportional Counter-properties and Possible Applications" by N. Broll, M. Henne and W. Kreutz. Analytical application note No. 271, Siemens AG, W. Germany (1980).
- (13) Kopp, M. K. (1979). *Rev. Sci. Instrum.* **50**, 382-383.
- (14) "Preliminary Test-report on the Use of the Position Sensitive Detector LETI (Jobin Yvon, France) in Combination with the Kratky-camera System" by P. Laggner. Institut für Röntgenfeinstrukturforschung, Graz, Austria (1981).

4

Data Treatment

O. GLATTER

Institut für Physikalische Chemie der Universität Graz, Graz, Austria

I.	Mathematical description of the experimental effects	119
A.	The collimating system	120
B.	The detector	123
C.	Wavelength effect	124
D.	Combined formulae	124
II.	Preliminary data treatment	125
III.	Smoothing, desmearing and Fourier transformation	126
A.	Introduction	126
B.	Multi-step procedures	128
C.	Single step procedure – Indirect Transformation Method	131
D.	Resolution	136
E.	Special transformations	139
F.	Simulations	149
IV.	Evaluation of molecular parameters and normalization	149
A.	Molecular weight	150
B.	Normalization – particle scale	152
C.	Structural parameters	153
V.	Calculation of scattered intensities and distance distributions of models	156
A.	Calculations of scattered intensities	157
B.	Calculation of the distance distribution function of models	162
	References	163

The theoretical basis of small angle scattering and the techniques for obtaining experimental scattering curves have been described in the two preceding chapters. The experimental data have to be transformed to correspond to an ideal experimental design, in order to be interpretable with the aid of the available theories. The mathematical procedures and the computer programs which are necessary for these transformations are discussed in this chapter. A survey of the most important general methods for the interpretation is given in the

following chapter. This division into two chapters is not meant to indicate that data treatment and interpretation are two independent problems. On the contrary, these two chapters plus the two preceding ones constitute a unit as they are closely related.

The methods presented in these two chapters are predominantly developed in the field of investigation of biological macromolecules in solution but most of them can be used in all fields of application. Additional methods developed for special applications are described in the several chapters of the section "Applications" of this book. The contrast variation technique is described separately in Chapter 6.

The following questions have to be answered in the chapters "Data Treatment" and "Interpretation".

How are the experimental results related with the general theory?

What is the content of information of the experiment?

Which results can be determined directly from the data?

How can the experimental situation be optimized?

How can additional information about the system under investigation be taken into account?

This chapter will be mainly restricted to the presentation of the existing analytical and numerical methods while the aspects of interpretation and a final conclusive discussion will be given at the end of the next chapter.

The mathematical description of the experimental situation (Section I of this chapter) is the basis for the preliminary data treatment (Section II) and for all correction procedures which are described in Section III. Normalization techniques and methods for the evaluation of molecular parameters are reviewed in Section IV; Section V deals with the calculation of scattered intensities and distance distributions of model systems.

I. Mathematical Description of the Experimental Effects

The ideal experimental design, i.e. point-like primary beam with high energy, point-like sample and detector, can never be attained in a real experiment (Chapter 3). The various effects caused by the most common experimental design are discussed separately in the following sections.

A. The Collimating System

The collimating system used in the majority of applications is a slit system whose slit length (or slit height) is very large compared to the slit width perpendicular to the slit length. Let $I_0(x, t)$ be the two-dimensional intensity

distribution of the primary beam entering the sample, where t is the coordinate from the centre of the primary beam in the direction of the slit length and x is the coordinate perpendicular to t . Simple geometrical considerations show that the intensity distribution $I_0(x, t)$ can be written as a product of two independent distributions, such as

$$I_0(t, x) = P(t) \cdot Q(x) \quad (1)$$

This independence is true with sufficient accuracy for most practical applications. The two-dimensional collimation effect can then be split into two one-dimensional effects.

1. SLIT LENGTH EFFECT

Let us assume for the moment that the profile $Q(x)$ is infinitely narrow. The line-shaped primary beam with its intensity distribution $P(t)$ causes a *smeared* scattered intensity $\tilde{I}(m)$. The experimental abscissa m measures the distance between scattered beam and centre of the primary beam in the plane of registration, m is related to the reduced angular variable h and the scattering angle 2θ by the relations

$$h = \frac{4\pi}{\lambda} \cdot \sin \theta \quad (2a) \qquad \text{and} \qquad 2\sin\theta \approx \frac{m}{a} \quad (2b)$$

The combination of Eqns (2a) and (2b) gives

$$m \approx \frac{\lambda \cdot a}{2\pi} \cdot h \quad (3)$$

with λ being the wavelength of the radiation and a the distance between the sample and the plane of registration.

The smeared intensity $\tilde{I}(m)$ is the integral over the theoretical intensity $I(m)$ weighted by the intensity function $P(t)$. The argument of the integrand results from a simple geometrical consideration by Guinier and Fournet (1947a, b) and (1955) (see Fig. 1a).

$$\tilde{I}(m) = \int_{-\infty}^{\infty} P(t) \cdot I(\sqrt{(m^2 + t^2)}) dt = 2 \int_0^{\infty} P(t) \cdot I(\sqrt{(m^2 + t^2)}) dt \quad (4)$$

The intensity distribution $P(t)$ can always be transformed into an even function. Equation (4) assumes that the primary beam entering the sample has no divergence in the direction of the coordinate t . Therefore it is necessary to measure the intensity profile as far as possible from the sample (distance a^*), normally in or near the plan of registration (distance a). This profile can be used as a virtual parallel profile in the sample plane (Fig. 1b). If the distance a^* is not

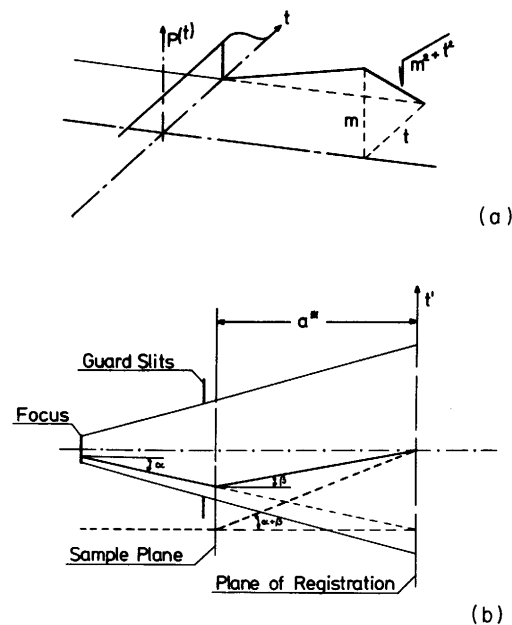


FIG. 1. (a) Geometrical description of the slit length effect. (b) Definition of the intensity profile $P(t)$ as a virtual parallel beam.

exactly equal to the distance a used for the registration of $\hat{I}(m)$, the profile must be subjected to the linear transformation

$$P(t) = P_a * (k \cdot t') \quad (5)$$

with $k = a/a^*$.

2. SLIT WIDTH EFFECT

This effect is caused by the intensity profile $Q(x)$, i.e. by the extension of the primary beam perpendicular to the slit length. It can be described by the convolution integral

$$\hat{I}(m) = \int_{-\infty}^{\infty} Q(x) \cdot I(m-x) dx = \widetilde{QI} = Q * I \quad (6)$$

The function $Q(x)$ cannot be assumed to be an even function. The profile $Q(x)$ should be measured in the plane of registration for the same reasons as discussed for the slit length profile.

B. The Detector

The detector window has a finite size. The limiting detector slits are adjusted according to the size of the primary beam profiles $P(t)$ and $Q(x)$ (see Chapter 3). Again, we assume that the slit length to be large compared to the slit width.

1. DETECTOR SLIT LENGTH

The detector slit length has the same effect as the extension of the primary beam $P(t)$. However, it is not necessary to evaluate a new smearing integral. One can show that it is possible to combine the two effects (detector slit length and $P(t)$) by a convolution of the profile $P(t)$ with a step function corresponding to the detector slit length. This convolution is already performed experimentally if the profile $P(t)$ is recorded with the same detector window.

2. DETECTOR SLIT WIDTH

As with the detector slit length, the detector slit width causes an additional smearing effect. Since the primary beam profile $Q(x)$ is usually measured with the same detector slit width as the scattering curve, it is not necessary to make additional corrections.

3. DEPTH OF THE DETECTOR

If a position sensitive counter is used it results in an additional smearing effect if the X-rays do not enter the counter perpendicular to the wire. The degree of smearing is influenced by the vertical projection and by the absorption effect (Henne, 1976). The smearing integral is given by

$$I_d(m) = \int_{(1-d/a)m}^m I(m') \cdot Z(m-m', m') dm' \quad (7)$$

d is the total depth of the counter and the kernel Z is given by

$$Z(y, m) = \frac{\mu a}{m} \left[(1 - e^{-\mu d})^{-1} \right] e^{-(\mu a/m)y} \quad (8)$$

with μ being the absorption coefficient. The width of the smearing integral (7) is given by $m \cdot d/a$. This is a relative small number for usual configuration ($a \approx 20$ cm, $d \approx 0.4$ cm), and the effect can therefore be neglected if the measurements do not reach into the wide angle range.

C. Wavelength effect

The smearing effect caused by a wavelength distribution $W(\lambda')$ in the primary beam can be described by the wavelength integral (Guinier and Fournet, 1955)

$$I_\lambda(m) = \int_0^\infty W(\lambda') \cdot I\left(\frac{m}{\lambda'}\right) d\lambda' \quad (9)$$

where $\lambda' = \lambda/\lambda_0$ and λ_0 is the mean wavelength used in Eqn (2a). From this equation we see that the wavelength effect is zero for $h = 0$ and that the effective smearing interval increases linearly with the scattering angle. The accurate experimental determination of $W(\lambda')$ is rather difficult, and the wavelength distribution is therefore often approximated by a sum of two delta functions (K_α and K_β -line, see Zipper, 1969). This is only a rough approximation. It does not take into account the contribution of the white radiation in the region between 1,5 and 2,0 Å, which is detected with high efficiency by the counter. The wavelength profile is of great importance for neutron small angle scattering where the half width of the wavelength distribution is usually around 10%.

D. Combined Formulae

If the experimental set-up is such that detector depth effects can be neglected, the correction for the remaining three effects can be performed with one single formula:

$$I_{\text{exp}}(m) = 2 \int_{-\infty}^{\infty} \int_0^{\infty} \int_0^{\infty} Q(x) \cdot P(t) \cdot W(\lambda') \cdot I\left(\frac{\sqrt{(m-x)^2 + t^2}}{\lambda'}\right) d\lambda' dt dx \quad (10)$$

In the application of this formula the integrals have to be computed in the sequence: wavelength integral, slit length integral and slit width integral. If we want to connect the experimental scattering curve directly with the distance distribution $p(r)$, we have to consider the Fourier integral

$$I(h) = 4\pi \int_0^{\infty} \gamma(r) \cdot r^2 \frac{\sin hr}{hr} dr = 4\pi \int_0^{\infty} p(r) \frac{\sin(hr)}{hr} dr \quad (11)$$

where $p(r) = \gamma(r) \cdot r^2$.

Insertion of Eqn (11) into Eqn (10) yields:

$$I_{\text{exp}}(h) = 8\pi \int_{-\infty}^{\infty} dx \int_0^{\infty} dt \int_0^{\infty} d\lambda' \int_0^{\infty} dr Q(x) \cdot P(t) W(\lambda') p(r) \frac{\sin \beta}{\beta} \quad (12)$$

with $\beta = r \cdot [(h-x)^2 + t^2]^{1/2}/\lambda'$. The experimental variables t and x have to be reduced variables like h according to Eqn (2). The angular dependence of

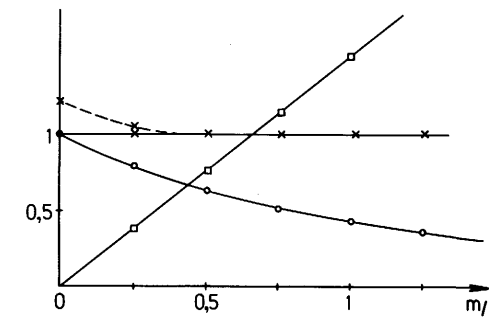


FIG. 2. Angular dependence of the ranges of integration of the smearing integrals: o--o slit length effect (slit length \bar{L}), x-x-x slit width effect, □-□-□ wavelength effect.

the smearing effect of the particular functions $P(t)$, $Q(x)$ and $W(\lambda')$ can be illustrated with the dependence of the effective range of integration on the angular position. The effect of slit length smearing decreases with increasing m -value as we can see from Fig. 2 where the $P(t)$ -function is assumed to be a step function with a full width of $2\bar{L}$.

The slit width effect is represented by a convolution integral and is therefore independent of the actual position. Contrary to the slit length integral, however, the integration runs from smaller m -values over the actual m -value to larger m -values. This gives rise to an enlargement of the real smearing effect near the central main maximum.

The wavelength effect (and the detector depth effect) increases linearly with the scattering angle and is zero at the origin. Scattering curves of quasi periodic shape (scattering function of a sphere: $\tau_h \approx \pi/R$) should not be measured with profiles $Q(x)$ and $W(\lambda')$ with an effective width equal to the period τ_h .

The general influence of all three smearing effects on the shape of the scattering curve is, that the curves are smoothed, i.e. maxima and minima are less pronounced and the slope of the curve is changed.

II. Preliminary Data Treatment

In most cases one is interested in the structure of particles in solution. The particle scattering curve is obtained by subtracting the scattering curve of the solvent (blank scattering) from the scattering curve of the solution. The concentration effect (interparticle interferences) is usually eliminated by considering a concentration series, i.e. one determines the scattering curves of several solutions of decreasing concentration. The extrapolation to zero concentration leads to the particle scattering curve free from concentration effects (see Chapter 7). The repetition of each measurement several times helps to

avoid systematic errors. Thus, one ends up with a large number of scattering curves which have to be averaged, extrapolated and subtracted taking into account the statistical significance of each individual curve. These preliminary steps of data reduction do not contain difficult mathematical operations, and they can easily be performed with a computer program (see Zipper, 1972).

III. Smoothing, Desmearing and Fourier Transformation

A. Introduction

The experimental scattering curve $I_{\text{exp}}(h)$ cannot be determined for the whole of reciprocal space ($0 \leq h \leq \infty$). At small h -values the measurement is limited by the unscattered primary beam, and at large h values by the progressive decrease of the signal to noise ratio. The scattered intensity is usually determined at discrete points (defined by the fixed position of the conventional counter or by the channel number of the position sensitive counter). According to counting statistics, the standard deviation of each data point is equal to the square root of the number of pulses registered by the counter.

The main target of the data processing is to obtain the two functions $I(h)$ and $p(r)$ from the experimental scattering curve $I_{\text{exp}}(h)$ represented by M data points. This situation is illustrated schematically in Fig. 3.

In the following, we shall restrict ourselves to non-oriented particles, for example particles in solution. In such a system, a large number of randomly oriented particles contribute to the physical scattering process, and the resulting spatial average leads to a loss of information: the three-dimensional electron density distribution $\rho(r)$ (describing the whole structure of the particle) is thereby reduced to the one-dimensional distance distribution function $p(r)$. We "observe" the particle indirectly by means of scattering. This physical process of scattering can be described mathematically by a Fourier transformation (transformation T_1 , Eqn (11)), which results in the unsmeared scattered intensity $I(h)$. Allowance for the various collimation effects (transformations $T_2 - T_4$) leads to the smeared scattered intensity; the experimental data points, $I_{\text{exp}}(h)$ are affected by the statistical error $\epsilon(h)$.

The target of data treatment is to obtain the functions $I(h)$ and $p(r)$ from the finite number of observed intensity values, i.e. to find the inverse of the transformations T_1 to T_4 . The procedure has to allow for the statistical accuracy (smoothing, least squares approximation), has to solve the desmearing problem and has to perform the Fourier transformation. These problems can be solved in several steps (multi-step procedures) or in one-step (single-step procedures). The smoothing and desmearing operations are performed prior to the Fourier transformation in the multi-step procedures. The problem of error accumulation

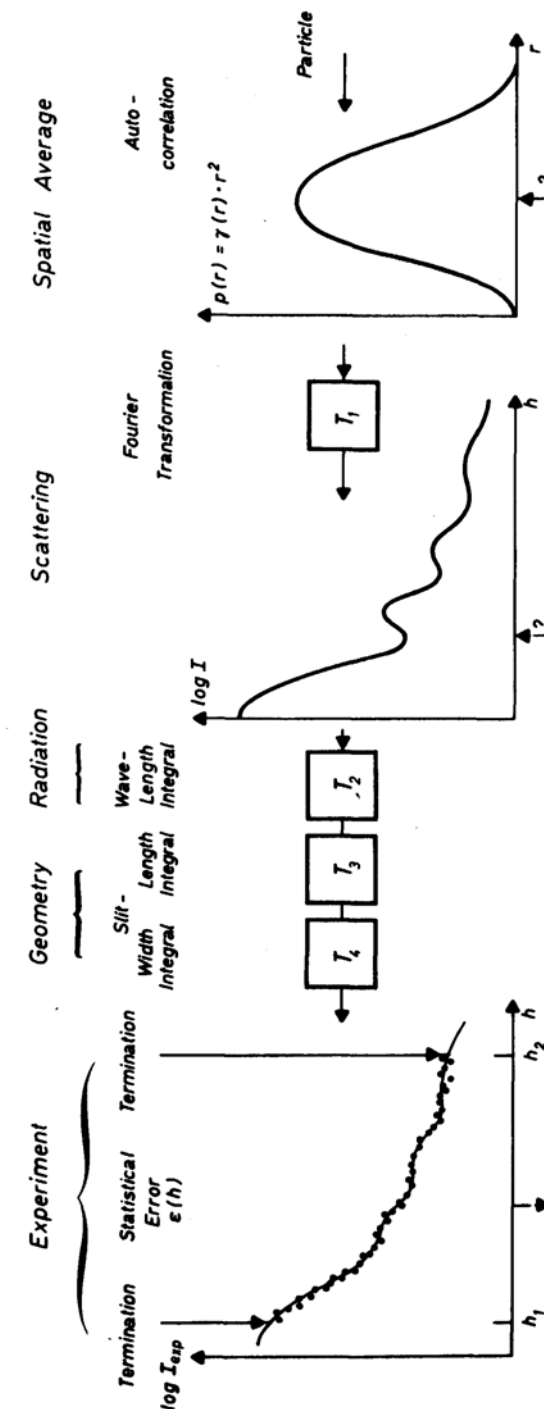


FIG. 3. Schematic representation of the correlation between a particle and its observable experimental scattering data.

is usually less severe in single-step procedures. In any case, the correct sequence: slit width, slit length and wavelength desmearing has to be observed (Glatter and Zipper, 1975). The essential problems of the desmearing procedure are the unavoidable smoothing of statistical fluctuations and the termination effect. The termination effect is also the main problem in Fourier transformation, since the direct inverse transformation T_1^{-1} requires in principle the knowledge of the scattering function for an infinite angular range. Any extrapolation of the scattering function may introduce systematic errors. Nevertheless, extrapolation is often performed towards zero angle to enable the estimation of several molecular parameters.

The number of desmearing procedures described in the literature is large and is still increasing (Guinier and Fournet, 1947a, b; 1955; Kratky *et al.*, 1951; Kratky *et al.*, 1960; Schmidt and Height, 1960; Syneček, 1960; Heine and Roppert, 1962; Heine, 1963; Fedorov *et al.*, 1965; Schmidt, 1965; Shchedrin and Feigin, 1966; Taylor and Schmidt, 1967, 1969; Lake, 1967; Hoßfeld, 1971; Vonk, 1971; Damaschun *et al.*, 1971; Patel and Schmidt, 1972; Glatter, 1972; 1974; Vonk, 1975; Jaeneke, 1975; Glatter, 1977b; Mazur, 1977; Schollmeyer *et al.*, 1977; Deutsch and Luban, 1978a, b; Moore, 1980). In addition, there exists several papers dealing with the smoothing problem (Damaschun *et al.*, 1968; Oelschlaeger, 1969; Brämer and Wenig, 1972).

B. Multi-step Procedures

1. SMOOTHING AND DESMEARING

Historically, the first desmearing procedures were developed for the most important effect, the slit length effect. Guinier and Fournet (1947a, b; 1955) described a method which assumes an infinitely long primary beam. This assumption holds if the profile $P(t)$ is constant within the region $t \geq h^*$ where the scattering intensity $I(h)$ with $h \geq h^*$ is negligibly small. The smearing integral equation is solved by an integration procedure with the integrand being by the first derivative of the smeared scattering function.

$$I(h) = -\frac{1}{\pi c} \int_0^\infty \frac{\tilde{I}'(\sqrt{(h^2 + t^2)}) dt}{\sqrt{(h^2 + t^2)}} \quad (13)$$

Estimation of the first derivative, however, is a serious problem, which necessitates a preliminary smoothing of the data.

Kratky *et al.* (1951) have extended the above method to include $P(t)$ -functions of trapezoidal shape.

Heine and Roppert (1962) have adapted this method to be carried out by a digital computer. A technique for the preliminary elimination of the slit

width effect was described by Kratky *et al.* (1960). This method requires symmetrical $Q(x)$ functions and the accuracy increases for decreasing width of the $Q(x)$ function.

The procedure of Schmidt (1965) and Taylor and Schmidt (1967) is a widely used improvement of Guinier's method. It assumes a Gaussian $P(t)$ -function, which allows partial integration and avoids the computation of the first derivative. The smoothing of the experimental data is performed by a piecewise approximation by polynomials. Experimental data have to be provided at relatively small equidistant intervals with equal accuracy. There is some loss of information at the innermost scattering points.

Damaschun *et al.* (1968, 1971) were the first to use the sampling theorem of Fourier transformation as a basis for a smoothing procedure. Their method takes an estimate of the maximum intraparticle distance as a physical smoothing condition. The desmearing is performed in a second step with the procedure of Heine and Roppert (1962).

Lake (1967) has described an iterative desmearing method, which is very simple and allows arbitrary slit functions $P(t)$ and $Q(x)$. Preliminary smoothing of the data is necessary, and the results are not always of sufficient quality (Schmidt, 1967; Walter *et al.*, 1974).

A procedure for the correction of the wavelength effect caused by the K_β -line has been developed by Zipper (1969). His method assumes a wavelength profile which is composed only by the K_α and the K_β line.

The first attempts to use a problem-specific function system for the approximation of small angle scattering curves was undertaken by Hoßfeld (1968). The innermost part of any scattering curve can be fitted perfectly by the Hermite-function with index zero which is a Gaussian function. Unfortunately, the approximation of the residual part by a series of Hermite functions shows poor convergence.

Several important new aspects are included in the procedure of Schelten and Hoßfeld (1971). This constrained weighted least squares technique, allowing arbitrary primary beam profiles, results in an approximation function with minimized second derivative. Cubic B-spline functions are used as a basic set. The smoothing effect is excellent, but the minimization of the second derivative has the danger of an uncontrolled flattening of maxima, in particular of the main maximum at zero angle. This effect increases with increasing statistical error.

The integral Eqn (4) is reduced to a linear system of equations in the procedure of Vonk (1971). Arbitrary slit length profiles $P(t)$ can be corrected, but the routine does not correct the slit width effect. A weighted approximation of the data is performed by a reduction of the actual number of unknowns calculated in one step of the solution. The termination effect and artificial oscillations caused by the statistical error are sometimes not negligible.

The desmearing procedure for the slit length effect developed by Strobl

(1970) has no restrictions to the primary beam function $P(t)$. The error propagation is discussed, but it is not a weighted least squares procedure. The method is appropriate for scattering curves containing sharp reflections, since the primary result is the integrated scattering function.

An improvement of the iterative method which overcomes most of the problems involved in Lake's procedure was described by me (1972, 1974). This new iterative method allows the correction of both geometrical effects and of the wavelength effect in one single step for arbitrary weighting functions $P(t)$, $Q(x)$ and $W(\lambda')$. The procedure has an implicit smoothing routine, the degree of smoothing is dependent on a freely selectable smoothing parameter and on the accuracy of the data. The iterative process is controlled by a weighted least squares condition. The number of necessary iterations is estimated by a convergence criterion, the termination effect is minimized. The method can be used for arbitrary types of scattering functions since no special mathematical function system is used. The accuracy of the result is comparable to the one of the experimental data, but it is impossible to perform a rigid error propagation analysis. Slight artificial oscillations may occur in the innermost part of the desmeared scattering function. A modification of this method for scattering curves with discrete reflexion was described by Jaeneke (1975).

The recent method of Deutsch and Luban (1978a, b) gives an exact, explicit solution of the slit length effect for arbitrary weighting functions. The slit length weighting function $P(t)$ has to be transformed by an integral equation. The solution is found through a Laplace transformation. This has first been done by Fedorov *et al.* (1968), who found that this procedure is not very useful for numerical calculations (Schmidt and Fedorov, 1978). Deutsch and Luban, who apparently were not aware of Fedorov's work, rediscovered the Laplace transform solution. The scattering curve must be extrapolated to $h = \infty$ in order to minimize truncation errors, and must be very carefully extrapolated to $h = 0$. For the latter extrapolation it is necessary to have zero slope and an "accurate" measure of the second derivative (radius of gyration) at $h = 0$; otherwise, unreasonable scattering functions are obtained (Schelten and Hendricks, 1978).

2. FOURIER TRANSFORMATION

A conventional Fourier transformation can be carried out after desmearing with any technique, in order to compute the distance distribution function:

$$p(r) = \frac{1}{2\pi^2} \int_0^\infty I(h) \cdot (hr) \cdot \sin(hr) dh \quad (14)$$

Here, the main problems are the termination effect and the influence of a remaining background scattering. These may cause such strong artificial

oscillations ("Fourier ripples") in the $p(r)$ -function that it becomes useless. The termination effect can be reduced by extrapolations of the scattering curve. The Guinier approximation can be used for the extrapolation to zero angle if the first data points are measured down to very small angles. Another extrapolation technique (Damaschun and Pürschel, 1971a, b) makes use of the Fourier sampling theorem and of an estimate D_{\max} for the maximum distance D of the particle. This method makes use only of the scattered intensities at the points $h_k = k \cdot \pi/D_{\max}$, no least squares approximation is involved to use intermediate points registered in the experiment.

The extrapolation to large angles can sometimes be performed with Porod's law (see Eqn 42 in Chapter 2). An artificial temperature factor (e^{-kh^2}) should not be applied to damp the Fourier ripples, since it leads to a loss of information. It will be demonstrated in the next part of this chapter that the termination effect can be minimized with the help of the Indirect Fourier Transformation method.

C. Single Step Procedure – Indirect Transformation Method

The Indirect Transformation Method (Glatter 1977a, b) combines the following demands: single step procedure, optimized general function system, weighted least squares approximation, error propagation, minimization of the termination effect and consideration of the physical smoothing condition given by the maximum intraparticle distance. This smoothing condition requires an estimate D_{\max} as an upper limit of the largest particle dimension D :

$$D_{\max} \geq D \quad (15)$$

If such an estimate can be given it follows that

$$p(r) = 0 \quad \text{for } r \geq D_{\max}$$

for scattering curves which are extrapolated to zero concentration (no interparticular interferences). For the following it is not necessary that the equality in Eqn (15) holds, i.e. D_{\max} need not to be a perfect estimate of D .

The function system should be defined in this range $0 \leq r \leq D_{\max}$ and a linear combination

$$p_A(r) = \sum_{v=1}^N c_v \varphi_v(r) \quad (16)$$

is used as an approximation to the distance distribution function $p(r)$.

Let N be the number of functions and c_v be the unknowns. The functions $\varphi_v(r)$ are chosen as cubic B-splines (Greville, 1969; Schelten and Hößfeld, 1971). They are defined as multiple convolution products of a step function and they represent curves with a minimum second derivative.

Each individual function φ_ν can be subjected to the transformations T_1 to T_4 . The intermediate result after the transformation T_1 represents scattering intensities without collimation effects corresponding to a distance distribution represented by $\varphi_\nu(r)$:

$$\Psi_\nu(h) = T_1\varphi_\nu(r) \quad (17)$$

Smeared intensities result after execution of all transformations

$$\chi_\nu(h) = T_4 T_3 T_2 T_1 \varphi_\nu(r) = T_4 T_3 T_2 \Psi_\nu(h) \quad (18)$$

The functions $\chi_\nu(h)$ constitute an optimized system for the approximation of scattering data from a particle with maximum dimension D_{\max} , measured under the conditions represented by $T_1 - T_4$. The coefficients c_ν are determined by a weighted least squares approximation to the experimental data $I_{\exp}(h)$.

A theoretical limitation for the number of functions $N = N_{\max}$ follows from the sampling theorem (Glatter, 1980b). This limitation leads to a relative small number of terms in the expansion Eqn (16) and may cause considerable termination effects. One of the main ideas of the indirect transformation technique is to start with a larger number of coefficients ($N > N_{\max}$) to guarantee a sufficient representation of the distance distribution function. These coefficients are then correlated by a stabilization routine. This technique could be explained as a reduction of the effective number of coefficients. Practical experience showed that this procedure gives better results than the usual unstabilized least squares routine with $N \leq N_{\max}$ (Glatter, 1980b). The stabilized least squares condition is given by

$$(L + \lambda N_{c'}) = \min. \quad (19a)$$

with

$$L = \int_{h_1}^{h_2} \left[I_{\exp}(h) - \sum_{\nu=1}^N c_\nu \chi_\nu(h) \right]^2 / \sigma^2(h) dh \quad (19b)$$

and

$$N_{c'} = \sum_{\nu=1}^{N-1} (c_{\nu+1} - c_\nu)^2 \quad (19c)$$

where h_1 and h_2 are the angles of the first and the last data point, $\sigma^2(h)$ is the estimated variance of the observed intensities and λ is a stabilization parameter (Glatter, 1977a, b).

Possible reasons for a breakdown of the stabilized least-squares algorithm are systematic errors in $I_{\exp}(h)$ and $\sigma(h)$, or the choice of inconsistent parameters (incorrect value for D_{\max} , or the use of too many spline functions – corresponding to an attempt to overinterpret the experimental data).

The coefficients c_ν , resulting from Eqn (19) define the solution in real space according to Eqn (16). The optimum fit to the observed data points is given by

$$I_A(h) = \sum_{\nu=1}^N c_\nu \chi_\nu(h) \quad (20)$$

and the desmeared scattering curve is defined by the series

$$I_A(h) = \sum_{\nu=1}^N c_\nu \Psi_\nu(h) \quad (21)$$

(see Fig. 4). The radius of gyration can be estimated from $p_A(r)$ as follows:

$$R_A^2 = \int_0^{D_{\max}} p_A(r) \cdot r^2 dr / 2 \int_0^{D_{\max}} p_A(r) dr \quad (22)$$

This approximation offers the advantage that the radius of gyration is calculated from the smeared data points, using the whole available scattering curve requiring only information on the maximum size D_{\max} . For this reason, this approximation frequently yields more accurate results than the Guinier approximation.

An approximate value for the intensity at zero angle can be computed in a similar way:

$$I_A(0) = 4\pi \int_0^{D_{\max}} p(r) dr \quad (23)$$

Numerical tests have demonstrated that the radius of gyration can be estimated from Eqn (22) with good accuracy even for situations where the Guinier approximation breaks down due to high termination values $h_1 D$. A comparison of the results of different approximation methods for two different types of particles is given in Fig. 5.

An additional advantage of the Indirect Transformation Method is the fact that it offers the possibility of calculating the propagated error band in real space. One has to keep in mind, however, that this error band represents only the error from counting statistics. Systematic errors in the measurements cannot be detected by such a general treatment. Sometimes, however, they are indicated by a breakdown of the stabilization procedure. Systematic errors introduced by the computational methods can be detected by means of simulations (see Section III.F4 of this chapter).

The efficiency of the Indirect Transformation Method is illustrated in Fig. 6: the example shows a simulated scattering curve of a sphere ($D = 200 \text{ \AA}$), smeared according to the slit length effect with a statistical error of 5%. The scattering angles of the first and the last data point are $h_1 = 0,016$ ($h_1 \cdot D_{\max} \approx 3,8$) and $h_2 = 0,06$. The solution was obtained with 20 splines, $D_{\max} = 1,25 \cdot D = 250 \text{ \AA}$. The accuracy of the radius of gyration, computed with Eqn (22) is 1,5%, the zero intensity can be estimated with an error of 2,5%. The error propagation analysis already developed in the first papers (Glatter, 1977a, b) was improved by a recent modification of the indirect transformation method (Moore, 1980). The error treatment is not only performed for the $p(r)$ function but also for all derived parameters like radius of gyration Rg , forward scatter $I(0)$ and so on.

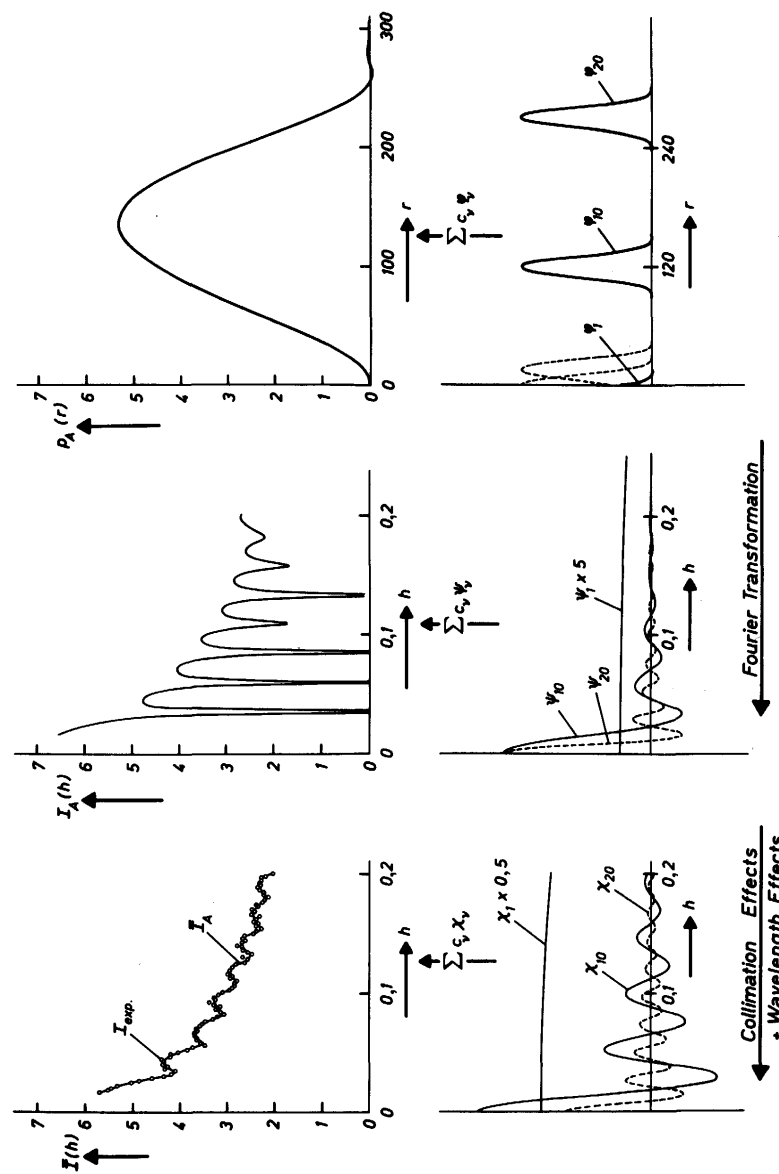


FIG. 4. Function systems $\varphi_\nu(r)$, $\Psi_\nu(h)$ and $x_\nu(h)$ used for the approximation of the scattering data in the indirect transformation method.

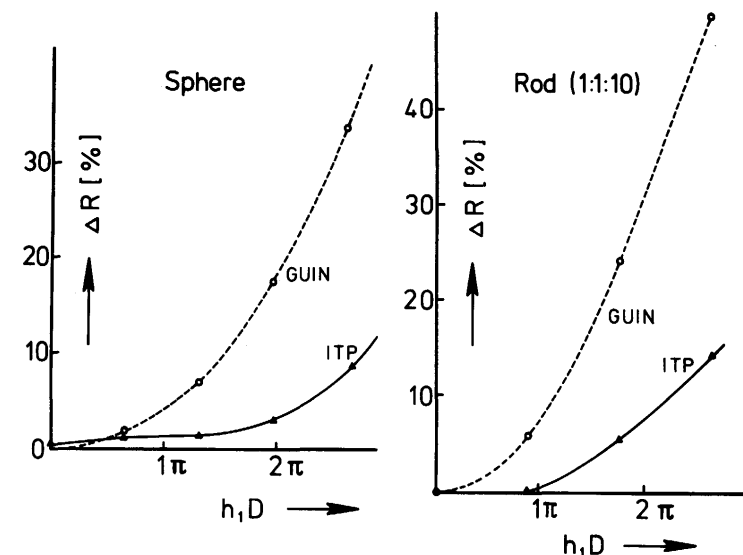


FIG. 5. Dependence of the accuracy of R determined by Guinier's approximation as well as calculated by the indirect transformation method on the angular resolution at small angles (h_1 = innermost measuring angle) for a sphere and a rod. The deviation ΔR of the experimental value from the model value is given in percentages.

Sine functions are used for the expansion in real space allowing much simpler mathematics as the Fourier transformation can be performed analytically and leads to $(\sin x/x)$ -functions in reciprocal space. The disadvantage of this function system is on the other hand that the termination effect and the errors introduced by non-eliminated background scattering is the same as in the conventional transformation technique. The desmearing problem is solved in the same way as in my method. Comparing the two methods one can say that both procedures give similar results for standard applications, the indirect transformation method is superior to the sine-function method of Moore if the termination and background effects are essential while the later method will be superior in cases of high resolution measurements, i.e. measurements with a high ratio of the h -values of the last and the first data point h_2/h_1 . The method of Moore is a cross between my indirect transformation method and the evaluation method of Damaschun and Pürschel (1971a, b) which is a direct Fourier filtering technique combined with the conventional desmearing routine. All three methods are Fourier filtering techniques using an estimate D_{\max} . This estimate can be found directly if $h_1 D_{\max} < \pi$ (Müller and Glatter, 1981; Moore, 1980) or by a cosine-transformation (Müller *et al.*, 1980).

The indirect transformation method has been modified for cylindrical and lamellar particles and for polydisperse systems (see Section III.E of this chapter).

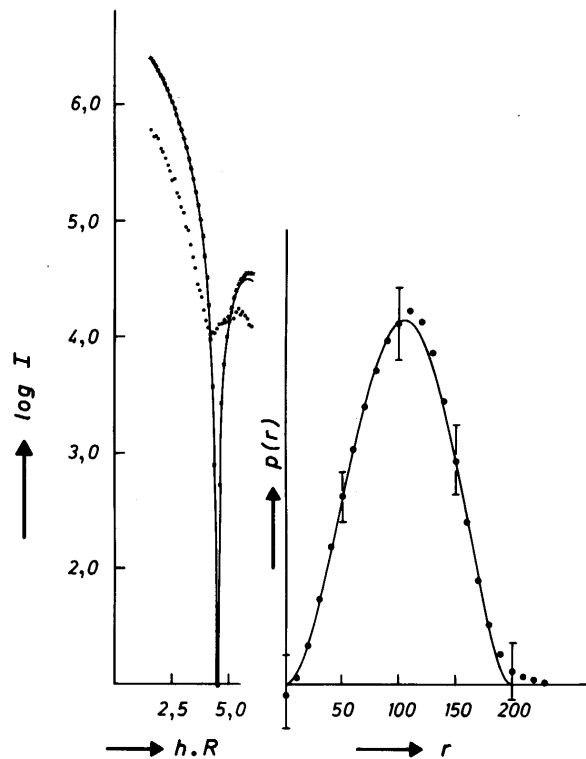


FIG. 6. Indirect transformation: *left part*: — theoretical scattering function of a sphere with radius $R = 100 \text{ \AA}$. ····· simulated data, smeared according to slit length effect, 5% statistics, $h_1 R = 1.6$; $h_2 R = 6.0$; $\Delta h R = 0.1$. ××× desmeared scattering function. *Right part*: — theoretical $p(r)$ function. ····· distance distribution with propagated error (I) computed from the simulated data using $D_{\max} = 250 \text{ \AA}$.

D. Resolution

1. MAXIMUM PARTICLE DIMENSION

It is common practice in the small angle literature to define the resolution from the lowest scattering angle h_1 using the Bragg relation

$$h_1 D_{\text{Bragg}} = 2\pi \quad \text{or} \quad D_{\text{Bragg}} = \frac{2\pi}{h_1} \quad (24)$$

In small angle scattering one is usually not concerned with periodical structures, but with scattering functions of isolated particle with finite extension in real space. It must therefore be emphasized that D_{Bragg} is only a special measure

for the smallest scattering angle which is not identical to the maximum dimension of particles that can be studied.

The sampling theorem of Fourier transformation (Shannon and Weaver, 1949; Bracewell, 1965) gives a clear answer to the question of largest particle size. If the scattering curve is observed at increments $\Delta h \leq h_1$ starting from a scattering angle h_1 , the scattering data contain the full information for all particles with maximum dimension D

$$D \leq \frac{\pi}{h_1} \quad (25)$$

The first application of this theorem to the problem of data evaluation was given by Damaschun and Pürschel (1971a, b). In practice one will have to stay well below this limit, i.e.

$$h_1 < \frac{\pi}{D} \quad \text{and} \quad \Delta h \ll h_1 \quad (26)$$

taking into account the loss of information due to counting statistics and smearing effects. An optimum value for $\Delta h = \pi/(6D)$ is claimed by Walter *et al.* (1974).

2. RESOLUTION

There is no clear answer to the question concerning the smallest structural detail, i.e. details in the $p(r)$ function that can be recognized from an experimental scattering function. The limiting factors are the maximum scattering angle h_2 , the statistical error $\sigma(h)$ and the weighting functions $P(t)$, $Q(x)$ and in particular $W(\lambda')$ for neutron experiments.

The resolution in the $p(r)$ function can be expressed mathematically if we introduce a sampling distance in real space. Such a sampling distance ΔR must fulfill the condition

$$\Delta R \geq \pi/h_2 \quad (27a)$$

if the scattering curve is known up to the scattering angle h_2 . The sampling limit given by Eqn (27a) can be used without systematic error only if the scattering intensity $I(h)$ is zero for all $h > h_2$. We have to keep in mind that we are discussing here only the termination effect and that the condition of Eqn (27a) is necessary but may not be sufficient for an exact representation of scattering curves with smearing effect and statistical error.

A sampling in real space is performed implicitly by the indirect transformation method. The sampling distance ΔR is given by the distance DRB between the knots of the spline functions. This distance is related to the upper limit for the maximum particle dimension D_{\max} and the number of splines N by

$$DRB = D_{\max}/N \quad (27b)$$

A theoretical limitation for the number of functions N would follow from the combination of the Eqns (27a) and (27b)

$$N_{\max} \leq \frac{h_2 \cdot D_{\max}}{\pi} \quad (27c)$$

The same number follows directly from the sampling theorem of Fourier transformation for an expansion of the distance distribution function in a series of sine functions

$$N_{\max} \leq \frac{h_2}{\Delta h} \leq \frac{h_2 \cdot D_{\max}}{\pi} \leq \frac{h_2}{h_1} \quad (27d)$$

taking into account Eqns (15) and (16). With a low ratio h_2/h_1 we end up with a relatively small number of terms in the series expansion. This may lead to considerable termination effects for sine-series with so-called Fourier ripples in the $p(r)$ function and with a scattering curve that drops to zero very rapidly for $h > h_2$. The indirect transformation technique working with spline functions and stabilization allows the use of larger numbers for N ($N > N_{\max}$) and can minimize the termination effects, i.e. Fourier ripples are negligible and scattering curves are not forced to zero at the limit \bar{h} with

$$\bar{h} = \frac{\pi}{\Delta R} = \frac{\pi}{DRB} \quad (28a)$$

and do not increase behind this "mirror point". This is shown, for example, for a scattering function of a sphere ($D = 200 \text{ \AA}$, $D_{\max} = 240 \text{ \AA}$, $N = 20$, $DRB = 12 \text{ \AA}$) without smearing effect and statistical errors in Fig. 7. The scattering curve is represented correctly in its details up to \bar{h} and the general trend is reproduced up to much larger angles, i.e. the problems of "undersampling" (Bracewell, 1965) are not essential for this technique. The real limitation for this technique is given by the numerical operations. The corresponding errors are not negligible for $N > 40$, i.e. scattering curves with a ratio $h_2/h_1 \geq 40$ can not be evaluated with sufficient accuracy with the indirect transformation technique.

3. INFORMATION CONTENT

The information content of a scattering curve can be defined by the maximum number of independent coefficients that can be derived from this curve. This number cannot be determined exactly but an upper estimate is given by Eqns (27c) and (27d), and we have to keep in mind that solutions with the indirect transformation technique with $N > N_{\max}$ do not have N independent coefficients. The information content cannot be increased by any extrapolation technique.

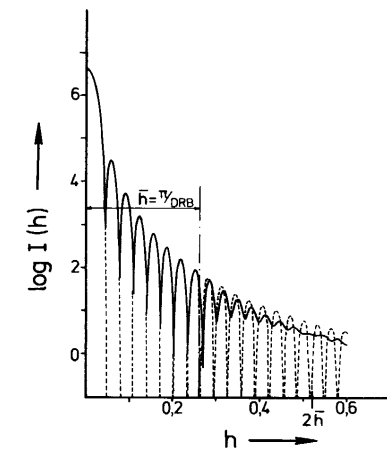


FIG. 7. Indirect transformation method: limitation of the resolution caused by the distance of the knots DRB . ----- Exact scattering function of a sphere, $D = 200 \text{ \AA}$; —— approximation with $DRB = 12 \text{ \AA}$, $D_{\max} = 240 \text{ \AA}$, $N = 20$.

Only the contrast variation technique, i.e. the registration of a series of scattering curves at different contrast may give a higher number of coefficients.

The question of information content is important for the problem of model fitting (see Chapter 5). One has to keep in mind that a number of N spline or sine coefficients do not allow to fit all possible N -parameter models. The transformation of coefficients of a series expansion into independent model parameters is a very complicated problem which does not have a unique solution.

4. DEFINITION OF THE ORIGIN

Quantities like m , t and x are measured from an experimental origin that can, in principle, be chosen arbitrarily.

The origin of the coordinate in the slit length direction should coincide with the centre of the $P(t)$ -function. For the slit width coordinate, it is common to use the centre of gravity as origin, but there exist good reasons to choose the maximum of $Q(x)$ if asymmetric $Q(x)$ -functions are to be corrected by the desmearing routine.

E. Special Transformations

There is no loss of information due to spatial averaging in the case of spherical particles and therefore it should be possible to calculate the radial electron density distribution from the scattering amplitudes.

A detailed evaluation of the scattering contribution of the cross-section would be of interest if the particles have a lamellar or cylindrical structure. Such calculations (Glatter, 1980b) must assume that the particles are homogeneous along the basal plane (lamellae) or along the cylinder axis (cylinder), i.e. the electron density can be written for lamellae (index t) as

$$\rho(r) = \rho_0 \cdot \rho_t(x) \quad (29a)$$

where ρ_0 is a constant and x is the normal distance from the central plane in the lamella; or for cylinders (index c) as

$$\rho(r) = \rho_0 \cdot \rho_c(r_c) \quad (29b)$$

where r_c is a vector in the cross-section plane perpendicular to the cylinder axis. There is again the situation that it should be possible to calculate ρ_t or ρ_c from the scattering amplitudes as there is no loss of information by spatial averaging in these two cases too.

Small angle scattering experiments measure the angular dependence of the scattering intensity. It is impossible to obtain scattering amplitudes which would allow the computation of the electron density by Fourier transformation. However, Fourier transformation of the scattering intensity gives the correlation function or the distance distribution function of the particle. This function is the so-called convolution square of the electron density distribution (Hoseman and Bagchi, 1962; Bracewell, 1965). The electron density distribution can be determined in principle by two different methods from the scattering intensity under the additional assumption of lamellar, cylindrical or spherical symmetry. The conventional procedure starts with the determination of the scattering amplitudes from the scattering intensities by a simple square root operation. The determination of the right sign – known as the so-called phase problem – is the main problem in this step. The critical regions near the zeros are influenced greatly by deviations from ideal symmetry, by polydispersity of the sample and by any experimental errors. These effects lead to the fact that there appear more or less pronounced minima instead of real zeros. There is no unique technique for the estimation of the best symmetrical approximation. The phase problem can sometimes be solved by contrast variation (Mateu *et al.*, 1972; Müller *et al.*, 1974).

Another possible procedure is the Fourier transformation of the scattering intensity and the subsequent computation of the electron density from the distance distribution function by a convolution square root technique. This method does not suffer from the phase problem. The integral transformations for the different symmetries are described in the following Sections III. E1-3 and the convolution square root technique is summarized for all three cases in Section III. E4.

1. SPHERICAL SYMMETRY

The radial electron density can be calculated from the square root of the scattering intensity in the case of spherical particles:

$$\rho(r) = \frac{1}{2\pi^2} \int_0^\infty (I(h))^{1/2} \cdot h^2 \cdot \frac{\sin hr}{hr} dh \quad (30)$$

The phase problem (ambiguity of the sign for the square root) can be resolved by contrast variation (Mateu *et al.*, 1972; Müller *et al.*, 1974). Use of the Indirect Transformation Method (Glatter, 1977a) minimizes the termination effect.

2. HANKEL TRANSFORMATION

The distance distribution of the cross-section of particles elongated in one direction (like cylinders) $p_c(r)$ is correlated to the total scattered intensity $I(h)$ through the equation

$$I(h) = 2\pi^2 L \int_0^\infty p_c(r) \cdot \frac{J_0(hr)}{h} dr = I_c(h) \cdot \frac{\pi \cdot L}{h} \quad (31)$$

where $J_0(hr)$ is the zero-order Bessel function, L is the length of the cylinder and $I_c(h)$ is the scattering intensity of the cross-section (see also Section IV.A in Chapter 2).

The inverse transformation is given by

$$p_c(r) = \frac{1}{2\pi} \int_0^\infty I_c(h) \cdot (hr) \cdot J_0(hr) dh \quad (32)$$

The Indirect Transformation Method offers a particularly convenient way to compute the distance distribution function of the cross-section $p_c(r)$ from the smeared experimental data by simply using Eqn (31) for the transformation T_1 (instead of Eqn (11)) (Glatter, 1980b).

If we assume cylindrical symmetry, and constant electron density along the cylinder axis, a simplification similar to the case of spherical symmetry applies. The radial electron density $\rho_c(r)$ can then be calculated from the Hankel transform

$$\rho_c(r) = \frac{1}{2\pi} \int_0^\infty (I_c(h))^{1/2} \cdot h \cdot J_0(hr) dh \quad (33)$$

(Fedorov and Aleshin, 1967; Fedorov, 1971).

3. COSINE TRANSFORMATION

One is interested in the distance distribution function of the thickness $p_t(r)$ if the particles under investigation are elongated in two directions (lamellae, thin vesicles). The function $p_t(r)$ is correlated with $I(h)$ by the equation

$$I(h) = 4\pi A \int_0^\infty p_t(r) \cdot \frac{\cos(hr)}{h^2} dr = \frac{A \cdot 2\pi}{h^2} \cdot I_t(h) \quad (34)$$

where A is the area to the plane of the lamella and I_t is the scattering intensity of the cross-section (see Section IV.B in Chapter 2). The inverse transformation is given by

$$p_t(r) = \frac{1}{\pi} \int_0^\infty I_t(h) \cos(hr) dh \quad (35)$$

Again, the Indirect Transformation offers the option of computing the function $p_t(r)$ directly from the smeared experimental data by using Eqn (34) instead of Eqn (11) for T_1 .

Let us assume a lamella whose electron density is only a function of the coordinate perpendicular to the lamellar plane (no in-plane inhomogeneity). If the electron density $\rho_t(r)$ is also centrosymmetric, we can calculate this function by the Cosine Transformation

$$\rho_t(r) = \frac{1}{\pi} \int_0^\infty (I_t(h))^{1/2} \cos(hr) dh \quad (36)$$

(Lesslauer *et al.*, 1972; Laggner *et al.*, 1979).

In the special case of thin spherical membranes ($R_a - R_i < 2R_i$) a similar relation between the function $P(r)$ and $I(h)$ applies.

$$P(r) = \frac{1}{\pi} \int_0^\infty I(h) \cdot h^2 \cdot \cos(hr) dh = 4\pi^2 (2\tilde{k}_+^2 - \hat{k}_+ k_+) \quad (37)$$

(Weik, 1974) with $k_+(r) = r \cdot \rho(r)$ for $0 \leq r \leq R_a$.

For the limit of a very thin shell ($R_a - R_i \ll R_a$) we get for small values of r the transition from $8\pi^2 \tilde{k}_+^2$ to $4\pi R^2 \cdot 2\pi p_t(r) = 2\pi \cdot 4\pi p_t(r)$ in agreement with Eqn (35), i.e. the function \tilde{k}_+ centred at $r=0$ is proportional to the function $p_t(r)$ and the approximation for lamellae can be applied. (For further details see Chapter 10.)

4. CONVOLUTION SQUARE ROOT

The cross-section correlation functions $\gamma_t(r)$ and $\gamma_c(r)$ are defined as the spatial average of the convolution square of the scattering length densities:

and

$$\gamma_t(r) = \rho_t(x) * \rho_t(-x) \quad (38)$$

$$\gamma_c(r) = \langle \rho_c(r_c) * \rho_c(-r_c) \rangle \quad (39)$$

The symbol $*$ stands for the mathematical operation called convolution and the symbol $\langle \rangle$ means averaging over all directions in the plane of the cross-section. The distance distribution functions can be defined by

$$p_t(r) = \gamma_t(r) \quad (40)$$

and

$$p_c(r) = r \gamma_c(r) \quad (41)$$

The connection between the cross-section scattering functions and the distance distribution functions is given by the Cosine- and Hankel-transformation of Eqns (34) and (31). The convolution square root is the inverse process to the convolution square, i.e. it allows the computation of $p_t(r)$ or $\rho_c(r)$ from $p_t(r)$ or $p_c(r)$.

It has already been shown for the one-dimensional problem (lamellar symmetry) by Hosemann and Bagchi (1952) and by Engel (1973) that the convolution square root operation has a unique solution (except for a factor ± 1) if the function has a finite range of definition and if the function is symmetrical. The first attempt for the one-dimensional case was made by Hosemann and Bagchi (1962). They solved the problem by discretization of the integral equation. The resulting non-linear equation system has a triangular matrix and can be solved stepwise. An improvement of this technique using an iterative procedure was given by Bradaczek and Luger (1978). A completely different method has been developed by Pape (1974). The method solves the phase problem implicitly by a system of linear equations originating from a sine series development of the correlation function.

All these methods have the property that they give results of sufficient accuracy only for exact input data. Statistical errors are not taken into account by these methods.

A weighted least squares technique for the one-dimensional case developed by Pape and Kreutz (1978) approximates the electron density distribution by a few Gaussian functions. The method is very sensitive to the first data set of the iteration, i.e. it requires good *a priori* information on the signs and positions of the Gaussians. A new method recently developed (Glatter, 1981) needs no such *a priori* information at all and can be applied to any of the three types of symmetry. The electron density is approximated in its range of definition by a linear combination of a finite number of functions that have to be linearly independent in this range:

$$\bar{\rho}(r) = \sum_{i=1}^N c_i \varphi_i(r). \quad (42)$$

N is the number of functions, r is the normal distance from the centre of symmetry, the $\varphi_i(r)$ are equidistant step functions (B splines of zero order) with a width ΔR allowing the analytical integration of the overlap integrals and the c_i are the heights of the step functions to be determined by the method. The function $\bar{p}(r)$ defined by Eqn (42) corresponds to a distance distribution function $\bar{p}(r)$ given by the equation:

$$\bar{p}(r) = \sum_{i=1}^N V_{ii}(r)c_i^2 + 2 \sum_{i>k} V_{ik}(r)c_i c_k \quad (43)$$

The overlap integrals $V_{ik}(r)$ state the overlap of the i th and the k th step shifted a distance r , taking into account the different geometries and the factors r and r^2 in the Eqns (41) and (11). These integrals have been computed analytically (see Glatter, 1981, tables 1-3).

The system of equations (43) is non-linear, but it can be solved by an iterative stabilized weighted least squares procedure starting with an arbitrary but normalized set of (constant) initial coefficients. The propagation of the statistical error of the input function $p(r)$ to the resulting $\bar{p}(r)$ function is defined by the covariance matrix of the solution coefficients c_i . Test series showed that the method converged under all the different test conditions independent of any *a priori* information on the solutions.

Real molecules investigated in an experiment will never fulfill the symmetry conditions perfectly. The results of the tests showed that the method gives satisfying results for slight deviations from the ideal symmetry, the $\bar{p}(r)$ function is a good symmetrical approximation and the fit of the $p(r)$ function and of the scattering function is adequate. This is illustrated in Fig. 8 by an oblate ellipsoid of revolution (1:1.2:1.2) with a two-step electron density distribution ($\rho_i = -0.6$; $\rho_a = 1.0$; $r_a = 53.11$ Å; $r_i = 38.11$ Å). The resulting electron density distribution $\bar{p}(r)$ is shown in Fig. 8a, the fit of the $p(r)$ function in Fig. 8b and the fit of the scattering curve in Fig. 8c.

Larger axial ratios like 1:1.5:1.5 or more lead to appreciable deviations in the $p(r)$ and $I(h)$ fit and the resulting $\bar{p}(r)$ function contains no significant information. The procedure can be employed as a test of symmetry as essential deviations from symmetry are always accompanied by poor approximations of the $p(r)$ function.

The influence of a finite extension of the particle in the direction of the lamella plane or of the cylinder axis is also an important question. The main part of this problem is the computation of the cross-section distance distribution functions $p_t(r)$ and $p_c(r)$. The effects of finite dimensions are negligible if the ratio of the maximum dimension of the particle D and the maximum dimension of the cross-section D_t or D_c is not smaller than ten, but a qualitative evaluation is possible even for smaller ratios (Glatter, 1980b). An example for the computation of $p_c(r)$ and $\rho_c(r)$ for an inhomogeneous cylinder is given in Fig. 9.

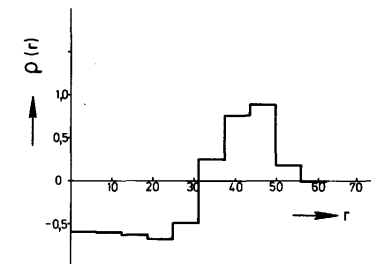


FIG. 8. (a) Electron density profile $\rho(r)$ obtained from an oblate ellipsoid of revolution (axial ratio 1:1.2:1.2) with a two-step electron density distribution ($\rho_i = -0.6$; $\rho_a = 1.0$; $r_a = 53.11$ Å; $r_i = 38.11$ Å).

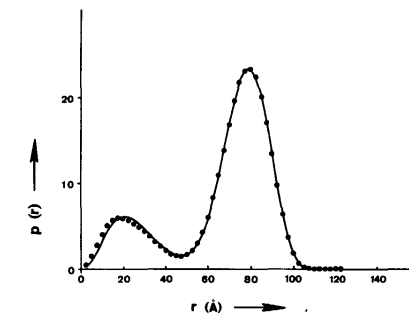


FIG. 8. (b) Fit of the $p(r)$ functions of the oblate ellipsoid model: $p(r)$ function of the model; —— best spherical approximation obtained by the convolution square root technique.

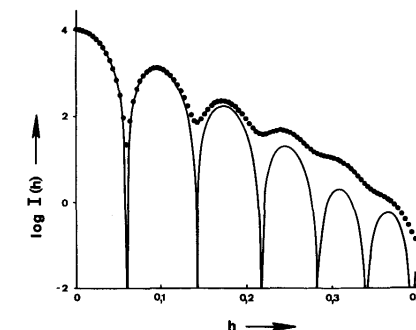


FIG. 8. (c) Fit of the $I(h)$ functions: scattering intensity of the model; —— best spherical approximation by the convolution square root technique.

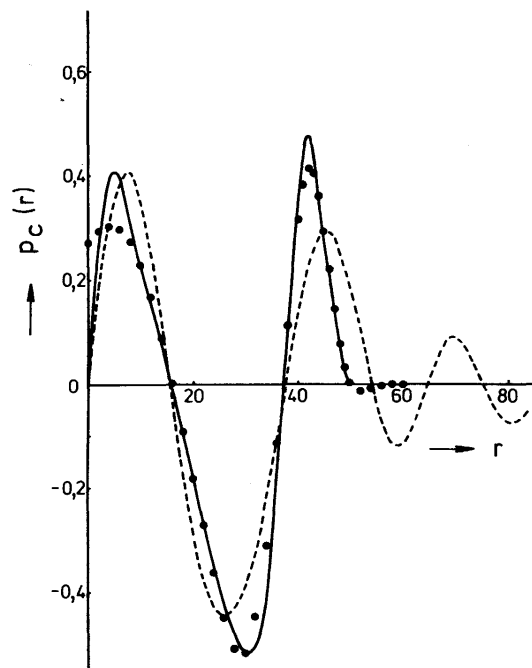


FIG. 9. Cross-section distance distribution function $p_c(r)$ of an inhomogeneous cylinder: — theoretical function for an infinitely long cylinder; ····· results from indirect transformation method; - - - results from direct (conventional) transformation.

The cylinder has the following dimensions: outer radius $R_o = 25 \text{ \AA}$, height $H = 250 \text{ \AA}$ ($H/2R_o = 5$), the electron density profile is a two-step function ($R_i/R_o = 0.7$; $\rho_i = -1.0$; $\rho_o = 1.0$). The scattering intensity is given in the range $0.03 \leq h \leq 0.3$ with an increment $\Delta h = 0.01$. The scattering intensity has been extrapolated to zero angle only for the direct transformation of Eqn (32). The $p_c(r)$ functions resulting from the direct transformation and from the indirect transformation method ($D_{\max} = 60 \text{ \AA}$; $DRB = 6 \text{ \AA}$; $h_1 = 0.08$) are shown in Fig. 9 together with the theoretical $p_c(r)$ function of an infinite long cylinder. The results from the indirect transformation deviate essentially from the theoretical function only in the innermost part below the resolution limit ($r < \pi/h_2 \approx 10 \text{ \AA}$) whereas the direct transform shows the usual termination ripples, the good agreement at very small r -values is insignificant and is caused by the multiplication of $\gamma_c(r)$ by the factor r according to Eqn (41).

The corresponding radial electron density profiles $\bar{\rho}_c(r)$ resulting from the convolution square root procedure ($N = 5$, $\Delta R = DRB = 6 \text{ \AA}$) are shown in Fig. 10.

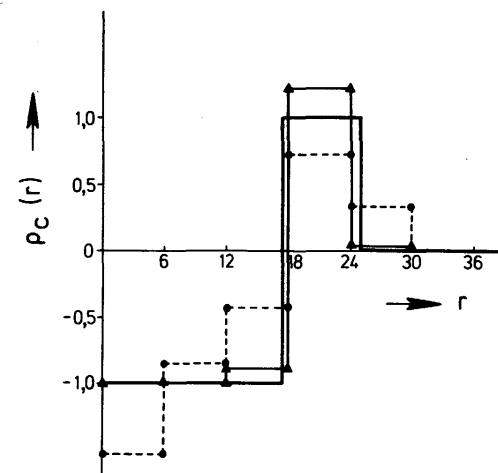


FIG. 10. Radial electron density distribution $\rho_c(r)$ according Fig. 10: — theoretical function; $\Delta-\Delta-\Delta$ five step model ($\Delta R = 12 \text{ \AA}$) obtained by convolution square root from indirectly transformed data; - - - five step model obtained from directly transformed data.

5. PARTICLE SIZE DISTRIBUTIONS

The scattering function of a polydisperse system is determined by the shape of the particles and by the size distribution. It is impossible to determine both the size distribution and the shape from a scattering experiment. We can assume a size distribution and can determine the shape, or more frequently assume the shape and try to determine the size distribution. The problems associated with finding the particle size distribution from the scattering curve are similar to the problems which have been discussed above in connection with the Fourier transformation. We shall assume that the scattered intensity results from an ensemble of particles of the same shape whose size distribution can be described by $D_n(R)$, where R is a size parameter and $D_n(R)$ denotes the number of particles of size R . Let us assume further that there are no interparticle interference or multiple-scattering effects. Then, the scattering function $I(h)$ is given by

$$I(h) = c_n \int_0^\infty D_n(R) \cdot R^6 \cdot i_0(hR) dR \quad (44)$$

c_n is a constant and $i_0(hR)$ is the normalized form factor of a particle of size R . There exist two ways for the computation of $D_n(R)$ (or $D_v = R^3 \cdot D_n(R)$) from $I(h)$: (a) by an inverse transformation like the Fourier transformation, the type of transformation depends on the assumed particle shape; (b) assuming the analytical form of $D(R, k_i)$ and adjusting the parameters k_i in reciprocal space. Again, one has to make an assumption concerning the particle shape.

(a) *Analytical Methods.* An explicit analytical solution for the special case of spherical particles was derived by Roess (1946) and Riseman (1952). These methods involve an integration over the scattering curve from zero to infinity. If it is possible to determine the Porod constant with sufficient accuracy (see Section III.C in Chapter 2) such transformations can be carried out without strong termination effects (Letcher and Schmidt, 1966; Brill and Schmidt, 1968; Brill *et al.*, 1968).

Similar transformations have since been developed for different types of particles: long cylinders (Fedorova, 1977), thin spherical shells (Fedorova and Emelyanov, 1977), thin cylinders (Schmidt *et al.*, 1978), thin circular discs (Schmidt *et al.*, 1978) and flat sheets (Pringle and Schmidt, 1977). A general analytical method for calculating particle-dimension distributions from scattering data was published recently by Fedorova and Schmidt (1978). The size distribution can be calculated using Titchmarsh-transformation if the scattering intensity can be expressed as a square of a Bessel function of the first kind and order ν . All these transformations make no approximation, but the solution function is very sensitive to the extrapolated part of $I(h)$.

(b) *Numerical Methods – Linear Models.* Here we have to distinguish between methods which approximate the function $D_n(R)$ with a special two parameter function (for example the so-called log normal distribution): Roess and Shull (1947), Hoseman (1951), Mittelbach and Porod (1965), Mittelbach (1965), Harkness *et al.* (1969), Neilson (1973), Plestil and Baldrian (1976), and more general approaches which permit a larger number of parameters: Hendricks *et al.* (1974), Plavnik *et al.* (1976), Vonk (1976) and Glatter (1980a).

The parameter estimation is comparatively easy for the two parameter models but the size distribution is biased to a considerable extent by the particular model that was assumed for the size distribution.

The general approaches start with a set of basis functions $\varphi_i(R)$

$$D_n(R) = \sum_{i=1}^N c_i \varphi_i(R) \quad (45)$$

where $N \leq 30$. Hendrick and Plavnik used a set of equally spaced delta functions, in a logarithmic scale and cubic B-splines are used as a basis set in my Indirect Transformation Method. All methods involve a stabilization condition minimizing the first or second derivative: Hendricks uses the additional constraint $c_i \geq 0$ in order to prevent negative values for the size distribution, Vonk needs a strong additional smoothing condition for the first and last parameter. The estimation of the weight of the several constraints (smoothing parameter) has to be performed by trial-and-error (Hendricks, Plavnik, Vonk) and can be determined by the stability plot method in my procedure. A similar graphical method for the estimation of the optimal stabilization parameter has been developed by

Vonk (1978). If Eqn (37) is used for the transformation T_1 instead of Eqn (11) in the indirect transformation method, the size distribution function $D_n(R)$ can be computed from the unsmoothed smeared scattering data.

The method of Vonk and my one were tested for the use of incorrect shape factors. The resulting size distributions are reasonable considering the incorrect assumptions. There exists no detailed comparison of the quality of the different procedures. Conditions for an ideal procedure could be defined as follows:

- (1) The solution should be a smooth function (minimized second derivative or similar constraints).
- (2) Minimized termination effect (no transformation ripples).
- (3) The function $D(R)$ should be positive.
- (4) The function $D(R)$ should be defined in a limited range ($R_{\min} < R < R_{\max}$). Unfortunately conditions (1)–(3) can be contradictory for narrow size distributions.

F. Simulations

Simulations can help to estimate systematic errors introduced by the data evaluation procedures and can be used for the optimization of the experimental design. Simulations are performed with exactly known model systems (test functions). These systems should be similar to the structures of interest. The model data are transformed according to the special experimental situation (collimation and wavelength effect), starting from the theoretical distance distribution and/or scattering function. Experimental data points are generated by sampling in a limited h -range and adding statistical noise from a random number generator. This simulated data set is subjected to the data evaluation procedure and the result is compared with the starting function. Such simulations can reveal the influence of each approximation applied in the various evaluation routines.

On the other hand they can also be used for the optimization of the experimental designs. The experimental situation is characterized by several contradictory effects: a large width for the functions $P(t)$, $Q(x)$ and $W(\lambda')$ leads to high statistical accuracy but considerable smearing effect. The quality of the results of the desmearing procedure is increased by high statistical accuracy (low σ), but decreased by large smearing effects.

IV. Evaluation of Molecular Parameters and Normalization

Several parameters can be evaluated directly from the scattering data. The most important are the molecular weight, the radius of gyration and the volume of the particle (Kratky, 1963).

A. Molecular Weight

1. PARTICLES OF ARBITRARY SHAPE

In the following we assume a scattering function corrected for collimation effect (desmeared) and for interparticle interference. The particle is measured in a homogeneous solution and has an isopotential specific volume v'_2 and z_2 mol. electrons per gram, i.e. the molecule contains $z_2 \cdot M$ electrons if M is the molecular weight. The number of effective mol.electrons per gram is given by

$$\Delta z_2 = (z_2 - v'_2 \cdot \rho_0) \quad (46)$$

when ρ_0 is the mean electron density of the solvent. The intensity of the primary beam is given by $I_0(x, t)$ (see Section I.A). The total energy per unit time irradiating the sample can be calculated by integration of the whole irradiated area A :

$$P = \int_A I_0(x, t) dt dx \quad (47)$$

The scattered intensity is correlated with the molecular weight by the equation:

$$I(h) = \frac{I_e \cdot \Delta z^2 \cdot M \cdot d \cdot N_L \cdot c \cdot P}{a^2} \cdot \phi(h) \quad (48)$$

where $I_e = 7,9 \times 10^{-26} [\text{cm}^2]$ is the Thomson factor which could be called "effective cross-section of the electron", d is the thickness of the sample, N_L is the Avogadro number and c the concentration in $[\text{g}/\text{cm}^3]$; a is the distance between the sample and the plane of registration in $[\text{cm}]$ and $\phi(h)$ is the normalized form factor of the molecule ($\phi(0) = 1$). The molecular weight can be determined from the intensity at zero angle $I(0)$:

$$M = \frac{I(0)}{P} \cdot \frac{a^2}{\Delta z^2 \cdot d \cdot c \cdot I_e \cdot N_L} = \frac{I(0)}{P} \cdot \frac{21,0 \cdot a^2}{\Delta z^2 \cdot d \cdot c} \quad (49)$$

(Kratky *et al.*, 1951).

2. ROD-LIKE PARTICLES

Introduction of Eqn (47), Chapter 2:

$$I(h) = I(0) \cdot \phi(h) = I_c(h) \cdot \frac{\pi L}{h} = I_c(0) \cdot \frac{\pi L}{h} \phi_c(h) \quad (50)$$

and consideration of the relation

$$\frac{I(0)}{I_c(0)} = \frac{\bar{\rho}^2 \cdot A^2 \cdot L^2}{\bar{\rho}^2 \cdot A^2} = L^2 \quad (51)$$

(where L is the length and A is the area of the cross-section of the particle) leads to

$$\phi(h) = \frac{I_c(0)}{I(0)} \cdot \frac{\pi L}{h} \phi_c(h) = \frac{\pi}{h \cdot L} \cdot \phi_c(h) \quad (52)$$

Equation (48) can be transformed by use of Eqn (52) into

$$I(h) \cdot h = \frac{\pi \cdot I_e \cdot \Delta z^2 \cdot M/L \cdot d \cdot N_L \cdot c \cdot P}{a^2} \phi_c(h) \quad (53)$$

If we introduce the mass per unit length $M_c = M/L$ and take into account that $\phi_c(h)|_{h \rightarrow 0} = 1$ we obtain

$$M_c = \frac{(I(h) \cdot h)|_{h \rightarrow 0}}{P} \cdot \frac{a^2}{\Delta z^2 \cdot d \cdot c \cdot I_e \cdot N_L} = \frac{I(h)h|_{h \rightarrow 0}}{P} \cdot \frac{6,68 a^2}{\Delta z^2 \cdot d \cdot c} \quad (54)$$

(Kratky and Porod, 1953).

3. FLAT PARTICLES

A similar derivation of the mass per unit area M_t of flat particles is possible by taking into account the corresponding relations:

$$I(h) = I(0) \cdot \phi(h) = I_t(h) \cdot \frac{A \cdot 2\pi}{h^2} = I_t(0) \cdot \frac{A \cdot 2\pi}{h^2} \cdot \phi_t(h) \quad (55)$$

and

$$\frac{I(0)}{I_t(0)} = \frac{\bar{\rho}^2 \cdot A^2 \cdot T^2}{\bar{\rho}^2 \cdot T^2} = A^2 \quad (56)$$

where A is the area of the particle plane and T is the thickness of the particle.

Introducing this into Eqn (48) leads to

$$I(h) \cdot h^2 = \frac{2\pi \cdot I_e \cdot \Delta z^2 \cdot (M/A) \cdot d \cdot N_L \cdot c \cdot P}{a^2} \cdot \phi_t(h) \quad (57)$$

From this equation we obtain the result by substitution of $M_t = M/A$ and consideration of $\phi_t(h)|_{h \rightarrow 0} = 1$

$$M_t = \frac{I(h) \cdot h^2|_{h \rightarrow 0}}{P} \cdot \frac{a^2}{2\pi \cdot \Delta z^2 \cdot d \cdot c \cdot I_e \cdot N_L} = \frac{I(h)h^2|_{h \rightarrow 0}}{P} \cdot \frac{3,34 a^2}{\Delta z^2 \cdot d \cdot c} \quad (58)$$

4. NORMALIZATION OF PRIMARY BEAM PROFILES

Equations (49), (54) and (58) are based on the power P (sometimes called "integrated intensity" (Eqn (47)). This requires scattered intensities that are desmeared with normalized profiles, i.e.

$$2 \int_0^\infty P(t) dt = \int_{-\infty}^\infty Q(x) dx = \int_0^\infty W(\lambda') d\lambda' = 1 \quad (59)$$

Most experimental techniques, however, determine not the total power of the primary beam but the power per unit length of the slit length function $P(t)$. (See Chapter 3.I.V.)

These experimental constraints have to be taken into account by a different normalization of $P(t)$:

$$2 \int_0^\infty P(t) dt = \bar{L} \quad (60)$$

where \bar{L} is the mean length of the profile. This can easily be attained for the usual trapezoidal $P(t)$ -function by the normalization

$$P(0) = 1,0 \quad (61)$$

A corresponding transformation factor has to be used if the integration of Eqn (4) is performed in the reduced angular scale t_h (h -scale),

$$t_h = T_{hm} t \quad (62)$$

$$\tilde{I}(h) = \frac{\lambda}{T_{hm}} \int_0^\infty P(t_h) \cdot I(\sqrt{(h^2 + t_h^2)}) dt_h \quad (63)$$

where $P(0) = 1,0$ and T_{hm} is given by

$$T_{hm} = \frac{2\pi}{\lambda a} \quad (64)$$

These normalizations are performed automatically by some desmearing algorithms (Glatter, 1974, 1977b).

B. Normalization – Particle Scale

If we call the scattered intensity of one particle $I_1(h)$, which takes into account that $I_1(0)$ is correlated with the number of excess electrons Δm through

$$I_1(0) = \Delta m^2 = M^2 \cdot \Delta z \quad (65)$$

we obtain the following relation by substitution into Eqn (49).

$$K = \frac{I_1(0)}{I(0)} = \frac{M^2 \cdot \Delta z^2}{I(0)} = \frac{M \cdot a^2}{I_e \cdot N_L \cdot P \cdot c \cdot d} \quad (66)$$

The scattered intensity of one particle (scattering curve in "particle scale") is thus given by

$$I_1(h) = I(h) \cdot K = I(h) \cdot \frac{M \cdot a^2}{I_e \cdot N_L \cdot P \cdot c \cdot d} \quad (67)$$

This scaling is a prerequisite for the calculation of the particle functions and of parameters like difference electron density, surface etc.

C. Structural Parameters

1. VOLUME

According to Porod (1951), the invariant Q is given by

$$Q = \int_0^\infty I(h) \cdot h^2 dh \quad (68)$$

In combination with the scattered intensity at zero angle, Q can be used to determine the volume of the particle:

$$V = 2\pi^2 \cdot \frac{I(0)}{Q} \quad (69)$$

Volume determinations are subject to errors as they rely on the validity of an extrapolation to zero angle (to obtain I_0) and to large angles (h^{-4} extrapolations).

2. SURFACE

The surface S of a particle is correlated with the scattered intensity (see Chapter 2, Section III.C) by

$$I_1(h)|_{h \rightarrow \infty} = (\Delta\rho)^2 \cdot \frac{2\pi}{h^4} \cdot S \quad (70)$$

where $I_1(h)$ is the scattered intensity of one particle (see Eqn (67)). Determination of the absolute intensity can be avoided if the following equation is used

$$O_s = \frac{S}{V} = \pi \frac{\lim_{h \rightarrow \infty} [I(h) \cdot h^4]}{Q} \quad (71)$$

The ratio S/V is called specific surface O_s and can be determined directly from the scattering curve without additional data, if the volume fraction w_1 of the solvent is assumed to be equal to unity, i.e. for infinite dilution (Mittelbach and Porod, 1965).

3. CROSS-SECTION, THICKNESS AND CORRELATION LENGTH

Expressions analogous to (68) exist for the relation between the cross-section area A of rod-like particles and the limiting value $(I(h) \cdot h)|_{h \rightarrow 0}$

$$A = \frac{(I(h) \cdot h)_{h \rightarrow 0}}{Q} \cdot 2\pi \quad (72)$$

and for the relation between the thickness T of lamellar particles and the limiting value $(I(h) \cdot h^2)_{h \rightarrow 0}$

$$T = \frac{(I(h) \cdot h^2)_{h \rightarrow 0}}{Q} \cdot \pi \quad (73)$$

but the experimental accuracy of the limiting values $(I(h) \cdot h)_{h \rightarrow 0}$ and $(I(h) \cdot h^2)_{h \rightarrow 0}$ is usually not very high.

The invariant can directly be obtained from a smeared scattering curve $\tilde{I}(h)$, provided the smearing originates from an infinitely long slit length profile $P(t)$:

$$\tilde{Q} = \int_0^\infty \tilde{I}(h) \cdot h \cdot dh = 2Q \quad (74)$$

The correlation length l_c (see Section III.B in Chapter 2) can be calculated directly from the experimental intensity without normalization

$$l_c = 2 \int_0^\infty \gamma_0(r) dr = \pi \int_0^\infty I(h) \cdot h \cdot dh / Q \quad (75)$$

If we consider the solution to be a two phase system with the volume parts w_1 and w_2 ($w_1 + w_2 = 1$) and the electron density difference $\Delta\rho$, the following relation holds for the mean square difference of the electron density

$$\overline{(\Delta\rho)^2} = w_1 \cdot w_2 (\Delta\rho)^2 \quad (76)$$

This value can be determined as follows:

$$\overline{\Delta\rho^2} = \frac{Q}{P} \frac{a^2}{2\pi^2 \cdot I_e \cdot d} \quad (77)$$

If we consider particles with internal electron density fluctuations Eqn (69) has to be modified:

$$V = \frac{2\pi^2 I(0)}{Q} \cdot \frac{\bar{\rho}^2}{\bar{\rho}^2} \quad (78)$$

where $\bar{\rho}^2 > \bar{\rho}^2$. If the volume is calculated from Eqn (69) neglecting the term $\bar{\rho}^2/\bar{\rho}^2$, one obtains the so-called correlation volume V_c , with $V_c < V$.

One has to bear in mind that there exist two different notations for most of these constants (Kratky, 1963; Pilz, 1973; Luzzati, 1960). For a comparison of the two notations, including transmitting equations I have recently derived, see Pilz *et al.* (1980).

4. RADIUS OF GYRATION

(a) Radius of Gyration of the Whole Particle. This parameter is defined in analogy to the radius of inertia in mechanics

$$R^2 = \frac{\int_V \rho(r_i) \cdot r_i^2 \cdot dV_i}{\int_V \rho(r_i) \cdot dV_i} \quad (79)$$

It can be obtained from the distance distribution function $p(r)$ (Eqn 11)

$$R^2 = \frac{\int_0^\infty p(r) \cdot r^2 \cdot dr}{2 \int_0^\infty p(r) \cdot dr} \quad (80)$$

or from the innermost part of the scattering curve (Guinier Approximation)

$$I(h) = I(0) \cdot e^{-\frac{h^2 R^2}{3}} \quad (81a)$$

A plot of $\log I(h)$ vs h^2 (Guinier plot) shows a linear descent with a negative slope α where

$$R = K \cdot \sqrt{\tan \alpha} \quad (81b)$$

(see Table 1 and Fig. 4, Chapter 8)

(b) Radius of Gyration of the Cross-section. In the special case of rod-like particles, the two-dimensional analogue of R is called the radius of gyration of the cross-section R_c . It can be obtained from

$$R_c^2 = \frac{\int_0^\infty p_c(r) \cdot r^2 \cdot dr}{2 \int_0^\infty p_c(r) \cdot dr} \quad (82)$$

or from the innermost part of the scattered intensity of the cross-section $I_c(h)$:

$$I_c(h) = I_c(0) \cdot e^{-\frac{h^2 R_c^2}{2}} \quad (83)$$

(see Table 1 and Fig. 11, Chapter 8)

(c) Radius of Gyration of the Thickness. A similar definition exists for lamellar particles. The one-dimensional radius of gyration of the thickness R_t can be calculated from

$$R_t^2 = \frac{\int_0^\infty p_t(r) \cdot r^2 \cdot dr}{2 \int_0^\infty p_t(r) \cdot dr} \quad (84)$$

or from the innermost part of the scattered intensity of the thickness $I_t(h)$

$$I_t(h) = I_t(0) \cdot e^{-h^2 R_t^2} \quad (85)$$

(see Table 1 and Fig. 16a, Chapter 8).

The radius of gyration is an interesting parameter for homogeneous particles. It is related to the geometrical parameters of simple homogeneous triaxial bodies as follows (Mittelbach, 1964):

$$\begin{aligned} \text{sphere (radius } r\text{)} \quad R^2 &= \frac{2}{5}r^2 \\ \text{hollow sphere (radii } r_1 \text{ and } r_2\text{)} \quad R^2 &= \frac{3}{5} \frac{r_2^5 - r_1^5}{r_2^3 - r_1^3} \\ \text{ellipsoid (semi-axes } a, b, c\text{)} \quad R^2 &= \frac{a^2 + b^2 + c^2}{5} \\ \text{prism with edge lengths } A, B, C \quad R^2 &= \frac{A^2 + B^2 + C^2}{12} \\ \text{elliptic cylinder (semi-axes } a, b; \text{ height } h\text{)} \quad R^2 &= \frac{a^2 + b^2}{4} + \frac{h^2}{12} = R_q^2 + \frac{h^2}{12} \\ \text{hollow cylinder (height } h \text{ and radii } r_1, r_2\text{)} \quad R^2 &= \frac{r_1^2 + r_2^2}{2} + \frac{h^2}{12} \end{aligned} \quad (86)$$

5. ABSCISSA SCALING

The various molecular parameters can be evaluated from scattered intensities with different abscissa scaling. The abscissa used in theoretical work is $h = (4\pi/\lambda) \sin \theta$, the most important experimental abscissa scales are $m = (\lambda a/2\pi) \cdot h = (1/T_{hm}) \cdot h$ (see Eqns (3) and (64)) and $2\theta \approx m/a = (\lambda/2\pi) \cdot h$. The formulae for the various parameters for the different scales are listed in Table 1.

V. Calculation of Scattered Intensities and Distance Distributions of Models

The following part of this chapter will give a survey of the most important procedures for the calculation of scattered intensities and distance distribution functions.

A. Calculations of Scattered Intensities

The scattering curves can be calculated semi-analytically for simple triaxial bodies and for models composed of some of these bodies.

1. TRIAXIAL MODELS

The scattering amplitude of simple triaxial bodies like ellipsoids, prisms and cylinders can be calculated analytically for any orientation. The spatial averaging has to be performed numerically. The error in these integrations can be kept below an arbitrary small limit by a sufficient decrease of the increment of integration. Such semi-analytical calculations have been performed for a large number of different models by Porod (1948), Mittelbach and Porod (1961a, b, 1962) and Mittelbach (1964).

2. MULTIBODY MODELS

Many molecules under investigation cannot be approximated satisfactorily by simple triaxial models. Therefore, semi-analytical methods were extended to models composed of several triaxial bodies (Haager, 1972). The scattering amplitudes of the individual constituent subunits are calculated analytically and added according to the particular orientation in the model. The total amplitude is squared and averaged over all orientations.

Again, integrations are performed numerically. The increment of integration is halved until the required accuracy is achieved. The number of intervals increases rapidly for larger h -values if the model is elongated. The computing time for the outer part of the scattering curve ($h \cdot D \geq 30$) can be in the order of several hours (UNIVAC 494). Models with inhomogeneous electron density can be simulated by a superposition of parts of differing electron density.

Models composed of only spherical subunits can be evaluated with the Debye formula (Debye, 1915)

$$I(h) = i_{el}(h) \sum_{i=1}^N \sum_{k=1}^N \rho_i V_i \rho_k V_k \phi_i(h) \cdot \phi_k(h) \frac{\sin(h \cdot d_{ik})}{h \cdot d_{ik}} \quad (87)$$

where the spatial average is carried out analytically.

3. METHOD OF FINITE ELEMENTS

Any model can be approximated by a finite number of very small homogeneous elements of variable electron density. The elements have to be smaller than the smallest structural detail of interest.

TABLE 1

$R = K \cdot \sqrt{\tan \alpha}$	$R = K \cdot \frac{\lambda a}{2\pi} \sqrt{\tan \alpha}$	$R = K \cdot \frac{\lambda}{2\pi} \sqrt{\tan \alpha}$
$\tan \alpha = \frac{\Delta \log I(h)}{\Delta h^2}$	$\tan \alpha = \frac{\Delta \log I(m)}{\Delta m^2}$	$\tan \alpha = \frac{\Delta \log I(2\theta)}{\Delta(2\theta)^2}$
$K = \sqrt{\frac{3}{\log e}} = 2,628$		
$R_t = K_t \cdot \sqrt{\tan \alpha}$	$R_c = K_c \cdot \frac{\lambda a}{2\pi} \sqrt{\tan \alpha}$	$R_c = K_c \cdot \frac{\lambda}{2\pi} \sqrt{\tan \alpha}$
$\tan \alpha = \frac{\Delta \log (I(h) \cdot h)}{\Delta h^2}$	$\tan \alpha = \frac{\Delta \log (I(m) \cdot m)}{\Delta m^2}$	$\tan \alpha = \frac{\Delta \log (I(2\theta) \cdot 2\theta)}{\Delta(2\theta)^2}$
$K_c = \sqrt{\frac{2}{\log e}} = 2,146$		
$R_t = K_t \cdot \frac{\lambda a}{2\pi} \sqrt{\tan \alpha}$	$R_t = K_t \cdot \frac{\lambda}{2\pi} \sqrt{\tan \alpha}$	
$\tan \alpha = \frac{\Delta \log (I(h) \cdot h^2)}{\Delta h^2}$	$\tan \alpha = \frac{\Delta \log (I(m) \cdot m^2)}{\Delta m^2}$	$\tan \alpha = \frac{\Delta \log (I(2\theta) \cdot (2\theta)^2)}{\Delta(2\theta)^2}$
$K_t = \sqrt{\frac{1}{\log e}} = 1,517$		
(Table continued)		
$V = 2\pi^2 \frac{I(0)}{Q}$	$V = \frac{\lambda^3 a^3 \cdot I(0)}{4\pi Q_m}$	$V = \frac{\lambda^3}{4\pi} \cdot \frac{I(0)}{Q_{2\theta}}$
$Q = \int I(h) \cdot h^2 dh$	$Q_m = \int I(m) \cdot m^2 dm$	$Q_{2\theta} = \int I(2\theta) \cdot (2\theta)^2 d(2\theta)$
$A = 2\pi \frac{(I(h) \cdot h)_0}{Q}$	$A = \frac{\lambda^2 a^2 \cdot ((m) \cdot m)_0}{2\pi Q_m}$	$A = \frac{\lambda^2}{2\pi} \cdot \frac{((2\theta) \cdot 2\theta)_0}{Q_{2\theta}}$
$T = \pi \frac{(I(h) \cdot h^2)_0}{Q}$	$T = \frac{\lambda a}{2} \cdot \frac{((m) \cdot m^2)_0}{Q_m}$	$T = \frac{\lambda}{2} \cdot \frac{((2\theta) \cdot (2\theta)^2)_0}{Q_{2\theta}}$
$M = \frac{I(0)}{P} \cdot \frac{K \cdot \frac{a^2}{c \cdot d \cdot (\Delta z)^2}}{c \cdot d \cdot (\Delta z)^2}$	$K = \frac{1}{I_e \cdot N_L} = 21,0$	
$M_c = \frac{(I(h) \cdot h)_0}{P} \cdot \frac{K \cdot \frac{a^2}{c \cdot d \cdot (\Delta z)^2}}{c \cdot d \cdot (\Delta z)^2}$	$M_c = \frac{((m)m)_0}{P} \cdot \frac{2K \cdot \frac{a}{c \cdot d \cdot (\Delta z)^2}}{c \cdot d \cdot (\Delta z)^2}$	$M_c = \frac{((2\theta)(2\theta))_0}{P} \cdot \frac{2K \cdot \frac{a^2}{c \cdot d \cdot (\Delta z)^2}}{c \cdot d \cdot (\Delta z)^2}$
$M_t = \frac{(I(h) \cdot h^2)_0}{P} \cdot \frac{K \cdot \frac{a^2}{c \cdot d \cdot (\Delta z)^2}}{c \cdot d \cdot (\Delta z)^2}$	$M_t = \frac{((m)m^2)_0}{P} \cdot \frac{2\pi K \cdot \frac{1}{c \cdot d \cdot (\Delta z)^2}}{c \cdot d \cdot (\Delta z)^2}$	$M_t = \frac{((2\theta)(2\theta)^2)_0}{P} \cdot \frac{2\pi K \cdot \frac{a^2}{c \cdot d \cdot (\Delta z)^2}}{c \cdot d \cdot (\Delta z)^2}$
$(\Delta p)^2 = \frac{Q}{P} \cdot \frac{a^2}{2\pi^2 \cdot d} \cdot K$	$(\Delta p)^2 = \frac{Q_m}{P} \cdot \frac{4\pi}{\lambda^3 \cdot a \cdot d} \cdot K$	$(\Delta p)^2 = \frac{Q_{2\theta}}{P} \cdot \frac{4\pi \cdot a^2}{\lambda^3 \cdot d} \cdot K$
	$K = \frac{10^{24}}{I_e} \left(10^{24} \dots \left[\frac{cm^3}{A^3} \right] \right)$	
$Q_s = \pi \cdot \frac{K}{Q}$	$Q_s = \frac{2\pi^2 \cdot K_m}{\lambda a \cdot Q_m}$	$Q_s = \frac{2\pi^2}{\lambda} \cdot \frac{K_{2\theta}}{Q_{2\theta}}$
$K = \lim_{h \rightarrow \infty} I(h) \cdot h^4$	$K_m = \lim_{m \rightarrow \infty} I(m) \cdot m^4$	$K_{2\theta} = \lim_{2\theta \rightarrow \infty} I(2\theta) \cdot (2\theta)^4$

(a) *Sphere Method.* In this method, the elements consist of spheres of equal size. The diameter of these spheres must be chosen independently of the distance between nearest neighbours, in such a way that the volume of the model is represented exactly by the sum of the volumes of all elements (which corresponds to a slight formal overlap between adjacent spheres). The scattering intensity is calculated using the Debye Formula (87), with $\phi_i(h) = \phi_k(h) = \phi(h)$. The bulk of the computing time necessary for such calculation is used by the computation of the reciprocal distances d_{ik} and by the computation of the $\sin x/x$ terms.

The number of reciprocal distances is determined by the number of elements N , which in turn depends on the required resolution. The number of $\sin x/x$ terms equals the number of h -values M multiplied by $N(N - 1)/2$. Computing times can be lowered drastically by the use of approximate d_{ik} -values. If the distances d_{ik} are quantized to multiples of $D_{\max}/10\,000$, the results have an error of less than 1% (D_{\max} is an upper estimate for the maximum distance D of the model), but the computing time for a model composed of 400 elements is lowered by a factor 10 (Glatter, 1980c). Models up to several thousand elements can be computed by this method within ten minutes CPU-time on a UNIVAC 1100/81 computer. In terms of CPU-time this method is superior to the semi-analytical method of Haager for nonglobular models.

The sphere method can be used for the computation of scattering curves of macromolecules from a known crystal structure. The weights of the atoms are given by

$$Z_{\text{eff}} = Z - \rho_0 V_{\text{eff}} \quad (88)$$

where V_{eff} is the apparent volume of the atom given by Langridge *et al.* (1960). This is a rough approximation for the influence of the solvent.

(b) *Cube Method.* This method has been developed independently by Fedorov *et al.* (1972, 1974a, b) and by Ninio and Luzzati (1972), mainly for the computation of scattered intensities for macromolecules in solution whose crystal structure is known. In the cube method the macromolecule is mentally placed in a parallelepiped, which is subdivided into small cubes (with edge lengths of 1–1.5 Å). Each cube is examined in order to decide whether it is inside the macromolecule or in the solvent region. After all the cubes have been considered, it is possible to represent the outline and the volume of the dissolved particle with good accuracy. The mathematical background of this method is described in detail by Fedorov *et al.* (1974a, b). The main shortcoming of the method consists in a rather rough account of the internal cavities accessible to the solvent. In the majority of cases these cavities are automatically taken into account in evaluating whether a given cube pertains to the molecule or to the solvent, but in a number of cases the method overestimates the number

of cavities accessible to the solvent. To overcome this shortcoming the “modified cube method” was recently developed (Fedorov and Denesyuk, 1978): if the distance from the centre of a cube not pertaining to the molecule to the nearest atom of the molecule is larger than $R + B$ (where R is the edge length of the cube and B is a parameter regulating the overall molecule volume), such a cube is considered a potential centre of a water molecule and this cube and the neighbouring 6 cubes are excluded from the macromolecule volume. The method is used for the investigation of changes in the conformation of biological macromolecules in solution (Fedorov and Denesyuk, 1978).

A somewhat different cube method for the calculation of scattering curves of models has been developed recently by Labischinski and Bradaczek (1977). The shape of the particle has to be defined piecewise by an analytical boundary. The particle is placed in a cube which is divided into $2^n \times 2^n \times 2^n$ sampling points (usually $64 \times 64 \times 64 = 262\,144$). The points inside the particle can now be determined automatically by the equations defining the analytical boundary. The Fourier transformation is performed with the Fast Fourier Transform technique.

The accuracy of the method is limited by the orthogonal sampling (difficulties with bent boundaries) and by the averaging over all directions in space which can be performed without essential problems only for globular structures. An image digitizing system for the computer input of structure models allows the graphical input of a model which is defined by its projections (Bradaczek *et al.*, 1979).

B. Calculation of the Distance Distribution Function of Models

The distance distribution function $p(r)$ can be calculated analytically only for a few simple models (Porod, 1948; Goodisman, 1980), in all other cases we have to use a finite element method with spheres. It is possible to define an analogous equation to the Debye formula of Eqn (87) in real space (Glatter, 1980c). The distance distribution function $p(r)$ can be expressed as

$$p(r) = \sum_{i=1}^N \rho_i^2 p_0(r, R_i) + 2 \sum_{i=1}^{N-1} \sum_{k=i+1}^N \rho_i \rho_k \bar{p}(r, d_{ik}, R_i, R_k) \quad (89)$$

$p_0(r, R_i)$ is the distance distribution function of a sphere with the radius R_i and electron density equal to unity, $\bar{p}(r, d_{ik}, R_i, R_k)$ is the cross term distance distribution between the i th and k th sphere (radii R_i and R_k) with a mutual distance d_{ik} .

Equations (89) (and (87)) can be used in two different ways for the calculation of model functions. Sometimes it is possible to approximate a macromolecule as an aggregate of some spheres of well defined size representing

different globular subunits. The form factors of the subunits are in such cases real parameters of the model. However, in most cases we have no such possibility and we have to use the method of finite elements, i.e. we fit our model with a large number of sufficiently small spheres of equal size, and, if necessary, different weight. The form factor of the small spheres is now not a real model parameter and introduces a limit of resolution.

Fourier transformation (Eqn 14) can be used for the computation of the distance distribution function of any arbitrary model if the scattering function of the model is known over a sufficient large range of h -values.

References

- Bracewell, R. (1965). "Fourier Transform and Its Applications". McGraw-Hill, New York.
- Bradaczek, H and Luger, P. (1978). *Acta Cryst. A* **34**, 681–683.
- Bradaczek, H., Denzer, P. and Labischinski, H. (1979). *J. Phys. E: Sci. Instrum.* **12**, 354–355.
- Brämer, R. and Wenig, W. (1972). *Kolloid Z. u. Z. Polymere* **250**, 414–416.
- Brill, O. L. and Schmidt, P. W. (1968). *J. Appl. Phys.* **39**, 2274–2281.
- Brill, O. L., Weil, C. G. and Schmidt, P. W. (1978). *J. Coll. Interf. Sci.* **27**, 479–492.
- Damaschun, G. and Pürschel, H. V. (1971a). *Acta Cryst. A* **27**, 193–197.
- Damaschun, G. and Pürschel, H. V. (1971b). *Mh. Chem.* **102**, 1146–1155.
- Damaschun, G., Müller, J. J. and Pürschel, H. V. (1968). *Mh. Chem.* **99**, 2243–2348.
- Damaschun, G., Müller, J. J. and Pürschel, H. V. (1971). *Acta Cryst. A* **27**, 11–18.
- Debye, P. (1915). *Ann. Physik* **46**, 809–823.
- Deutsch, M. and Luban, M. (1978a). *J. Appl. Cryst.* **11**, 87–97.
- Deutsch, M. and Luban, M. (1978b). *J. Appl. Cryst.* **11**, 98–101.
- Engel, P. (1973). *Z. Kristallogr.* **137**, 433–435.
- Fedorov, B. A. (1971). *Acta Cryst. A* **27**, 35–42.
- Fedorov, B. A. and Aleshin, V. G. (1967). English Transl. in *Polymer Sci. USSR* **8**, 1657.
- Fedorov, B. A. and Densyuk, (1978). *J. Appl. Cryst.* **11**, 473–477.
- Fedorov, B. A., Feigin, L. A. and Dembo, A. T. (1965). *Kristallografija* **10**, 788–790.
- Fedorov, B. A., Andreeva, N. A., Volkova, L. A. and Voronin, L. A. (1968). *Kristallografiya* **13**, 770–775. (Engl. Transl.: Sov. Phys. Crystallogr. (1969). **13**, 668–672.)
- Fedorov, B. A., Ptitsyn, O. B. and Voronin, L. A. (1972). *FEBS Lett.* **28**, 188–190.
- Fedorov, B. A., Ptitsyn, O. B. and Voronin, L. A. (1974a). *J. Appl. Cryst.* **7**, 181–186.
- Fedorov, B. A., Ptitsyn, O. B. and Voronin, L. A. (1974b). *Molekul. Biol. (Moscow)* **8**, 693–702.
- Fedorova, I. S. (1977). *J. Coll. Interf. Sci.* **59**, 98–105.
- Fedorova, I. S. and Emelyanov, V. B. (1977). *J. Coll. Interf. Sci.* **59**, 106–112.
- Fedorova, I. S. and Schmidt, P. W. (1978). *J. Appl. Cryst.* **11**, 405–411.
- Glatter, O. (1972). *Mh. Chem.* **103**, 1691–1694.
- Glatter, O. (1974). *J. Appl. Cryst.* **7**, 147–153.
- Glatter, O. (1977a). *Acta Phys. Austriaca* **47**, 83–102.
- Glatter, O. (1977b). *J. Appl. Cryst.* **10**, 415–421.
- Glatter, O. (1980a). *J. Appl. Cryst.* **13**, 7–11.
- Glatter, O. (1980b). *J. Appl. Cryst.* **13**, 577–584.
- Glatter, O. (1980c). *Acta Phys. Austriaca* **52**, 243–256.
- Glatter, O. (1981). *J. Appl. Cryst.* **14**, 101–108.
- Glatter, O. and Zipper, P. (1975). *Acta Phys. Austriaca* **43**, 307–310.
- Goodisman, J. (1980). *J. Appl. Cryst.* **13**, 132–134.
- Greville, T. N. E. (1969). "Theory and Applications of Spline Functions". Academic Press, New York and London.
- Guinier, A. and Fournet, G. (1947a). *J. Phys. Radium* **8**, 345.
- Guinier, A. and Fournet, G. (1947b). *Nature (London)* **160**, 501.
- Gunier, A. and Fournet, G. (1955). "Small Angle Scattering of X-Rays". Wiley, New York.
- Haager, O. (1972). Dissertation, Univ. Graz.
- Harkness, S. D., Gould, R. W. and Hren, J. J. (1969). *Phil. Mag.* **19**, 115–128.
- Heine, S. (1963). *Acta Phys. Austriaca* **16**, 144.
- Heine, S. and Roppert, J. (1962). *Acta Phys. Austriaca* **15**, 148–166.
- Hendricks, R. W., Schelten, J. and Schmatz, W. (1974). *Philos. Mag.* **30**, 819–837.
- Henne, M. (1976). Diplomarbeit Univ. Freiburg/Br.
- Hosemann, R. (1951). *Ergeb. Exakt. Naturwiss.* **24**, 142–221.
- Hosemann, R. and Bagchi, S. N. (1952). *Acta Cryst.* **5**, 749–762.
- Hosemann, R. and Bagchi, S. N. (1962). "Direct Analysis of Diffraction by Matter", North-Holland, Amsterdam.
- Hoßfeld, F. (1967). *Interner Bericht*, KFA Jülich.
- Hoßfeld, F. (1968). *Acta Cryst. A* **24**, 643–650.
- Jaeneke, L. (1975). Diplomarbeit Univ. Freiburg/Br.
- Kratky, O. (1963). *Progress in Biophys.* **13**, 105–173.
- Kratky, O., Porod, G. and Kahovec, L. (1951). *Z. Elektrochem.* **55**, 53–59.
- Kratky, O. and Porod, G. (1953). In "Die Physik der Hochpolymere" (H. A. Stuart, ed.), Vol. II. Springer Verlag, Berlin.
- Kratky, O., Porod, G. and Skala, Z. (1960). *Acta Phys. Austriaca* **13**, 76–128.
- Labischinski, H. and Bradaczek, H. (1977). *J. Appl. Cryst.* **10**, 363–364.
- Laggner, P., Gotto, A. M. and Morrisett, J. D. (1979). *Biochem.* **18**, 164–171.
- Lake, J. A. (1967). *Acta Cryst.* **23**, 191–194.
- Langridge, R., Marvin, D. A., Seeds, W. E., Wilson, H. R., Cooper, C. W., Wilkins, M. H. F. and Hamilton, L. D. (1960). *J. Mol. Biol.* **31**, 115.
- Lesslauer, W., Cain, J. E. and Blasie, J. K. (1972). *Proc. Nat. Acad. Sci. U.S.A.* **69**, 1499–1503.
- Letcher, J. J. and Schmidt, P. W. (1966). *J. Appl. Phys.* **37**, 649–655.
- Luzzati, V. (1960). *Acta Cryst.* **13**, 939–945.
- Mateu, L., Tardieu, A., Luzzati, V., Aggerbeck, L. and Scanu, A. M. (1972). *J. Mol. Biol.* **70**, 105–116.
- Mazur, J. (1977). NBS Technical Note 936.

- Mittelbach, P. (1964). *Acta Phys. Austriaca* **19**, 53–102.
- Mittelbach, P. (1965). *Kolloid-Z. u. Z. Polymere* **206**, 152–159.
- Mittelbach, P. and Porod, G. (1961a). *Acta Phys. Austriaca* **14**, 185–211.
- Mittelbach, P. and Porod, G. (1961b). *Acta Phys. Austriaca* **14**, 405–439.
- Mittelbach, P. and Porod, G. (1962). *Acta Phys. Austriaca* **15**, 122–147.
- Mittelbach, P. and Porod, G. (1965). *Kolloid-Z. u. Z. Polymere* **202**, 40–49.
- Moore, P. B. (1980). *J. Appl. Cryst.* **13**, 168–175.
- Müller, K. and Glatter, O. (1982). *Makromol. Chem.* in press.
- Müller, K., Laggner, P., Kratky, O., Kostner, G., Holasek, A. and Glatter, O. (1974). *FEBS Lett.* **40**, 213–218.
- Müller, J. J., Schmidt, P. W. and Damaschun, G. (1980). *J. Appl. Cryst.* **13**, 280–283.
- Neilson, G. F. (1973). *J. Appl. Cryst.* **6**, 386–392.
- Ninio, J. and Luzatti, V. (1972). *J. Mol. Biol.* **71**, 217–229.
- Oelschlaeger, H. (1969). *Acta Phys. Austriaca* **30**, 323–327.
- Pape, E. H. (1974). *Biophys. J.* **14**, 284–294.
- Pape, E. H. and Kreutz, W. (1978). *J. Appl. Cryst.* **11**, 421–429.
- Patel, I. S. and Schmidt, P. W. (1972). *J. Appl. Cryst.* **5**, 40–46.
- Pilz, I. (1973). In "Physical Principles and Techniques of Protein Chemistry" (S. J. Leach, ed.), Part C, pp. 141–243. Academic Press, New York and London.
- Pilz, I., Glatter, O. and Kratky, O. (1980). "Methods in Enzymology", Vol. 61, Part H, pp. 148–249. Academic Press, New York and London.
- Plavnik, G. M., Kozhevnikov, A. I. and Shishkin, A. V. (1976). *Doklady Akademii Nauk SSSR* **226**, 630–633.
- Plestil, J. and Baldrian, J. (1976). *Czech. J. Phys.* **B26**, 514–527.
- Porod, G. (1948). *Acta Phys. Austriaca* **2**, 255–292.
- Porod, G. (1951). *Kolloid-Z.* **124**, 83–114.
- Pringle, O. A. and Schmidt, P. W. (1977). *J. Coll. Interf. Sci.* **59**, 252–257.
- Riseman, J. (1952). *Acta Cryst.* **5**, 193–196.
- Roess, L. C. (1946). *J. Chem. Phys.* **14**, 695–697.
- Roess, L. C. and Shull, C. G. (1947). *J. Appl. Phys.* **18**, 308–313.
- Schelten, J. and Hendricks, R. W. (1978). *J. Appl. Cryst.* **11**, 297–324.
- Schelten, J. and Hoßfeld, F. (1971). *J. Appl. Cryst.* **4**, 210–223.
- Schmidt, P. W. (1965). *Acta Cryst.* **19**, 938–942.
- Schmidt, P. W. (1967). *J. Appl. Cryst.* **3**, 137–145.
- Schmidt, P. W. and Fedorov, B. A. (1978). *J. Appl. Cryst.* **11**, 411–416.
- Schmidt, P. W. and Hight, R. (1960). *Acta Cryst.* **13**, 480–483.
- Schmidt, P. W., Emelyanov, V. B. and Fedorova, I. S. (1978). *J. Colloid Interface Sci.* **67**, 226–233.
- Schmidt, P. W., Fedorova, I. W. and Emelyanov, V. B. (1979). *J. Colloid Interface Sci.* **67**, 234–239.
- Schollmeyer, E., Tschang, Ch., Hirt, P. and Herlinger, H. (1977). *Makromol. Chem.* **178**, 2079–2087.
- Shannon, C. E. and Weaver, W. (1949). "The Mathematical Theory of Communication". University of Illinois Press, Urbana.
- Shchedrin, B. M. and Feigin, L. A. (1966). *Acta Cryst.* **11**, 159–163.
- Strobl, G. R. (1970). *Acta Cryst.* **A26**, 367–375.
- Syneček, V. (1960). *Acta Cryst.* **13**, 378–380.
- Taylor, T. R. and Schmidt, P. W. (1967). *Acta Cryst.* **25**, 293–296.
- Taylor, T. R. and Schmidt, P. W. (1969). *J. Appl. Cryst.* **2**, 143.
- Vonk, C. G. (1971). *J. Appl. Cryst.* **4**, 340–342.
- Vonk, C. G. (1975). *J. Appl. Cryst.* **8**, 340–341.
- Vonk, C. G. (1976). *J. Appl. Cryst.* **9**, 433–440.
- Vonk, C. G. (1978). Private communication.
- Walter, G., Kranold, R. and Becherer, G. (1974). *Stud. Biophys.* **47**, 49–62.
- Weik, D. (1974). *Biophys. J.* **14**, 233–235.
- Zipper, P. (1969). *Acta Phys. Austriaca* **30**, 143–151.
- Zipper, P. (1972). *Acta Phys. Austriaca* **36**, 27–38.

5

Interpretation

O. GLATTER

Institut für Physikalische Chemie der Universität Graz, Graz, Austria

I. Introduction	167
II. Homogeneous particles	170
A. Globular particles	170
B. Rod-like particles	171
C. Flat particles	173
D. Composed structures – aggregation, subunits	175
E. Chain molecules	179
III. Hollow and inhomogeneous particles	181
A. Globular particles	181
B. Rod-like particles	183
C. Flat particles	186
D. Spherical vesicles	188
IV. Interparticle-interference, concentration effect	189
A. Liquid type	189
B. Gas-type	191
V. Background	191
VI. Optimization of model parameters	192
A. Models	193
B. Parameter-fit	193
VII. Conclusion	195
References	196

I. Introduction

This chapter deals with the possibilities of structure determination from small angle scattering experiments. It is restricted to dilute monodisperse solutions. Special methods for chain molecules and dense systems are described in Chapters 12, 13 and 14.

Only in a few cases of distinct symmetry (see Chapter 4) can structural details be computed in a straightforward manner. In the majority of cases, structural

details have to be deduced indirectly, either from the shape of the scattering function in reciprocal space or from the distance distribution function in real space. In general, one has to resort to trial and error techniques, considering the fit of experimental results with the corresponding functions of models. The problem of finding the correct class of possible models is the crucial point in this procedure; subsequently, the model parameters can be optimized taking into account the statistical accuracy of the experimental data. The classification can be done either in real space or in reciprocal space.

The relevant functions in real space ($\gamma(r)$, $p(r)$, $p_c(r)$, $p_t(r)$, $G(l)$ and $\rho(r)$) and in reciprocal space ($I(h)$, $I_c(h)$, $I_t(h)$ and $F(h)$) were defined in Chapters 2 and 4.

The chord distribution function $G(l)$ (defined in Chapter 2) cannot be calculated with sufficient accuracy from experimental data to be of importance for the interpretation of these data. The scattering functions show best special features of symmetry. As an example, any scattering function of monodisperse particles with spherical symmetry shows distinct minima. These minima are considerably flattened in the case of cubes (Fig. 1a). The corresponding differences in real space ($p(r)$ -function) are not so clear-cut (Fig. 1b). But in general, the interpretation of scattering functions in reciprocal space are hampered by the highly abstract nature of this domain. Thus, it is very difficult to quantify errors in the model from deviations between the experimental scattering curve and the model scattering curve. This argument applies especially to smeared scattering curves. On the other hand, the distance distribution function

$$p(r) = \gamma(r) \cdot r^2 \quad (1)$$

has a clear geometrical definition. This function (multiplied by the factor 4π) represents for homogeneous particles the number of distances within the particle, i.e. the number of lines with lengths r which are found in the combination of any small volume element i with any other volume element k . The situation is a little bit more complicated in the case of inhomogeneous particles as we have to take into account the difference electron density at the volume elements. Thus the $p(r)$ -function of inhomogeneous particles is proportional to the number of pairs of difference electrons separated by the distance r which are found in the combination of any volume element i with any other volume element k of the same particle. The number of pairs of difference electrons is given by the number of pairs of volume elements multiplied by the product of the number of difference electrons n_i and n_k situated in the corresponding volume elements (see Fig. 2). Regions with opposite signs of difference electron density give negative contributions to $p(r)$, i.e. $p(r)$ can be negative in some regions.

A qualitative classification of shape and internal structure of the particle can be obtained directly from $p(r)$ (Glatter, 1979). In addition to that, several structural parameters can be determined quantitatively, e.g. the maximum intraparticle distance D , since $p(r)$ drops to zero at $r = D$.

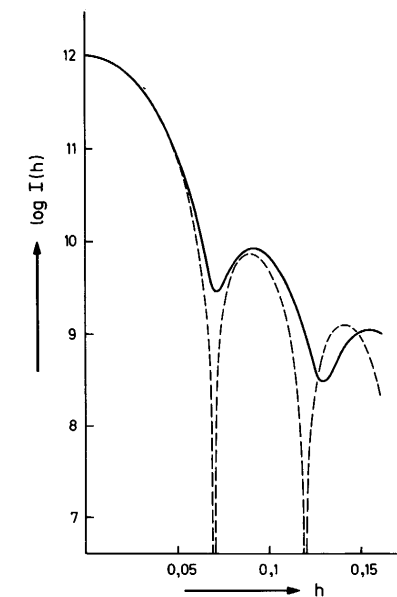


FIG. 1.(a) Comparison of the scattering functions of a sphere (----) and a cube (—) with the same radius of gyration.

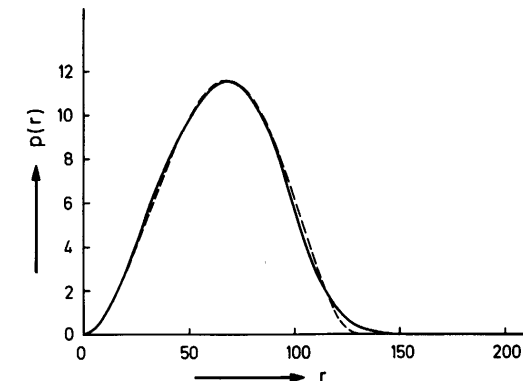
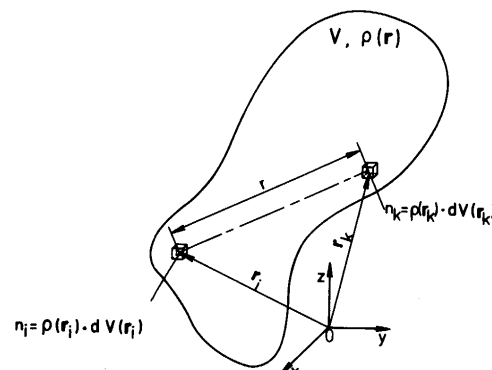


FIG. 1.(b) Distance distribution function of a sphere (----) and a cube (—) with the same radius of gyration and the same scattering intensity at zero angle.

The $p(r)$ -function and the corresponding propagated statistical error band can be calculated with minimized termination effect with the Indirect Transformation Method described in Chapter 4. Chapter 6 describes the method of contrast variation, which can be used to separate $p(r)$ into three functions; of these, the function $p_1(r)$ (coming from $\rho_c(r)$) corresponds to the distance

FIG. 2. Illustration for the definition of $p(r)$.

distribution originating from the overall shape, and $p_2(r)$ (coming from $\rho_s(r)$) corresponds to the distance distribution originating from electron density inhomogeneities within the particle ("inner structure"). Each of these two functions can be interpreted as described in the present chapter: $p_1(r)$ simply has to be treated as a homogeneous particle, while $p_2(r)$ should be treated as an inhomogeneous particle whose mean electron density is identical to the one of the solvent.

II. Homogeneous Particles

The electron density difference $\Delta\rho = \rho_c$ is constant and $p(r)$ has the simple geometrical definition (number of distances).

A. Globular Particles

The distance distribution of a sphere can be evaluated analytically (Porod, 1948):

$$p(r) = 12x^2(2 - 3x + x^3) \quad x = \frac{r}{D} \quad (2)$$

if D is the diameter of the sphere. This function has its maximum near $r = D/2$ ($x \approx 0.525$). Let $r(\text{Max})$ be the r -value of the maximum of $p(r)$. For any deviation from spherical shape, the ratio $M = r(\text{Max})/D$ decreases in the following sequence: globular particles, flat particles, rod-like particles. These findings can be rationalized with the following considerations: long distances contribute in globular particles from three dimensions, in flat particles from two dimensions and in rod-like particles only from one dimension.

B. Rod-like Particles

An important class are particles elongated in one direction which have a constant cross-section of arbitrary shape (long cylinders and prisms). The cross-section A (with maximum dimension d) should be small in comparison to the length L of the whole particle

$$d \ll L \quad L = (D^2 - d^2)^{1/2} \approx D \quad (3)$$

For such particles, $p(r)$ will increase linearly with decreasing r -values, starting from $r = L$. $p(r)$ is given by

$$p(r) = \frac{2}{4\pi} \int_r^L \int_A \int_A \rho_c^2 \cdot df_1 df_2 dx = \frac{1}{2\pi} \cdot \rho_c^2 \cdot A^2 (L - r) \quad (4)$$

(see Fig. 3). This equation shows that the slope of the linear part is proportional to the square of the area of the cross-section:

$$\tan \alpha = -\frac{dp}{dr} = \frac{A^2 \cdot \rho_c^2}{2} \quad (5)$$

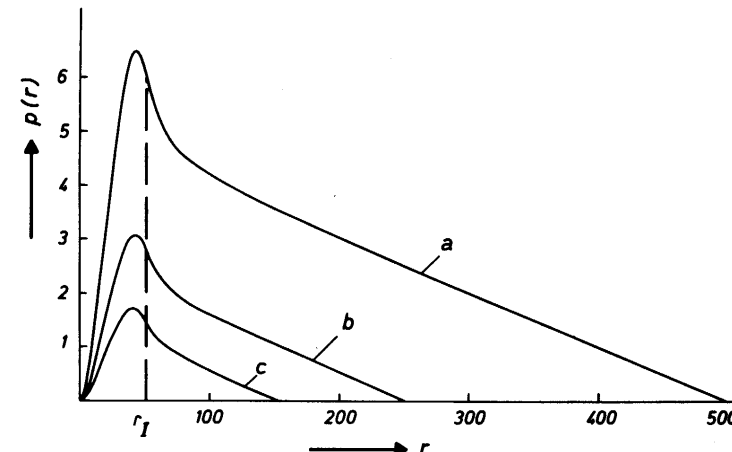


FIG. 3. Distance distributions from homogeneous prisms with edge lengths of: (a) 50:50:500 Å; (b) 50:50:250 Å; (c) 50:50:150 Å.

In principle, Eqn (5) can be used to determine the cross-section area A from the slope of the linear part of $p(r)$ for rod-like particles, if the particle electron density ρ_c is known. However, since the linear part of $p(r)$ will be sensitive to errors in the innermost part of $I(h)$, application of Eqn (5) requires a very critical consideration of systematic errors in this region (extrapolation to zero concentration etc.).

Deviations from Eqn (4) appear as soon as the approximations of Eqn (3) break down, i.e. as soon as the dimension of the cross-section is no longer negligibly small. The $p(r)$ function has a maximum in the region $0 \leq r \leq d$ (the actual position depends on the shape of the cross-section and on the ratio d/D) and is linear for $r > d$ (see Fig. 3). Test calculations have shown that an approximate limit for the occurrence of a linear part can be found from the condition

$$\frac{D}{d} > 2,5 \quad (6)$$

(see Fig. 3).

The point of inflection r_I (Fig. 3) between the maximum and the linear region gives a rough indication for the size of the cross section. This is illustrated with a few examples in Table 1.

TABLE 1
 r_I as a Function of the Dimensions for Various Prisms

Cross-section dimension [Å]	Length [Å]	Distance corresponding to the point of inflection [Å]
50 × 50	150	52
	250	52
	500	52
40 × 40	400	42
80 × 20	400	78
160 × 10	400	155

It should be emphasized that r_I is usually difficult to determine exactly, particularly for particles near the limit given by Eqn (6). r_I has a clear-cut geometrical meaning only for circular cylinders, for which it is equal to the diameter.

The scattering curves of rod-like particles show a pronounced central maximum and broad side maxima, depending on the size of the cross-section ($I_c(h)$) (Fig. 4). The cross-section intensities $I_c(h)$ drop to zero in the Guinier range, caused by the finite length of the particles.

This impedes the accurate determination of the radius of gyration of the cross-section R_c . The distance distribution function of the cross-section $p_c(r)$ can be calculated with Eqns (32), Chapter 4 if $I(h)$ is known up to sufficiently large angles to include some of the subsidiary maxima originating from the cross-section. The termination effect of such calculations is always appreciable (Chapter 4, Fig. 9). The function p_c drops to zero at $r = d$.

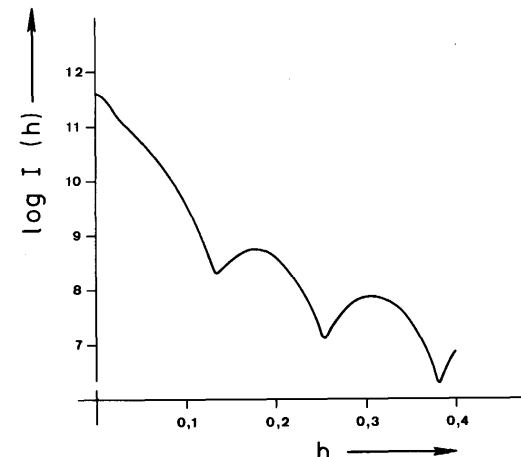


FIG. 4. Scattering intensity of a homogeneous prism with edge lengths of 50:50:250 Å.

C. Flat Particles

The form of the $p(r)$ function of flat particles, i.e. particles elongated in two dimensions (discs, flat prisms) is more complicated. An analytical expression can be given for infinite thin circular discs (Porod, 1948)

$$p(r) = \frac{16}{\pi} x (\arccos x - x\sqrt{1-x^2}), \quad x = \frac{r}{D} \quad (7)$$

Intuitively, one can rationalize the main features with the following consideration: let us take a point in the centre of the lamella (Fig. 5a-c). For very small values of r ($r \leq d$; d = thickness of the lamella), $p(r)$ will increase with the second power of r , since the number of distances is proportional to the surface of a sphere with radius r (Fig. 5a). If $r > d$, most of the sphere lies outside the lamella and $p(r)$ will increase roughly linearly, since the intersecting plane between lamella and sphere approximates a circular cylinder for $r \geq d$ (Fig. 5b). Figure 5c illustrates the situation for still larger r -values; if the centre of the cylinder is near the edge of the lamella, some of the cylinder will lie outside the lamella ("boundary losses"). Evidently, these boundary losses increase with increasing r , and eventually cause $p(r)$ to drop to zero for $r \geq D$. It should be emphasized that the above "linear" range usually can not be observed, since the boundary losses are effective also at small r -values.

Thus, we expect a quadratic increase for the region $r < d$, a more or less linear increase for $r > d$ (first term of the power series in Eqn (7)) and a drop to zero at $r = D$. This is shown in Fig. 6a for 3 lamellae of different thickness d .

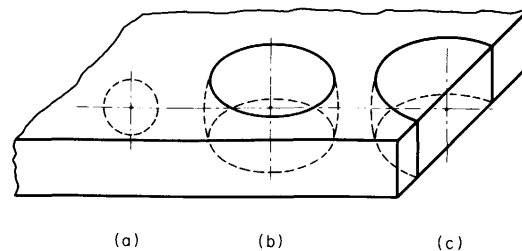


FIG. 5. Distances in a lamellar particle.

The transition at $r = d$ cannot be seen clearly in this plot, but a convex behaviour at $r > d$ can be recognized distinctly.

The situation becomes much clearer if we use the function

$$f(r) = \gamma(r) \cdot r = \frac{p(r)}{r} \quad (8)$$

This function is more useful for lamellar particles than $p(r)$. Values of $f(r)$ for the lamellae in Fig. 6a are plotted in Fig. 6b. As expected, the curves start with a linear increase. At $r = d$ the curves become almost linear, the slight decrease is due to boundary losses. The thickness d of the particle can be read from the transition point.

The limiting value A of the function $f(r)$, resulting from an extrapolation of the quasi linear part towards $r = 0$, contains information about the area of the basal plane of the lamella, according to

$$A = f(r)|_{r \rightarrow 0} = \frac{\rho_c^2}{r} \int \frac{2\pi r \cdot d}{4\pi} dv = \frac{\rho_c^2 \cdot F \cdot d^2}{2} = \frac{\rho_c^2 \cdot V \cdot d}{2} \quad (9)$$

The extrapolation to $r = 0$ is the more accurate the larger the ratio D/d (see Fig. 6b). In practice, the shape of the function $f(r)$ will allow the recognition of a lamellar particle and the determination of its thickness.

The transition from elongated rods with compact cross-sections to elongated lamellae is demonstrated for the example of three prisms (with edges a, b, c) with constant cross-section ($a \cdot b = \text{const.}$) and constant length $c = L$ (see Fig. 7a). The ratio of the edge length is: (1) 4:4:40, (2) 2:8:40 and (3) 1:16:40. The corresponding $p(r)$ -functions show a linear descent with the same slope dp/dr since all the particles are elongated, have the same cross-section and fulfill condition (6). The increasing dimension of the cross-section from (1) to (3) causes a decrease in the length of the linear descent and a shift of the maximum to larger r -values. The increasing lamellar character can be seen from the $f(r)$ functions in Fig. 7b. The quadratic prism (1) does not indicate any lamellar structure, whereas the lamellar shape of prisms (2) and (3) can easily be

recognized. The thickness d and the basal area $A_t = b \cdot c$ can be estimated. As mentioned above, the point of inflection r_I gives an approximate value for the larger edge length. It should be emphasized that such a clear-cut direct classification is not possible in reciprocal space.

Figures 8a and 8b give a comparison between a globular particle (sphere $r = 19.1 \text{ \AA}$), a rod-like particle (prolate ellipsoid with semi-axes 10:10:30) and a flat particle (oblate ellipsoid with semi-axes 23.2:23.2:4.6), all having the same number of excess electrons ($I(0)$) and the same radius of gyration (Fig. 8a). The ellipsoids have a larger maximum dimension D than the sphere and their ratio M for the position of the maximum is smaller. These properties are most significant for the prolate ellipsoid. The corresponding $p(r)$ function can be classified as a rod-like particle with varying cross-section, indicated by the nonlinear descent towards $r = D$. The point of inflection r_I indicates a mean diameter of 18 \AA .

The oblate ellipsoid can be recognized as a flat particle by a consideration of $f(r)$ (Fig. 8b). Its mean thickness (obtained from the position of the transition point) is about 8 \AA . This function, however, does not indicate the variable thickness. The difference between the oblate ellipsoid and a similar prism (35.8:35.8:8.2) are so insignificant that they may be within experimental errors (see Glatter, 1979). The distance distribution of the sphere can be classified as a globular particle (large M -value). The spherical symmetry can be detected in reciprocal space or from $p(r)$ by the application of the deconvolution technique indicating a homogeneous sphere. The zeros of the scattered intensity and the height of the subsidiary maxima give an indication for a homogeneous sphere in reciprocal space too. The decrease of the M -value for the ellipsoid leads, in reciprocal space, to a diminution of the decrease of the main-maximum as compared to the sphere. The classification of the two ellipsoids is not so clear-cut in reciprocal space. Using the Guinier plots for the cross-section intensity $I_c(h)$ and the thickness intensity $I_t(h)$, it could be possible to classify the prolate ellipsoid as a rod-like particle and the oblate ellipsoid as a flat particle, but this division is not unambiguous.

D. Composed Structures – Aggregation, Subunits

1. DIMERS

The formation of dimers can be analysed qualitatively with the $p(r)$ function. An illustrative example is given in Fig. 9a-d. A prolate ellipsoid with axial ratio 1:1:2 is taken as monomer. The $p(r)$ function of the monomer indicates an elongated particle with decreasing cross-section toward the ends. The difference distance distribution of the lines connecting the two subunits in the dimer results from the subtraction of the distance distribution of the two monomers

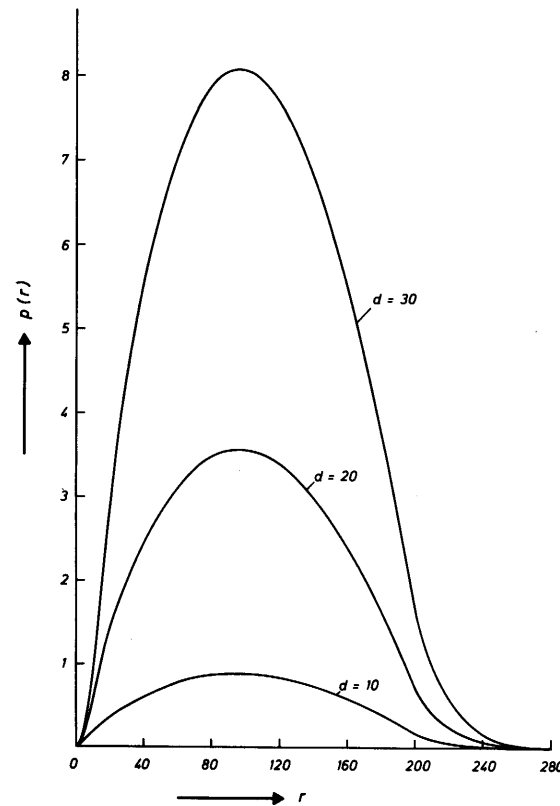


FIG. 6.(a) $p(r)$ functions of lamellar particles with the same basal plane ($100 \times 100 \text{ \AA}$) and varying thickness d . (a) $d = 10 \text{ \AA}$; (b) $d = 20 \text{ \AA}$ and (c) $= 30 \text{ \AA}$.

from the distance distribution of the dimer. The difference between the parallel (Fig. 9a) and the linear arrangement (Fig. 9b) is obvious. Almost all of the difference distribution of the parallel arrangement lies within the distance distribution of the monomer, whereas the linear arrangement contributes up to twice the maximum dimension of the monomer. The two rectangular configurations of *T*-type (Fig. 9c) and *L*-type (Fig. 9d) lie between the linear and parallel arrangement. The maximum of the difference distribution is at larger r -values for the *L*-type than for the *T*-type. For such a rough analysis it is not necessary to have an exact shape analysis of the monomer.

The hump at large r -values is typical for dimers whose constituent monomers can still be recognized, otherwise the hump disappears like in the case of axial aggregation of cylinders. Similar analyses can be carried out for the formation of dimers from globular or lamellar monomers.

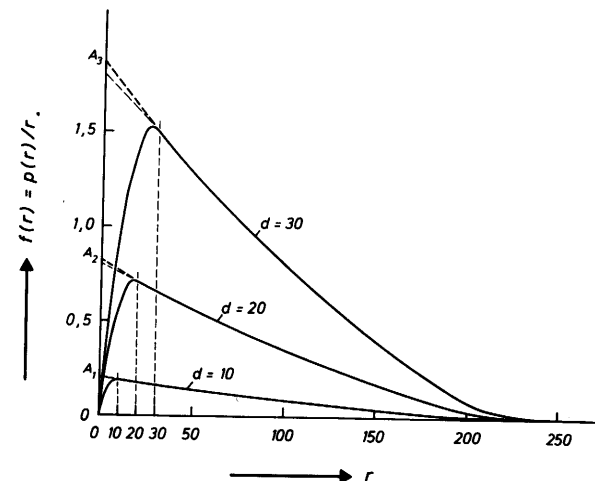


FIG. 6.(b) The functions $f(r) = p(r)/r$ of the particles described in (a). The transition points are signalled by the vertical dashed lines.

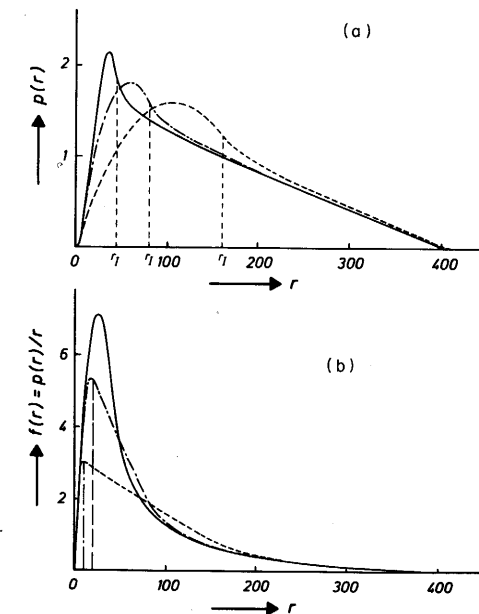


FIG. 7. Three prisms with constant length L (400 \AA) and a constant cross-section but varying length of the edges: — $40 \times 40 \text{ \AA}^2$; - - - $80 \times 20 \text{ \AA}^2$; - · - $160 \times 10 \text{ \AA}^2$. Part (a) $p(r)$ function. Part (b) $f(r) = p(r)/r$.

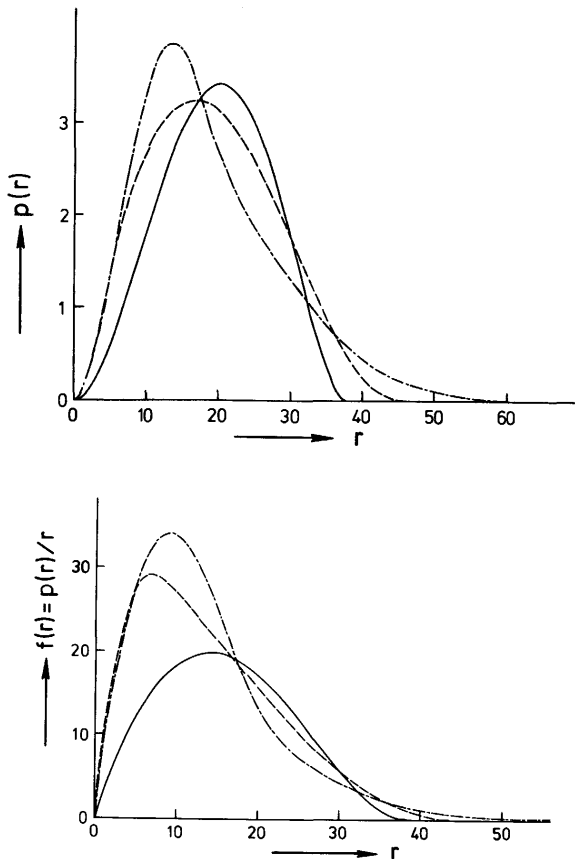


FIG. 8. Comparison of the $p(r)$ and $f(r)$ function of a sphere (—), a prolate ellipsoid of revolution 1:1:3 (---), an oblate ellipsoid of revolution 1:1:0.2 (- - -) with the same radius of gyration. (a) (above) $p(r)$ function. (b) (below) $f(r)$ function.

Higher aggregates can generally not be classified unambiguously. Additional information from other sources, like the occurrence of symmetry, can simplify the problem.

In reciprocal space we can use only the radii of gyration R , R_c and R_t for a rough classification.

2. SUBUNITS

Particles which consist of aggregates of a relatively large number of identical subunits show the overall structure of the whole particle at low resolution. At larger angles (high resolution) the influence of the individual subunits can be

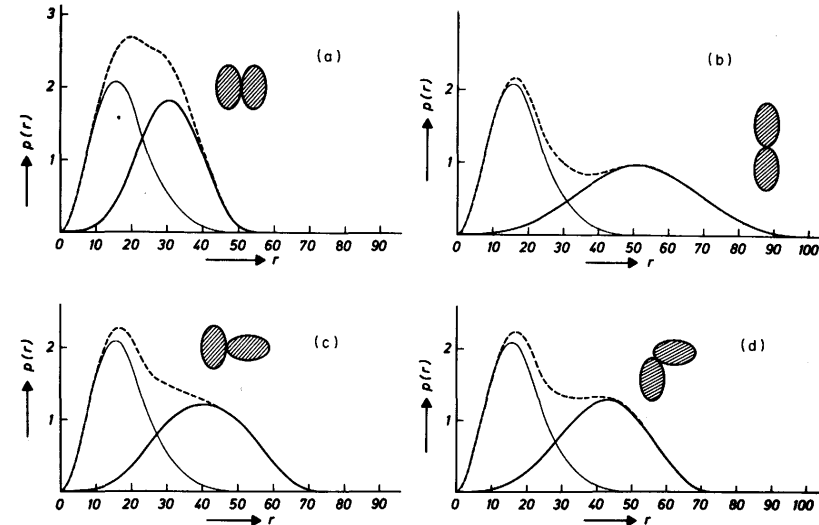


FIG. 9. Distance distribution function $p(r)$ from dimer models built from prolate ellipsoids. — monomers, --- dimers, - - - difference between dimers and monomers. (a) parallel formation, (b) linear formation, (c) T-type, (d) L-type.

seen. In the special case of globular or spherical subunits, it is possible to determine the size of the subunits from the position of the minima of the corresponding shape factors (Glatter, 1972). The $p(r)$ function shows inter-subunit distances convoluted with the $p(r)$ function of the form factor (Glatter, 1980). More information about the subunit-arrangement can be obtained from $p(r)$ if the scattering curve is divided by an approximate form factor (Glatter, 1972). A common situation in practical applications is shown in the next example. The enzyme DNA-dependent RNA polymerase is composed of four subunits (Fig. 10). The structure of the subunits was known from earlier small angle scattering experiments (Stöckel *et al.*, 1979; Meisenberger *et al.*, 1980a). Model 2 shows a possible configuration with a centre-to-centre distance of the two larger subunits of 7 nm as suggested by the preceding experiments. Comparison of the corresponding $p(r)$ function with the experimental data (Meisenberger *et al.*, 1980b) shows that the maximum is situated at larger r values for the model. This maximum can be shifted to the right position by a reduction of the centre-to-centre distance to 5 nm (model 1).

E. Chain Molecules

Methods of interpretation for this type of molecules are discussed in detail in Chapter 12. The scattering curve of a worm-like chain can be approximated by the Debye formula

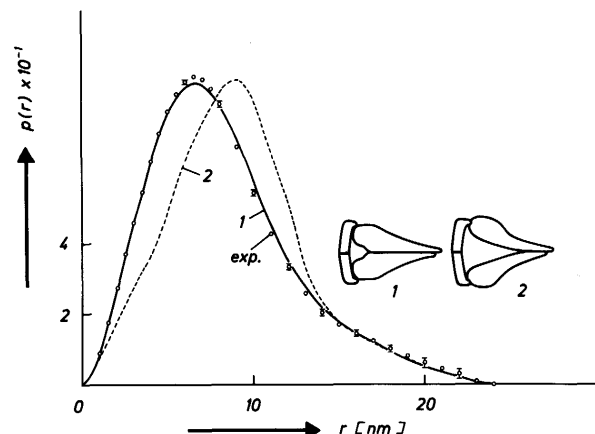


FIG. 10. Comparison of the experimental $p(r)$ function of a core enzyme $\circ \circ \circ$ (Meisenberger et al., 1980) with the theoretical one of model 1 (—) and model 2 (---).

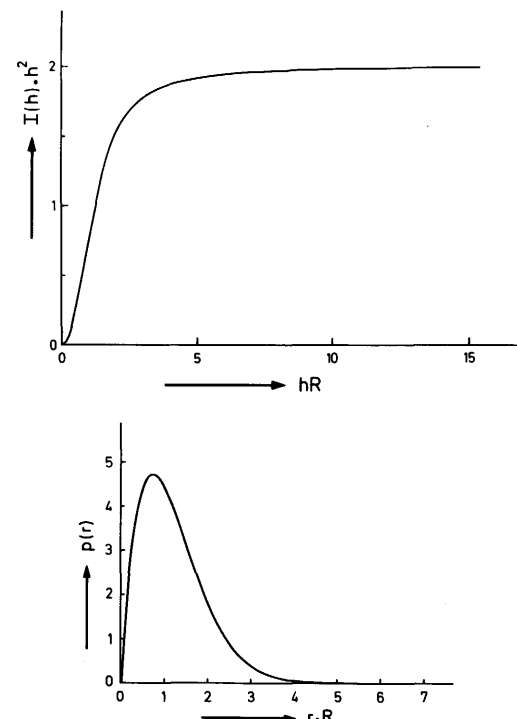


FIG. 11. (a) (above) Scattering function of a chain molecule according to Debye in a $I(h) \cdot h^2$ versus h plot. (b) (below) The corresponding distance distribution function.

$$i(h) = \text{const.} \frac{2}{x^2} [e^{-x} - 1 + x] \quad (10)$$

with $x = R^2 \cdot h^2$. The scattering curve shows a linear plateau for large h values in a plot $I(h) \cdot h^2$ versus h (Fig. 11a). The corresponding distance distribution function is shown in Fig. 11b.

III. Hollow and Inhomogeneous Particles

A. Globular Particles

1. HOLLOW SPHERE

The hollow sphere is the hollow particle of greatest practical importance. The distance distribution function is known analytically (Glatter, 1979):

$$p(r) = \begin{cases} \rho_c^2 \left[\frac{4\pi}{3} (R_a^3 - R_i^3) r^2 - (R_a^2 + R_i^2) \pi \cdot r^3 + \frac{\pi}{6} \cdot r^5 \right] & 0 \leq r \leq (R_a - R_i) \\ \rho_c^2 \left[\frac{\pi}{2} (R_a^2 - R_i^2)^2 \cdot r \right] & (R_a - R_i) \leq r \leq 2R_i \\ \rho_c^2 \left[\frac{\pi}{2} (R_a^2 - R_i^2)^2 \cdot r - \frac{4\pi}{3} R_i^3 \cdot r^2 \right. \\ \left. + \pi R_i^2 \cdot r^3 - \frac{\pi}{12} r^5 \right] & 2R_i \leq r \leq (R_a + R_i) \\ \rho_c^2 \left[\frac{4\pi}{3} R_a^3 \cdot r^2 - R_a^2 \pi \cdot r^3 + \frac{\pi}{12} r^5 \right] & (R_a + R_i) \leq r \leq 2R_a \end{cases} \quad (11)$$

if R_i is the inner radius and R_a is the outer radius ($2R_a = D$).

For thin spherical shells we can write

$$d = R_a - R_i, \quad R_a = R_m + d/2 \quad \text{and} \quad R_i = R_m - d/2 \quad (12)$$

Substitution into (11) yields

$$p(r) = \rho_c^2 \cdot 2\pi \cdot R_m^2 \cdot d^2 \cdot r \approx \frac{\rho_c^2 V \cdot d}{2} \cdot r \quad (13)$$

for the linear part (second row in Eqn 11).

The limiting case of a very thin spherical shell corresponds to a special case of a flat particle. Therefore, it is interesting to study its $f(r)$ function. The linear region is horizontal due to the special shape of this body (in analogy to Eqn (9)), the height of this plateau is given by Eqns (11) and (12):

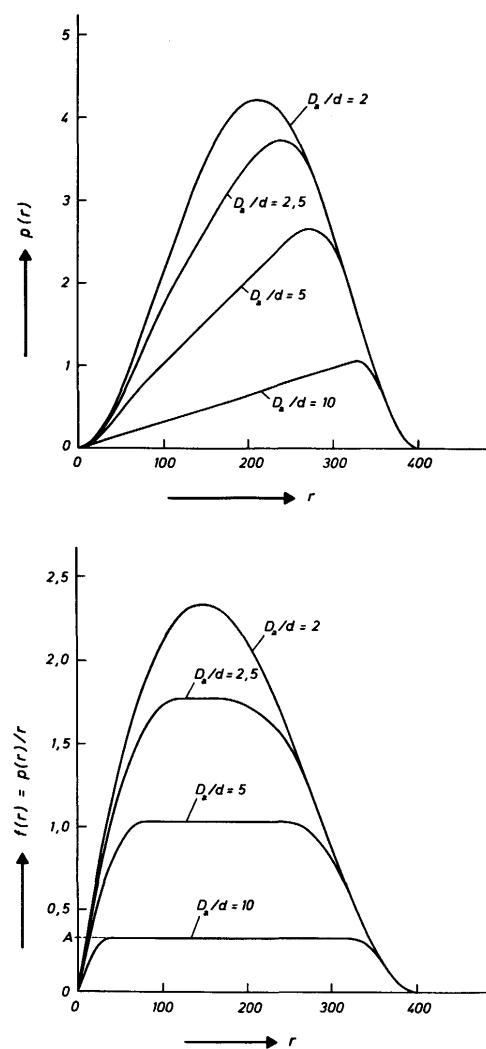


FIG. 12. (a) (above) Hollow spheres — $p(r)$ functions: D_a is the outer diameter, d the thickness of the shell. $D_a/d = 2$ represents a full sphere, $D_a = 400 \text{ \AA}$. (b) (below) Hollow spheres as in Fig. 12a, $f(r)$ functions: A is the height of the plateau.

$$A = \rho_c^2 \cdot \frac{\pi}{2} (R_a^2 - R_i^2)^2 = \rho_c^2 \cdot 2\pi R_m^2 d^2 \simeq \rho_c^2 \frac{Vd}{2} \quad (14)$$

The transition from a thin-walled sphere to a full sphere is shown in Fig. 12a and Fig. 12b.

The scattered intensity of hollow spheres is very similar to the scattered intensity of a homogeneous sphere and can be expressed analytically as

$$\begin{aligned} J(h) = & \rho_c^2 \cdot 16\pi^2 \left[R_a^3 \frac{\sin(hR_a) - hR_a \cos(hR_a)}{(hR_a)^3} \right. \\ & \left. - R_i^3 \frac{\sin(hR_i) - hR_i \cos(hR_i)}{(hR_i)^3} \right]^2 \end{aligned} \quad (15)$$

The height of the side maxima increases with increasing R_i . The "degree of hollowness" R_i/R_a can be determined from this height only if one is sure that the particle under examination is a homogeneous hollow sphere.

2. SPHERICAL MULTILAYER MODELS

Distance distribution functions of spherical multilayer models with alternating signs of the excess electron density are illustrated in Fig. 13. The rough qualitative conclusions that can be made from the $p(r)$ function are as follows: under the assumption of a compact structure, the occurrence of minima in the $p(r)$ function signals the existence of regions of electron density with alternating sign. The number of such regions is equal to the number of maxima in the $p(r)$ function, provided the particles are spherical (sharp minima in the scattering curve) and the shells have approximately the same dimensions (thickness). The radial electron density distribution can be computed from the $p(r)$ function by means of the convolution square root technique described in Chapter 4.

B. Rod-like Particles

1. RADIAL INHOMOGENEITY

The $p(r)$ functions of an elongated cylinder with constant electron density along the cylinder axis and varying electron density of cylindrical symmetry $\rho_c(x)$ (x is the distance from the cylinder axis) are shown in Fig. 14. The $p(r)$ function differs from the one of a homogeneous cylinder for r -values smaller than the cylinder diameter. A linear descent at large r -values can still be observed. Its slope is given by the equation

$$\tan \alpha = -\frac{dp}{dr} = \frac{A^2 \cdot \bar{\rho}_c^2}{2\pi} \quad (16)$$

A is the area of the cross-section and

$$\bar{\rho}_c = \frac{1}{A} \int_A \rho_c(x) df \quad (17)$$

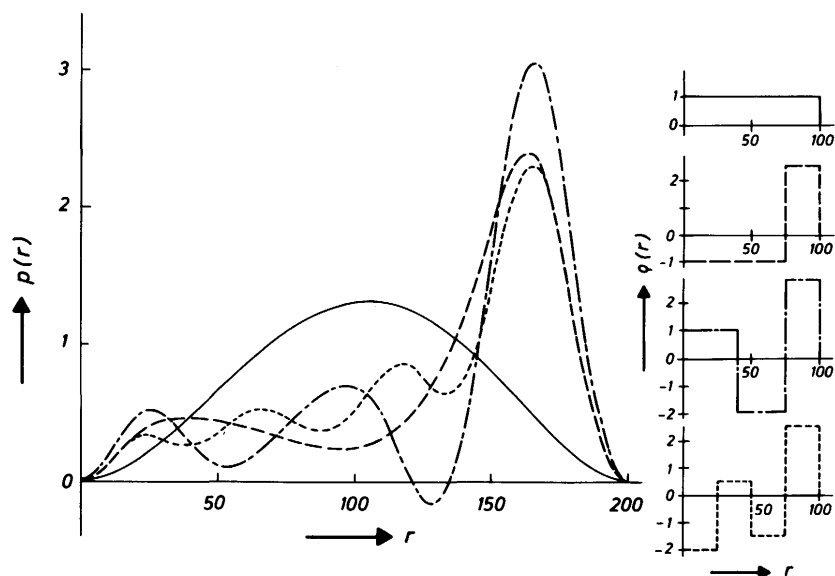


FIG. 13. Spherical multilayer models with constant outer diameter of 200 Å. $p(r)$ functions in the left part, electron density profiles in the right part of the figure.

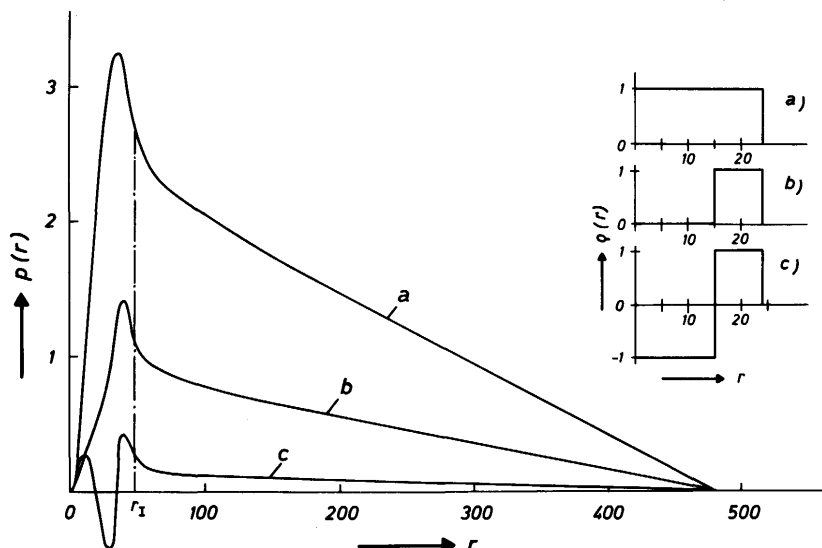


FIG. 14. Circular cylinder with a constant length of 480 Å and an outer diameter of 48 Å. (a) Homogeneous cylinder, (b) hollow cylinder, (c) inhomogeneous cylinder. The $p(r)$ functions are shown on the left side, the corresponding electron density distributions $\rho(r)$ on the right side.

If we compare the homogeneous cylinder with the hollow cylinder we see that the maximum of the $p(r)$ function of the hollow cylinder is located at larger distances, since the small distances from the core are missing. The slope of the linear descent is lower due to the smaller cross-section area. The $p(r)$ function of the inhomogeneous cylinder shows a negative region, i.e. there are distances which connect regions with opposite signs more frequently than regions with the same sign. The maximum is caused by the outermost shell (see hollow cylinder). The linear descent is always positive, even if $\bar{\rho}_c$ is negative. The linear region coincides with the abscissa if $\bar{\rho}_c = 0$. This would be the case in the evaluation of the structural term $p_2(r)$ ($I_s(h)$) in the contrast variation method. Again, the scattering curve $I(h)$ is of no practical importance for the classification. If the $p(r)$ with its linear descent has allowed us to classify the experimental data as scattering data from an elongated cylindrical particle we can calculate the cross-section distance distribution function $p_c(r)$ (Eqns (31) and (32) in Chapter 4). Assuming cylindrical symmetry (indicated by distinct side maxima in the $I_c(h)$ function) we can again compute the radial electron density distribution $\rho_c(r)$ in a straight-forward manner with the convolution square root technique from $p_c(r)$.

2. AXIAL INHOMOGENEITY

Particles with a homogeneous cross-section but with inhomogeneities along the long axis show a modification of the $p(r)$ function in the whole range of definition $0 < r < D$. Periodical changes of the electron density are assumed in the model shown in Fig. 15a: its $p(r)$ function is compared with $p(r)$ for a homogeneous cylinder having the same mean electron density. The corresponding scattering functions are shown in Fig. 15b. The periodical changes in the electron density lead to the periodical ripples in $p(r)$ and to sharp maxima in $I(h)$ which could be explained as broadened reflections of odd orders. In the special case $\bar{\rho} = 0$ (internal structure term $p_2(r)$ in the contrast variation method), one observes a $p(r)$ function that deviates from zero in the whole range $0 \leq r \leq D$. Oscillations about the linear descent can also occur for cylinders with homogeneous electron density but varying cross-section, like a linear assembly of spheres. In this case the $p(r)$ function can be constructed from a set of equally spaced delta functions with linear decreasing coefficients, convoluted with the distance distribution of a pair of spheres with the corresponding mutual distance.

Inhomogeneities which are mixtures of the axial and radial type (real two- or three-dimensional functions) can not be interpreted without additional information.

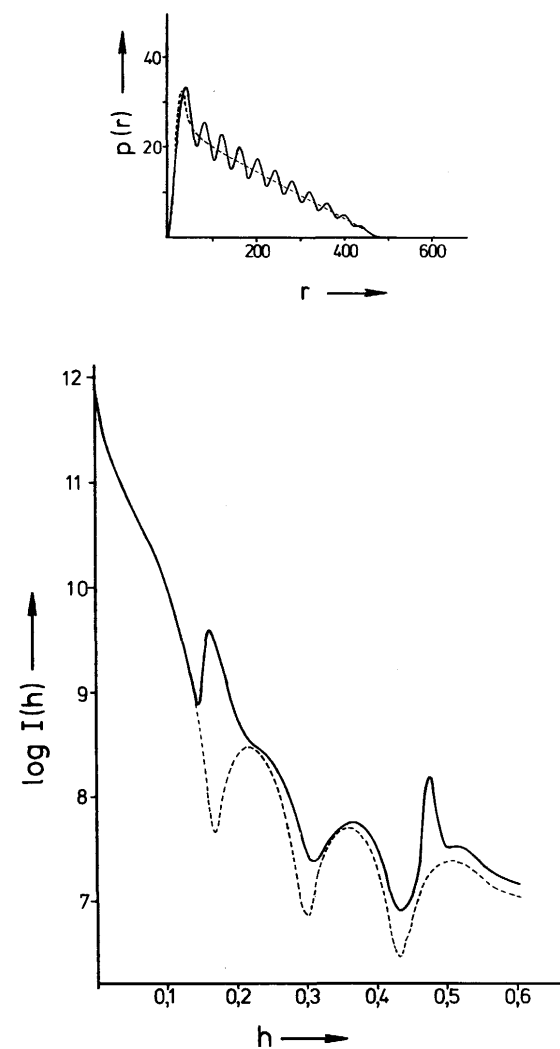


FIG. 15. Inhomogeneous circular cylinder with periodical changes of the electron density along the cylinder axis compared with a homogeneous cylinder with the same mean electron density. (a) above $p(r)$ function; (b) (below) scattering intensity, — inhomogeneous cylinder, - - - homogeneous cylinder.

C. Flat Particles

1. CROSS-SECTIONAL INHOMOGENEITIES

Lamellar particles with varying electron density perpendicular to the basal plane, i.e. $\rho = \rho_t(x)$ (x is the distance from the central plane) show properties

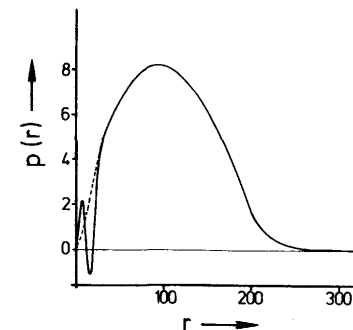


FIG. 16. $p(r)$ function of a lamellar particle. The full line corresponds to an inhomogeneous particle, $\rho_t(x)$ is a three-step function with the values $+1, -1, +1$. The broken line represents the homogeneous lamella with $\rho = +1$.

similar to that of rod-like particles with radial inhomogeneity. The $p(r)$ function deviates from the $p(r)$ function of the homogeneous lamella between $0 < r < T$ and can be negative in this region. An example is given in Fig. 16. The $p(r)$ function coincides with that of a homogeneous lamella of the same dimensions and the same mean electron density for $r > T$. The function $p_2(r)$ ($\bar{\rho}_t = 0$) drops to zero behind $r = T$. To obtain the extrapolated $f(r)$ function Eqn (9) has to be modified as follows:

$$B = f(r)|_{r \rightarrow 0} = \frac{\bar{\rho}_t^2 \cdot A \cdot T^2}{2} = \frac{\bar{\rho}_t^2 \cdot V \cdot T}{2} \quad (18)$$

with

$$\bar{\rho}_t = \frac{1}{T} \int_{-T/2}^{T/2} \rho_t(x) dx \quad (19)$$

Again we can calculate the cross-section functions $p_t(r)$ with Eqns (34) and (35) in Chapter 4 if the lamellar structure has been realized from the $f(r)$ function and the convolution square root technique gives the best symmetrical approximation for $\rho_t(r)$.

2. IN-PLANE INHOMOGENEITY

Lamellae with a homogeneous cross-section but inhomogeneities along the basal plane have $p(r)$ functions which deviate from $p(r)$ of the corresponding homogeneous lamella (with the same mean electron density) in the range of the whole particle $0 < r < D$. The amplitude of oscillations is a measure for the degree of in-plane inhomogeneity. The general problem – cross-sectional plus in-plane inhomogeneities – occurs in the study of membranes: these particles show a pronounced cross-section structure with additional in-plane inhomogeneities (see Chapter 10).

D. Spherical Vesicles

Inhomogeneous spherical vesicles can be discussed as thin inhomogeneous hollow spheres or, in a rough approximation, as bent flat particles. We shall content ourselves with a discussion of vesicles with spherical symmetry, i.e. $\rho = \rho(r)$. Under this assumption, the distance distribution functions $p(r)$ and $f(r)$ deviate from the corresponding functions of a homogeneous particle (with the same dimensions and the same mean electron density) within the two regions $0 < r < d$ ($d = R_a - R_i$) and $2R_i < r < 2R_a$. In this special case one can calculate the function $P(r)$ according to Weik (1974) (see Chapter 4, Section III. E3). The function $P(r)$ has two non-zero regions at $0 < r < d$ and $2R_i < r < 2R_a$ and is equal to zero wherever $f(r)$ is horizontal (see Fig. 17).

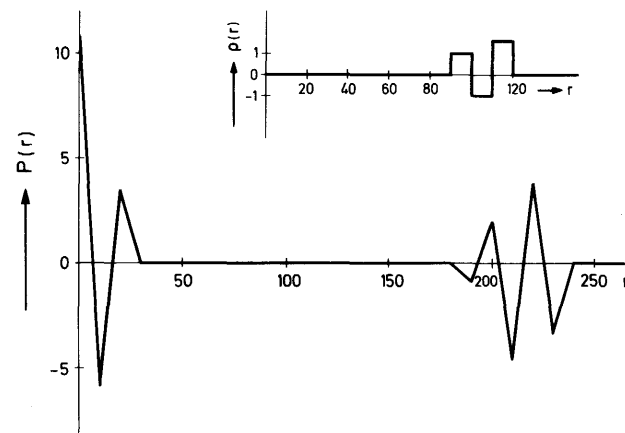


FIG. 17. $\rho(r)$ and $P(r)$ of a spherical vesicle when $\rho(r)$ is an asymmetrical profile, generating an asymmetrical $P(r)$ function in the range $2R_i < r < 2R_a$.

The scattering curve shows high frequency oscillations (according to the dimension of the vesicle) modulated with a low frequency curve (according to the density profile $\rho(r)$) (Fig. 18). The high frequency oscillations are appreciably damped for spherical vesicles with a size distribution in the mean diameter or for nonspherical vesicles and $P(r)$ is smeared out in its second part ($2R_i < r < 2R_a$) for such particles. This second part must be known for the determination of asymmetrical electron density profiles.

The limiting case of an infinitely large vesicle coincides with a lamellar particle (for further details see Chapter 10).

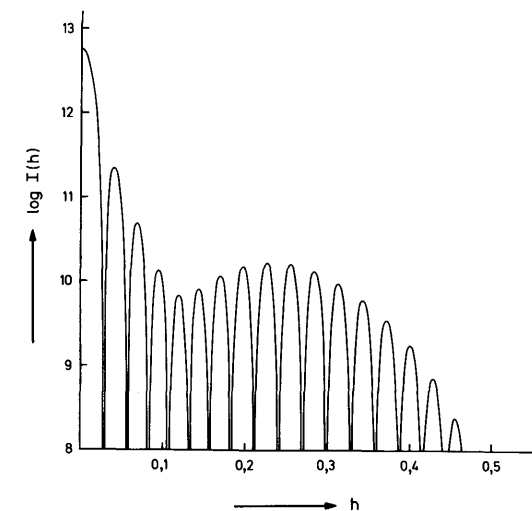


FIG. 18. Scattering function of the spherical vesicle defined in Fig. 17.

IV. Interparticle-interference, Concentration Effect

A general discussion of this effect is given in Chapter 2, Section V. No unique mathematical description of this effect is available at present. There exist only some qualitative considerations (Guinier and Fournet, 1955; Kratky and Porod, 1956; Porod, 1972).

A. Liquid Type

This type of concentration effect occurs most frequently in practical small angle work, and it can lead to a considerable distortion of the $p(r)$ function: $p(r)$ is lowered (as compared to the isolated particle) for increasing r -values and passes through a negative minimum in the region of the maximum distance D . At still larger distances, $p(r)$ shows damped oscillations about zero. This can be shown theoretically for the so-called hard sphere model (Fig. 19a) and it is also found in many experiments with nonspherical particles (see for example Fig. 6 in Chapter 8).

The influence of the interparticle-interference on the scattering curve manifests itself in a decrease of the scattered intensity at small angles (Fig. 19b). A

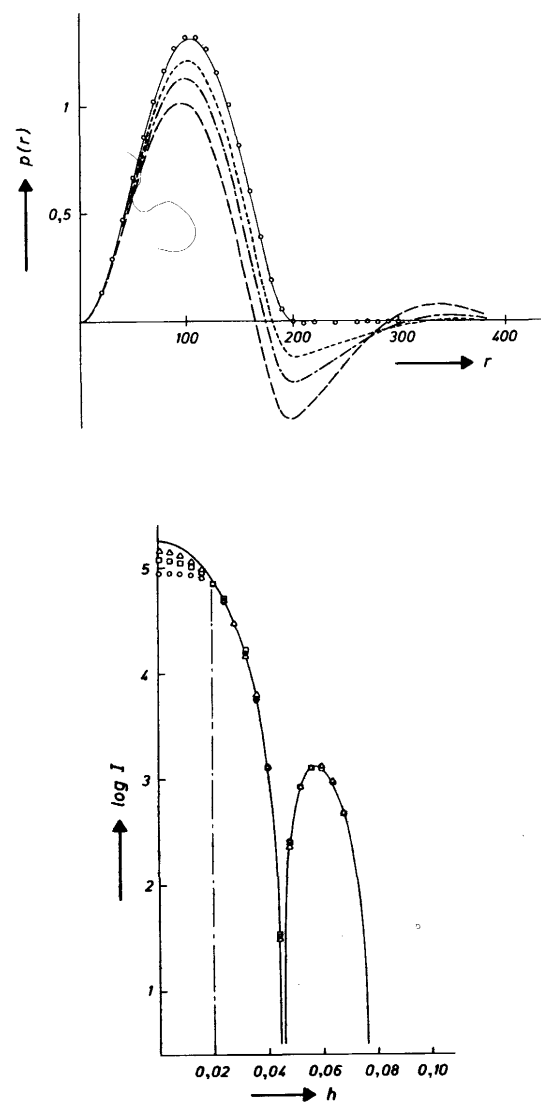


FIG. 19. (a) (above) Distance distribution – hard sphere interference model. Theoretical $p(r)$ functions: — $\theta = 0$, --- $\theta = 0,25$, -·-·— $\theta = 0,5$, -·-·- $\theta = 1,0$. Circles: Results from indirect transformation: $\theta = 0,5$, $h_1 R = 2,0$. 2% statistical noise, $D_{\max} = 300 \text{ \AA}$, $\Delta R_g = 0,5\%$, $\Delta I_0 = 1,2\%$. (b) (below) Interference effect – hard sphere model $R = 100 \text{ \AA}$: Scattering functions for different concentration factors θ ; $\theta = 8v_0/v_1$. —: $\theta = 0$; Δ: $\theta = 0,25$; □: $\theta = 0,5$; ○: $\theta = 1,0$. Dashed vertical line: termination for indirect transformation (first data point at $h \cdot R = 2,0$).

rough approximation which yields a fair representation of the experimental findings was given by Guinier and Fournet (1955) for the hard sphere model:

$$I_{HS}(h) = \text{const. } \phi^2(hR_a) \frac{1}{1 + \theta \cdot \phi(2hR_a)}. \quad (20)$$

$\theta = 8v_0/v_1$ is the packing parameter, R_a is the radius of the sphere and $\phi(hR_a)$ is the scattering amplitude of a sphere with radius R_a . The apparent radius of gyration decreases with increasing concentration. The length of the linear range of the Guinier plot can be extended by the interference effect for nonspherical particles. Thus a long linear Guinier plot is no guarantee for the complete elimination of the concentration effect. Remaining concentration effects cannot be recognized in reciprocal space, but they can clearly be seen from the $p(r)$ function.

It should be noted that minima at zero angles could also arise from inhomogeneous particles, but their $p(r)$ function ends with a positive part provided the particle does not have a dipole structure.

Sometimes it is impossible to measure a series of concentrations, e.g. if the structure of the particle depends on the concentration. In such cases one can attempt to reduce the contribution of the interparticle interferences by neglecting the innermost part of the scattering curve in the evaluation of the experimental data. The problems of increasing termination effects can be overcome with the indirect transformation method (Fig. 19a). However, if the concentrations are high ($\theta > 0,5$), the interparticle interferences can no more be treated as perturbations which can be eliminated.

B. Gas-type

In this case one observes a tendency for particle aggregation and therefore an increase in the $p(r)$ function at large r -values, corresponding to an increase of the scattered intensity at very small angles. A reduction of this type of interference effect by omitting the innermost data points is not possible and there exist no general methods for the interpretation of such data.

V. Background

In a first approximation, the scattering background can be approximated as a constant term. Elimination of the background can only be properly performed if the scattering curve shows a h^{-4} -course (h^{-3} for slit smeared functions). Neglect of background-eliminations leads to strong oscillations in the $p(r)$ function (conventional Fourier transformation) or to an increase of the $p(r)$

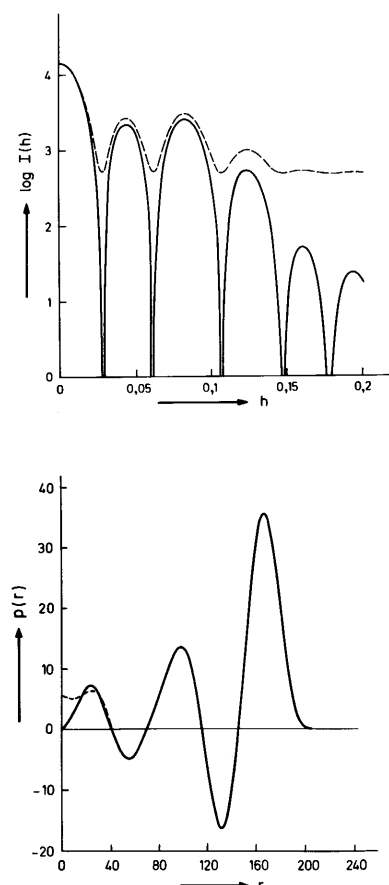


FIG. 20. (a) (above) Scattering function of the three-step spherical multilayer model in Fig. 13. — exact scattering function, --- scattering function with an additional constant background. (b) (below) Distance distribution functions computed from the scattering functions in Fig. 20a with the indirect transformation method.

function at $r = 0$ if the indirect transformation method is used (see Fig. 20), but the interpretation is not severely impeded by this increase at $r = 0$.

VI. Optimization of Model Parameters

The techniques for a classification of the experimental results were described in the preceding part of this chapter. Once the right class of particle shape is found from the $p(r)$ function and the scattered intensity, one can start with model

calculations and model refinement in order to obtain the optimum set of model parameters.

A. Models

1. GEOMETRICAL MODELS

We can construct geometrical models which are defined by some model parameters (triaxial bodies like sphere, ellipsoid, cylinder, prism etc. and composed models). Parameters are quantities like the length of axes or edges, angles between axes etc. More complicated models can be constructed by a combination of several smaller bodies.

2. MATHEMATICAL MODELS

A large number of three-dimensional structures can in principle be described with spherical harmonics which are solutions for a special type of differential equation (see Chapter 6). Sufficient convergence within a few coefficients can only be expected for globular structures. In other words: the necessary restriction to a small number of coefficients leads to a strong restriction of possible structures.

Both types of models (geometric and mathematical) represent an arbitrary restriction to a limited number of solutions, and the model parameters cannot be calculated directly in either case. They have to be optimized by trial and error methods.

B. Parameter-fit

1. GEOMETRICAL MODELS

The traditional way for the parameter estimate for simple triaxial models consisted of an optical comparison of model scattering function with the desmeared experimental data in a plot which avoids the scaling problems (i.e. $\log I$ vs $\log h$). A large number of model curves for several triaxial bodies was available from the calculation of Porod (1948) and Mittelbach (1964). The difficulties in the optimization are caused by restriction to simple geometrical models, by the existence of several local minima in a general least squares technique and by the problem of error propagation.

The discussion of deviations between model and experimental data is more convenient in real space ($p(r)$ -function) than in reciprocal space. Another possibility is the calculation of smeared model scattering functions and a fit of the parameters directly on the experimental data (Sjöberg, 1978). The

classification is difficult with this procedure, but the method is suitable for the final steps of model refinement and it avoids the problem of error propagation.

2. MATHEMATICAL MODELS

A wide class of homogeneous particles (so-called star-shaped domains) can be represented by

$$\rho_c(r) = \begin{cases} 1 & 0 \leq r \leq F(\omega) \\ 0 & \text{elsewhere} \end{cases} \quad (21)$$

where ω is a unit vector defining the orientation. The boundary $F(\omega)$ can be expanded into a series of spherical harmonics $Y_{lm}(\omega)$:

$$F(\omega) = \sum_{l=0}^{\infty} \sum_{m=-l}^l f_{lm} Y_{lm}(\omega) \quad (22)$$

where the f_{lm} are the unknown structure parameters. The corresponding scattering function $I(h)$ can be expanded into a power series

$$I(h) = \sum_{n=0}^{\infty} a_n \cdot h^{2n} = 4\pi \sum_{n=0}^{\infty} \frac{(-1)^n}{(2n+1)!} \left[\int_0^{\infty} p(r) \cdot r^{2n} \cdot dr \right] \cdot h^{2n} \quad (23)$$

There exists an analytical relationship between the coefficients a_n and f_{lm} (Stuhrmann *et al.*, 1977), but there is no direct way for the calculation of the f_{lm} from the set of a_n , i.e. the expansion coefficients f_{lm} must still be estimated by an iterative trial and error procedure and the advantage of the possibility of an exact analytical description cannot be used for a direct calculation of the structure. The coefficients a_n vary over many orders of magnitude and their accuracy decreases with increasing n . The higher moments of the $p(r)$ -function (Eqn 23) depend highly on the outer part of this function, especially on the maximum distance D . On the other hand, one has to deal with a rapidly increasing number of unknowns f_{lm} with increasing n , since $l \leq n$ and $-l < m < l$.

The maximum number of model parameters N can be estimated roughly from the range of registration. But one has to be very careful, because it is possible to construct N parameter models which cannot be resolved. If we take, for example, a spherical vesicle with a three step electron density profile we have 6 parameters, but the width of the steps could be much smaller than the resolution given by Eqn (27a) in Chapter 4. On the other hand, we may have chosen a model that cannot fit the data with N parameters, for example, if we use spherical harmonics for the representation of a long cylinder.

Anyhow we must bear it in mind that we cannot determine models with many more parameters than N . In such cases we must have additional information about the subject under investigation.

VII. Conclusion

Summarizing Chapters 4 and 5 one can say that X-ray small angle scattering is a matured technique for the investigation of non-periodic scattering media like macromolecules in solution or inhomogeneities in a solid matrix. The mathematical corrections and transformations necessary for the evaluation and interpretation of experimental data can be performed with efficient computer programs existing as well for standard applications as for special problems. Therefore, there exist no basic problems avoiding the evaluation of scattering data. The collimation effects can be eliminated and the necessary transformations can be performed with sufficient accuracy in spite of the restricted range of registration and the statistical errors.

Some integral parameters like the radius of gyration R , the molecular weight M_r , the volume V and so on can be computed directly in a straightforward manner from the experimental data. However, the loss of information caused by the spatial average do not allow a direct and unique determination of the structure of the substance under investigation but it is possible to make a rough classification and to distinguish between globular, cylindrical and lamellar particles. This discrimination could be improved by an orientation of the particles in solution. The theoretical fundamentals for small angle scattering from solutions of flow-oriented colloidal particles have been published by Sjöberg (1980). The research activities are going on in the direction of experimental applications. Such experiments could bring a considerable progress and would be a basis for a comparison and combination of X-ray small angle scattering and quasi-elastic light scattering.

In the case of inhomogeneous particles it is possible to calculate the electron density distribution under the assumption of special symmetries. This would not be possible for asymmetrical objects. The information content about such systems can be increased considerably by the contrast variation method (see Chapter 6). The contrast can be varied much more for neutrons than for X-rays.

The situation is the same for triangulation measurements. With such experiments one tries to determine the mutual distance between regions of high scattering cross-section (i.e. high contrast). This technique has been developed for X-ray small angle scattering by Kratky and Worthmann (1947) and by Hoppe (1972, 1973). The synthesis of special heavy-atom markers allowed an application to biological macromolecules (Vainshtein *et al.*, 1980), but the method was applied with great success only in the field of neutron small angle scattering (Engelman *et al.*, 1975; Engelman and Moore, 1975; Stöckel *et al.*, 1977). The next step after the rough classification of the experimental data is the refinement of models. The models are designed taking into account additional *a priori* information about the system. The corresponding distance distribution functions and scattering functions are compared with the experimental data and the fit is

optimized by variation of the free model parameters. There exist elaborated general computer routines for the computation of model functions. The fitting procedure can be rationalized by a standard least squares technique.

Models which do not coincide with the experiment must be excluded, agreement of model functions with experimental data qualifies the model as a possible structure, but one has to bear it in mind that there might exist other possible structures if they cannot be excluded by additional information.

References

- Engelman, D. M. and Moore, P. B. (1975). *Ann. Rev. Biophys. Bioeng.* **4**, 219–241.
Engelman, D. M., Moore, P. B. and Schoenborn, B. P. (1975). *Proc. Nat. Acad. Sci., U.S.A.* **72**, 3888–3892.
Glatter, O. (1972). *Acta Phys. Austriaca* **36**, 307–315.
Glatter, O. (1979). *J. Appl. Cryst.* **12**, 166–175.
Glatter, O. (1980). *Acta Phys. Austriaca* **52**, 243–256.
Guinier, A. and Fournet, G. (1955). "Small Angle Scattering of X-Rays". Wiley, New York.
Hoppe, W. (1972). *Isr. J. Chem.* **10**, 321–333.
Hoppe, W. (1973). *J. Mol. Biol.* **78**, 581–585.
Kratky, O. and Porod, G. (1956). *Z. Phys. Chem.* **7**, 236–241.
Kratky, O. and Worthmann, W. (1947). *Monatsh. Chem.* **76**, 263–281.
Meisenberger, O., Pilz, I. and Heumann, H. (1980a). *FEBS Lett.* **112**, 39–41.
Meisenberger, O., Heumann, H. and Pilz, I. (1980b). *FEBS Lett.* **122**, 117–120.
Mittelbach, P. (1964). *Acta Phys. Austriaca* **19**, 53–102.
Porod, G. (1948). *Acta Phys. Austriaca* **2**, 255–292.
Porod, G. (1972). *Mh. Chem.* **103**, 395–405.
Sjöberg, B. (1978). *J. Appl. Cryst.* **11**, 73–79.
Sjöberg, B. (1980). *J. Appl. Cryst.* **13**, 154–162.
Stöckel, P. et al. (1977). Presented at the 4th International Conference on "Small Angle Scattering". Gatlinberg, Tenn.
Stöckel, P., May, R., Strell, I., Cejka, Z., Hoppe, W., Heumann, H., Zillig, W., Crespi, H., Katz, Z. Z. and Ibel, K. (1979). *J. Appl. Cryst.* **12**, 176–185.
Stuhrmann, H. B., Koch, M. H. J., Parfait, J., Haas, J., Ibel, K. and Crichton, R. R. (1977). *Proc. Nat. Acad. Sci., USA* **74**, 2316–2320.
Vainshtein, B. K., Feigin, L. A., Lvov, Yu. M., Gvozdev, R. I., Marakushev, S. A. and Likhtenshtein, G. I. (1980). *FEBS Lett.* **116**, 107–110.
Weik, D. (1974). *Biophys. J.* **14**, 233–235.

6

Contrast Variation

H. B. STUHRMANN

EMBL bei DESY, Hamburg, W. Germany

I.	Introduction	197
II.	The scattering density	198
III.	The multipole expansion	200
	A. Spherical and isometric structures	202
	B. The shape of compact macromolecules	203
IV.	Contrast variation	204
	A. Zero angle scattering	208
	B. The radius of gyration	209
	C. Isomorphous replacement methods	210
	References	213

I. Introduction

Any elastic scattering process can in principle be used for structure determination of the target. This is also true if the molecules which give rise to the scattering pattern are randomly oriented. The well known Debye equation

$$I(h) \simeq \sum_{i=0}^N \sum_{j=0}^N f_i f_j \frac{\sin h|\mathbf{r}_i - \mathbf{r}_j|}{h|\mathbf{r}_i - \mathbf{r}_j|} \quad (1)$$

relates a molecule characterized by N atoms with the form factor f located at \mathbf{r}_i to the scattering $I(h)$. This equation has originally been derived to explain X-ray scattering by gas molecules. It is the starting point of any analysis of gas-like systems.

Thermodynamics emphasize the close relationship between the properties of gases and dilute solutions (H. Eisenberg, 1968). As $I(0)$ is proportional to the square of the number of atoms in a molecule it is not surprising that the

scattering pattern of macromolecules relatively early attracted the attention of X-ray diffractionists. Macromolecules consist of thousands of atoms. We want to turn our attention to that class of macromolecules which have a rigid structure and it is also assumed that the solution contains only one kind of molecules. Such a solution could be prepared by dissolving a protein crystal.

It is true that crystallizing proteins have been objects of research in small angle scattering. However, there is a wide class of biomolecules which share the purity of dissolved crystals but which do not (yet) crystallize. These are the structures of increased interest in small angle scattering of solutions. As there is high biochemical evidence that a purified active protein consists of equal molecules the question for structure determination can be justified. However, this raises the next question: what can we expect from small angle scattering? The amount of information which can be obtained from small angle scattering has been estimated by Luzzati (1979). It appears that a small angle curve might yield about 20 to 30 parameters of the macromolecular structure.

This very encouraging finding opens the next question. Which of the thousands of pieces of the macromolecular structure should we determine as we dispose of only 20 to 30 from our small angle experiment? It is at this point that the ways of small angle scientists become divergent. Depending on the preference for certain classes of macromolecules the analysis will assume different forms. There are integrals of the weighted small angle scattering function and its transform which have a simple geometrical meaning, like molecular mass, radius of gyration, volume, specific surface, mean curvature of the surface. The latter ones are related to a specific model, the molecular shape.

The fact that shape determination is a very attractive way of analysing small angle scattering reflects several typical assumptions: the reference to an atomic structure as it has been assumed in Eqn (1) is abandoned. In addition, any intra-molecular structure is either ignored or eliminated by some rough estimations (i.e. by the assumption of the asymptotic h^{-4} dependence of $I(h)$ at large h). As long as the resolution is not better than a few diameters of the solvent molecules (5–10 Å) the model of smooth macromolecular boundaries can be made plausible (Ninio *et al.*, 1972; Fedorov *et al.*, 1972).

II. The Scattering Density

It is clear that small angle scattering is a method which in the best case can determine a molecular structure at low resolution. It is therefore practical to replace the atomic model by a function which describes the density of the atomic form factors in a volume element. In the case of X-ray scattering, the form factor is proportional to the number of electrons of the atom. Therefore the electron density is a convenient measure of the potential encountered by

a crossing X-ray photon or neutron. The form factors do not depend in a regular way on the atomic number in the case of neutron scattering. The coherent scattering lengths b vary as a function of the atomic number isotope and nuclear spin state in an apparently irregular way, as neutrons are scattered by nuclei. The scattering length of hydrogen is negative ($-0,372 \cdot 10^{-12}$ cm) and that of its heavier isotope deuterium is strongly positive ($+0,67 \cdot 10^{-12}$ cm). Carbon ($b = 0,66 \cdot 10^{-12}$ cm) and oxygen ($b = 0,58 \cdot 10^{-12}$ cm) have similar values, whereas b of nitrogen ($=0,95 \cdot 10^{-12}$ cm) is one of the highest known in thermal neutron scattering. For comparison we mention that the scattering length of one electron in X-ray scattering is $0,28 \cdot 10^{-12}$ cm. The scattering lengths of other atoms are just multiples of this number. The scattering lengths in neutron scattering are similar to those of the first row of the periodic table in the case of X-ray scattering (Bacon, 1975).

With these numbers in mind we can calculate the scattering density of most of the biomolecules. By definition the scattering density is given as the ratio between the sum of coherent scattering lengths of nuclei (or atoms) divided by the volume occupied by these atoms.

$$\rho = \frac{\sum b_i}{V} = \frac{[\text{cm}]}{[\text{cm}^{-3}]} = [\text{cm}^{-2}] \quad (2)$$

For water we obtain in the case of X-ray scattering

$$\rho = \frac{6 \cdot 10^{23}}{18} (2 + 8) 0,28 \cdot 10^{-12} = 9,3 \cdot 10^{10} \text{ cm}^{-2}$$

In the case of neutron scattering the calculation is similar: The scattering density of H₂O is:

$$\rho = \frac{6 \cdot 10^{23}}{18} [2(-0,37) + 0,58] \cdot 10^{12} = -0,56 \cdot 10^{10} \text{ cm}^{-2}$$

The scattering density of D₂O is:

$$\rho = \frac{6 \cdot 10^{23}}{20} \cdot 1,1 [2 \cdot 0,66 + 0,58] \cdot 10^{-12} = +6,3 \cdot 10^{10} \text{ cm}^{-2}$$

In a similar way scattering densities of more complicated molecules can be calculated. It turns out that the neutron scattering density of biological material (proteins, DNA, RNA, lipids) is in the boundaries of the scattering density of light and heavy water (H. Stuhrmann, 1974). The relative scattering densities with respect to water are similar with X-rays.

III. The Multipole Expansion

The evaluation of certain structure parameters (M_r, R, V etc.) from $I(h)$ is a first approach. A more systematic structure analysis will start from a Fourier series where the consideration of a finite number of Fourier coefficients defines the resolution. For a single molecule model the expansion of the excess scattering density $\rho(r)$ with respect to the solvent as a series of spherical harmonics Y_{lm} appears to be natural (Stuhrmann, 1970a-c).

$$\rho(r) = \sum_{l=0}^L \sum_{m=-l}^l \rho_{lm}(r) Y_{lm}(\omega) \quad (3)$$

$r = (X, Y, Z) \equiv (r, \omega)$; L is an arbitrary number depending on the required precision. ω is a unit vector and r is the distance from the origin along the direction of ω . ω represents the polar and the azimuthal angle. The angular symmetry of the Y_{lm} is related to those of the multipoles: $l = 0$ (monopole), $l = 1$ (dipole), $l = 2$ (quadrupole), etc. There are $2m + 1$ Y_{lm} for each l which correspond to well known wave functions in spectroscopy: $l = 0$ (s), $l = 1$ (p_x, p_y and p_z), $l = 2$ ($5d$ functions). However, the dimensions of the radial functions $\rho_{lm}(r)$ are much larger and they are calculated as projections of $\rho(r)$ onto the spherical harmonics

$$\rho_{lm}(r) = \int \rho(r) Y_{lm}^*(\omega) d\omega \quad (3a)$$

The Fourier transform of $\rho(r)$ is developed as a series of spherical harmonics as well:

$$A(h) = \sum_{l=0}^L \sum_{m=-l}^l A_{lm}(h) Y_{lm}(\Omega) \quad (4)$$

$h = (h, \Omega)$, h is the momentum transfer and Ω is a unit vector in the reciprocal space. The relation between the function $A_{lm}(h)$ and $\rho_{lm}(r)$ is given by the Hankel transform with spherical Bessel functions j_l as a kernel.

$$A_{lm}(h) = \left(\frac{2}{\pi}\right)^{1/2} i^l \int_{r=0}^{\infty} \rho_{lm}(r) j_l(hr) r^2 dr \quad (5)$$

The diffraction pattern of randomly oriented particles must be a mathematical quantity which is independent of the actual orientation. From a vector in three-dimensional space we know that its length is conserved on rotation (i.e. $r^2 = x^2 + y^2 + z^2$). Equation 4 describes $A(h)$ in a space with more than 3 coordinates. Again, it is the scalar product which turns out to be the measurable quantity of small angle scattering (Stuhrmann, 1970a):

$$\begin{aligned} I(h) &= 2\pi^2 [A_{00}^2(h) + A_{10}^2(h) + \dots] \\ &= 2\pi^2 \sum_{l=0}^L \sum_{m=-l}^l |A_{lm}(h)|^2 \equiv \langle A|A \rangle \end{aligned} \quad (6)$$

Equation (6) is equivalent to Eqn (1).

However, there are marked differences in the appearance of the Debye equation of SAS and its multipole expansion. Equation (1) consists of $N^2 - N$ distinct interference terms of weighted sine waves, originating from N volume elements of integration of $\rho(r)$. There are no distinct interference terms in Eqn (6). Each partial structure $\rho_{lm}(r) Y_{lm}(\omega)$ produces its own small angle scattering curve $|A_{lm}(h)|^2$. It appears that the analysis of $I(h)$ cannot be unique, as different sums of $|A_{lm}(h)|^2$ yielding the same $I(h)$ reflect different structures $\rho(r)$.

The analysis of $I(h)$ in terms of multipole contributions to SAS is not quite arbitrary. As $A_{lm}(h)$ starts with h^l only the monopole ($l = 0$) of the structure will give rise to SAS of zero angle. The scattered intensity at zero angle is proportional to the square of the total excess scattering length of the particle.

$$\begin{aligned} I(0) &\approx 2\pi^2 A_{00}^2(0) = 4\pi \left[\int \rho_{00}(r) r^2 dr \right]^2 \\ &= 4\pi \left[\int_r \int_{\omega} \rho(r, \omega) Y_{00}(\omega) r^2 dr d\omega \right]^2 = \left[\int_V \rho(r) d^3r \right]^2 \end{aligned} \quad (7)$$

Equation (7) is the basis of molecular weight determination.

At very small angles $I(h)$ is described by a parabola:

$$I(h) \approx 1 - \frac{1}{3} R^2 h^2 \pm \dots \quad (8)$$

After appropriate choice of the origin the first moment of the dipole terms can be eliminated and the radius of gyration R is simply given by the second moment of the monopole $\rho_{00}(r)$:

$$R^2 = \frac{\int \rho(r) r^2 d^3r}{\int \rho(r) d^3r} = \frac{\int \rho_{00}(r) r^4 dr}{\int \rho_{00}(r) r^2 dr} \quad (9)$$

The coefficients associated with higher powers of h consist in general of more than one multipole. Unless a certain model is preferred, there is no way to attribute definite weights to various multipoles.

A. Spherical and Isometric Structures

The easiest way to deal with the multipole expansion of small angle scattering (Eqn 6) is to assume a spherical (monopole) structure:

$$\begin{aligned} I(h) &= 2\pi^2 A_{00}^2(h) \\ &= 4\pi \left[\int_{r=0}^{\infty} \rho_{00}(r) \frac{\sin hr}{hr} r^2 dr \right]^2 \end{aligned} \quad (10)$$

Usually $I(h)$ in this case exhibits a number of minima where $I(h)$ is close to zero. Other methods (e.g. electron microscopy) will be used to confirm the spherical surface of the particle. Once the sequence of signs of the extremes of $A_{00}(h)$ is established, the sine transformation of $A_{00}(h)$ yields the radial density distribution $\rho_{00}(r)$ of the sphere. This is a most useful result from small angle scattering which cannot be obtained by other methods.

For isometric structures (viruses, lipoproteins, chromatin monomers) it is necessary to add higher multipoles ($l \geq 5$) to the predominant monopole term (Finch and Holmes, 1967)

$$\rho(r) = \sum_{l=0}^L \rho_{l0}(r) \left\{ \sum_{m=-l}^l a_{lm} Y_{lm}(\omega) \right\} \equiv \sum_{l=0}^L \rho_{l0} H_l(\omega) \quad (11)$$

The coefficients a_{lm} determine the symmetry of the particle: their calculation is described by Cohan (1958) for the icosahedral case. As the decoration is often confined to a shell, the radial functions associated with spherical harmonics of higher order can be approximated by

$$\rho(r) = \frac{1}{\sqrt{4\pi}} \rho_{00}(r) + \sum_{l=1}^L \rho_l \delta(r - R) H_l(\omega) \quad (12)$$

The scattered intensity of this structure is

$$I(h) = 2\pi^2 \{A_{00}^2(h)\} + 4\pi \sum_{l=1}^L \rho_l^2 R^4 j_l^2(hr) \quad (13)$$

which just gives the contribution of the l th spherical Bessel function. This is often the case with spherical viruses, where the only important non-spherically symmetric contrast at low resolution originates from the projecting tips of protein subunits, all at essentially the same radius. For the evaluation of $\rho(r)$ from the transform of $I(h)$, Chapter 4 should be consulted.

As pointed out by Klug (unpublished work cited by Finch and Holmes, 1967), the icosahedral symmetry of isometric viruses leads to a useful separation of zero and higher order harmonics in their scattering patterns. Symmetry leads

to "selection rules" for terms in the spherical harmonic expansion of a density distribution or its corresponding Fourier transform. For the icosahedral case, the permitted orders are given by $l = 6p + 10q + 15r$ ($p, q, r = 0, 1, 2, \dots$) (Laporte, 1948; Cohan, 1958; Finch and Holmes, 1967; Jack and Harrison, 1975). The first non-zero term is therefore $l = 6$. Highly subdivided icosahedral surface lattices often have very weak low orders, so that the first strong, non-spherically symmetric term in the expression may, for instance, be $l = 18$ or 20 . This is the case with tomato bushy stunt virus (TBSV), where the projecting tips of protein subunits, clustered at twofold and local twofold positions, provide the major source of low resolution contrast, besides the monopole term (S.C. Harrison, 1969; Jack and Harrison, 1975).

The separation of the monopole term from the higher harmonics starts from the observation that non-zero order terms become significant at spacings which correspond to fractions of the diameter of the whole molecule. Often, however, the zero order term obviously continues to dominate, and higher order terms can be regarded as background. In PM2 phages, the bilayer so dominates the density fluctuations that $A_{00}^2(h)$ is the only clearly visible part of the scattered intensity out to 25 Å (Harrison *et al.*, 1971).

B. The Shape of Compact Macromolecules

Particles of uniform density offer a welcome constraint of the general structure $\rho(r)$, as the multipoles $\rho_{lm}(r)$ are no longer independent. Since at high contrast the contribution of the internal structure of the particle to SAS becomes negligibly small, the shape model is quite realistic.

Let us describe the outer surface of a compact protein molecule by a unique function $F(\omega)$ (Stuhrmann, 1970b, c, 1975; Stuhrmann *et al.*, 1977)

$$\begin{aligned} \rho(r) &= 1 \quad \text{if } 0 < r < F(\omega) \\ &= 0 \quad \text{elsewhere} \end{aligned} \quad (14)$$

The introduction of this model into Eqn (5) results in

$$A_{lm}(h) = \left(\frac{2}{\pi} \right)^{1/2} i^l \int_{r=0}^{F(\omega)} \int_{\omega} Y_{lm}^*(\omega) j_l(hr) r^2 dr d\omega \quad (15)$$

The relationships between the A_{lm} with different l correspond to those of the Bessel functions. The development of $F(\omega)$ as a series of spherical harmonics and $j_l(hr)$ as a power series is chosen in order to facilitate the integration of Eqn (15). With

$$j_l(hr) = \sum_{p=0}^{\infty} \frac{(-1)^p (hr)^{l+2p}}{2^p p! [2(l+p)+1]!!} \equiv d_{lp}(hr)^{l+2p}$$

integration yields

$$A_{lm}(h) = \left(\frac{2}{\pi}\right)^{1/2} i^l \sum_{p=0}^{\infty} \frac{d_{lp}}{l+2p+3} f_{lm}^{(l+2p+3)} h^{l+2p} \quad (16)$$

On introduction of $A_{lm}(h)$ from Eqn (16) into Eqn (6), the scattered intensity results in a power series of h^2 :

$$I(h) = \sum c_n h^{2n} \quad (17)$$

where the coefficients c_n depend in a non-linear way on the parameters f_{lm} of the structure (Stuhrmann, 1970b, 1970c; Stuhrmann *et al.*, 1977):

$$\begin{aligned} c_n &= c_n \{f_{lm}\} \quad n = 0, 1, 2, 3 \\ l &= 0, 1, 2, 3, \dots \quad -l < m < l \end{aligned} \quad (18)$$

The analysis of small angle scattering data in terms of shape models has been applied mostly to globular proteins. This class of macromolecules does not display any inhomogeneous density distribution at low resolution, thus justifying a sharply contrasted black and white picture as a model for protein molecules in solution. The coincidence of experimental and calculated scattering curves proves that the suggested model is not wrong. In order to prove that it is probably the right one, a thorough search for other possible models has to be made. The investigation of the uniqueness can be made easier when expansions of the shape as a series of functions (e.g. spherical harmonics) are chosen because the resolution is well controlled by the number of coefficients taken into account (Stuhrmann *et al.*, 1977). The evaluation of f_{lm} from c_n is rather easily performed in those cases where the structure in question does not differ too much from a sphere. Long rods and extended sheet structures are less amenable to this kind of analysis.

IV. Contrast Variation

Morphological studies of globular macromolecules by small angle scattering start from the assumption that the scattering pattern originates from macromolecules, the boundaries of which enclose regions of constant scattering density. This may be a good approximation especially at low resolution if the mean scattering density of the solute differs very much from that of the solvent. The scattering density of the macromolecule then displays a sharp "black and white" picture. The relevant parameter which defines the quality of the picture is the contrast $\bar{\rho}$ which is given as the difference between the mean scattering density of the dissolved particle and the solvent:

$$\bar{\rho} = \bar{\rho}_{\text{solute}} - \bar{\rho}_{\text{solvent}} \quad (19)$$

Equation (15) also holds for each volume element: the excess scattering density of the solute therefore is

$$\rho(r) = \rho(r)_{\text{solute}} - \rho(r)_{\text{solvent}} \equiv \rho(r)_{\text{solute}} - \bar{\rho}_{\text{solvent}} \quad (20)$$

There are two states of $\rho(r)$ which are very different. At very high contrast, precisely speaking at infinitely high contrast, the inner structure of globular particles is no longer contributing to small angle scattering. The other state concerns the appearance of $\rho(r)$ at vanishing contrast. The fluctuations of the intramolecular density distribution around the mean scattering density of the solute are then rendered visible. It is therefore an appealing idea to define (Stuhrmann and Kirste, 1965)

$$\rho(r) = \bar{\rho} \rho_c(r) + \rho_s(r) \quad (21)$$

where $\rho_c(r)$ and $\rho_s(r)$ represent the molecule at infinite and zero contrast respectively.

$\rho_c(r)$ is the space excluded to solvent molecules. In the case of neutron scattering of proteins in H_2O/D_2O mixtures the influence of dissociating protons has to be taken into account. As the H/D exchange ratio of the dissociating hydrogens of a protein depends on the H_2O/D_2O ratio of the solvent, effects of H/D exchange will modify $\rho_c(r)$. If one starts with $\rho_s(r)$ having a particular H/D composition due to the H_2O/D_2O composition of the solvent, then the increase in $\rho(r)$ will be less than a given decrease in solvent density in those parts of the solute molecule that contain exchangeable hydrogens. This effect is taken into account by $\rho_c(r) < 1$. If the density of exchangeable protons of the solute equals that in the solvent, $\rho_c(r)$ will be zero. $\rho_c(r)$ remains unity in those volume elements not occupied by water and exchangeable hydrogens.

By Fourier transformation, the amplitude A has the same form as $\rho(r)$

$$A(h) = \bar{\rho} A_c(h) + A_s(h) \quad (22)$$

Using Eqn (6) the contrast dependence of small angle scattering follows a quadratic polynomial in $\bar{\rho}$:

$$\begin{aligned} I \sim \langle A | A \rangle &= \langle \bar{\rho} A_c + A_s | \bar{\rho} A_c + A_s \rangle \\ &= \bar{\rho}^2 \langle A_c | A_c \rangle + \bar{\rho} (\langle A_c | A_s \rangle + \langle A_s | A_c \rangle) + \langle A_s | A_s \rangle \\ &\equiv \bar{\rho}^2 I_c(h) + \bar{\rho} I_{cs}(h) + I_s(h) \end{aligned} \quad (23)$$

In Eqn (23) a real contrast has been assumed. There are some nuclei (e.g. Cd^{113} , Gd^{157} , Sm^{149}) which undergo resonant scattering at thermal energies of neutrons. Due to an additional phase shift during the scattering process, the scattering length b is no longer a real number but gets its adequate description by a complex b

$$b = b_0 + b' + ib''$$

where b' and b'' are the real and imaginary parts varying strongly with the wavelength in the resonance region and $\bar{\rho}_0$ is encountered far away from the resonance. With X-ray scattering this phenomenon is quite common to all atoms. Near their K , L and M absorption edges the atomic form factor will show an anomalous dispersion which is due to electron transitions of the K , L or M shell of the atoms. The magnitude of the corresponding f' and f'' are similar to those of b' and b'' in the case of neutron scattering and amount to 5 to 15 electrons (Phillips *et al.*, 1978).

Assuming a complex scattering density $\bar{\rho}' + i\bar{\rho}''$ in a region $\rho_a(r)$, Eqn (21) is extended:

$$\rho(r) = [\bar{\rho}_0 \rho_c(r) + \rho_s(r)] + (\bar{\rho}' + i\bar{\rho}'') \cdot \rho_a(r) \quad (21a)$$

Small angle scattering as described in Eqn (23) will change into a slightly different form.

$$\begin{aligned} I(h) &= (\bar{\rho}'^2 + \bar{\rho}''^2) I_a(h) + \bar{\rho}' [\bar{\rho}_0 I_{ac}(h) + I_{as}(h)] \\ &\quad + [\bar{\rho}_0^2 I_c(h) + \bar{\rho} I_{cs}(h) + I_s(h)] \end{aligned} \quad (23a)$$

$I_a(h)$ is the scattering function of anomalous scatterers. $I_{ac}(h)$ and $I_{as}(h)$ are cross terms resulting from the convolution of $\rho_a(r)$ with $\rho_c(r)$ and $\rho_s(r)$ respectively.

Equation (23a) is quite general. For instance, it may be used when the configuration of heavy atoms in a protein is going to be studied.

If anomalous scatterers are distributed homogeneously over the whole excluded volume $\rho_c(r)$ or in the solvent, then $\rho_a(r)$ becomes equal to $\rho_c(r)$. The excess scattering density then is described by

$$\rho(r) = (\bar{\rho}_0 + \bar{\rho}' + i\bar{\rho}'') \rho_c(r) + \rho_s(r) \quad (21b)$$

and Eqn (23a) is reduced to

$$I(h) = [(\bar{\rho}_0 + \bar{\rho}^{-1})^2 + \bar{\rho}''^2] I_c(h) + (\bar{\rho}_0 + \bar{\rho}') I_{cs}(h) + I_s(h) \quad (23b)$$

It appears that the real part of the structure factor is most interesting in the complex contrast variation (CCV) method, as there is no linear dependence of $I_{ac}(h)$ on the imaginary part of $\bar{\rho}$. The advantage of the CCV method compared to other methods of contrast variation may be considerable as no chemical changes of the solution are involved. Very often the mean density of proteins can be matched by addition of sugar ($\bar{\rho}_0 = 0$). Then, for instance, the contrast in a sugar solution containing RbBr could easily be varied near the K absorption edges of rubidium ($\lambda_K = 0.815 \text{ \AA}$) and bromine ($\lambda_K = 0.920 \text{ \AA}$). Synchrotron radiation is most convenient for the selection of arbitrary wavelengths.

From Eqn (23) it appears that the measurement of $I(h)$ at three different contrasts (i.e. scattering densities of the solvent) is sufficient for the determination

of the basic scattering function $I_c(h)$, $I_{cs}(h)$ and $I_s(h)$. In practice about ten different solvent densities are chosen in order to evaluate the basic scattering functions.

$I_c(h)$ is the shape scattering function which can be used for shape determination as described before. $I_s(h)$ can be measured directly at vanishing contrast. Appropriate solvent mixtures can be very often achieved. However, $\text{H}_2\text{O}/\text{D}_2\text{O}$ mixtures are most convenient for matching the density of the particle (Stuhrmann *et al.*, 1975; Stuhrmann, 1979).

$I_{cs}(h)$ is the transform of an averaged convolution square of the internal structure $\rho_s(r)$ and the shape $\rho_c(r)$. Contrary to $I_c(h)$ and $I_s(h)$ which are real scattering functions, the mixed term $I_{cs}(h)$ can assume positive and negative values.

Contrast variation is a low resolution method. As the shape factor $I_c(h)$ decreases with h^{-4} at greater angles its influence is usually no longer measurable at $h \cdot D > 30$. $I_s(h)$ is dominant in the wide angle range. The method of contrast variation has been developed independently in protein crystallography (Bragg and Perutz, 1952) and in small angle scattering of protein solutions (Stuhrmann and Kirste, 1965).

It has been of transient interest in protein crystallography where it has been replaced by isomorphous heavy atom replacement. The contrary was the case for small angle scattering, where the low resolution quality of this method did not present an additional drawback at all. With the availability of powerful neutron sources contrast variation has now become a still flourishing technique in neutron small angle scattering (H. Stuhrmann and A. Miller, 1978).

There are a few relationships between the basic scattering functions which may be useful for both checking the consistence of the data and establishing a symmetry of the structure $\rho(r)$. From Eqn (23) the following inequality can be derived:

$$|I_{cs}(h)| \leq 2[I_c(h)I_s(h)]^{1/2} \quad (24)$$

For spherical particles, that is if $\rho(r) = \rho_{00}(r) (4\pi)^{-1/2}$, the inequality (24) becomes an equation.

$$I(h) \approx A_{00}^2(h) = [\bar{\rho} A_{00}^c(h) + A_{00}^s(h)]^2 \quad (25)$$

The linear dependence of the square root of $I(h)$ on $\bar{\rho}$ is a necessary condition for the absence of higher multipoles with $l \neq 0$ of $\rho(r)$. The choice of sign is relatively easy if data from contrast variation are available. In general $\rho_c(r)$ will be positive and therefore $A_{00}^c(0)$ must be positive too. If $I_{cs}(h)$ changes its sign at h_0 , either $A_{00}^c(h)$ or $A_{00}^s(h)$ will change its sign. At least one of the functions $I_c(h)$ and $I_s(h)$ should have a minimum at h_0 . As long as the minima of $I_c(h)$ and $I_s(h)$ do not coincide at h_0 , determination of the sign $A_{00}^c(h)$ and $A_{00}^s(h)$ is quite unambiguous. This has been used in the study of lipoproteins and spherical viruses (Stuhrmann *et al.*, 1975).

In a similar way equations for the contrast dependence of more than one multipole can be written. The redundancy of the data will be lost, which makes any conclusions less reliable. For non-spherical particles the analysis is very often restricted to the contrast dependence of zero angle scattering and of the radius of gyration.

A. Zero Angle Scattering

Since at $h = 0$ only the monopole term ($l = 0$) of $\rho(r)$ enters into $I(h)$ the square of zero angle scattering is a linear function of the scattering density of the solvent:

$$[I(0)]^{1/2} \approx A(0) = \bar{\rho} A_c(0) = \bar{\rho} \int \rho_c(r) d^3r = \bar{\rho} V_c \quad (25a)$$

Strictly speaking, this is only true if the scattering amplitudes of the atoms are real numbers, since

$$A(0) = \sum_i b_i$$

If nuclei or atoms with complex scattering lengths (anomalous dispersion) are present in the solute or the solvent, then Eqn (20) contains complex numbers. The square root $I(0)$ is no longer a linear function of the solvent density

$$[I(0)]^{1/2} \approx A(0) = [(\bar{\rho}_0 + \bar{\rho}')^2 + \bar{\rho}''^2]^{1/2} A_c(0)$$

In the following considerations the complex parts of the contrast are dropped. If $\rho_c(r) = 1$ inside the protein molecule, then V_c equals to the real volume V . As mentioned above, the contrast variation in neutron scattering is achieved in a most elegant way by isotopic replacement of the solvent. In the case of aqueous solutions, H_2O/D_2O mixtures cover a wide range of scattering densities from $-0.56 \cdot 10^{10} \text{ cm}^{-2}$ with H_2O to $6.35 \cdot 10^{10} \text{ cm}^{-2}$ with D_2O . For both neutron and X-ray scattering the scattering density can be changed by chemical replacement of the solvent (addition of salts, sugars etc. to H_2O or H_2O/D_2O mixtures). This in general will have a different influence on $\rho_c(r)$ and can be used to determine the inner solvation of the protein molecule. A very recent result from small angle scattering of ferritin with X-ray synchrotron radiation showed that the change of the structure factor of heavy atoms (iron) with the wavelength can be used as well for contrast variation and in the sense of isomorphous replacement methods (Stuhrmann, 1980).

A plot of the square root of the extrapolated zero angle scattering versus the solvent results in a straight line, the intercept of which with the abscissa provides the scattering density of the solute. This is also $I_s(0)$. If the solution contains macromolecules of different density then $I(0)$ will reach a positive minimum value at a solvent composition with a scattering density equal to the mean

scattering density of the polydisperse solution. From the height of the minimum $I(0)$, the mean square deviation of the scattering density distribution can be estimated (Stuhrmann and Duée, 1975).

B. The Radius of Gyration

Among the parameters of $\rho(r)$ determined from small angle scattering the squared radius of gyration

$$R^2 = \frac{\int \int \rho(r)\rho(r')|r - r'|^2 d^3r d^3r'}{2 \int \int \rho(r)\rho(r') d^3r d^3r'} \quad (26)$$

is most easily accessible (Eqn 8).

Inserting Eqn (21) into the definition of the radius of gyration gives

$$R^2 = R_c^2 + \frac{\alpha}{\bar{\rho}} - \frac{\beta}{\bar{\rho}^2} \quad (27)$$

The constants independent of the contrast are:

$$\alpha = \frac{1}{V_c} \int \rho_s(r) r^2 d^3r$$

$$\beta = \frac{1}{V_c^2} \int \int \rho_s(r)\rho_s(r') r \cdot r' d^3r d^3r'$$

$$R_c^2 = \frac{1}{V_c} \int \rho_c(r) r^2 d^3r$$

In a plot of R^2 versus $1/\bar{\rho}$ the intersection with the ordinate gives R_c^2 , the square of the radius of gyration of the molecular shape and from the tangent of the curve in $1/\bar{\rho} = 0$ the second moment α of the spherical average of the internal structure can be derived. If $\rho(r)$ is approximated by a core surrounded by a spherical shell, then it can be shown that α is positive if the shell has a higher density than the core (e.g. proteins and more pronounced with lipoproteins and chromatin) and negative if the core has a higher density (e.g. in ferritin, ribosomes). On the other hand, β is always positive; it describes the displacement of the centre of mass as a function of the contrast (Stuhrmann and Miller, 1978).

For complex contrasts (compare Eqn 23a) Eqn 27 will assume a slightly different form:

$$R^2 = R_c^2 + \frac{(\bar{\rho}_0 + \bar{\rho}')}{(\bar{\rho}_0 + \bar{\rho}')^2 + \bar{\rho}''^2} \cdot \frac{\alpha}{V_c} - \frac{1}{(\bar{\rho}_0 + \bar{\rho}')^2 + \bar{\rho}''^2} \cdot \frac{\beta}{V_c^2} \quad (27a)$$

often $\bar{\rho}_0$ will be large compared to the complex parts $\bar{\rho}'$ and $\bar{\rho}''$. Then Eqn (27a) is reduced to

$$R^2 = R_c^2 + \frac{1}{\bar{\rho}_0 + \bar{\rho}'} \cdot \frac{\alpha}{V_c} - \frac{1}{(\bar{\rho}_0 + \bar{\rho}')^2} \cdot \frac{\beta}{V_c^2} \quad (27b)$$

Recent small angle X-ray scattering experiments of ferritin with synchrotron radiation have shown a marked dependence of the apparent radius of gyration on the real part of the structure factor of iron near the absorption edge ($\lambda_K = 1,734 \text{ \AA}$) (Stuhrmann, 1980) (Fig. 1).

C. Isomorphous Replacement Methods

Contrast variation can be regarded as a special isomorphous replacement. The label is given by the volume function $\rho_c(r)$, an admittedly very big label. A label which is comparable in size to the structure is supposed to resolve $\rho_s(r)$ unsatisfactorily. The inequality of Eqn (24) demonstrates this fact. The advantage of $\rho_c(r)$ as a label is its high scattering intensity $I_c(h)$ which can be measured easily. Heavy atoms as labels on the other hand would resolve the structure much better. Though the role of heavy atom labels in small angle scattering would not be of the same outstanding importance as in protein crystallography, they still provide a net of heavy atom sites which reflect the three-dimensional structure of the particle (Hoppe, 1972).

Heavy atoms have not been tried in small angle scattering until recently when an intramolecular distance was determined using mercury labels (Feigin *et al.*, 1978). Anomalous dispersion effects might give similar results. Experiments of the latter type are presently tried with synchrotron radiation.

With larger structures (e.g. ribosomes) the introduction of more powerful scatterers is important. There are two ways of achieving this. (1) The scattering length of one atom or the number of heavy atoms concentrated around a site is increased. Higher scattering lengths for X-rays are encountered with certain nuclei (e.g. ^{57}Fe at 14.4 KeV has a scattering length which is nearly 20 times larger than that of the 26 electrons of the iron atom). However, this technique has not yet become feasible as the resonance condition reduces very much the probability of such a transition. (Mössbauer *et al.*, 1970). In principle synchrotron radiation can furnish brighter sources of Mössbauer radiation than radioactive sources (Trammell *et al.*, 1978). In practice the increase of the scattering from a label is achieved by increasing its size.

Though this is not impossible with heavy atom complexes in X-ray scattering, the isotopic replacement in neutron scattering still offers the easier way. (2) Deuterated protein subunits in quaternary structures or deuterated proteins

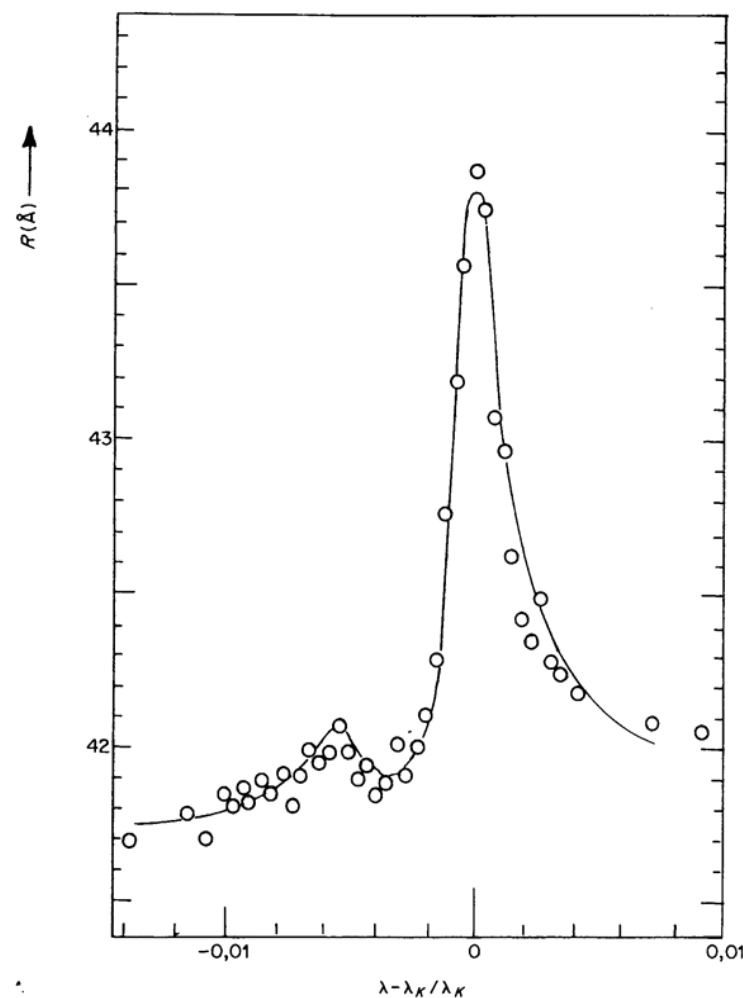


FIG. 1. Dependence of the apparent radius of gyration R of Ferritin on the wavelength. Near the K -absorption edge of iron at the wavelength $\lambda_K = 1,734 \text{ \AA}$, the real part and the imaginary part of atomic form factor of iron change considerably. The variation of R reflects the change of the real part f' of the form factor of iron only. From Eqn (23a) it can be deduced that $R = a + bf'$. The full line is f' as calculated from the imaginary part f'' of iron. f'' is proportional to the absorption coefficient of iron, which has been measured simultaneously with R .

in ribosomes are convenient labels which have become very useful in small angle scattering. These labels are big enough in order to provide a measurable signal in small angle scattering and they are small enough in order to be a useful probe for structure resolution. So far it has been the practice to deuterate two

distinct subunits *A* and *B* in a complex biomolecule, in order to determine the distance *d* between their centres of mass. In order to measure the relevant interference function

$$J_d(h) \sim \frac{\sin hd}{hd} \quad (28)$$

it is necessary to measure four samples which differ in the deuteration of *A* and *B*. Denoting deuteration by the index *D* and normal subunits by the index *H*, $J(h)$ is obtained as a superposition of four scattering functions (Kratky and Worthmann (1947); Hoppe, 1972; Engelman and Moore, 1972)

$$J = [I(A_D, B_D) + I(A_H, B_H)] - [I(A_D, B_H) + I(A_H, B_D)] \quad (29)$$

At low resolution $J(h)$ equals $J_d(h)$. It has, however, to be emphasized that $J(h)$ does not only depend on the distance between the labels, as it has been supposed for $J_d(h)$. $J(h)$ is a two particle scattering function. How this fact enters into the analysis becomes clearer from the consideration of the corresponding distance distribution function.

We assume that the diameters of the subunits are much smaller than their mutual distance. Then the measurable distinct distance distribution function represents the projection of the mass of the subunits onto the connecting line. This idea is still a good guide when the labelled subunits get closer to each other. In order to make full use of the wealth of the interference function $J(h)$, it has to be measured with great accuracy. So far the precision of the neutron scattering experiments allowed the determination of *d* only. In some cases guesses on possible asymmetries of the subunits and their mutual orientations could be made (Langer *et al.*, 1978).

As the biochemical reconstitution methods for the introduction of deuterated probes to a desired site are rapidly improving, it is possible to have a single protonated protein in a deuterated environment. A lower proton content means only small incoherent neutron scattering. Under these conditions small angle scattering of single proteins in a ribosome can be measured and a structure determination of ribosomal proteins *in situ* is at hand (Nierhaus *et al.*, 1978). As ribosomes consist of RNA and proteins, both components have to be deuterated to such a degree that their scattering lengths become equal.

These conditions have to be established by intramolecular contrast variation. In addition, the $\text{H}_2\text{O}/\text{D}_2\text{O}$ mixture (more than 90% D_2O) has to be adjusted to the scattering density of the deuterated ribosomal proteins and RNA. The development of intramolecular contrast variation will contribute to the elucidation of the internal structure of large biomolecules in a way that cannot be achieved by variation of the solvent density only.

References

- Bacon, G. E. (1975). "Neutron Diffraction". Oxford University Press, Oxford.
- Bragg, W. L. and Perutz, M. F. (1952). *Acta Cryst.* **5**, 277–283.
- Cohan, N. V. (1958). *Proc. Cambridge Philos. Soc.* **54**, 28–41.
- Eisenberg, H. and Cohen, G. (1968). *J. Mol. Biol.* **37**, 355–362.
- Engelman, D. M. and Moore, P. B. (1972). *Proc. Nat. Acad. Sci. USA* **72**, 3888–3892.
- Fedorov, B. A., Pfitsyn, O. and Voronin, L. A. (1972). *FEBS Lett.* **28**, 188–190.
- Feigin, L. A., Lvov, Yu. M., Gochar, N. A., Likhtenstein, G. I. and Marakushev, S. A. (1978). *Kristallographia* **23**, 749–755 (in Russian).
- Finch, J. T. and Holmes, K. C. (1967). "Methods in Virology" (K. Maramorosh and H. Koprowski, eds), Vol. 3, pp. 351–474. Academic Press, New York and London.
- Harrison, S. C. (1969). *J. Mol. Biol.* **42**, 457–483.
- Harrison, S. C., Caspar, P. L. D., Camerini-Otero, R. D. and Franklin, R. M. (1971). *Nat. New Biol.* **229**, 197–201.
- Hoppe, W. (1972). *Israel J. Chem.* **10**, 321–333.
- Jack, A. and Harrison, S. C. (1975). *J. Mol. Biol.* **99**, 15–25.
- Kratky, O. and Worthmann, W. (1947). *Monatsh. Chem.* **76**, 263–281.
- Langer, J. A., Engelman, D. M. and Moore, P. B. (1978). *J. Mol. Biol.* **119**, 463.
- Laporte, O. (1948). *Z. Naturforsch.* **3A**, 447–456.
- Luzzati, V. and Tardieu, A. (1979). "Biophysics and Bioengineering". Volume 9 (in press).
- Mössbauer, R. L., Parak, F. and Hoppe, W. (1970). *Ber. Bunsenges. Phys. Chem.* **74**, 1207–1216.
- Nierhaus, K. H., Stuhrmann, H. B. and Miller, A. (1978). "Research Proposal for the Use of Neutron Beams of the ILL-HER".
- Ninio, J., Luzzati, V. and Yaniv, M. (1972). *J. Mol. Biol.* **71**, 217–229.
- Phillips, J. C., Templeton, D. H., Templeton, L. K. and Hodgson, K. O. (1978). *Science* **201**, 257–259.
- Stuhrmann, H. B. (1970a). *Acta Cryst.* **A26**, 297–306.
- Stuhrmann, H. B. (1970b). *Z. phys. Chemie, Frankfurt* **72**, 177–184.
- Stuhrmann, H. B. (1970c). *Z. phys. Chemie, Frankfurt* **72**, 185–198.
- Stuhrmann, H. B. (1974). *Appl. Cryst.* **7**, 173–178.
- Stuhrmann, H. B. (1975). "Brookhaven Symposia in Biology", No. 27, pp. IV3–19.
- Stuhrmann, H. B. and Duée, E. D. (1975). *J. Appl. Cryst.* **8**, 538–542.
- Stuhrmann, H. B. and Kirste, R. G. (1965). *Z. physik. Chemie, Frankfurt* **46**, 247–250.
- Stuhrmann, H. B. (1979). *Chemie un unserer Zeit* **13**, 11–22.
- Stuhrmann, H. B. (1980). *Acta Cryst.* **A36**, 996–1001.
- Stuhrmann, H. B. and Miller, A. (1978). *J. Appl. Cryst.* **11**, 325–345.
- Stuhrmann, H. B., Tardieu, A., Mateu, L., Sardet, C., Luzzati, V., Aggerbeck, L. and Scanu, A. M. (1975). *Proc. Nat. Acad. Sci. USA* **72**, 2270–2273.
- Stuhrmann, H. B., Koch, M. H. J., Parfait, J., Haas, J., Ibel, K. and Crichton, R. R. (1977). *Proc. Nat. Acad. Sci. USA* **74**, 2316–2320.
- Trammell, G. T., Hannon, J. P., Ruby, S. L., Flinn, Paul, Mössbauer, R. L. and Parak, F. (1978). *AIP Conf. Proc.* **38**, 46–49.

7

Experimental Practice

K. MÜLLER

*Institut für Röntgenfeinstrukturforschung der Österreichischen Akademie der
Wissenschaften und des Foschungszentrums Graz, Graz, Austria*

I.	Equipment	216
A.	Sources of errors of the experimental measuring points	216
B.	Supplementary measurements	218
II.	Samples for SAXS	220
A.	Kinds of samples	220
B.	Sample thickness and amount	221
C.	Exposure time	224
D.	Radiation damage	224
III.	Particle scattering	224
A.	Purity of solution	225
B.	Concentration effect	225
C.	Contrast	227
D.	Computation of the difference solution-blank	229
E.	Background subtraction	232
F.	Partial specific volume	233
G.	Preliminary evaluations	235
	References	235

In the following the main steps of a common SAXS measuring routine are described, possible sources of errors are mentioned and suggestions are made on how to avoid them. Besides remarks on the general measuring technique, some special problems involved in the measurement of particle scattering in solution are described. Peculiarities of other techniques recording the scattering of solids, fibres etc. will be found in Chapters 12 and 14.

I. Equipment

A. Sources of Errors of the Experimental Measuring Points

1. INTENSITY FLUCTUATIONS OF THE X-RAY SOURCE

Fluctuations of the primary intensity do not only cause errors when the step scanning method is employed but also in the case of position sensitive registration whenever a blank must be subtracted from the scattering.

Therefore, it is necessary to control the constancy by means of a monitor as described in Chapter 3.I, or by an ionization chamber positioned in the path of the beam, or by periodically repeated control measurements using a standard scattering sample. Short time fluctuations will cancel out partially in the step scanning mode when the curves are measured repeatedly and averaged.

2. INSTABILITY OF THE COUNTER POSITION

This problem arises only in connection with the step scanning method as a consequence of the limited mechanical precision of the goniometer support (c. $\pm 1\mu\text{m}$ for high quality instruments). In the case of very steep curves, especially if differences are to be calculated, these imperfections may lead to considerable errors. Again, repeated registration with subsequent averaging is the best help.

3. CHANGES OF THE GEOMETRY OF THE CAMERA SET-UP

Possible changes of the camera alignment or of the focal position also lead to errors of the measured scattering function. Therefore, the primary beam geometry as well as the position of the centre of gravity of the beam must be controlled periodically. Considerable progress with a view to the stability was achieved by the construction of the so-called compact camera.

4. INCONSTANT VACUUM

Air contributes increasingly to the entire scattering with increasing angle. At 5° scattering angle, for example, the air scattering caused by a 20 cm vacuum tube at 1 bar pressure is approximately as strong as the scattering of a usual glass capillary filled with a dilute macromolecular solution.

As a consequence, measurements are commonly carried out in a vacuum of only a few millibars. Continuously working pumps are to be preferred

compared with systems switching off and on when upper and lower levels are exceeded, since the pressure fluctuations that occur may cause changes of the camera blank scattering up to 100%, and intensity changes up to 1% even, in the case of the most powerful scattering samples.

5. SAMPLE TEMPERATURE

The scattered intensity depends on the temperature of the sample. In general, the dependence is positive and is higher, the higher the thermal expansion coefficient is. Solids may show an increase in the scattering intensity of 1% and more per degree Celcius, whereas the scattering of a water fille capillary increases only c. 0,15% per degree Celcius (depending on the scattering angle).

To avoid errors, the sample container should be thermostatized either by water or electronically by a Peltier cuvette to $\pm 0,1^\circ\text{C}$ (Leopold, 1969).

6. INSTABILITIES OF THE REGISTRATION ELECTRONICS

The sources of possible errors which can be caused by the electronics are manifold due to the variety of electronical set-ups. For example, shifts of the operating voltage of the counter tubes, dejustment of the discriminator, broadening of the pulse height distribution of the counter at the end of its lifetime etc.

If obvious errors of the scattering curves cannot be explained otherwise, a thorough check of the electronics will be useful.

7. CHANGES OF THE SAMPLE

Chemical alterations of the sample caused or accelerated by the radiation or also by other reasons can change the entire scattering pattern. Once again, a greater number of relatively short scans to be averaged is advantageous, compared with only one or a few extended scans, since changes in the scattering can easily be detected in time.

A measure for all these possible errors together is the ratio between the mean deviation of the measured intensities at identical angular positions in different scans from the mean value compared with the statistical error of the mean value. In the ideal case of no systematic experimental errors this value becomes unity, i.e. the measuring points are only afflicted with the statistical noise.

Practical experience shows that this ratio approaches unity sooner, the more scans are registered.

B. Supplementary Measurements

1. PRIMARY BEAM GEOMETRY

For the sake of desmearing, the geometry of the beam cross-section must be known.

In principle the same registration form should be applied as for the measurement, to keep the errors comparable. In any case, the primary beam must be attenuated by mass absorption filters before registration. If polychromatic radiation is used it is essential to switch off the pulse height discrimination because of the shift of the spectrum towards short wavelengths by the filters. Otherwise, the counter might be already overcharged although the registered intensity is apparently low.

The beam dimensions must be measured in the plane of registration or transformed to it (see Chapter 4).

Position sensitive counters are capable of measuring beam width and length by adjusting them in the horizontal and perpendicular directions.

In the step scanning mode the intensity distribution across the beam width $Q(x)$ is measured pointwise using the same receiving slit as for the measurement. The obtained profile is then already convoluted with the slit width and is directly used for the desmearing procedure.

The beam length is usually measured by a narrow perpendicular slit which is moved stepwise across the beam in its $P(t)$ direction. For desmearing, this profile must be convoluted with the receiving slit length. The symmetry of $P(t)$ and the shape of $Q(x)$ are important means for controlling the alignment of the camera.

The zero point of the abscissa can be chosen arbitrarily within the profile $Q(x)$. The only condition is that all measured intensities including $Q(x)$ are related to this point. Usually, but not necessarily, the centre of gravity of $Q(x)$ is chosen.

2. WAVELENGTH DISTRIBUTION

If polychromatic radiation is used, the obtained scattering can be corrected mathematically provided the spectrum of the X-ray light is known. This can be measured by an X-ray spectrograph, usually applying a Si- or Ge-crystal. The different absorption of the crystal for different wavelengths can either be determined experimentally using an additional spectrograph or in the case of selected crystals, also by computation (Pinsker, 1978).

Figure 1 shows such a profile for Cu-radiation (45 kV), convoluted with the λ -sensitivity distribution of a Xenon-filled proportional counter.

Position sensitive counters are capable of direct wavelength distribution

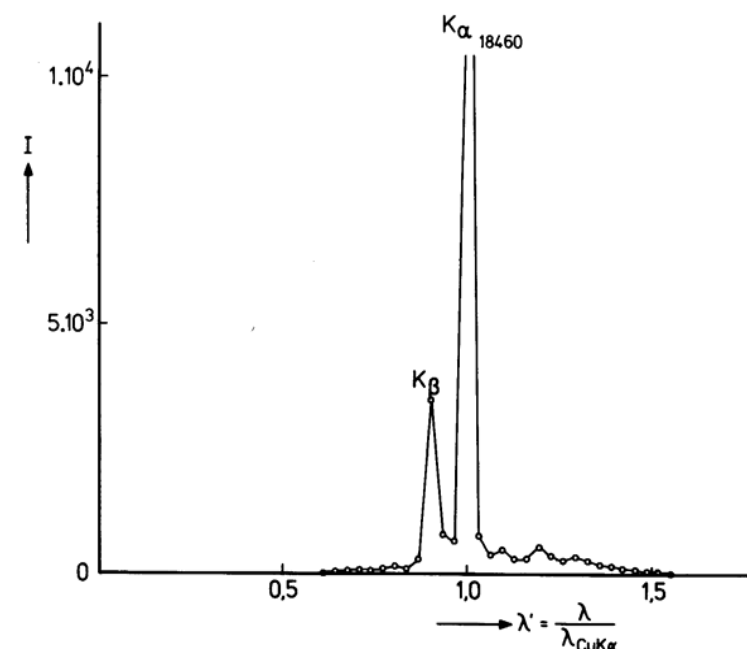


FIG. 1. Wavelength distribution of Cu-radiation registered with a xenon-filled proportional counter in units of λ -Cu-K α (intensities are given in arbitrary units). Beside the characteristic K α and K β lines practically no contributions of shorter wavelength are observed (since they are not absorbed by the counter gas). The obvious presence of longer wavelength, however, should be considered for an exact wavelength desmearing procedure.

measurement by analysing not the position pulse spectrum but the energy spectrum with the multichannel analyser.

A simplified method is to take into account only the predominant contributions of the characteristic K α - and K β -radiation, neglecting the other wavelengths. For this method, introduced by Zipper (1969), the intensity ratio of K α and K β , called γ , must be determined.

However, as shown in Fig. 2, the quality of the desmearing method using the whole spectrum (Glatter, 1977, Müller and Glatter, 1982) is superior to the γ -method correcting only for the K β contribution, especially with respect to the resolution of the minima. For curves without side maxima the γ -method yields quite satisfactory results.

3. PRIMARY INTENSITY

For absolute scale measurements, as necessary for molecular weight, volume and absolute electron density level determinations, the intensity of the primary

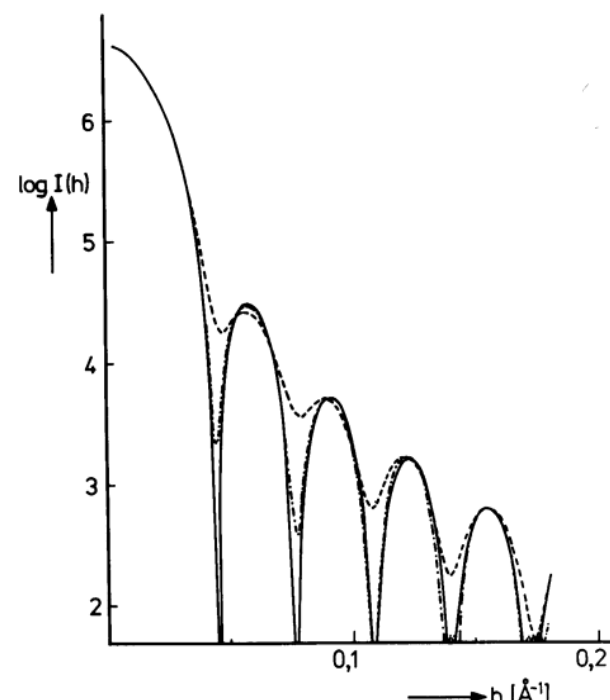


FIG. 2. Wavelength desmearing of the scattering function of a sphere. The full line represents the theoretical scattering curve. The broken lines were obtained from a simulated experimental curve derived from the exact function by artificial smearing (beam length, beam width, wavelength profile) and adding statistical noise and subsequent desmearing, in the one case (---) applying the γ -method, in the other one (----) using the wavelength distribution $w_{\lambda'}$. The latter treatment leads to better resolution especially in the region of the minima.

beam must be known. The methods in use have already been described in Chapter 3.I. Since the primary beam is weakened by the sample the attenuation factor of the sample (including eventual cuvettes) must be taken into account.

II. Samples for SAXS

A. Kinds of Samples

SAXS is a versatile method with regard to the variety of materials which can be investigated, that are densely packed, oriented specimen like fibres of synthetic or natural polymers (cellulose, collagen, silk etc.), amorphous and crystalline solids without orientation like glasses, metals, ceramics and polymers, powders and meltings, suspensions and colloidal solutions.

Homogeneous solids are exposed to the X-ray beam in the form of foils or thin platelets, fibres are gathered up into bundles and liquids are poured into cuvettes.

In any case it is essential that the irradiated region of the sample is quite homogeneous especially with respect to its density and thickness. In the case of solids this requirement can easily be fulfilled. Powders and fibres must be prepared carefully to realize this condition. The single fibres of the bundle should be parallel without application of strong stretching forces, since the structure of the material could be changed. Sometimes it is useful to pass the bundle through a glass capillary to achieve homogeneity.

The material of the cuvettes for liquid measurements must not absorb nor scatter X-ray too strongly. Cuvettes with plano-parallel walls of thin quartz, mica or glass platelets have proved to work well, as also the Mark capillaries, having glass walls of only 0,001 cm thickness. Such a capillary weakens a polychromatic X-ray (Cu-radiation) by the factor 0,7. The capillaries must have homogeneous wall thickness, uniform diameters and must not have any curvature in the irradiated region (for use in connection with slit collimation systems). The scattering of a glass capillary is shown in Fig. 3.

A particular problem in measuring liquids is the frequently observed formation of air bubbles within the capillary. This might be prevented by keeping the sample for several hours at a temperature higher than that employed for the measurement.

Also short evaporation can help, however solutions can change their concentration. If the bubbles cannot be removed in this way vibrations or shaking can make them float to the surface. Viscous liquids often cannot be rid of bubbles, except by refilling or by centrifugation which, however, bears the considerable risk of destroying the cuvette.

Dust and other slight macroscopical impurities are not disturbing since they scatter to immeasurable small angles.

For adjustment of the cuvette, it is filled with a strongly absorbing material, preferably with a saturated solution of CsCl, for example, and adjusted in the beam by electronical or optical (screen) means to the right position.

B. Sample Thickness and Amount

To achieve maximum scattering intensity the thickness of the sample must have an optimum value. On the one hand the scattered intensity increases linearly with the thickness and on the other hand the absorption by the sample increases, however, exponentially. The optimum thickness, d_{opt} , is

$$d_{\text{opt}} = \frac{1}{\mu} \quad (1)$$

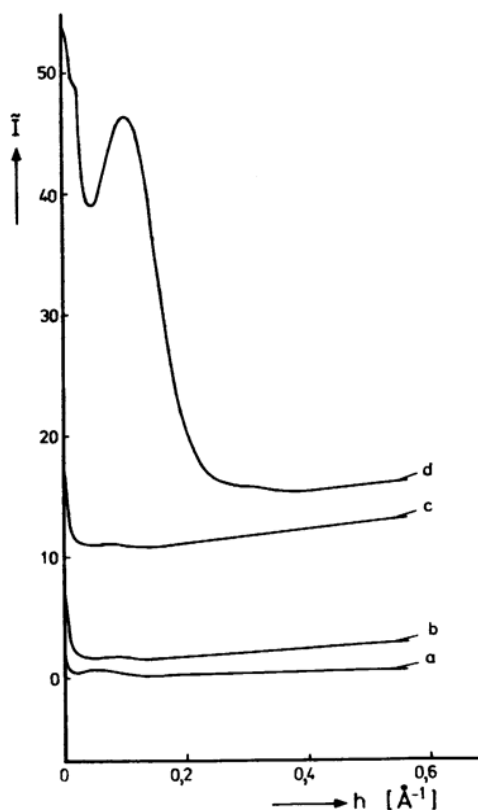


FIG. 3. Scattering of the evacuated camera (a), of the camera with empty glass capillary (b), of the camera with a water filled capillary (c) and of the camera with a capillary filled with a 10% (mass concentration) detergent micellar solution (d). (The intensities correspond to a primary intensity of 2×10^5 c.p.s. measured with Cu-radiation, 1.3 kVA, 40 μm entrance slit, 100 μm receiving slit and a beam length of 1.6 cm in the plane of registration.)

where μ is the linear absorption coefficient. This coefficient can either be calculated approximately from the mass absorption coefficient of the individual elements of the material, by weighted summation according to the equation

$$\mu = \left[\sum_{n=1}^i \left(\frac{\mu}{\rho} \right)_i \cdot p_i \right] \cdot \bar{\rho} \quad (2)$$

(p_i = mass fraction of i th element, $(\mu/\rho)_i$ = mass absorption coefficient of the i th element, $\bar{\rho}$ = mean density of the entire sample at the measuring temperature), or by simple measurement of the attenuation of the beam. Preferably, the latter method will be applied since absorption measurements are done routinely

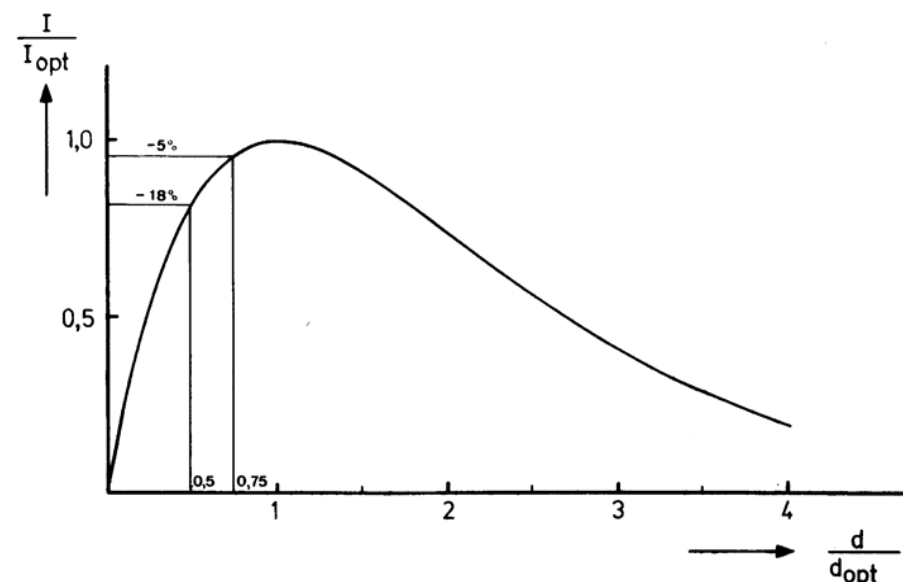


FIG. 4. Dependence of the scattering intensity in units of I_{opt} on the sample thickness given in units of d_{opt} . The values of d only correspond to the pure sample thickness. The thickness of the cuvette walls must be taken into account separately.

anyway for absolute scale determinations. Furthermore, the calculation of μ is complicated if monochromatic light is not used.

In the case of cuvettes or capillaries being used as containers for liquid samples, the absorption of the empty cuvette must be taken into account for an accurate measurement. Otherwise, since the walls of the cuvette only contribute to the absorption but not to the scattering of the sample in it, one obtains too small a value for the optimum thickness, which may lead to a loss of scattered intensity up to 10% (see Fig. 4).

The precise thickness of the sample as needed for absolute scale measurements can be determined directly by a micrometer for solid probes or by a calibrated microscope. However, it can also be determined from the measured attenuation according to Lambert Beer if the absorption coefficient has been calculated. The problems of this latter method have been already mentioned above.

Theoretically, the minimum amount of sample is determined by the area of the irradiated sample and the optimum thickness. For mounting on an appropriate sample holder, however, the planar size will have to be somewhat larger than required by the geometry of the beam passing through it. In the case of liquid, approximately 0.1 cm^3 is needed. For solutions, the amount of solute

depends on the concentration which, as a rule, is in the range of 10–0,1% mass fraction, according to the scattering power (electron density contrast) and interparticle interference effect. In general, thus, a sample amount of 10 mg will be highly sufficient for one SAXS measurement. If a determination of the partial specific volume for molecular weight or absolute electron density determination is desired, much higher quantities are necessary (100–200 mg).

C. Exposure Time

General rules for calculating the exposure time cannot be given. Depending on primary beam intensity, scattering power of the sample, type of registration and desired precision of the scattering curve, the measurement of one sample may take from a few minutes (strong scatterers like solid polymers, fibres etc.; position sensitive counter) up to several to ten hours (dilute solutions; step scanning method). Using photographic films, efficient pictures are commonly obtained after 1–10 hours of exposure, according to the sensitivity of the film. In the case of solutions, the expenditure of time is even higher since it is necessary to have measurements of the blank scattering of the solvent and concentration series for elimination of the interparticle interference effect.

D. Radiation Damage

A further requirement for the samples is that they must not be changed by the radiation during the exposure time. A general prediction whether this will be the case or not cannot be made. Experience, however, shows that the usual radiation doses only very seldom cause measurable structural changes.

Platelets of Lupolen, for example, as used as calibrated standard samples showed a decrease in scattered intensity of 1% after absorption of approximately 10 Mrad. This corresponds to $\approx 10^{15}$ absorbed CuK α pulses, or an exposure time of several thousand hours (depending on the primary beam intensity). For enzymes, in some cases an accelerated decrease of the activity has been observed as an effect of the X-rays. However, these changes in the activity are not usually accompanied by any measurable change in the scattering pattern.

Nevertheless, it is advisable to test the stability of the sample by comparisons of the scattering of repeatedly measured scans.

III. Particle Scattering

Measurements of particles in solution involve some additional experimental problems and practical aspects that shall be discussed in the following.

A. Purity of Solution

Solutions must be monodisperse, otherwise the obtained measuring quantities will represent average values. In special cases this condition does not need to be fulfilled strictly, e.g. if the molecules of the contamination differ in size by several orders of magnitude from the main component, so that the angular ranges of scattering are so different that the mutual influence becomes negligible. Another example is a system forming an association equilibrium. If the structure and scattering function of the monomer is known, the structure of the aggregate can be calculated from the measured scattering curve.

For really polydisperse solutions the information that can be obtained by SAXS is restricted to the size distribution function, provided the shape of the particles is known, and vice versa.

To test monodispersity in principle, all methods for separation and analysis of macromolecules are suitable, however, it is not necessary to apply oversensitive methods. In general a preparation showing one single, homogeneously migrating peak in the ultracentrifuge will be sufficiently pure for a SAXS measurement.

B. Concentration Effect

The concentration of the solution must be known for absolute scale measurements and for the calculation of the partial specific volume. The latter especially may be very sensitive to even small errors of the concentration which thus strongly influences the value of the molecular weight. In general, the effect of the concentration will be the more influencing the smaller the net electron density contrast between solute and solvent.

Consequently, the concentration must be determined with the highest possible accuracy.

For a correct treatment the scattering curve must be extrapolated to zero concentration in order to eliminate the interparticle interference effect. Therefore, it is necessary to measure a series of concentrations and to extrapolate the scattering to infinite dilution.

Since an exact treatment of the interparticle interference effects is hardly possible because of the lack of a basic theory (with the exception of hard sphere interaction models) (Guinier *et al.*, 1955) with limited applicability, several methods of extrapolation are in use as shown in Fig. 5.

Linear extrapolation of the intensities (Fig. 5a) often works well when the concentration effect is weak and the concentrations are low.

It is also possible to extrapolate individual parameters like R , $I(0)$, Q separately (Fig. 5c), however, frequently there is also no linear dependence observed at higher concentrations.

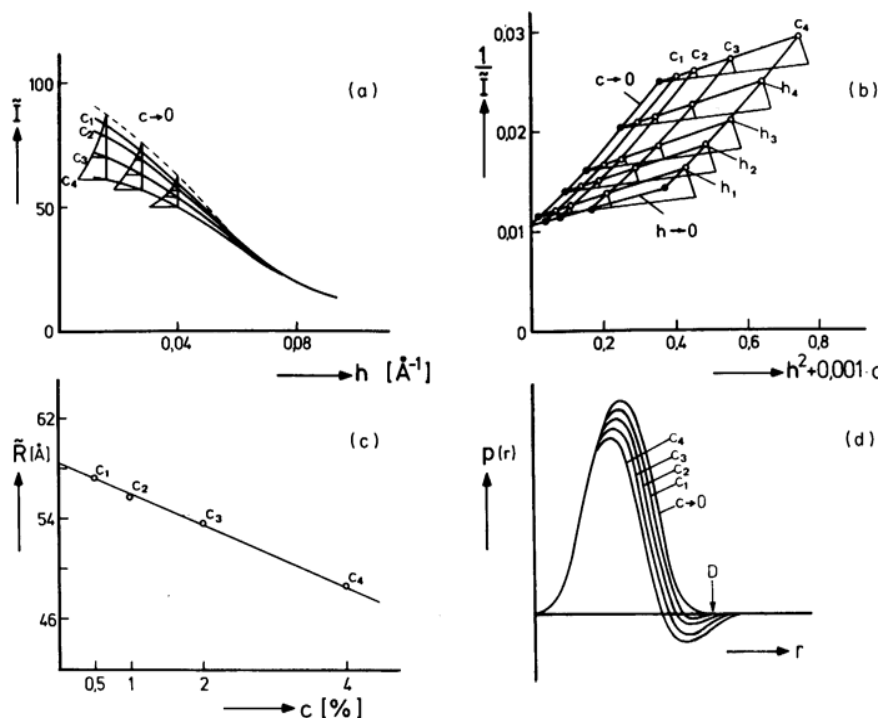


FIG. 5. Different ways for extrapolation to zero concentration. (a) The smeared scattering functions are directly extrapolated. The length of the horizontal lines within the triangles are proportional to the concentration. However, especially at higher concentrations, frequently no linear dependence is found. (b) The radii of gyration are extrapolated. The extrapolated scattering curve is reconstructed from the course of the corresponding Gaussian curve. (c) Zimm-plot. In the $1/\tilde{I}$ v. h^2 plot the scattering curves take a nearly linear form so that extrapolation to zero angle ($h \rightarrow 0$) is possible. The extrapolation to zero concentration is done in analogy to (b). (d) In any case the distance distribution function as obtained by indirect Fourier transformation reflects the concentration effect by the negative oscillation in the region of D .

Better linearity is often achieved by the Zimm plot (Fig. 5b) developed for simultaneous extrapolation to zero scattering angle and to zero concentration in the related field of light scattering.

In any case it is advisable to test the extrapolated curve by Fourier transformation. The obtained distance distribution function should not exhibit a negative trough in the region of the maximum dimension, as shown in Fig. 5d, when the interparticular interference effect has really been eliminated.

Depending on the highest concentration three to five dilutions will be sufficient in practice. Since the difference between the individual concentrations should not be too large (not more than a factor of two), more scans are recommended when starting with highly concentrated solutions. Since the interference

effect depends on the size, structure, charge etc. of the particle and also on the solvent, no general rule can be given as to what concentration the dilution series must be extended downwards. In general, dilutions of 1–0.5% mass fraction will be sufficient. For measurements up to larger angles where the concentration effect disappears, only the highest concentration will be used because of its scattering power.

Since the interference effect usually becomes negligible beyond values of $h \cdot D > 5$ (again depending on the actual system), the lower concentrations need only to be measured up to this angle. Beyond this value the curves should coincide, provided they have been normalized to unity concentration and to their individual absorption coefficients. It will be useful to measure up to somewhat larger angles for a sufficient range of overlapping.

If the curves, nevertheless, do not fit together, errors of the concentration will be responsible. If they differ in their slope so that overlapping becomes impossible, changes of the material by dilution must be considered. For very high concentrations ($> 10\%$) there is another explanation imaginable, i.e. incorrect computation of the difference between solution and solvent scattering as a consequence of the non-negligible volume fraction of the solute (see Section III.D).

C. Contrast

The contrast $\Delta\rho$ strongly influences the scattering power of the dissolved particles and, moreover, the entire scattering pattern for systems with inhomogeneous internal electron density distribution (see Chapter 6). Therefore, it is essential to choose a solvent providing an appropriate contrast.

For homogeneous particles it will be desirable to adjust the contrast to as high as possible with respect to the gain of intensity.

For an advanced treatment of the scattering of particles with an internal structure, measurements at a series of contrasts (positive and negative) must be carried out. In several cases it will be useful to adjust the solvent to specific contrasts in order to match the scattering of individual parts of the molecule with a certain, known electron density. If a detailed analysis of the characteristic scattering functions is not aimed for, it will be sufficient to measure at one high contrast to obtain determination of the overall shape. If the distance distribution function shows a smooth course without any fluctuations this might serve as a criterion for believing that at this contrast the influence of the internal structure is already negligible.

The actual contrast $\Delta\rho$ is

$$\Delta\rho = \rho_2 - \rho_1 \quad \begin{cases} 2 = \text{solute} \\ 1 = \text{solvent} \end{cases} \quad (3)$$

The individual electron densities ρ_i (in $e \cdot \text{\AA}^{-3}$) are obtained from

$$\rho_i = z_i \cdot \bar{v}_i \cdot N_A \cdot 10^{-24} \quad (4)$$

where z_i is the electron concentration in gram-electrons ($= N_A$ electrons) per gram substance. For pure components z is simply calculated from the chemical composition

$$z = \frac{\sum_j n_j \cdot N_j}{\sum_j n_j \cdot A_j} \quad (5)$$

j = number of different elements the compound consists of, n_j = number of atoms of each individual element, N_j = number of electrons of a single atom of j th element, A_j = atomic weight of the j th element.

If several compounds are mixed (buffers, solvents with additives for contrast adjustment) the former expression is to be weighted by the mole-fractions (m_i) of the i compounds

$$z = \frac{\sum_i m_i \sum_j n_j \cdot N_j}{\sum_i m_i \sum_j n_j \cdot V_j} \quad (6)$$

In aqueous solutions, alcalihalogenides or carbohydrates are usually used for contrast adjustment. Figure 6 shows the dependence of the electron densities of aqueous solutions of sodium bromide, glycerol and sucrose on the mole percentage.

The additive itself should be chosen carefully with respect to minimum X-ray adsorption, maximum contrast shift at minimum concentration and the chemical properties of the macromolecular solute, since no changes of the structure may be caused by the added compound.

For a correct determination of the characteristic functions it is, moreover, necessary that the excluded volume of the particle is invariant and that no specific interactions or solvent penetration occurs in dependence of the solvent composition. In some cases this condition will not be fulfilled exactly, but sufficiently so that the errors remain below the resolution of the experiment. In the case of sensible structures, however, like some proteins or aggregation complexes being in equilibrium with monomers in solution, for example, dramatic structural changes or even complete disruption of the entire structure may occur. In the case of polyelectrolytes, for example, it is to be expected that added salts will more easily interact with the charged surface than, for example, glycerol, which is known to have a stabilizing effect on several biological structures.

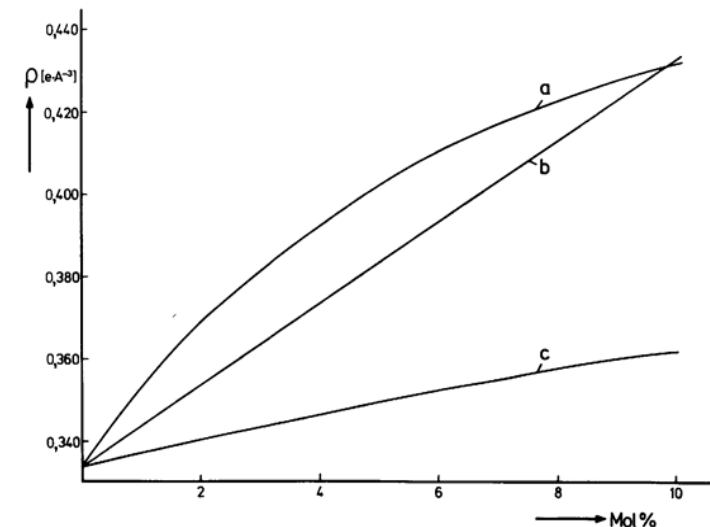


FIG. 6. Dependence of the contrast shifting effect of sucrose (a), sodium bromide (b) and glycerol (c) in dependence of the concentration of the additive in aqueous solution. ρ = electron density of the solution in electrons per \AA^3 .

Different electrolytes may behave quite differently (Hey *et al.*, 1976). In any case the invariance of the structure in different solvents should be tested as far as possible. A possibility for a partial verification by combining X-ray and density measurements was described recently (Aggerbeck *et al.*, 1978).

For neutron scattering the problem of contrast adjustment is much less difficult since a wide range of contrasts can be covered by simple variation of the $\text{H}_2\text{O}/\text{D}_2\text{O}$ mixing ratio, however, there arise also problems due to proton : deuteron exchange reactions between solvent and solute.

D. Computation of the Difference Solution-blank

To obtain a particle scattering curve the difference between the scattering of the solution and the solvent must be calculated. This is commonly done by simple subtraction of the scattering of the solvent filled capillary (often called blank scattering) from that of the solution. Thereby it should be considered that the total scattering of the solution $i_2(h)$ is the square of the sum of the scattering amplitudes generated by all kinds of electron density inhomogeneities the beam meets along its path. These are formed essentially by the entire sample volume including the capillary, by the volume excluded by the dissolved particles, by electron density fluctuations within the particle and by the short range electron density inhomogeneities of the solvent. The

fluctuations within the particle might be separated into those of colloidal dimensions, thus being resolved by the measured scattering function (usually called internal structure), and into those unresolved short range fluctuations, yielding the so-called background scattering, being practically constant at larger angles.

(For comparison with model scattering functions it is necessary to decide whether this separation is justified. It is not when models with atomic resolution, for example those derived from crystal structure analysis data, are used, since then the background is part of the particle scattering. In the unusual case of models, the structural details of which compare with the resolution that can be reached experimentally ($\sim 10\text{--}5 \text{ \AA}$), this dissection will be reasonable.)

$$i_2(h) = (a_s(h) + a_v(h) + a_i(h) + a_{if}(h) + a_{sf}(h))^2 \quad (7)$$

$a_s(h)$, $a_v(h)$, $a_i(h)$, $a_{if}(h)$ and $a_{sf}(h)$ are the scattering amplitudes of the entire sample (s), of the excluded volume of the particles (v), of the internal structure (resolved) (i), of the internal electron density fluctuations (not resolved – background) (if) and of the fluctuations within the solvent (sf). The terms a_v and a_i together contribute to what we call particle scattering a_p .

Since $i_1(h)$, the blank scattering, is an analogy

$$i_1(h) = (a_s + a_{sf})^2 \quad (8)$$

the difference $i_2(h) - i_1(h)$ is not identical to the particle scattering because of the interference terms and the term $a_{if}(h)$.

Nevertheless, it is possible to obtain the particle scattering as a good approximation. a_s and all corresponding cross-terms are negligible since the size of the sample is extremely large as compared with the particles. Consequently a_s will be practically zero at the first measuring point, even at highest resolution.

Also, the remaining interference terms will be very small according to the considerable differences of the dimensions of the individual inhomogeneities, except the interparticle interference term (J_p) which must be considered in practice, especially at higher concentrations. Consequently, the proper scattering of the solution $i_2(h)$ is in a good approximation:

$$i_2(h) = i_{sf}(h) + i_p(h) + i_{if} + J_p \quad (9)$$

Since by the same approximation $i_1(h) = i_{sf}(h)$ the difference curve

$$i_2(h) - i_1(h) = i_p(h) + i_{if}(h) + J_p \quad (10)$$

($i_1(h)$ = scattering function of the solvent) differs from the true particle curve only by the term $i_{if}(h)$, which can be considered as a constant background and eliminated by subtraction (see below), and by the interparticle interference term J_p , which is eliminated by extrapolation to zero concentration (see above).

From the experimental point of view the following considerations should be kept in mind:

(1) The experimental conditions must be identical during the measurement of the solution and the blank. Intensity fluctuations of the primary beam, especially, must be monitored in some way and considered for the difference calculation. The cuvette must be the same for both measurements. Also, the measuring temperature should be identical. Although the scattering intensity of water changes not more than 1–2% per 10°C in the range of room temperature, this might significantly influence the course of the difference curve at larger angles, where the solution scattering intensity frequently is less than 10% higher than the blank scattering. Also, the temperature dependence of the contrast should be considered.

(2) The composition of the solvent used for the blank measurements must be identical to that in the actual solution. Deviations originating in Donnan-equilibrium for solutions of charged macromolecules which have been prepared by dialysis usually can be neglected.

(3) The counting rates must be chosen with view to the decreasing intensity difference at larger angles. The relative error F of an individual point of the difference curve is

$$F = \frac{1}{\sqrt{N}} \cdot \frac{q^2 + 1}{q - 1} \quad (11)$$

where N is the number of counts accumulated for both solution and blank scattering (equal rates assumed for blank and solution), and q is the intensity ratio $i_2(h)/i_1(h)$. If this ratio is, say, 10 (at small hD values), F is about 1% when 10^5 pulses have been counted. If q is 1,05 (at large hD values) F becomes about 30% at the same pulse rate (see Fig. 3). This clearly shows that the pulse rate must be chosen with respect to the accuracy of the scattering at larger angles, if any interpretation of this part of the scattering function is intended.

If a constant time is chosen for all points (e.g. position sensitive counter), this time must allow counting rates for the measuring points at largest angles which are sufficient for the desired accuracy. The points at smaller angles are then registered with unnecessary accuracy. In the step scanning mode a constant preset count is to be preferred.

(4) The curves must be normalized to identical absorption. Especially for higher concentrated solutions, the absorption might differ by 10 and more percent.

(5) In the case of concentrated solutions, the volume fraction of the solute must be taken into account: at large hD values the sample scattering curve is no longer controlled by the form factor of the particle but predominantly by

the short range fluctuations within the particle. With respect to a correct elimination of this background, the blank scattering, i.e. the electron density fluctuations of the solvent, must only be subtracted to such an extent that corresponds to the volume fraction of the solvent in the solution (Damascshun *et al.*, 1979). For this aim, an additional measurement of the scattering of the empty cuvette $i_c(h)$ (see Fig. 3) is necessary. The correct particle scattering curve including the background is then obtained from

$$i_p(h) + i_{if}(h) = i_2(h) - (1 - w_2) \cdot i_1(h) - w_2 \cdot i_c(h) \quad (12)$$

Also this equation is an approximation assuming additivity of intensities and neglecting the cross terms. At low volume fractions of the solute (w_2) the effect will be small. At higher concentrations, however, considerable errors will be observed (negative intensities at larger angles, deviations from the h^3 -law).

(6) A further problem of measurements at large angles is that the blank scattering reflects the liquid structure of the solvent. It is difficult to judge whether this structure will be changed by the solute and how far the difference curve will be influenced by this effect at large angles.

E. Background Subtraction

The only remaining contribution to the desired particle curve is the background scattering. The term $i_{if}(h)$, however, can be determined according to Porod (1951) and Luzzati (1960) respectively, from the course of the difference curve at large angles, which should follow the equations

$$i(h) = \frac{P}{h^4} + i_{if}(h) \quad (13)$$

$$\tilde{i}(h) = \frac{P}{h^3 2\pi} + i_{if}(h) \quad (14)$$

$i_{if}(h)$ is, in good approximation, taken to be a constant in the measured angular range. From the slope of an appropriate plot ($\tilde{i}(h)^3 \cdot h^3$ against h^3) $i_{if}(h)$ can be determined (Fig. 7). (It should be mentioned that Porod's law only holds for idealized scattering particles with a smooth surface and step-like electron density difference to the solvent, however in practice it often can be used in this connection with success.) The intersection with the ordinate represents the Porod-constant, which allows extrapolation of the curves beyond the measuring range. This is important for all kinds of evaluations including an integration of the scattering function from zero to infinity, conventional Fourier transformation and the determination of the invariant according to Porod.

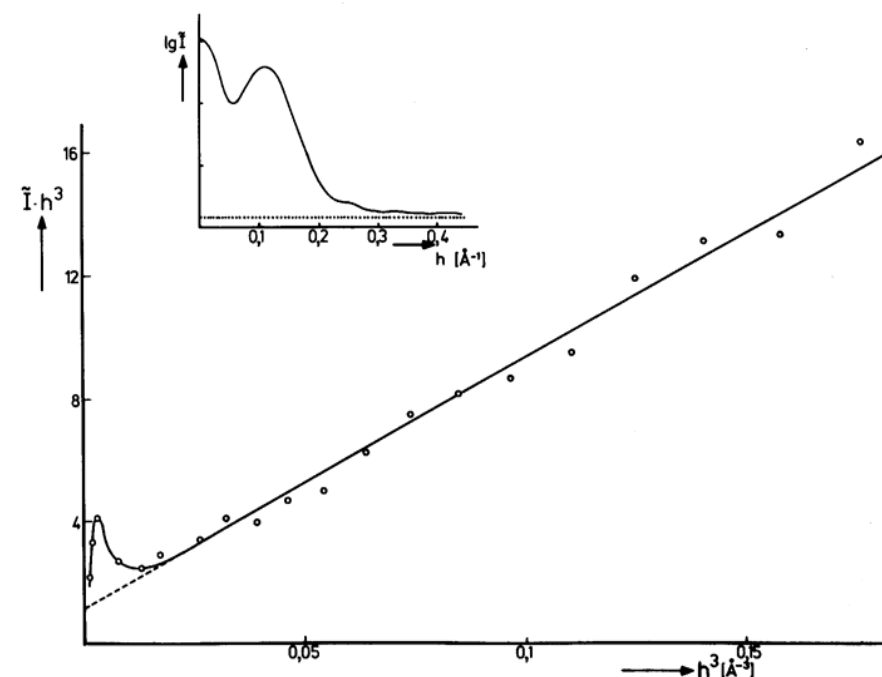


FIG. 7. Determination of the scattering background from the $\tilde{I} \cdot h^3$ v. h^3 plot of a detergent micelle scattering curve. From the slope of the straight line, the background (dotted line in the insert) to be subtracted can be derived.

F. Partial Specific Volume

For any absolute scale measurement, i.e. the measurement of the molecular weight or the determination of absolute electron density levels, the partial specific volume must be known.

This quantity is necessary to define that volume associated with the scattering particle which deviates in its mean electron density from that of the solvent. For a simple two component system, i.e. a solution composed of only one pure solute and a pure solvent, it corresponds to the linear increase in the volume of the solution when an infinitesimally small amount of solute is added, and can be described in terms of the density increment (Casassa and Eisenberg, 1964)

$$\frac{dp}{dc_2} = 1 - \vartheta_2 \rho_1 \quad (15)$$

(ρ = density of the solution, c_2 = concentration, ϑ_2 = partial specific volume of the solute, ρ_1 = density of the solvent).

In practice one measures the density difference between the solvent and solutions of several finite concentrations. The values obtained are called apparent partial specific volumes ϕ'_2

$$\phi'_2 = \rho_1^{-1}(1 - \Delta\rho \cdot c^{-1}) \quad (16)$$

($\Delta\rho$ = density difference between solution of concentration c and the solvent). The partial specific volume can be derived by extrapolation of these values to zero concentration.

Possible interactions between solvent and solute are thus eliminated and the scattering function is extrapolated to zero concentration. Frequently, however, the concentration dependence of ϕ'_2 will be found to be very small, so that at not very high concentrations ϕ'_2 is practically identical to \bar{v}_2 (Pilz and Czerwenka, 1973).

For multicomponent systems a more complex treatment is necessary. If the solvent, for example, contains additional compounds of low molecular weight (salts, buffer substances, additives for contrast adjustment), the interaction of these molecules with the dissolved macromolecules must be taken into account (Eisenberg, 1976), by means of preferential interaction terms.

The apparent partial specific volume then can be defined in analogy to Eqn (15) as

$$\frac{d\rho}{dc_2} = 1 - \phi'_2 \cdot \rho^0 \quad (17)$$

however, ϕ'_2 is not a specific molar quantity in this case since it includes contributions of mutual interactions of the components.

For a three component system, for example, a more accurate equation is

$$\frac{d\rho}{dc_2} = (1 - \bar{v}_2 \rho^0) + \xi_3 \cdot (1 - \bar{v}_3 \cdot \rho^0) \quad (18)$$

where \bar{v}_3 is the partial specific volume of component 3 (salt, sucrose etc.) and ξ_3 is the preferential interaction parameter. \bar{v}_2 is assumed to be a constant. Since this is a very important question, methods have been developed to test the invariance of \bar{v}_2 (Aggerbeck *et al.*, 1978). However, it is difficult to distinguish reliably the effects of volume change, preferential interaction and solvent penetration, which possibly may be caused by alterations of the solvent composition.

To determine the apparent specific volume, high precision density measurements are necessary. Usually these are performed with help of the digital densitometer (Kratchy *et al.*, 1969). This instrument reaches a high accuracy, especially when operated with a monitor oscillator (Lagninger and Stabinger, 1976) so that even the smallest temperature fluctuations are cancelled out. Thus in most cases the accuracy of the ϕ'_2 values is not limited by the density

measurement but by the errors of the concentration. Obviously, the measurements must be carried out at the same temperature as the X-ray experiment and also the solvent composition must be identical for both.

G. Preliminary Evaluations

Several pieces of information can be derived directly from the smeared particle scattering curve. These might be a valuable help for the subsequent evaluation procedure.

Provided the condition $h_1 \cdot D \leq \pi$ is fulfilled (h_1 = lowest measured scattering angle) the smeared curve should follow the Guinier approximation and show a linear course in the $\log \tilde{i}$ against h^2 plot from which the smeared radius of gyration can be determined. The quadruplicity of this value means a rough estimate of the maximum particle dimension can be achieved.

A steep increase in the intensity at the innermost angles deviating from the Guinier line indicates the presence of aggregates or other large molecular arrangements. Deviations from the Guinier line at larger angles to higher intensities will be due to anisometric structures, whereas deviations to lower intensities indicate highly isometrical particles.

A curvature of the $\log \tilde{i}/h^2$ -line in the Guinier range usually originates in insufficient monodispersity.

The scattering intensity at zero angle $i(0)$ can be calculated as a good approximation from the smeared $\tilde{i}(0)$ using the equation (Kratchy *et al.*, 1960)

$$i(0) = \tilde{i}(0) \cdot \sqrt{\left(\frac{\ln 10 \cdot \operatorname{tg}\alpha}{\pi}\right)} \quad (19)$$

($\operatorname{tg}\alpha$ is the slope of the Guinier straight line).

Also the invariant Q can be determined from the smeared curve.

$$Q = 2\tilde{Q} \quad (20)$$

and

$$\tilde{Q} = \int_{h_1=0}^{h_2} i(h) \cdot h \cdot dh + \int_{h_2}^{\infty} \frac{P}{h^3} \cdot h \cdot dh \quad (21)$$

The constant P can be derived from the analysis of the scattering background (see Section III.E). Thus one obtains information on the molecular weight and the volume of the dissolved particles from the "crude" data.

References

- Aggerbeck, L., Yates, M., Tardieu, A. and Luzatti, V. (1978). *J. Appl. Cryst.* 11, 466-472.

- Casassa, E. F. and Eisenberg, H. (1964). *Advan. Protein Chem.* **19**, 287–394.
Damaschun, G., Müller, J. J. and Bielka, H. (1979). ‘Methods in Enzymology’,
Vol. LIX (K. Moldave and L. Grossmann, eds).
Eisenberg, H. (1976). ‘Biological Macromolecules and Polyelectrolytes in
Solution’. Clarendon Press, Oxford.
Glatter, O. (1977). *J. Appl. Cryst.* **10**, 415–421.
Guinier, A. and Fournet, G. (1955). ‘Small Angle Scattering of X-Rays’. Wiley,
New York.
Hey, M. J., Clough, J. M. and Taylor, D. J. (1976). *Nature* **262**, 807–809.
Kratky, O., Porod, G. and Skala, Z. (1960). *Acta Phys. Austriaca* **13**, 76–128.
Kratky, O., Leopold, H. and Stabinger, H. (1969). *Z. Angew. Phys.* **27**, 273–277.
Laggner, P. and Stabinger, H. (1976). *J. Colloid Interface Sci.* **5**, 91–96.
Leopold, H. (1969). *Elektronik* **18**, 350–351.
Luzzati, V. (1960). *Acta Cryst.* **13**, 939–945.
Müller, K. and Glatter, O. (1982). *Makromolek. Chem.* (in press).
Pilz, I. and Czerwanka, G. (1973). *Makromolek. Chem.* **170**, 185–190.
Pinsker, Z. G. (1978). ‘Dynamic Scattering of X-Rays in Crystals’. Springer-
Verlag, Berlin.
Porod, G. (1951). *Kolloid-Z.* **124**, 83–114.
Zipper, P. (1969). *Acta Phys. Austriaca* **30**, 143–151.

8

Proteins

I. PILZ

Institut für Physikalische Chemie der Universität Graz, Graz, Austria

I. Introduction	240
II. Preparatory steps	241
A. Preparation of protein solutions	241
III. General data evaluation	243
A. Elimination of concentration effects	244
B. Molecular parameters	247
C. Shape	252
IV. Special data evaluation	256
A. Spherical proteins	256
B. Elongated proteins	256
C. Lamellar proteins	261
V. Structure of proteins	268
A. Secondary structure	268
B. Tertiary structure	270
C. Quaternary structure	274
VI. Structural changes	282
A. General	282
B. Enzymes	282
C. Structural changes in immunoglobulins	284
D. Denaturation, association-dissociation	284
VII. Polydisperse solutions	285
A. General	285
B. Two-component systems	285
C. Equilibrium data	286
VIII. Special applications	287
A. Intermolecular structure	287
B. Synchrotron radiation	287
References	289

I. Introduction

On the basis of their structure, proteins are usually classified into two categories, fibrous proteins and globular proteins. The *fibrous* proteins, such as keratins, fibroin, myosin and collagen, are normally insoluble in aqueous media. The *globular* proteins, on the other hand, are usually soluble in aqueous buffers, with the exception of the special group of proteins which are integral components of membrane structures.

In this chapter we want to discuss only the water-soluble globular proteins, including such important groups as enzymes, antibodies, hormones etc. In these proteins the polypeptide chains often form certain regions of regular secondary structures, like α -helical or pleated sheet structures, but these regions are always rather limited and the polypeptide chain is folded into a complex tertiary structure. It is known that many biological functions of the globular proteins are determined by their three-dimensional structure. The globular proteins may consist of one single polypeptide chain or of a smaller or larger number of polypeptide chains, which together form highly complex quaternary structures. The biological function is very often dependent on the ability of this tertiary or quaternary structure to respond to the interaction with other molecules by conformational changes.

Thus, the knowledge of the detailed three-dimensional structure is the key to the understanding of the biological function. At the present time, X-ray structure analysis of protein crystals is the only method by which detailed structural information, at the level of atomic resolution, may be obtained. But the method also has some limitations and disadvantages, which necessitate the application of other methods. First, the protein must be crystallized and heavy atom derivatives have to be prepared. With many proteins it is a serious problem getting suitable crystals, and hence the conditions (i.e. the solvent, ionic strength, pH etc.) under which the protein is studied are ultimately determined by the crystallization procedure and it is usually not possible to care for biological conditions. Secondly, the protein molecules in the crystal are held together by forces which are not present under biological conditions in solution. According to the experience obtained so far, the solvent conditions and the crystallization seem to have no or only little influence on the structure, but there are also examples where differences were found between the protein structure in crystal and in solution (see Section V.B). The great advantage of SAXS lies in the possibility of performing the measurements in any desired solvent under biological conditions and in the ability to follow changes of the structure, which may occur by changing the external conditions.

A third limitation on crystallographic studies is the fact that biological processes are dynamic, while the X-ray crystallographic studies, which take several days or weeks, are essentially static. Small angle X-ray studies are usually

also static, but by using high power X-ray sources and position sensitive detectors it becomes possible to follow dynamic processes which are not too fast (see Section VIII.B).

In the following we want to discuss the kind of information that can be obtained on the secondary, tertiary and quaternary structure of the so-called "globular proteins" by small angle X-ray scattering. ("Globular" does not mean that all of these proteins are nearly spherical; there are also elongated or flat molecules – but as compared to the very elongated fibrous proteins it is justifiable to call them "globular".) We will deal mainly with the water soluble proteins and in the first part of this chapter the usual experimental procedures and the basic evaluations will be described. In the second part some newer applications will be discussed. Unfortunately there are at the moment no published applications available for some new interpretation procedures described in Chapter 5.

II. Preparatory Steps

A. Preparation of Protein Solutions

Usually several questions, which are of interest to biochemists who intend to perform a small angle X-ray experiment on a protein, concern practical details like: total amount of protein necessary; special requirements of solvent (buffer); optimal concentration of the protein; radiation damage. Since the sample preparation has been already discussed in a general way in Chapter 7 we will only deal with some supplements concerning protein solutions.

1. TOTAL AMOUNT OF SAMPLE

As a general rule, a total amount of about 20 mg protein is the lower limit. Exact measurements, which involve frequent repetitions, require a total amount of 100–200 mg. 5–10 mg, however, may be enough for a preliminary investigation yielding rough overall parameters for the molecule.

2. CHOICE OF SOLVENTS

Proteins are usually dissolved in buffers or salt solutions of low concentration. The only requirement of the SAXS method concerns the electron density. As already pointed out in Chapters 2, 4 and 7, the scattered intensity is a function of the electron density difference between solute and solvent. Since the electron density difference between protein and water is in itself not very high, salt concentrations of more than 1 M should be avoided and light ions should be

preferred to heavy ions. The solvent scattering at high salt concentrations (especially of heavy ions as, for example, CsCl) can easily mask the scattering of the protein.

In any case, a complete series of concentrations of the protein must be measured, as already mentioned in Chapter 7. One usually prepares a stock solution and dialyses against the desired buffer. An important rule shall be stressed again: the solvent used as blank solution (for the determination of the background scattering) must be identical in composition and chemical potential to the solvent used for the protein. This requirement is usually best fulfilled by dialysis. Special procedures may be necessary whenever dialysis is unsuitable (such as in the presence of large amounts of sucrose, which is occasionally used to vary the electron density – Schausberger and Pilz, 1977).

3. CONCENTRATION OF PROTEIN SOLUTIONS

For globular proteins, concentration effects can usually only be neglected for concentrations below 1 mg ml^{-1} . Proteins in aqueous solutions, however, produce such a small excess scattering (see Chapters 2 and 7) that statistical errors become inhibitively large for concentrations below about 3 mg ml^{-1} . This makes it necessary to study a concentration series and to extrapolate it to infinite dilution. As a rule four or five solutions with concentrations in the range between 3 mg ml^{-1} and 30 mg ml^{-1} should be measured. As concentration effects are apparent only at relatively small angles, much higher concentrations ($50\text{--}100 \text{ mg ml}^{-1}$) can be used for investigating the tail end of the scattering curve where the intensity is very weak. These highly concentrated solutions make it possible to measure details of the scattering curve (maxima, minima) at large angles with sufficient accuracy.

4. HOMOGENEITY

To derive exact data from SAXS, all macromolecular particles in the system must be identical in size and shape. Only in truly monodisperse solutions is it possible to obtain exact structural parameters. Since proteins often tend to form aggregates, it is always necessary to test the protein solution using other physical techniques before investigating SAXS. A minimal criterion is that the solute shows a single symmetrical peak in the sedimentation pattern in the analytical ultracentrifuge (compare also Chapter 7).

If there are aggregates, one must try to remove them by such methods as gel filtration, electrophoresis, electrofocusing or centrifugation. These methods, of course, fail if there is an association-dissociation equilibrium; however, in such cases it is sometimes possible to obtain essential information on the protein as shown in Section IV.B4.

Sometimes the formation of aggregates can be prevented by changing the temperature, buffer, ionic strength etc. or by adding some reagents. But in any case one has to prove carefully whether or not these conditions change the native conformation of the protein.

5. RADIATION DAMAGE

A question which occurs in the course of every small angle investigation concerns the possible damage to the protein due to the absorbed X-rays. SAXS only records the morphology of the biological macromolecule, independent of its functional activity. That is, a loss in activity can be detected by SAXS only if it is accompanied by a significant change in morphology. Very small structural changes, which affect only part of a chain or dislocate a few atoms, are invisible for SAXS as long as the measurement is restricted to the usual small angle region; (the possibility of getting information on smaller structural changes is discussed in Section V). In other words, a damage to the molecule due to radiation or other factors does not influence the small angle curve as long as there is no structural change in the order of magnitude mentioned above.

As an approximate rule, proteins do not suffer much damage if the duration of X-ray exposure does not exceed about 10 hours (with the usual X-ray generators operated with 50 kV and 30 mA). According to our experience many samples do not lose any more activity after that period of irradiation than a non-irradiated reference sample. On the other hand, there are a number of proteins which are much more sensitive to irradiation. Some of them dissociate and others, for instance some IgG antibodies and enzymes, aggregate under the influence of X-ray radiation. In such cases one has to look for conditions which prevent the dissociation or aggregation as far as possible, or to change the solution as soon as an aggregation or dissociation starts. Another possibility (if enough sample is available) is to measure in a cuvette through which the solution is pumped from a reservoir. Sometimes the use of very low intensity X-rays, or a completely monochromatic radiation (using a graphite crystal, see Chapter 3), prevents the aggregation.

Morphological changes which may occur during irradiation can be monitored by the change of the scattered intensity as a function of time. Repeated recording of the same curve can easily detect and help to eliminate such affects (see Chapter 7).

III. General Data Evaluation

We assume that the following preparatory steps, which are described in detail in the preceding chapters of this book, are already done: measurement of a

concentration series of a monodisperse solution of a protein, subtraction of the blank scattering, normalization of the scattering curve to unit concentration ($I(h)/c$ -curves), desmearing (correction of collimation and wavelength effects), and Fourier transformation. Thus we have the final scattering curves of the various concentrated solutions in the reciprocal space and their most useful presentations in the real space – the $p(r)$ functions. The general data evaluation, which is always the first step with all the various types of evaluation, shall be illustrated in some detail by a practical example in order to explain the way in which molecular parameters can be obtained.

A. Elimination of Concentration Effects

It should again be borne in mind that all of the equations discussed in Chapters 4 and 5 are valid only for sufficiently dilute solutions. A solution is only sufficiently dilute if the distances between the macromolecules in solution are so irregular and so large that no phase relations (interparticle interferences) exist between the waves scattered by the single molecules. On the other hand the scattered intensity becomes too weak and the statistical errors too high by using protein concentrations below about 3 mg ml^{-1} . Thus we have to measure, in any case, a concentration series and to extrapolate to zero concentration.

Interparticle interference usually leads to a decrease of the scattered intensity with increasing concentration at small angles as shown in Fig. 1 for different concentrations of haemocyanin *Astacus leptodactylus*, which is chosen as an example in this chapter (Pilz *et al.*, 1980). Since the distances between the macromolecules in solution are large as compared to the distances within the macromolecules, the concentration effects due to interparticle interference only occur at small angles, according to the law of reciprocity. At larger angles the scattering $\tilde{I}(h)/c$ -curves of all concentrations should coincide (Fig. 1).

The magnitude of the concentration effect depends on the shape and charge of the particle and the solvent (see also Chapter 7). No general function exists which would allow prediction of the magnitude of the concentration effect. Good approximations have been given by Guinier and Fournet (1955) and Porod (1972). In the practical case the magnitude of concentration effects can be seen best by plotting the scattering curves of the various concentrated solutions, normalized to unit concentration, in the way shown in Fig. 1. This plot also shows whether it is necessary to measure any further concentrations.

The different ways normally used for the extrapolation to zero concentration are shown in Figs 2 and 3. The upper (and lower, respectively) thick line is the extrapolated curve; the extrapolation can be carried out either in the normal plot ($\tilde{I}(h)/c$ -values against h , Fig. 2) or in the Zimm plot (known from light scattering, Fig. 3). Within that small angular range at which the scattering curves of the higher concentrated solutions deviate clearly from those of the lower

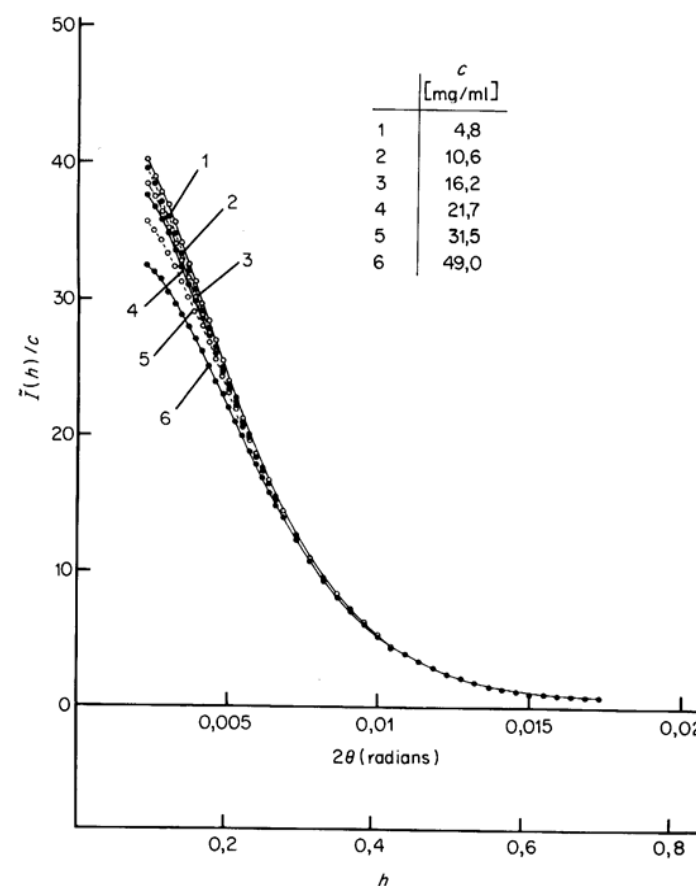


FIG. 1. Slit-smeared scattering curves of a protein (haemocyanin of *Astacus leptodactylus*) for the indicated concentrations c . The curves are normalized to $c = 1$ by plotting \tilde{I}/c ; $h = 4\pi \sin \theta/\lambda$ and λ the wavelength of the CuK_α -line = 0.154 nm (the same holds for all figures given in this chapter); 2θ = scattering angle; \tilde{I} slit-smeared scattering intensity.

ones, the concentrations are plotted in arbitrary units parallel to the abscissa at each measured scattering angle as shown in Figs 2 and 3 (Cleemann and Kratky, 1960). Scattering curves of solutions with relatively low protein concentrations can be extrapolated usually in either of the two plots (normal and Zimm) to zero concentration. If one is forced to use highly concentrated solutions the more precise extrapolation in the Zimm plot should be preferred.

A third possibly way is to calculate the radius of gyration R from the Guinier plot for each concentration (Fig. 4) and to plot the R -values against the concentration c as shown in Fig. 5. Obviously, this extrapolation is only meaningful when the Guinier plot of the curves follows a well defined straight line, as

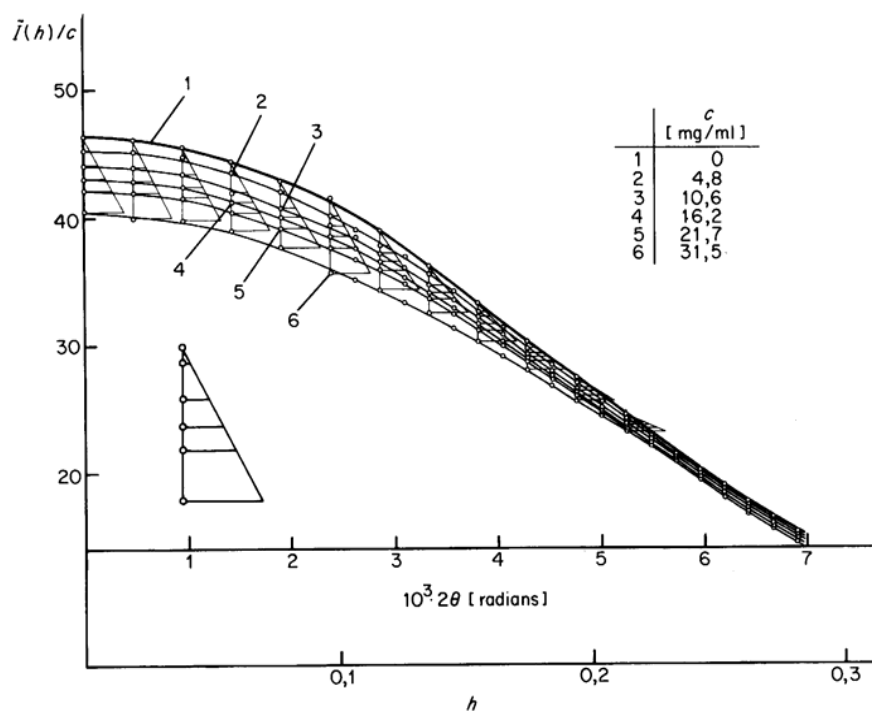


FIG. 2. Innermost portions of the scattering curves shown in Fig. 1. The curves are extrapolated to zero concentration (curve 1) by plotting the corresponding concentration at different scattering angles parallel to the abscissa in arbitrary units, as indicated.

illustrated in Fig. 4. All extrapolations to zero concentration can be done with the smeared (as in Figs 2–5) or unsmeared curves. We routinely perform all three extrapolation procedures on the smeared and unsmeared curves of the same system. An agreement of the extrapolated curves is a good indication that no serious error was introduced by the extrapolation procedure.

Another valuable hint for the correctness of the extrapolation to zero concentration uses the $p(r)$ functions (see Chapter 5). This function is affected considerably by interparticle interferences. It is lowered with increasing distance r and goes through a minimum in the region of the maximum distance D of the particle, as already pointed out by Damaschun *et al.* (1973). In Fig. 6 the distance distribution functions for haemocyanin in various concentrations are shown. It is clearly seen that the minimum is most pronounced for the highest concentration and that it disappears for the curve extrapolated to zero concentration. The $p(r)$ function ends with a negative part only for particles having regions with different electron density of different signs at the distal ends. Since such a

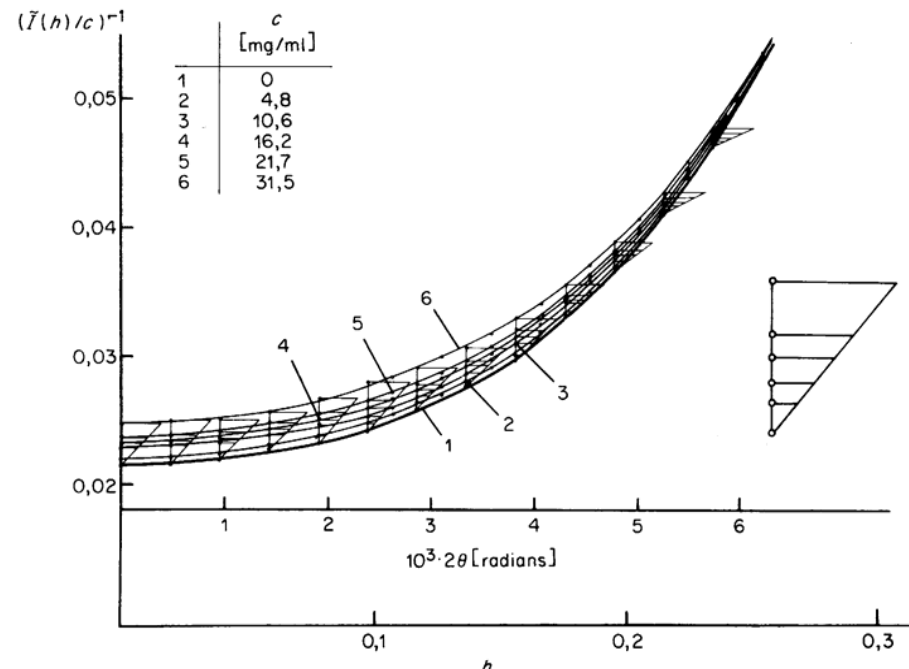


FIG. 3. Innermost portions of the scattering curves shown in Fig. 1 in a Zimm-plot. The curves are extrapolated to zero concentration in the same way as described in Fig. 2.

configuration can be excluded for proteins, concentration effects can easily be recognized from the $p(r)$ functions.

B. Molecular Parameters

1. RADIUS OF GYRATION

The radius of gyration R of a dissolved particle is one of the most important and most precise parameters obtained by SAXS and it can be determined in several different ways.

The most common method uses the Guinier approximation described in detail in Chapters 2 and 4. Figure 4 shows the Guinier straight lines of haemocyanin *Astacus leptodactylus* in various concentrations. From the slopes of the straight lines the radii of gyration can be calculated. It should again be pointed out that the smallest angle measured has to be $h \leq \pi/D$ (see Chapter 4). Extrapolation to zero concentration (compare Figs 2, 3 and 5) yields $\tilde{R} = 6,56$ nm (smeared value) (final desmeared value: $R = 6,90$ nm).

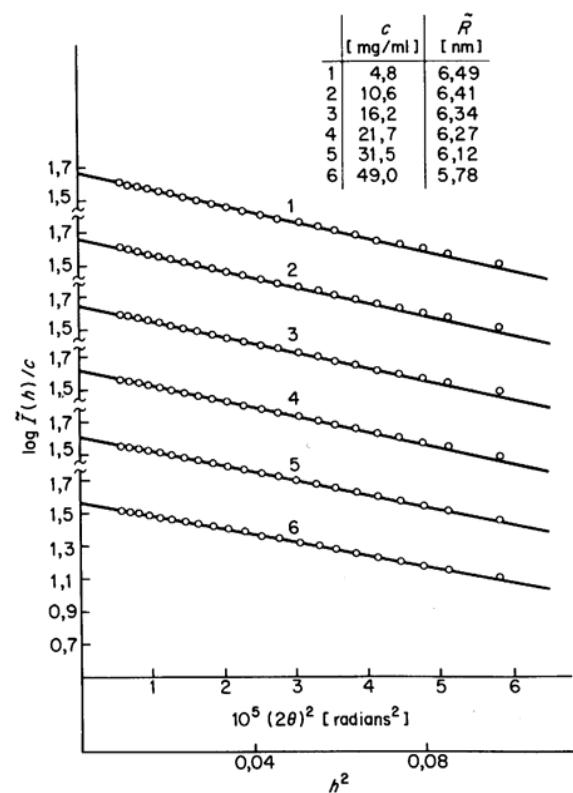


FIG. 4. Guinier plots of the innermost portions of the scattering curves shown in Fig. 1. The values of the slit-smeared radii of gyration \tilde{R} obtained for the different concentrations are indicated.

The radius of gyration can also be determined from the distance distribution function ($p(r)$). This method is particularly powerful when used in connection with the indirect Fourier transformation described in Chapter 4. It has the advantage that the whole scattering curve is used for the determination of the radius of gyration and not only the innermost portion as is the case with the Guinier method. Using this method we found for haemocyanin that $R = 6,92$ nm.

A third way to estimate the radius of gyration is only possible for homogeneous and isometric particles, whose shape does not deviate strongly from a sphere or cube as is sometimes the case with globular proteins. The scattering curve of these particles usually shows well pronounced maxima and minima and R can be calculated from the position h_1 of the first subsidiary maximum

$$R = \frac{4,5}{h_1} \quad (1)$$

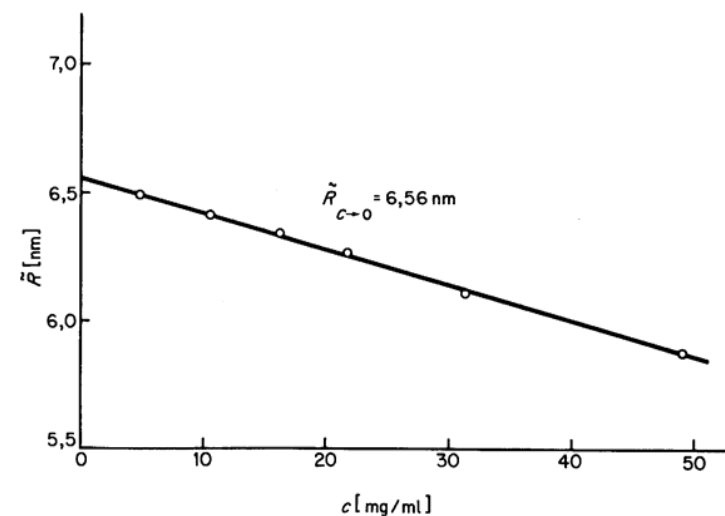


FIG. 5. Slit-smeared radii of gyration \tilde{R} calculated from Fig. 4 plotted against the protein concentration c .

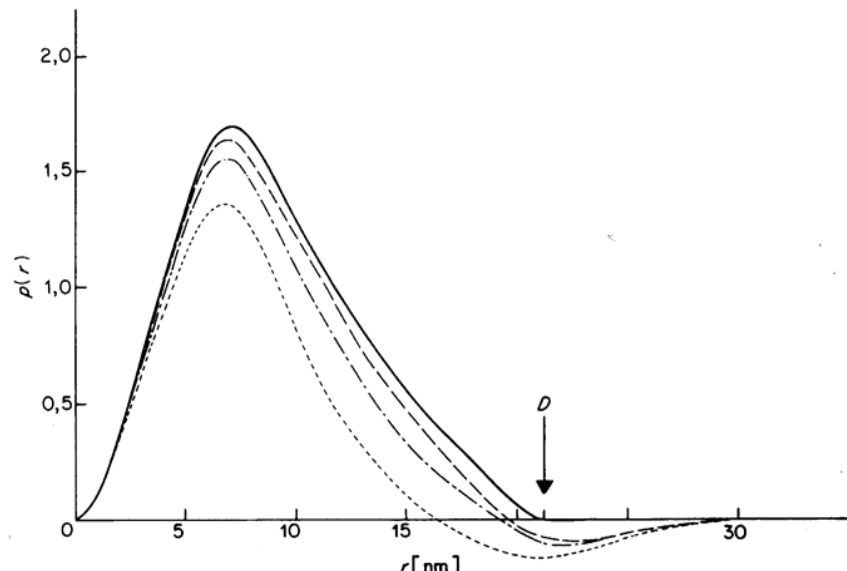


FIG. 6. Distance distribution functions $p(r)$ for various concentrated solutions of the haemocyanin of *Astacus leptodactylus*. Curve (---), $c = 48 \text{ mg g}^{-1}$; curve (- - -), $c = 21,6 \text{ mg g}^{-1}$; curve (----), $c = 4,8 \text{ mg g}^{-1}$, curve (—), c extrapolated to zero; D = maximum distance of the particle.

2. MOLECULAR WEIGHT

The molecular weight M_r is calculated using Eqn (42) (Chapter 4). Especially with proteins, it is necessary to determine the isopotential specific volume v'_2 as accurately as possible (see Chapter 7) because it enters the equation in the square of a relatively small difference thus leading to a strong amplification of errors. (Errors of 1% in the v'_2 value, for instance, produce errors of 4–5% in the value of M_r , when proteins are investigated in the usual dilute buffers.) (Z_1 , the number of moles of electrons per gram of the solute (protein), generally has the value 0,535 for proteins.)

The intensity at zero angle $I(0)$ is usually obtained by extrapolation to zero concentration shown in Figs 2 and 3 and the intensity of the primary beam is measured using one of the methods described in Chapter 3, Section I. For haemocyanin *Astacus leptodactylus* M_r was found to be $854\,000 \pm 5\%$.

3. VOLUME

The volume V of the protein particle is determined by Eqn (62), Chapter 4; $I(0)$, the intensity at zero angle and the invariant Q enter the equation. Q is given by the integral

$$Q = \int_0^\infty I(h) \cdot h^2 dh = \int_0^{h^*} I(h) \cdot h^2 dh + \frac{k_1}{h^*} \quad (2)$$

Obviously, it is not possible to record the scattered intensity up to the angle ∞ . The integration is therefore carried out numerically with Simpson's formula up to a relatively large angle h^* ; the remaining tail end of the curve is integrated analytically: according to Porod (1951), the tail end of a scattering curve oscillates about $k_1 h^{-4}$. The tail end constant k_1 is determined from a suitable plot ($I(h)$ v. h^{-4}), which should oscillate about a straight line with slope k_1 . This determination, however, is never very accurate, and the analytically computed portion of the invariant (i.e. the term k_1/h^* , see Eqn (2)) should be as small as possible. Usually, its contribution to the total of Q is less than 10%. Figure 7 shows the plot $I(h) \cdot h^2$ v. h . The invariant is equal to the area under this curve. Analytical integration started at the angle h^* . The value thus obtained for the volume of haemocyanin is $1,07 \times 10^4 \text{ nm}^3$.

It may be necessary to point out that Eqn (2) is exactly valid only for particles with homogeneous electron density and the volume can be determined therefore with much less accuracy than, for instance, the radius of gyration.

A method for approximate calculations of the volume of compact homogeneous particles by use of a finite portion of the scattering curve has been suggested by Kayushina *et al.* (1974).

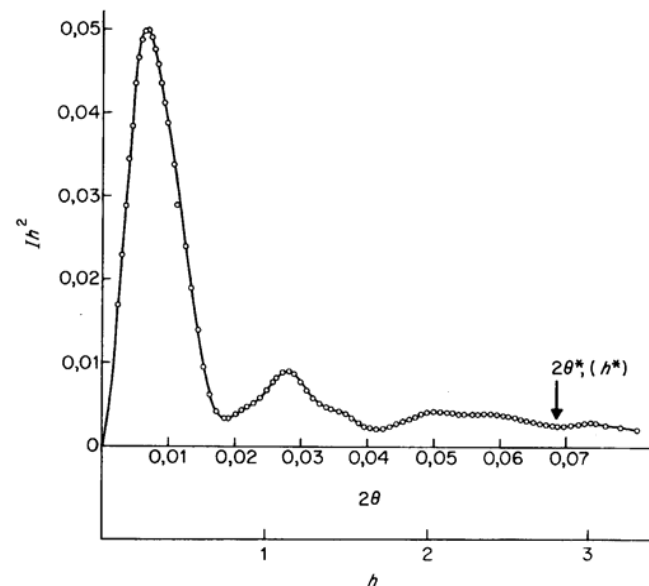


FIG. 7. Plot of $I(h) \times h^2$ v. h used for the calculation of the invariant Q of haemocyanin of *Astacus leptodactylus*. From zero angle up to $(2\theta)^*$ (resp. h^*) the integration is carried out by Simpson's formula.

4. DEGREE OF HYDRATION

Water molecules are essential structural features in proteins, both in the crystal and in solution; the volume of the dissolved protein determined by SAXS is always a "hydrated volume" including a smaller or larger number of water molecules, which are loosely bound between the folded polypeptide chains and subunits forming the complete structure. It is of some interest to know this degree of hydration (or degree of swelling) f_s . It can be calculated from the hydrated particle volume V , the molecular weight M_r and the isopotential specific volume v'_2

$$f_s = \frac{N_L V}{v'_2 M_r 10^{21}} \quad (3)$$

From this the number of grams of water per gram of protein can be calculated

$$\text{grams H}_2\text{O/grams protein} = v'_2(f_s - 1).$$

For haemocyanin *Astacus leptodactylus* f_s was found to be 1,37 which corresponds to about 0,3 g H₂O per gram of protein.

The commonly used expressions "degree of swelling" or "degree of hydration"

are sometimes misleading. The idea of these expressions is not that a protein is swollen in water like a sponge, but that the relatively low resolution obtained by SAXS does not allow determination of only the protein volume. Water molecules in small curves and clefts in between the polypeptide chains belong to the volume determined by SAXS and are the reasons for the difference between the volume of the pure protein mass and that determined by SAXS. Therefore the expression "degree of hydration" is to be preferred to the misleading expression "degree of swelling".

5. MAXIMUM DIAMETER

It follows immediately from its definition that the distance distribution function $p(r)$ is zero for all distances larger than the maximum particle diameter. Figure 6 shows the maximum distance D of haemocyanin *Astacus leptodactylus* to be 21.5 nm.

6. OTHER STRUCTURAL PARAMETERS

The SAXS parameters discussed so far (radius of gyration, molecular weight, volume and maximum diameter) are the ones most commonly used to characterize dissolved particles. There are a number of other structural parameters applicable to the description of a general colloid-type distribution of matter.

One of these parameters is the *specific inner surface* O_s (see Chapters 2 and 4), which is identical with S/V , whereby S corresponds to the inner surface of the dissolved particle and V is the volume of the particle.

The *transversal or intersection length* \bar{l} is defined as the average of all intercepts obtained by intersecting the disperse phase in all possible directions. It is proportional to the inverse of the specific inner surface; for a system of identical particles

$$\bar{l} = \frac{4}{O_s} = \frac{4V}{S} \quad (4)$$

C. Shape

The object of the interpretation of SAXS of proteins is to get detailed knowledge of their structure, which may contribute to the understanding of their biological function. In general, a structure analysis from SAXS data cannot start from an atomic model as the experiment does not allow such a resolution.

The structural parameters of the macromolecule mentioned so far can be calculated directly from the scattering curve or its Fourier transform; they are independent of the model. Information on the shape of a protein is usually obtained by a trial and error procedure. The basic strategy is to look for models

which have the same structural parameters and to compare the experimental curves with the curves calculated for various models. This process can be carried out in reciprocal space (with the scattering curve), and in real space (with the distance distribution function). All models not equivalent in scattering can be rejected, models whose scattering curve coincides (within the experimental error) with the observed curve are accepted and presented for discussion (see Chapter 4).

It should be pointed out that the coincidence of experimental and calculated scattering curves only proves that the model is equivalent in scattering. To prove that a detailed model is the only right one is not possible. Furthermore, it should be mentioned that the analysis of small angle X-ray scattering as discussed in this chapter in terms of shape models is only meaningful for chemically homogeneous structures, like proteins, which have only small density fluctuations within the molecule. In this case the scattering is mainly determined by the shape of the particle and the contribution of the internal structure becomes negligibly small at low resolution.

The overall shape – whether the molecule is spherical, flat, elongated, contains hollow spaces etc. – can be suggested if the scattered intensity is known to high precision. In summary we can say that SAXS provides valuable information concerning tertiary and quaternary structure of proteins and there are also first attempts to apply SAXS to problems concerning the secondary structure of proteins. The possibilities of obtaining this information is discussed with practical examples in more detail in Section V. In the following, we will confine ourselves to the basic procedure in which an overall shape can be determined.

The first idea of the overall shape of a macromolecule is obtained from a comparison of its scattering curve with theoretical curves of simple triaxial full and hollow bodies with various geometries and various axial and hollow-space ratios. It is most convenient to use double-logarithmic plots for this purpose, since a comparison in this plot depends only on the shape of the molecule and is independent of the size of the particle and the scattered intensity. An example is shown in Fig. 8 for haemocyanin, whose experimental curve is compared with those of a sphere and ellipsoids of various axial ratios.

Deviations between the observed and theoretical curves of simple triaxial bodies may be explained by consideration of a more complicated model. For proteins, such deviations from the theoretical curve of a homogeneous, triaxial body can usually be explained by deviations from a simple triaxial shape or in terms of a well defined substructure, e.g. originating from the arrangement of subunits. In other words, this substructure causes deviations from the assumption of homogeneous electron density implicit in the simple triaxial models.

Since there is a very great variety of possible substructures, one should use any accessible information for the construction of a detailed model. Sometimes it is possible to split a protein into fragments, dissociation products or smaller

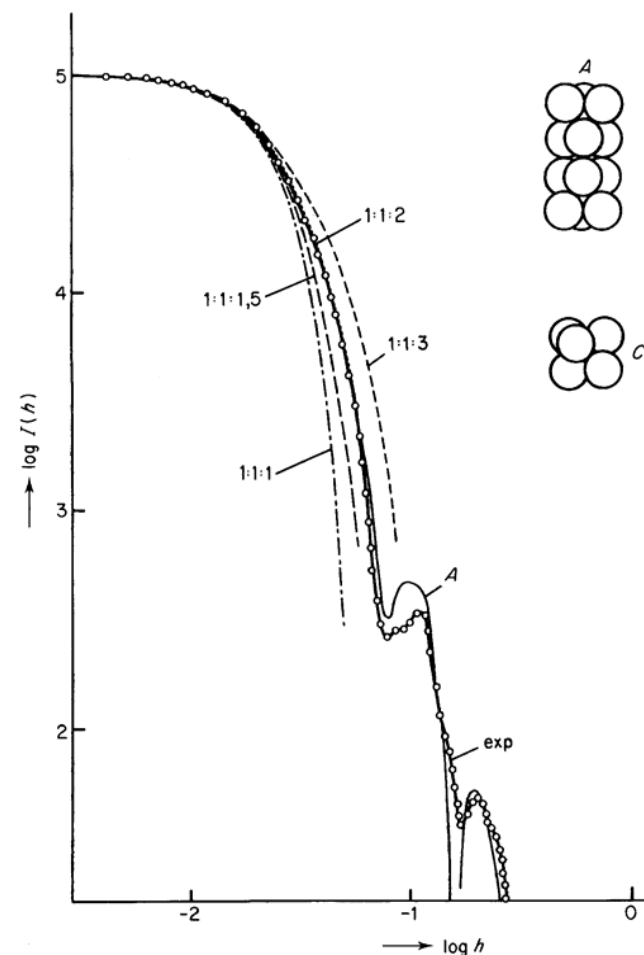


FIG. 8. Comparison of the experimental curve of the haemocyanin of *Astacus leptodactylus* with theoretical curves of a sphere (1:1:1), various ellipsoids of revolution of the given axial ratios and the Model A in a log-log plot. C is the model of the monomer.

subunits without changing their conformation. The knowledge of the structural parameters and the overall shape of these fragments or subunits can be a valuable help in finding a model for the whole protein, as shown in Section V.C4. Further information obtained from biochemical studies, such as number and size of polypeptide chains, may give valuable hints to the number and size of subunits. Electron microscopy may yield useful information concerning their arrangement. Finally, from the SAXS curve itself, information on subunits can be obtained as discussed in Section V.C3.

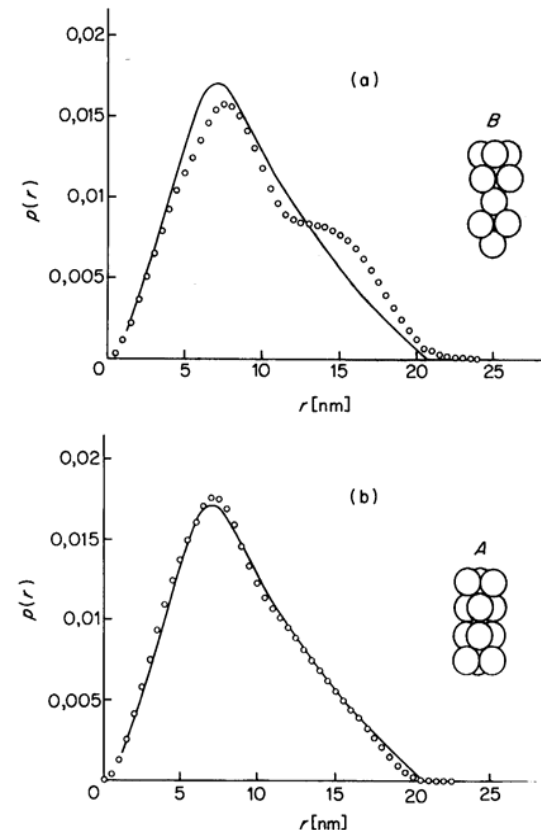


FIG. 9. Distance distribution function $p(r)$ of the haemocyanin of *Astacus leptodactylus* (○○○) compared with the calculated $p(r)$ -function of (a) model B and (b) of model A.

Now let us go back to our practical example of haemocyanin *Astacus leptodactylus*. From the comparison with simple triaxial bodies in Fig. 8 we get the information that its overall shape is somewhat elongated with a main axial ratio of about 1:1:2 and that it can be described to a first approximation by a simple ellipsoid or cylinder of homogeneous electron density.

The information from biochemical studies was a valuable help in discovering that this protein is a dimer which can be split into two monomers, each consisting of six nearly identical subunits. The investigation of the monomers allowed the presentation of model C (Fig. 8) for the monomers, which is equivalent in scattering.

The next question was to find out in which way these monomers were arranged to form the dimer. A larger number of models were calculated arranging

the monomers in symmetrical and asymmetrical ways and assuming that they were connected either very loosely by touching only at one point or by overlapping of larger areas.

Distinguishing between these models is possible, for instance, by the comparison of the distance distribution functions. Model A in Fig. 9b, for instance, fits well the experimental $p(r)$ functions and the scattering curve in the reciprocal space (Fig. 8), while Model B in Fig. 9a shows clear deviations. Model B has a low electron density in between the monomers which causes a decrease in the distances in the range of 12 nm and, of course, an increase of the larger distances in the range of 16 nm, clearly seen by the minimum and the shoulder in the model curve.

IV. Special Data Evaluation

A. Spherical Proteins

For particles with spherical symmetry it is possible to determine, besides other structural parameters, the radial electron density distribution from the Fourier transform of the scattering amplitudes, and from $p(r)$ functions obtained by the indirect Fourier transformation (see Chapter 4). Lipoproteins and the spherical viruses (resp. their protein shells) especially show a highly spherical symmetry. Since these groups of proteins and the determination of the radial electron density distribution are discussed in detail in Chapters 9 and 10, we want to cite only a few papers dealing with spherical proteins. Fischbach and Anderegg (1965) and Bieling *et al.* (1966) determined the radial electron density distribution of apoferritin, Anderegg (1967) and Zipper *et al.* (1971) those of different viruses and their protein shells.

B. Elongated Proteins

Although most of the water-soluble proteins have a globular shape, some are known to be elongated either in the monomeric form or in the form of rod-like aggregates.

1. CROSS-SECTIONAL FACTOR

As already discussed in Chapter 2, the scattering curve of a particle, one dimension of which is very large in comparison to its other dimensions, can be split into two factors, one factor which is related to the length of the rod-like particles and depends upon $1/h$ and the cross-sectional factor $I_c(h)$. Multiplying the scattering curve by h , the factor of the length can be eliminated and the

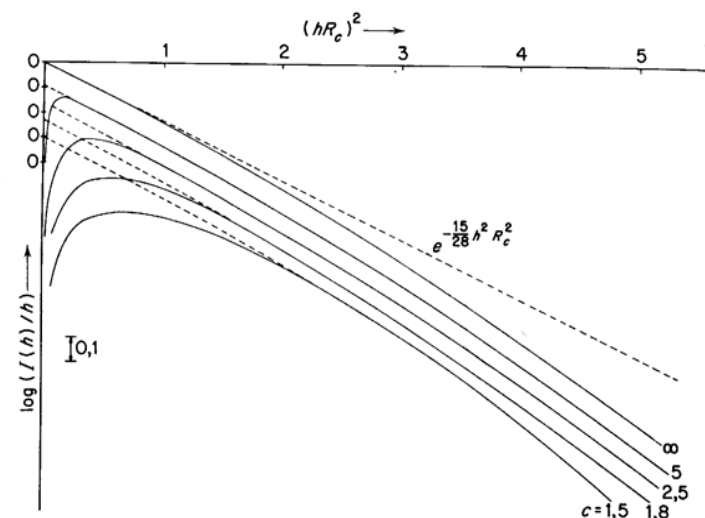


FIG. 10. Theoretical cross-section curves of ellipsoids with an axial ratio 1:1: c shown in Guinier plot (Mittelbach, 1964).

curve then obtained represents only the cross-sectional factor $I_c(h)$, i.e. $I(h) \cdot h$. From the cross-sectional factor a number of parameters concerning the cross-section can be calculated; the radius of gyration of the cross-section R_c , molecular weight per unit length M_c and the area A_c of the cross-section. A comparison of the cross-sectional factor with theoretical curves of various cross-sections give information on the shape of the cross-section. Isotropic cross-sections show the steepest curves, while increasing anisotropy leads to a flattening of the cross-section curves.

There are not many proteins which are extremely long in comparison with their cross-sections, and thus correspond to the requirements stated above. In practice it is therefore of more general interest to see whether it is also possible to obtain information on the cross-sections of particles with a length which is only a few times larger than the other dimensions.

In Fig. 10 the cross-section curves (Mittelbach, 1964) of ellipsoids with the axial ratio 1:1: c are shown in the Guinier plot. These curves lead to two conclusions:

- (1) The cross-section curves of particles the lengths of which are only several times their diameters differ from the cross-section curves of very long particles (dashed line) by their low intensities at very small angles. This low intensity becomes the more pronounced, that is, the curve deviates already from the Guinier straight line at correspondingly larger angles, the smaller the length the particle is in comparison to its diameter.

This low intensity at small angles is readily understood since particles which are not very long naturally lack large intraparticulate distances and thus also the corresponding scattering at small angles.

(2) It is seen from Fig. 10, that the Guinier linearity of the cross-section factor is already apparent at a ratio of diameter to length of about 1:2. One can thus obtain rough information about the cross-section of a protein molecule which is only about twice as long as its diameter. Exact data on the cross-section, however, can be usually obtained only when the ratio diameter to length is clearly larger than 1:2. The evaluation is done by correcting the low-angle region of the cross-section factor, in the manner illustrated in Fig. 10, that is, by extrapolating the scattering curves to zero angle (dashed lines).

From these corrected cross-section curves for particles, which are not very elongated, all parameters of the cross-section (R_c , M_c , A_c , anisotropy) discussed above for very long particles, can be determined. Furthermore, the cross-section can be calculated not only for rigid rods, but also for slightly bent rods.

2. CROSS-SECTION FROM THE $p(r)$ -FUNCTION

An elongated particle can also be recognized directly from the form of the distance distribution function. Particles with a constant cross-section (long cylinders or prisms) show a characteristic linear decrease at large r -values, as pointed out in Chapter 5 (compare Fig. 3). A necessary condition for recognizing a cross-section is again that the maximum dimension of the cross-section c_{\max} is much smaller than the maximum dimension D of the whole particle

$$\frac{D}{c_{\max}} \geq 2,5 \quad (7)$$

From the slope of the linear region at large r -values the area A_c of the cross-section can be calculated. Since the method for obtaining information about the cross-section also from the $p(r)$ function, has only recently been developed (Glatter, 1979), no published practical examples are so far available. The calculation of the distance distribution function $p_c(r)$ and radial inhomogeneity is described in Chapter 5.

3. LENGTH OF THE PARTICLES

When the length of a protein particle does not exceed 100 nm, it is possible to determine not only the radius of gyration of the cross-section R_c but also the radius of gyration R of the whole particle, provided that in very long particles sufficiently small angles are measured. When R and R_c are known, the length L of the particle can be directly calculated from

$$R^2 - R_c^2 = \frac{L^2}{12} \quad (5)$$

for a prism, and

$$R^2 - R_c^2 = \frac{c^2}{5} \quad (6)$$

for an ellipsoid, where c is the largest semi-axis.

4. PRACTICAL EXAMPLE

Beef liver glutamate dehydrogenase may serve as an example, since this enzyme forms elongated aggregates. The enzyme was studied by Sund *et al.* (1969) in a concentration range of 1 mg ml^{-1} to 33 mg ml^{-1} ; in this range of concentration the glutamate dehydrogenase exists as a mixture of aggregates, the average molecular weight of which increases from about $0,5 \times 10^6$ to 2×10^6 with increasing concentration.

But while the radius of gyration R and the molecular-weight M_r of the whole particle varies greatly in the concentration range under investigation, the cross-section curves show almost identical slopes in the Guinier plot (Fig. 11). The radii of gyration of the cross-section R_c , calculated from the slopes of the straight lines, and the masses per unit length M_c , calculated from the intensities at zero angle, are also identical as seen in the plot of the R_c and M_c values versus the enzyme concentration c (Fig. 12). It can be clearly seen that both the radii of gyration and the masses per unit length of the cross-section are independent of the concentration and thus independent of the size of the associated molecules. This proves that with this enzyme a linear aggregation takes place in the direction of the long axis while the cross-section remains unchanged.

By comparing the shape of the experimental cross-section curves with theoretical curves for elliptical cross-sections of varying axial ratios, it is also possible to obtain information on the shape of the cross-section. Figure 13 shows this comparison for solutions of various concentrations and it is seen that regardless of the concentration, there is always a largely isotropic cross-section which is either circular or slightly elliptical.

The data which can be obtained on the size and shape of the whole molecule are, because of the mixture of aggregates, much less accurate; nevertheless, it can be shown from these data, too, that a linear association must take place. From the radii of gyration R obtained for the whole particles and the known R_c value, the average length L of the aggregates can be calculated. If these lengths are plotted against the average molecular weights (Fig. 14) it can be seen that there is a linear association; that is, the lengths increase in proportion to the molecular weights of the aggregates. Generally we can say that in any case where data on the cross-section of a particle can be calculated, a more

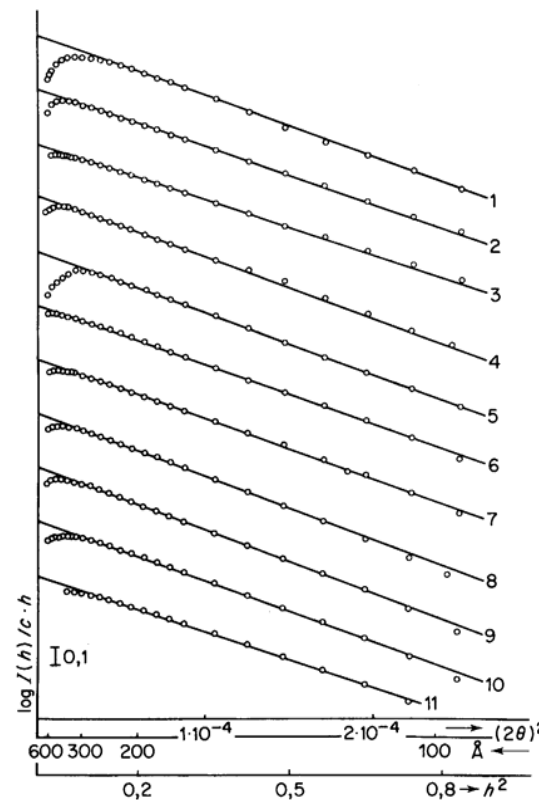


FIG. 11. Guinier plot of the cross-section factors of glutamate dehydrogenase recorded for eleven different concentrations in the range between 1 mg ml^{-1} and 33 mg ml^{-1} . The resulting values for the radius of gyration of the cross-section R_c and the mass per unit length M_c are plotted against the concentration in Fig. 12 (Sund *et al.*, 1969).

detailed picture of its shape is obtained. With very long particles (several thousand angstroms), the length of which cannot be determined by SAXS, at least information on the shape and mass per unit length of the cross-section can be obtained. With associating proteins the type of association may be determined as shown with glutamate dehydrogenase.

5. RADIAL ELECTRON DENSITY DISTRIBUTION

As already discussed in Chapter 4 it is possible to calculate the radial electron density distribution of a circular cross-section of very elongated particles using the Hankel transform (Fedorov and Aleshin, 1966; Fedorov, 1970).

Fedorov *et al.* (1977) studied microtubule structures by this method.

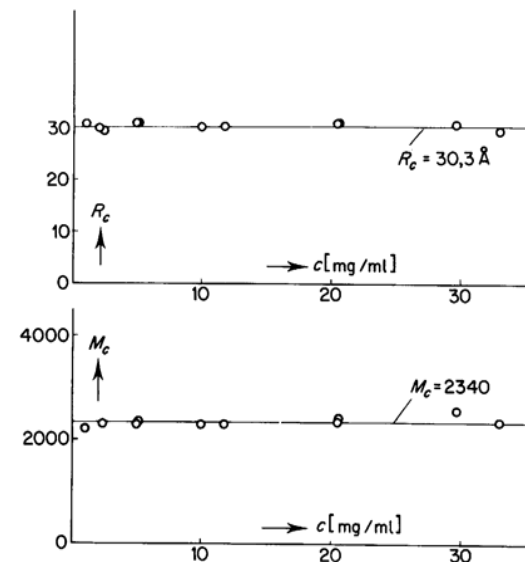


FIG. 12. Radius of gyration of the cross-section R_c and mass per unit length M_c of glutamate dehydrogenase as a function of the concentration c (Sund *et al.*, 1969).

Microtubules in solution form hollow cylinders, the length of which considerably exceeds their diameter. Figure 15 shows the obtained electron density distribution of the microtubule cross-section (electron density $\rho(r)$ plotted against the radial distance r). The distribution function shows the presence of an internal cavity (or very low density region) with a diameter of about 140 Å. The external diameter of the cylinder is about 290 Å and the wall thickness about 75 Å. Similar studies have been performed on tobacco mosaic virus (Fedorov, 1971) and on flagella from *Salmonella* (Yamaguchi *et al.*, 1974).

C. Lamellar Proteins

1. THICKNESS-FACTOR

By a lamella we understand a particle in which two dimensions are large compared with the third dimension (the thickness T). As already discussed in Chapter 2 the scattering curve of a lamellar particle is composed of a factor of the area, which is proportional to h^{-2} , and a thickness factor of the Gaussian type. By multiplying the scattering curve by h^2 the factor of the area can be eliminated and the remaining thickness factor can be plotted according to Guinier. From the slope of the straight line thus obtained, the radius of gyration R_t of the thickness is calculated, which when multiplied by $\sqrt{12}$ gives the thickness T itself, provided that the flat particle has a homogeneous electron density.

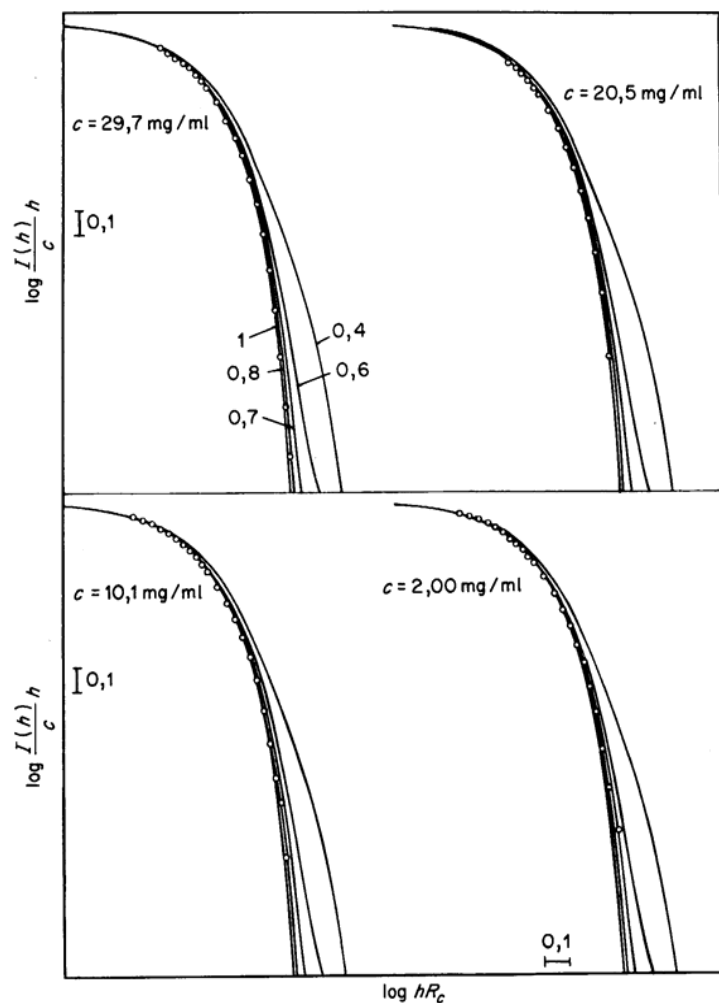


FIG. 13. Comparison of the experimental cross-section curve (\circ) with theoretical curves (full lines) for elliptical cross sections with axial ratios $(2a:2b)$ between 1:1 and 1:0.4 (in log-log plot). c is the concentration of glutamate dehydrogenase (Sund *et al.*, 1969).

Though these relations are calculated for particles the thickness of which is very small as compared to the dimensions of the plane of the lamella, the thickness of lamellar particles can still be determined even if the length and the width of the particle are only about twice or three times larger than the smallest dimension (the thickness). In analogy to the cross-section curves of not very elongated rods, a lack of intensity at small angles is also observed in this case for the same reasons.

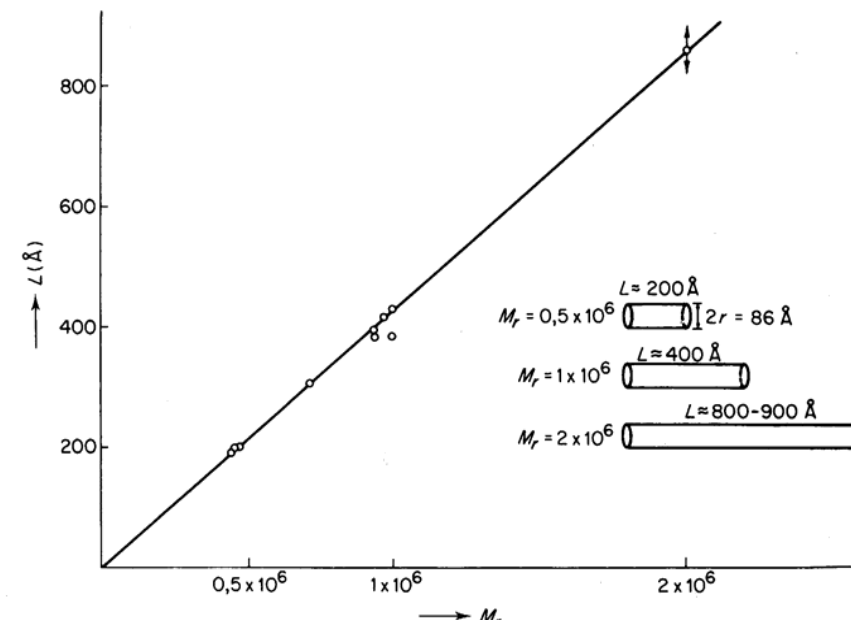


FIG. 14. Average length L of glutamate dehydrogenase particles in phosphate buffer, pH 7.6, as a function of the average molecular weight M_r (Sund *et al.*, 1969).

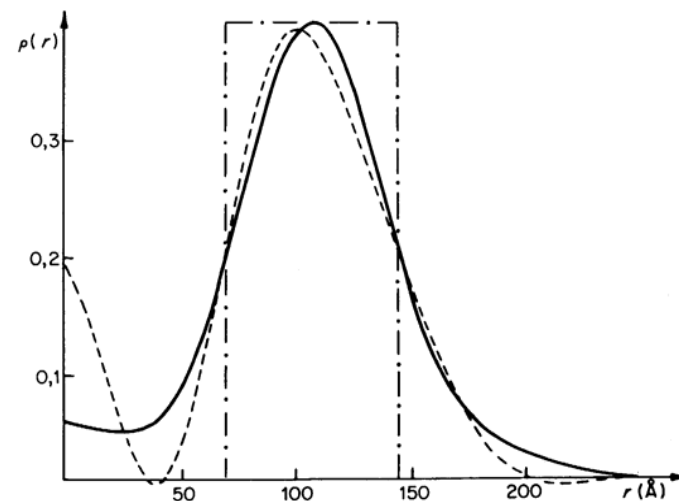


FIG. 15. Function of electron density distribution $\rho(r)$ of the microtubule cross-section. (—) Function corresponding to the alternating order of signs (+ - + -) of the scattering amplitude; (---) function corresponding to a less reliable variant of sign alteration (+ - + +) of the scattering amplitude; (- - -) cylinder with the internal diameter of 140 \AA and 290 \AA , respectively; r = radius of the circular cross-section (Federov *et al.*, 1977).

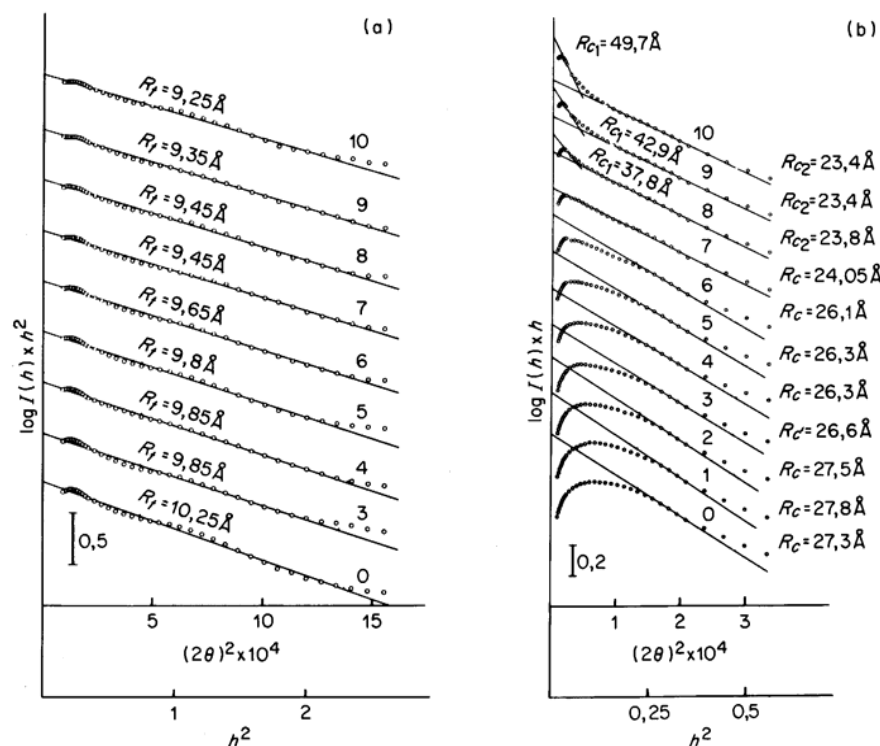


FIG. 16. Thickness plots (a) and cross-section plots (b) of aggregating substrate-free malate synthase. Time interval between subsequent curves: 5.7 hours; R_t = radius of gyration of the thickness; R_c = radius of gyration of the cross-section (Zipper and Durchschlag, 1980a).

The precision of the determination of the thickness is, however, usually not as great with proteins as that for the determination of the cross-sections of elongated particles (see also Chapter 10). Thickness can be determined not only with plane lamellar particles but also with bent lamellar (Pilz *et al.*, 1970) or flat star-shaped particles (Wilhelm *et al.*, 1977).

2. THICKNESS FROM THE $p(r)/r$ -FUNCTION

The thickness of flat particles can be determined also in the real space from the $p(r)$ function or better from the $p(r)/r = f(r)$ function as discussed in Chapter 5. The shape of the $f(r)$ function allows the recognition of lamellar particles. Flat particles with cross-sectional or in-plane inhomogeneity are discussed in Chapter 5.

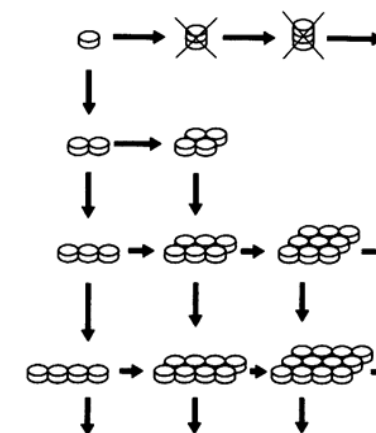


FIG. 17. Tentative schema of X-ray induced aggregation of malate synthase, derived from small angle X-ray scattering measurements (Zipper and Durchschlag, 1980b).

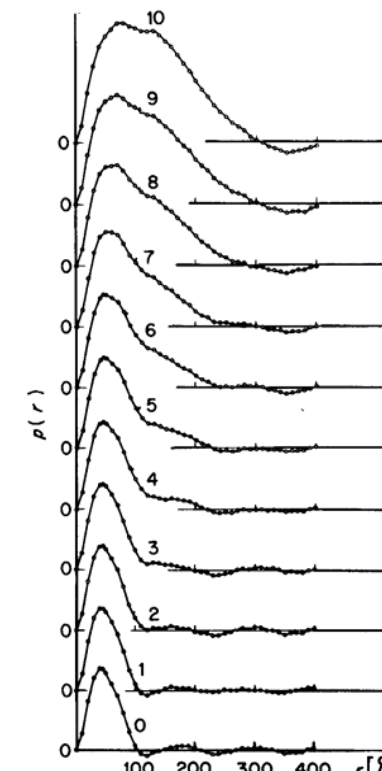


FIG. 18. Distance distribution functions $p(r)$ of aggregating substrate-free malate synthase. Time interval between subsequent curves: 5.7 hours (Zipper and Durchschlag, 1980a).

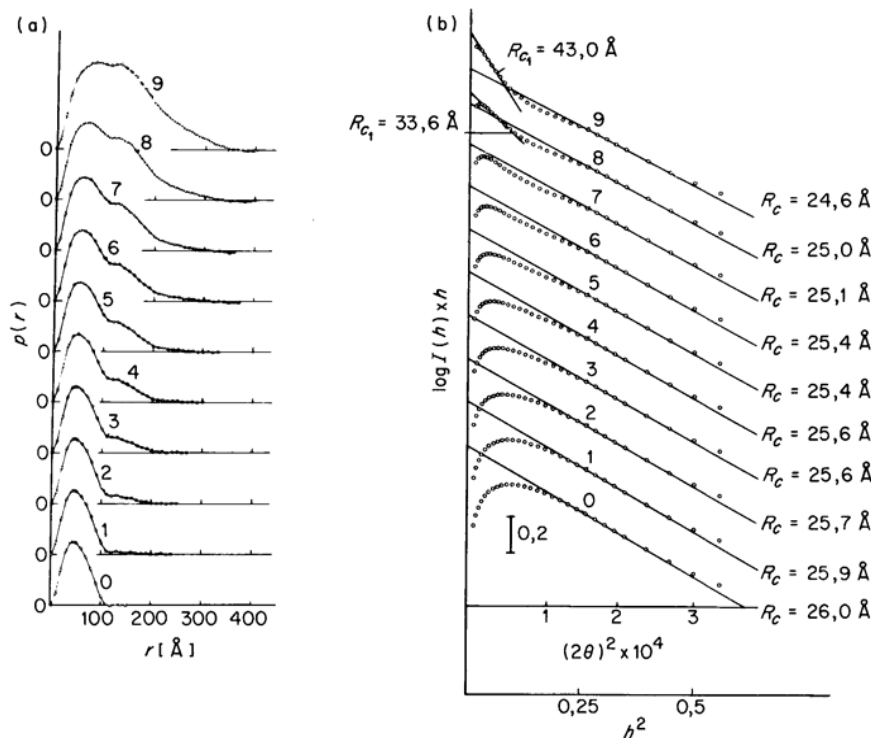


FIG. 19. Computer simulation of the aggregation process: distance distribution functions $p(r)$, (a) and cross-section plots (b), calculated for various stages of aggregation; R_c = radius of gyration of the cross-section (Zipper and Durchschlag, 1980c).

3. PRACTICAL EXAMPLES

The malate synthase studied by P. Zipper and H. Durchschlag (1978a, 1978b) may serve as an example for lamellar proteins. The shape of the enzyme is best approximated by a flat ellipsoid of revolution with the axes $a = b = 6.1$ nm and $c = 2.2$ nm.

Usually, enzymes are not affected by the exposure to X-rays in the course of a small angle investigation. Malate synthase showed a clearly different behaviour. Zipper and Durchschlag observed considerable changes in the scattering behaviour after prolonged irradiation. The radius of gyration and molecular weight increased as a function of irradiation time, indicating an aggregation to larger particles. This effect was studied systematically by varying the time of exposure to X-rays and the intensity of the incident radiation.

These small angle investigations did not only yield information on the aggregation rate, but also on the aggregation process itself: it turned out that the

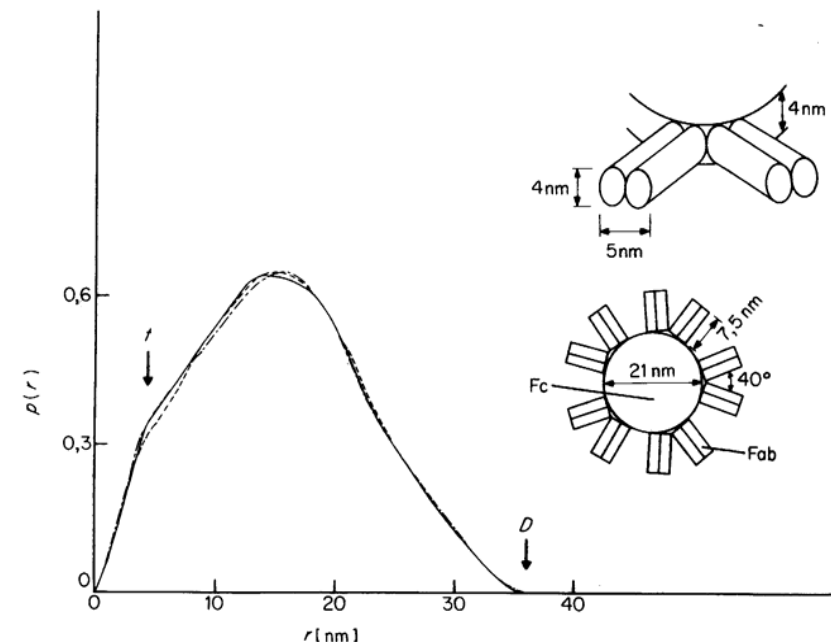


FIG. 20. Distance distribution function $p(r)$ of a human Waldenström IgM compared with the $p(r)$ function of the model shown in the figure, which has a thickness of 4 nm indicated by a kink at about 4 nm (arrow) (Wilhelm *et al.*, 1977).

thickness factor remains unchanged during aggregation (Fig. 16a). This rules out a stacking of the disc-like particles in the direction of the rotation axis (like coins in a moneyroll). Small aggregates show one and higher aggregates show two cross-section factors (Fig. 16b), which led the authors to suggest the association pattern indicated in Fig. 17. The first few molecules aggregate in one direction forming a linear row of side-by-side particles. This leaves the thickness of the flat particles unchanged and one cross-section factor is found, corresponding to the cross-section of the linear row of particles. For larger oligomers, aggregation in a second direction has to be assumed, indicated by the existence of a second cross-section factor. This aggregation pattern is also supported by the distance distribution function $p(r)$ (Fig. 18). The maximum distance increased stepwise, each step being roughly equal to the diameter of a single enzyme molecule (Zipper and Durchschlag, 1980a).

All samples investigated became more and more polydisperse in the course of the aggregation. The authors performed a computer simulation of the assumed aggregation model, calculating distance distribution function and cross-section curves for the various states of aggregation (Fig. 19). The agreement with the corresponding experimental curves (Fig. 16b and Fig. 18) is quite striking. It

illustrates that sometimes even quite complex polydisperse systems can be successfully investigated by the small angle X-ray scattering technique.

A thickness factor was found also for the macroglobulin molecule IgM which is best described by the flat star-shaped model seen in Fig. 20 (Wilhelm *et al.*, 1977). IgM molecules show, also, a tendency to form dimers and trimers. It was found that no increase in the thickness takes place upon aggregation. This is only possible by combining the molecules side by side as is shown for the first steps with the malate synthase in Fig. 17.

V. Structure of Proteins

In this section I want to discuss the information on the secondary, tertiary and quaternary structure of a protein that can be obtained by SAXS.

A. Secondary Structure

It seems necessary to point out that SAXS is not especially suitable for obtaining information on the secondary structure; optical rotary dispersion (ORD) and circular dichroism (CD), for instance, are preferable in this case. But it is, of course, a great advantage if it is possible to obtain, besides the information on the tertiary and quaternary structure, also hints concerning the type of secondary structure mainly present in the protein (α -helix, β -structure). Information on the secondary structure means, of course, an increase in structural resolution, which always requires the knowledge of the scattering curve to wider angles.

Grigoryev *et al.* (1971) tried to find empirical rules connecting the characteristics of large X-ray scattering with the secondary structure of polypeptide chains. First of all they studied synthetic polypeptides having in solution an α -helical, pleated sheet and coil-like structure. They found that α -helical and β -structures cause specific maxima, which appear at large scattering angles. In Fig. 21a the scattering curves of poly-L-glutamic acid (PGA) at large angles are shown, and in Fig. 21c those of poly-S-carboxamethyl-L-cysteine (PCMC). The curve with the maximum in Fig. 21a represents the α -helical structure of PGA in the uncharged state, while the curve with the maximum in Fig. 21c presents the β -structure of PCMC. The difference in the scattering curves and especially the difference in the position of the maximum reflects the difference between α -helical structure and β -structure of the polypeptides. With the ionization of PGA and PCMC accompanied by their transition to the coil-like state, the maxima on the scattering curves disappear (curve 2 in Fig. 21a and 21c).

In order to ascertain that observed differences in the maxima are due to the secondary structure of PGA and PCMC and not to the difference in the side-chain, the authors also investigated the scattering of poly-L-lysine (PL), which

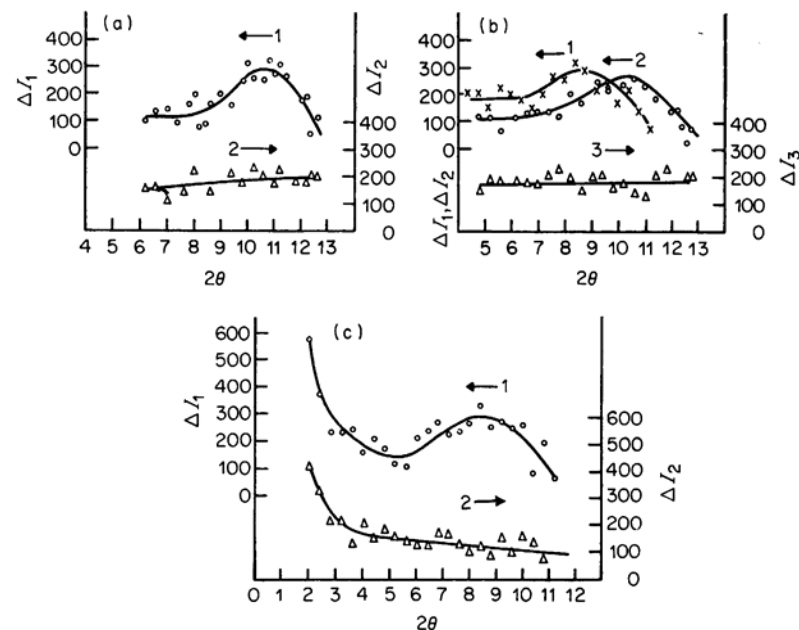


FIG. 21. Outer portions of the scattering curves of the following substances: (a) 2% aqueous PGA solution: (1) 0.2 M LiCl, pH 4.65; (2) 0.1 M LiCl, pH 7.0. (b) 4% aqueous PL solution: (1) 0.22 M LiCl, pH 10.8, 12–14°C; (2) 0.17 M LiCl, pH 11.5 after heating for 30 min at 50°C; (3) 0.22 M LiCl, pH 7.0. (c) 3% aqueous PCMC solution: (1) 0.06 M NaCl, pH 4.5; (2) 0.06 M NaCl, pH 9.0 (Grigoryev *et al.*, 1971).

may have an α -, β - and coil-like structure, depending on temperature and pH of the medium. At low temperatures non-ionized PL has an α -helical structure and the position of the maximum in Fig. 21b (curve 2 corresponds to the maximum of PGA (α -helical structure) in Fig. 21a. By heating to 50°C a transition of the α -helical structure of PL to the β -structure takes place accompanied by a shift of the maximum (curve 1 Fig. 21b), the position of which now corresponds to the β -structure of PCMC (Fig. 21c). As with PGA and PCMC the maximum in the scattering curve of PL disappears with the transition to the coil-like structure effected by ionization (curve 3, Fig. 21b).

Ptitsyn *et al.* (1974) investigated as the next step the characteristic scattering of four globular proteins, two of which (myoglobin and lysozyme) have a predominantly α -helical structure, and the other two (α -chymotrypsin and immunoglobulin G) mainly a β -structure. They observed maxima in the same angular region as has been found for the synthetic polypeptides, which practically disappeared upon denaturation. But although it is clear that the intra-molecular packing within the protein is reflected at large angles it is difficult

to correlate clearly certain scattering characteristics to different types of secondary structure.

The authors tried to develop a method, which allows to a certain extent the interpretation of the scattering characteristics at large angles in terms of intramolecular packing of a protein chain (Ptitsyn *et al.*, 1974).

Ishimure *et al.* (1977) studied the conformation of the synthetic polypeptide poly (*N*-carbobenzoxy-L-lysine) in different solvents. They determined the mass per unit length M_c and the radius of gyration of the cross-section R_c in four different solvents (dimethyl formamide, pyridine, *m*-cresol and hexamethylphosphoric triamide). The M_c -values confirmed that poly (*N*-carbobenzoxy-L-lysine) exists in an α -helical conformation in these solvents. From the increase in the R_c -value in the order of *m*-cresol < dimethyl formamide < pyridine < hexamethylphosphoric triamide the authors conclude that the side-chain conformation varies with the kind of solvent from a loose contact with the main chain (in *m*-cresol) to a moderately extended conformation (in hexamethylphosphoric triamide).

Hamada *et al.* (1977) studied poly (L-tyrosine) in dimethyl formamide and concluded that it exists in this solvent in the form of a right-handed α -helix.

Summarizing, one can say that at present valuable information on the secondary structure of synthetic polypeptides can be obtained, but it is difficult to get similar information on proteins.

B. Tertiary Structure

In any case the tertiary structure of a protein can be approximated by the shape of a simple triaxial body of certain dimensions. Usually good agreement with the results of X-ray crystallography studies is obtained, as summarized in the paper of Kratky and Pilz (1978). It is impossible to mention all investigations concerning the tertiary structure of proteins published so far; only a few articles dealing with special methods may be enumerated. Summarizing papers are given by Kratky (1963), Pessen *et al.* (1973), Pilz (1973), Kratky and Pilz (1972) and Pilz *et al.* (1979a).

1. CONTRAST VARIATION

As already mentioned the scattering of homogeneous proteins is mainly determined by their shape; contributions to the scattering by the internal structure of the protein can be neglected at low resolution. By variation of the electron density of the solvent, however, the shape scattering term can be separated from the scattering term of the inner structure (contrast variation method, Stuhrmann, 1973; Stuhrmann and Miller, 1978; Chapter 6). The method is especially suitable for neutron-scattering, because in this case the

variation of the scattering density can be done by applying various D_2O/H_2O mixtures. By SAXS the variation of the electron density of the solvent is only possible by using highly concentrated sugar solutions (up to 60%), glycerol (up to 90%) or salt. The difficulty in applying this method in SAXS is that it only works correctly if the structure of the solute is not influenced by the different solvents. According to our experience there are often changes of the isopotential specific volume (lysocyme, papain, Schausberger and Pilz, 1977; haemocyanin *Helix pomatia*, Berger *et al.*, 1976). With myoglobin, on the other hand, the method worked well (Stuhrmann, 1970a). Luzzati *et al.* (1976) point out clearly that the application of the density-contrast method is generally based upon two assumptions: (a) the sample is an ideal solution of identical particles; (b) each particle has a volume associated with it inside of which the scattering-density distribution is independent of the scattering density of solvents. Tardieu *et al.* (1976) and Aggerbeck *et al.* (1978) indicate how the validity of conditions (a) and (b) can be tested.

If a macromolecule is composed of two chemically distinct components, which differ clearly in scattering density, it is possible to mask the scattering of one of the components by an appropriate choice of the solvent (see Chapter 6). When the density of the solvent is made equal to that of one of the components, this component becomes invisible for the X-rays and only the remaining part of the structure remains visible. Ferritin, for instance, consists of a mineral iron core, surrounded by a spherical shell of regularly arranged protein subunits. With a concentrated sugar solution (55% sucrose) the excess scattering of the protein shell nearly vanishes and the observed scattering is caused only by the iron core, which can be studied in this way without cleaving the molecule into the distinct components (Fischbach and Anderegg, 1965).

The contrast variation method has proved very suitable for studying systems which are composed of two components of different scattering density such as protein-nucleic acid (ribosomes, see Chapters 6 and 9) or protein-lipid (Chapter 10). Intrinsic membrane proteins belong also to systems of this type since it is not possible to dissolve these proteins in aqueous buffers because of their amphiphilic nature. Pseudo-solutions of these proteins can only be obtained by using detergents, which replace the hydrophobic environment of the lipid membrane. Thus only a two-component system protein-detergent can be studied in aqueous solutions as discussed in detail in Chapter 10 and in Osborne *et al.* (1978) and Sardet *et al.* (1976).

2. LARGE-ANGLE SCATTERING

Fedorov and Denesyuk (1977) found that the so-called "large-angle" region (from several degrees to about 20 degrees) has a high sensitivity to the type of polypeptide chain packing. The immense variety of possible tertiary and

quaternary structures of proteins, however, does not allow analysis of the protein structure itself, but the change (or lack of change) which can take place either in the molecule at the transition from crystal to solution or during the functioning of the protein can be studied. The investigations are based upon the known protein structure in the crystal; the scattering curve of this structure is calculated and compared with the experimental scattering curve of the protein in solution. In case of a divergence between calculated and measured curves the protein structure is modified by the authors according to physical and functional considerations in order to obtain the best agreement between the curves.

The problem with this comparison is the fact that it is impossible to take exactly into account an ion or water shell which may influence the experimental scattering curve and the surface of the particle. However, it can be assumed that proteins do not have such a pronounced shell as highly charged polyelectrolytes (nucleic acids etc.). In any case, one has to check carefully whether the observed differences between experimental and calculated curves are not within the experimental error and/or within the uncertainty of the calculations assuming various surfaces and van der Waal's radii for the atoms.

Fedorov and Denesyuk (1978) compared, for instance, the scattering curve calculated for the crystallized sperm-whale myoglobin (Watson, 1966) to the scattering curve measured in solution. They found a divergence at larger angles, which could be interpreted by a structural change occurring when the protein passes from crystal to solution. Assuming a small increase up to 2 Å of the distance between the hairpin GH and the other part of the molecule, the calculated and measured curve could be fitted as shown in Fig. 22. (To decide between modification I and II, shown in the figure, was not possible.)

The main difficulty in calculating the scattering at large angles is — as already mentioned — to take correctly into account the solvent influence and this requires the determination of the volume of the macromolecule inaccessible to the solvent. Fedorov *et al.* (1972) and Ninio *et al.* (1972) introduced the "cube method" which was modified later by Fedorov and Denesyuk (1977). In this modified "cube method" the macromolecule is placed into a parallelepiped, which is subdivided into small cubes with edges of 1–1.5 Å. Each cube is examined in order to decide whether it belongs to the macromolecule or to the solvent (see Chapter 4).

Some further interesting applications of the cube method will be mentioned. Timschenko *et al.* (1976) found that the structure of hen egg-white lysozyme in solution differs from the structure in the crystal and these authors explain the difference by a small opening of the substrate-binding cleft. A much larger difference was found for phage T4 lysozyme and the authors mention that this investigation "shows for the first time that the enzyme structure in solution can substantially differ from its crystalline structure" (Timschenko *et al.*, 1978a). Bovine pancreatic ribonuclease and its complex with an inhibitor on the other

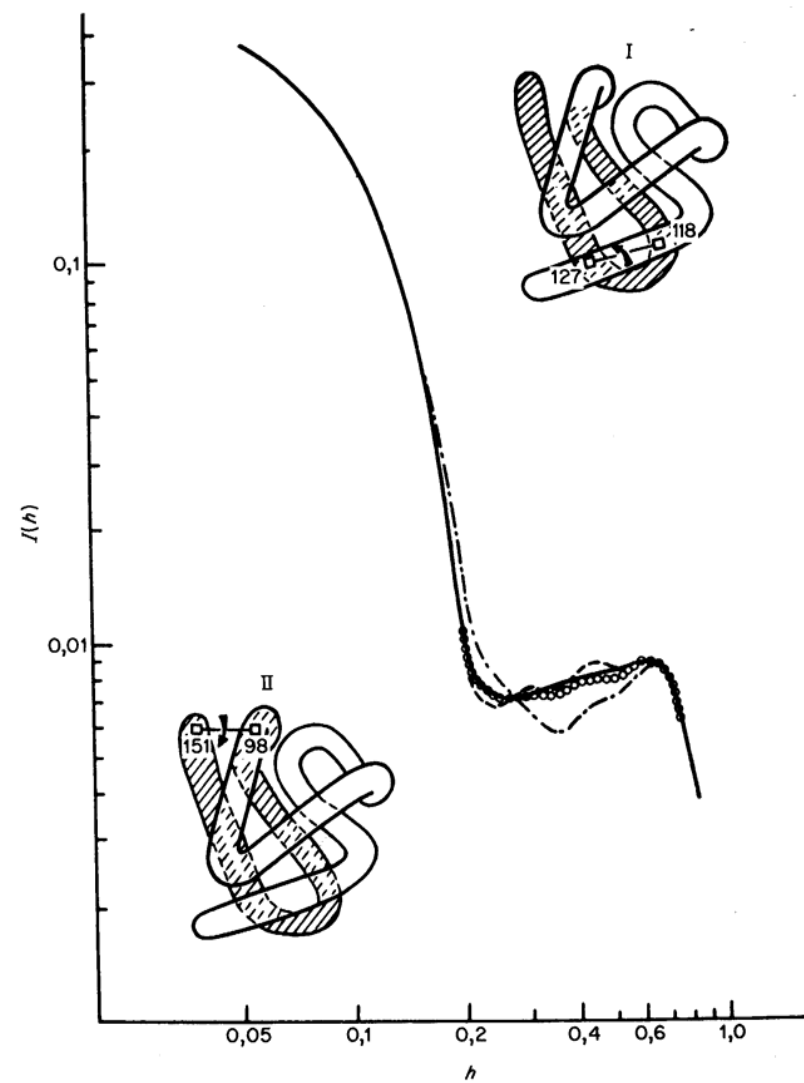


FIG. 22. Theoretical scattering curves of sperm whale myoglobin and its structural modifications. The sperm whale myoglobin structure in crystal (---) and two modifications obtained by shifting or rotating parts of the peptide chain by 5° to 10°; modification I (ooooo), modification II (---); experimental curve (—) (Fedorov and Denesyuk, 1978).

hand did not show structural differences between the state in solution and in crystal (Timschenko *et al.*, 1978b).

Information on the surface of a particle may be obtained in special cases from the distribution of chords $G(r)$, when the scattered intensity at large angles can be determined with high accuracy. $G(r)$ is zero at the origin for particles with a smooth surface; a non-zero value indicates discontinuities of a particle surface ("sharp edged particle"). The accuracy of the method is discussed in Chapter 2; a practical example is given by Gulik *et al.* (1976) on methionyl-tRNA synthetase.

C. Quaternary Structure

1. GENERAL

Many proteins are complexes built of several subunits. One of the most important prerequisites for the understanding of the mechanism of these complexes is the knowledge of their quaternary structure. The method of SAXS has proved very suitable for obtaining information on the quaternary structure of proteins. A large number of detailed models of quaternary structures of proteins have been suggested from SAXS investigations over the last decade.

Since there is an infinite variety of possible quaternary structures, one should use any accessible information for the construction of a detailed model to save time in computing and to reduce the structures being in consideration. The following information can be obtained from SAXS itself: molecular parameters, overall shape, cross-section or thickness of elongated or flat particles, information on the substructure as discussed in Sections V.C3 and V.C4. Pieces of information from other methods are also a valuable help as discussed in Section III.C. In a detailed model the quaternary structure of proteins is usually approximated by arranging a few simple triaxial bodies (spheres, cylinders, ellipsoids etc.) or by simulating a shape by a large number (up to several thousands) of spheres or cubes (see Chapter 4, Section V).

Whenever the comparison between experimental and calculated scattering curve is extended to large angles, one has to take into account that the small spheres cause maxima and minima (usually only the minima are clearly seen) at larger angles dependent on their size as discussed in the following (Section V.C3).

The structure of a particle can also be described by a series of multipole components, i.e. by additive composition of a term with spherical symmetry (monopole) and corresponding terms with dipole, quadropole etc. symmetry. Addition of the scattering curves of the multipoles results in the whole scattering curve and a determination of the structure is possible by decomposing the experimental scattering curve into the curves which correspond to the different multipoles (Stuhrmann, 1970b; Harrison, 1969; Stuhrmann and Miller, 1978; see Chapter 6).

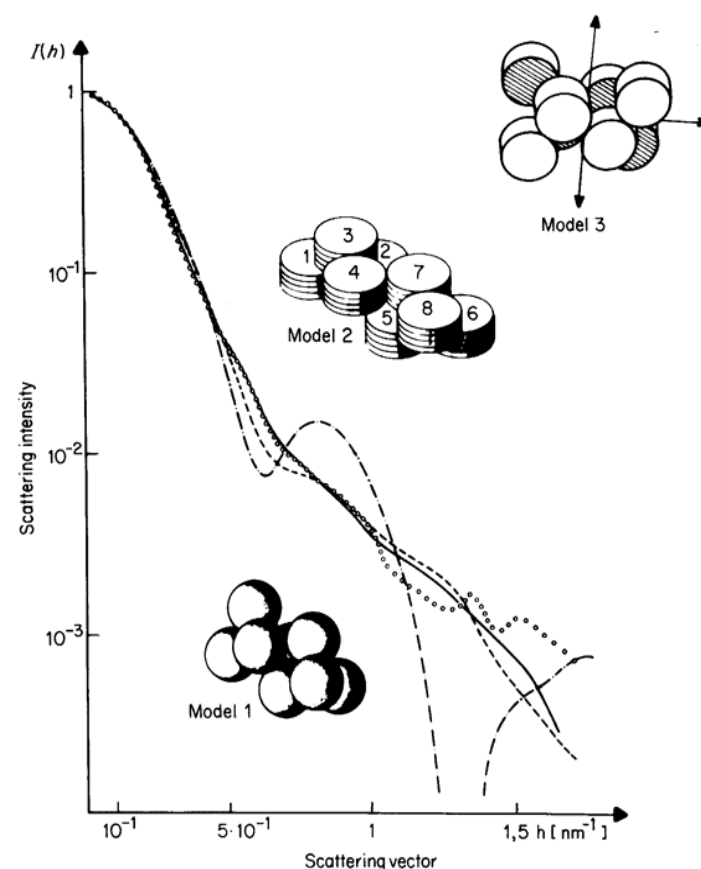


FIG. 23. Experimental scattering curve (○○○) of phosphofructokinase from Baker's yeast with theoretical scattering curves of model 1 (----), model 2 (- - -) and model 3 (—) (Plietz *et al.*, 1978).

2. PRACTICAL EXAMPLES

As an example, some models calculated by Plietz *et al.* (1978) for the phosphofructokinase from baker's yeast are shown in Fig. 23. The best agreement with the experimental curve gives model 3, which is composed of 8 cylindrical subunits and has three 2-fold axes. All models were calculated by the program of Rolbin *et al.* (1973); each model was approximated by about 2000 spheres.

The comparison between experimental and calculated curves can be done in reciprocal space as shown in Fig. 23 or in real space. In Fig. 20 the distance distribution function of a human Waldenström macroglobulin IgM is compared with that of the model shown in the figure. Although SAXS can not give, in

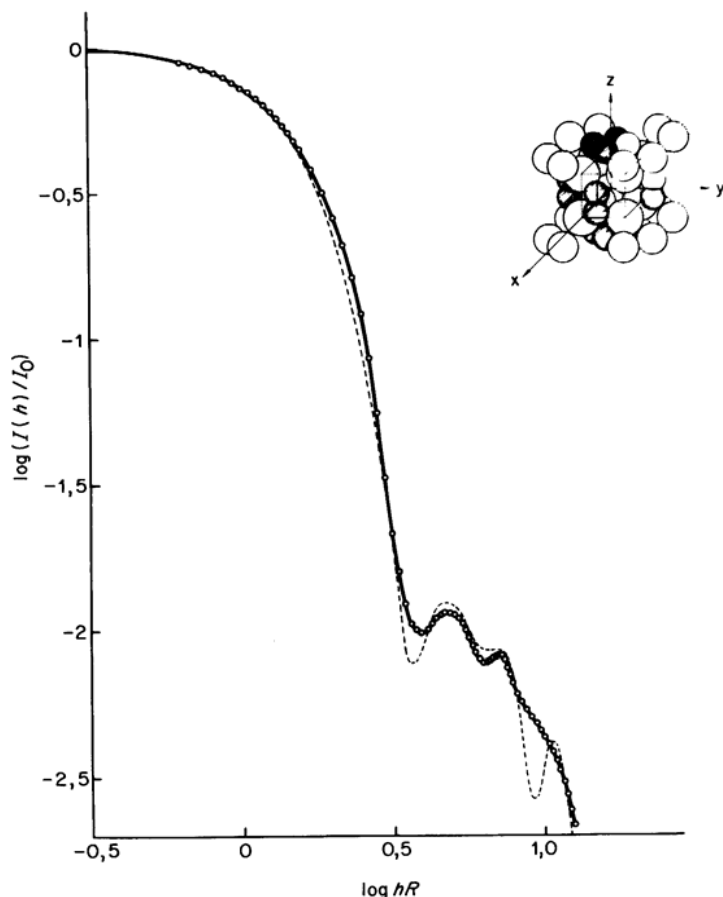


FIG. 24. Comparison of the experimental scattering curve (oooo) of the pyruvate dehydrogenase core complex from *E. coli* with the theoretical curve of the model shown in the figure (Durchschlag, 1975a).

principle, information on the flexibility of a macromolecule, Wilhelm *et al.* (1978) could show that this human IgM is a rather flat molecule. The Fab-arms have to lie in the plane of the Fc-arms. Only a slight flexibility is possible. It can be excluded that the Fab-arms are bent out to a high extent from the Fc-plane like a spider, as suggested by some electron microscopic pictures. The model was calculated by the program APDIST of Glatter (Chapter 4, Section V.A3a), the shape was simulated with 1680 spheres.

The quarternary structure suggested by Durchschlag (1975a, 1975b) for the pyruvate dehydrogenase core complex from *E. coli* is shown in Fig. 24. He

determined not only the usual but nearly all molecular parameters obtainable by SAXS. Some further detailed quaternary structures were suggested by Bode *et al.* (1972) for bacterial flagella, by Folkhard *et al.* (1977) for fatty acid synthetase from pig liver, by Damaschun *et al.* (1978) for the glycoprotein ceruloplasmin, by Stöckel *et al.* (1973) for the giant respiratory protein haemoglobin *Tubifex tubifex* and by Notbohm *et al.* (1979) on chromatin.

3. SIZE OF SUBUNITS

Some proteins are composed of a large number of identical spherical or nearly spherical subunits. In this case it is possible to get information on the size of the subunits from the scattering at large angles. As already mentioned a higher resolution of a structure always requires a measurement at comparatively larger angles. The scattering curve of the haemocyanin *Helix pomatia* (Pilz *et al.*, 1972; Pilz *et al.*, 1974; Berger *et al.*, 1977) shown in Fig. 25 may illustrate this fact. When only the decrease of the main maximum is measured one can obtain only the information that the protein has a rather isotropic shape. Including the four subsidiary maxima into the measurement increases the resolution and one can find that the overall shape of this haemocyanin is best described by a hollow cylinder of certain dimensions. When the scattering curve can also be measured at large angles, where the intensity has already dropped down by five orders of magnitude one can get information on the substructure, in this case on the sub-units, too. (To carry out the measurements with sufficient accuracy also at larger angles requires, however, large amounts of sample, highly concentrated solutions, a very long time of measurement and a sample stable to X-ray irradiation.)

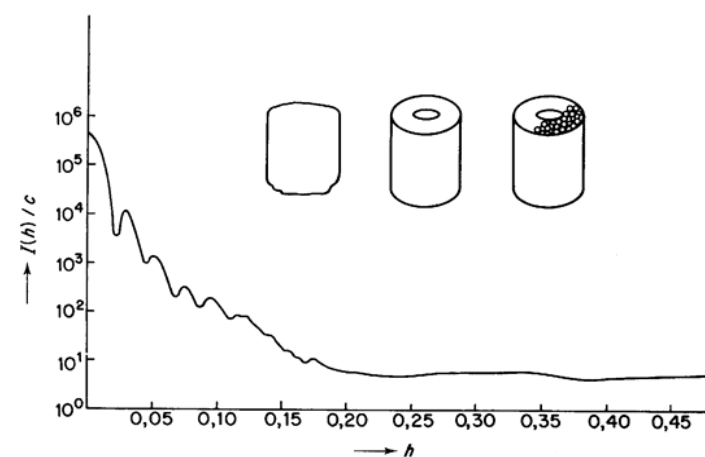


FIG. 25. Scattering curve of the haemocyanin *Helix pomatia*; explanation of the models in the text.

Debey's (1915) scattering theory of the molecular gas can be applied to a molecule consisting of nearly identical, nearly spherical subunits (Glatter, 1972; Kratky, 1947, 1948). Since Debey's scattering function always contains the shape factor of the spherical subunits, the zero points of the latter (compare Chapter 2) also have to appear in the scattering curve of the whole particle. Consequently, the radius of gyration of the subunits (compare Chapter 2) and their diameter, assuming spherical shape, can be calculated from the position of the minima. The above assumptions (identical and spherical subunits) are true if

$$\frac{h_{01}}{h_{02}} = 1,73$$

where h_{01} and h_{02} are the positions of the first two minima.

To be sure that the minima are really due to the subunits and are not influenced by the overall shape, the whole haemocyanin molecule was cleaved into dissociation products – into halves, tenths and twentieths. The shape of these products is seen in Fig. 26; the fact that the same minima were found at nearly the same positions proves that the minima are caused by the subunits and not by the overall shape which is quite different for the whole haemocyanin and the dissociation products. The model built up from the subunits which fits best the scattering curve is seen in Fig. 27.

Paradies and Vettermann (1978) determined in a similar way the radius of gyration of the subunits of the phosphofructokinase from *Dunaliella salina* and Notbohm *et al.* (1979) the size of the subunits of the protein core in tightly packed chromatin.

4. CLEAVING IN FRAGMENTS

In any case it is a valuable help for the model calculations for quaternary structures to split a larger molecule into fragments, dissociation products, subunits etc., when this can be done without changing its structure. The knowledge of the size and shape of these fragments as determined by SAXS reduces the possible quaternary structures drastically. As an example, the immunoglobulin IgG shall be mentioned. It can be split, as illustrated schematically in Fig. 28, by enzymes into different fragments, Fab', Fc and (Fab')₂. The shape of the Fab' and Fc fragment of a human IgG (Pilz *et al.*, 1976) could be best approximated by the combination of two cylinders. To find a model for the whole IgG molecule, the models of the fragments were arranged in different ways to obtain the best fit (Pilz *et al.*, 1977).

It should be noted that nearly correct values were obtained for the scattering data and the asymmetry factor as early as 1955 (Kratky *et al.*, 1955). These measurements yielded a remarkably precise molecular weight from absolute intensity measurements, based on photographic data, using solutions of 8% and

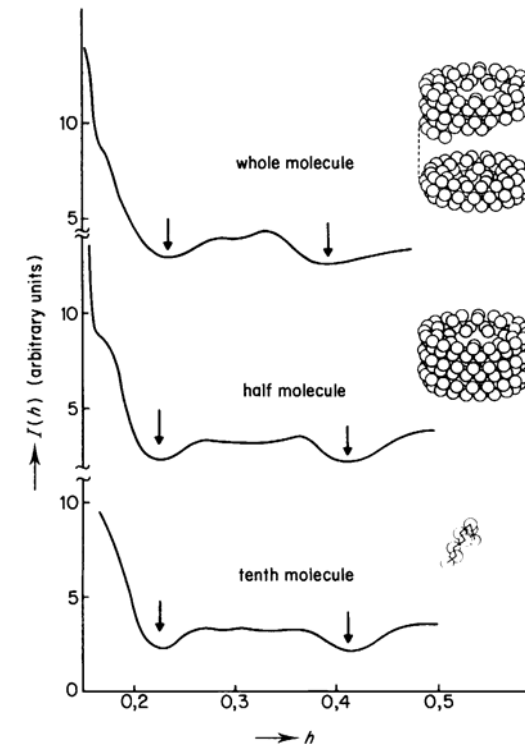


FIG. 26. Outer parts of the scattering curve of the whole molecule of the haemocyanin *Helix pomatia* and its dissociation products (halves and tenths).

16% concentration. The insignificance of interference effects is as expected for a particle of very anisotropic shape (Kratky and Porod, 1956). In 1963 Kratky *et al.* obtained the shape of the overall scattering curve of human IgG. This characteristic shape with a break in the cross-section curve has been observed many times since then for other Immunoglobulins. The shape appears to be a consequence of the particular subunit structure of Immunoglobulins (Pilz *et al.*, 1970).

The model for haemocyanin *Helix pomatia* (Fig. 27) was found in a similar way by arranging the tenths, twentieths and halves and the model for haemocyanin *astacus leptodactylus* was built up from the monomers (Fig. 8). A model for the DNA-dependent RNA-Polymerase consisting of the core ($\alpha_2\beta\beta'$) and the initiation factor σ was determined by studying separately the subunits α_2 , $\alpha_2\beta$ and σ (Meisenberger *et al.*, 1980, 1981).

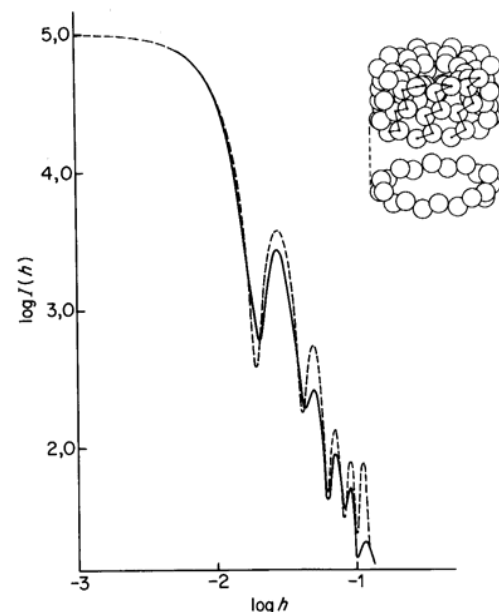


FIG. 27. Experimental scattering curve of the β -haemocyanin *Helix pomatia* compared with the theoretical curve of the model shown in the figure; the arrangement of the tenths in the molecule is indicated (Berger *et al.*, 1977).

5. THE LABEL TRIANGULATION METHOD

This method was developed in 1947 by Kratky and Worthmann for determining intramolecular distances of heavy atoms in dissolved polymers. This method was extended by Engelman and Moore (1972) and Hoppe (1972) who suggested the use of the method for the determination of the spatial arrangement of subunits in protein complexes. The principle of the method is the following: after appropriate labelling of the subunits the distances between the subunits of a complex can be determined by X-ray or neutron scattering experiments. The labels can be heavy atoms in X-ray work or deuterated subunits in the case of neutron scattering. For studying protein complexes it is necessary that the complex can be split into subunits and regenerated from it to the native structure. In this way a protein complex can be recombined from normal subunits and subunits marked with heavy or deuterated subunits. This method is especially suitable for neutron scattering since it is very difficult to introduce a sufficient amount of heavy atoms into the subunits, but relatively easy to label by deuteration of the subunits. (Deuterated subunits can be obtained, for example, by culturing *E. coli* cells in heavy water medium.) The

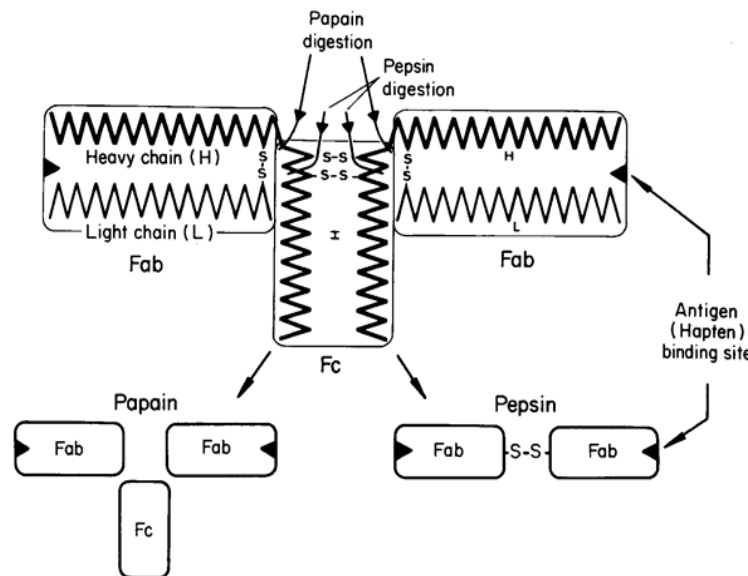


FIG. 28. Schematic illustration of the digestion of the IgG-immunoglobulin molecule into different fragments by the enzyme papain and pepsin. The two specific combining sites for antigens are at the opposite ends of the molecule in the Fab regions. The region where the disulfide bridges are drawn is called the "hinge" region.

investigation of these labelled protein complexes allows the distances between the subunits to be deduced and the relative positions within the protein complex to be calculated, as discussed in detail in Chapter 9.

As pointed out in Chapter 9, the label triangulation method has found its greatest application so far in the study of *E. coli* ribosomes. The location of the proteins in the 30S ribosomal subunit was determined by the group of Engelman and Moore (1975) and Moore *et al.* (1978); similar studies on the 50S ribosomal subunit were performed by Hoppe *et al.* (1975) and Serdyuk and Grenader (1975).

Up until now the following applications of this new method to proteins are known. Stöckel *et al.* (1978) studied the protein complex of the DNA-dependent RNA-polymerase using neutron scattering and labelling of the subunits by deuteration. Feigin *et al.* (1978) determined the distance between heavy atom labels in Histidine Decarboxylase by SAXS. The distance between Hg-labels connected to SH-groups of cysteine was found to be 69 ± 2 Å. The authors estimate also the contribution made by the heavy atom markers to the scattering. A protein with a molecular weight of 100 000 requires a marker consisting of about four heavy atoms with atomic number 80–90 to allow the registration of the scattering of the marker. Newer applications of this method are described by Vainshtein *et al.* (1979, 1980).

Czer *et al.* (1978) determined the distance between two binding sites of an IgG antibody molecule (see Fig. 28). As antigen, a dextran (molecular weight 40 000) was used, the antigen was bound to the divalent IgG antibody and the distance between the two dextrans could be determined by the contrast variation method (see Chapter 6), by measuring the dextran-antibody complexes in various mixtures of H₂O/D₂O. Since the dextran scattering density does not differ very much from that of the antibody, the distance could be determined only with large statistical error.

VI. Structural Changes

A. General

SAXS is well suited to the investigation of conformational changes, which may be induced through interaction with small molecules (effectors). Of special interest is, of course, the question whether there is a conformational change of the enzyme structure when it works (binding of ligands etc.). Of similar interest is the question whether antigens cause a conformational change of the structure of antibodies upon binding. Furthermore, the investigation of structural changes which may occur by changing the solvent conditions (presence or absence of special ions as Mg⁺⁺, change of ionic strength, pH, temperature etc.) is often important.

While the shape of a dissolved macromolecule can only be deduced indirectly from a comparison with model structures, relative changes of shape and dimensions can be determined with higher accuracy. The following examples may show the possibility of studying structural changes with SAXS.

B. Enzymes

A good example of the magnitude of detectable morphological change is the human haemoglobin molecule: the allosteric structural change upon addition and removal of oxygen can be clearly seen by SAXS (Conrad *et al.*, 1969). The haemoglobin molecule has overall dimensions of about 6 nm, and the maximum movement of a polypeptide chain is 0.6 nm. Much smaller structural changes, which effect only part of a chain or dislocate a few atoms, are invisible for SAXS (only large angle studies – as mentioned in Section V.B2 – may permit a somewhat better resolution).

McDonald *et al.* (1979) found that yeast hexokinase in solution exhibits a large conformational change upon binding glucose or glucose 6-phosphate.

The decrease in the radius of gyration by about 1 nm upon binding glucose or glucose 6-phosphate suggests that the closing of the slit between the two lobes of hexokinase observed in the crystal structures occurs in solution when either glucose or glucose 6-phosphate is bound.

Müller *et al.* (1972) studied yeast pyruvate kinase and found a decrease in the radius of gyration by 0.1 nm upon charging the enzyme with the allosteric ligand. This structural change is believed to produce a decrease in anisotropy of the enzyme upon binding the ligand.

Durchschlag *et al.* (1971) studied the glyceraldehyde-3-phosphate dehydrogenase; this enzyme consists of four chemically identical subunits which bind one molecule of NAD each. The authors studied the structural changes caused by NAD and observed a volume contraction depending on the degree of saturation with NAD. Full saturation (i.e. four NAD molecules per enzyme molecule) decreases the volume by 7%. The authors could also state clearly, that the mechanism of binding is not a sequential but an allosteric one. Simon (1972) investigated D-glyceraldehyde-3-phosphate dehydrogenase from mammalian skeletal muscle and observed also a slight decrease in the radius of gyration by 0.08 nm upon binding of four NAD molecules. To determine such a small change in R, Simon had to develop a special method, which allows direct determination of differences in the radius of gyration.

Pilz *et al.* (1979) studied the phenylalanine specific tRNA Synthetase in the free state and after binding the tRNA^{Phe} and observed a small contraction of the enzyme upon binding of tRNA reflected by a clear decrease in the radius of gyration and a shift of the distance distribution function to smaller distances.

Zipper and Durchschlag (1978) investigated malate synthase from Baker's Yeast and found that binding of substrate and substrate analogue causes small structural changes, which are reflected mainly by a slight decrease in the radius of gyration, a decrease in the maximum diameter and an increase in the radius of gyration of the thickness.

Kuntz *et al.* (1978) studied two of the five multiple forms of beef liver catalase (cat I and cat V) using various biochemical and biophysical techniques. They found that the two molecules cat I and cat V differ not only in the volume and radius of gyration as determined by SAXS but also in their isoelectric points and surface charges. A model for the quaternary structure of the beef liver catalase is suggested. Since cat I and cat V can be interconverted the observed structural changes are assumed to be caused by conformational changes.

Paradies and Vettermann (1978) investigated the phosphofructokinase from *Dunaliella salina* in the absence and presence of the ligand fructose and found in the presence of the ligand a much lower R-value indicating a more compact spherical structure of the enzyme after ligand binding.

C. Structural Changes in Immunoglobulins

Of special interest in immunochemistry is the question whether a change of conformation takes place within an antibody molecule upon the binding of the specific antigen. A comparison between the scattering data of the free antibody and after saturation with antigen should answer this question. However, antigens are usually larger molecules and it is difficult to differentiate between changes in the scattering data caused by the addition of the antigen and changes which are due to a conformational change in the antibody itself (Laggner *et al.*, 1971). This difficulty could be overcome by using, instead of the whole antigens, only its reactive group, the hapten, which is a very small molecule, the mass of which can be neglected upon addition to the antibody molecule. A difference between the molecular parameters can be attributed completely to a conformational change of the antibody.

Pilz *et al.* (1973, 1974b) studied IgG antibodies ($M_r = 150\,000$) before and after interaction with the specific hapten ($M_r = 350$, resp. 850). In every case a significant change in the conformation was observed, the radius of gyration and volume decreased by 2–8% depending upon the degree of saturation with hapten. Similar results were obtained by Czer *et al.* (1977) using neutron scattering.

The next question of interest was, whether it is possible to localize this conformational change within the molecule. For this purpose the IgG antibody was cleaved by enzymes into its fragments as shown in Fig. 28. Each of the two Fab'-fragments has one active binding site for hapten. These fragments were studied in the absence and presence of the specific hapten. No changes of conformation were observed with these fragments upon the interaction with hapten (Pilz *et al.*, 1975). These findings lead to the conclusion that the conformational change does not take place within the Fab' fragment but relatively far away in the area of the hinge region and/or in the Fc-fragment (see Fig. 28).

To prove this assumption the hinge region was modified by cleaving the disulphide bonds in the hinge region by reduction and alkylation. The fact that this modification influenced the observed structural changes significantly allows the conformational change to be localized within the area of the hinge region and the Fc fragment (Pilz *et al.*, 1979c).

D. Denaturation, Association-dissociation

SAXS is also very suitable for following denaturation or association-dissociation processes. The spatial unfolding of the native structure of a protein upon denaturation, for instance, can be clearly followed by the increase in the radius of gyration (Kirste *et al.*, 1969). The reversible pH-denaturation of albumin was studied by Laggner *et al.* (1971). The equilibrium between the monomeric and

dimeric form of DNA-dependent RNA-polymerase depending on the ionic strength of the solution was studied by Pilz *et al.* (1972) by investigating the change in the radius of gyration.

VII. Polydisperse Solutions

A. General

Usually, a monodisperse solution of protein particles is a necessary prerequisite for SAXS investigations. From polydisperse solutions only average molecular parameters can be obtained whereby, it should be borne in mind, that the median \bar{M}_r -value is a weight average while the median \bar{R} -value is a Z-average. There are, however, special circumstances where valuable information can be obtained even from polydisperse systems. The accuracy of the obtained molecular parameters is, of course, much lower than with homodisperse solutions. For a system of particles which have the same shape but differ in size, a particle size distribution can be calculated (see Chapter 4, Section III.E5).

Many proteins show a strong tendency to form aggregates in solution. Often information on the type of the aggregation process can be obtained from SAXS. As already mentioned (Section IV.B), the glutamate dehydrogenase associate in a linear fashion; the cross-section of the aggregates is always the same, only the length increases with the molecular weight. With malate synthase, on the other hand, the thickness factor remains unchanged during aggregation, and Zipper and Durchschlag (1978) performed a computer simulation of the assumed aggregation model, as discussed in detail in Section IV.C.

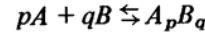
B. Two-component Systems

Many enzymes exist in different states of aggregation, like rabbit muscle glycogen phosphorylase which coexists as dimer and tetramer. Frequently, only one of these aggregation states can be obtained in a pure form in solution. The other components can only be studied in a paucidisperse system containing both aggregation states. If sufficiently accurate structural parameters are obtainable for one of the components from studies on the monodisperse system, it may be possible to calculate the structural parameters of the other component from the scattering curve of the paucidisperse solution. This was done by Puchwein *et al.* (1970) for the glycogen phosphorylase aggregates and by Witz *et al.* (1964) for β -Lactoglobulin.

An example for a system which exists in various states (globular particles and elongated aggregates) is the native and renatured silk fibroin of *Bombyx mori* (Kratky *et al.*, 1964; Kratky *et al.*, 1955; Kratky and Pilz, 1955).

C. Equilibrium Data

In special cases it is possible also to obtain equilibrium data from SAXS. The accuracy of such results obtained from more or less polydisperse solutions is, of course, rather limited; but it can be high enough, as shown by Österberg *et al.* (1975), to decide which type of complex is formed between two macromolecules *A* and *B*, when the equilibrium of the system is described by the general reaction



which has the associated equilibrium constant β_{pq} . Österberg *et al.* (1975) showed by analysis of SAXS data that the predominant complex (*AB*) formed in solution between lysine: tRNA ligase (*A*) from yeast and tRNA (*B*) consists of two ligase molecules and one molecule of tRNA (A_2B -type).

For a sufficiently diluted system the scattered intensity *I* at any angle can be written as the sum of intensities scattered from all types of particles in the solution, i.e.

$$I = I_A + I_B + \sum \sum I_{pq}$$

where I_A , I_B and I_{pq} are the scattered intensities from the molecules *A*, *B* and the complexes $A_p B_q$, respectively. The intensity contributed by each type of particle at a particular small angle depends on its concentration, its molecular weight and the excess electrons Δz (see Chapter 4). The scattered intensity increases with an increase in any of these parameters.

Let us compare the scattered intensity *I* on the following two systems assuming the *same total concentration* of *A* and *B* in both cases. The first system consists of a mixture of *A* and *B* without any complex between the two. The other system contains free *A* and *B* particles plus complexes of the type $A_p B_q$. As a result of the higher molecular weight of the complexes, the second system will show a higher scattered intensity at sufficiently small angles. The intensity difference ΔI between the two systems depends only on the complex; it is the difference between the intensity *I* of the two systems containing components plus complex (i.e. *A*, *B*, $A_p B_q$) and the intensity $I_{Atot} + I_{Btot}$ of the system containing only *A* and *B* (with the same total concentration of *A* and *B*). I_{Atot} and I_{Btot} have to be recorded separately for each component (ligase *A* and tRNA *B*):

$$\Delta I = I - I_{Atot} - I_{Btot}$$

By the assumption that only one single complex $A_p B_q$ predominates in solution it is possible to determine from ΔI what type of complex predominates. The authors suggest also a model for the ligase (Österberg *et al.*, 1973) and for the complex.

In a similar study, the complex formation between 5-SrRNA and the L-18

protein of the *E. coli* 50 S ribosome subunit was studied by Österberg and Garret (1977).

VIII. Special Applications

A. Intermolecular Structure

The SAXS technique can also be used to get information on the intermolecular structure of proteins in highly concentrated solutions. Haemoglobin, for instance, has a concentration of 330 g l^{-1} in the red human blood cells, and the physical and biochemical properties of these concentrated solutions depend on the haemoglobin concentration. It is, therefore, of special interest to get information on the intermolecular structure and interaction potentials in oxi- and deoxyhaemoglobin solutions.

Zinke *et al.* (1978a) investigated scattering curves of haemoglobin solutions in a concentration range from 30 g l^{-1} to 370 g l^{-1} (Fig. 29). Using the Zernicke-Prins equation (Zernicke and Prins, 1927) they calculated the pair correlation function for the dissolved haemoglobin molecules as shown in Fig. 30 for oxihaemoglobin. The haemoglobin molecules have a "short-range-order-structure" whereby the range of order increases with the concentration and amounts to about 4 molecule diameters at 324 g l^{-1} . The most probable distance between the oxihaemoglobin molecules decreases with increasing concentration and is about 6.5 nm for a concentration of 324 g l^{-1} as deduced from the position of the first maximum in Fig. 30.

Furthermore, Zinke *et al.* determined the potential function of the haemoglobin-haemoglobin interaction on the basis of fluid theories. They found that the course of the pair potential functions depends on the concentration; the potential minimum lies 1.2–1.5 nm above the largest oxihaemoglobin diameter.

The values obtained for deoxyhaemoglobin solutions are nearly identical to those of the oxihaemoglobin except the deoxyhaemoglobin solution with the highest concentration (370 g l^{-1}), which seems to have a much more ordered structure.

B. Synchrotron Radiation

It seems that synchrotron radiation will play an important role when kinetic aspects are considered. The synchrotron X-ray radiation is very intense and diffraction patterns of fibrous structures (for instance muscles) can be obtained in a few seconds. Thus the observation of association and dissociation processes or larger conformational changes, which alter the radius of gyration, should be possible by synchrotron radiation, when the technique is refined.

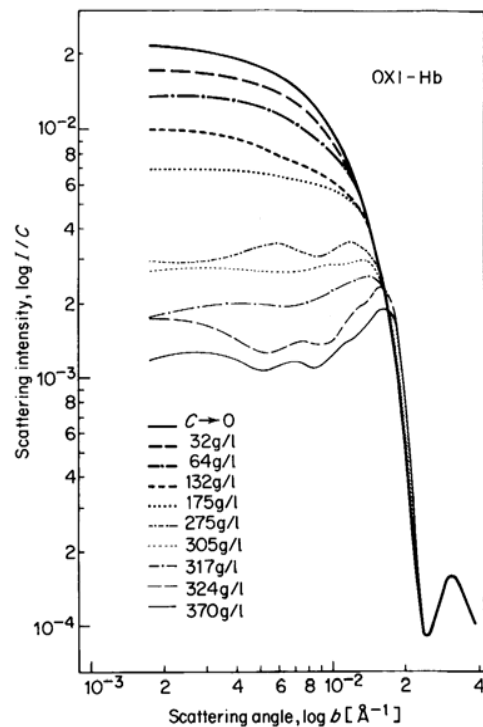


FIG. 29. Concentration dependence of the oxihaemoglobin scattering curves ($b = 1/D_{\text{Bragg}}$; Zinke *et al.*, 1978).

Another advantage of synchrotron radiation is given by the extremely low divergence of the incident beam. The scattering patterns observed in the range between 0.1 mrad and 10 mrad result from spacings of about 10–10 000 nm (Stuhrmann, 1978). Since these dimensions are typical for a number of large biological macromolecules, such as viruses, phages, mitochondria, DNA etc., synchrotron radiation may become especially suitable for these structural investigations.

On the other hand, there are serious experimental limitations. One important point is the increase in temperature of the sample due to photon absorption. Another limiting factor is the very low maximum counting rate of the position sensitive detector used. For detailed information see Chapter 3.II and Stuhrmann (1978).

First results on solutions of proteins are reported by Bordas and Randall (1978). The authors point out that the immediate object of these experiments was to establish the validity of the method for protein solutions and they measured only one very highly concentrated solution (50 mg ml^{-1}) of different

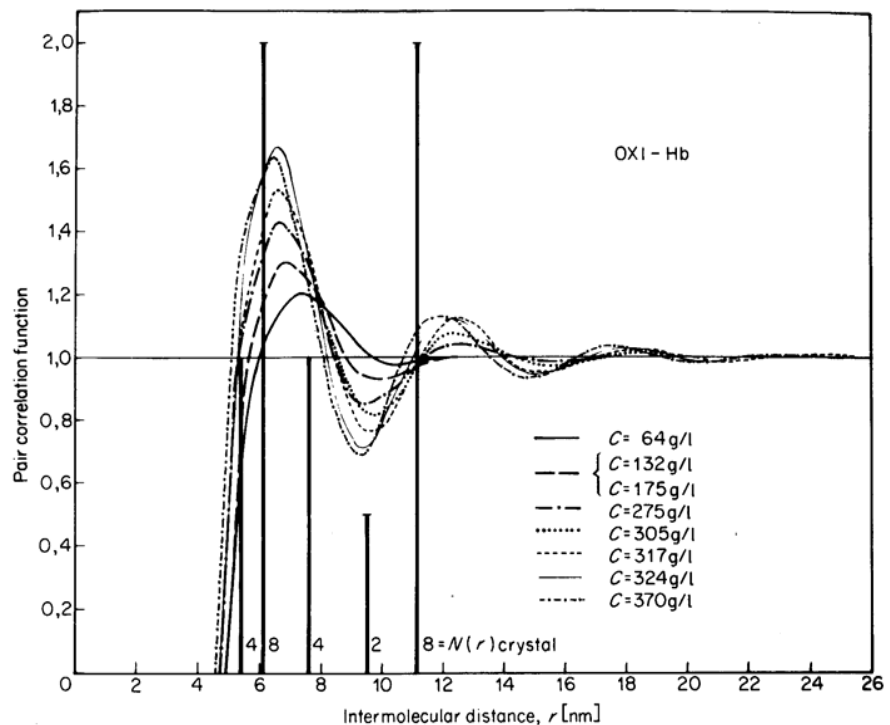


FIG. 30. Concentration dependence of the pair correlation function of oxihaemoglobin. $N(r)$ -number of neighbouring molecules in the haemoglobin crystal of space group $p4_32_12$.

proteins (catalase, myoglobin, bovine serum albumin and ferritin). Runs of 2–3 min exposure were made of all specimens and approximate values of the radii of gyration were calculated from the Guinier plots. An extrapolation to zero concentration was not possible since no concentrations series were measured. However, the R -values found are similar to those determined exactly by normal SAXS. The accuracy of these measurements is at the moment far below the accuracy obtained by the usual SAXS.

References

- Aggerbeck, L., Yates, M., Tardieu, A. and Luzzati, V. (1978). *J. Appl. Cryst.* **11**, 466–472.
- Anderegg, J. W. (1967). In "Small-Angle X-Ray Scattering" (H. Brumberger, ed.), pp. 243–265. Gordon and Breach, New York.
- Berger, J., Pilz, I., Witters, R. and Lontie, R. (1976). *Z. Naturforsch.* **31c**, 238–244.

- Berger, J., Pilz, I., Witters, R. and Lontie, R. (1977). *Eur. J. Biochem.* **80**, 79–82.
- Bielig, H. J., Kratky, O., Rohns, G. and Wawra, H. (1966). *Biochem. Biophys.* **112**, 110–118.
- Bode, W., Engel, J. and Winklmaier, D. (1972). *Eur. J. Biochem.* **29**, 313–327.
- Bordas, J. and Randall, J. T. (1978). *J. Appl. Cryst.* **11**, 434–441.
- Cleemann, J. C. and Kratky, O. (1960). *Z. Naturforsch.* **15b**, 525–535.
- Conrad, H., Mayer, A., Thomas, H. P. and Vogel, H. (1969). *J. Mol. Biol.* **41**, 225–229.
- Czer, L., Franek, F., Gladkikh, I. A., Nezlin, R. S., Novotny, J. and Ostvanevich, Yu. N. (1977). *FEBS Lett.* **80**, 329–331.
- Czer, L., Franek, F., Gladkikh, I. A., Nezlin, R. S., Novotny, J. and Ostvanevich, Yu. M. (1978). *FEBS Lett.* **93**, 312–316.
- Damaschun, G., Damaschun, H., Pürschel, H. V. and Ruckpaul, K. (1973). In "Abhandlungen der Akademie der Wissenschaften der DDR", pp. 289–296.
- Damaschun, G., Damaschun, H., Dembo, A. T., Kayushina, R. L., Kröber, R., Moskow, K. A., Müller, J. J., Neifakh, S. A., Rolbin, J. A., Shavlovsky, M. M. and Zirwer, D. (1978). *Stud. biophys. Berlin* **71**, 53–76.
- Debey, P. (1915). *Ann. Physik* **46**, 809–824.
- Durchschlag, H. (1975a). *Biophys. Struct. Mechanism.* **1**, 169–188.
- Durchschlag, H. (1975b). *Biophys. Struct. Mechanism.* **1**, 153–168.
- Durchschlag, H., Puchwein, G. and Kratky, O. (1971). *Eur. J. Biochem.* **19**, 9–22.
- Engelman, D. M. and Moore, P. B. (1972). *Proc. Nat. Acad. Sci. U.S.A.* **69**, 1997–1999.
- Engelman, D. M., Moore, P. B. and Schoenborn, B. P. (1975). *Proc. Nat. Acad. Sci. U.S.A.* **72**, 3888–3892.
- Fedorov, B. A. (1970). *Molekul. Biol.* **4**, 69–75.
- Fedorov, B. A. (1971). *Acta Cryst.* **A27**, 35–42.
- Fedorov, B. A. and Aleshin, V. G. (1966). *Vysokomol. Soed.* **8**, 1506–1513.
- Fedorov, B. A. and Denesyuk, A. I. (1977). *Acta Cryst.* **B33**, 3198–3204.
- Fedorov, B. A. and Denesyuk, A. I. (1978). *FEBS Lett.* **88**, 114–117.
- Fedorov, B. A., Ptitsyn, O. B. and Voronin, L. A. (1972). *FEBS Lett.* **28**, 188–190.
- Fedorov, B. A., Sphungin, I. L., Gelfand, V. I., Rosenblat, V. A., Damaschun, G., Damaschun, H. and Papst, M. (1977). *FEBS Lett.* **84**, 153–155.
- Feigin, L. A., Gochar, N. A., Likhtenstein, G. I., L'vov, Yu. M. and Marakushev, S. A. (1978). *Kristallografija* **23**, 749–755.
- Fischbach, F. A. and Anderegg, J. W. (1965). *J. Mol. Biol.* **14**, 458–473.
- Folkhard, W., Felser, B. and Pilz, I. (1977). *Eur. J. Biochem.* **81**, 173–178.
- Glatter, O. (1972). *Acta Physica Austriaca* **36**, 307–315.
- Glatter, O. (1979). *J. Appl. Cryst.* **12**, 166–175.
- Grigoryev, A. I., Vokova, L. A. and Ptitsyn, O. B. (1971). *FEBS Lett.* **14**, 189–191.
- Guinier, A. and Fournet, G. (1955). In "Small-Angle Scattering of X-Rays". Wiley, New York.
- Gulik, A., Monteilhet, C., Dessen, P. and Fayat, G. (1976). *Eur. J. Biochem.* **64**, 295–300.
- Hamada, F., Ishimuro, Y., Hayashi, T. and Nakajima, A. (1977). *Biopolymers* **16**, 2351–2361.

- Hoppe, W. (1972). *Israel J. Chem.* **10**, 321–333.
- Hoppe, W., May, R., Stöckel, P., Lorenz, S., Erdmann, V. A., Wittman, H. G., Crepsi, H. L., Katz, J. J. and Ibel, K. (1975). *Brookhaven Symp. Biol.* **27**, IV, 39–48.
- Ishimuro, Y., Hamada, F. and Nakajima, A. (1978). *Macromolecules* **11** (2), 382–387.
- Kayushina, R. L., Rol'bin, Yu. A. and Feigin, L. A. (1974). *Kristallografiya* **19**, 1161–1165.
- Kirste, R. G., Schulz, G. V. and Stuhrmann, H. B. (1969). *Z. Naturforsch.* **24b**, 1385–1392.
- Kratky, O. (1947). *Monatsh. Chem.* **76**, 325–333.
- Kratky, O. (1948). *J. Polym. Sci.* **3**, 195–204.
- Kratky, O. (1963). *Prog. Biophys. Chem.* **13**, 105–173.
- Kratky, O. and Pilz, I. (1955). *Z. Naturforsch.* **10b**, 388–395.
- Kratky, O. and Pilz, I. (1972). *Quarterly Reviews of Biophysics* **5**, 481–537.
- Kratky, O. and Pilz, I. (1978). *Quarterly Reviews of Biophysics* **11**, 39–70.
- Kratky, O. and Porod, G. (1956). *Zeitschrift für Physikalische Chemie, Neue Folge* **7**, 236–241.
- Kratky, O. and Worthmann, W. (1947). *Monatsh. Chem.* **76**, 263–281.
- Kratky, O., Pilz, I. and Sekora, A. (1955). *Z. Naturforsch.* **10b**, 510–518.
- Kratky, O., Porod, G., Sekora, A. and Paletta, B. (1955). *J. Polymer Sci.* **16**, 163–175.
- Kratky, O., Pilz, I., Schmitz, P. J. and Oberdorfer, R. (1963). *Z. Naturforschg.* **18b**, 180–188.
- Kratky, O., Wawra, H., Pilz, I., Sekora, A. and Deinse, van A. (1964). *Monatsh. Chem.* **95**, 359–372.
- Kuntz, G., Stöckel, P. and Heidrich, H. G. (1978). *Hoppe-Seyler's Z. Physiol. Chem.* **359**, 959–973.
- Laggner, P., Kratky, O., Palm, W. and Holasek, A. (1971). *FEBS Lett.* **15**, 220–223.
- Laggner, P., Kratky, O., Palm, W. H. and Holasek, A. (1971). *Monatsh. Chem.* **102**, 1729–1744.
- Luzzati, V., Tardieu, A., Mateu, A. and Stuhrmann, H. B. (1976). *J. Mol. Biol.* **101**, 115–127.
- McDonald, R. C., Steitz, T. A. and Engelman, D. M. (1979). *Biochemistry* **18**, No. 2, 338–342.
- Meisenberger, O., Pilz, I. and Heumann, H. (1980). *FEBS Lett.* **112**, 39–41; **120**, 57–60; **122**, 117–120; (1981) *FEBS Lett.* **123**, 22–24.
- Mittelbach, P. (1964). *Acta Phys. Austriaca* **19**, 53–102.
- Moore, P. B., Langer, J. A. and Engelman, D. M. (1978). *J. Appl. Cryst.* **11**, 479–482.
- Müller, K., Kratky, O., Röschlau, P. and Hess, B. (1972). *Hoppe-Seyler's Z. Physiol. Chem.* **353**, 803–809.
- Ninio, J., Luzzati, V. and Yaniv, M. (1972). *J. Mol. Biol.* **71**, 217–229.
- Notbohm, H., Hollandt, H., Meissner, J. and Harbers, E. (1979). *Int. J. Biolog. Macromolecules* **1**, 180–184.
- Osborne, H. B., Sardet, C., Villaz, M. M. and Chabre, M. (1978). *J. Mol. Biol.* **123**, 177–206.
- Österberg, R. and Garrett, A. (1977). *Eur. J. Biochem.* **79**, 67–72.
- Österberg, R., Sjöberg, B., Rymo, L. and Lagerkvist, U. (1973). *J. Mol. Biol.* **77**, 153–158.

- Österberg, R., Sjöberg, B., Rymo, L. and Lagerkvist, U. (1975). *J. Mol. Biol.* **99**, 383–400.
- Paradies, H. H. and Vettermann, W. (1978). *Arch. Biochem. Biophys.* **191**, 169–181.
- Pessen, H., Kumosinski, T. F. and Timasheff, S. N. (1973). In "Methods in Enzymology", Vol. XXVII, Part D, pp. 151–209.
- Pilz, I. (1973). In "Physical Principles and Techniques of Protein Chemistry", (S. J. Leach, ed.) Part C, pp. 141–243. Academic Press, New York and London.
- Pilz, I., Herbst, M., Kratky, O., Oesterhelt, D. and Lynen, F. (1970). *Eur. J. Biochem.* **13**, 55–64.
- Pilz, I., Puchwein, G., Kratky, O., Herbst, M., Haager, O., Gall, W. E. and Edelman, G. M. (1970). *Biochemistry*, **9**, 211–219.
- Pilz, I., Glatter, O., Kratky, O. and Moring-Claesson, O. (1972a). *Z. Naturforsch.* **27B**, 518–524.
- Pilz, I., Kratky, O. and Rabussay, D. (1972b). *Eur. J. Biochem.* **28**, 205–220.
- Pilz, I., Kratky, O., Licht, A. and Sela, M. (1973). *Biochemistry* **12**, 4998–5005.
- Pilz, I., Engelborghs, Y., Witters, R. and Lontie, R. (1974a). *Eur. J. Biochem.* **42**, 195–202.
- Pilz, I., Kratky, O. and Karush, F. (1974b). *Eur. J. Biochem.* **41**, 91–96.
- Pilz, I., Kratky, O., Licht, A. and Sela, M. (1975). *Biochemistry* **14**, 1326–1333.
- Pilz, I., Schwarz, E. and Palm, W. (1976). *Eur. J. Biochem.* **71**, 239–247.
- Pilz, I., Schwarz, E. and Palm, W. (1977). *Eur. J. Biochem.* **75**, 195–199.
- Pilz, I., Glatter, O. and Kratky, O. (1979a). In "Methods in Enzymology", Vol. 61, pp. 148–249.
- Pilz, I., Goral, K. and Haar, F. v. d. (1979b). *Z. Naturforsch.* **34c**, 20–26.
- Pilz, I., Schwarz, E., Durchschein, P., Licht, A. and Sela, M. (1979c). *Proc. Nat. Acad. Sci. U.S.A.* **77**, 117–121.
- Pilz, I., Goral, K., Hoyarts, M., Lontie, R. and Witters, R. (1980). *Eur. J. Biochem.* **105**, 539–543.
- Plietz, P., Damaschun, G., Koppenschläger, G. and Müller, J. J. (1978a). *FEBS Lett.* **91**, 230–232.
- Plietz, P., Damaschun, G., Koppenschläger, G. and Müller, J. J. (1978b). *Acta Biol. Med. German.* **37**, 513–517.
- Porod, G. (1951). *Kolloid-Z.* **124**, 83–114.
- Porod, G. (1972). *Monatsh. Chem.* **103**, 395–405.
- Ptitsyn, O. B., Fedorov, B. A. and Voronin, L. A. (1974). *Studia biophysica* **47**, 9–25.
- Puchwein, G., Kratky, O., Gölker, C. F. and Helmreich, E. (1970). *Biochemistry* **9**, 4691–4698.
- Rolbin, J. A., Kayushina, R. L., Feigin, L. A. and Schedrin, B. M. (1973). *Kristallographija* **18**, 701–710.
- Sardet, C., Radieu, A. and Luzzati, V. (1976). *J. Mol. Biol.* **105**, 383–407.
- Schausberger, A. and Pilz, I. (1977). *Makrom. Chem.* **178**, 211–225.
- Serdyuk, I. N. and Grenader, A. K. (1975). *FEBS Lett.* **59**, 133–136.
- Simon, I. (1972). *Eur. J. Biochem.* **30**, 184–194.
- Stöckel, P., Mayer, A. and Keller, R. (1973). *Eur. J. Biochem.* **37**, 193–200.
- Stuhrmann, H. B. (1970a). *Z. phys. Chem. Neue Folge* **72**, 185–198.
- Stuhrmann, H. B. (1970b). *Acta Cryst. A* **26**, 297–306.
- Stuhrmann, H. B. (1973). *J. Mol. Biol.* **77**, 363–369.
- Stuhrmann, H. B. (1978). *Quarterly Reviews of Biophysics* **11**, I, 71–98.

- Stuhrmann, H. B. and Miller, A. (1978). *J. Appl. Cryst.* **11**, 325–345.
- Sund, H., Pilz, I. and Herbst, M. (1969). *Eur. J. Biochem.* **7**, 517–525.
- Tardieu, A., Mateu, L., Sardet, C., Weiss, B., Luzzati, V., Aggerbeck, L. and Scanu, A. M. (1976). *J. Mol. Biol.* **101**, 129–153.
- Timschenko, A. A., Ptitsyn, O. B., Dolgikh, D. A. and Fedorov, B. A. (1978a). *FEBS Lett.* **88**, 105–108.
- Timschenko, A. A., Ptitsyn, O. B., Troitsky, A. V. and Denesuk, A. I. (1978b). *FEBS Lett.* **88**, 109–113.
- Vainshtein, B. K., L'vov, Yu. M., Feigin, L. A., Gvozdev, R. I., Marakushev, S. A., and Likhtenstein, G. I. (1979). *Doklady Akademii Nauk SSSR* **247**, 974–978.
- Vainshtein, B. K., Feigin, L. A., L'vov, Yu. M., Gvozdev, R. I., Marakushev, S. A. and Likhtenstein, G. I. (1980). *FEBS Lett.* **116**, 107–110.
- Watson, H. C. (1969). *Prog. Stereochem.* **4**, 229–333.
- Wilhelm, P., Pilz, I., Palm, W. and Bauer, K. (1977). *Eur. J. Biochem.* **84**, 457–463.
- Witz, J., Timasheff, S. N. and Luzzati, V. (1964). *J. Amer. Chem. Soc.* **86**, 168–173.
- Yamaguchi, T., Wakabayashi, K. and Mitsou, T. (1974). *Biochem. Biophys. Acta* **372**, 450–456.
- Zernike, F. and Prins, J. A. (1927). *Z. Phys.* **41**, 184–192.
- Zinke, M. (1978). *Studia biophysica Berlin* **73**, 235–236 and Microfiche 1/44–56.
- Zinke, M., Damaschun, G., Müller, J. J. and Ruckpaul, K. (1978). *Studia biophysica Berlin* **71**, 135–136.
- Zipper, P. and Durchschlag, H. (1978a). *Eur. J. Biochem.* **87**, 85–99.
- Zipper, P. and Durchschlag, H. (1978b). *Z. Naturforsch.* **33c**, 504–510.
- Zipper, P. and Durchschlag, H. (1980a). *Monatsch. Chem.* **111**, 1367–1390.
- Zipper, P. and Durchschlag, H. (1980b). *Rad. Environm. Biophys.* **18**, 99–121.
- Zipper, P. and Durchschlag, H. (1980c). *Z. Naturforsch.* **35c**, 890–901.
- Zipper, P., Kratky, O., Hermann, R. and Hahn, T. (1971). *Eur. J. Biochem.* **18**, 1–9.

9

Nucleic Acids and Nucleoproteins

P. ZIPPER

Institut für Physikalische Chemie der Universität Graz, Graz, Austria

I. Nucleic acids	296
A. DNA and model polynucleotides	296
B. High molecular weight RNA (H-RNA)	299
C. Low molecular weight RNA	302
II. Viruses	304
A. Isometric viruses	304
B. Rod-like viruses	310
C. Large bacteriophages	311
III. Ribosomes	312
A. Ribosomes and ribosomal subunits	312
B. Polysomes	317
IV. Chromatin	317
A. Nucleosomes and core particles	318
B. Chromatin, chromosomes and nuclei	320
References	321

Among the various constituents of living systems, nucleic acids play the central role. They carry the genetic information and take part in the various mechanisms which provide for the replication of this information and for its translation into protein structures. In the cell, nucleic acids occur in manyfold forms, either in the free state or closely associated with proteins and other components as, for instance, in ribosomes and in chromatin. Nucleic acids are also the essential components in viruses.

In the exploration of the three-dimensional structure of nucleic acids and of the various nucleoproteins, small angle scattering, besides other techniques such as X-ray crystallography and electron microscopy, has contributed a good deal of important information on the size, shape and internal structure of these particles.

Since it is impossible to give here a full account of all the hundreds of papers

dealing with small angle studies on nucleic acids and related particles, this chapter is only intended to represent a survey of the essential applications of small angle solution scattering in the field of nucleic acids research and a first and necessarily very brief introduction to specific working procedures. For details, the reader must always refer to the original literature.

According to the diversity of occurrence and structure of nucleic acids and nucleoproteins, the chapter is divided into four parts which successively deal with small angle studies on isolated nucleic acids, on viruses, on ribosomes, and on chromatin.

I. Nucleic Acids

A. DNA and Model Polynucleotides

The double helix as the structural principle of DNA and its dimensions in the crystalline state are now well established. In dilute solution linear double-stranded DNA behaves like a stiff chain. Due to the rigidity of the molecule and its low mass per unit length, the overall size of native DNA is much too large to allow measurements of the innermost portion of the scattering curve. Thus neither the radius of gyration nor the molecular weight of undegraded DNA molecules can be determined by SAXS. The determination of these parameters for DNA which has been degraded by sonification may also be a rather difficult task (cf. Wawra *et al.*, 1970).

In the experimentally accessible angular range (cf. Fig. 1), the SAXS curve of linear DNA reflects essentially the rod-like shape of shorter sections of the molecule and enables the establishment of parameters concerning the cross-section of the DNA double helix such as the mass per unit length M_c and the cross-sectional radius of gyration R_c . The periodicities along the chain, due to the double-helical structure, cause the occurrence of maxima in the wide-angle region of the scattering curve (Kirste and Oberthür, 1969; Bram and Beeman, 1971). The supercoiling of circular DNA, on the other hand, causes the appearance of maxima at small and very small angles (Brady *et al.*, 1976; Benham *et al.*, 1980).

In that angular range from which R_c and M_c are derived, interparticulate interferences do not influence much the DNA scattering curve (this holds particularly in the presence of salts), thus an extrapolation of the data to zero concentration may often be omitted (cf. Luzzati *et al.*, 1961a, 1967a; Kratky, 1963; Bram and Beeman, 1971). At smaller angles, however, the shape of the scattering curve varies considerably with the concentration of DNA (Kirste and Oberthür, 1969; Wawra *et al.*, 1970).

DNA, like other nucleic acids, is a polyelectrolyte. In aqueous solution,

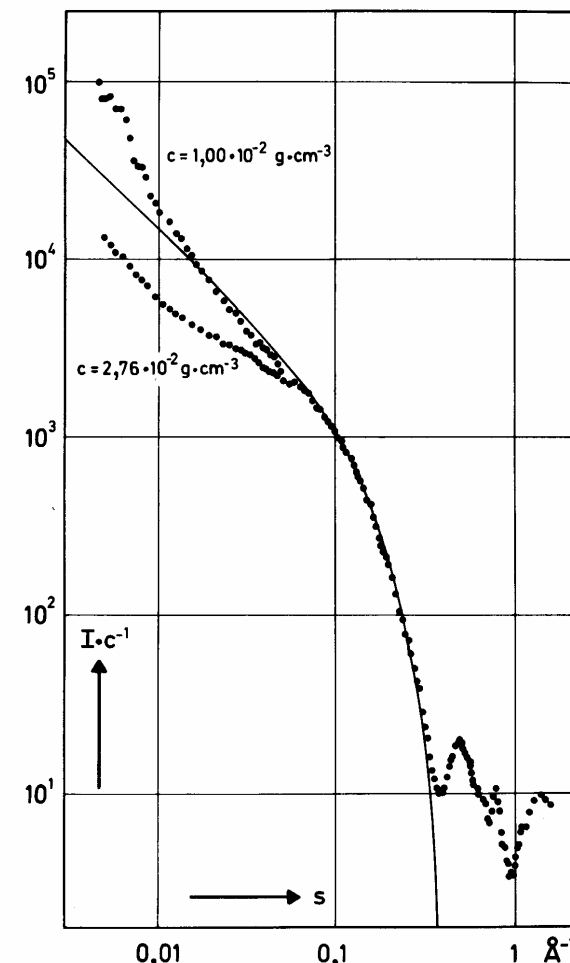


FIG. 1. SAXS and WAXS curve of DNA from herring sperm. The solid curve is the theoretical scattering function for infinitely long rods. ($s = 4\pi/\lambda \cdot \sin \vartheta [\text{\AA}^{-1}]$). From Kirste and Oberthür (1969).

nucleic acids may interact with water molecules or small electrolytes. The influence of this interaction on the number of excess electrons must be taken into account accordingly when molecular weights or related parameters are determined from SAXS measurements. This can be done by making use of the electron density increment $(\partial\rho/\partial c_2)_\mu$ at constant chemical potentials (Eisenberg and Cohen, 1968) or of the parameter Δz (cf. Zipper and Büinemann, 1975) properly defined via the isopotential specific volume v'_2 (Kupke, 1972):

$$\Delta z = z_2 - z_s d_s v'_2 + \sum_{i \neq 2} \xi_i (z_i - z_s)$$

Fortunately, the contribution of the term containing the interaction parameter ξ_i is not very important, thus omitting this term does usually not involve a great error. Strictly, the solutions must be in dialysis equilibrium with the respective solvents, and the density measurements to determine v'_2 should be performed, if possible, with the same solutions and solvents as used for the SAXS experiments.

In the early SAXS studies on DNA and other nucleic acids the above conditions were usually not fulfilled (cf. Luzzati *et al.*, 1967a, for a procedure to eliminate solvation effects). Nevertheless, those studies yielded M_c values which were close to the theoretical value for the *B* form of DNA. A critical recalculation of some of these M_c values has been presented by Eisenberg and Cohen (1968).

For the determination of the parameters R_c and M_c , Luzzati and co-workers evaluated directly the slit-smeared scattering curves by comparing them in double-logarithmic plots with the theoretical slit-smeared scattering functions for infinitely long rods (Luzzati *et al.*, 1961a, 1961b, 1962, 1964, 1967a, 1967b; Witz and Luzzati, 1965). The more recommendable procedure is, of course, the evaluation of cross-section Guinier plots of the desmeared scattering curves (cf. Kratky, 1963; Wawra *et al.*, 1970; Gulik *et al.*, 1970; Bram and Beeman, 1971; Zipper, 1973; Zipper and Bünnemann, 1975).

Bram and Beeman (1971) observed that in the cross-section Guinier plots for DNA two straight lines can actually be drawn from which two different pairs of values for R_c and M_c can be derived. The authors interpreted this finding on the basis of a core and shell model in which a low-density Debye-Hückel layer of counter-ions surrounded a high-density core of partially ionized DNA. According to this model, the larger value for R_c would represent the entire cross-section of core and shell, while the smaller R_c would be related more to the cross-section of DNA itself. Actually, values for M_c close to the theoretical value for the *B* form of DNA (as salt) were only obtained from the intercept of the steeper of the two straight lines.

A perturbation of the solvent in the vicinity of DNA was also assumed by Luzzati *et al.* (1961a, 1967a) because of the observed decrease of R_c with increasing electron density of the solvent. However, the existence of two cross-section factors in the SAXS curves was obviously obscured in these studies by the evaluation procedure already described. On the other hand, Gulik *et al.* (1970), who found that the cross-section curve of poly *rC* can be approximated by the sum of two Gaussians, explained this finding by the helical structure and not by the assumption of a core and shell structure.

Double straight lines in cross-section Guinier plots of DNA or polynucleotide

scattering curves have also been observed by Zipper (1973) and Zipper and Bünnemann (1975). Another core and shell model for DNA was derived by Wawra *et al.* (1970) from SAXS measurements on highly diluted solutions.

The dependence of the parameters R_c and M_c of DNA on the nature and concentration of counter-ions was investigated mainly by Luzzati *et al.* (1967a) and by Bram and Beeman (1971). Structural transitions of DNA and of poly *rA*, poly *rU* and poly *rC*, as caused by temperature, pH or denaturing agents, were also studied by Luzzati and co-workers (Luzzati *et al.*, 1964, 1967b; Witz and Luzzati, 1965; Gulik *et al.*, 1970); structural transitions of poly [$d(A - s^4T) \cdot d(A - s^4T)$] due to variation of salt concentration by Zipper (1973).

The determination of the parameters R_c and M_c for complexes of DNA with various ligands (proflavine, actinomycin, actinomine, mercury compounds) was used to study structural changes of DNA due to ligand binding (Luzzati *et al.*, 1961b; Wawra *et al.*, 1970; Zipper *et al.*, 1972, 1978, 1982a; Zipper and Bünnemann, 1975). The quantitative interpretation of changes of R_c is not unambiguous, because these changes may reflect, besides the trivial effect of the ligand, structural changes of the DNA as well as changes in the distribution of ions around the DNA. On the other hand, changes of M_c can arise, apart from the increase of mass due to the ligand, only from structural changes of the DNA. For a correct determination of the M_c of DNA-ligand complexes the isopotential specific volumes of the complexes and the binding ratios r_b must be known. Then changes of M_c upon ligand binding, from $M_{c,o}$ to $M_{c,r}$, can be interpreted directly in terms of changes of the length l per nucleotide pair or of the length L of the double helix:

$$\frac{L_r}{L_o} = \frac{l_r}{l_o} = \frac{[1 + r_b M_L / M_{NP}] M_{c,o}}{M_{c,r}}$$

M_L and M_{NP} designate the molar mass of one ligand and one nucleotide pair respectively.

Comparative studies of the secondary structure of DNA and other polynucleotides in solution were performed by Bram (1971a, 1971b, 1971c) and Bram and Beeman (1971). By comparison of the experimental WAXS curves with theoretical curves calculated for various models, the author could show that the secondary structure varies with the base composition. SAXS and WAXS measurements were also used to study the secondary and the supramolecular structure of condensed DNA and condensed DNA-spermine complexes in dependence upon the experimental conditions (Damaschun *et al.*, 1978a, 1978b; Becker *et al.*, 1979).

B. High Molecular Weight RNA (H-RNA)

In contrast to most DNAs, RNA usually consists of a chemically single strand. Since this is capable of bending back on itself it may form both rigid

double-helical segments besides unpaired regions, which are more flexible. This is clearly reflected by the scattering behaviour. At medium scattering angles where the rod-like structure of the segments of the H-RNA molecule dominates the scattering, the scattering curve is similar to that of DNA. At small scattering angles, on the other hand, the scattering is dominated by the three-dimensional arrangement of the rod-like segments; thus the intensity is higher than it would be when the rod-like segments scattered independently (cf. Timasheff *et al.*, 1961; Timasheff, 1964). The wide angle region of the scattering curve reflects the secondary structure of the double-helical regions of H-RNA (Damaschun *et al.*, 1978b).

The early SAXS studies on H-RNAs from different sources were confined mainly to the determination of the cross-section parameters R_c and M_c from the rod-type region of the scattering curves and to an interpretation of the deviations at smaller angles from the theoretical curves for infinitely long rods in terms of the mean length of the rod-like segments (Timasheff *et al.*, 1961; Witz *et al.*, 1965; Luzzati *et al.*, 1967b).

The structure, especially the superstructure, of H-RNA depends on the presence of ions, preferably of Mg^{2+} . In the presence of sufficient amounts of Mg^{2+} , the RNA molecule adopts a fairly compact structure, whereas in the absence of these ions as much less compact, more extended structure is favoured. The first complete SAXS curve of compact H-RNA (from phage MS2) was measured by Zipper *et al.* (1973a, 1974, 1975; cf. Fig. 2). At small scattering angles the scattering curve was found to be similar to that for an elongate flat particle; the parameters M , R , D , M_c , R_c , and R_t , all referring to the entire RNA molecule, were determined partly from the scattering curve itself, and partly from the $p(r)$ function. From the rod-type region of the SAXS curve at larger angles a second pair of values for R_c and M_c could be determined, which referred to the substructure of the RNA molecule; the M_c value allowed an estimate of the double-helix content. An almost perfect fit of the experimental SAXS curve was obtained by theoretical curves for models which simulated both the overall shape and the substructure of the RNA molecules.

The transition of MS2 RNA from the extended structure in the absence of ions to the compact structure by addition of Mg^{2+} was also studied by SAXS (Clauwaert *et al.*, 1977; Zipper *et al.*, 1982b). For the RNA molecule in the extended form, only parameters concerning the cross-section of the entire molecule and of the rod-like segments could be determined by SAXS. While the R_c and M_c for the segments were found to be widely independent of the Mg^{2+} concentration, the R_c and M_c for the overall shape increased with the Mg^{2+} concentration. For each Mg^{2+} concentration, the length L of the RNA particle was calculated from the ratio of the known molar mass M and the experimental M_c , and the radius of gyration R of the entire molecule was then estimated from L and the experimental R_c . The estimated R were found to be

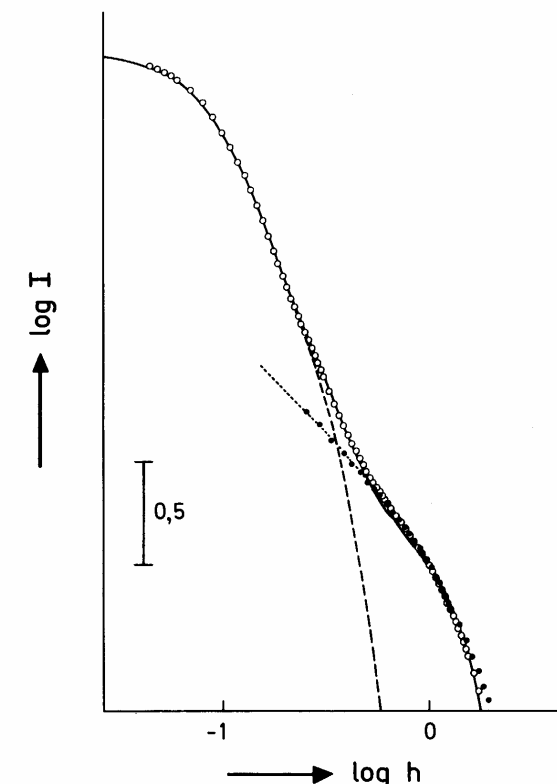


FIG. 2. SAXS curves of the RNA from phage MS2 in the presence (○) or absence (●) of Mg^{2+} . The long-dashed curve is the theoretical scattering function for an oblate elliptic cylinder (axial ratio 1,9 : 1 : 0,3), the short-dashed curve is the theoretical scattering function for infinitely long rods; the solid curve has been calculated for a coil model which simulates both the overall shape and the substructure of the RNA molecules. ($h = 4\pi/\lambda \cdot \sin \vartheta$ [nm $^{-1}$]). After Zipper *et al.* (1975, 1982b).

in good agreement with the R as measured directly by means of light scattering. Further SAXS studies on MS2 RNA concerned the influence of temperature on the structure of native and of formaldehyde-denatured RNA; the formation of random coils at high temperatures could be established by the determination of the persistence length (Zipper *et al.*, 1973a, 1982b).

The 16-S ribosomal RNA is another H-RNA, the complete scattering curve of which has been measured by SAXS (Folkhard *et al.*, 1975). The analysis of the scattering curve and its fit by a model curve were performed similarly as with MS2 RNA. The authors investigated also the complex of 16-S RNA with the ribosomal protein S4.

The 16-S RNA binding site for the protein S4 can be isolated. This S4-RNA

was studied by Österberg *et al.* (1977) who determined M and R and fitted the slit-smeared SAXS curve by the theoretical slit-smeared curve for an oblate ellipsoid (for the curve-fitting technique cf. Sjöberg, 1978). Recently, SANS studies were performed on similar fragments of 16-S RNA (12-S RNA, 13-S RNA) and on their complexes with protein S4 and other ribosomal proteins (Serdyuk *et al.*, 1980a, 1980b; Österberg *et al.*, 1980a, b). In the studies on the complexes, contrast variation by H_2O/D_2O exchange (cf. Section III) was used to mask the RNA in order to study the proteins *in situ*.

C. Low Molecular Weight RNA

Two different kinds of low molecular weight RNA have been studied extensively by SAXS, namely various species of *tRNA* and the 5-S ribosomal RNA. In both cases, the experimental SAXS curves could not be fitted well by the theoretical curves for simple models such as ellipsoids or cylinders.

In the case of *tRNA*, several authors tried to fit the experimental curves by the curves for rather detailed models derived from various clover-leaf base-pairing configurations (Lake and Beeman, 1967, 1968; Connors *et al.*, 1969; Ninio *et al.*, 1969, 1972). Model curves were calculated in the Beeman group by replacing each nucleotide with three scattering units (phosphate, ribose, base); Ninio's calculations were performed by means of the cube method, using the coordinates of all non-hydrogen atoms.

A different approach to finding a model equivalent in scattering to *tRNA* was chosen by Kratky *et al.* (1969) and Pilz *et al.* (1970). They fitted the SAXS curve of *tRNA^{Phe}* by the curve for a model composed of one large and two small ellipsoids. This L-shaped model was suggested by the finding of two different cross-section factors in the SAXS curve of *tRNA^{Phe}*.

While in most of the earlier SAXS studies on *tRNA* the radius of gyration had been determined as the only molecular parameter besides curve fitting (for an exception, cf. Krigbaum and Godwin, 1966), Pilz *et al.* (1970) determined a variety of parameters such as M , R , V , M_c , R_c , and hydration. Moreover, measurements were performed at low and at high temperatures. The observed increase in R upon heating was found to be correlated with the increase of UV absorption. The determination of a persistence length from the measurements at 70°C established the random coil conformation of *tRNA* at this temperature. The reversible break-down of the tertiary structure of *tRNA* upon heating was also reflected by the reversible disappearance of a side-maximum in the SAXS curve. A similar study as with *tRNA^{Phe}* was also performed with *tRNA^{Ser}* (Pilz *et al.*, 1977).

A dependence of R of *tRNA^{Phe}* on the nature of the counter-ions (Li^+ , K^+ , Cs^+ , Mg^{2+} , Ba^{2+}) was established by Pilz *et al.* (1971). R was found to increase

slightly with the molecular weight of the counter-ions. High concentrations of Mg^{2+} (or the presence of spermine) lead to a considerable increase in R because of dimerization of the *tRNA* (Laggner *et al.*, 1980). Recently, the influence of counter-ions (Na^+ , K^+ , Mg^{2+}) was also investigated in a SANS study on *tRNA^{Phe}* (Li *et al.*, 1980). The scattering behaviour in D_2O was found to be highly dependent on the nature of the ions, probably due to the electrostriction of water.

Ninio *et al.* (1972) investigated *tRNA^{Val}* in different states. While the R of the unacylated and of the acylated form of the molecule were practically the same, significant differences between the SAXS curves were observed at larger angles.

Complexes of various *tRNAs* with aminoacyl-*tRNA* synthetases were investigated both by SAXS (Österberg *et al.*, 1975; Pilz *et al.*, 1979) and SANS (Giegé *et al.*, 1977; Dessen *et al.*, 1978; Zaccai *et al.*, 1979).

The size and shape of 5-S RNA was investigated by Connors and Beeman (1972) and by Österberg *et al.* (1976a). Both groups of authors determined the radius of gyration as the only molecular parameter and attempted to fit the experimental scattering curves by model curves. These were calculated similarly as has been described for *tRNA* (cf. Lake and Beeman, 1968). As compared to *tRNA*, the SAXS curve of 5-S RNA falls off more slowly, suggesting that the particle is more anisometric than *tRNA* (Connors and Beeman, 1972). The best fit of the SAXS curve was achieved by a Y-shaped model (Österberg *et al.*, 1976a). Müller *et al.* (1980, 1981) studied 5-S RNA by SAXS and WAXS.

Österberg and Garrett (1977) and Österberg (1979) investigated also binary and ternary complexes of 5-S RNA with the ribosomal proteins L18 and L25. These proteins are of similar size as 5-S RNA (Österberg *et al.*, 1976b; Österberg, 1979). The stoichiometry of the complexes and their stability constants were determined by means of X-ray titration studies. For this purpose, SAXS measurements were performed on several series of solutions in which the concentration of one component (protein) was varied whereas the concentrations of the other components (RNA alone or RNA and the other protein) were kept constant. The scattering of the pure components was recorded separately. The difference between the absolute intensity of the complex solution and the sum of the absolute intensities of the corresponding solutions of pure components, all measurements taken at a constant small scattering angle, were then evaluated by using a method developed by Österberg (cf. Österberg *et al.*, 1975). The results of the titration studies were used to correct the SAXS curves of the complex solutions for the contributions of free components prior to the determination of the parameters R and M and the analysis of the curves for the shape and structure of the complexes. Recently, 5-S RNA and some of its complexes with ribosomal proteins were also investigated by SANS (May *et al.*, 1980b).

II. Viruses

The first SAXS studies on isotropic solutions of viruses were performed by Leonard *et al.* (1951, 1953) who investigated several plant viruses of highly isometric sphere-like shape. Since then numerous SAXS studies have been performed which deal with viruses or related particles of similar isometric shape. Only a few SAXS studies were performed on isotropic solutions of anisometric viruses such as the rod-like tobacco mosaic virus. Some large bacteriophages such as T2 which contains a head and a tail have also been investigated by SAXS. More recently, the method of SANS was also applied successfully to virus research. A list of viruses studied by SAXS or SANS is given in Table 1.

A. Isometric Viruses

Because of the high isometry of these viruses, their scattering curves are, especially at small and moderate angles, similar to the scattering curves for spheres or hollow spheres and contain, like these curves, several distinct side-maxima (cf. Fig. 3). In some SAXS studies, the size of viruses was therefore estimated simply by comparison of the positions of the maxima and minima in the experimental curves with the positions of the extrema in the theoretical curves for solid and hollow spheres (Leonard *et al.*, 1951, 1953; Schmidt *et al.*, 1954; Finch *et al.*, 1967). This method, however, can only be an approximation because viruses contain several components of different electron density (RNA or DNA, protein, sometimes also lipids) which are not uniformly distributed over the entire virus. Moreover, the isometric viruses are not truly spherical; the icosahedral symmetry of their protein shell was established by X-ray diffraction and electron microscopy (cf. Caspar and Klug, 1962). Both the non-uniform density distribution and the deviations from spherical symmetry influence the scattering curve.

As was established by Harrison (1969) and Stuhrmann (1970), the scattering intensity $I(h)$ of a quasi-spherical particle can be expressed by the following sum.

$$I(h) = A_0(h)^2 + \sum_n A_n(h)^2$$

where $A_0(h)$ is the Fourier transform of the spherically averaged radial electron density distribution of the particle and the $A_n(h)$ are terms that depend on the not spherically symmetric components of the particle density. At $h = 0$ only the zero-order amplitude $A_0(h)$ contributes to scattering while the higher order terms $A_n(h)$ equal zero. They are also small at low values of h and only

TABLE 1. Selected Small Angle X-ray (X) and Neutron (N) Scattering Studies on Viruses

alfalfa mosaic virus	X	Van DomeLEN and Beeman, 1962
	N	Cusak <i>et al.</i> , 1981
adenovirus, hexon	X	Teig-Jensen <i>et al.</i> , 1972; Berger <i>et al.</i> , 1978
broad bean mottle virus	X	White, 1962; Anderegg, 1967; Finch <i>et al.</i> , 1967; White and Fischbach, 1973
brome grass mosaic virus	X	Anderegg <i>et al.</i> , 1963; Anderegg, 1967
cauliflower mosaic virus	N	Jacrot <i>et al.</i> , 1976, 1977; Chauvin <i>et al.</i> , 1978a
frog virus 3	N	Chauvin <i>et al.</i> , 1979
polyoma virus	X	Cuillel <i>et al.</i> , 1979
satellite tobacco necrosis virus	X	Jack and Harrison, 1975
Sindbis virus	X	Sjöberg, 1977
southern bean mosaic virus	X	Chauvin <i>et al.</i> , 1977
	X	Harrison <i>et al.</i> , 1971b
	X	Leonard <i>et al.</i> , 1951, 1953; Schmidt and Taylor, 1967
squash mosaic virus	N	Jacrot, 1976; Jacrot <i>et al.</i> , 1977
tomato bushy stunt virus	X	Anderegg, 1967
tobacco mosaic virus	X	Leonard <i>et al.</i> , 1953; Harrison, 1969
tobacco necrosis virus	N	Chauvin <i>et al.</i> , 1978b
turnip yellow mosaic virus	X	Kratky <i>et al.</i> , 1957; Malmon, 1957; Longley, 1963; Fedorov, 1971
(wild) cucumber mosaic virus	X	Leonard <i>et al.</i> , 1951, 1953
	X	Schmidt <i>et al.</i> , 1954
	N	Jacrot <i>et al.</i> , 1977
	X	Anderegg <i>et al.</i> , 1961; Anderegg, 1967; Jack and Harrison, 1975
phages:	N	Jacrot <i>et al.</i> , 1977
DD2	X	Boyarintseva <i>et al.</i> , 1973c; Feigin <i>et al.</i> , 1974
fd	N	Torbet, 1979
fr, MS2, R17	X	Fischbach <i>et al.</i> , 1965; Anderegg, 1967; Zipper <i>et al.</i> , 1971a, 1971b, 1973b
Pf1	N	Jacrot <i>et al.</i> , 1977
PM2	X	Torbet, 1979
	X	Harrison <i>et al.</i> , 1971a; Satake <i>et al.</i> , 1980
	N	Schneider <i>et al.</i> , 1978
P22	X	Earnshaw <i>et al.</i> , 1976; Earnshaw and Harrison, 1977; Earnshaw and King, 1978
S _D	X	Boyarintseva <i>et al.</i> , 1973a, 1973b, 1974b, 1977; Feigin <i>et al.</i> , 1974
T2	X	Boyarintseva <i>et al.</i> , 1974a; Feigin <i>et al.</i> , 1974
T7	N	Agamalian <i>et al.</i> , 1979
λ	X	Earnshaw and Harrison, 1977; Künzler and Berger, 1978; Earnshaw <i>et al.</i> , 1979
φ29	X	Subirana <i>et al.</i> , 1979

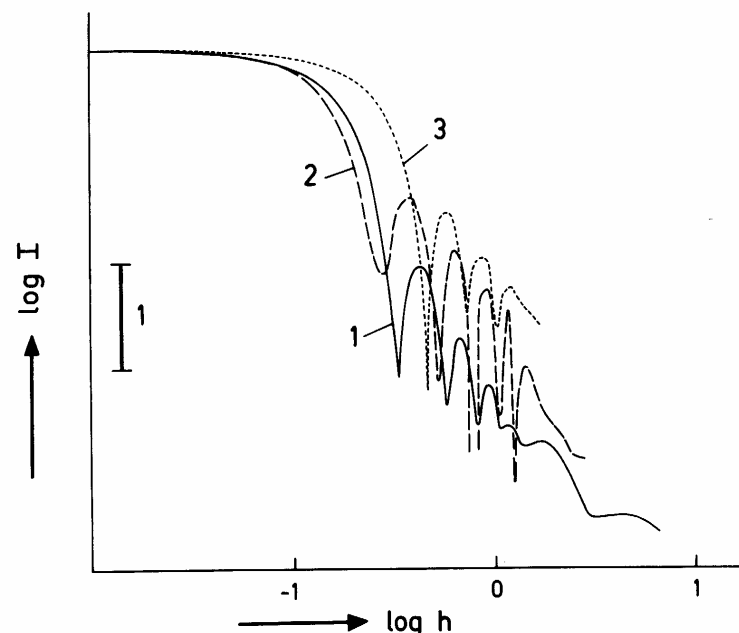


FIG. 3. Normalized SAXS curves of phage *fr* in dilute buffer ($\rho_s = 336 \text{ e nm}^{-3}$; curve 1) and in sucrose solution ($\rho_s = 427 \text{ e nm}^{-3}$; curve 3), and of empty capsids of phage *fr* (artificial top component; curve 2). After Zipper *et al.* (1971a, 1973b).

contribute to the scattering significantly at larger h values. According to the icosahedral selection rule (cf. Finch and Holmes, 1967) the first possible higher-order term is that with $n = 6$; however, depending on the surface structure of the virus, terms with $n < 18$ may be insignificant (Harrison, 1969). In a limited angular range ($0 \leq h \leq h_{\max}$), the square root $F(h)$ of the scattering intensity $I(h)$ can therefore be considered as a good approximation to $A_0(h)$, thus the radial electron density distribution may be calculated from it. The upper limit h_{\max} is related to the resolution at which the structure of the virus particle departs from spherical symmetry; this is of the magnitude of the inter-subunit distances in the protein shell (Harrison, 1969; Earnshaw *et al.*, 1976). Experience has shown that usually the zero-order amplitude $A_0(h)$ remains dominant up to h values which correspond to spacings of about 10–20% of the virus diameter, though even in this angular range departures from spherical symmetry might be responsible for the generally observed lack of true zeros in the scattering curves.

Interparticle interferences may influence the scattering curve considerably only in the region of the central maximum. In the range of the first side-maximum the influence of interferences is already insignificant, even at very

high concentrations (Harrison, 1969). The analysis of the interference effects in terms of the pair correlation function $g(r)$ may yield information on the interparticle interactions (Schmidt and Taylor, 1967).

Determinations of the molecular weight of isometric viruses by SAXS or SANS were seldom performed (cf., for example, Zipper *et al.*, 1971a; Sjöberg, 1977; Chauvin *et al.*, 1977; Cuillel *et al.*, 1979). The radius of gyration was determined mostly from Guinier plots of the scattering curve, sometimes also from the $p(r)$ function (cf. Zipper *et al.*, 1973b) or from the position of the first side-maximum in the scattering curve (cf. Zipper *et al.*, 1971a; Sjöberg, 1977). The $p(r)$ and $\gamma(r)$ functions have also been used to determine the diameter of virus particles independently of any model assumptions (Zipper *et al.*, 1973b; Jacrot, 1976; Jacrot *et al.*, 1977; Chauvin *et al.*, 1978b).

Anderegg *et al.* (1961) were the first who calculated the radial excess electron density distribution $\Delta\rho(r)$ of viruses in solution by Fourier inversion of the $F(h)$ curve. This curve was obtained from the positive or negative square root of $I(h)$; the central maximum was taken positive, subsequent maxima were used with alternating signs. Intensities near the minima of the $I(h)$ curve were ignored. The $F(h)$ curve was drawn such that it fitted the data calculated from the intensity maxima and passed through zero in between. The $F(h)$ curve was multiplied by a Gaussian "artificial temperature factor" which reduced the amplitude to 0.1 of its value at the cut-off point (that was after the fifth maximum). Similar procedures were also used in other SAXS studies on viruses, both in the Anderegg group (White, 1962; Anderegg *et al.*, 1963; Fischbach *et al.*, 1965; White and Fischbach, 1973) and by other authors (e.g. Zipper *et al.*, 1971a, 1973b).

A somewhat different method of obtaining the $F(h)$ curve was applied by Harrison and co-workers (Harrison, 1969; Harrison *et al.*, 1971a, 1971b; Earnshaw *et al.*, 1976) who used photographic instead of counter recording of the scattered radiation. They drew a smooth base-line through the minima in the densitometer tracings and subtracted this curve as a background. By this subtraction, the intensity reached zero between the maxima, however the heights of the maxima were also reduced, in contrast to Anderegg's procedure. Both the subtraction of a background and the application of an artificial temperature factor were assumed to damp the influence of higher-order harmonics on the transforms (Harrison, 1969). For an exception from the use of alternating signs of the maxima, cf. Harrison *et al.* (1971b).

The $\Delta\rho(r)$ functions obtained by direct Fourier transformation of the $F(h)$ curve are afflicted with termination errors, even if an artificial temperature is used (these factors do not really eliminate the termination effects). Therefore, a direct comparison of these $\Delta\rho(r)$ curves with simple models which are usually concentric shells of different density is not adequate. A better way is to calculate, first, the amplitude curve of the model and to transform it in exactly

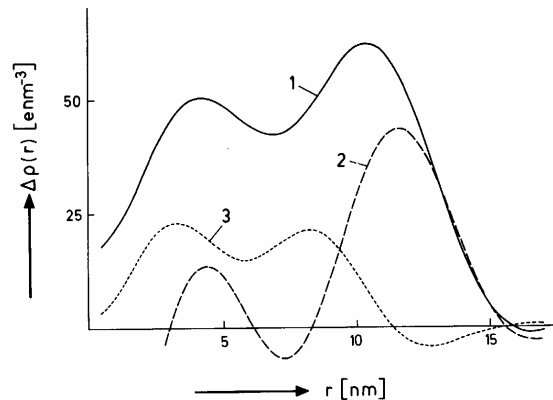


FIG. 4. Radial excess electron density distributions as calculated from the scattering curves shown in Fig. 3. Curve 1 represents the whole phage f_1 , curve 2 its protein coat; curve 3 is the RNA core as seen at vanishing protein contrast. After Zipper *et al.* (1971a, 1973b).

the same way as the $F(h)$ curve of the virus. Since the $\Delta\rho(r)$ curve so calculated is then afflicted with the same errors due to the Fourier inversion as the experimental $\Delta\rho(r)$ function, both functions can be compared with each other (Anderegg *et al.*, 1961, 1963; Fischbach *et al.*, 1965; Zipper *et al.*, 1971a).

The indirect Fourier transformation by means of Glatter's method (approximation of the $F(h)$ curve by the Fourier transforms of a set of splines representing the $\Delta\rho(r)$ function; Glatter, 1977) has not been applied to viruses so far. Another kind of indirect Fourier transformation was used by Sjöberg (1977, 1978), Schneider *et al.* (1978) and Chauvin *et al.* (1978b), who fitted the slit-smeared scattering curves of shell models to the experimental slit-smeared scattering curves of viruses. For future studies the convolution square-root technique (Glatter, 1981) which avoids the phase problem should also be taken into consideration.

The $\Delta\rho(r)$ functions obtained from SAXS measurements of viruses in dilute buffer do not always allow localization of the different components within the virus particle unambiguously. Though the electron density of the nucleic acid itself is higher as compared to that of protein, different extents of hydration may compensate or even overcompensate the electron density difference between nucleic acid and protein component in the virus (cf. Fig. 4 and below). In viruses which contain large amounts of lipids these may be localized very easily because of the negative excess electron density of the lipid hydrocarbons (cf. Harrison *et al.*, 1971a, 1971b).

The localization of protein and nucleic acid within the virus is facilitated when virus-like protein particles which contain no nucleic acid are available. SAXS measurements on such empty capsids have helped to determine the

radial dimensions of the protein coat of several viruses (Schmidt *et al.*, 1954; Anderegg *et al.*, 1961; Anderegg, 1967; Zipper *et al.*, 1973b).

Another way to get insight into the radial distribution of protein and nucleic acid within the virus is the variation of the contrast to the virus particle. In SAXS this can be achieved by increasing the electron density of the solvent by addition of appropriate substances; e.g. ammonium sulfate, sodium sulfate, sucrose, or melezitose have been used for this purpose (Harrison, 1969; Harrison *et al.*, 1971a; Zipper *et al.*, 1971a; White and Fischbach, 1973). In this way, however, the electron density of the solvent can only be made equal to the electron density of the protein component of the virus, so that the nucleic acid alone causes SAXS, but the solvent electron density cannot be increased to such an extent as required to match the higher electron density of the nucleic acid. It is the main advantage of SANS over SAXS, that by appropriate choice of the H_2O/D_2O ratio in the solvent, the contrast for either the protein or the nucleic acid can be made zero; thus the distinction between protein and nucleic acid domains is easier than with SAXS (cf. Jacrot *et al.*, 1976, 1977; Jacrot, 1976; Chauvin *et al.*, 1977, 1978a, 1978b, 1979; Schneider *et al.*, 1978; Cuillel *et al.*, 1979).

Because virus particles are penetrated by solvent, the spherically averaged excess electron density $\Delta\rho(r)$ can be expressed by the following relation (Harrison, 1969):

$$\Delta\rho(r) = [1 - \phi_s(r)] \cdot [\rho_p(r) - \rho_s]$$

where $\phi_s(r)$ is the volume fraction at radius r which is penetrable by solvent of the electron density ρ_s (i.e. the same electron density as for the surrounding solvent) and $\rho_p(r)$ was called the intrinsic electron density of the particle. By measurements in solvents of different electron densities ρ_s , the radial functions $\phi_s(r)$ and $\rho_p(r)$ can be determined. Since sugar molecules are larger than water molecules, only part of the space accessible to water is also penetrable by sugar molecules. When, therefore, the contrast variation is achieved by the addition of sugars, $\phi_s(r)$ represents the volume fraction accessible to the sugar molecules, and $\rho_p(r)$ includes, besides the anhydrous virus, also those regions of hydration water from which sugar molecules are excluded by their size. The dependence of the extent of penetration on the size of the sugar molecules was demonstrated by White and Fischbach (1973).

As the mean hydration of the entire virus can be derived from the ratio of its total volume to the "dry" volume, the extent of hydration of the only protein- or nucleic acid-containing regions can be estimated from the ratios of the theoretical excess electron densities for anhydrous protein or nucleic acid to the experimental $\Delta\rho(r)$ values (cf. Anderegg *et al.*, 1963; Fischbach *et al.*, 1965; Zipper *et al.*, 1971a).

Though the appearance of higher-order harmonics in the scattering curves of

viruses at large angles limits the possible resolution of the spherically symmetric density distribution, the $\Delta\rho(r)$ functions obtained so far have certainly enriched our knowledge on the structure of viruses or virus-related particles. In some special applications, for instance, the radial density distribution has been used to unveil the structures of various kinds of empty capsids for which controversial models had been proposed (Zipper *et al.*, 1971b, 1973b), or to elucidate the pathways in the assembly of phage heads (Earnshaw *et al.*, 1976, 1979; Earnshaw and King, 1978; Künzler and Berger, 1978), or to study the polymorphism of viruses (Chauvin *et al.*, 1978a).

On the other hand, an analysis of the higher-order terms in the scattering curve may yield information on the surface organization of the virus particles. A first attempt in this direction has been undertaken by Jack and Harrison (1975). By using icosahedral harmonics, the authors calculated scattering curves for point models representing different types of clustering of the protein sub-units. The zero-order term was assumed to be identical to the scattering from a solid sphere with the same radius as the virus. The comparison of these curves with experimental curves led the authors to the conclusion that, particularly in the case of small viruses, the deviations of the experimental scattering curves from those for solid spheres may be accounted for by deviations from spherical symmetry rather than by radial density fluctuations, and that low-order harmonics contribute significantly to the scattering. In such a case, the calculation of $\Delta\rho(r)$ could yield misleading results. It is, however, questionable whether the conclusions drawn by the authors hold generally.

The package of the nucleic acid within the virus may give rise to intensity maxima at large angles, e.g. in the 2.5 nm region (Earnshaw *et al.*, 1976; Earnshaw and Harrison, 1977), while the secondary structure of the nucleic acid leads to a characteristic scattering pattern in the wide angle region (Earnshaw *et al.*, 1976).

B. Rod-like Viruses

The methods applied in the small angle studies on isotropic solutions of rod-like viruses were essentially the conventional procedures for elongate particles. Accordingly, mainly cross-section parameters such as R_c , M_c or the radius r_c of the cross-section were determined (Kratky *et al.*, 1957; Malmon, 1957; Longley, 1963; Torbet, 1979). For two components of alfalfa mosaic virus, even the innermost portion of the SAXS curve was measured and the radius of gyration and the length were determined from it (Van Domelen and Beeman, 1962). A SANS contrast variation study on this virus was recently performed by Cusack *et al.* (1981).

An attempt to calculate the radial excess electron density distribution over the cross-section of the cylindrical tobacco mosaic virus has been undertaken

by Fedorov (1971), who applied the Hankel transformation to the scattering curve measured by Malmon (1957). Since from the theory this method is restricted to infinitely long cylindrical particles, a special extrapolation of the scattering curve to zero angle was necessary to compensate for the finite length of the virus particles. The problem of missing zeros for the determination of the amplitude was solved in a similar way as by Anderegg *et al.* (1961) for the isometric viruses. The obtained $\Delta\rho(r)$ function was of only low resolution as imposed by the poor quality of the experimental data.

C. Large Bacteriophages

In contrast to isometric or rod-like viruses, large phages are often composed of a head and a tail, the shape of the head being somewhat elongated as, for example, in phage T2 or more isometric. While the tail of phage T2 has a length similar to the length of the head, phages with a much shorter tail are also known. Even in the case of phage T2 the tail volume amounts to less than 10% of the total volume of the phage, thus the scattering from the head of the phage dominates the scattering curve.

For phages with isometric heads, the spherically symmetric term of the structure is dominant the shorter the tail. When the tail is sufficiently short, the scattering curves of such phages can be treated like those of isometric viruses; thus, for instance, the radial excess electron density distribution can be calculated (Earnshaw *et al.*, 1976; Boyarintseva *et al.*, 1977). This has been done even in the case of non-isometric empty capsids (Subirana *et al.*, 1979).

Feigin and co-workers (Feigin *et al.*, 1974; Boyarintseva *et al.*, 1974a, 1977) measured the SAXS from several large phages, among them T2, and compared the experimental curves with the curves for various models. In the case of phage T2, the true Guinier range of the scattering curve is at unaccessibly small angles due to the large overall size of the phage. Therefore, the value for R that can be derived from the innermost portion of the measured SAXS curve refers to the phage head alone and not to the entire phage. However, the best fit of the experimental SAXS curve of the phage was obtained with models consisting of a head and a tail.

Boyarintseva *et al.* (1974b) applied the contrast variation method (by addition of sucrose or of various salts) to study the size and shape of the DNA space within the head of phage S_D . The observed sharpening of the maxima and minima in the SAXS curve upon raising the electron density of the solvent suggested the DNA space to be of spherical shape. The WAXS curve of phage S_D was compared with theoretical curves for the various forms of DNA as calculated by Bram (1971a); the experimental data were found to be consistent with the B form (Feigin *et al.*, 1974). SANS contrast variation was applied to phage T7 (Agamalian *et al.*, 1979).

III. Ribosomes

Ribosomes are rather complex ribonucleoprotein particles consisting of three different species of RNA and more than 50 different proteins. Under appropriate conditions, the ribosome can be split reversibly into two different subunits, each subunit containing also both RNA and protein. The complete disruption into the various constituents and reassembly of the subunits from the constituents is also possible.

This section deals with small angle scattering from entire ribosomes, ribosomal subunits and polysomes. Small angle scattering from isolated ribosomal nucleic acids (5-S, 16-S) has already been discussed in Section I.

A detailed review of the results of small angle studies in the field of ribosome research has been published recently (Damaschun *et al.*, 1979).

A. Ribosomes and Ribosomal Subunits

Because of the non-concentric distribution of RNA and protein in the ribosomal particle, ribosomes possess a much lower degree of symmetry than viruses. This and the more anisometric shape lead to scattering curves which are completely different from those of isometric viruses (cf. Fig. 5 with Fig. 3). For dilute solutions, they show a rather smooth course at small angles, with some modulations or weak maxima at moderate angles (Hill *et al.*, 1969; Venable *et al.*, 1970; Serdyuk and Grenader, 1977). A similar scattering behaviour can also be observed with the ribosomal subunits (Hill *et al.*, 1969; Serdyuk and Grenader, 1977; Serdyuk *et al.*, 1977, 1979; Serdyuk, 1979). According to Serdyuk, the scattering in the moderate angle region reflects features of the RNA compact packing. At high concentrations, an additional maximum occurs at small angles because of interparticulate interferences (Venable *et al.*, 1970).

SAXS of entire ribosomes or ribosomal subunits at only one solvent electron density can only yield rather limited information on the particles under investigation. Only the maximum dimension of the particles can be deduced unambiguously from the $p(r)$ function. Already the correct interpretation of the radius of gyration or the approximation of the experimental SAXS curve by a model curve would require additional informations on the internal structure of the particles. The assumption of a homogeneous density distribution is only an insufficient approximation (cf. Hill *et al.*, 1969, 1970; Kayushina and Feigin, 1969; Serdyuk *et al.*, 1970; Hill and Fessenden, 1974; Damaschun *et al.*, 1974; Paradies *et al.*, 1974).

Information on the internal structure of ribosomal particles is available from measurements at several different contrasts. Besides the conventional contrast variation techniques by solvent exchange, as applied, for example, in the case of viruses, three further approaches have been used for the study of the internal

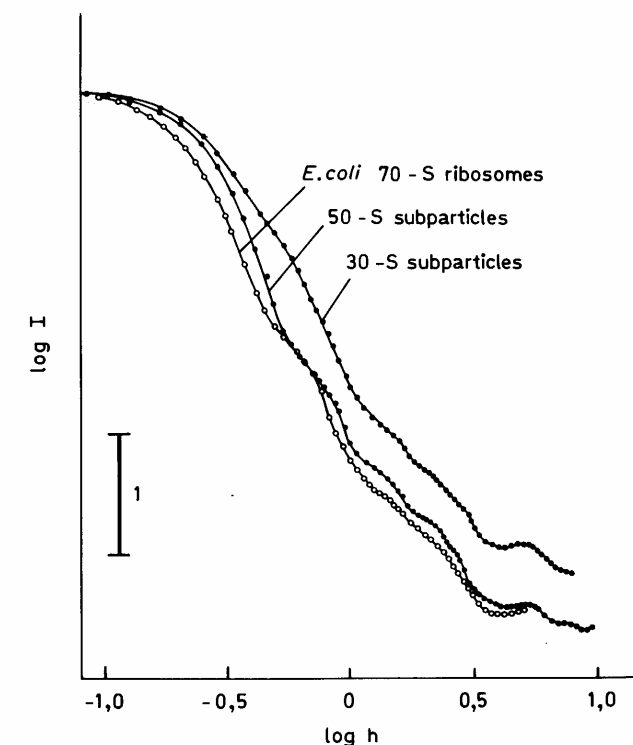


FIG. 5. SAXS curves of ribosomes and ribosomal subparticles from *E. Coli*. After Serdyuk and Grenader (1977).

structure of ribosomes: the contrast variation by the joint use of different types of radiation (X-rays, neutrons, light), the contrast variation by specific deuteration, and the label triangulation technique. Apart from the first of these approaches, SAXS plays a negligible role in the elucidation of the internal structure of ribosomal particles as compared to SANS. For recent reviews of the different approaches see Koch and Stuhrmann (1979), Serdyuk (1979) and Moore and Engelman (1979).

1. CONTRAST VARIATION BY SOLVENT EXCHANGE

Only a few contrast variation studies were performed by means of SAXS, by raising the electron density of the solvent by addition of sucrose (Smith, 1971; Tolbert, 1971). This method does not work well with ribosomes because of their incomplete penetration by sucrose (cf. discussion by Serdyuk and Grenader, 1977).

Contrast variation by H_2O/D_2O exchange for SANS is also not free from

difficulties, because by substituting D₂O for H₂O in the solvent a number of exchangeable protons of the solute will be replaced with deuterium, an effect which must be taken into account accordingly. Nevertheless, SANS contrast variation studies on ribosomes and ribosomal subunits have proved to be very successful. They can yield the following results (cf. Stuhrmann *et al.*, 1976, 1977, 1978; Beaudry *et al.*, 1976).

The linear dependence of the square root of the zero intensity on the scattering density of the solvent yields the average scattering density of the particles at zero contrast, their volume and their molecular weight. The dependence of the squared radius of gyration on the inverse of the contrast yields the radius of gyration of the particles at infinite contrast and the parameters α and β . The sign of α is an indicator for the internal distribution of scattering density; a negative value for α , as found, for example, for the ribosomal subunits, signals that a dense core is surrounded by a less dense shell. The size of β is a measure for the displacement of the centres of mass of the RNA and the protein component in the particles. The radii of gyration at the points where either the protein or the RNA is contrast-matched equal the respective radii of gyration for the RNA or the protein component. Similarly, the $p(r)$ functions at the matchpoints for protein or RNA correspond to the RNA-RNA or protein-protein distance distributions, respectively. The analysis of the shape scattering function $I_C(h)$ in terms of spherical harmonics may yield the shape of the particles.

2. JOINT USE OF DIFFERENT TYPES OF RADIATION

The radius of gyration R of a particle which consists of the two components protein and RNA is related to the radii of gyration R_P and R_R of the two components *in situ* by

$$R^2 = x_P R_P^2 + (1 - x_P) R_R^2 + x_P(1 - x_P)L^2$$

where L is the spatial separation of the centres of mass of the two components and x_P is the relative scattering fraction of the protein component (cf. Serdyuk and Grenader, 1975). For a given sample, the value for x_P depends on the type of radiation used for the scattering experiment. It can be calculated from the chemical composition and the specific volumes of the components in the case of X-rays or neutrons, or from the refractive index increments and the specific volumes in the case of light. The squares of the different radii of gyration as obtained from scattering experiments (in H₂O or D₂O as solvent) by using X-rays, light or neutrons as primary radiation are plotted versus x_P . A linear dependence, as it is found in the case of ribosomal subunits, indicates that the separation L between the centroids of protein and RNA must be very small. In this case, the linear extrapolation of the data to $x_P = 0$ and $x_P = 1$ yields

directly the radii of gyration R_R and R_P of the components *in situ* (Serdyuk, 1975, 1979; Serdyuk and Grenader, 1975, 1977; Serdyuk *et al.*, 1977, 1979).

3. SPECIFIC DEUTERATION

Another alternative method to contrast variation by solvent exchange is the specific deuteration of the RNA or the proteins of the ribosomal subunits by manipulating the growth conditions (Moore *et al.*, 1974, 1975). By substituting deuterium for hydrogen in non-exchangeable positions, the internal distribution of scattering density of the particle is altered. The specific deuteration method may be combined most advantageously with the solvent exchange technique (Crichton *et al.*, 1977). Contrast variation studies on entire ribosomes which were reconstituted from one deuterated and one protonated subunit reveal a strong parabolic dependence of the squared radius of gyration on the inverse of the contrast. The accordingly high value for the parameter β allows in this case the determination of the distance between the centres of the two subunits (Koch *et al.*, 1978).

By sophisticated techniques it is also possible to obtain ribosomal particles which are deuterated so specifically that both the RNA and all but one or two selected protonated proteins can be contrast-matched by the same H₂O/D₂O mixture (May *et al.*, 1980a). This recent approach offers new possibilities for studying the shape of ribosomal proteins *in situ* as well as for the label triangulation technique (cf. below).

Specific deuteration, in addition to SAXS and normal SANS, has also been used to study the interaction of a ribosomal protein with the small ribosomal subunit (Laughrea *et al.*, 1978).

4. LABEL TRIANGULATION TECHNIQUE

While the aforementioned approaches are able to unveil, at low resolution, the distribution of protein and RNA in ribosomal particles and subunits, mainly by analysis of the radii of gyration obtained at different contrasts, the label triangulation technique is capable of elucidating even the spatial arrangement of the various protein molecules within the particles by determination of their mutual distances. Additionally, information can be obtained on the size, shape and orientation of the protein molecules *in situ*. The method is based on the former work of Kratky and Worthmann (1947) and was introduced for the study of biomolecules by Hoppe (1972, 1973) for the X-ray case and by Engelman and Moore (1972) for the neutron case. For the investigation of ribosomal particles, however, only SANS is actually applied.

The method makes use of the fact that the ribosomal subunits can be reassembled from their constituents. Thus it is possible to obtain particles in which one or two protein molecules are labelled by the incorporation of deuterium while the rest of the particle is protonated. Scattering measurements must be performed with two different solutions of particles: one solution containing equal amounts of reassembled particles with two deuterated proteins and of reassembled particles with all proteins protonated, the other solution containing equal amounts of reassembled particles with only one or the other of the proteins of the pair deuterated. The difference between the intensities scattered from these two solutions is an interference function reflecting the spatial separation of the two proteins in the particle. If the protein molecules can be approximated by spheres, the interference function $\Delta I(h)$ is related to the distance L between the centres of the molecules by

$$\Delta I(h) = 2f_1 f_2 \frac{\sin hL}{hL}$$

where f_1 and f_2 are the transforms of the spheres. The evaluation of the position of the first zero of the interference function allows a sufficiently accurate measurement of the distance L even if the protein molecules are not spherical (Hoppe *et al.*, 1975; Moore *et al.*, 1977).

A Fourier inversion of the interference function yields a distribution function $p(r)$ of the length of all vectors joining the deuterium atoms in one protein molecule with those in the other molecule (Engelman *et al.*, 1975a, 1975b). The following data can be derived from this distribution function (cf. Moore and Engelman, 1979): the separation between the protein pair can be deduced from the position of the maximum of $p(r)$ or from the first moment of $p(r)$ (Moore *et al.*, 1977; Langer *et al.*, 1978). The second moment of $p(r)$, which is a function of the separation between the protein molecules and of their individual radii of gyration, allows a determination of the latter parameters (Moore *et al.*, 1978). The breadth of the distribution function depends on the orientation and the shape of the two protein molecules. Since the axial ratios of the protein molecules can be estimated from their radii of gyration and molecular volume, the relative orientation of the proteins can be deduced if they are appreciably extended in shape (Moore and Engelman, 1977).

A series of distance measurements between different protein pairs can be combined by means of triangulation to estimate the locations of the various protein molecules within the ribosomal particles (Moore *et al.*, 1977, 1978; Langer *et al.*, 1978; Moore and Weinstein, 1979; May, 1978; Schindler *et al.*, 1979). Finally, models of the quaternary structure of ribosomal particles can be tested by comparison of experimental and theoretical scattering curves (cf. Spirin *et al.*, 1979).

B. Polysomes

Polysomes are complexes of ribosomes with mRNA. The SAXS curve of polysomes differs considerably from that of the corresponding free ribosomes, e.g. by the occurrence of additional maxima at small angles (Müller *et al.*, 1978; Damaschun *et al.*, 1979). The joint analysis of the two scattering curves can yield *inter alia* the following data on the polysome structure: the difference between the squared radii of gyration of the polysomes and the free ribosomes can be evaluated in terms of the mean distance of the ribosomal centres of mass from the centre of gravity of the entire polysome. The ratio of the zero intensities of the polysomes and the free ribosomes allows an estimate of the mean number of ribosomes attached to one mRNA molecule. The quotient of the polysome and ribosome scattering curves yields an interaction term which is related to the mutual distances between the ribosomes in the polysome. The average number of ribosomes on a mRNA molecule may also be derived from this interaction term at larger angles. A Fourier inversion of the interaction term yields a distance distribution function from which the distances between the centres of the next and second neighbours can be deduced. Using these distances and the mean number of ribosomes in a polysome, the interaction term and the scattering curve can be calculated for various models and compared with the curves obtained from the SAXS experiment.

IV. Chromatin

Chromatin is the deoxyribonucleoprotein complex contained in the chromosomes of eukaryotes. It appears to have a hierarchical structure. The fundamental subunit is the nucleosome, which can be isolated after limited nuclease digestion of the nuclei. It contains about 200 base pairs of DNA which are complexed with two sets of four different proteins (histones); a further histone (H1) is also associated with the nucleosome. A fragment of the nucleosome, the core particle, is obtained after further nuclease digestion. It lacks the histone H1 and the linker region of nucleosomal DNA; the remaining DNA is about 140 base pairs in length and is wound around the octameric core of histones. In chromatin, supercoiling of the string of nucleosomes (the nucleofilament) leads to higher-order structures. *In vitro* structural transitions can be induced, e.g. by the addition of monovalent or divalent cations.

The first reports on SAXS studies on solutions of chromatin appeared in 1959 and further studies were performed some years later (Luzzati and Nicolaieff, 1959, 1963; Nicolaieff, 1967; Bram and Ris, 1971). The scattering curves obtained from dilute solutions indicated a rod-like structure; measurements on concentrated solutions (gels) established the occurrence of a variety

of intensity maxima, e.g. at Bragg spacings of 11 nm, 5.5 nm and 3.7 nm. A founded interpretation of these experimental findings (as well as of similar results from X-ray fibre diffraction; cf. Wilkins *et al.*, 1959; Pardon *et al.*, 1967) suffered at that time, however, from the lack of additional information on chromatin structure.

This situation improved significantly when the subunit concept of chromatin was developed (mainly from electron microscopic and nuclease digestion studies) and neutron scattering was applied to study chromatin and its subunit.

Recent reviews of small angle studies in the field of chromatin research have been given by Pardon *et al.* (1978), Pardon (1979), Bram *et al.* (1978), Hjelm *et al.* (1978) and Baldwin *et al.* (1979).

A. Nucleosomes and Core Particles

SANS contrast variation studies on nucleosomes and core particles provided convincing evidence that in these particles the DNA is external to a protein core. This followed from the positive value of the parameter α as derived from plots of R^2 versus the reciprocal contrast (Pardon *et al.*, 1975; Hjelm *et al.*, 1977; Suau *et al.*, 1977). Hjelm *et al.* and Suau *et al.* determined also the volume of the nucleosome and of the core particle and derived and analysed the three basic scattering functions $I_C(h)$, $I_S(h)$ and $I_{CS}(h)$ to separate shape and internal structure. The shape function $I_C(h)$ has side-maxima, e.g. a broad maximum at Bragg spacings of about 3.5–3.7 nm. This maximum occurs also in the scattering curve itself, particularly in 100% D₂O.

Baldwin *et al.* (1978) performed SANS on core particles by varying the contrast by addition of small molecules (glycerol, sucrose) at fixed H₂O/D₂O ratios. The analysis of $I(0)$ and of R yielded information on the amount of bound water and on its distribution (cf. also Kneale *et al.*, 1977).

Further SANS measurements on nucleosomes or core particles were performed by, among others, Bradbury *et al.* (1975) and Baudy *et al.* (1976); SANS and SAXS measurements by Pardon *et al.* (1977); SAXS and WAXS studies by Damaschun *et al.* (1977, 1980, cf. Fig. 6).

SANS studies on a histone complex (called core protein) established a radius of gyration similar to the value for the intact core particle under conditions where the protein dominates the scattering, but only half the molecular weight of the protein of the core particle (Wooley *et al.*, 1977; Pardon *et al.*, 1978). This histone complex also gives a 3.5 nm side-maximum.

The maximum dimensions of nucleosomes, core particles and core protein were determined from $p(r)$ functions (Suau *et al.*, 1977; Lilley *et al.*, 1978).

The analysis of the experimental findings resulted in the establishment of models for core particles and nucleosomes which were tested by comparison of the model curves with the experimental scattering curves or the basic

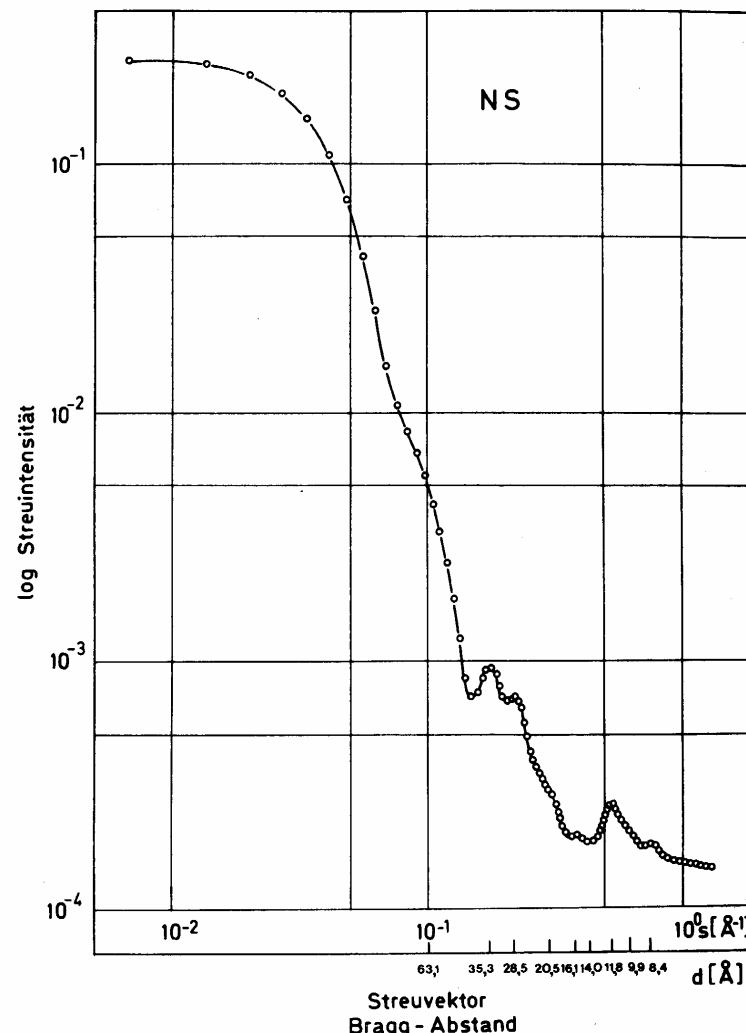


FIG. 6. SAXS and WAXS curve of 11-S nucleosomes (core particles) from rat thymus. ($s = 4\pi/\lambda \cdot \sin \vartheta [\text{\AA}^{-1}]$; d = Bragg spacing [\AA]). From Damaschun *et al.* (1977).

scattering functions (cf., for example, Hjelm *et al.*, 1977; Pardon *et al.*, 1977; Richards *et al.*, 1977; Lilley *et al.*, 1978; Suau *et al.*, 1977; Damaschun *et al.*, 1977; Bram, 1978).

SANS studies of the radii of gyration of small oligomers of chromatin subunits were performed to determine the centre-to-centre separation between the subunits (Pardon *et al.*, 1978; Pardon, 1979). The X-ray patterns of concentrated

gels of individual chromatin subunits were found to be similar to those for intact chromatin (Pardon *et al.*, 1978).

B. Chromatin, Chromosomes and Nuclei

The scattering behaviour of chromatin depends on several factors, such as the concentration of chromatin, the nature and concentration of small ions, or the contrast.

The occurrence of a series of partly concentration-dependent small angle maxima in the scattering from concentrated gels or fibres of chromatin has attracted most of the interest. Since these maxima appear at spacings greater than the dimensions of the DNA double helix they gave the first evidence for a regular structure in chromatin other than the double helix. (Maxima due to the DNA double helix appear in the wide angle region of the scattering curve; cf. Bram, 1971a.)

While originally the small angle maxima were thought to have a common origin and were ascribed mainly to the DNA component, SANS contrast variation studies convincingly demonstrated that the various maxima show a different behaviour on contrast variation (Baldwin *et al.*, 1975; Bradbury *et al.*, 1975). It is now generally accepted that the 3.7 nm maximum is due to the structure of the subunit. The 11 nm peak, on the other hand, may reflect a repeat distance between the subunits along the nucleofilament, the pitch of a regular helical structure (solenoid), or even also interparticle effects in an extended liquid-type array (cf. Pardon, 1979; Spencer and Staynov, 1980).

The occurrence of additional maxima in scattering curves of chromatin, chromosomes and intact nuclei at very small angles (i.e. very large Bragg spacings), indicative of higher-order structures, was described by Bram *et al.* (1974b, 1975), Baudy and Bram (1979) and Ibel (1980).

Notbohm *et al.* (1979) analysed the positions of the minima in chromatin SAXS curves and compared them with the minima in simulated curves for models.

Contrast variation in SANS measurements on chromatin is usually performed by variation of the H₂O/D₂O ratio, but contrast variation by addition of small molecules or by use of chromatin with deuterated histones or deuterated DNA is also applied (cf. Bradbury *et al.*, 1975, 1977; Ibel, 1980).

SAXS and SANS studies on dilute solutions of chromatin yielded information on the cross-section parameters R_c and M_c (Luzzati and Nicolaieff, 1963; Nicolaieff, 1967; Bram and Ris, 1971; Aleksanyan *et al.*, 1975; Sperling and Tardieu, 1976; Hollandt *et al.*, 1979; Bram *et al.*, 1974a, 1977; Baudy and Bram, 1978). The obtained values depend on the experimental conditions and clearly reflect a structural transition from the nucleofilament to a higher-order structure at high ionic strength or in the presence of divalent cations. The enormous

increase in R_c (from about 3 nm to about 9 nm) and in M_c upon raising the ionic strength was studied in detail by Suau *et al.* (1979). The authors calculated also the $p(r)$ function of the cross-section by the Hankel transformation.

The slight increase of R_c (for the nucleofilament) with the reciprocal contrast, as observed in SANS studies (Baudy and Bram, 1978; Suau *et al.*, 1979), indicates that also in the nucleofilament cross-section the DNA is on the outside, surrounding a protein core.

References

- Agamalian, M. M., Drabkin, G. M., Dovgikov, A. A., Lvov, Yu. M. and Ronto, D. (1979). Submitted to *Kristallografiya*.
- Aleksanyan, V. I., Vorobev, V. I. and Fedorov, B. A. (1975). *Biopolymers* **14**, 1133–1142.
- Anderegg, J. W. (1967). In "Small-Angle X-Ray Scattering" (H. Brumberger, ed.), pp. 243–265. Gordon and Breach, New York.
- Anderegg, J. W., Geil, P. H., Beeman, W. W. and Kaesberg, P. (1961). *Biophys. J.* **1**, 657–667.
- Anderegg, J. W., Wright, M. and KAESBERG, P. (1963). *Biophys. J.* **3**, 175–182.
- Baldwin, J. P., Boseley, P. G., Bradbury, E. M. and Ibel, K. (1975). *Nature* **253**, 245–249.
- Baldwin, J. P., Braddock, G. W., Carpenter, B. G., Kneale, G. G., Simpson, J. K., Suau, P., Hjelm, R. P. and Bradbury, E. M. (1978). *J. Appl. Cryst.* **11**, 483–484.
- Baldwin, J. P., Boulter, E., Braddock, G. W., Bradbury, E. M., Cary, P. D., Carpenter, B. G., Kneale, G. G. and Suau, P. (1979). In "Gene Function" (S. Rosenthal *et al.*, eds), *Proc. FEBS Meet.*, Vol. 51, pp. 171–191. Pergamon Press, Oxford.
- Baudy, P. and Bram, S. (1978). *Nucleic Acids Res.* **5**, 3697–3714.
- Baudy, P. and Bram, S. (1979). *Nucleic Acids Res.* **6**, 1721–1729.
- Baudy, P., Bram, S., Vastel, D., Lepault, J. and Kitzis, A. (1976). *Biochem. Biophys. Res. Commun.* **72**, 176–183.
- Beaudry, P., Petersen, H. U., Grunberg-Manago, M. and Jacrot, B. (1976). *Biochem. Biophys. Res. Commun.* **72**, 391–397.
- Becker, M., Misselwitz, R., Damaschun, H., Damaschun, G. and Zirwer, D. (1979). *Nucleic Acids Res.* **7**, 1297–1309.
- Benham, C. J., Brady, G. W. and Fein, D. B. (1980). *Biophys. J.* **29**, 351–366.
- Berger, J., Burnett, R. M., Franklin, R. M. and Grüttner, M. (1978). *Biochim. Biophys. Acta* **535**, 233–240.
- Boyarintseva, A. K., Dembo, A. T., Tikhonenko, T. I. and Feigin, L. A. (1973a). *Dokl. Akad. Nauk SSSR* **209**, 721–729.
- Boyarintseva, A. K., Dembo, A. T., Tikhonenko, T. I. and Feigin, L. A. (1973b). *Dokl. Akad. Nauk SSSR* **212**, 487–489.
- Boyarintseva, A. K., Dembo, A. T., Tikhonenko, T. I. and Feigin, L. A. (1973c). *Dokl. Akad. Nauk SSSR* **213**, 462–465.
- Boyarintseva, A. K., Dembo, A. T. and Feigin, L. A. (1974a). *Kristallografiya* **19**, 105–109.

- Boyarintseva, A. K., Dembo, A. T., Feigin, L. A., Petrovskii, G. V., Sholer, J. and Tikhonenko, T. I. (1974b). *Stud. Biophys.* **47**, 83–84.
- Boyarintseva, A. K., Rolbin, Yu. A. and Feigin, L. A. (1977). *Dokl. Akad. Nauk SSSR* **237**, 709–712.
- Bradbury, E. M., Baldwin, J. P., Carpenter, B. G., Hjelm, R. P., Hancock, R. and Ibel, K. (1975). *Brookhaven Symp. Biol.* **27**, IV, 97–117.
- Bradbury, E. M., Hjelm, R. P., Carpenter, B. G., Baldwin, J. P., Kneale, G. G. and Hancock, R. (1977). In "The Molecular Biology of the Mammalian Genetic Apparatus" (P. Ts'o, ed.), Vol. I, pp. 53–70. Elsevier-North Holland, Amsterdam.
- Brady, G. W., Fein, D. B. and Brumberger, H. (1976). *Nature* **264**, 231–234.
- Bram, S. (1971a). *J. Mol. Biol.* **58**, 277–288.
- Bram, S. (1971b). *Nature New Biol.* **232**, 174–176.
- Bram, S. (1971c). *Nature New Biol.* **233**, 161–164.
- Bram, S. (1978). *Biochem. Biophys. Res. Commun.* **81**, 684–691.
- Bram, S. and Beeman, W. W. (1971). *J. Mol. Biol.* **55**, 311–324.
- Bram, S. and Ris, H. (1971). *J. Mol. Biol.* **55**, 325–336.
- Bram, S., Butler-Browne, G., Bradbury, E. M., Baldwin, J., Reiss, C. and Ibel, K. (1974a). *Biochimie* **56**, 987–994.
- Bram, S., Baudy, P., Butler-Browne, G. and Ibel, K. (1974b). *Biochimie* **56**, 1339–1341.
- Bram, S., Butler-Browne, G., Baudy, P. and Ibel, K. (1975). *Proc. Nat. Acad. Sci. USA* **72**, 1043–1045.
- Bram, S., Baudy, P., Lepault, J. and Hermann, D. (1977). *Nucleic Acids Res.* **4**, 2275–2282.
- Bram, S., Kouprach, S. and Baudy, P. (1978). *Cold Spring Harbor Symp. Quant. Biol.* **42**, 23–29.
- Caspar, D. L. D. and Klug, A. (1962). *Cold Spring Harbor Symp. Quant. Biol.* **27**, 1–24.
- Chauvin, C., Jacrot, B. and Witz, J. (1977). *Virology* **83**, 479–481.
- Chauvin, C., Pfeiffer, P., Witz, J. and Jacrot, B. (1978a). *Virology* **88**, 138–148.
- Chauvin, C., Witz, J. and Jacrot, B. (1978b). *J. Mol. Biol.* **124**, 641–651.
- Chauvin, C., Jacrot, B., Lebeurier, C. and Hirth, L. (1979). *Virology* **96**, 640–641.
- Clauwaert, J., De Clercq, R., Ribitsch, G. and Zipper, P. (1977). "Fourth International Conference on Small-Angle Scattering of X-Rays and Neutrons, Programs and Abstracts", p. 48, Abstr. PE-3.
- Connors, P. G. and Beeman, W. W. (1972). *J. Mol. Biol.* **71**, 31–37.
- Connors, P. G., Labanauskas, M. and Beeman, W. W. (1969). *Science* **166**, 1528–1530.
- Crichton, R. R., Engelmann, D. M., Haas, J., Koch, M. H. J., Moore, P. B., Parfait, R. and Stuhrmann, H. B. (1977). *Proc. Nat. Acad. Sci. USA* **74**, 5547–5550.
- Cuillel, M., Tripier, F., Braunwald, J. and Jacrot, B. (1979). *Virology* **99**, 277–285.
- Cusack, S., Miller, A., Krijgsman, P. C. J. and Mellema, J. E. (1981). *J. Mol. Biol.* **145**, 525–543.
- Damaschun, G., Müller, J. J., Bielka, H. and Böttger, M. (1974). *Acta biol. med. germ.* **33**, 817–823.

- Damaschun, G., Müller, J. J. and Bielka, H. (1979). *Methods Enzymol.* **59**, 706–750.
- Damaschun, H., Damaschun, G., Pospelov, V. A. and Vorobev, V. I. (1980). *Molec. Biol. Rep.* **6**, 185–191.
- Damaschun, H., Damaschun, G., Fenske, H., Lindigkeit, R., Müller, J. J., Pospelov, V. J. and Vorobev, V. J. (1977). *Acta biol. med. germ.* **36**, K13–K17.
- Damaschun, H., Damaschun, G., Becker, M., Buder, E., Misselwitz, R. and Zirwer, D. (1978a). *Acta biol. med. germ.* **37**, 569–576.
- Damaschun, H., Damaschun, G., Becker, M., Buder, E., Misselwitz, R. and Zirwer, D. (1978b). *Nucleic Acids Res.* **5**, 3801–3809.
- Dessen, P., Blanquet, S., Zaccai, G. and Jacrot, B. (1978). *J. Mol. Biol.* **126**, 293–313.
- Earnshaw, W. C. and Harrison, S. C. (1977). *Nature* **268**, 598–602.
- Earnshaw, W. and King, J. (1978). *J. Mol. Biol.* **126**, 721–747.
- Earnshaw, W., Casjens, S. and Harrison, S. C. (1976). *J. Mol. Biol.* **104**, 387–410.
- Earnshaw, W. C., Hendrix, R. W. and King, J. (1979). *J. Mol. Biol.* **134**, 575–594.
- Eisenberg, H. and Cohen, G. (1968). *J. Mol. Biol.* **37**, 355–362.
- Engelman, D. M. and Moore, P. B. (1972). *Proc. Nat. Acad. Sci. USA* **69**, 1997–1999.
- Engelman, D. M., Moore, P. B. and Schoenborn, B. P. (1975a). *Proc. Nat. Acad. Sci. USA* **72**, 3888–3892.
- Engelman, D. M., Moore, P. B. and Schoenborn, B. P. (1975b). *Brookhaven Symp. Biol.* **27**, IV, 20–37.
- Fedorov, B. A. (1971). *Acta Cryst. A* **27**, 35–42.
- Feigin, L. A., Dembo, A. T. and Boyarinseva, A. K. (1974). *J. Appl. Cryst.* **7**, 164–167.
- Finch, J. T. and Holmes, K. C. (1967). In "Methods in Virology" (K. Maromosch and H. Koprowski, eds), Vol. 3, pp. 351–474. Academic Press, New York and London.
- Finch, J. T., Leberman, R. and Berger, J. E. (1967). *J. Mol. Biol.* **27**, 17–24.
- Fischbach, F. A., Harrison, P. M. and Anderegg, J. W. (1965). *J. Mol. Biol.* **13**, 638–645.
- Folkhard, W., Pilz, I., Kratky, O., Garrett, R. and Stöffler, G. (1975). *Eur. J. Biochem.* **59**, 63–71.
- Giegé, R., Jacrot, B., Moras, D., Thierry, J. C. and Zaccai, G. (1977). *Nucleic Acids Res.* **4**, 2421–2427.
- Glatter, O. (1977). *Acta Phys. Austriaca* **47**, 83–102.
- Glatter, O. (1981). *J. Appl. Cryst.* **14**, 101–108.
- Gulik, A., Inoue, H. and Luzzati, V. (1970). *J. Mol. Biol.* **53**, 221–238.
- Harrison, S. C. (1969). *J. Mol. Biol.* **42**, 457–483.
- Harrison, S. C., Caspar, D. L. D., Camerini-Otero, R. D. and Franklin, R. M. (1971a). *Nature New Biol.* **229**, 197–201.
- Harrison, S. C., David, A., Jumblatt, J. and Darnell, J. E. (1971b). *J. Mol. Biol.* **60**, 523–528.
- Hill, W. E. and Fessenden, R. J. (1974). *J. Mol. Biol.* **90**, 719–726.
- Hill, W. E., Thompson, J. D. and Anderegg, J. W. (1969). *J. Mol. Biol.* **44**, 89–102.

- Hill, W. E., Anderegg, J. W. and Van Holde, K. E. (1970). *J. Mol. Biol.* **53**, 107–121.
- Hjelm, R. P., Kneale, G. G., Suau, P., Baldwin, J. P., Bradbury, E. M. and Ibel, K. (1977). *Cell* **10**, 139–151.
- Hjelm, R. P., Baldwin, J. P. and Bradbury, E. M. (1978). In "Methods in Cell Biology" (G. Stein *et al.*, eds), Vol. 18, pp. 295–325. Academic Press, New York and London.
- Hollandt, H., Notbohm, H., Riedel, F. and Harbers, E. (1979). *Nucleic Acids Res.* **6**, 2017–2027.
- Hoppe, W. (1972). *Israel J. Chem.* **10**, 321–333.
- Hoppe, W. (1973). *J. Mol. Biol.* **78**, 581–585.
- Hoppe, W., May, R., Stöckel, P., Lorenz, S., Erdmann, V. A., Wittmann, H. G., Crespi, H. L., Katz, J. J. and Ibel, K. (1975). *Brookhaven Symp. Biol.* **27**, IV, 38–48.
- Ibel, K. (1980). "Fifth International Conference on Small-Angle Scattering, Program & Abstracts", p. 238.
- Jack, A. and Harrison, S. C. (1975). *J. Mol. Biol.* **99**, 15–25.
- Jacrot, B. (1976). *Rep. Prog. Phys.* **39**, 911–953.
- Jacrot, B., Pfeiffer, P. and Witz, J. (1976). *Phil. Trans. Roy. Soc. London Ser., B* **276**, 109–112.
- Jacrot, B., Chauvin, C. and Witz, J. (1977). *Nature* **266**, 417–421.
- Kayushina, R. L. and Feigin, L. A. (1969). *Biofizika* **14**, 957–962.
- Kirste, R. G. and Oberthür, R. C. (1969). *Makromol. Chemie* **127**, 301–303.
- Kneale, G. G., Baldwin, J. P. and Bradbury, E. M. (1977). *Quart. Rev. Biophys.* **10**, 485–527.
- Koch, M. H. J. and Stuhrmann, H. B. (1979). *Methods Enzymol.* **59**, 670–706.
- Koch, M. H. J., Parfait, R., Haas, J., Crichton, R. R. and Stuhrmann, H. B. (1978). *Biophys. Struct. Mechanism* **4**, 251–262.
- Kratky, O. (1963). *Progr. Biophys. Mol. Biol.* **13**, 105–173.
- Kratky, O. and Worthmann, W. (1947). *Monatsh. Chem.* **76**, 263–281.
- Kratky, O., Paletta, B., Porod, G. and Strohmaier, K. (1957). *Z. Naturforsch. 12b*, 287–292.
- Kratky, O., Pilz, I., Cramer, F., von der Haar, F. and Schlimme, E. (1969). *Monatsh. Chem.* **100**, 748–749.
- Krigbaum, W. R. and Godwin, R. W. (1966). *Science* **154**, 423.
- Künzler, P. and Berger, H. (1978). *J. Appl. Cryst.* **11**, 496–497.
- Kupke, D. W. (1972). In "Physical Principles and Techniques of Protein Chemistry" (S. J. Leach, ed.), Part C, pp. 1–75. Academic Press, New York.
- Laggnan, P., Nilsson, L. and Rigler, R. (1980). "Fifth International Conference on Small-Angle Scattering, Program & Abstracts", pp. 144–145.
- Lake, J. A. and Beeman, W. W. (1967). *Science* **156**, 1371–1373.
- Lake, J. A. and Beeman, W. W. (1968). *J. Mol. Biol.* **31**, 115–125.
- Langer, J. A., Engelman, D. M. and Moore, P. B. (1978). *J. Mol. Biol.* **119**, 463–485.
- Laughrea, M., Engelman, D. M. and Moore, P. B. (1978). *Eur. J. Biochem.* **85**, 529–534.
- Leonard, B. R., Anderegg, J. W., Kaesberg, P., Shulman, S. and Beeman, W. W. (1951). *J. Chem. Phys.* **19**, 793–794.

- Leonard, B. R., Anderegg, J. W., Shulman, S., Kaesberg, P. and Beeman, W. W. (1953). *Biochim. Biophys. Acta* **12**, 499–507.
- Li, Z. G., Giegé, R., Zaccai, G., Oberthür, R. and Jacrot, B. (1980). "Fifth International Conference on Small-Angle Scattering, Program & Abstracts", p. 146.
- Lilley, D. M. J., Richards, B. M., Pardon, J. F., Cotter, R. I. and Worcester, D. L. (1978). In "Gene Expression" (B. F. C. Clark *et al.*, eds), *Proc. FEBS Meet.*, Vol. 43, pp. 213–222. Pergamon Press, Oxford.
- Longley, W. (1963). Ph.D. Thesis, London University.
- Luzzati, V. and Nicolaieff, A. (1959). *J. Mol. Biol.* **1**, 127–133.
- Luzzati, V. and Nicolaieff, A. (1963). *J. Mol. Biol.* **7**, 142–163.
- Luzzati, V., Nicolaieff, A. and Masson, F. (1961a). *J. Mol. Biol.* **3**, 185–201.
- Luzzati, V., Masson, F. and Lerman, L. S. (1961b). *J. Mol. Biol.* **3**, 634–639.
- Luzzati, V., Luzzati, D. and Masson, F. (1962). *J. Mol. Biol.* **5**, 375–383.
- Luzzati, V., Mathis, A., Masson, F. and Witz, J. (1964). *J. Mol. Biol.* **10**, 28–41.
- Luzzati, V., Masson, F., Mathis, A. and Saludjian, P. (1967a). *Biopolymers* **5**, 491–508.
- Luzzati, V., Witz, J. and Mathis, A. (1967b). In "Genetic Elements. Properties and Function" (D. Shugar, ed.), pp. 41–55. Academic Press, London and New York.
- Malmon, A. G. (1957). *Acta Cryst.* **10**, 639–642.
- May, R. (1978). Thesis, Technische Universität München.
- May, R. P., Nierhaus, K. H., Simpson, K., Stuhrmann, H. B. and Wurmbach, P. (1980a). "Fifth International Conference on Small-Angle Scattering, Program & Abstracts", p. 152.
- May, R., Stöckel, P., Strell, I., Hoppe, W., Lorenz, S. and Erdmann, V. A. (1980b). "Fifth International Conference on Small-Angle Scattering, Program & Abstracts", p. 137.
- Moore, P. B. and Engelman, D. M. (1977). *J. Mol. Biol.* **112**, 228–234.
- Moore, P. B. and Engelman, D. M. (1979). *Methods Enzymol.* **59**, 629–638.
- Moore, P. B. and Weinstein, E. (1979). *J. Appl. Cryst.* **12**, 321–326.
- Moore, P. B., Engelman, D. M. and Schoenborn, B. P. (1974). *Proc. Nat. Acad. Sci. USA* **71**, 172–176.
- Moore, P. B., Engelman, D. M. and Schoenborn, B. P. (1975). *J. Mol. Biol.* **91**, 101–120.
- Moore, P. B., Langer, J. A., Schoenborn, B. P. and Engelman, D. M. (1977). *J. Mol. Biol.* **112**, 199–234.
- Moore, P. B., Langer, J. A. and Engelman, D. M. (1978). *J. Appl. Cryst.* **11**, 479–482.
- Müller, J. J., Damaschun, G. and Bielka, H. (1978). *Eur. J. Biochem.* **90**, 547–553.
- Müller, J. J., Welfle, H. and Damaschun, G. (1980). *Stud. Biophys.* **79**, 119–120.
- Müller, J. J., Welfle, H., Damaschun, G. and Bielka, H. (1981). *Biochim. Biophys. Acta* **654**, 156–165.
- Nicolaieff, A. (1967). In "Small-Angle X-Ray Scattering" (H. Brumberger, ed.), pp. 221–241. Gordon and Breach, New York.
- Ninio, J., Favre, A. and Yaniv, M. (1969). *Nature* **223**, 1333–1335.
- Ninio, J., Luzzati, V. and Yaniv, M. (1972). *J. Mol. Biol.* **71**, 217–229.
- Notbohm, H., Hollandt, H., Meissner, J. and Harbers, E. (1979). *Int. J. Biol. Macromol.* **1**, 180–184.
- Österberg, R. (1979). *Eur. J. Biochem.* **97**, 463–469.

- Österberg, R. and Garrett, R. A. (1977). *Eur. J. Biochem.* **79**, 67–72.
- Österberg, R., Sjöberg, B., Rymo, L. and Lagerkvist, U. (1975). *J. Mol. Biol.* **99**, 383–400.
- Österberg, R., Sjöberg, B. and Garrett, R. A. (1976a). *Eur. J. Biochem.* **68**, 481–487.
- Österberg, R., Sjöberg, B. and Garrett, R. A. (1976b). *FEBS Lett.* **65**, 73–76.
- Österberg, R., Sjöberg, B., Garrett, R. A. and Ungewickell, E. (1977). *FEBS Lett.* **80**, 169–172.
- Österberg, R., Sjöberg, B., Garrett, R. A. and Müller, R. (1980a). *Nucleic Acids Res.* **8**, 6221–6231.
- Österberg, R., Sjöberg, B., Liljas, A., Müller, R., Garrett, R. A. and Littlechild, J. (1980b). "Fifth International Conference on Small-Angle Scattering, Program & Abstracts", p. 235.
- Paradies, H. H., Franz, A., Pon, C. L. and Gualerzi, C. (1974). *Biochem. Biophys. Res. Commun.* **59**, 600–607.
- Pardon, J. F. (1979). In "Chromatin Structure and Function. Molecular and Cellular Biophysical Methods. Part A" (C. A. Nicolini, ed.), pp. 187–216. Plenum Press, New York, London.
- Pardon, J. F., Wilkins, M. H. F. and Richards, B. M. (1967). *Nature* **215**, 508–509.
- Pardon, J. F., Worcester, D. L., Wooley, J. C., Tatchell, K., Van Holde, K. E. and Richards, B. M. (1975). *Nucleic Acids Res.* **2**, 2163–2176.
- Pardon, J. F., Worcester, D. L., Wooley, J. C., Cotter, R. I., Lilley, D. M. J. and Richards, B. M. (1977). *Nucleic Acids Res.* **4**, 3199–3214.
- Pardon, J. F., Cotter, R. I., Lilley, D. M. J., Worcester, D. L., Campbell, A. M., Wooley, J. C. and Richards, B. M. (1978). *Cold Spring Harbor Symp. Quant. Biol.* **42**, 11–22.
- Pilz, I., Kratky, O., Cramer, F., von der Haar, F. and Schlimme, E. (1970). *Eur. J. Biochem.* **15**, 401–409.
- Pilz, I., Kratky, O., von der Haar, F. and Cramer, F. (1971). *Eur. J. Biochem.* **18**, 436–441.
- Pilz, I., Malnig, F., Kratky, O. and von der Haar, F. (1977). *Eur. J. Biochem.* **75**, 35–41.
- Pilz, I., Goral, K. and von der Haar, F. (1979). *Z. Naturforsch.* **34c**, 20–26.
- Richards, B. M., Pardon, J. F., Lilley, D. M. J., Cotter, R. I., Wooley, J. C. and Worcester, D. L. (1977). *Cell Biol. Int. Rep.* **1**, 107–116.
- Satake, H., Akutsu, H., Kania, M. and Franklin, R. M. (1980). *Eur. J. Biochem.* **108**, 193–201.
- Schindler, D. G., Langer, J. A., Engelman, D. M. and Moore, P. B. (1979). *J. Mol. Biol.* **134**, 595–620.
- Schmidt, P. W. and Taylor, T. R. (1967). *Phys. Fluids* **10**, 885–888.
- Schmidt, P. W., Kaesberg, P. and Beeman, W. W. (1954). *Biochim. Biophys. Acta* **14**, 1–11.
- Schneider, D., Zulauf, M., Schäfer, R. and Franklin, R. M. (1978). *J. Mol. Biol.* **124**, 97–122.
- Serdyuk, I. N. (1975). *Brookhaven Symp. Biol.* **27**, IV, 49–60.
- Serdyuk, I. N. (1979). *Methods Enzymol.* **59**, 750–775.
- Serdyuk, I. N. and Grenader, A. K. (1975). *FEBS Lett.* **59**, 133–136.
- Serdyuk, I. N. and Grenader, A. K. (1977). *Eur. J. Biochem.* **79**, 495–504.
- Serdyuk, I. N., Smirnov, N. I., Ptitsyn, O. B. and Fedorov, B. A. (1970). *FEBS Lett.* **9**, 324–326.
- Serdyuk, I. N., Grenader, A. K. and Kotelianskii, V. E. (1977). *Eur. J. Biochem.* **79**, 505–510.
- Serdyuk, I. N., Grenader, A. K. and Zaccai, G. (1979). *J. Mol. Biol.* **135**, 691–707.
- Serdyuk, I. N., Gogia, Z. V., Venyaminov, S. Yu., Khechinashvili, N. N., Bushuev, V. N. and Spirin, A. S. (1980a). *J. Mol. Biol.* **137**, 93–107.
- Serdyuk, I. N., Shpungin, J. L. and Zaccai, G. (1980b). *J. Mol. Biol.* **137**, 109–121.
- Sjöberg, B. (1977). *Eur. J. Biochem.* **81**, 277–283.
- Sjöberg, B. (1978). *J. Appl. Cryst.* **11**, 73–79.
- Smith, W. S. (1971). Ph.D. Thesis, University of Wisconsin.
- Spencer, M. and Staynov, D. Z. (1980). *Biophys. J.* **30**, 307–316.
- Sperling, L. and Tardieu, A. (1976). *FEBS Lett.* **64**, 89–91.
- Spirin, A. S., Serdyuk, I. N., Shpungin, J. L. and Vasiliev, V. (1979). *Proc. Nat. Acad. Sci. USA* **76**, 4867–4871.
- Stuhrmann, H. B. (1970). *Acta Cryst. A* **26**, 297–306.
- Stuhrmann, H. B., Haas, J., Ibel, K., De Wolf, B., Koch, M. H. J. and Parfait, R. (1976). *Proc. Nat. Acad. Sci. USA* **73**, 2379–2383.
- Stuhrmann, H. B., Koch, M. H. J., Parfait, R., Haas, J., Ibel, K. and Crichton, R. R. (1977). *Proc. Nat. Acad. Sci. USA* **74**, 2316–2320.
- Stuhrmann, H. B., Koch, M. H. J., Parfait, R., Haas, J., Ibel, K. and Crichton, R. R. (1978). *J. Mol. Biol.* **119**, 203–212.
- Suau, P., Kneale, G. G., Braddock, G. W., Baldwin, J. P. and Bradbury, E. M. (1977). *Nucleic Acids Res.* **4**, 3769–3786.
- Suau, P., Bradbury, E. M. and Baldwin, J. P. (1979). *Eur. J. Biochem.* **97**, 593–602.
- Subirana, J. A., Lloveras, J., Lombardero, M. and Vinuela, E. (1979). *J. Mol. Biol.* **128**, 101–106.
- Teig-Jensen, B., Furugren, B., Lindquist, I. and Philipson, L. (1972). *Monatsh. Chem.* **103**, 1730–1736.
- Timasheff, S. N. (1964). *Biochim. Biophys. Acta* **88**, 630–641.
- Timasheff, S. N., Witz, J. and Luzzati, V. (1961). *Biophys. J.* **1**, 525–537.
- Tolbert, W. R. (1971). Ph.D. Thesis, University of Wisconsin.
- Torbet, J. (1979). *FEBS Lett.* **108**, 61–65.
- Van Domelen, B. H. and Beeman W. W. (1962). *Biochim. Biophys. Acta* **61**, 872–875.
- Venable, J. H., Spencer, M. and Ward, E. (1970). *Biochim. Biophys. Acta* **209**, 493–500.
- Wawra, H., Müller, W. and Kratky, O. (1970). *Makromol. Chemie* **139**, 83–102.
- White, R. A. (1962). Ph.D. Thesis, University of Wisconsin.
- White, R. A. and Fischbach, F. A. (1973). *J. Mol. Biol.* **75**, 549–558.
- Wilkins, M. H. F., Zubay, G. and Wilson, H. R. (1959). *J. Mol. Biol.* **1**, 179–185.
- Witz, J. and Luzzati, V. (1965). *J. Mol. Biol.* **11**, 620–630.
- Witz, J., Hirth, L. and Luzzati, V. (1965). *J. Mol. Biol.* **11**, 613–619.
- Wooley, J. C., Pardon, J. F., Richards, B. M., Worcester, D. L. and Campbell, A. M. (1977). *Fed. Proc.* **36**, 810.

- Zaccai, G., Morin, P., Jacrot, B., Moras, D., Thierry, J. C. and Giegé, R. (1979). *J. Mol. Biol.* **129**, 483–500.
- Zipper, P. (1973). *Eur. J. Biochem.* **39**, 493–498.
- Zipper, P. and Büinemann, H. (1975). *Eur. J. Biochem.* **51**, 3–17.
- Zipper, P., Kratky, O., Herrmann, R. and Hohn, T. (1971a). *Eur. J. Biochem.* **18**, 1–9.
- Zipper, P., Kratky, O. and Schubert, D. (1971b). *FEBS Lett.* **14**, 219–221.
- Zipper, P., Kratky, O., Büinemann, H. and Müller, W. (1972). *FEBS Lett.* **25**, 123–126.
- Zipper, P., Folkhard, W. and Clauwaert, J. (1973a). *Hoppe-Seyler's Z. Physiol. Chem.* **354**, 1262–1263.
- Zipper, P., Schubert, D. and Vogt, J. (1973b). *Eur. J. Biochem.* **36**, 301–310.
- Zipper, P., Folkhard, W. and Clauwaert, J. (1974). *J. Appl. Cryst.* **7**, 168.
- Zipper, P., Folkhard, W. and Clauwaert, J. (1975). *FEBS Lett.* **56**, 283–287.
- Zipper, P., Ribitsch, G., Schurz, J. and Büinemann, H. (1978). *Hoppe-Seyler's Z. Physiol. Chem.* **359**, 1170.
- Zipper, P., Ribitsch, G., Schurz, J. and Büinemann, H. (1982a). Submitted for publication.
- Zipper, P., Ribitsch, G., Folkhard, W., Schurz, J., De Clercq, R. and Clauwaert, J. (1982b). In preparation.

10

Lipoproteins and Membranes

P. LAGGNER

*Institut für Röntgenfeinstrukturforschung der Österreichischen Akademie der
Wissenschaften und des Forschungszentrums Graz, Graz, Austria*

I. Introduction	329
II. Serum lipoproteins	330
A. High density lipoproteins (HDL)	331
B. Low density lipoproteins (LDL)	337
C. The pathological lipoprotein X (Lp-X)	346
D. Reconstitution experiments	347
III. Membranes	349
A. Phospholipid bilayers	349
B. Solubilized membrane proteins	353
Acknowledgements	355
References	357

I. Introduction

In this chapter I shall attempt to give a concise review of the small angle scattering studies in the field of lipids and lipid-protein complexes of biological origin. According to the general theme of this book, the treatment will be confined to examples of particle scattering, i.e. to the analysis of small angle scattering from dilute, unoriented systems. Many important contributions to this area have come from X-ray and neutron diffraction studies on condensed, oriented systems, in particular of lipids and membranes. However, a coverage of this area would exceed the scope of the present review and the reader must be referred to the substantial review literature (Luzzati, 1968; Levine, 1972; Shipley, 1973; Worcester, 1976; Schoenborn, 1976).

Most of the structures to be discussed here are either corpuscular or lamellar: the normal plasma lipoproteins are generally isotropic, frequently spherically symmetrical particles. In these cases the ultimate result of small angle scattering

studies is a description of both external morphology and internal structure. A different situation prevails with the lamellar structure of lipids and membranes: here, the overall dimensions of the typically formed hollow vesicles are rather ill defined and frequently, by at least one order of magnitude, larger than the lamellar cross-section, and hence a description of overall size and shape is highly problematic if not impossible. However, under the condition of the absence of structural discontinuities within the lamellar plane it is possible to determine the lamellar thickness and the cross-sectional electron density distribution. This condition is clearly not fulfilled by natural membranes which are in many cases known to consist of laterally separated domains of proteins and lipids. It is, hence, normally impossible to obtain significant structural data from experiments with plasma membranes in random dispersion. This problem can be circumvented with some promise for success by chemically dissecting the membrane structure into its components and to study these separately. A considerable wealth of information has thus been obtained for various membrane lipids and in the past few years there emerged also several promising small angle scattering investigations of solubilized membrane proteins.

The theoretical background applying to this type of work has been extensively reviewed in Chapters 2, 5 and 6. In this chapter, the emphasis will lie on the practical possibilities and limitations of small angle scattering in this field of application.

II. Serum Lipoproteins

The lipoproteins occurring in normal blood serum constitute a broad spectrum of particles containing different proportions of specific protein components and polar and apolar lipids. The molecular weights range from approximately 2×10^5 to 10^8 . This spectrum can be separated by appropriate techniques, e.g. by density gradient ultracentrifugation, resulting in fractions of different buoyant densities (for extensive reviews on the general physical and chemical properties see Scanu and Wisdom, 1972; Scanu *et al.*, 1975; Laggner, 1976, 1981).

These buoyant densities are generally used to define in operational terms individual lipoprotein classes as High Density (HDL), Low Density (LDL) and Very Low Density Lipoproteins (VLDL). An alternative classification based upon the nature of the apoprotein constituents uses immunochemically similar "protein families" designated by capital letters A, B, C etc. (Alaupovic, 1972; see also reviews by Jackson *et al.*, 1976; Morrisett *et al.*, 1977) thus, for example, defining those species as lipoprotein A which contain only apo A proteins. Both terminologies have been used in the original studies and will also be adopted in the present review.

The most general physical and chemical characteristics of the lipoprotein

TABLE 1
General Physical and Chemical Characteristics of Lipoprotein Density Classes

	VLDL	LDL	HDL
Hydrated density (g/cm^3) ^a	0,95–1,006	1,006–1,063	1,063–1,21
Molecular weight	$5-10 \times 10^6$	$2-5 \times 10^6$	$2-5 \times 10^5$
Diameter (\AA) ^b	300–1000	200–300	90–140
<i>Components (weight-%)^c</i>			
Protein	< 10	25	45–55
Phospholipids	15–20	22	30
Cholesterol	< 10	8	5
Cholesteryl Esters	5	37	20
Triglycerides	50–70	10	3
Carbohydrate	< 1	~ 1	< 1

^a Apparent hydrated density from density gradient ultracentrifugation.

^b Average diameters of globular particles from electron microscopic data.

^c These are average values. Variations occur between individual donors and depending on the isolation procedure.

density classes are summarized in Table 1. It should be borne in mind, however, that these density classes do not represent discrete macromolecular species but are only systematic cuts out of a multimodal distribution of particle sizes and composition. For purposes of X-ray small angle scattering analysis it is obviously necessary to go further in the separation and to take all preparatory measures to ensure as good an approximation to monodispersity as possible. In practice the homogeneity has to be tested carefully by other methods, e.g. by analytical ultracentrifugation. Nevertheless, these tests also have their limitations and it is therefore necessary critically to consider the possible influences of polydispersity on the small angle scattering results. Moreover it cannot be excluded that a lipoprotein fraction which is homogeneous with respect to its hydrated density and molecular weight consists of nonidentical particles varying somewhat in their chemical composition and possibly also in their fine structure. The small angle scattering pattern will therefore generally represent an average result for the particular fraction under study and not necessarily reflect the structure of one single sort of particles.

A. High Density Lipoproteins (HDL)

1. THE SCATTERING PATTERNS

The physical and chemical characteristics of the HDL subfractions hitherto investigated by X-ray small angle scattering are summarized in Table 2. Quite normally, the analytical data from different preparations of the same subfraction

TABLE 2
Physical and Chemical Data of HDL Subfractions

	HDL ₃ ^a	LpA ₃ ^d	p-HDL ₃ ^b	HDL ₂ ^c	LpA ₂ ^d	LpC ^d
Molecular weight ($\times 10^{-5}$)	1,75	1,9–2,1	2,1	3,6	3,6	4,6
Partial Specific Volume ($\text{cm}^3 \text{g}^{-1}$) at 4°C	0,848	0,859	0,88	0,914	0,903	0,905
Mean Electron Density (e nm ⁻³)	385	381	375	361	365	365
Radius of Gyration at Infinite Contrast (nm)	4,06	4,2	4,1	—	4,7	—
<i>Composition (weight %)</i>						
Protein	55	58,0	44	41,2	42,0	35,0
Phospholipid	25	23,1	22	29,5	31,9	31,7
Cholesterol	4	3,9	3	5,4	5,5	4,7
Cholesteryl Esters	13	13,0	26	16,2	18,0	21,2
Triglycerides	3	2,0	5	7,7	2,6	7,5

^a from Tardieu *et al.* (1976);

^b from Atkinson *et al.* (1974a);

^c from Shipley *et al.* (1973);

^d from Laggner and Müller (1978).

show some variations which exceed the normal errors of the analytical methods. Most probably this reflects minor variations in the preparative methods used.

Three different subfractions of the HDL spectrum have been investigated so far in the author's laboratory, designated as LpA₃ (Laggner *et al.*, 1972, 1973), LpA₂ (Müller *et al.*, 1974) and LpC (Laggner *et al.*, 1976). LpA₂ and LpA₃, respectively, represent human HDL₂ and HDL₃ subfractions which contain only apolipoproteins A-I and A-II, whereas the fraction termed LpC is an HDL₂ fraction containing more than 80% apolipoproteins of the C-family and the remainder being apolipoproteins A.

The scattering curves of these three HDL fractions in isotonic NaCl solution are shown in a double-logarithmic plot in Fig. 1. It can be seen that by multiplication of the angular variable h with a suitably chosen factor x , corresponding to a linear shift in the logarithmic plot, the positions and relative heights of the secondary maxima for the lipoprotein species can be brought to an almost perfect coincidence (Laggner and Müller, 1978b). Taking, arbitrarily, $x = 1$ for LpA₃, the optimal values for LpA₂ and LpC are $x = 0,85$ and $0,76$, respectively. The ratio of these factors corresponds well to the reciprocal ratio of the maximum particle dimensions of 10 nm, 12 nm and 14,5 nm for LpA₂ and LpC, respectively, obtained from the pair distance distribution functions $p(r)$ (see Fig. 1). Both the real space and reciprocal space representations of the scattering results show a close structural similarity to these particle species.

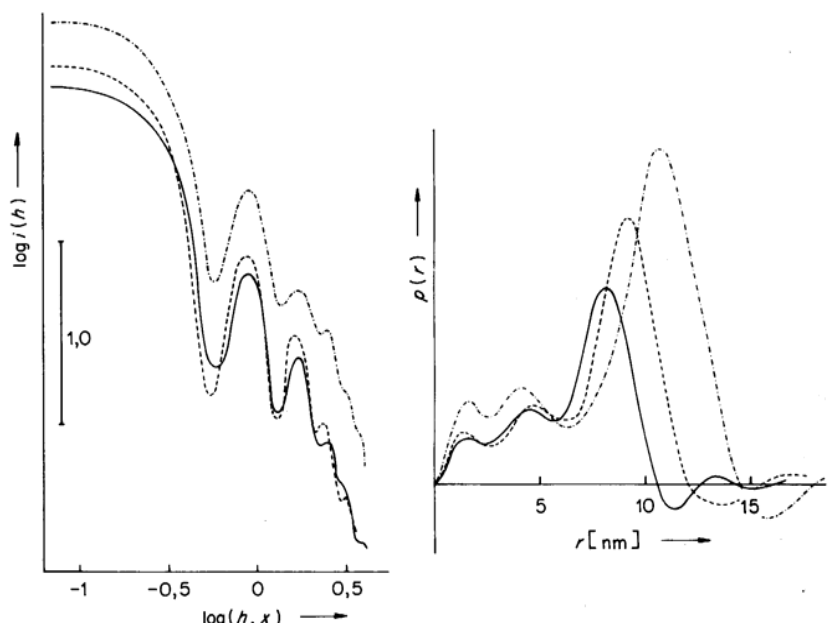


FIG. 1. Scattering curves $i(h)$ and distance distribution functions $p(r)$ of high density lipoprotein subclasses: LpA₃ (—), LpA₂ (---), LpC (-·-·-) in 0,15 M NaCl. The factors x in the angular scale are 1,0, 0,85 and 0,76 for LpA₃, LpA₂ and LpC, respectively. (From Laggner and Müller, 1978).

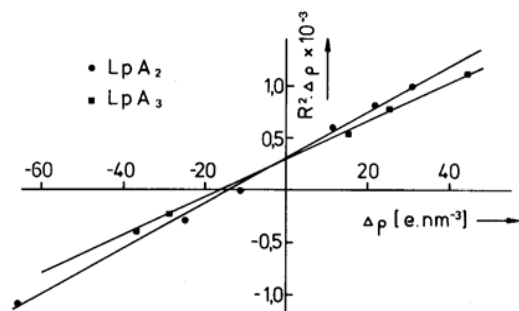


FIG. 2. Dependence of the radius of gyration R of LpA₂ (●) and LpA₃ (■) on the electron density contrast $\Delta\rho$, measured in sucrose solutions of different concentrations. (From Laggner and Müller, 1978).

The well developed secondary maxima and minima in the scattering curves, as well as the steep descent of the $p(r)$ function towards the maximum diameter immediately reflects a compact, highly isotropic structure. From the positive values of the second moment of the electron density distribution as obtained from the contrast dependence of the radius of gyration, R (Fig. 2), it follows

that the particles consist of a high electron density shell and a low electron density core (Stuhrmann, 1974; see also Chapter 6). Moreover, the linear course of $R^2 \cdot \Delta\rho$ versus $\Delta\rho$ demonstrates that the centres of gravity of the different electron density regions within the particles coincide. The slopes of these lines yield the radii of gyration at infinite contrast, i.e. the radii of gyration of the excluded volume. For LpA₃ and LpA₂ these values are 4.2 nm and 4.7 nm, respectively, corresponding to diameters for the equivalent sphere of 10.8 nm and 12.1 nm. Comparing this to the maximum dimensions from the $p(r)$ functions suggests strongly that the particles are indeed close to spherical.

Qualitatively very similar observations were reported by Shipley *et al.* (1972) on human HDL₂, by Atkinson *et al.* (1974a) on porcine HDL₃, and by Tardieu *et al.* (1976) on human HDL₃. The latter authors attempted the evaluation of the characteristic scattering functions $i_v(h)$ and $i_s(h)$, of the excluded volume and of the internal structure, respectively, from contrast variation experiments. They also made use of the distribution of chords $G(r)$ (Mering and Tchoubar, 1968) to extract information on the overall size and the relative locations of high and low electron density regions. Although this approach involves the assumption of only two discrete levels of electron density within the particle and despite the fact that the function $G(r)$ relies heavily on the accuracy in the low intensity outer part of the scattering curve, the qualitative interpretation is similar to what has been concluded from the $p(r)$ function as outlined above. The absolute dimensions resulting from this treatment are somewhat larger (maximum diameter for HDL₃: 13 nm) than those obtained for LpA₃ in the author's laboratory, which might be due both to differences in the samples and to the different ways of data evaluation. It is clear, however, that in practice the reliability of the dimensions obtained from the $p(r)$ function is superior to that from the distribution of chords, $G(r)$.

2. THE SPHERICALLY AVERAGED STRUCTURE

Under the above conditions it is justifiable to underly the assumption of quasi-spherical structure to the further evaluation of the data. In this case, there exist two alternative possibilities to determine the radial electron density distribution: (a) Fourier transformation of the amplitudes $F(h)$ (see Chapter 4), and (b) deconvolution of the pair distance distribution function $p(r)$. Only recently a practicable numerical method for performing the deconvolution of $p(r)$ has been developed (convolution square root technique by Glatter, 1981) and so far its use has been limited to a study of Low Density Lipoproteins (see Section II.B). In the following the three practical problems encountered in the more widely used approach of Fourier transformation of $F(h)$ shall be discussed.

(a) *The Problem of Non-zero Minima.* Ideally, the particle scattering function of spherically symmetric structures displays minima going to zero between the secondary maxima. In experimental practice with macromolecular structures, however, several conditions prevent the observation of such zero-minima: most obviously, the very fact of molecular structure precludes ideal sphericity; with lipoproteins, moreover, a minor degree of size heterogeneity will also contribute to the filling up of the minima. The same effect may be produced by time dependent deformation due to the structural flexibility which is a well established feature of most lipid-protein complexes.

Apart from these structural causes, the experimental technique, involving statistical noise as well as the procedures of desmearing and monochromatization, suffers from shortcomings which may be equally responsible for the filling-up of minima and it is clear that the various factors cannot be disentangled.

In the author's laboratory it became customary with scattering curves as given by the HDL subclasses to extrapolate the minima to zero since the majority of the above effects bear more strongly to the minima than to the maxima. An example of this procedure is shown in Fig. 3a. Atkinson *et al.* (1974a) and Tardieu *et al.* (1976) have proposed to decompose the scattering functions into two separate terms, one being ascribed to the spherical average and the other to the deviation from sphericity. The non-sphericity term is assumed to take the shape of a smooth curve connecting the minima of the total scattering curve, thus creating zero-minima for the sphericity term (Fig. 3b). It is evident, however, that this background subtraction is a largely arbitrary approach since no unique description for the background term can be given and since it neglects all experimental errors which may not be negligible at all, particularly with curves obtained by extrapolation as, for example, the shape function $i_v(h)$ at infinite contrast.

To a certain extent, therefore, either of the above methods for obtaining zero minima is to some extent debatable; however, if the experimentally obtained minima are sharp and low as compared to the maxima, the final results from both approaches are rather similar.

(b) *The Problem of Curve Termination.* Due to the inherently limited angular range covered by small angle scattering experiments the result of Fourier transformation can only provide a low-resolution description of the structure under investigation. Furthermore, it is well known that considerable errors incur if the amplitudes are cut off and thus set equal to zero beyond the largest measured angle h_{\max} : an oscillating function with a wavelength of π/h_{\max} is thus generated and superimposed on the structurally relevant $\Delta\rho(r)$ function. To minimize this effect, the method of indirect Fourier transformation (for details, see Chapter 4) has been used in the author's laboratory. An example for the application of this method to the data of LpA₃ is given in Fig. 4. In any case, it is advisable to

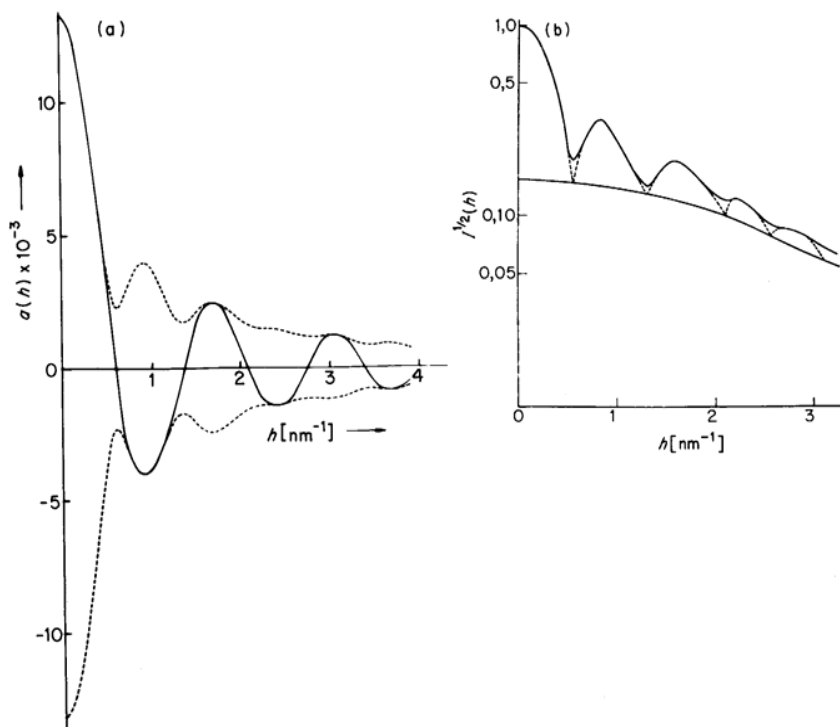


FIG. 3. Two possibilities for constructing the amplitudes $a(h)$ from experimental scattering data. (a) Extrapolation of the minima to zero; this method has been generally employed in studies from the author's group; (b) subtraction of an artificial background to allow for deviations from spherical symmetry as used by Atkinson *et al.* (1974a).

test the initially used function $F(h)$ and the choice of the number of auxiliary Spline functions, N_s , and of the Lagrange multiplier λ (see Chapter 4) by reverse transformation and comparison to the experimental scattering curve. For the refinement of the fit, the approximation by simple electron density step functions may in some cases prove most convenient.

(c) *The Phase Problem.* Despite its paramount importance in the Fourier transformation of amplitudes, the problem of the *a priori* undefined signs of the individual maxima has not yet seen a complete formal solution in the field of small angle scattering. This ambiguity further reduces the resolution of such experiments. It can be solved by contrast variation experiments only for the first few maxima: for the refined $\Delta\rho(r)$ functions obtained from any possible phase combination (starting with the sign of the first maximum as known from the net electron density contrast) the theoretical second moment is calculated and compared to the experimentally found value, i.e. the intercept at $\Delta\rho = 0$

in the plot of $R^2 \Delta\rho$ versus $\Delta\rho$. In the case of scattering curves from HDL this allows the phase assignment to the first four maxima for which alternating signs have been thus obtained. The relatively low contribution by the following maxima and the high experimental error in the larger angular region makes attempts to increase the resolution by including further maxima very difficult. The formal resolution with regard to details in the internal structure in terms of the smallest Bragg's value is approximately 1,1 nm for the case of the HDL subfractions studied in the author's laboratory.

3. RESULTS FOR HDL SUBFRACTIONS

The electron density distributions obtained by Indirect Fourier transformation for LpA_3 , LpA_2 and LpC are shown in Fig. 5. Closely similar results have been obtained by Shipley *et al.* (1972) on HDL_2 and by Tardieu *et al.* (1976) on HDL_3 from human serum and by Atkinson *et al.* (1974a) on porcine HDL_3 .

These results, together with considerations regarding the chemical composition and the volume requirements for the individual lipid and protein constituent, have led to the postulation of a molecular model (Fig. 6) which essentially consists of a spherical micellar arrangement of the apolar lipids in the particle core surrounded by an outer hydrophilic surface formed by protein and polar phospholipid headgroups. In this model the interdigitation between the core lipids and the hydrocarbon chains of the phospholipids is a significant feature as it provides an explanation for the size variations observed with HDL subfractions. Since the length of a cholestryloleate molecule in fully extended conformation is approximately 3,7 nm, which is close to the core diameter of LpA_3 , the phospholipid hydrocarbon chains are in this case considered to be interdigitated into the core lipids with their full length, thus posing a lower limit to the overall particle size consistent with this structural model. The upper limit is given by the minimum length of interdigitation which is postulated to be the case in LpC , where the core radius corresponds almost to the sum of the extended lengths of a cholestryloleate molecule plus an 18:1 hydrocarbon chain. The external shell thickness is consistent with a two-dimensional, highly α -helical protein network into which the polar phospholipid headgroups are intercalated. A detailed discussion of the considerations leading to this model and a comparison to other existing models has been presented elsewhere (Laggner and Müller, 1978).

B. Low Density Lipoproteins (LDL)

By its chemical composition, LDL differs from HDL most significantly in its higher content in apolar lipids, cholestryloesters and triglycerides, which amount

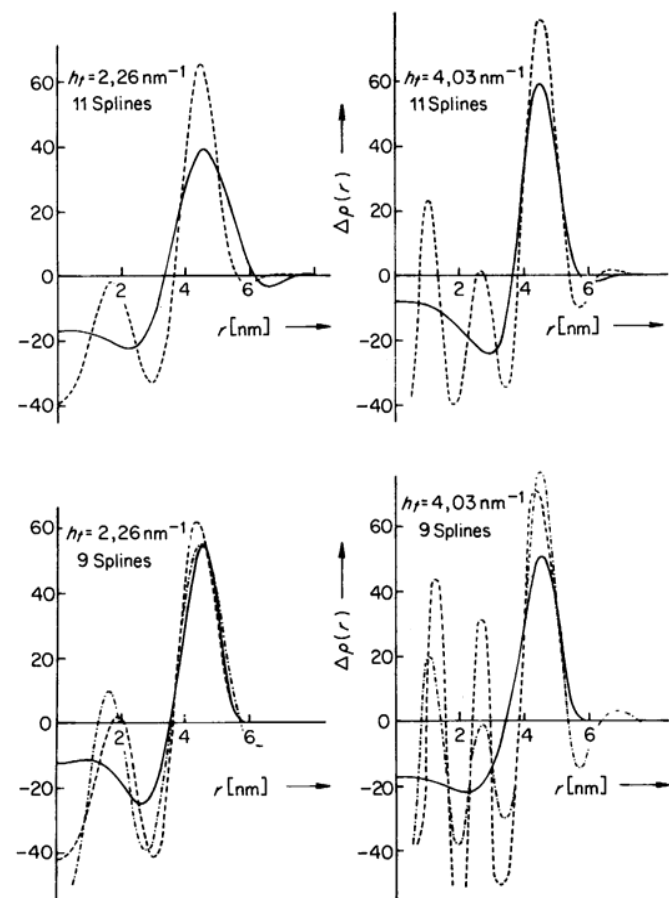


FIG. 4.(a) Radial electron density profiles of LpA_3 obtained by indirect Fourier transformation of the amplitudes in Fig. 3a. The graphs show the influence of curve termination and of the number of Spline function used (see Chapter 4). — optimally stabilized; - - less stabilized; - · - by direct Fourier transformation. (From Laggner and Müller, 1978).

to about half of the total weight, and its relatively low protein and phospholipid content, and it is hence obvious that the molecular arrangement within this lipoprotein class must be different from HDL. The first X-ray small angle investigation of LDL by Mateu *et al.* (1972) has indicated that LDL particles display quasi-spherical structure with strong internal electron density variations. The overall size of the particles has been estimated from this study to be approximately 26 nm. The radial electron density distribution calculated from the amplitudes by Fourier transformation led these authors to the proposal of a detailed molecular model. However, this model has later been rejected on the basis of methodically more advanced studies (Laggner *et al.*, 1976; Tardieu *et al.*, 1976).

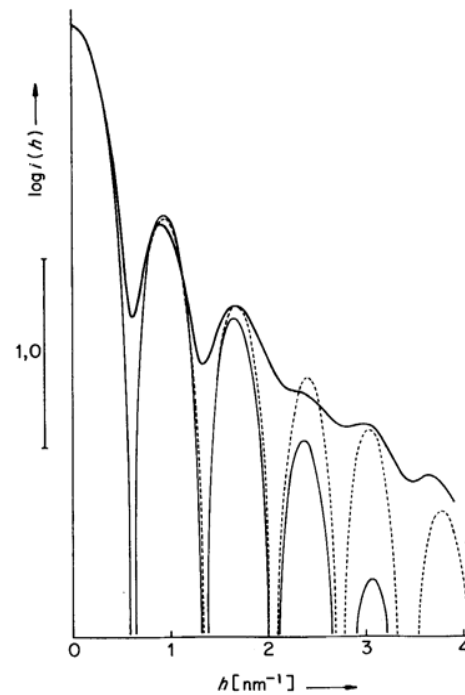


FIG. 4.(b) Comparison of the theoretical scattering curves for the optimally stabilized (light full line) and less stabilized electron density profile (---) to the desmeared experimental results (heavy full line). (From Laggner and Müller, 1978).

In the following, the three independent experimental approaches, which have led to the present understanding of the structural principle of LDL, will be briefly reviewed.

1. CONTRAST VARIATION

Attempts to evaluate the characteristic scattering functions (see Chapter 6) from a series of experimental scattering curves obtained at different electron density contrasts have been carried out independently by Tardieu *et al.* (1976) and by the author's group (Müller *et al.*, 1978). From these studies it became evident that particularly the shape scattering function $i_v(h)$ is afflicted by considerable errors since it is obtained from extrapolation of scattering data restricted to a relatively narrow range of electron densities to infinite contrast. Moreover, this approach also requires constancy of the scattering volume and absolute electron density of the particle throughout the entire range of solvents used in the contrast variation series.

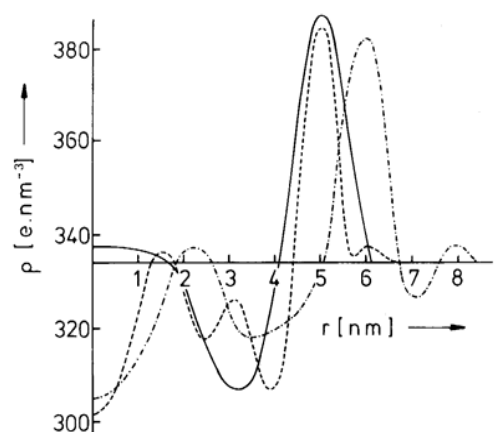


FIG. 5. Radial electron density profiles of LpA₂ (— from Müller *et al.*, 1974; --- from Laggner, 1978a) and of LpC (----). (From Laggner and Müller, 1978).

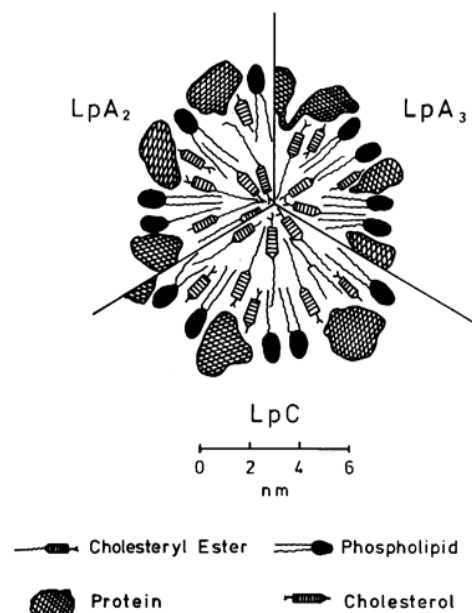


FIG. 6. Cross-sectional molecular model of three HDL subfractions, LpA₃, LpA₂, and LpC (from Laggner and Müller, 1978).

Aggerbeck *et al.* (1978) and Luzzati *et al.* (1979) have attempted to verify this condition for the case of LDL (from hyperlipidemic rhesus monkey) in NaBr solutions. Two methodically different tests were performed. In the first one the amplitude at zero angle $\sqrt{i}(0)$ was determined as a function of solvent electron density. This should result in a linear dependence if the absolute number of electrons within the scattering particles remained constant throughout the whole range of NaBr concentrations. An approximately linear dependence was observed between NaBr concentrations of 1,7 M and 6 M. However, in a similar experiment using sucrose to change the contrast, we have been able to show that particularly at low sucrose concentrations the plot of \sqrt{i} versus ρ_0 solvent departs significantly from linearity (Müller *et al.*, 1978). Since no results have been reported by Aggerbeck *et al.* for NaBr in the low contrast region, the hypothesis of a constant volume and electron density remains debatable. Also the second test used by Aggerbeck *et al.*, i.e. the attempt to determine a "preferential interaction parameter" by precision densimetry, fails to be conclusive since, according to the thermodynamic analysis of multicomponent systems (Casassa and Eisenberg, 1964; Eisenberg, 1976; Lee *et al.*, 1979), this parameter requires the measurement of the density increment under two conditions, i.e. first, under identical chemical potential of the solvent components in solvent and solution (dialysis equilibrium) and, secondly, under identical molal concentrations in solvent and solution. Aggerbeck *et al.* only determined the density increment of LDL in dialysis equilibrium in a series of NaBr solutions and, for simplification, made the *a priori* assumption that each lipoprotein particle is accompanied by a fixed amount of water impenetrable to NaBr. Thus, a partial specific volume of $0,9628 \text{ cm}^3 \text{ g}^{-1}$ and a quantity of 0,09 g of water associated to LDL were calculated. Using these values together with the known chemical composition of LDL a net electron density of $344,4 \text{ e nm}^{-3}$ was calculated and compared to the values of $341,7 \text{ e nm}^{-3}$ obtained from the abscissa intercept in the function of $\sqrt{i}(0)$ versus ρ_0 . This comparison is hardly in favour of the above assumptions since it can be easily shown that a broad variation in the composition of the preferentially bound solvent would result in net electron densities between these two limits.

For these reasons an interpretation of the volume scattering function $i_v(h)$ and hence also of the particle volume V obtained from $i_v(h)$ according to

$$V = 2\pi^2 \cdot \frac{i_v(0)}{\int_0^\infty i_v(h) \cdot h^2 \cdot dh}$$

is based on considerable uncertainties (note that V is the result of double extrapolation, first to infinite contrast to obtain $i_v(h)$, and second to infinite angle h). In a study on LDL from hyperlipidemic rhesus monkey Luzzati *et al.* (1979) used the ratio of R_v^3/V , where R_v is the radius of gyration at infinite contrast,

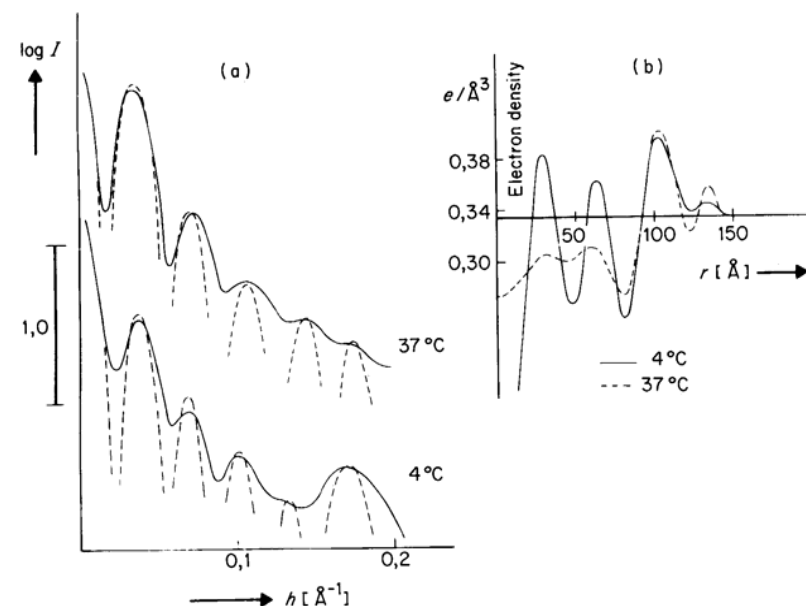


FIG. 7. (a) Scattering curve of LpB from human low density lipoproteins in 0.15 M NaCl at 4°C and 37°C (—). The dotted lines represent the theoretical scattering curves for the radial electron density profiles shown in (b). (b) Radial electron density profiles obtained by Fourier transformation of the amplitudes $\pm I^{1/2}(h)$. (From Laggner *et al.*, 1977a).

as an argument for strong departure from spherical shape. On the other hand, for human LDL we have found that there exists close agreement between the radius of a sphere calculated from R_v ($r = \sqrt{(5/3)} \cdot R_v = 11.6 \text{ nm}$) and the maximum particle diameter of 23–25 nm obtained from the $p(r)$ function, supporting strongly quasi-spherical shape of the particle (Müller *et al.* 1978).

The internal structure scattering function $i_s(h)$ can be obtained with much better accuracy since it is obtained by interpolation rather than by extrapolation and the contrast matching solvent is only approximately 0.3 M sucrose or 0.4 M NaBr. Tardieu *et al.* (1976) have calculated a spherically averaged radial electron density distribution from the amplitudes at zero contrast. The results are very similar to those obtained from our experiments in 0.15 M NaCl buffer (Laggner *et al.*, 1976), where LDL has still a finite net contrast, with the typical appearance of strong positive-to-negative variations of the electron density in the particle core (Fig. 7). The internal separation of high and low electron density regions is also reflected by the pair distance distribution $p(r)$ which shows strong fluctuations at $r < 15 \text{ nm}$ (Fig. 8b). By calculating the theoretical contrast dependence of structure models with other than radial symmetry, the postulated spherical symmetry of LDL has been further supported (Müller

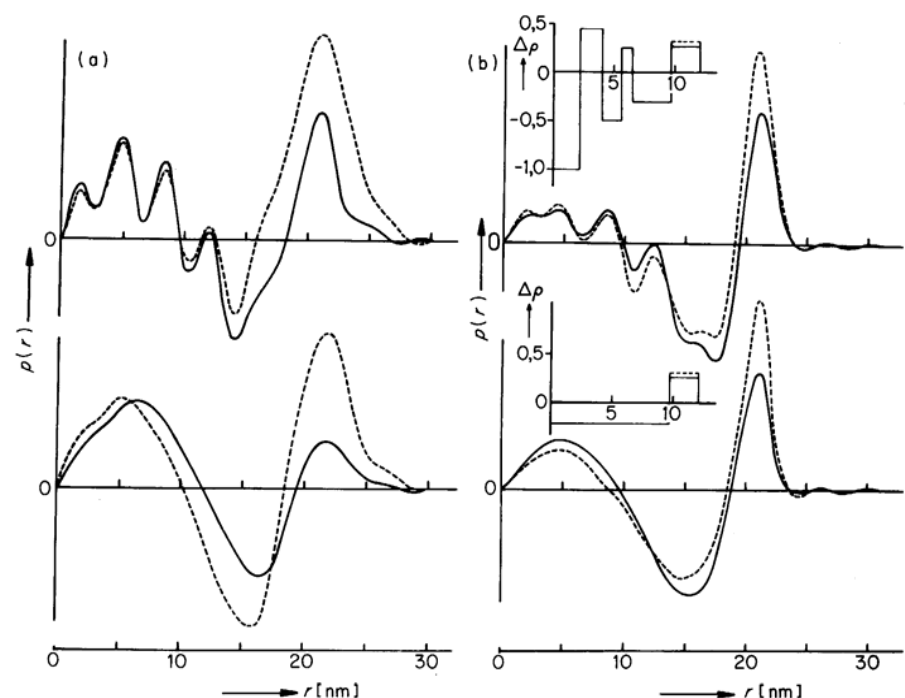


FIG. 8. (a) The effect of partial removal of proteins from low density lipoprotein by trypsin digestion on the distance distribution functions $p(r)$ at 4°C (upper frame) and 37°C (lower frame). (b) Theoretical distance distribution functions calculated for the electron density step models shown in the inserts. (From Laggner *et al.*, 1978a).

et al., 1978). Neutron scattering data by Stuhrmann *et al.* (1975) and by Laggner *et al.* (1981) were also in support of spherical symmetry.

2. TEMPERATURE VARIATION

Following the important finding, first published by Deckelbaum *et al.* (1975), that the cholestrylo esters within LDL undergo a reversible thermotropic transition similar to the liquid-crystalline to isotropic phase change of isolated cholestrylo esters, two independent studies were conducted to study in detail the temperature dependence of small angle scattering by LDL (Atkinson *et al.*, 1977; Laggner *et al.*, 1977a). These studies demonstrated that the two inner electron density maxima at 3.0 and 6.5 nm observed at 4°C are abolished upon heating above 30°C, whereas the external high electron density shell remains practically unaffected (Fig. 10). Excellent agreement was found to exist between the volume of the temperature sensitive core and the volume requirements

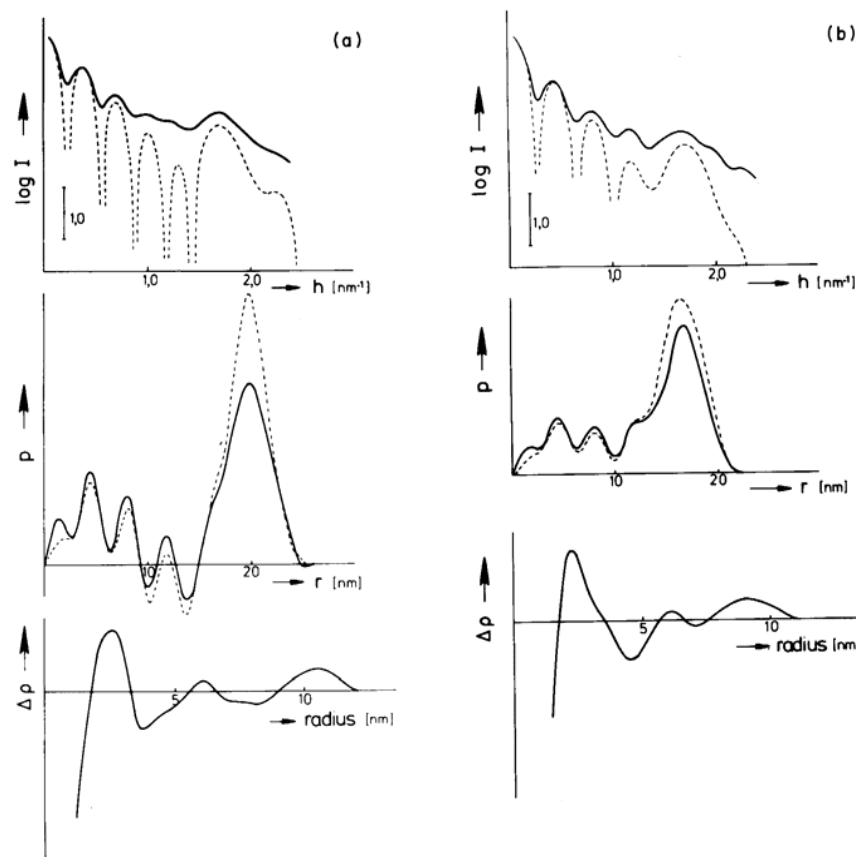


FIG. 9. Deconvolution of the pair distance distribution functions $p(r)$ for porcine LDL₁ (a) and LDL₂ (b). Top and middle frames show the experimental (—) and approximated (---) scattering functions $I(h)$ and distance distribution functions $p(r)$, respectively. Bottom frames show the resulting radial electron density contrast distributions.

calculated for the cholesteryl ester moiety within one LDL particle of molecular weight $2,4 \times 10^6$. This interpretation was also supported by the results obtained from X-ray small angle scattering on two subfractions of porcine LDL (Jürgens *et al.*, 1981) where the electron density maxima at 3 and 6,5 nm have also been obtained by deconvolution of the $p(r)$ function (Fig. 9). This, together with the original observation by Deckelbaum *et al.* (1975) suggested that the core of the LDL particle consists largely of cholesteryl esters which undergo an order-disorder transition. The surface shell is hence occupied by the polar constituents, protein, phospholipid and unesterified cholesterol.

Mateu *et al.* (1977, 1978) have reported that the maximum at $h = 1,7 \text{ nm}^{-1}$, disappears reversibly upon freezing or dehydration. These authors, therefore,

suggested that this maximum reflects an ordered arrangement in the surface structure since this region would be first affected by freezing or dehydration. However, since the studies by partial proteolytic removal of protein from the surface of LDL (see below) has shown no effects on the maximum at $h = 1,7 \text{ nm}^{-1}$ this interpretation would require further convincing evidence. On the other hand, the finding of Mateu *et al.* can be reconciled with the idea of an ordered cholesteryl ester arrangement as the cause for the $h = 1,7 \text{ nm}^{-1}$ maximum by considering the overall structural flexibility of lipoproteins: it is likely that the forces exerted by freezing or dehydration are sufficient to deform the whole particle to such an extent that the regularity in the apolar lipid arrangement is abolished.

3. LIMITED PROTEOLYTIC DIGESTION

Further support for the above interpretation of the X-ray scattering data and some information about the structural role of the protein in LDL has been obtained by studies on LDL particles from which some 20% of the protein had been removed by trypsin digestion (Laggner *et al.*, 1978). The qualitative similarity of the scattering curves (Fig. 8a), and of the temperature dependence of the maximum at $h = 1,7 \text{ nm}^{-1}$, suggested that the overall structural principle is not affected by the limited proteolytic digestion. The $p(r)$ functions (Fig. 8b) reveal the fact that removal of protein affects mainly the frequency of large intraparticle distances, confirming that degradation occurs at the particle surface. Since the 3,6 nm periodicity at distances < 14 nm remains entirely unaffected by protein removal, it can be assumed with certainty that this regularity is not directly related to the protein structure. Combining the information gathered by the various approaches we have suggested a schematic structural representation for LDL as shown in Fig. 10. A similar model has been suggested by Atkinson *et al.* (1977) by using the additional information from crystallographic data on cholesteryl myristate (Craven and De Titta, 1976).

Tardieu *et al.* (1976) have suggested that the surface on LDL may feature extended protruding "spikes" of 8 nm length. In view of the results obtained from the above experiments it is evident that these spikes, if existent, are not related to the protein moiety. On the other hand, a recent study by neutron small angle scattering on selectively deuterated LDL (Laggner *et al.*, 1981) has shown that the second major surface component, the phospholipid polar head groups, are arranged in an approximately spherical shell of 10–11 nm radius, so that this species also fails to be responsible for the suggested spikes. From a more recent study on rhesus monkey LDL with a higher molecular weight ($3,7 \times 10^6$) Luzzati *et al.* (1979) made their third proposal regarding the surface structure: it was postulated that the protein moiety is arranged in

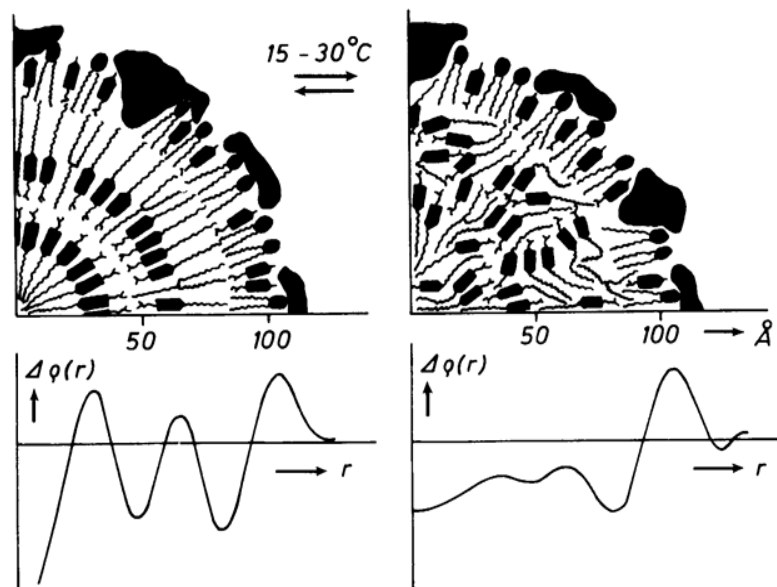


FIG. 10. Molecular interpretation (upper frame) of the radial electron density profile (lower frame) of low density lipoproteins below and above the thermotropic transition. Symbols used are similar to those defined in Fig. 6. (From Laggner *et al.*, 1977a).

discrete globes in a tetrahedral symmetry at the surface of a spherical core. The arguments for this are mainly based upon some unique features observed in freeze etching electron micrographs. It cannot be excluded that the X-ray data held in favour of this model are in fact consequences of a minor particle size heterogeneity and of the problems involved in the evaluation of the characteristic scattering function $i_v(h)$ (see Section B1).

C. The Pathological Lipoprotein X (Lp-X)

This abnormal lipoprotein occurring in the plasma of patients with certain hyperlipidemias (Seidel, 1977) is characterized by the almost complete absence of cholestryl esters and the high abundance of phospholipids and cholesterol. A recent study by the author's group has provided some quantitative structural information (Laggner *et al.*, 1977b). The distance distribution function indicated that the structure is basically determined by single lamellae of 5–6 nm thickness with strong positive-negative electron density fluctuations across the lamellar thickness (Fig. 11). A definition of the maximum particle dimension could not be obtained from the $p(r)$ function, indicating that the particles are larger than 30 nm and probably heterogeneous in size and shape. The cross-sectional structure of the lamella was analysed both by Fourier transformation of the

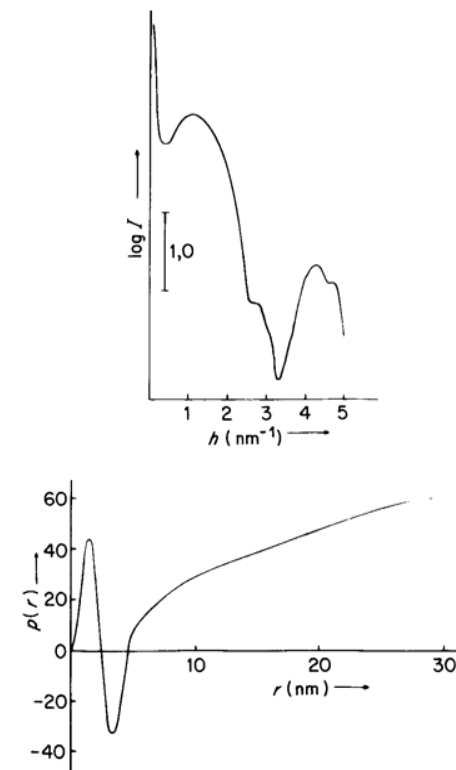


FIG. 11. The pathological Lipoprotein-X: Scattering curve (top) and distance distribution function $p(r)$ (below). (From Laggner *et al.*, 1977b).

thickness-amplitude $\pm \sqrt{(I(h)h^2)}$ as well as by trial-and-error deconvolution of the cross-section correlation function $\gamma_t(r)$ (Fig. 12). Both approaches indicated the typical pattern of a lipid bilayer of 5.1 nm thickness.

D. Reconstitution Experiments

An important task in the investigation of lipoprotein structure is the evaluation of the structural roles played by the individual apoprotein species in the complex formation with lipids. So far, two studies have been reported in the literature, in which reconstituted apolipoprotein-phospholipid complexes were investigated by X-ray small angle scattering. Atkinson *et al.* (1976) have studied the complex formed between the apolipoprotein from porcine HDL, which consists predominantly of one protein species very similar to human apoA-I, and dimyristoylphosphatidylcholine. The complex was found to have a disc-like structure with major axes of 11.0 nm and 5.5 nm, respectively. The internal

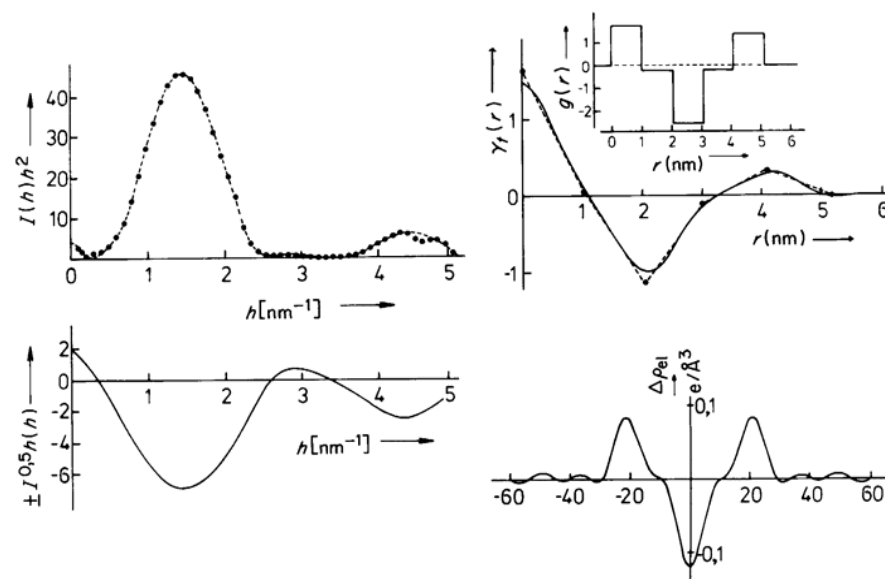


FIG. 12. Lipoprotein-X. Left: lamellar thickness factor $I_t(h) = I(h) \cdot h^2$ and thickness amplitude $I(h)^{0.5} \cdot h$. Right: correlation function $\gamma_t(r)$ (top) and electron density profile in the direction normal to the lamellar plane obtained by Fourier transformation of $I_t(h)$ and $\pm \sqrt{I_t(h)}$ (bottom). The insert (top right) shows a five-step electron density profile $g(r)$ found by iterative deconvolution of $\gamma_t(r)$ (adapted from Laggner *et al.*, 1977b).

electron density distribution could be approximated by a low electron density core surrounded by a 0.85 nm thick shell of high electron density. Very similar results have been obtained for the complex formed by the interaction of apo C-III (molecular weight: 9300) from human Very Low Density Lipoprotein with dimyristoylphosphatidylcholine vesicles (Laggner *et al.*, 1979) at a protein-to-lipid weight ratio of 0.25:1. The X-ray small angle scattering data (Fig. 13) indicated again a disc-like shape, however with a considerably longer major axis: the optimally fitting ellipsoid had an axial ratio of $16 \times 16 \times 5$ nm with a two-level internal electron density distribution (ratio of electron densities core: shell = -0.7:1.0) and an external shell thickness of 1 nm. A schematic view of the structure is shown in Fig. 12b. It has to be noted, however, that the formation of a disc-like structure is not exclusively a function of the protein, but also of the particular lipid species employed, since it has been found that the interaction between apo C-III with egg yolk phosphatidylcholine vesicles, which has a different fatty acyl chain composition, does not lead to a similar disruption of the vesicle structure, but seems to induce a flattening of the spherical lipid vesicles (Laggner, Gotto and Morrisett, unpublished observations).

All these investigations have shown that the protein moieties are located

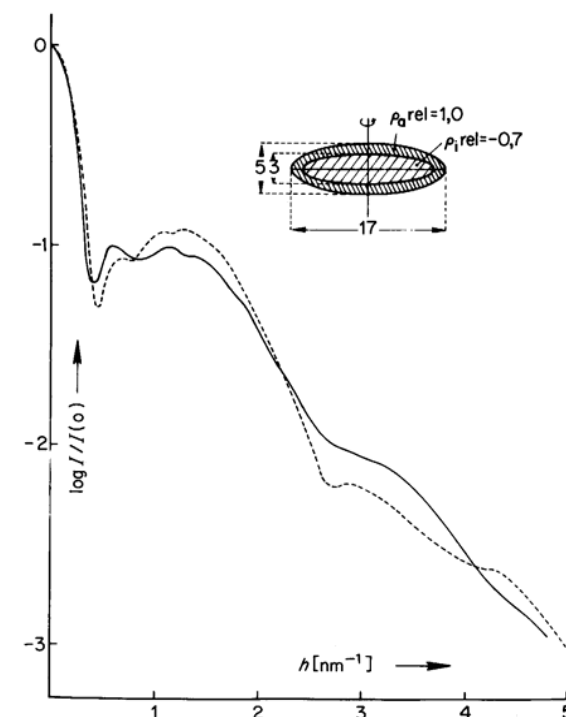


FIG. 13. Reconstituted complex between apolipoprotein C-III and dimyristoylphosphatidylcholine (weight ratio 0.25:1): comparison between experimental (—) and theoretical scattering curve (---) of the oblate ellipsoidal model shown in the insert.

predominantly at the polar periphery of the complexes which confirms the view obtained from the studies on native HDL subfractions.

III. Membranes

A. Phospholipid Bilayers

The phospholipid bilayer structure is now generally considered to be the fundamental structural element in biological membranes. The first direct evidence for this fact was provided by X-ray scattering studies of Wilkins *et al.* (1971) and Engelmann (1971) on ultrasonicated aqueous dispersions of phospholipids and on natural membranes. Ultrasonication of phospholipid dispersions leads to a disruption of the large, multilamellar liquid crystalline aggregates and to the formation of relatively small, hollow spherical vesicles (diameter in the order of several hundred Å) (Papadimitriou and Miller, 1967; Huang, 1969; Bangham

et al., 1974). Wilkins *et al.* (1971) and Lesslauer *et al.* (1971) have shown that the scattering pattern of such vesicle dispersions is dominated by the electron density profile along a line perpendicular to the plane of the spherical shell, and that the contribution from the limited size of the vesicles and from the curvature is low. For an infinitely thin spherical shell structure with radius r , the curvature produces a modulation of the intensity pattern with zero minima spaced in angular distances of $\Delta\theta = \pi/r$. To a first approximation, this modulation is also shown by spherical shell structures where the shell thickness is in the order of – but still smaller than – the inner diameter (Fig. 14). It is clear that a heterogeneity in r or deviations from sphericity will lead to a smearing out of this modulation in $I(h)$, so that essentially only the envelope, i.e. the Fourier transform of the correlation function across the shell thickness can be observed. This has also been demonstrated by model calculations (Atkinson *et al.*, 1974b). A mathematical formalism for the description of the scattering from spherical vesicles has been given by Moody (1975) who discussed in detail the validity of the “flat sheet” approximation to spherical vesicles and proposed criteria by which the features of membrane asymmetry and sidedness might be discerned. In experimental practice, however, this important aspect may prove difficult to be realized since the distinctions rely heavily on the intensities in the region of the scattering minima where the precision of the data is obviously lowest.

Wilkins *et al.* (1971) did not attempt to calculate quantitatively the electron density profile by Fourier transformation. However, they noted that the amplitude calculated from the scattering data closely resembled those calculated for model bilayer profiles and, from the similarity of this pattern to the scattering curves of dispersions of *Mycoplasma laidlawii* or erythrocyte membranes, concluded that lipid bilayer structure is present to a large extent also in these natural systems. Lesslauer *et al.* (1971, 1972), in a study on the location of lipophilic fluorescent probe molecules in phosphatidylcholine vesicles, first suggested that the electron density profile may be obtained by direct deconvolution of the Fourier transform of the thickness scattering factor $I(h) \cdot h^2$, according to the theories of Hosemann and Bagchi (1966). However, in their treatment it has to be implicitly assumed that the resulting electron density profile is symmetric in order to be unique. This constraint has to be considered as serious since ample evidence exists for the fact, that even in vesicles consisting of only one lipid species, the packing densities are different in the inner and outer monolayer (Huang and Mason, 1978). Weick (1974) has derived a formalism by which, for the case of monodisperse vesicle samples, both the convolution square $\hat{g}^2(r)$ and the convolution product $\hat{g}\hat{g}(r)$ of the electron density profile can be determined (where $g(r) = r \cdot \rho(r)$). This method has been applied to studies of the thylakoid membranes of *Rhodopseudomonas Sphaeroides* (Pape *et al.*, 1974). In principle, the analysis of these two functions should allow

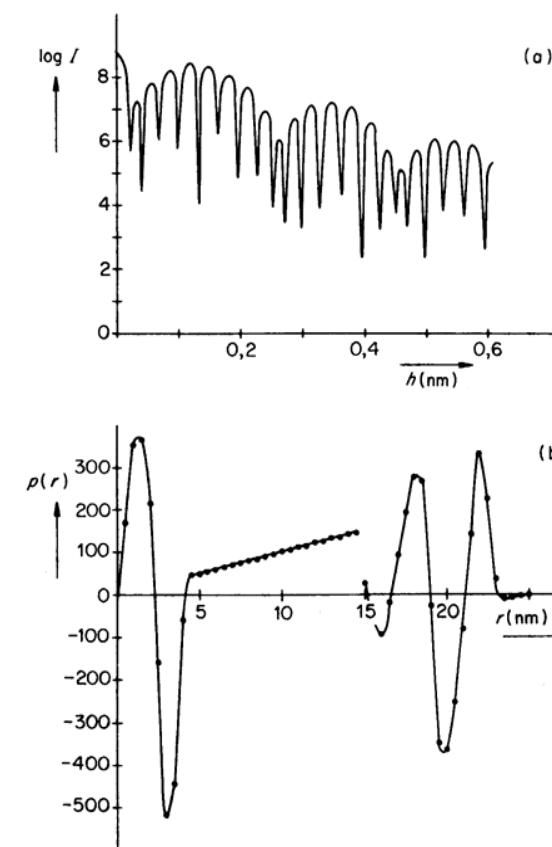


FIG. 14. (a) Theoretical scattering curve of a hollow spherical shell structure (vesicle) with the electron density profile typical for a phospholipid layer. (b) Distance distribution function $p(r)$ (outer part divided by 10).

the evaluation of the membrane asymmetry. Two conditions, however, have to be fulfilled: (a) the thickness of the shell has to be smaller than the inner diameter of the vesicle, and (b) all vesicles have to be of the same size. While the first condition is easily met by many systems, the second condition appears to rule out this possibility for most of the known vesicle preparations. Thus the problem of the evaluation of asymmetry in bilayer structures is at present still unresolved.

Despite the above shortcomings, the method has certain advantages over the study of multilamellar, ordered bilayer systems. Unilamellar vesicles, by their physical nature, can only be studied in relatively dilute solutions and in many respects the properties of the phospholipid bilayer in single-shelled vesicles resemble more closely the situation of phospholipids in plasma membranes.

TABLE 3
Structural Parameters of Dimyristoylphosphatidylcholine – Vesicles

$\theta^\circ C$	$\phi' \text{ cm}^3 \text{ g}^{-1}$	M^a	d nm	area/molecule nm ² ^b
10	0,933	$2,9 \times 10^6$	4,8	0,49
20	0,952	$2,7 \times 10^6$	4,5	0,52
30	0,978	$3,2 \times 10^6$	4,3	0,54

^a Calculated from the absolute intensity at zero angle.

^b Calculated from ϕ' and d assuming equal packing density at both sides of the bilayer.

Moreover, interactions of the single bilayer with any low molecular substance added to the solution can be studied, which is complicated in the case of multilamellar preparations due to the presence of more than one phase (e.g. hydrated lipid phase *plus* excess water). Thus it still appears rewarding to study in detail the X-ray scattering of single lipids and lipid mixtures in the form of vesicles, and their interaction with biologically interesting substances. Such studies have recently been initiated in the author's laboratory (Laggner, 1978b; Laggner *et al.*, 1979) and a brief review of the studies so far completed shall be given in the following.

Multilamellar phospholipid dispersions are known to undergo a reversible liquid crystalline phase transition at temperatures which are characteristic for the chemical structure of the individual phospholipid species (Chapman *et al.*, 1967; for reviews, see Chapman, 1973; Lee, 1977a, b). To study the structural changes involved in this phenomenon in single bilayer membranes, we have investigated the X-ray small angle scattering of vesicle preparations of the synthetic phospholipid, dimyristoyl phosphatidylcholine (C_{14} -chains) at three temperatures in the range of the transition. The results of these studies are summarized in Figs 14 and 15 and in Table 3. The scattering curves display the two characteristics of the vesicle structure, i.e. (a) the broad maxima corresponding to the transform of the bilayer profile, and (b) the superimposed modulation arising from the $(\sin hr/hr)^2$ term of the spherical shell with average radius r . From the $p(r)$ function (Fig. 14) it is evident that, despite the use of molecular sieve chromatography in the course of the preparation, the vesicle population is still far from monodisperse and hence the estimation of vesicle size is afflicted with some error.

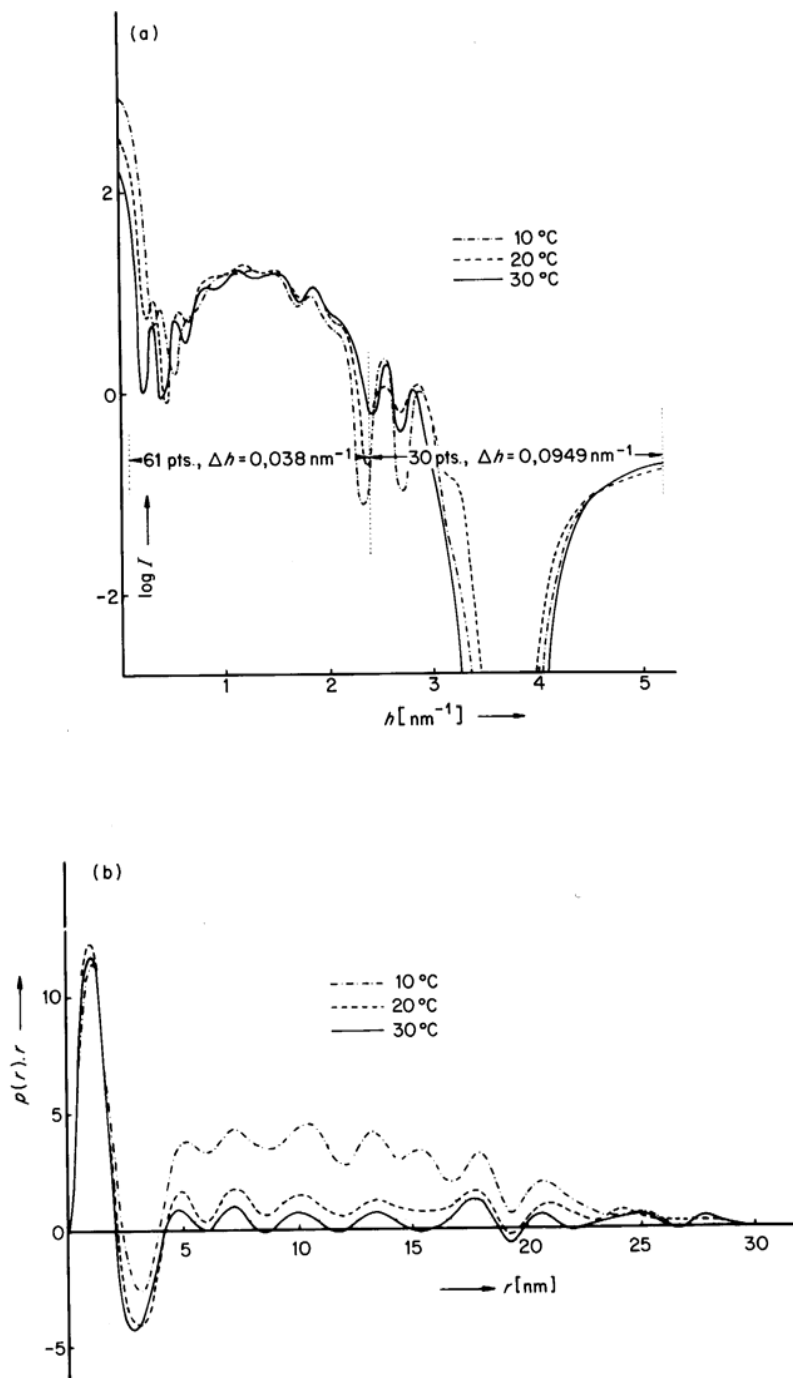
Much clearer, however, is the information about the bilayer thickness which is obtained with good accuracy by using the flat sheet approximation in the desmearing process (see Chapter 4). The result in this case is the correlation function $\gamma_t(r)$ along a line perpendicular to the bilayer plane (Fig. 15) and a desmeared curve which lacks the features of the hollow spherical structure. The lamellar thickness can be obtained from the point where $\gamma_t(r)$ finally approaches zero (Fig. 16), with an error of $\approx 2 \text{ \AA}$. It is clearly seen that the bilayer thickness

decreases with increasing temperature through the transition range. Together with the supplementary information about the partial specific volume measured with the hollow oscillator density meter in the reference mode (Laggner and Stabinger, 1976), a number of important structural parameters of the bilayers can be calculated (Table 3). It must be noted that this method of determination of the bilayer thickness involves no *a priori* assumptions with regard to the nature and extent of hydration, as are necessary in the calculation of the single bilayer thickness from lamellar repeat distances in multilamellar liposomes, and hence is a highly reliable and accurate method. The area *per* lipid molecule calculated from the thickness and the isopotential specific volume ϕ' , however, is certainly only an average value since, as discussed above, no distinction between inner and outer monolayer can be made.

In summary, the evaluation of small angle scattering curves from unilamellar lipid vesicles is a source for important direct information about the structure and structural changes of lipid bilayers.

B. Solubilized Membrane Proteins

Most natural membranes contain comparable amounts of lipids and proteins which are arranged in the plane of the membrane with little or no long range order (a remarkable exception being the purple membrane of halobacteria) (Blaurock and Stoeckenius, 1971; see review by Henderson, 1977). Thus the small angle scattering contains contributions from both the lamellar cross-section and the in-plane distribution of molecular components. It is hence, highly problematic to extract any conclusive information from scattering studies on random dispersions of biological membranes. There exists the possibility, however, of solubilizing individual membrane proteins by the use of suitable detergents (Helenius and Simons, 1976) and to study the detergent-protein complex by X-ray small angle scattering. If it can be assumed that the replacement of the endogenous membrane lipids by detergent does not lead to structural alterations of the protein – this can be tested indirectly, e.g. by measuring the enzymatic activity or other biochemical properties – the information from such studies can lead to valuable insights into the structure of the protein in the membrane. However, since it is generally not straightforward by such preparative procedures that such monodisperse systems which are suitable for investigation by X-ray small angle scattering are obtained, this approach has so far only been successfully applied on the rhodopsin-detergent complex prepared from retinal rod outer membranes (Sardet *et al.*, 1976). This study is an instructive example for the potential and limitations of such experiments. Rhodopsin (molecular weight 39,100) was extracted from the membranes by the detergent dodecyldimethylamine oxide (DDAO), and by column chromatography and sedimentation experiments it was found that the rhodopsin-detergent complex



is, to a good approximation, monodisperse. The complex consisted of one rhodopsin molecule and approximately 150 detergent molecules.

In equilibrium with the protein-detergent complex, the solution also contained pure detergent micelles. Thus, to obtain the scattering curve of the complex, a blank scattering curve obtained from detergent solution in equilibrium concentration had to be subtracted. It is obvious that this procedure involves the danger of considerable errors and therefore the interpretation of the results was only based upon the innermost part of the curves, essentially the Guinier range. The analysis was limited to five parameters: the particle weight, volume, radius of gyration and, from contrast variation, the average electron density, and the second moment of the electron density fluctuations inside the particle. On this basis a molecular model was proposed for the rhodopsin-detergent complex which consists essentially of an elongated protein structure (maximum length $\approx 95 \text{ \AA}$) spanning a flat detergent micelle. From this it was suggested that in the retinal rod outer segment membranes, the rhodopsin molecules exist as integral proteins spanning the membrane cross-section. These results are, in some of their quantitative aspects, at variance with the neutron diffraction results of Yaeger *et al.* (1976) and Saibil *et al.* (1976) which were obtained from intact retinas and isolated retinal rod outer segments, respectively. These studies, therefore, are instructive examples for the substantial problems encountered in attempts to determine membrane structure by scattering and diffraction methods.

It can be safely predicted that future studies by neutron scattering or diffraction will bring about important advances in this field due to its ample possibilities to vary the scattering contrasts of individual membrane components, either by $\text{H}_2\text{O}/\text{D}_2\text{O}$ variation or by selective deuteration. However, since only few centres exist at the moment where neutron studies can be conducted, the potential of X-ray methods will continue to find its use in providing a comparatively inexpensive and valuable source for structural information on biological membranes.

Acknowledgements

I wish to express my gratitude to Professor O. Kratky for his continuous interest and support, and to my colleagues Drs G. M. Kostner and K. W. Müller, for their

FIG. 15. Dimyristoylphosphatidylcholine vesicles at temperatures around the transition range: (a) scattering curves after desmearing by indirect Fourier transformation using 30 spline functions to define the three-dimensional distance distribution functions. (b) Distance distribution functions. The positive-negative fluctuation at small values of r defines the shell thickness, the trough at approximately 19 nm indicates an average diameter of the vesicle (measured from the low electron density centre of the bilayer), and the gradual decrease at $r > 22 \text{ nm}$ gives a crude estimate for the overall vesicle size.

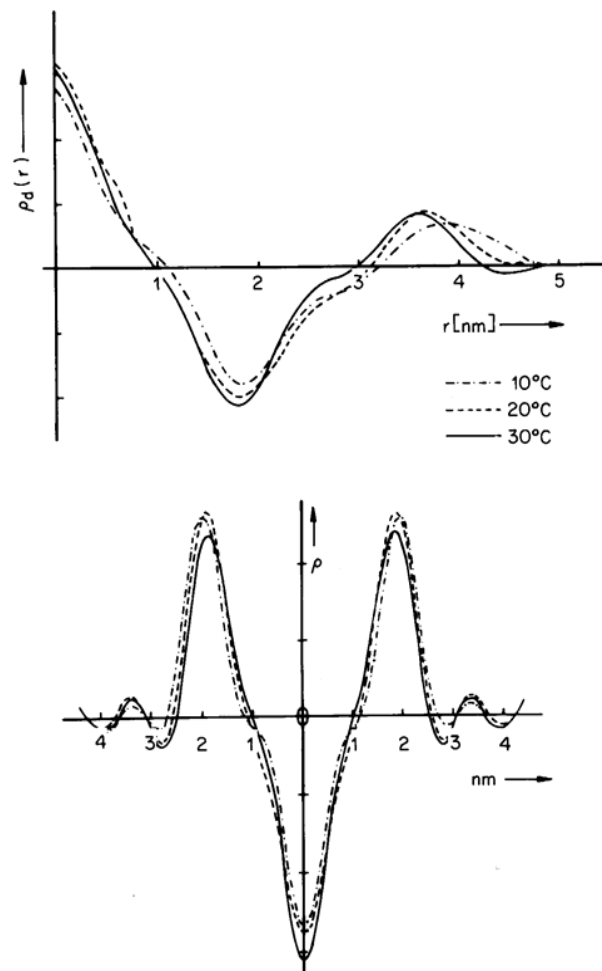


FIG. 16. Top: correlation function $\gamma_t(r)$ along a line perpendicular to the bilayer plane of dimyristoylphosphatidylcholine vesicles as obtained from the data in Fig. 15a, according to the "flat sheet" approximation. Bottom: Electron density profile assuming a plane of symmetry in the centre of the bilayer.

active contributions to the work cited from our group. Technical assistance by Miss D. Roblegg and Mrs. U. Rakusch is also gratefully acknowledged. Our original work has been supported generously by the Österreichischer Fonds zur Förderung der Wissenschaftlichen Forschung.

References

- Aggerbeck, L., Yates, M., Tardieu, A. and Luzzati, V. (1978). *J. Appl. Cryst.* **11**, 466–472.
- Alaupovic, P. (1972). In "Protides of Biological Fluids" (H. Peeters, ed.), pp. 9–19. Pergamon Press, Oxford.
- Atkinson, D., Davis, M. A. F. and Leslie, R. B. (1974a). *Proc. R. Soc. London B* **186**, 165–180.
- Atkinson, D., Hauser, H., Shipley, G. G. and Stubbs, J. M. (1974b). *Biochim. biophys. Acta* **339**, 10–29.
- Atkinson, D., Smith, H. M., Dickson, J. and Austin, J. P. (1976). *Eur. J. Biochem.* **64**, 541–547.
- Atkinson, D., Deckelbaum, R. J., Small, D. M. and Shipley, G. G. (1977). *Proc. Nat. Acad. Sci. USA* **74**, 1042–1046.
- Bangham, A. D., Hill, M. W. and Miller, N. G. A. (1974). In "Methods in Membrane Biology" (E. D. Korn, ed.), Vol. 1, p. 1. Plenum Press, New York.
- Blaurock, A. E. and Stoeckenius, W. (1971). *Nature New Biol.* **233**, 152–154.
- Casassa, E. F. and Eisenberg, H. (1964). *Advan. Protein Chem.* **10**, 287–394.
- Chapman, D. (1973). In "Biological Membranes" (D. Chapman and D. F. H. Wallach, eds), Vol. 2, pp. 91–144. Academic Press, London and New York.
- Chapman, D., Williams, R. M. and Ladbrooke, B. D. (1967). *Chem. Phys. Lipids* **1**, 445–475.
- Craven, B. M. and De Titta, G. T. (1976). *J. Chem. Soc., Perkin Trans. 2*, 514–822.
- Deckelbaum, R. J., Shipley, G. G., Small, D. M., Lees, R. S. and George, P. K. (1975). *Science, N.Y.* **190**, 392–394.
- Eisenberg, H. (1976). "Biological Macromolecules and Polyelectrolytes in Solution". Clarendon Press, Oxford.
- Engelman, D. M. (1971). *J. molec. Biol.* **58**, 153–165.
- Glatter, O. (1981). *J. Appl. Cryst.* **14**, 101–108.
- Helenius, A. and Simons, K. (1976). *Biochim. biophys. Acta* **415**, 29–79.
- Henderson, R. (1977). *Ann. Rev. Biophys. Bioeng.* **6**, 87–109.
- Hosemann, R. and Bagchi, S. N. (1966). "Direct Analysis of Diffraction by Matter". North Holland, Amsterdam.
- Huang, C. (1969). *Biochemistry* **8**, 344–351.
- Huang, C. and Mason, J. T. (1978). *Proc. nat. Acad. Sci. USA* **75**, 308–310.
- Jackson, R. L., Morrisett, J. D. and Gotto, A. M., Jr. (1976). *Physiol. Rev.* **56**, 259–316.
- Jürgens, G., Knipping, G. M. J., Zipper, P., Kaynshina, R., Degovies, G. and Laggner, P. (1981). *Biochemistry* **20**, 3231–3237.
- Laggner, P. (1976). In "Low Density Lipoproteins" (C. E. Day and R. S. Levy, eds), pp. 49–69. Plenum Press, New York.
- Laggner, P. (1978a). In "Protides of the Biological Fluids" (H. Peeters, ed.), Vol. 25, pp. 59–66. Pergamon Press, Oxford.
- Laggner, P. (1978b). *Studia Biophys.* **74**, 11–12.
- Laggner, P., Goldstein, S. and Chapman, M. J. (1978). *Biochem. Biophys. Res. Commun.* **82**, 1332–1339.
- Laggner, P. (1981). In "High Density Lipoproteins" (C. E. Day, ed.), pp. 43–72, Marcel Dekker, New York.
- Laggner, P. and Müller, K. (1978). *Quart. Rev. Biophys.* **11**, 371–425.

- Laggner, P. and Stabinger, H. (1976). In "Colloid and Interface Science" (M. Kerker, ed.), Vol. 5, 91–96. Academic Press, New York.
- Laggner, P., Kratky, O., Kostner, G., Sattler, J. and Holasek, A. (1972). *FEBS Lett.* **27**, 53–57.
- Laggner, P., Müller, K., Kratky, O., Kostner, G. and Holasek, A. (1973). *FEBS Lett.* **33**, 77–80.
- Laggner, P., Müller, K., Kratky, O., Kostner, G. and Holasek, A. (1976). *J. Colloid Interface Sci.* **55**, 102–108.
- Laggner, P., Degovics, G., Müller, K., Kratky, O., Kostner, G. and Holasek, A. (1977a). *Hoppe Seyler's Z. Physiol. Chem.* **358**, 771–778.
- Laggner, P., Glatter, O., Müller, K., Kratky, O., Kostner, G. and Holasek, A. (1977b). *Eur. J. Biochem.* **77**, 165–171.
- Laggner, P., Gotto, A. M., Jr. and Morrisett, J. D. (1979). *Biochemistry* **18**, 164–171.
- Laggner, P., Kostner, G., Rakusch, U. and Worcester, D. (1981). *J. Biol. Chem.* (In press).
- Lee, A. G. (1977a). *Biochim. Biophys. Acta* **472**, 237–281.
- Lee, A. G. (1977b). *Biochim. Biophys. Acta* **472**, 285–344.
- Lee, J. C., Gekk, K. and Timasheff, S. N. (1979). In "Methods in Enzymology" (C. H. W. Hirs and S. N. Timasheff, eds.), Vol. 61, pp. 26–57.
- Lesslauer, W., Cain, J. and Blasie, J. K. (1971). *Biochim. biophys. Acta* **241**, 547–566.
- Lesslauer, W., Cain, J. E. and Blasie, J. K. (1972). *Proc. Nat. Acad. Sci., USA* **69**, 1499–1503.
- Levine, Y. K. (1972). In "Progress in Biophysics and Molecular Biology" (J. A. V. Butler and D. Noble, eds), Vol. 24, pp. 9–74. Pergamon Press, Oxford.
- Luzzati, V. (1968). In "Biological Membranes" (D. Chapman, ed.), pp. 71–123. Academic Press, London and New York.
- Luzzati, V., Aggerbeck, L. P. and Tardieu, A. (1979). *J. molec. Biol.* **131**, 435–473.
- Mateu, L., Tardieu, A., Luzzati, V., Aggerbeck, L. and Scanu, A. M. (1972). *J. molec. Biol.* **101**, 105–116.
- Mateu, L., Kirchhausen, T. and Camejo, G. (1977). *Biochim. Biophys. Acta* **487**, 243–245.
- Mateu, L., Kirchhausen, T. and Camejo, G. (1978). *Biochemistry* **17**, 1436–1440.
- Mering, J. and Tchoubar, D. (1968). *J. Appl. Cryst.* **1**, 153–165.
- Moody, M. F. (1975). *Acta Cryst. A31*, 8–15.
- Morrisett, J. D., Jackson, R. L. and Gotto, A. M., Jr. (1977). *Biochem. Biophys. Acta* **472**, 93–133.
- Müller, K., Laggner, P., Kratky, O., Kostner, G., Holasek, A. and Glatter, O. (1974). *FEBS Lett.* **40**, 213–218.
- Müller, K., Laggner, P., Glatter, O. and Kostner, G. (1978). *Eur. J. Biochem.* **82**, 73–90.
- Papahadjopoulos, D. and Miller, N. (1967). *Biochim. biophys. Acta* **135**, 624–638.
- Pape, E. M., Menke, W., Weick, D. and Hosemann, R. (1974). *Biophys. J.* **14**, 221–232.
- Sabil, H., Chabre, M. and Worcester, D. (1976). *Nature* **262**, 266–270.
- Sardet, C., Tardieu, A. and Luzzati, V. (1976). *J. Molec. Biol.* **105**, 383–407.
- Scanu, A. and Wisdom, C. (1972). *Ann. Rev. Biochem.* **41**, 703–730.
- Scanu, A., Edelstein, C. and Keim, P. (1975). In "The Plasma Proteins" (F. Putnam, ed.), Vol. 1, pp. 317–391. Academic Press, New York and London.
- Schoenborn, B. P. (1976). *Biochim. biophys. Acta* **457**, 41–55.
- Seidel, D. (1977). *Klin. Wschr.* **55**, 611–623.
- Shipley, G. G. (1973). In "Biological Membranes" (D. Chapman and D. F. H. Wallach, eds), Vol. 2, pp. 1–89. Academic Press, London and New York.
- Shipley, G. G., Atkinson, D. and Scanu, A. M. (1972). *J. Supramol. Struc.* **1**, 98–104.
- Stuhrmann (1974). *J. Appl. Cryst.* **7**, 173–178.
- Stuhrmann, H. B., Tardieu, A., Mateu, L., Sardet, C., Luzzati, V., Aggerbeck, L. and Scanu, A. M. (1975). *Proc. Nat. Acad. Sci. USA* **72**, 2270–2273.
- Tardieu, A., Mateu, L., Sardet, C., Luzzati, V., Aggerbeck, L. and Scanu, A. M. (1976). *J. molec. Biol.* **101**, 123–153; erratum *ibid.* **105**, 459–460.
- Weick, D. (1974). *Biophys. J.* **14**, 233–235.
- Wilkins, M. H. F., Blaurock, A. E. and Engelman, D. M. (1971). *Nature New Biol.* **230**, 72–76.
- Worcester, D. (1976). In "Biological Membranes" (D. Chapman and D. F. H. Wallach, eds), Vol. 3, pp. 1–46. Academic Press, London and New York.
- Yaeger, M., Schoenborn, B. P., Engelman, D. M., Moore, P. B. and Stryer, L. (1976). *J. molec. Biol.* **137**, 315–348.

11

Natural High Polymers in the Dissolved and Solid State

O. KRATKY

*Institut für Röntgenfeinstrukturforschung der Österreichischen Akademie der
Wissenschaften und des Forschungszentrums Graz, Graz, Austria*

I. Natural High Polymers in Solution	361
A. Review of the Theory	361
B. Experimental Results	367
II. Natural High Polymers in the Dense Form and in the “Loosened-up” State	373
A. The Supermolecular Structure of Cellulose	373
B. Remarks to the Supermolecular Structure of Silk Fibroin	384
References	385

I. Natural High Polymers in Solution

It is the aim of this section to give information on mass, size and shape of dissolved natural high polymer molecules. The interpretation of SAXS measurements lies in the same general theory for both natural and synthetic high polymers. In the following, we will anticipate in possibly the most simple presentation, a selection of the theoretical bases, from the viewpoint of their application to the readily performed measurements on *natural* high polymers.

A. Review of the Theory

1. SHAPE OF THE SCATTERING CURVE

An important basic model for the macromolecule in solution is the so-called wormlike chain.^{(1),(2)} It consists of a chain whose axis is subject to a continuous

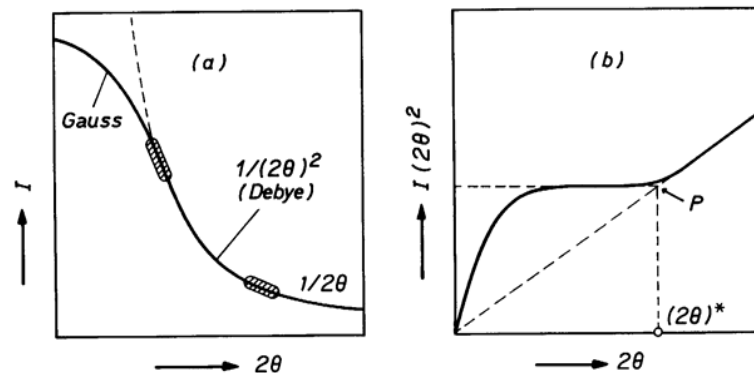


FIG. 1. Schematic drawing of the scattering curve of a coiled chain molecule (Gaussian coil).

and completely random change of direction at every point along the axis. The degree of coiling is characterized by a "persistence length". If we start from an arbitrary origin moving along the chain and determine the current direction cosine with the direction at the origin, this quantity will drop from its starting value of 1 and will, in average, exponentially approach zero. The distance measured along the chain from the origin to the point with the average value $1/e$ is called persistence length a . The scattering curve of such a dissolved chain molecule, frequently referred to as a Gaussian coil, consists of three regions (Fig. 1a).

The innermost part follows approximately a Gaussian curve, it is due to the overall shape of the globular particle. A Guinier plot of this part of the curve, therefore, yields the radius of gyration of the whole particle.

Due to the reciprocity between scattering angle and dimension of the scattering region, the shape of the scattering curve at larger angles will be dominated by structural elements, the size of which decreases with increasing scattering angle. The outermost part of the curve, the tail end, will, therefore, have the shape of the scattering curve of a needle, i.e. $I \approx 1/2\theta$, since it corresponds to very small regions of the molecule which are always more or less straight. This, however, is only so if the length of regions that can be considered approximately straight is large compared to the diameter of the chain, which appears to be true for many natural high polymers. However, as this cross-section is of finite area, we have, both for a "gas of needles" and for coiled macromolecules,

$$I = I_c x 1/2\theta \quad I_c = I x 2\theta$$

Here I_c is the "cross-section factor" which is determined by the dimension of the cross-section. For its dependence on the scattering angle those general relations practically hold which are valid for elongated particles. Therefore, by

plotting $\ln I_c = \ln I \times 2\theta$ v. $(2\theta)^2$ and extrapolating to zero angle we obtain, on the one hand, $(I_c)_0 = (I \times 2\theta)_0$ and, on the other, the slope $\tan \alpha$ of the terminal tangent, the square root of which is proportional to the radius of gyration of the cross-section R_c . The relation holds:

$$R_c = K \sqrt{(-\tan \alpha)_0}, \quad K = \frac{\lambda}{2\pi} \sqrt{\frac{2}{10 \log e}} = 0,526 \quad (1)$$

The intermediate portion of the I -curve, originating from larger subsections of the molecule which can be visualized as random arrangements of chain elements, follows the relationship $1/(2\theta)^2$.⁽³⁾ In an $I \times (2\theta)^2$ v. 2θ plot, this region becomes horizontal (Fig. 1b); in the same plot the $1/2\theta$ tail end follows an ascending line, the extension of which to the left passes through the origin, and the Gaussian region drops down towards zero at $2\theta = 0$. The more extended the molecule, the larger are the regions from needle-shaped molecule sections and the further towards smaller angles does the $1/2\theta$ branch extend. The abscissa value $(2\theta)^*$ of the intersection point P of the two linear extrapolations is, therefore, an important characteristic parameter for the shape of the molecule (Fig. 1b).

The first quantitative computations dealt with very large molecular coils, i.e. molecules whose chain length L (i.e. the length of the hypothetically, fully extended molecule, the "hydrodynamic length") is a large multiple x of the persistence length a (it is half of Kuhn's statistic chain element).^{(2),(4)} The Gaussian region of these molecules becomes so narrow that it defies observations. The theoretical curves for all Gaussian coils become identical when plotted against the quantity μ which is defined as follows:

$$\mu = \frac{4\pi \sin \theta}{\lambda} a \approx \frac{4\pi \theta}{\lambda} a \quad (2)$$

In a $I\mu^2$ v. μ plot we find the transition point simply by intersecting the $1/(2\theta)^2$ branch and the $1/2\theta$ branch, both pictured in the correct relative intensities at an abscissa value $\mu^+ = 6/\pi = 1,91$,^{(4),(5)} the persistence length a can thus easily be calculated from the experimentally observed θ^+ of the transition point, using the equation

$$1,91 = \frac{4\pi \theta^+}{\lambda} a \quad (3)$$

For coils of "finite" size it is clear *a priori*, that the drop in the innermost region of Fig. 1b becomes broader as a becomes smaller. The shape of the curve in the neighbourhood of the transition point is, however, not trivially predictable. Of a number of approaches to this problem, the most successful turned out to be the statistical computation following a "Monte-Carlo-Algorithm", which

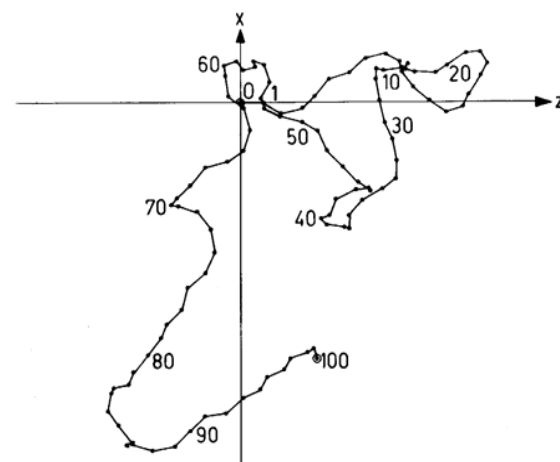


FIG. 2. Chain consisting of straight lines with fixed angle between adjacent segments and randomly chosen azimuth.

involved the use of random configurations. These numerical computations were based on the model of a flexible segment chain, the segments of which consist of infinitely thin lines. The model is largely equivalent to the wormlike chain, but the continuously bent segments are replaced by straight ones. The angle between adjacent segments is fixed (e.g. $\cos \alpha = 0.9$), but the direction is arbitrary through a randomly chosen azimuth.^{(6),(7)}

Figure 2 shows an example for such a model⁽⁸⁾ and Fig. 3 shows the result of several computations for chains the length of which is varied between 18 and 100 times their persistence length.⁽⁷⁾ The following four points should be stressed:

- (1) The intermediate branch of the curve, which in the $I \times (2\theta)^2$ v. 2θ plot is horizontal for infinitely large coils, is now inclined, but it approaches a horizontal course for large chain lengths.
- (2) μ^+ is observed to be around 2.3 between $x = 16$ and $x = 100$. This value is not, in principle, in disagreement with the smaller value $\mu^+ = 1.91$ for very large molecule chains, since the Monte-Carlo method has so far not been applied to molecules beyond $x = 100$, due to the prohibitively large computing times.
- (3) The model is certainly unrealistic insofar as in real molecules the chain has a finite diameter. As long as this diameter is small compared to the persistence length, the scattering curve will simply have to be multiplied with the corresponding cross-section factor; in the transition region, this cross-section factor will not differ very much from the zero-angle limit. The natural high polymers investigated so far show this behaviour.

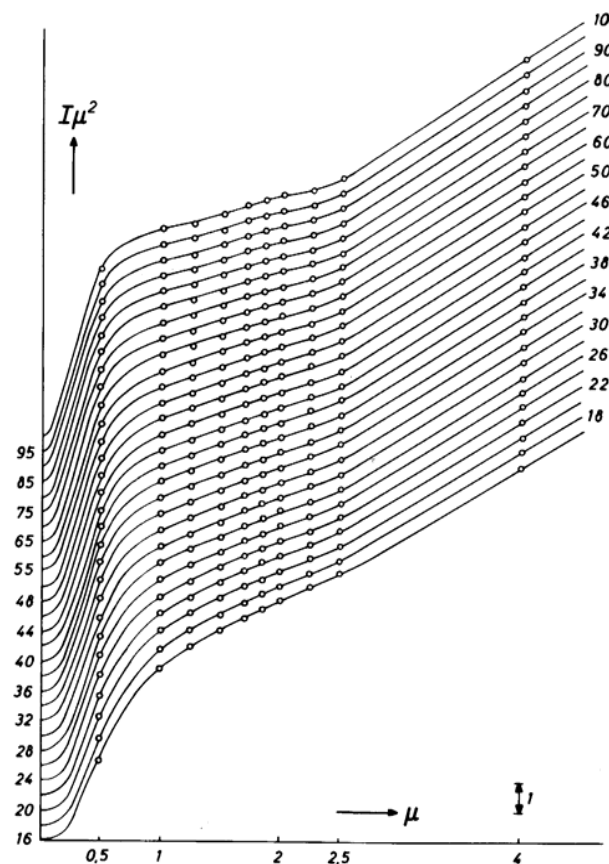


FIG. 3. Scattering curves in the $I \cdot \mu^2$ v. μ plot of segment chains, the lengths of which vary between 18 and 100 persistence lengths.

- (4) Whereas the curves generated with the Monte-Carlo technique show a clearly defined bend in the transition region, the transition point, however, in analytically calculated curves (compare Chapter 12) is less apparent and has to be obtained through extrapolation using larger portions of the curve.

2. MASS DETERMINATION

The molecular weight M_r can be calculated from the absolute intensity of the scattering curve at zero angle, i.e. from the ratio of I_0 and the primary intensity P_0 :^{(9),(10)}

$$M_r = K \frac{I_0 a^2}{P_0 \cdot T \cdot c (z_2 - v'_2 \rho_1)^2}; \quad K = \frac{1}{i_0 N} = 21,0 \quad (4)$$

a = distance sample – plane of registration, T = thickness of the sample in cm, c = concentration of the solution in g ml^{-1} , z_2 = number of electrons in 1 g solute, v'_2 = isopotential specific volume, ρ_1 = electron density of solvent.

The accurate determination of the isopotential specific volume amounts to a very accurate determination of the densities of solvent and solution (with known solute concentrations) (compare Chapter 7). Experimentally, this can be very tedious for solvents with low boiling point and large thermal expansion coefficient. It is apparent from Eqn (4) that small errors in v'_2 have drastic effects on the calculated molecular weight. There is, however, one way to circumvent this problem:⁽¹¹⁾ the limit $I \times 2\theta$ at large angles is a constant, provided the thickness is small compared to the persistence length. Its value is connected with the mass per unit length M_c according to:⁽¹⁰⁾

$$M_c = \frac{2}{i_0 \cdot N \cdot \lambda} \cdot \frac{a^2 \lim(I \times 2\theta)}{P_0 \cdot T \cdot c (z_2 - v'_2 \rho_1)^2}; \quad \frac{2}{i_0 \cdot N \cdot \lambda} = 27,3 \quad (5)$$

The quotient M_r/M_c is obviously the hydrodynamic length L (\AA). We find

$$L = \frac{\lambda I_0}{2 \lim(I \times 2\theta)} \quad (6)$$

v'_2 , c , T and P_0 cancel in this quotient, which makes L independent of errors in these quantities. From L we immediately obtain the molecular weight if the length l and the weight M_m of the monomer are known:

$$M_L = \frac{L}{l} M_m \quad (7)$$

Numerator and denominator in Eqn (6) have to originate from the same measurement and one has to make sure that I_0 is not affected by interparticle interference effects. It is obvious that M_c , M_L and L are connected according to:

$$M_c = \frac{M_L}{L} \quad (8)$$

From L , using Eqn (6), and a , using Eqn (3), we obtain $x = L/a$; Fig. 4 which shows the connection between x and $y = R/a$, derived again from Monte-Carlo calculations. It can conveniently be used to find the radius of gyration R_{calc} . Its value can be compared with the one obtained from a Guinier plot. The two values should agree, provided the assumption of Gaussian statistics holds and the solution is monodisperse.

So far, we have always assumed that the scattering particles consist of

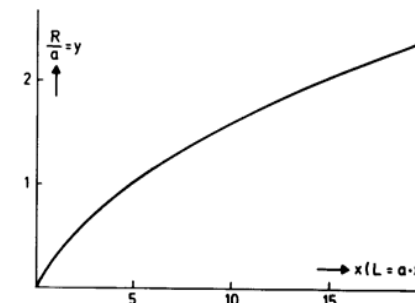


FIG. 4. Connection between R/a and L/a .

individual, coiled chain molecules, i.e. that there is no association. To justify this assumption, it is necessary to compute a “degree of association”, by multiplying M_c according to Eqn (5) with the length l of the monomer and dividing it through its molecular weight M_m .

B. Experimental Results

Several characteristic examples will be described.

1. HIGH-MOLECULAR CELLULOSE NITRATES

The classical rheologic investigations by Staudinger have demonstrated that cellulose nitrates are not extensively coiled in solution, i.e. the persistence length is large compared to the diameter of the chain. The theory of the infinitely thin wormlike chain can, therefore, be applied, and a curve of the type shown in Fig. 1b is to be expected from a $I \times (2\theta)^2$ v. 2θ plot. Measurements on high-molecular cellulose nitrate ($D_p = 3500$, dissolved in acetone) demonstrate that this is indeed true⁽¹¹⁾ (Fig. 5). The μ^+ -value exhibits a strong dependence on the concentration in such a way, that solutions with higher concentration show a shorter persistence length. At the time of these measurements, a value of $\mu^+ = 1,6$ was used and yielded the a -values displayed in Fig. 5. According to the current state of the theory, μ^+ should rather be higher which would result in correspondingly higher a -values. A representative constant for the degree of coiling would be obtained by an extrapolation of the apparent persistence lengths to zero concentration.

A determination of the molecular weight has not so far been possible due to insufficient resolution. The mass per unit length from Eqn (5), however, was determined at a very early stage. (In fact, this was the first absolute measurement on chain molecules all together.) Within the accuracy of these measurements,

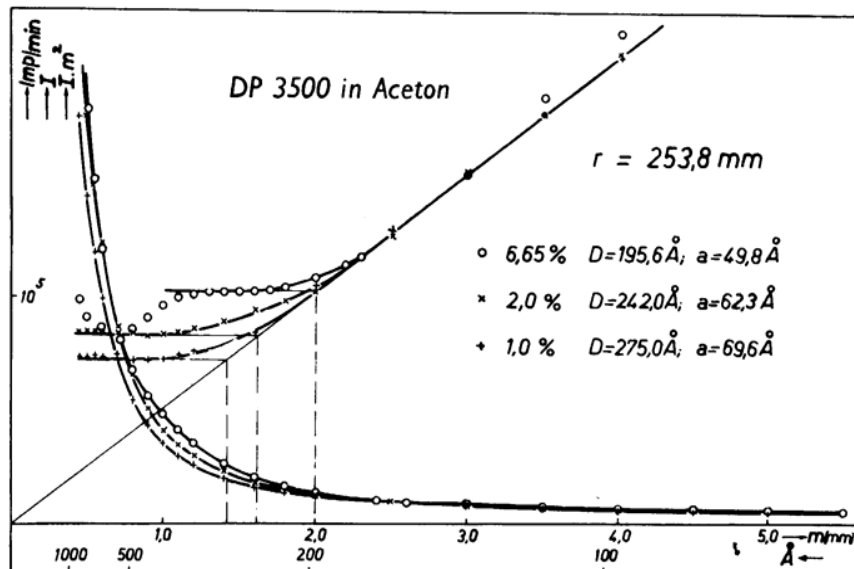


FIG. 5. Scattering curves of high-molecular cellulose nitrate, dissolved in acetone. Concentration 6,65, 2,0 and 1,0%.

the value expected for the *monomer* molecule was obtained. The indirectly obtained model of Staudinger concerning the solution-state of high polymers has thus received very convincing support through a more direct method.

2. LOW-MOLECULAR CELLULOSE NITRATES

A rather great number of investigations were performed on cellulose nitrates with molecular weights around 30 000.⁽¹²⁾ In the following we describe the evaluation on a few selected examples. The persistence length can be derived from a clear-cut bend in a $I \times (2\theta)^2$ v. 2θ plot, which is expected for a segmented chain, but not for a worm-like chain (compare Chapter 12, Fig. 8). From that one might conclude that the segmented chain model is, in some respects, superior to the worm-like chain model, although the segmented chain is only one way to approximate the worm-like chain by short, linear segments. The bend is even more apparent in an $I \times (2\theta)$ v. $1/2\theta$ plot (Fig. 6).⁽¹³⁾

The molecular weight of these substances was determined by the two different methods: from the absolute intensity according to Eqn (4) and from Eqns (6) and (7).

The agreement is, in general, very good, which is demonstrated by one of the investigated examples represented in Table 1. If the radius of gyration is determined from a Guinier plot (R_{exp}), one always obtains higher values than

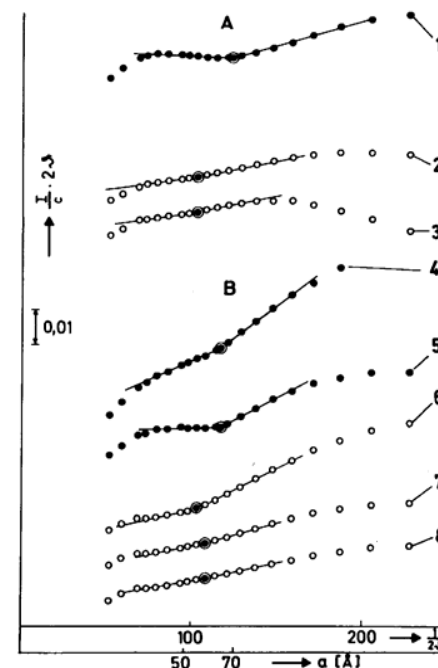


FIG. 6. Scattering curves in the $I/c \cdot 2\theta$ v. $1/2\theta$ plot of low-molecular cellulose nitrate. (○) fresh sample, (●) aged samples, (A) in acetone, (B) in a mixture of solvents (the numbers refer to different concentrations).

TABLE 1. Measurements on a Sample of Low-molecular Cellulosenitrate

Solvent	R_{exp}^a	R_{calc}	M_r	M_L	$a (\text{\AA})$
Acetone	120	108	34 400	34 400	58
Mixture of ethylalkohol and ethylacetate	119	108	35 600	35 600	60

^a Values are extrapolated to zero concentration.

if the determination is based on Fig. 4 (R_{calc}). The most probable reason for this discrepancy is the polydispersity of the samples.

3. HEPARIN

This substance is used pharmacologically as a blood anticoagulant. Due to its high negative charge, it exhibits typical polyelectrolyte behaviour in aqueous solutions, from which one expects a strong concentration-dependence of the

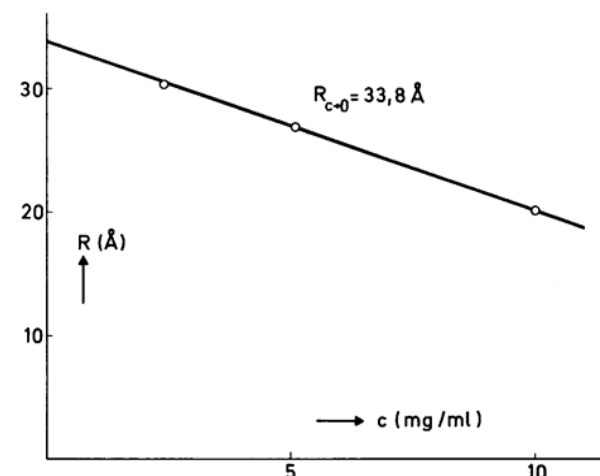


FIG. 7. Dependence of the radius of gyration on the concentration of heparin.

scattering behaviour. The derivation of reliable structural parameters, therefore, requires scrutiny of the extrapolation of scattering curves to zero concentrations.

All measurements were performed on the same Heparin preparation.⁽¹⁴⁾ The molecular weight derived from the absolute intensity yielded $M_r = 12\,900$, which agrees excellently with the values obtained from sedimentation ($M_r = 12\,600$) and viscosity measurements ($M_r = 12\,500$). The mass per unit length was also derived from the absolute intensity and yields $M_c = 54,5$. Since the chemical structure is known, one can calculate this quantity on the basis of the plausible assumption, that the length of the monomer is identical to half the cell length (5,15 Å); one thus obtains $(M_c)_{\text{theor}} = 52,7$ Å in very good agreement with the experiment. This computation of M_c also involved the assumption that the Na^+ counter-ions are sufficiently close to the polyion, so that their weights can be added and complications due to dissociation can be neglected. The good agreement between the experimental and the theoretical mass per unit length supports this idea.

Division of M_r by M_c yields the length of the molecule; one obtains $L = 237$ Å if the experimental value and $L = 245$ Å if the theoretical value for M_c is used.

As expected, the radius of gyration depends heavily on the concentration; extrapolation of the values found from the Guinier-plots gives $R = 33,8$ Å (Fig. 7).

The $I \times (2\theta)^2$ v. 2θ plot shows a distinct bend (Fig. 8), whose position yields the persistence length $a = 21,1$ Å. With this value and $x = 237/21,2 = 11,2$ we obtain from Fig. 4: $r_{\text{calc}} = 35,9$ Å, which shows a good agreement with the value from the Guinier plot.

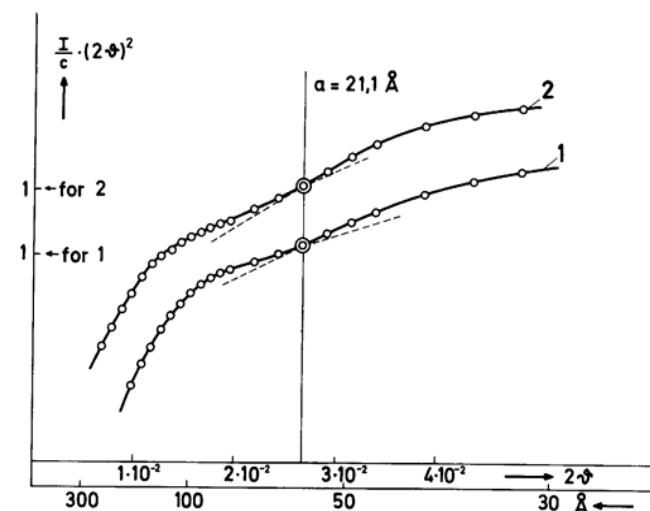


FIG. 8. $I/c(2\theta)^2$ v. 2θ plot for a heparin solution.

Heparin can thus be considered a textbook example for a Gaussian coil, whose mass, overall dimension and shape (degree of coiling) can be conveniently obtained from SAXS measurements. The present example also demonstrates that several approximations in the above theory are fully justified.

4. DEXTRANE AS AN EXAMPLE FOR A BRANCHED FIBRE MOLECULE

So far we have discussed unbranched chain molecules; if the coils contain no more than few branches, it is plausible that the determination of M_r , M_c , R_c and a remains unchanged and the length L evaluated from Eqn (6) corresponds to the sum of lengths of all branches. The radius of gyration of the overall molecule, however, is smaller than the value obtained from a and L according to Fig. 4.

The present chapter, however, deals with a different type of branching, i.e. molecules consisting of one main chain with many small side chains; this type of branching will be called "comb-like" branching. According to Garg and Stivala,⁽¹⁵⁾ dextran hydrolyzates correspond to this model. The authors have used the relationships for unbranched chain molecules, assuming that the resulting values for M_c and R_c will include an averaged contribution from the side chains. Although they have not given an explicit new theory which rigidly justifies such a procedure, it is intuitively plausible. Their results are summarized in Table 2.

M_r is the molecular weight from small angle scattering for the starting material

TABLE 2

	246 000	105 000	74 500	42 000	12 000
M_r	246 000	105 000	74 500	42 000	12 000
R_c	6,05	6,10	4,32	2,65	2,00
M_c accord. to (5)	58,81	44,99	60,00	35,68	34,46
M_c accord. to (8)	58,57	42,17	43,82	37,84	33,80
L	7 820	3 340	2 370	1 335	380
P	1 518	649	460	259	74
L_b	4 200	2 490	1 700	1 110	355
P_b	816	484	330	216	69
ΔL	3 620	850	670	225	25
ΔP	702	165	130	43	5
$f = P/16$	95	41	29	16	5
r	7	4 (7)	4	3	1
s	9	12 (16)	11	13	14
M_c accord. to (9)	55,9	42,0 (45,2)	42,9	38,7	33,7

and several dextrans obtained by hydrolysis. The radius of gyration of the cross-section R_c decreases with the molecular weight. The mass per unit length for the unbranched dextran can be computed for the monomer molecular weight (162 Dalton) and from its length (5,15 Å), yielding $M_c = 31,5$ Dalton. If branching occurs, the experimental M_c has to exceed this value. This is indeed so, since M_c increases from 34 to 59 with increasing molecular weight. It is obvious that the values obtained according to (5) and (8) agree very well. If we calculate the overall length L with Eqn (6), the resulting value will obviously correspond to the length of an unbranched molecule of equal molecular weight. The division of M_r by 162 yields the degree of polymerization P of the overall molecule. If, on the other hand, we compute the molecule length from (8), using the experimental value for M_c , we obtain the length L_b of the backbone. Division by 5,15 Å yields the degree of polymerization of the backbone P_b .

$L - L_b = \Delta L$ is, thus, the total chain length of the side-chains and $P - P_b = \Delta P$, their degree of polymerization.

Chemically, the backbone links (1,6 bonds) can be distinguished from the links between backbone and side-chains (1,3 bonds); independent of the degree of degradation, the ratio of 1,6 bonds to 1,3 bonds is always about 16. The total number of side-chains f is, therefore, simply $P/16$. The degree of polymerization of one branch r is given by $\Delta P/f$; and the number of monomer units between two branches along the backbone is given by $s = P_b/f$. The quantities r and s thus characterize the comb structure. The table shows that the degree of polymerization and the side-chain length increases with the molecular weight. It is obvious that this model permits a computation of the mass per unit length, according to

$$M_c = 162(r + s)/5,15s = 31,46(r + s)/s \quad (9)$$

The agreement with the values derived through Eqn (8) is excellent, which supports the underlying model.

One fact we have to accept without rigid explanation: the persistence length (from $I \times (2\theta)^2$ v. θ plot) clearly decreases with increasing molecular weight (Fig. 9).

5. NUCLEIC ACIDS, VIRUSES

The behaviour of the different nucleic acids (DNA, high-molecular weight RNA and low-molecular weight RNA) and the rod-like viruses in solution are discussed in Chapter 9.

II. Natural High Polymers in the Dense Form and in the "Loosened-up" State

About half a century ago the small angle scattering of various solid materials was discovered⁽¹⁶⁾⁻⁽¹⁹⁾ and qualitatively correctly interpreted as being connected with their colloidal structure. One of these substances was cellulose.⁽¹⁶⁾ Several years later, attempts were made to start to develop a quantitative interpretation of small angle scattering. Shortly after Guinier's⁽²⁰⁾ famous paper, which attempted an explanation of the phenomenon in terms of the scattering of independent colloidal particles ("particulate scattering"), it became apparent⁽²¹⁾⁻⁽²³⁾ that one has to distinguish between two types of object, whose small angle scattering must be treated differently: diluted systems, for which the particulate scattering concept is valid, and densely packed systems, whose scattering is dominated by interparticle interference effects.

The majority of small angle results on natural solid high polymers deal with cellulose. We shall, therefore, mainly confine ourselves to the discussion of the possibilities of SAXS with this substance as a representative example for natural solid high polymers as well as for densely packed systems. In this connection we shall restrict to the diffuse small angle scattering, and will exclude a discussion of sharp small angle reflections on the meridian.

A. The Supermolecular Structure of Cellulose

1. QUALITATIVE INFORMATION ABOUT THE RIBBON-SHAPE OF CELLULOSE MICELLES

Investigation of the high angle scattering had shown by the 1920s that cellulose molecules aggregate to form long bundles, so-called micelles. If tension

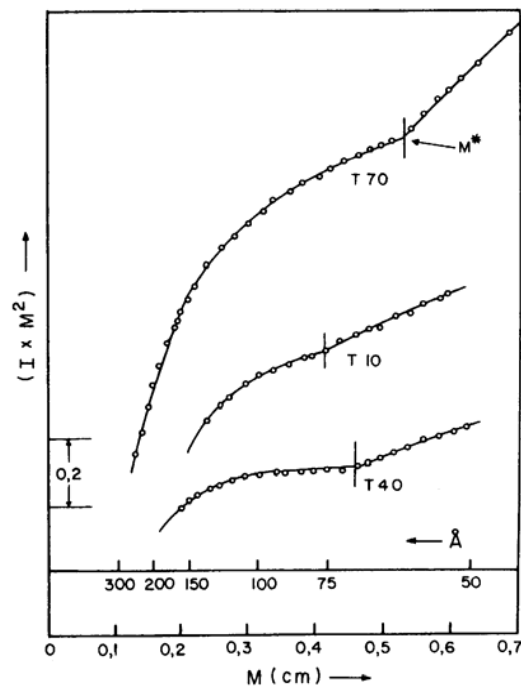


FIG. 9. Scattering curves in the $I \cdot m^2$ v. m plot of dextranhydrolysates. The molecular weights are 74 500 (for T_{70}), 12 000 (for T_{10}) and 42 000 (for T_{40}).

is applied to a plastic regenerated cellulose sample (film), the main axes of the micelles orient parallel to the direction of stress. At the same time, a characteristic line-shaped small angle interference effect can be observed on the equator (i.e. perpendicular to the direction of stress), which leads to the qualitatively correct interpretation that the supermolecular domains are much more extended parallel to the direction of stress than perpendicular to it. If a film is treated by stretching *and* rolling, it is possible to obtain an orientation with respect to two axes. If such a rolled band is oriented in a pinhole-camera with the stretching direction parallel to the X-ray beam, the resulting X-ray pattern is, unlike that of a sample which was only treated by stretching, no more rotationally symmetric: the scattering effect is anisotropic, as shown in Fig. 10. In this figure, the stretching direction and the rolling plane are perpendicular to the plane of the paper, the latter intersects the plane of the paper in a vertical line through the origin. From Fig. 10, one can immediately conclude that the lateral dimensions of the supermolecular domain are larger in the rolling plane than the ones perpendicular to it, since the scattering diagram is a reciprocal image of the true dimensions. Deformation processes can also be

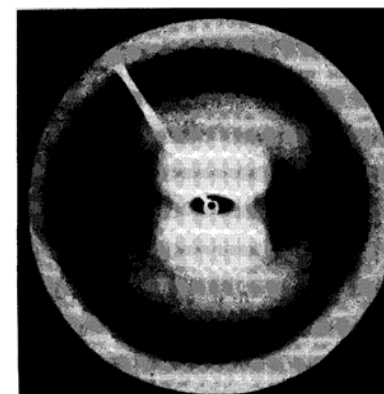


FIG. 10. X-ray diagram of a stretched and rolled film of regenerated cellulose, irradiated in the stretching direction; rolling plan is perpendicular to the plane of the paper and intersects it in a vertical line.

investigated by studying changes in the arc length of equator reflections in the wide angle X-ray diagram. In this way, the same above result (ribbon-shaped micelles) was obtained.⁽²⁴⁾ Other investigations have complemented the model by demonstrating that the micelles are linked together by amorphous regions to form micellar strands.⁽²⁵⁾

Additional crucial observations concerning the micellar structure of cellulose were reported by Heikens *et al.*,⁽²⁶⁾ who demonstrated that swelling modifies the otherwise diffuse and monotonously decreasing equator scattering of oriented cellulose, in such a way that points of inflection and even maxima can frequently be observed. These maxima correspond to periodicities between 70 and 90 Å, which obviously represent the sum of particle thickness and width of the interparticle gap. More important, however, is the conclusion that the diameters of the ribbon-shaped micelles are apparently rather uniform.

2. PREPARATION OF LOOSENERED-UP REGENERATED CELLULOSE AND THE AIM OF ITS INVESTIGATION

A valuable contribution to the study of cellulose was the idea to loosen up regenerated cellulose, in such a way that the micellar strands are separated from each other far enough to be considered independent particles; their scattering curves can then be interpreted according to the principles of particulate scattering.

Suitable materials are the so-called "air-swollen" cellulose samples, which are prepared according to Hermans *et al.*^{(27),(28)} by suspending highly swollen regenerated cellulose in an organic solvent, until the organic phase has replaced

the water of hydration. Subsequently, the fibres are dried to evaporate the organic liquid. This procedure yields porous gels which have retained the voids of the water-swollen state. These gels are called "air-swollen" cellulose fibres; they can be prepared with varying degrees of swelling ($q = 1,05-6$). We shall start the following discussion under the plausible assumption that through the preparation procedure the parallel alignment of neighbouring micelles, which is notably present in the water-swollen state, has given place to an extensive randomness. The results of the investigations to be discussed will justify this assumption, which is of crucial importance for the data evaluation: elongated or planar particles show practically no interparticle interference, as long as they are randomly oriented.⁽²⁹⁾ On the other hand, it is clear that, with progressively denser packing, sterical effects will force a parallel ordering of the particles, an "ordering in small domains". For lower degrees of swelling, we thus expect increasing interparticle interference.

In the following, we shall discuss research on the above described air-swollen fibres for the whole attainable range of swelling degree s . Most of the available possibilities of the small angle technique were applied in this work.^{(30),(31)}

3. CROSS-SECTION DETERMINATION FROM THE CURVE-SHAPE OF LOOSENERED-UP REGENERATED CELLULOSE

Figure 11 shows the Guinier-plot of the cross-section factor for three samples which are compatible with end-tangents of equal slope. The highest-swollen sample ($q = 5,98$) shows in the innermost part of its curve a rise in intensity beyond the Guinier-line, which we assume to be caused by the presence of micellar aggregates called "clusters". The sample with $q = 2,2$ shows a clear interference effect which, however, is confined to the innermost portion of the curve. The interference effect of the third sample ($q = 1,16$) extends so far out, that one could not unequivocally draw the end-tangent without recourse to the other two curves. The radius of gyration of the cross-section calculated from the Guinier tangents is $R_c = 47 \text{ \AA}$.

Moreover, $(Im)_0$ ($m \approx 2\theta \cdot a$) can be estimated from the three curves; this quantity permits a computation of the cross-sectional area A according to the following equation:⁽¹⁰⁾

$$A = \frac{(Im)_0 (a\lambda)^2}{Q' 2\pi} \quad (10)$$

Q' are the invariants determined from the Guinier-extrapolated curves (Fig. 11). The resulting values for A agree well with each other (Table 3). If we assume a rectangular cross-section, we can calculate its axes α and β from R_c and A according to:

$$A = \alpha \cdot \beta; \quad R_c^2 = \frac{1}{12} (\alpha^2 + \beta^2)$$

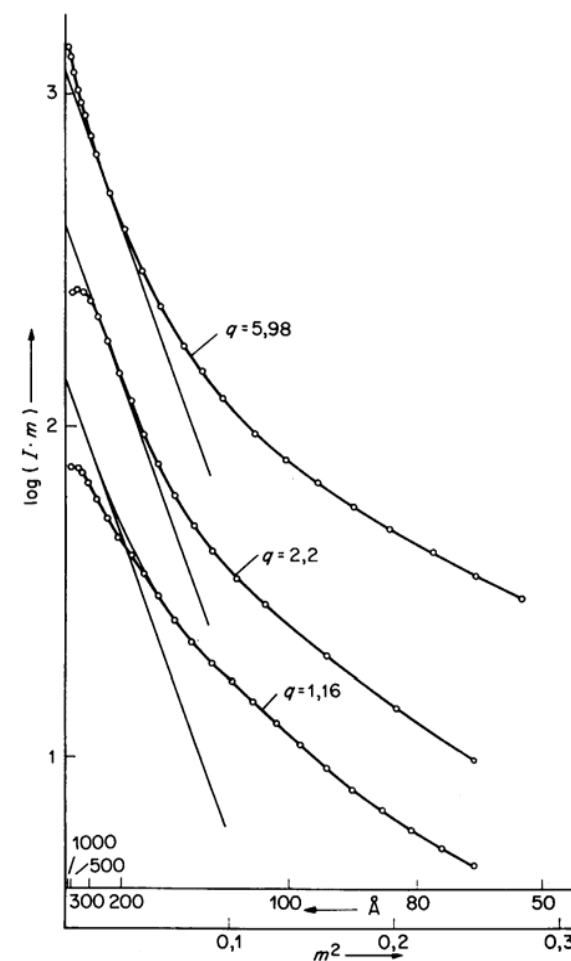


FIG. 11. Cross-section factor of three samples of air-swollen regenerated cellulose in the Guinier-plot.

TABLE 3

q	5,98	2,2	1,16
r	0,875	0,514	0,23
q'	6,84	4,29	5,45
f	0,147	0,635	0,964
A	9300	9000	9260
α	152,5	150	152,3
β	61	60,0	60,9
M_c	7740	6770	7370

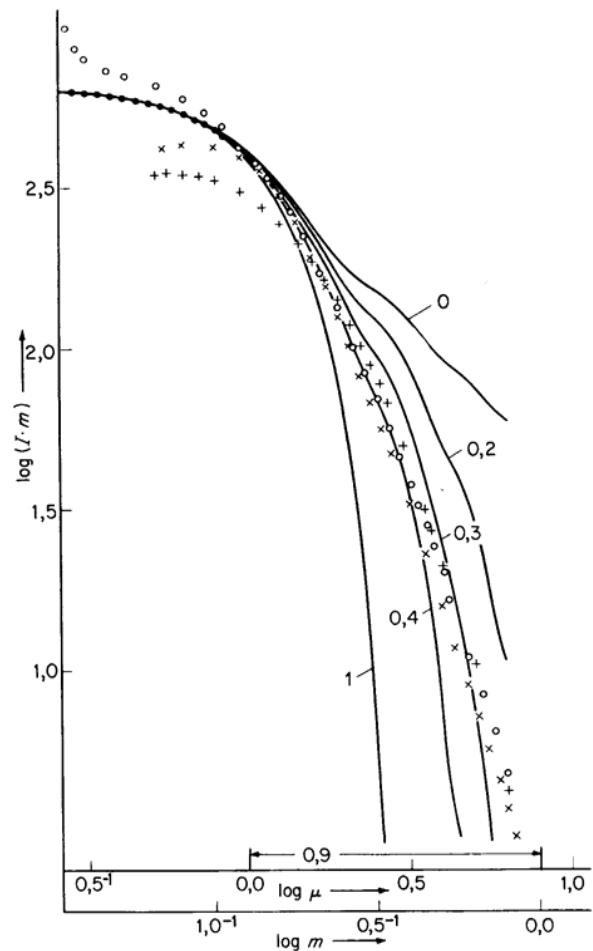


FIG. 12. A comparison of theoretical cross-section curves with experimental curves. The q -values are: (○) 5,98; (×) 2,2; (+) 1,16.

The results (Table 3) are in the order $\alpha = 150 \text{ \AA}$ and $\beta = 60 \text{ \AA}$.

A comparison of the experimental cross-section curve, with theoretical curves for different axial ratios (Fig. 12), yields a ratio $\beta/\alpha \approx 0,4$, which is in excellent agreement with the above values. At very small angles, the three samples show deviations from the theoretical curve in the logarithmic plot of Fig. 12. This phenomenon and its reason were already discussed in the context of Fig. 11.

The results discussed so far are compatible with an essentially monodisperse system. Nevertheless, the possibility might be considered that the cross-section is less anisotropic, which could be compensated for by a polydispersity in the

dimensions of its side axes. The experimental inner surface, however, agrees with the one of monodisperse micelles with the above axial ratio. Any decrease in anisotropy would lead to a decrease in the inner surface and, therefore, introduce a discrepancy with the experiment. In addition to that, the small angle scattering in Fig. 10 which is the expression for the cross-section anisotropy corresponds quite well to the above axial ratio.

One might also consider the opposite extreme, where one of the two side axes is allowed to become "infinitely" long. Janeschitz-Kriegl *et al.*⁽³²⁾ have shown that, with this lamella-model, the observed cross-section curve can only be accounted for if a moderate polydispersity in the lamella-thickness is assumed. However, this model appears unlikely since one would expect a more pronounced anisotropic small angle scattering of the rolled cellulose, when irradiated in the direction of stress, than is observed (Fig. 10). All in all, the interpretation which is based on an essentially monodisperse cross-section appears to be realistic.

4. USE OF ABSOLUTE INTENSITY – THE CLUSTER FRACTION

So far, we have only used the *shape* of the scattering curves to obtain information about the cross-section of the micellar strands. However, the absolute intensity, i.e. the ratio of scattered intensity and primary intensity, allows "weighing"-operations to be performed, which are useful as a supplement and as a control for the particle shape. In the present case, the quantity of interest is the mass per unit length, according to

$$M_c = K \cdot \frac{(Im)_0}{P_0} \frac{a}{t \cdot c \cdot z^2}; \quad K = 27,3 \quad (12)$$

(z = moles of electrons per gram of cellulose = 0,53). Obviously, the experimental mass per unit length should be in agreement with the value calculated from cross-section and known intensity. Attempts in this direction, however, led to large discrepancies, particularly for samples with a low degree of swelling. The reason soon became obvious: Eqn (12) can only yield correct results if *all* the cellulose is present in the form of individual and well separated micellar strands. The equation breaks down if some of the material is in the form of aggregation (clusters), whose scattering is beyond the experimentally observable angular range.

The question is easily settled by a comparison of the theoretically calculated invariant with the experimentally observed one: Eqn (13) yields the theoretical invariant from the elemental composition of cellulose

$$Q/P_0 = K \cdot t \cdot a \cdot w_1 \cdot w_2 (\Delta\rho)^2; \quad K = 8,34 \times 10^{-3} \quad (13)$$

(w_1 and w_2 are the volume fractions of air and cellulose, $\Delta\rho$ the electron density

difference, which is nearly identical to the electron density of cellulose), whereas the experimental invariant is obtained according to

$$Q'/P_0 = \int_0^\infty Im^2 dm/P_0 \quad (14)$$

We find that $r = Q'/Q$ is always smaller than 1 (Table 3). Obviously, it was not possible to sufficiently "loosen-up" all the substance, i.e. besides the isolated micellar strands there are still large aggregates ("clusters"), whose scattering is beyond the experimentally observable angular range. For a detailed discussion we refer to the original publications^{(30),(31)} and only mention that r can be used to compute the cluster fraction f (Table 3) and the degree of swelling q' in the unclustered domain.

Now we return to the problem of computing the mass per unit length; Eqn (12) has to be modified to account for the cluster formation. The values average at about 7300 Å (Table 3) and agree well enough between the three samples. If we calculate the mass per unit length from the axes α and β and the known density of cellulose (1.61 g cm^{-3}), we obtain a value of 8640, which is about 18% larger than the one from the modified Eqn (12). In view of various idealizing assumptions and the difficulties of the measurements the agreement is satisfactory; furthermore, the fact that only 40% of the micellar strands are in a crystalline state and 60% in an amorphous state (as determined from high angle X-ray scattering) could in view of the reduced average density at least partly account for the discrepancy.

5. DIRECT OBSERVATIONS OF THE CLUSTER FRACTIONS AT SMALLEST ANGLES

If the above given interpretation for the deficiency of the absolute value of the invariant and the calculation of the cluster fraction f is correct, it should (at least in principle) be possible to observe the scattering of the clusters at sufficiently small angles and obtain from the experiment the full invariant corresponding to the elemental composition (according to Eqn (13)). This was attempted for the sample with $q = 5.98$. The result is presented in Fig. 13: the right branch of the curve plus the dashed extrapolation to $m = 0$ was already used for the above analysis of the disperse fraction. The low angle maximum in the Im^2 plot is new, which originates from the clusters. If we now redetermine the invariant Q'' (using Eqns (13) and (14)), we obtain

$$r = \frac{Q''}{Q} = 1.056$$

This coincidence is even better than could be expected, in view of the many experienced sources of errors which influence the value of r . The measurements,

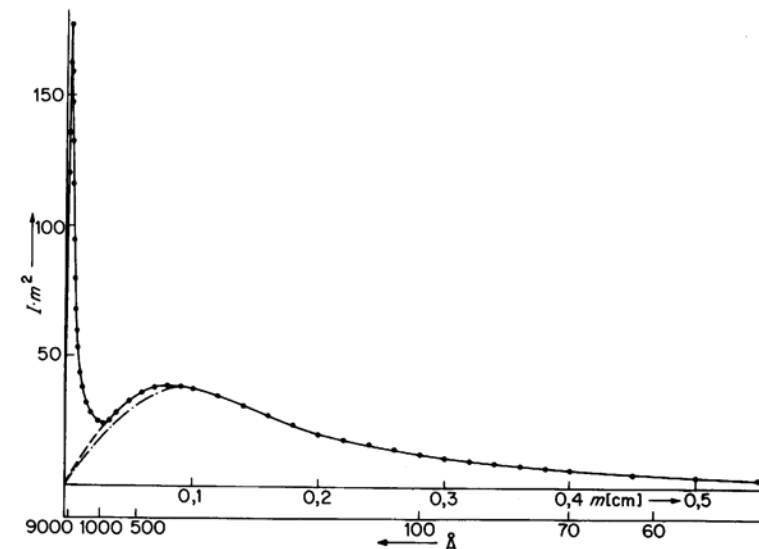


FIG. 13. $I \cdot m^2$ v. m plot for the sample with $q = 5.98$, included the zone of the very smallest scattering angles.

which are extended to a resolution of 9000 Å Bragg's value (corresponding to 0.17 mrad), were only possible because the scattered intensity was high enough to permit extremely sharp collimation.

6. THE INNER SURFACE

There is yet another possibility for checking the correctness of the cluster model.

Figure 14 shows a plot of the ratio $Im^4/Q' = k/Q'$, the value of which at large angles yields the specific inner surface of the unclustered domain.^{(33),(34)} This parameter, on the other hand, can be easily estimated for elongated bands of known cross-section. These values are presented in Fig. 14 as lines parallel to the abscissa.^{(30),(31)} The agreement is excellent, particularly for medium- and high-swollen samples.

The concept presented for the supermolecular structure of cellulose is thus verified in a number of ways. It is surprising that the possibility of loosening a micellar system to make it more suitable for small angle observations seems to be rather unpopular, in spite of its benefits. While, for example, every electron-microscopist routinely brings his sample into a state best suited for experimental observation, small angle researchers have so far largely neglected such possibilities.

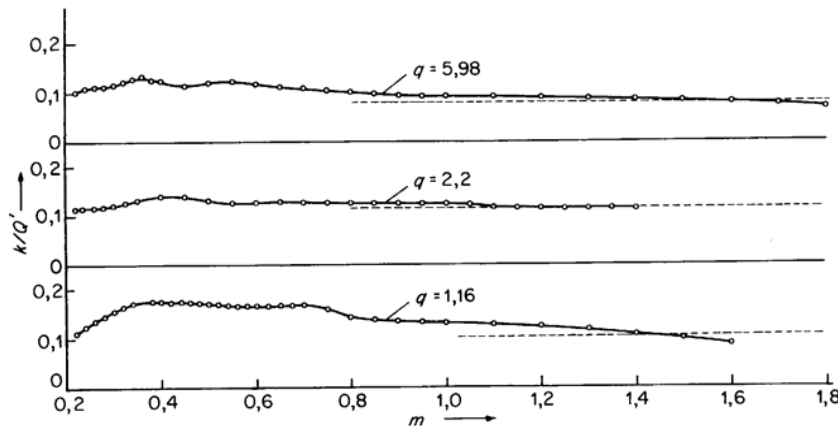


FIG. 14. $I \cdot m^4/Q'$ v. m plot in the tail end of the scattering curves. The marked points represent the measurements, the dotted lines are calculated under the assumption of a cross-section $60 \times 150 \text{ \AA}$ and the computed unclustered fraction ($1 - f$).

7. CELLULOSE OF VERY LOW DEGREES OF SWELLING AND IN THE DENSE STATE

Sterical considerations exclude a random packing if the void interparticle volume decreases to the order of several percent of the total volume. Since there is a tendency towards the formation of lamellar structures, it is possible to base the interpretation of such systems on the model of lamellar stacks.

For such systems, Porod's theory⁽³⁵⁾ is applicable; according to his theory, an Im^2 plot should show a maximum, which yields the average lamellar thickness through a direct application of Bragg's equation. For a fibre with $Q = 1.05$, however, the experimental maximum is so broad that one has to assume a large degree of polydispersity (in contrast to the high air-swollen samples). Moreover, it is remarkable that the thus obtained lamellar thickness of 40 \AA ⁽³¹⁾ is considerably smaller than the 60 \AA obtained from the particle scattering of loosened-up cellulose. P. H. Hermans' model for the lamellar splitting of micelles⁽³⁶⁾ makes it plausible that for such tightly packed systems any splitting has to lead to a decrease in the apparent average thickness. On the other hand, neighbouring lamellae can also stick together. Both effects lead to a considerable increase in the apparent polydispersity.

Let us turn to the dense celluloses, which occur in the native fibre and in the commercially produced rayon fibres. Here, the structure of lamellar stacks disappears due to excessive sticking of micelles. However, since regenerated celluloses show macroscopic densities varying by several percent, spaces of some sort have to be present. Stern⁽³⁷⁾ and P. H. Hermans *et al.*⁽³⁸⁾⁻⁽⁴⁰⁾ have

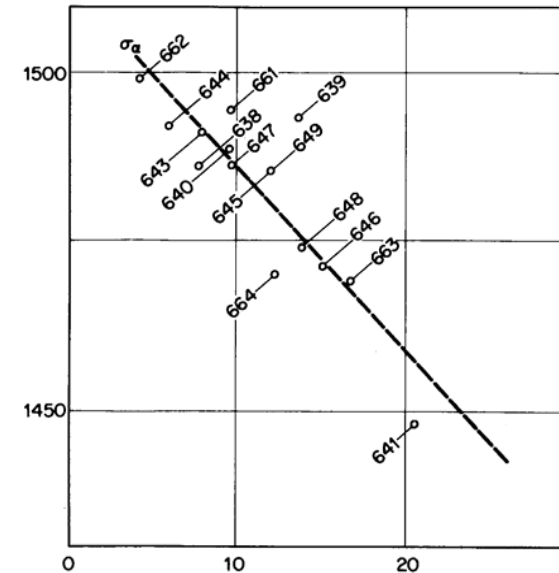


FIG. 15. Connection between density kg m^{-3} (ordinate) and absolute value of the invariant for different rayons.⁽³⁸⁾

demonstrated that useful information about these spaces can be obtained from the absolute value of the invariant: from the crystalline-amorphous composition, which one knows from wide angle measurements to be around 40% crystalline and 60% amorphous, and the known electron density of the two phases, one can compute the minimum value of the invariant. Only the sample with the highest density (nr. 662 in Fig. 15) showed this value, while for several other samples of lower macroscopic density the invariant always exceeded the theoretical minimum. Hermans *et al.* suggest the presence of voids, i.e. they assume a three-phase system (with air being the third phase). According to the equation

$$\overline{(\Delta\rho)^2} = \frac{K}{t \cdot a} \frac{Q}{P_0}; \quad K = 1.2 \times 10^2 \quad (15)$$

the mean square fluctuation of the electron density is directly proportional to the absolute value of the invariant. For a three-phase system, on the other hand, $\overline{(\Delta\rho)^2}$ can be calculated from the equation⁽³⁷⁾

$$\overline{(\Delta\rho)^2} = (\rho_3 - \rho_2)^2 w_3 \cdot w_2 + (\rho_3 - \rho_1)^2 w_3 \cdot w_1 + (\rho_2 - \rho_1)^2 w_2 \cdot w_1 \quad (16)$$

Let us label the crystalline cellulose as phase 3, the amorphous cellulose as phase 2 and the voids as phase 1: the first term in the above equation corresponds to the contrast between the two solid phases, while the second and the

third terms originate from the contrast between the solid phases and the voids. The electron density difference between the solid phases and the air phase is about ten times larger than the difference between the two solid phases; since electron density differences are squared in the above equation, it is easy to show that already 1% of the voids have a larger effect than the maximum crystalline-amorphous contrast. Hermans *et al.* have computed that one has to assume an air volume of 0,75% for the sample Nr. 641 with the lowest density. However, the density difference (1,50 v. 1,45) requires 3% voids. Since the resolution of these measurements did not exceed a Bragg spacing of 300 Å, it is quite plausible to ascribe this discrepancy to the existence of larger voids which were beyond experimental observations.

Later, similar studies were performed on 60 different celluloses, with considerably better resolutions (2000 Å).⁽⁸⁾ Again, the crystalline-amorphous contrast could not account for all the scattering power. Voids between 0,04% (which is practically zero) and 0,7% had to be assumed, in quite good agreement with Hermans. It was also attempted to correlate the void volume with a certain textile quality, the so-called "loop tenacity", and it was found that a very low void volume leads to poor loop tenacity. It was speculated that a good fibre has to have a minimum "reserve" of voids to absorb tensions caused by inhomogeneous mechanical stress.

The first extensive investigations into the voids in cellulose as a function of the production conditions and subsequent treatment, were carried out by Statton.⁽⁴¹⁾

Another approach to the study of natural cellulose fibres, which does not rely on any *a priori* model, consists of a direct application of Porod's general theory^{(33),(34)} to determine various characteristic parameters, such as specific inner surface, transversal length and coherence length. Ratto and co-workers have used this approach to study mercerized Jute⁽⁴²⁾ and Sisal⁽⁴³⁾ fibres.

B. Remarks on the Supermolecular Structure of Silk Fibroin

If one dissolves the cocoon fibres of the silk worm *Bombyx mori* in copper(II)-ethylenediamine and dialyses the solution, one obtains a clear, aqueous solution of "renatured" silk fibroin (Colemann and Howitt).⁽⁴⁴⁾ Upon standing, this solution is converted into a turbid gel. Such gels can be converted into air-swollen solid samples by a procedure similar to the one applied to cellulose (i.e. exchange of water with alcohol, and subsequent drying under vacuum). Since both kinds of samples (gels and air-swollen) show very similar small angle scattering which clearly reveals aggregation to supermolecular particles, we shall treat them together in the current chapter on solid high polymers, although the gels exhibit a high-viscous aggregation state, which could also qualify them as solutions.

Extensive investigations have in all cases revealed bar-shaped particles,⁽⁴⁵⁾ whose one side-axis is always around 60 Å, whereas the length of the other one scatters around fractions of 180 Å. These measurements, however, were carried out on rather concentrated gels (4–20%). An extension to more diluted gels would be desirable.

References

- (1) Porod, G. (1949). *Monatsh. Chem.* **80**, 251.
- (2) Kratky, O. and Porod, G. (1949). *Rec. trav. Chim. Pays-Bas* **68**, 1106.
- (3) Debye, P. (1947). *J. Physic. Colloid Chem.* **51**, 18.
- (4) Porod, G. (1953). *J. Polymer Sci.* **10**, 157.
- (5) Kratky, O. (1962). *Kolloid-Z. Z. f. Polymere* **182**, 7.
- (6) Peterlin, A. (1960). *J. Polymer Sci.* **47**, 403.
- (7) Heine, S., Kratky, O. and Roppert, J. (1962). *Makrom. Chem.* **56**, 150.
- (8) Kratky, O. (1966). *Pure Appl. Chem.* **12**, 483.
- (9) Kratky, O., Porod, G. and Kahovec, L. (1951). *Z. Elektrochem.* **55**, 53.
- (10) Kratky, O. (1963). *Progr. Biophys.* **13**, 105.
- (11) Heine, S., Kratky, O., Porod, G. and Schmitz, P. J. (1961). *Makrom. Chem.* **44–46**, 682.
- (12) Kratky, O., Leopold, H. and Puchwein, G. (1967). *Kolloid-Z. Z. f. Polymere* **216**, 215.
- (13) Zipper, P., Krigbaum, W. R. and Kratky, O. (1969). *Kolloid-Z. Z. f. Polymere* **235**, 1281.
- (14) Stivala, S. S., Herbst, M., Kratky, O. and Pilz, I. (1968). *Arch. Biochem. Biophys.* **127**, 795.
- (15) Garg, S. K. and Stivala, S. S. (1978). *J. Polymer Sci. Polymer Physics Ed.* **16**, 1419.
- (16) Mark, H. (1932). In "Physik und Chemie der Zellulose", p. 139. J. Springer, Berlin.
- (17) Warren, B. E. (1934). *J. Chem. Phys.* **2**, 551.
- (18) Krishnamurti, P. (1930). *Ind. J. Phys.* **5**, 473.
- (19) Hendricks, S. B. (1932). *Z. Kristallogr. Mineral* **83**, 503.
- (20) Guinier, A. (1937). *C.R. Acad. Sci. Paris* **204**, 1115.
- (21) Kratky, O. (1938, 1942). *Naturwiss.* **26**, 94; **30**, 542.
- (22) Kratky, O. (1940). *Z. Elektrochem.* **46**, 550.
- (23) Kratky, O., Sekora, A. and Treer, R., (1942). *Z. Elektrochem. Ber. Bunsenges. physikal. Chemie* **48**, 587.
- (24) Baule, B., Kratky, O. and Treer, R. (1941). *Z. Physik. Chem.* **B50**, 255.
- (25) Kratky, O. (1938). *Kolloid-Z.* **84**, 149.
- (26) Heikens, D., Hermans, P. H., van Velden, P. F. and Weidinger, A. (1953). *J. Polymer Sci.* **11**, 433.
- (27) Hermans, P. H. and de Leeuw, A. J. (1938). *Kolloid-Z.* **83**, 58.
- (28) Hermans, P. H. and Platzek, P. (1939). *Z. physik. Chem.* **A185**, 260.
- (29) Kratky, O. and Porod, G. (1956). *Z. physik. Chem.* **7**, 236.
- (30) Kratky, O. and Miholic, G. (1963). *Mh. Chem.* **94**, 151.
- (31) Kratky, O. and Miholic, G. (1963). *J. Polymer Sci. Part C2*, 449.
- (32) Janeschitz-Kriegl, H., Kratky, O. and Porod, G. (1952). *Z. Elektrochem. Ber. Bunsenges. physikal. Chemie* **56**, 146.

- (33) Porod, G. (1951). *Kolloid-Z.* **124**, 83.
- (34) Porod, G. (1952). *Kolloid-Z.* **125**, 51.
- (35) Porod, G. (1949). *Acta Physica Austriaca* **3**, 66.
- (36) Hermans, P. H. (1949). In "Physics and Chemistry of Cellulose Fibres". Elsevier, Amsterdam.
- (37) Stern, F. (1955). *Trans. Far. Soc.* **51**, 430.
- (38) Hermans, P. H., Heikens, D. and Weidinger, A. (1959). *J. Polymer Sci.* **35**, 145.
- (39) Heikens, D. (1959). *J. Polymer Sci.* **35**, 139.
- (40) Hermans, P. H. and Weidinger, A. (1960). *Makromol. Chem.* **39**, 67.
- (41) Statton, W. O. (1956, 1962). *J. Polymer Sci.* **22**, 385; **58**, 205.
- (42) Ratho, T. and Sahu, N. C. (1971). *J. Colloid Interface Sci.* **37**, 115.
- (43) Ratho, T., Patel, A. and Singhal, O. P. (1974). *J. Polymer Sci.* **12**, 2595.
- (44) Coleman, D. and Howitt, F. O. (1946). *Proc. Roy. Soc. London* **A190**, 145.
- (45) Kratky, O., Pilz, I. and Sekora, A. (1955). *Z. Naturforsch.* **10b**, 510.

12

Synthetic Polymers in Solution

R. G. KIRSTE

Johannes-Gutenberg-Universität, Fachbereich Chemie Institut für Physikalische Chemie, Mainz, W. Germany

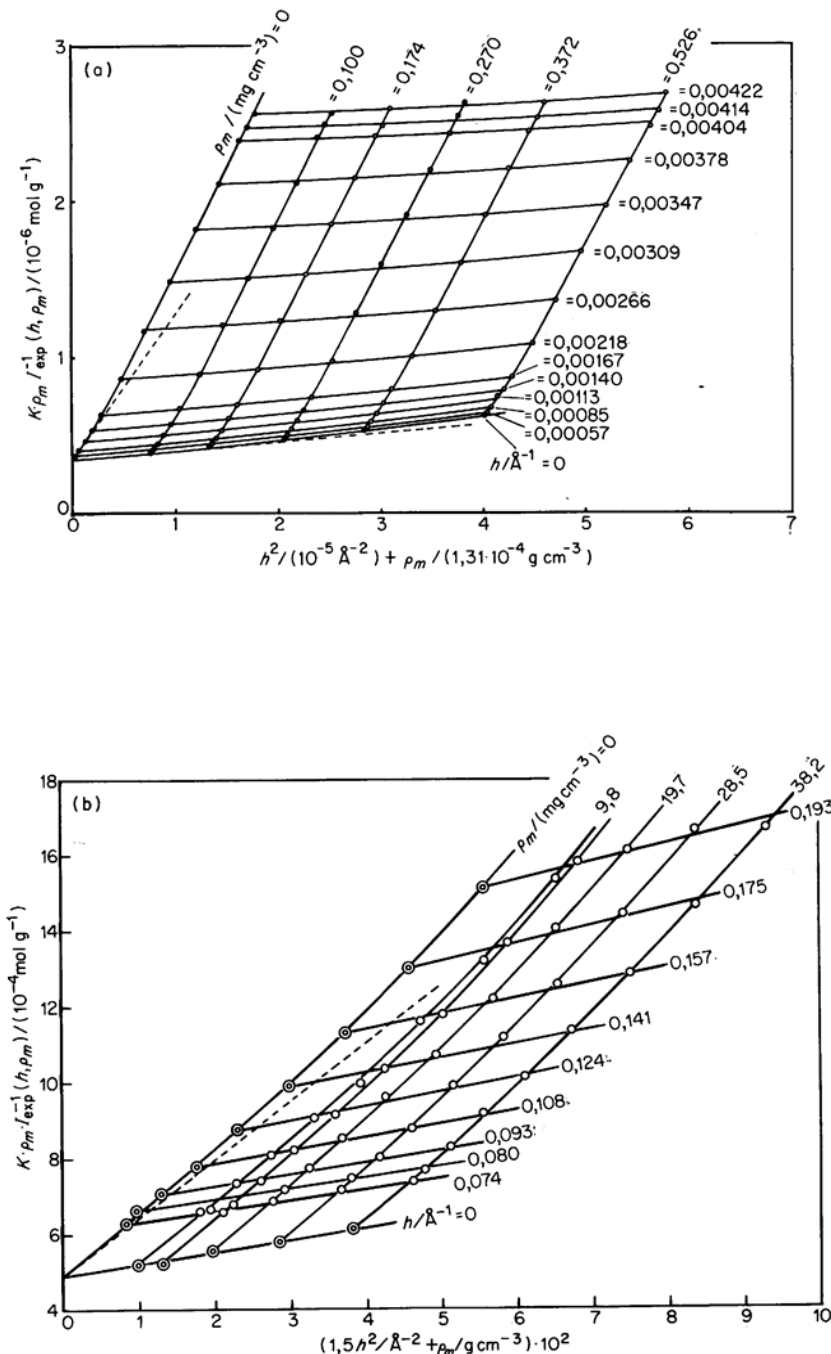
R. C. OBERTHÜR

Institut Max von Laue – Paul Langevin, Grenoble, France

I. Introduction	387
II. Coil models	392
A. Unperturbed coils	392
B. Perturbed coils	397
III. Scattering functions of coil molecules	401
A. Unperturbed coils	401
B. Perturbed coils	416
IV. Some specific experimental applications	419
A. Molar mass, radius of gyration and second virial coefficient	419
B. Analysis of the scattering function	422
V. Conclusion	428
References	429

I. Introduction

The subject of this chapter is the scattering of electromagnetic radiation by dilute solutions of polymer molecules and especially the influence of the statistical chain conformation of single polymer chains on the scattering pattern. In the scattering by a set of single macromolecules inter- and intramolecular interferences occur. The scattered intensity $I_{\text{exp}}(h, \rho_m)$, measured as a function of momentum transfer h and the mass concentration ρ_m of the polymer, usually expressed in g cm^{-3} , may be treated according to Zimm (1948) and Flory and Bueche (1958)



$$\frac{K \cdot \rho_m}{I_{\text{exp}}(h, \rho_m)} = \frac{1}{M \cdot I_n(h)} + 2A_2 \cdot Q_{FB}(h) \cdot \rho_m + \dots \quad (1)$$

M is the molar mass of the dissolved polymer, expressed in g(mol)^{-1} and $I_n(h)$ is the single particle scattering function, normalized in such a way that $I_n(0) = 1$ (structure factor). The first term on the right of Eqn (1) is merely due to intramolecular interferences, whereas the higher terms reflect the influence of intermolecular interferences. A_2, A_3 etc. are the virial coefficients of osmotic pressure Π from the series expansion

$$\frac{\Pi}{\mathcal{R} \cdot T \cdot \rho_m} = \frac{1}{M} + A_2 \rho_m + A_3 \rho_m^2 + \dots \quad (2)$$

where \mathcal{R} is the gas constant and T the absolute temperature. The function $A_2 \cdot Q_{FB}(h)$ reflects the average spatial arrangement of two polymer particles during their mutual approach with $Q_{FB}(h)$ normalized to 1 at $h = 0$. It tends to zero with increasing h , so that the effect of intermolecular interferences at a given concentration can be neglected at sufficiently high values of h .

At ideal osmotic pressure ($A_2 = A_3 = \dots = 0$) the intermolecular interferences are cancelled, so that $I_{\text{exp}}(h, \rho_m)$ becomes proportional to ρ_m and Eqn (1) reduces to

$$[I_{\text{exp}}(h, \rho_m)]_{\text{ideal}} = K \cdot \rho_m \cdot M \cdot I_n(h) \quad (3)$$

In the case of X-ray scattering the meaning of K is obtained by comparison with Eqn (48) in Chapter 4

$$K = \frac{e^4}{m^2 \cdot c^4} \cdot \frac{P \cdot (\Delta z)^2 \cdot d \cdot N_A}{a^2} \quad (4)$$

The plot of $K \cdot \rho_m / I_{\text{exp}}(h, \rho_m)$ versus $h^2 / \text{\AA}^{-2} + \text{constant} \cdot \rho_m / (\text{g} \cdot \text{cm}^{-3})$, called Zimm-plot (Fig. 1) allows a simultaneous extrapolation to $h = 0$ and $\rho_m = 0$, which yields $1/M$ as the ordinate intercept.

The line with $h = 0$ has the equation

$$\lim_{h \rightarrow 0} \frac{K \cdot \rho_m}{I_{\text{exp}}(h, \rho_m)} = \frac{1}{M} \cdot (1 + 2A_2 \cdot M \cdot \rho_m + \dots) \quad (5)$$

from which the thermodynamic analysis of the dilute system can be performed. The line with $\rho_m = 0$ has the equation

FIG. 1. Zimm-plots of (a) LS-data of PS in toluene at 25°C (Rahlwes, 1974): $M_w = 2.95 \cdot 10^3 \text{ g(mol)}^{-1}$; $U = 0.05$; $\langle R^2 \rangle_z^{1/2} = 900 \text{ \AA}$; $A_2 = 2.2 \cdot 10^{-4} \text{ cm}^3 \cdot \text{mol g}^{-2}$. (b) SAXS-data of PMMA (80% syndiotactic) in acetone at 20°C (Kirste and Wunderlich, 1968): $M_w = 2.04 \cdot 10^3 \text{ g(mol)}^{-1}$; $U = 0.35$; $\langle R^2 \rangle_z^{1/2} = 11.9 \text{ \AA}$; $A_2 = 14.6 \cdot 10^{-4} \text{ cm}^3 \cdot \text{mol g}^{-2}$. The dashed straight lines represent the initial slopes of $K \cdot \rho_m / I_{\text{exp}}$ against h^2 and against ρ_m , respectively.

$$\lim_{\rho_m \rightarrow 0} \frac{K \cdot \rho_m}{I_{\text{exp}}(h, \rho_m)} = \frac{1}{M \cdot I_n(h)} = \frac{1}{M} \cdot \left(1 + \frac{\langle R^2 \rangle}{3} \cdot h^2 \pm \dots \right) \quad (6)$$

and provides for the determination of $I_n(h)$, which contains all information on the shape and the conformation of the isolated macromolecule in solution. The initial slopes of Eqn (5) versus ρ_m and Eqn (6) versus h^2 yield the second virial coefficient A_2 and the mean square radius of gyration $\langle R^2 \rangle$, respectively, without any conditions. In practice however, where a measurable part of the scattering curve must be used for the extrapolations according to Eqns (5) and (6), the obtained values of A_2 and $\langle R^2 \rangle$ often greatly depend on the range over which the extrapolation has been performed and on the extrapolation procedure itself.

For the extrapolation of the concentration dependent scattering of polymer coils a square root plot (cf. Yamakawa, 1971, Chapter VII) of the reciprocal intensity ($\sqrt{(K \cdot \rho_m / I_{\text{exp}}(h, \rho_m))}$) versus ρ_m presuming $A_3 = A_2^2 \cdot M/3$ is often more suitable for an accurate determination of A_2 than an ordinary Zimm-plot.

For the extrapolation of the angular dependence of the scattered intensity, the square root plot again gives the best linearization of the scattering function of monodisperse statistical coil molecules for $I_n(h) \approx 1$ (cf. Kirste and Wunderlich, 1968; Yamakawa, 1971, Chapter VII), whereas a Zimm-plot shows a straight line only for the scattering function of polymer samples with a peculiar, broad molecular weight distribution (see below). A Guinier-plot (see Chapter 4), however, is more suitable for the extrapolation of the scattering of the collapsed coils of globular proteins. Figure 2 shows the coincidence and the deviations between the described extrapolation curves and scattering curves of a representative (Gaussian coil, see below) and two limiting (sphere, rod) conformations of macromolecules in solution.

Since, in general, a Zimm-plot yields a higher value and a Guinier-plot a lower value for the mean square radius of gyration of a polymer coil, a combination of both plots can be used for a better estimate of $\langle R^2 \rangle$ (Kirste and Wunderlich, 1968).

Equation (1) has the same form in X-ray and coherent neutron small angle scattering (SAXS, SANS) as well as in light scattering (LS). Only the expressions for the constant K are different. Therefore, light and neutron scattering data can be used for the verification of scattering functions as well. Typical differences between light scattering and X-ray small angle scattering become evident from a comparison of the Zimm-plots in Figs 1a and b.

If a coil is formed by a polymer chain, the chain length, the flexibility of the chain, its atomic structure and the intramolecular segment-segment interactions between distant parts of the chain will influence the statistics of distances between scattering centres, so that individual chain properties must

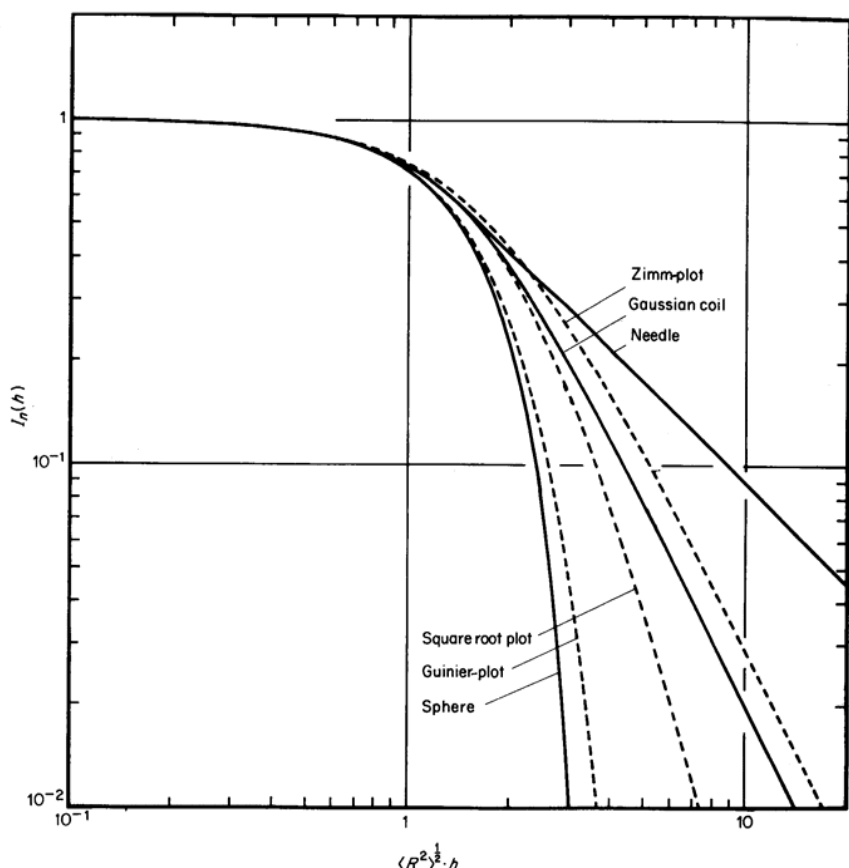


FIG. 2. Structure factors (drawn curves) for a rod (Eqn 44), a Gaussian coil (Eqn 33) and a sphere (Eqn 16 in Chapter 2), reduced to the same radius of gyration in a double logarithmic plot, together with the functions (dashed curves), which yield a straight line in a Zimm-plot ($I_n^{-1}(h) = 1 + \langle R^2 \rangle \cdot h^2/3$), in a square root plot ($I_n^{-1/2}(h) = 1 + \langle R^2 \rangle \cdot h^2/6$) and in a Guinier-plot ($\log_e I_n(h) = 1 - \langle R^2 \rangle \cdot h^2/3$).

be discussed in connection with the scattering. Furthermore, synthetic polymers exhibit a more or less pronounced heterogeneity in the molecular weight, so that in the usual evaluation according to Eqn (6) the weight average of the molar mass M_w and the z-average of the structure factor $\langle I_n(h) \rangle_z$ and hence of the mean square radius of gyration $\langle R^2 \rangle_z$ is obtained (Zimm, 1948).

All these features can be considered in the calculations of scattering functions $\langle I_n(h) \rangle_z$ of coil molecules based on more or less realistic approaches to the properties of real systems, whereas in other cases, the evaluation of scattering curves may be limited to the extrapolation of M_w , $\langle R^2 \rangle_z$ and A_2 from the

experimental data and calculation of $\langle R^2 \rangle_z$ and A_2 as a function of M_w for the different coil models.

II. Coil Models

A polymer chain may consist of N links, numbered from 1 to N . If two links i and j and their separation $|i - j|$ are considered, one can differentiate between two types of intersegmental interactions (Fig. 3).

(i) The so-called short range (longitudinal) interactions, which act along the chain from neighbour to neighbour. The nature of these interactions are bond forces and hindrance of rotation. These interactions approach zero if $|i - j|$ increases without limit. One can assume that the hindrance of rotation in coiled macromolecules is influenced by about five next neighbours.

(ii) The so-called long range (transversal) interactions, which act across (perpendicular to) the chain and the distance law of which is independent of $|i - j|$. In athermic solutions the long range interactions are caused by the Born-repulsion between the atoms of approaching polymer segments and thus closely related to the segmental volume, while attractional van-der-Waals forces between the polymer segments are cancelled by the solvent. Therefore this type of interactions is also called excluded volume effect.

The short range interactions are present in each polymer coil and only slightly affected by the solvent. The long range interactions on the other hand are strongly affected by the solvent. Under definite conditions the Born-repulsion is compensated by attractional interactions yielding a second virial coefficient $A_2 = 0$. This is the so-called theta-point of polymer solutions, which is analogous to the Boyle-point of gases and where the polymer solution shows a pseudo-ideal behaviour. Hence, to a first approximation, at the theta-point the long range interactions are cancelled.

On this fact a differentiation between two types of coils may be based:

- (i) coils without long range interaction (unperturbed coils, Gaussian coils)
- (ii) coils with long range interaction and thus exhibiting an excluded volume effect (perturbed coils, expanded coils).

A. Unperturbed Coils

1. LINEAR CHAINS

The distance r_{ij} between two skeletal atoms i and j of a coiled chain molecule varies with time. In unperturbed coils the following statement on the mean square interatomic (intersegmental) distance $\langle r_{ij}^2 \rangle$ and on its probability

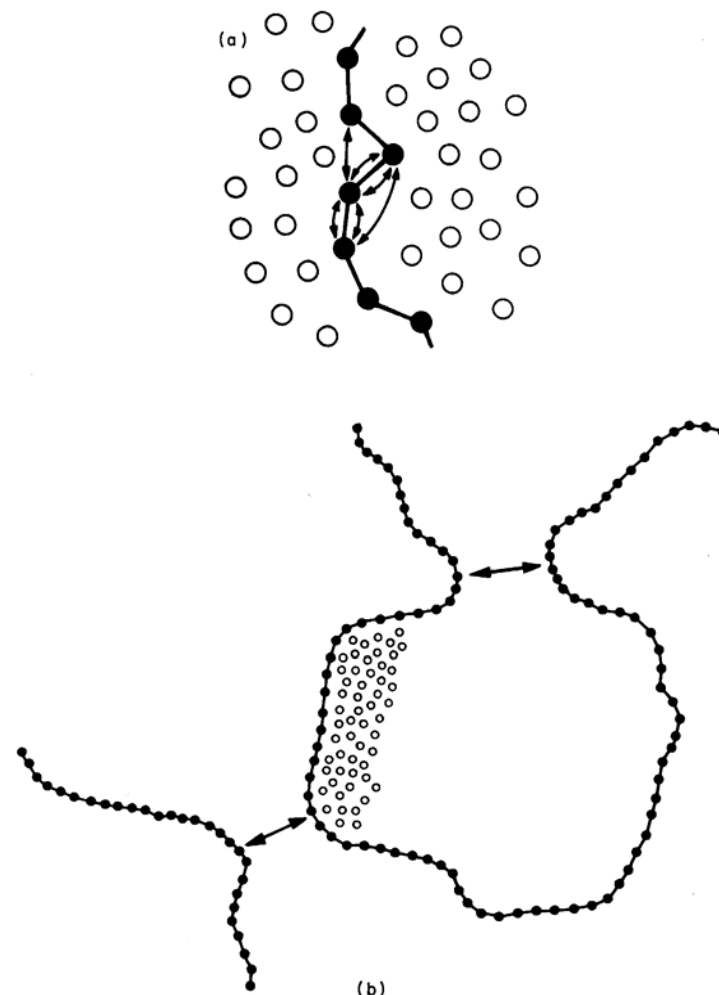


FIG. 3. Schematic picture of the action of (a) short range (longitudinal) interactions and (b) long range (transversal) interactions in polymer solutions. Solvent molecules are presented by open circles.

distribution $p\langle r_{ij} \rangle$ can be made (Flory, 1953, 1969). If the contour length of the chain between i and j is called L_{ij} with

$$L_{ij} = |i - j| \cdot l_0 \quad (7)$$

then for the limit $L_{ij} \rightarrow \infty$

$$\langle r_{ij}^2 \rangle = b \cdot L_{ij} \quad (8)$$

and the mean square end-to-end distance of the whole chain reads

$$\langle r_{ee}^2 \rangle = b \cdot L = b^2 \cdot n \quad (8a)$$

where $L = b \cdot n$ is the contour length of the whole chain. The length b is a constant for a coil and is called the statistical chain element; n is the number of statistical chain elements in the chain. It is the quantity b which in fact reflects the short range interactions between adjacent polymer segments along the chain and hence the overall flexibility of the chain. With the same restrictions as Eqn (8) the expression

$$p(r_{ij}) = \left(\frac{3}{2\pi \cdot \langle r_{ij}^2 \rangle} \right)^{3/2} \cdot 4\pi \cdot r_{ij}^2 \cdot \exp \left(-\frac{3r_{ij}^2}{2\langle r_{ij}^2 \rangle} \right) \quad (9)$$

is valid. A coil which exhibits this Gaussian distribution for all its intersegmental distances is called a Gaussian coil. Again with the restriction $L \rightarrow \infty$ the mean square radius of gyration of unperturbed coils is given by

$$\langle R^2 \rangle = \frac{\langle r_{ee}^2 \rangle}{6} = \frac{b \cdot L}{6} \quad (10)$$

or with $M_L = M/L$, the molar mass per unit length

$$\langle R^2 \rangle = \frac{b}{6 \cdot M_L} \cdot M = K_{r,0} \cdot M \quad (11)$$

where $K_{r,0}$ is a characteristic parameter of the individual polymer (characteristic ratio of $\langle R^2 \rangle/M$, cf. Flory, 1969, p. 37).

The simplest model of an unperturbed coil is the freely jointed chain of Kuhn (1934); N vectors of equal length b are linked together in such a way that the angular orientation of each vector relative to its neighbours is random (random walk with constant step length in three dimensions, random flight). In this model Eqns (8) and (8a) hold for each $N \geq 1$. Furthermore, since $b = l_0$ (cf. Eqn 7)

$$\langle r_{ij}^2 \rangle = b^2 \cdot |i - j| \quad (12)$$

The radius of gyration of this chain is given by (cf. Flory, 1969, p. 11)

$$\langle R^2 \rangle = \frac{b^2 \cdot N \cdot (N + 2)}{6(N + 1)} \quad (13)$$

which reduces to Eqn (10) with $b \cdot N = L$ for sufficiently long chains.

The special importance of Kuhn's model for real unperturbed chains lies in the fact that it provides a concrete picture of their respective statistical chain elements b , i.e. a real unperturbed chain has a statistical chain element which is equal to the bond length in that freely jointed chain which agrees with the real chain in $\langle R^2 \rangle$ and L (equivalent chain). Another unperturbed coil model is the valence angle chain (Eyring, 1932). $N + 1$ skeletal atoms are linked together by N vectors of length l_0 with a fixed valence angle α (Fig. 4). The

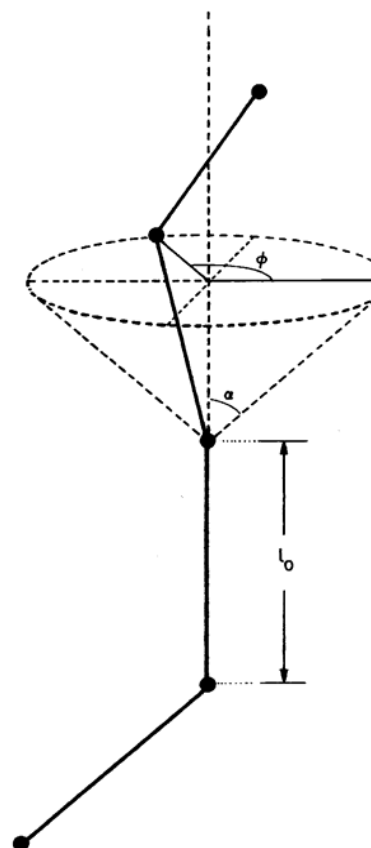


FIG. 4. Characterization of a valence angle chain. α = valence angle, ϕ = angle of rotation; l_0 = bond length.

atoms are numbered from 0 to N and the vectors from 1 to N . The contour length L_{ij} between the atoms i and j is given by Eqn (7). If the rotation is free, the mean square distance between atoms i and j is given by

$$\langle r_{ij}^2 \rangle = l_0 \cdot L_{ij} \cdot \frac{1 + \cos \alpha}{1 - \cos \alpha} - 2l_0^2 \cdot \frac{\cos \alpha}{(1 - \cos \alpha)^2} \cdot (1 - \cos^{|i-j|} \alpha) \quad (14)$$

In the limit $|i - j| \rightarrow \infty$, this reduces to

$$\langle r_{ij}^2 \rangle = l_0 \cdot L_{ij} \cdot \frac{1 + \cos \alpha}{1 - \cos \alpha} \quad (15)$$

which fits Eqns (8), (8a), (10) and (11) with

$$b = l_0 \cdot \frac{1 + \cos \alpha}{1 - \cos \alpha} \quad (16)$$

In 1949, Kratky and Porod proposed a procedure for the construction of threads, which show a continuous transition from a rod-like to a coiled shape with increasing length (worm-like chain). This model coil turned out to provide a large range of applicability to real chains. It is called the persistence chain model. The construction procedure starts from a freely rotating valence angle chain (Fig. 4). A limiting process is defined in which α and l_0 simultaneously approach zero and N tends to infinity in such a way that the contour length $L = N \cdot l_0$ and the overall flexibility characterized by b (Eqn 16) are maintained constant. The expression for $\langle r_{ij}^2 \rangle$ (Eqn 14) then changes in the following manner:

$$\langle r_{ij}^2 \rangle = b \cdot L_{ij} - \frac{1}{2} b^2 \cdot (1 - e^{-2L_{ij}/b}). \quad (17)$$

This equation includes rod-like and coil behaviour, if one looks at the limiting cases. One obtains

$$\langle r_{ij}^2 \rangle = L_{ij}^2 \quad \text{for } L_{ij} \rightarrow 0 \quad (18)$$

and

$$\langle r_{ij}^2 \rangle = b \cdot L_{ij} \quad \text{for } L_{ij} \rightarrow \infty. \quad (19)$$

The parameter $n = L/b$ (number of chain elements in the whole chain) may serve as a stiffness parameter, because with increasing stiffness (at constant L) the number of chain elements decreases, i.e. the terms "short chain" and "stiff chain" essentially envisage the same object.

The radius of gyration of the persistence chain (Benoit and Doty, 1953) is given by

$$\langle R^2 \rangle = \frac{b \cdot L}{6} \cdot \left[1 - \frac{3}{2n} + \frac{3}{2n^2} - \frac{3}{4n^3} \cdot (1 - e^{-2n}) \right] \quad (20)$$

Instead of the statistical chain element, Kratky and Porod use the persistence length a , which is defined as the average sum of the projections of all vectors $j \geq i$ on the direction of vector i if $L \rightarrow \infty$. It turns out that $a = b/2$. Another concrete meaning of a elucidates from the exponential in Eqn (17), which is the limiting expression of $\cos^{|i-j|} \alpha$ in Eqn (14); thus a is the length of such a piece L_{ij} of the chain the bending angle α_{ee} of which (between both its ends) obeys $\langle \cos \alpha_{ee} \rangle = 1/e \approx 0.368$.

The concept of the persistence chain has been extended by Kirste (1967) with the introduction of a persistence of curvature and torsion in addition to the persistence of direction of Kratky and Porod. As for the "worm-like chain", a persistence thread is formed by the limiting process $l_0 \rightarrow 0$, $\alpha \rightarrow 0$ and $N \rightarrow \infty$ starting from a valence angle chain. However, in addition, the angle of rotation φ (Fig. 4) is hindered and underlies simultaneously a limiting process. Thus smoothed persistence chains with additional parameters for preferred curvature and torsion can be obtained (Kirste, 1971; Oberthür, 1978).

In Figs 5a-c the influence of an increasing persistence of curvature characterized by the radius of preferred curvature R_{curv} at constant overall chain flexibility characterized by the statistical chain element b is shown.

A still closer approach to the individual behaviour of real coiled chain molecules has been attempted by Volkenstein (1963), Birshtein and Ptitsyn (1966) and Flory (1969) through a description of the short range interactions in the polymer chain by a map of conformational energies of the different rotational states. Through a statistical weighing process the individual chain dimensions, and especially $K_{r,0}$ of Eqn (11) are obtained.

2. BRANCHED AND CIRCULAR GAUSSIAN COILS

If f Gaussian coils of equal length are linked together at the same point with one of their ends, a Gaussian star molecule is obtained. Its mean square radius of gyration $\langle R^2 \rangle_{\text{star}}$ in comparison with that of a linear Gaussian coil of the same chain length $\langle R^2 \rangle_{\text{lin}}$ is given by (Zimm and Stockmayer, 1949)

$$\frac{\langle R^2 \rangle_{\text{star}}}{\langle R^2 \rangle_{\text{lin}}} = \frac{3f - 2}{f^2} \quad (21)$$

If two Gaussian coils with the same end-to-end distance r_{ee} are linked together at their four ends, a Gaussian ring is formed with a mean square radius of gyration $\langle R^2 \rangle_{\text{ring}}$ just half of that of the corresponding linear molecule of the same chain length (Zimm and Stockmayer, 1949)

$$\frac{\langle R^2 \rangle_{\text{ring}}}{\langle R^2 \rangle_{\text{lin}}} = \frac{1}{2} \quad (22)$$

It becomes evident from Eqns (21) and (22) that both branching and cyclization of polymer chains lead to a more compact coil structure in comparison with that of the corresponding linear chain.

B. Perturbed Coils

If in a solution of polymer coils the chemical potential of the solvent is non-ideal ($A_2 \neq 0$), the coil size is different from that in the unperturbed state. If $A_2 > 0$ (good solvent) the coil is expanded due to prevailing intersegmental repulsion, and if $A_2 < 0$ (poor solvent) it is shrunk due to prevailing intersegmental attraction. A relation between the mean square radius of gyration and the molar mass is (Flory, 1953, Chapter XIV; Peterlin, 1955)

$$\langle R^2 \rangle = K_{r,\epsilon} \cdot M^{1+\epsilon} \quad (23)$$

instead of Eqn (11). This is primarily an experimental relation, obtained from viscosity and light scattering experiments within a molecular weight range of

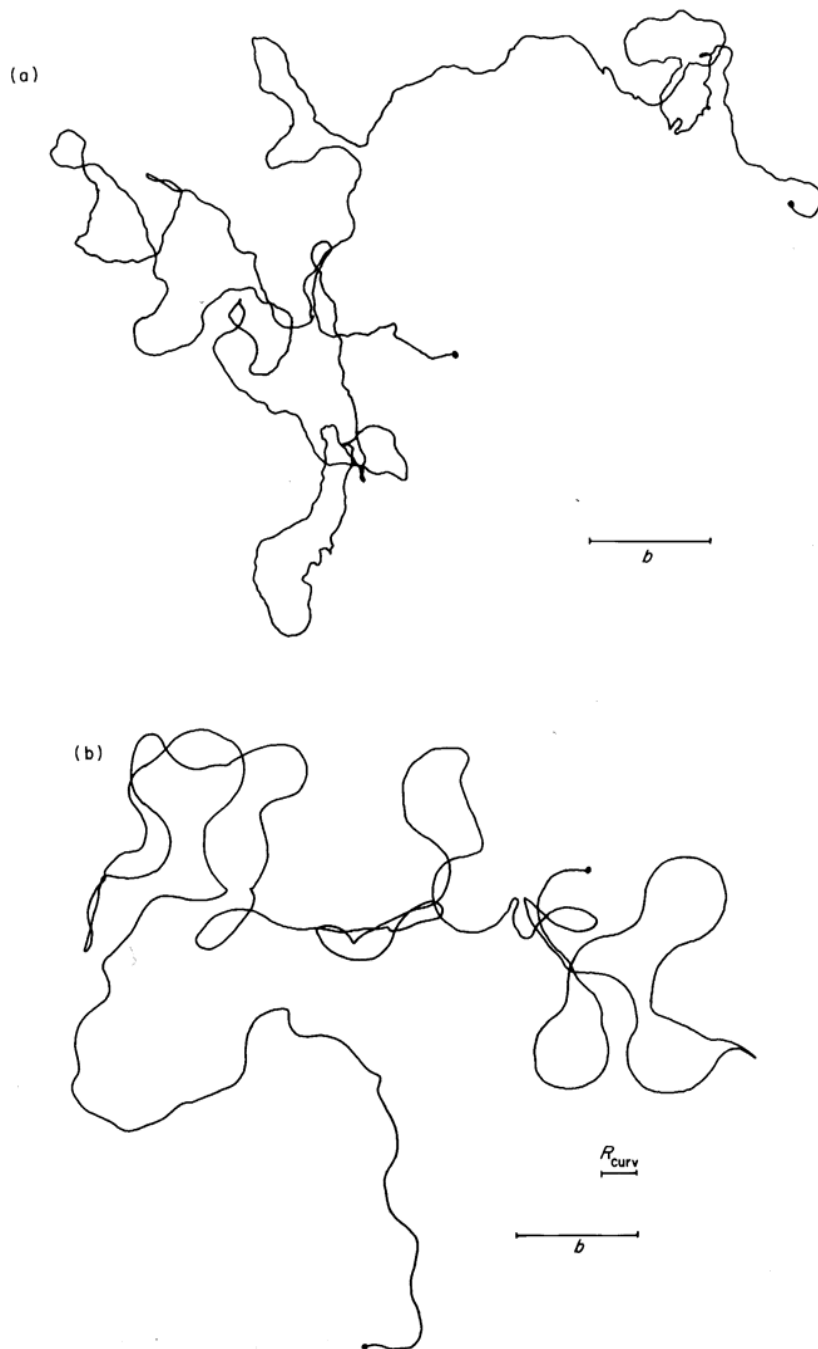


FIG. 5. Projections of computer-generated persistence coils of a length $L = 50b$ with constant persistence of direction ($b = \text{constant}$) and increasing persistence of curvature, characterized by the ratio of the radius of preferred curvature R_{curv} to the statistical chain element b : (a) $R_{\text{curv}}/b = 0$ (Kratky-Porod Chain), (b) $R_{\text{curv}}/b = 0,28$, (c) $R_{\text{curv}}/b = 0,62$.

about one or two orders of magnitude. According to these experiments ϵ is a monotonic function of A_2 : $\epsilon < 0$ for $A_2 < 0$; $\epsilon = 0$ at $A_2 = 0$ (thus recovering Eqn (11)) and $\epsilon > 0$ for $A_2 > 0$. It is an interesting experimental feature that ϵ rapidly approaches a limiting value near 0,2 with increasing A_2 (Schulz and Kirste, 1961). More accurate measurements have shown that ϵ is a function of the molecular weight. Even in good solvents one finds $\epsilon \approx 0$ for short chain molecules. With increasing chain length the value of ϵ becomes larger and again tends to a limit close to 0,2 (Kirste and Wild, 1969).

In an attempt to explain this behaviour, the random walk, unrestricted and only governed by short range sequential rules, which essentially characterizes all models of unperturbed coils, is now performed in a three-dimensional lattice and restricted by the condition that it must not return to any previously occupied lattice site (self-avoiding walk), thus simulating the repulsion between distant chain segments (cf. Fig. 3).

Calculations based on this model result in the relation

$$\langle r_{ij}^2 \rangle = A \cdot |i - j|^{1+\epsilon} \quad (24)$$

for the mean square distance $\langle r_{ij}^2 \rangle$ between two occupied lattice sites as a function of the number of steps $|i - j|$ of the walk in between, which may be compared with Eqn (12). A is a numerical constant. It turns out that $\epsilon \approx 0,2$ if $|i - j|$ tends to infinity, independent of the lattice type (cf. McKenzie, 1976). The mean square end-to-end distance of the perturbed model chain is obtained immediately from Eqn (24) and may be written, after conversion of the total

number of steps N in the self-avoiding walk, to the molar mass M of the polymer chain, in the form

$$\langle r_{ee}^2 \rangle = K_{e,\epsilon} \cdot M^{1+\epsilon} \quad (25)$$

from which the mean square radius of gyration

$$\langle R^2 \rangle = \frac{K_{e,\epsilon}}{(2+\epsilon) \cdot (3+\epsilon)} \cdot M^{1+\epsilon} = K_{r,\epsilon} \cdot M^{1+\epsilon} \quad (26)$$

is obtained, in agreement with the experimental relation of Eqn (23). Equally, for the limit of $|i-j| \rightarrow \infty$ an intersegmental distance distribution within the perturbed chain is approached, which may be written as (Fisher, 1966)

$$p(r_{ij}) = C \cdot r_{ij}^s \cdot \exp \left[-\left(\frac{r_{ij}}{\sigma} \right)^t \right] \quad (27)$$

with

$$C = \frac{t}{\sigma^{s+1} \cdot \Gamma \left(\frac{s+1}{t} \right)} \quad \text{and} \quad \sigma^2 = \frac{\langle r_{ij}^2 \rangle \cdot \Gamma \left(\frac{s+1}{t} \right)}{\Gamma \left(\frac{s+3}{t} \right)}$$

and where t is related to ϵ by $t = 2/(1-\epsilon)$.

With $\epsilon = 0$ and $s = t = 2$ the Gaussian distribution of Eqn (9) is recovered. Since the above relations on perturbed chains are not rigorous deductions from the described model, but based on analytical approaches to computer-simulations of the self-avoiding walk, several authors have used different values of ϵ , s and t in their calculations of scattering functions of expanded coils

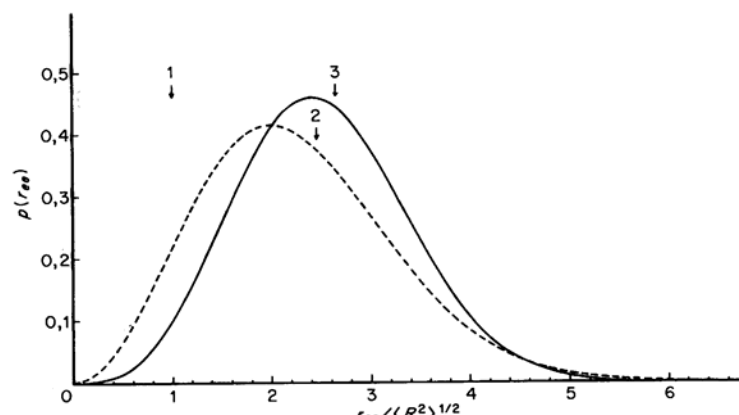


FIG. 6. End-to-end distance distribution functions, corresponding to the scattering curves of Fig. 14, for a perturbed coil (drawn curve) with $\epsilon = 0.2$, $s = 2.8$ and $t = 2.5$ and for a Gaussian coil (dashed curve) with $\epsilon = 0$, $s = t = 2$. Arrow 1 indicates the root mean square radius of gyration for both coils, arrows 2 and 3 the root mean square end-to-end distances for the Gaussian coil and the perturbed coil respectively.

(see Section III.B). However, values of $\epsilon = 0.2$, $s = 2.8$ and $t = 2.5$ seem to give the best agreement with concrete experimental data (cf. Fig. 23). The corresponding intersegmental distance distribution function is narrower than a Gaussian distribution (Fig. 6) and it shows that especially short intersegmental distances are avoided in the expanded coil.

III. Scattering Functions of Coil Molecules

Scattering functions of single polymer coils may be calculated according to the formula of Debye (1915) for the scattering of X-rays by single molecules

$$I_n(h) = \frac{1}{N^2} \cdot \sum_{i=1}^N \sum_{j=1}^N \left\langle \frac{\sin h \cdot r_{ij}}{h \cdot r_{ij}} \right\rangle , \quad (28)$$

where N is the total number of scattering centres.

Since the distance r_{ij} is variable with time, the average of the interference terms of each spacing has to be taken. This can be done appropriately if the distribution function $p(r_{ij})$ is known:

$$\left\langle \frac{\sin h \cdot r_{ij}}{h \cdot r_{ij}} \right\rangle = \int_0^\infty p(r_{ij}) \cdot \frac{\sin h \cdot r_{ij}}{h \cdot r_{ij}} \cdot dr_{ij} \quad (29)$$

Generally, it must be taken into consideration that $p(r_{ij})$ depends explicitly on i , j and N . But it is always assumed that only $|i-j|$ through $\langle r_{ij}^2 \rangle$ enters into this function. The physical meaning of this simplification is, that the temporal distribution of the distances between two segments with the separation $|i-j|$ along the chain does not depend on the total chain length. This assumption is exactly valid in unperturbed chains, whereas it is an approximation in perturbed ones.

Nevertheless, for all cases of practical interest to be considered in this chapter we may write Eqn (28) in the form

$$I_n(h) = \frac{2}{N^2} \sum_{|i-j|=0}^N (N - |i-j|) \cdot \int_0^\infty p(r_{ij}) \frac{\sin h \cdot r_{ij}}{h \cdot r_{ij}} \cdot dr_{ij} \quad (30)$$

Here $(N - |i-j|)$ is obviously the statistical weight of each $|i-j|$ in the linearly ordered set of N scattering centres. Thus Eqn (30) can be evaluated if both $p(r_{ij})$, and its parameter $\langle r_{ij}^2 \rangle$ as a function of $|i-j|$ are known.

A. Unperturbed Coils

1. SCATTERING FUNCTION OF MONODISPERSE GAUSSIAN COILS

The simplest procedure for obtaining a coil scattering function is the introduction of the Gaussian distribution of Eqn (9) together with Eqns (7) and (8)

into Eqn (30). For this distribution the integral of Eqn (29) can be solved analytically and it yields

$$\left\langle \frac{\sin h \cdot r_{ij}}{h \cdot r_{ij}} \right\rangle = \exp \left[-\frac{h^2 \cdot \langle r_{ij}^2 \rangle}{6} \right] \quad (31)$$

So Eqn (30) becomes

$$I_n(h) = \frac{2}{N^2} \sum_{|i-j|=0}^N (N - |i-j|) \cdot \exp \left[-\frac{h^2 \cdot \langle r_{ij}^2 \rangle}{6} \right] \quad (32)$$

with

$$\langle r_{ij}^2 \rangle = b^2 \cdot |i-j|$$

Equation (32) has been calculated by Debye (1947) with the result

$$I_n(h) = \frac{2(e^{-x} + x - 1)}{x^2} \quad (33)$$

with $x = \langle R^2 \rangle \cdot h^2$.

A characteristic feature of this function is its asymptotic h^{-2} -course for large h (Fig. 7a):

$$\lim_{h \rightarrow \infty} I_n(h) = \frac{2}{x} \left(1 - \frac{1}{x} \right) \quad (34a)$$

and

$$\lim_{h \rightarrow \infty} h^2 \cdot I_n(h) = \frac{2}{\langle R^2 \rangle} \left(1 - \frac{1}{h^2 \cdot \langle R^2 \rangle} \right) \quad (34b)$$

If the scattering function is normalized to the molar mass M , this equation enables the determination of the characteristic ratio $\langle R^2 \rangle / M = K_{r,0} = b / 6M_L$ immediately from the asymptotic h^{-2} course:

$$\lim_{h \rightarrow \infty} h^2 \cdot M \cdot I_n(h) = \frac{12M_L}{b} \cdot \left(1 - \frac{6M_L}{h^2 \cdot M \cdot b} \right) \quad (34c)$$

With $M_L = M_0/p_0$ (M_0 = molar mass of the monomer unit, p_0 pitch of the monomer unit in the extended chain conformation), also the statistical chain element can be obtained.

The corresponding scattering law for the star-shaped polymer with f branches reads (Benoit, 1953)

$$I_n(h) = \frac{2}{x^2} \left[\frac{f}{2} (f-1) e^{-\frac{2x}{f}} - f(f-2) e^{-\frac{x}{f}} + x + \frac{f}{2} (f-3) \right] \quad (35)$$

where $x = nb^2h^2/6 = f^2(3f-2)\langle R^2 \rangle h^2$, and n denotes the number of statistical chain elements in the coil. At large h this function approaches the same h^{-2} asymptote as Eqn (33) (Fig. 7a):

$$\lim_{h \rightarrow \infty} I_n(h) = \frac{2}{x} \left[1 + \frac{2}{x} \left(\frac{f^2 - 3f}{4} \right) \right] \quad (36a)$$

$$\lim_{h \rightarrow \infty} h^2 \cdot I_n(h) = \frac{6f - 4}{f^2 \langle R^2 \rangle} \left[1 + \frac{(f/2 - 1)(f^2 - 3f)}{f^2 h^2 \langle R^2 \rangle} \right] \quad (36b)$$

$$\lim_{h \rightarrow \infty} h^2 \cdot M \cdot I_n(h) = \frac{12M_L}{b} \left[1 + \frac{12M_L}{h^2 Mb} \right] \quad (36c)$$

A similar behaviour is exhibited by a Gaussian ring, the structure factor of which may be approached by series expansions for high and for low values of h (cf. Casassa, 1965). Its asymptotic h^{-2} -course is approached as follows (Fig. 7a):

$$\lim_{h \rightarrow \infty} I_n(h) = \frac{2}{x} \left[1 + \frac{2}{x} \right] \text{ with } x = nb^2h^2/6 = 2\langle R^2 \rangle h^2 \quad (37a)$$

$$\lim_{h \rightarrow \infty} h^2 \cdot I_n(h) = \frac{1}{\langle R^2 \rangle} \left[1 + \frac{1}{h^2 \langle R^2 \rangle} \right] \quad (37b)$$

$$\lim_{h \rightarrow \infty} h^2 \cdot M \cdot I_n(h) = \frac{12M_L}{b} \left[1 + \frac{12M_L}{h^2 Mb} \right] \quad (37c)$$

Since Eqn (33) actually was deduced for the limit of infinitely long chains (cf. Eqns (8) and (9)), a good agreement with experimental scattering curves, including the asymptotic behaviour of Eqns (34a-c), can be expected only if $L \gg b$ and $r_{ij} \gg b$. In practice this means that Eqn (33) is obeyed (with a deviation of less than 1%) by high molecular weight polymers under theta-conditions with $M/M_L = L \gtrsim 250b$ at low values of momentum transfer h (large r_{ij}) with $h \cdot b \lesssim 0.3$ and with a narrow molar mass distribution of the sample with a non-uniformity of $U \lesssim 0.05$ (cf. seq.).

To overcome these restrictions in the interpretation of the scattering of polymer molecules, further refinements of the previous calculation have been performed.

2. SCATTERING FUNCTION OF POLYDISPERSE GAUSSIAN COILS

The shape of the scattering function is influenced by the molecular weight distribution in the following way:

$$M_w \cdot \langle I_n(h) \rangle_z = \int_0^\infty I_n(h, M) \cdot M \cdot m(M) \cdot dM = M_w \left(1 - \frac{\langle R^2 \rangle_z}{3} \cdot h^2 + \dots \right) \quad (38)$$

where $m(M)$ is the mass distribution function of the polymer, M_w is the weight average of the molar mass, whereas $\langle I_n(h) \rangle_z$ and $\langle R^2 \rangle_z$ are the z-averages of the structure factor and the mean square radius of gyration, respectively.

The inversion of this transform would yield the molecular weight distri-

bution from the measured scattering intensity and the known monodisperse scattering function $I_n(h, M)$. This has been tried recently by Greschner (1973). However, the calculation shows that for practical use an inaccessibly high accuracy of the intensity measurements (better than 0.1%) would be necessary.

In 1948, Zimm combined Eqn (33) with a Schulz-distribution of the molar mass (Schulz, 1939)

$$m(M) = \frac{1}{\Gamma(k+1)} \cdot \left(\frac{k+1}{M_w} \right)^{k+1} \cdot M^k \cdot \exp \left[-(k+1) \cdot \frac{M}{M_w} \right] \quad (39)$$

with

$$k = 1/U \quad \text{and} \quad U = \frac{M_w}{M_n} - 1$$

U the non-uniformity is a measure of the width of the distribution function, and M_n is the number average molar mass. Though Eqn (39) is a special type of molecular weight distribution function, it can be used in many cases, especially if the polymer has been fractionated and the molecular weight distribution exhibits only one narrow peak. The result of Zimm's calculation presented in a more convenient form (Greschner, 1973) may be written as

$$\langle I_n(h) \rangle_z = \frac{2[(1 + U \cdot \xi)^{-\frac{1}{U}} + \xi - 1]}{(1 + U) \cdot \xi^2} \quad (40)$$

with

$$\xi = \frac{\langle R^2 \rangle_z}{1 + 2U} \cdot h^2$$

This function again exhibits an asymptotic h^{-2} -course like Eqn (33) (Fig. 7):

$$\lim_{h \rightarrow \infty} \langle I_n(h) \rangle_z = \frac{2}{1 + U} \left(\frac{1}{\xi} - \frac{1}{\xi^2} \right) \quad (41a)$$

$$\lim_{h \rightarrow \infty} h^2 \cdot \langle I_n(h) \rangle_z = \frac{2(1 + 2U)}{(1 + U) \langle R^2 \rangle_z} \cdot \left(1 - \frac{1 + 2U}{h^2 \cdot \langle R^2 \rangle_z} \right) \quad (41b)$$

$$\lim_{h \rightarrow \infty} h^2 \cdot M_w \cdot \langle I_n(h) \rangle_z = \frac{12M_L}{b} \cdot \left(1 - \frac{6M_L}{h^2 \cdot M_n \cdot b} \right) \quad (41c)$$

So the statistical chain element b can be determined in the same way as in the case of monodisperse coils.

The occurrence of M_n in the asymptote (Eqn 41c) may be used for a simultaneous determination of M_w from $h \rightarrow 0$ and of M_n from $h \rightarrow \infty$ in a Zimm-plot as suggested by Benoit (1953), according to

$$\lim_{h \rightarrow 0} [M_w \cdot \langle I_n(h) \rangle]^{-1} = \frac{1}{M_w} + \frac{\langle R^2 \rangle_z \cdot h^2}{3M_w} \quad (42a)$$

and

$$\lim_{h \rightarrow \infty} [M_w \cdot \langle I_n(h) \rangle]^{-1} = \frac{1}{2M_n} + \frac{\langle R^2 \rangle_w \cdot h^2}{2M_w} \quad (42b)$$

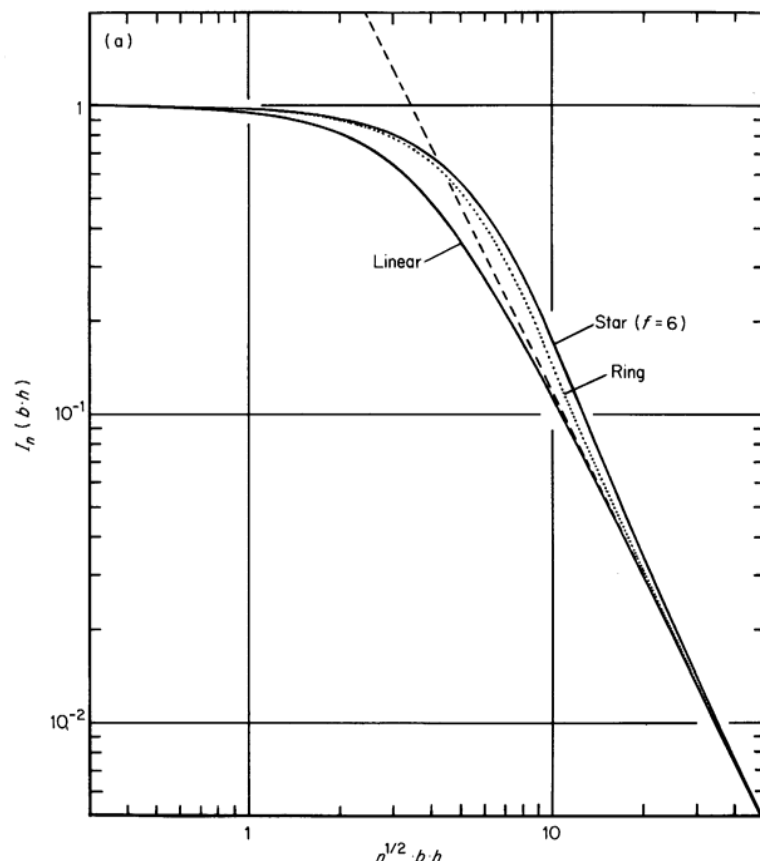


FIG. 7(a).

which can be derived from Eqn (38) immediately and is in fact independent of a given molecular weight distribution. For a criticism of an evaluation procedure based on these equations see Greschner (1973).

From Eqn (40) it follows that for $U < 1$ the scattering curve in a Zimm-plot has an upwards and for $U > 1$ a downwards curvature, whereas for $U = 1$ it corresponds exactly to a straight line (cf. Eqns 42a, b and Fig. 1a, b), which can be used as a rough estimate of U . In general, however, the non-uniformity is obtained from other techniques and then introduced for correction. If a polymer sample is given with a certain M_w and a certain $\langle R^2 \rangle_w$, one may ask whether a monodisperse coil with $M = M_w$ exhibits a radius of gyration $\langle R^2 \rangle$ which is identical to $\langle R^2 \rangle_w$ of the polydisperse sample. The answer is that this is true only if $\langle R^2 \rangle \propto M$. In this case $\langle R^2 \rangle_z$ may be corrected to $\langle R^2 \rangle = \langle R^2 \rangle_w$ by the equation of Altgelt and Schulz (1960) provided that the heterogeneity of M can be approximated by Eqn (39):

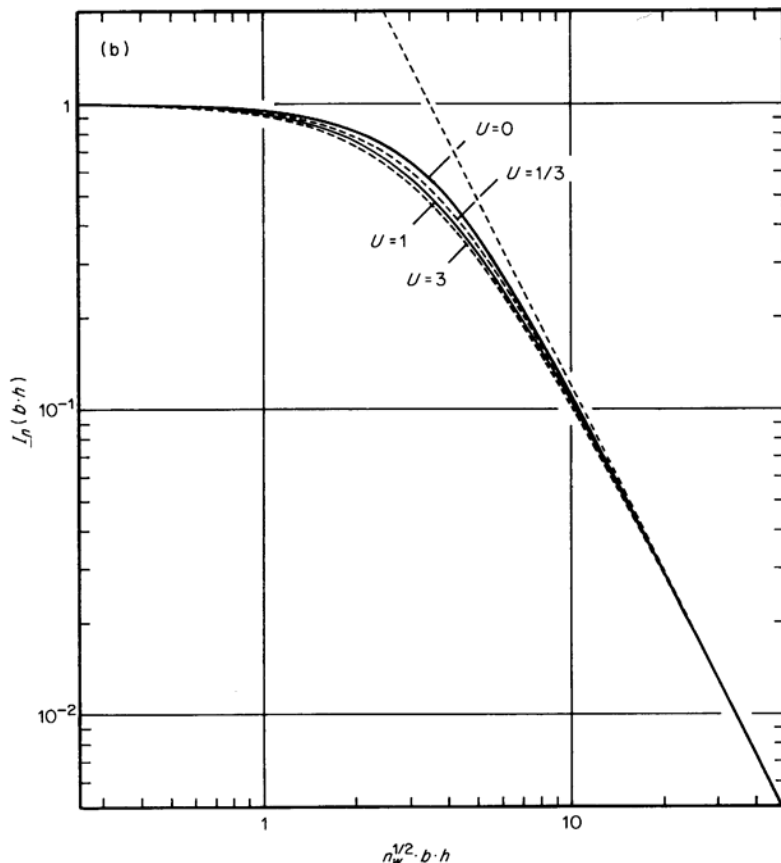


FIG. 7. Structure factors of Gaussian coils. (a) Linear, circular and six branched star-shaped Gaussian coils. (b) Linear Gaussian coils with increasing polydispersity (Schulz distribution) characterized by non-uniformity U . The dashed straight line is the h^{-2} -asymptote which is approached by all curves for $h \rightarrow \infty$.

$$\langle R^2 \rangle = \frac{1+U}{1+2U} \langle R^2 \rangle_z \quad (43)$$

In all other cases (e.g. persistence coils, rods and expanded coils), however, more complex equations must be used to correct the radius of gyration for the polydispersity of the sample (Oberthür, 1978) (cf. Fig. 17).

The best possibility for the direct determination of the polydispersity by scattering experiments results from the deviation of the scattering curve of a polydisperse sample from that of a monodisperse sample as shown in Fig. 7. For $U=1$ the maximum deviation is as big as 12%. If the scattering curve of a polymer sample under theta-conditions can be taken in the range of this maximum

deviation with an error of less than 0.3%, a non-uniformity of $U \approx 0.01$ can still be detected by a least squares fit of Eqn (40) to the experimental data (Hack and Meyerhoff, 1978).

This procedure, however, is limited to small values of U , where the type of the distribution function is of minor importance. Furthermore, since the validity of Eqn (33) with an accuracy of about 0.1% is demanded, it should be restricted to polymer coils with a length of $L \gtrsim 1000b$ and a range of momentum transfer of $h \cdot b \lesssim 0.1$, where the influence of the structure of the polymer thread on the scattering is still negligible.

3. SCATTERING FUNCTIONS OF PERSISTENCE CHAINS

A persistence chain is made up of an infinitely thin filament, which is subjected to a specified bending procedure, and hence tends to the formation of a statistical coil. Its scattering function therefore should approach the scattering of a Gaussian coil (Eqn 33) for $h \rightarrow 0$ and $L \rightarrow \infty$, and it should approach the scattering of an infinitely thin and long rod for $h \rightarrow \infty$.

The structure factor of an infinitely thin rod (needle) of length L (see Fig. 2) has been calculated by Neugebauer (1943):

$$I_n(h) = \frac{2}{h \cdot L} \cdot \left[Si(h \cdot L) - \frac{1 - \cos(h \cdot L)}{h \cdot L} \right] \quad (44)$$

where

$$Si(x) = \int_0^x \frac{\sin x}{x} \cdot dx.$$

For $h \rightarrow \infty$ this function tends to an asymptotic h^{-1} course, which is approached from below:

$$\lim_{h \rightarrow \infty} I_n(h) = \frac{\pi}{h \cdot L} - \frac{2}{h^2 \cdot L^2} \quad (45)$$

If the scattering function is normalized to the molar mass of the rod and multiplied by h^2 , this asymptotic equation reads

$$\lim_{h \rightarrow \infty} h^2 \cdot M \cdot I_n(h) = \pi \cdot M_L \cdot h - \frac{2M_L}{L} \quad (45a)$$

For $L \rightarrow \infty$, on the other hand, Eqn (44) reduces to the scattering of an infinitely thin and long rod, which in the same presentation as the previous equation is given by

$$\lim_{L \rightarrow \infty} h^2 \cdot M \cdot I_n(h) = \pi \cdot M_L \cdot h \quad (46)$$

This equation corresponds to a straight line through the origin in a plot of $h^2 \cdot M \cdot I_n(h)$ versus h , the slope of which allows the determination of the mass per unit length M_L of the thread.

Such a plot, usually called a Kratky-plot, has been suggested by Kratky and Porod (1949) to visualize the transition from the coil scattering behaviour according to Eqn (33) with an asymptote parallel to the abscissa (Eqn 34c) to the asymptotic rod scattering behaviour of Eqn (46). This transition obviously only depends on the flexibility of the chain. The point of intersection between both asymptotes is obtained from

$$\frac{12M_L}{b} = \pi \cdot M_L \cdot h^* \quad \text{yielding } h^* \cdot b = 3,820 \quad (47)$$

Consequently, from the intersection point the statistical chain element b can be obtained without knowledge of the absolute intensity of the scattering, in contrast to the use of Eqn (34c).

These considerations give a sketch of the principal course of the scattering function of a persistence chain (cf. Fig. 16), its correct calculation, however, has encountered great difficulties.

In 1960 Peterlin used a new way to calculate model scattering functions of polymer coils: the Monte Carlo method. This method has since been applied by many authors and the results in some cases proved to be more elucidating than those from analytical calculations. In Monte Carlo calculations, a great number of random conformations of the thread are generated by a computer. The scattering function is then calculated according to Eqn (28), where the average is taken over all the generated conformations, usually in the order of 1000. In these calculations, of course, it is not possible to perform strictly the limiting process $\alpha \rightarrow 0$, $l_0 \rightarrow 0$, $N \rightarrow \infty$ (cf. page 396). Only small values of α and l_0 can be chosen.

A good example for Monte Carlo calculations of the scattering curves of persistence chains in a wide range of relative chain length $L/b = n$ has been given by Heine *et al.* (1962), who used $\cos \alpha = 0,9$ and $l_0 = b/20$. The obtained results show a good agreement with later analytical calculations.

Three different analytical approaches finally have solved the problem of the scattering of the Kratky-Porod-chain: using a modified Daniels distribution Sharp and Bloomfield (1968) obtained

$$M \cdot I_n(h) = \frac{2M \cdot (e^{-x} + x - 1)}{x^2} + \left[\frac{4}{15} + \frac{7}{15x} - \left(\frac{11}{15} + \frac{7}{15x} \right) e^{-x} \right] \cdot M_L \cdot b \quad (48)$$

with

$$x = \frac{L \cdot b \cdot h^2}{6}$$

For $L > 10b$ and $b^2 \cdot h^2 < 10$ this function is valid with an accuracy better than 1%.

Yamakawa and Fujii (1974) used a series expansion of the average of the interference term of each spacing given in Eqn (29):

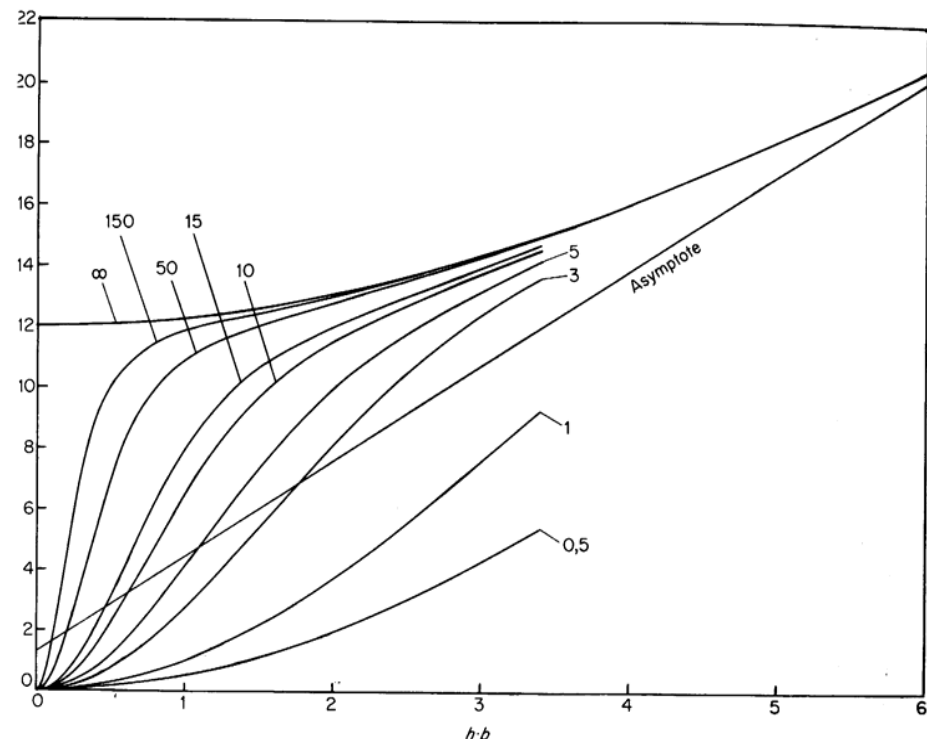


FIG. 8. Scattering functions of Kratky-Porod-chains. The parameter is $n = L/b$, $n = 0,5 - 15$: Yamakawa and Fujii (1974); $n = 50$ and 150 : Sharp and Bloomfield (1968); $n = \infty$: des Cloizeaux (1973). The asymptote corresponds to Eqn (51b).

$$\left\langle \frac{\sin h \cdot r_{ij}}{h \cdot r_{ij}} \right\rangle = \exp \left[-\frac{h^2 \cdot \langle r_{ij}^2 \rangle}{6} \right] \cdot \sum_{m=0}^{\infty} g_{2m} \cdot h^{2m} \quad (49)$$

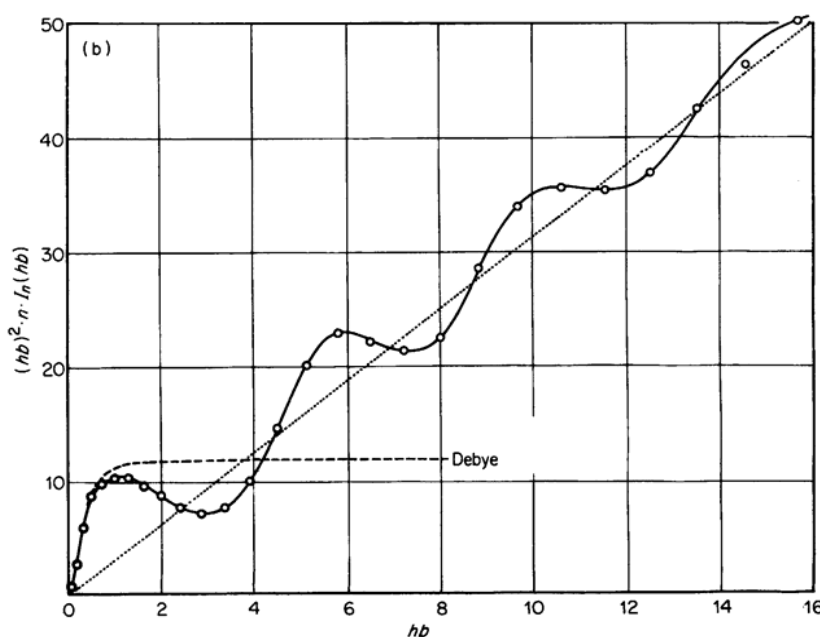
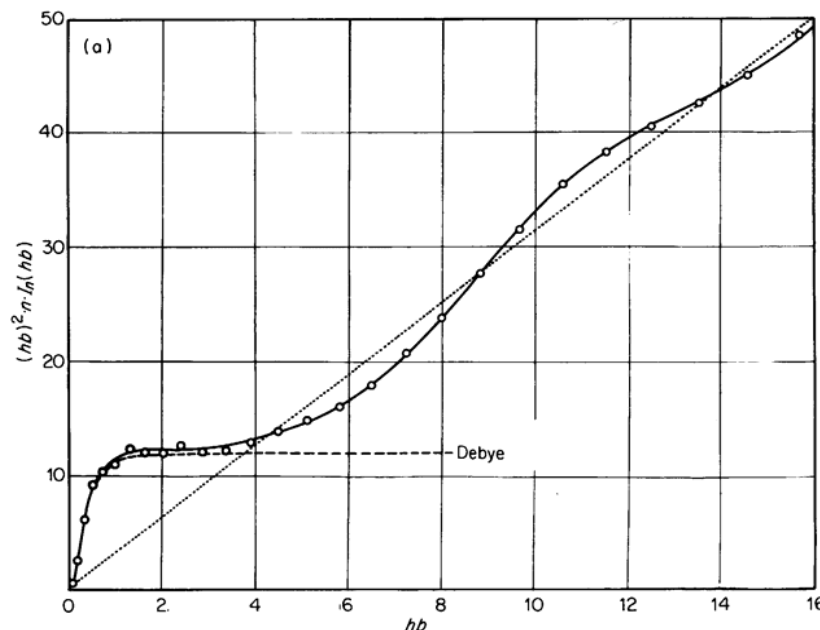
Here $\sum g_{2m} \cdot h^{2m}$ is the Hermite's expansion with $g_0 = 1$, $g_2 = 0$ and

$$g_{2m} = \sum_{k=0}^{m-2} \frac{(-1)^{m-k} \langle r_{ij}^2 \rangle^k \langle r_{ij}^{2(m-k)} \rangle}{(3!)^k \cdot k! [2(m-k)+1]!} - \frac{(m-1) \langle r_{ij}^2 \rangle^m}{(3!)^m \cdot m!} \quad (50)$$

for $m \geq 2$.

The coefficients have been calculated up to g_{22} , which affords the calculation of the moments of the distance distribution (cf. page 394) up to $\langle r_{ij}^{22} \rangle$. Especially the scattering of short persistence chains at low values of $h \cdot b$ (cf. Fig. 8) can be obtained by this method, whereas the convergence of this procedure becomes poorer at large values for the chain length and for $h \cdot b$.

For the infinitely long chain at all values of the reduced momentum transfer $h \cdot b$ the exact solution of the scattering function of the Kratky-Porod chain has been given by des Cloizeaux (1973) in a series expansion.



For the limits of $h \rightarrow 0$ his function is reduced to

$$\lim_{\substack{L \rightarrow \infty \\ h \rightarrow 0}} h^2 \cdot M \cdot I_n(h) = \frac{12M_L}{b} + \frac{4M_L \cdot b}{15} \cdot h^2 \quad (51a)$$

which may be obtained from Eqn (48) as well, whereas for the limits of $h \rightarrow \infty$ des Cloizeaux's function reads

$$\lim_{\substack{L \rightarrow \infty \\ h \rightarrow \infty}} h^2 \cdot M \cdot I_n(h) = \pi \cdot M_L \cdot h + \frac{4M_L}{3b}. \quad (51b)$$

This corresponds to a straight line parallel and above the asymptote of Eqn (46) (Fig. 8), and may be compared with Eqn (45a).

In Fig. 8 the function of des Cloizeaux is plotted together with those of Yamakawa and two examples of Sharp and Bloomfield (Eqn 48). It becomes evident that for $L/b = n > 50$, Eqn (48) has attained the function of des Cloizeaux within the given limits, which in turn approaches its asymptote (Eqn 51b) in a strongly damped oscillation (cf. Fig. 21). This means that the scattering of a Kratky-Porod chain can be expressed by means of two functions with an accuracy better than 1%, if only its length exceeds 50 statistical chain elements.

If an increasing persistence of curvature in addition to the persistence of direction of the Kratky-Porod chain is introduced into a persistence chain, regularities are produced in the distance distribution of the coiled filaments. These regularities are reflected in the scattering curves. Kirste (1967) has calculated a series of scattering curves with an increasing ratio of the radius of preferred curvature to the statistical chain element R_{curv}/b by the described Monte Carlo procedure. The results (Fig. 9a and b) show an increasing deviation from the Debye scattering curve of Eqn (33) even at low values of $h \cdot b$, whereas at large $h \cdot b$ the scattering curves show asymptotic oscillations around the scattering function of the thin rod of infinite length (Eqn 46), the periods of which are shifted to lower values of momentum transfer h with increasing radius of preferred curvature R_{curv} at constant statistical chain element b . The reliability of the method follows from the fact that the same procedure applied to the Kratky-Porod chain yielded a function which agrees with the described analytical results within a few percent.

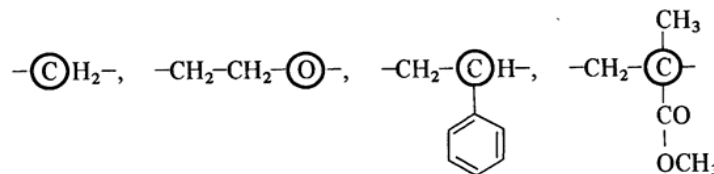
FIG. 9. Scattering functions of persistence chains of length $L = 100b$ with constant persistence of direction and increasing persistence of curvature (cf. Figs 5b and c), together with the functions of an infinitely long rod (dotted line, Eqn 46) and a Gaussian coil (dashed curve, Eqn 33): (a) $R_{\text{curv}}/b = 0.28$, (b) $R_{\text{curv}}/b = 0.62$.

4. SCATTERING FUNCTIONS OF INDIVIDUAL POLYMER CHAINS

Recently Yoon and Flory (1975, 1976a, b) used the statistical conformations of individual synthetic polymers based on conformational energy maps (rotational isomeric state model) for the calculation of scattering functions. They carried out the calculations for polymethylene (PM), polyethylene oxid (PEO), as well as for polystyrene (PS) and polymethylmethacrylate (PMMA) of varying tacticity.

Partly the scattering curves were obtained from a series expansion in terms of the even moments $\langle r_{ij}^{2m} \rangle$ of the individual distance distributions (cf. Eqn 49) and partly from Monte Carlo calculations based on the statistical weight of the different rotational isomers derived from the conformational energies.

For each monomeric group one atom was taken as a point scatterer marked by a circle in the following structural formulae:



This procedure results in a sequence of points representing the structure of the polymer in solution.

First of all the scattering curve of the PM-chain calculated by the Monte Carlo procedure (open circles in Fig. 10) will be considered. From $C_\infty = 6,87$ (Flory, 1969, p. 170) the characteristic ratio of Eqn (11) can be obtained according to

$$K_{r,0} = \frac{\langle R^2 \rangle}{M} = \frac{N_0 \cdot l_0^2 C_\infty}{6 \cdot M_0} = 0,191 \text{ Å}^2 \cdot \text{mol} \cdot \text{g}^{-1} \quad (52)$$

where $l_0 = 1,53 \text{ Å}$ is the length of a skeletal bond. $N_0 = 1$ is the number of bonds and $M_0 = 14,0 \text{ g mol}^{-1}$ the molar mass of the monomer unit CH_2 . Since the number of monomer units in the chain, for which the scattering function has been calculated (Yoon and Flory, 1976a), is $X + 1 = 1001$, its molar mass is $M = 1,40 \cdot 10^4 \text{ g mol}^{-1}$.

From these data, the Debye scattering function according to Eqn (33) can be calculated. It turns out that it permits a satisfactory description of the PM-scattering only up to $h \approx 0,05 \text{ Å}^{-1}$. However, a better approximation to the PM-coil is attained by a Kratky-Porod chain with $M_L = 11,04 \text{ g} \cdot \text{mol}^{-1} \cdot \text{Å}^{-1}$ (pitch per monomer unit of the extended (all-trans) PM-chain $p_0 = 1,268 \text{ Å}$) and hence $b = 12,68 \text{ Å}$ and $L/b = n = 100$. Application of Eqn (48) together with the function of des Cloizeaux (1973) yields the corresponding scattering

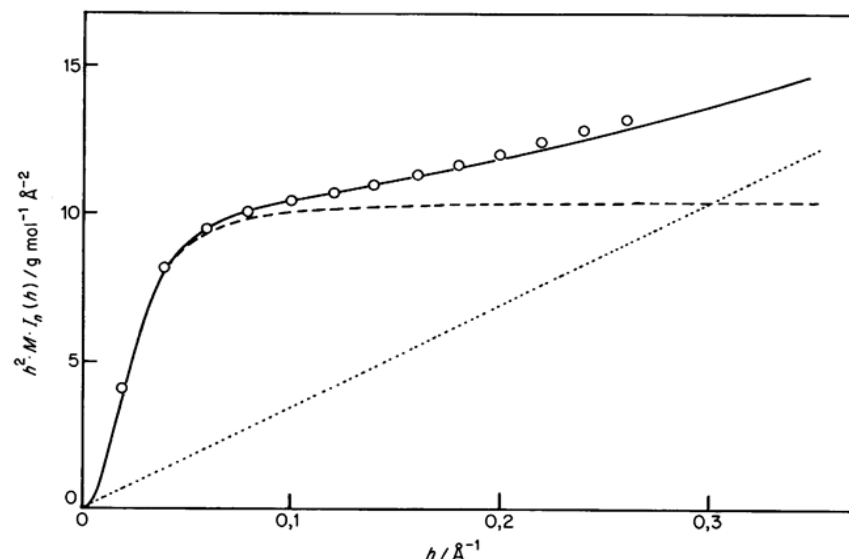


FIG. 10. Scattering functions for PM-chains according to Monte-Carlo-calculations of Yoon and Flory (1976a) for $M = 1,40 \cdot 10^4 \text{ g}(\text{mol})^{-1}$ (open circles), together with the scattering functions of a Gaussian coil (dashed curve) and a Kratky-Porod chain (drawn curve) with the same characteristics ($M_L = 11,04 \text{ g}(\text{mol} \cdot \text{Å})^{-1}$; $b = 12,68 \text{ Å}$). The dotted straight line is the corresponding scattering asymptote of a rod (Eqn 46).

function. Its coincidence with the calculated PM-scattering up to $h \approx 0,2 \text{ Å}^{-1}$ possibly reflects the similarity in the random choice of the rotational angle φ (Fig. 4) in both the bending mechanism of the Kratky-Porod chain and the PM-chain. The deviations at larger values of h may be due to the finite values of α , l_0 and φ (Fig. 4) for the PM-chain in contrast to the continuous worm-like chain.

The most striking example of the application of the rotational isomeric state model for the description of polymer chains, however, pertains to PMMA.

Since its monomer unit has an asymmetric C-atom, this polymer can exist in an isotactic (*i*-PMMA) and in a syndiotactic (*s*-PMMA) configuration (Fig. 11).

As demonstrated in Fig. 12, both configurations show appreciable differences in their scattering behaviour (Yoon and Flory, 1975, 1976b). First of all the chain flexibilities are different as reflected by the different heights of the Debye plateaus (isotactic: $C_\infty = 10,3$; syndiotactic: $C_\infty = 7,5$). Then, especially in the case of *s*-PMMA, the course of the scattering curve exhibits pronounced deviations from the Debye-function even at low h -values. This peculiar behaviour must be born in the conformational particularities of the PMMA chain.

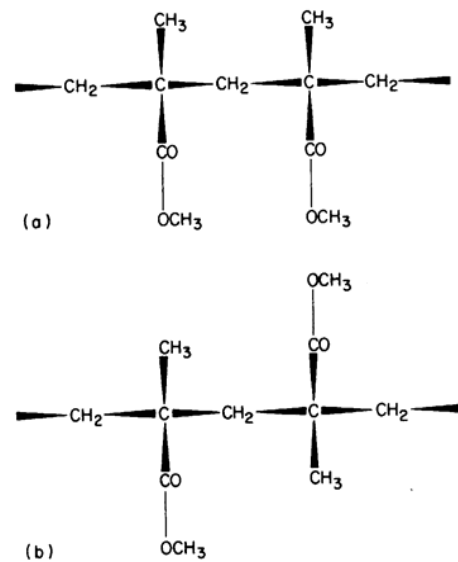


FIG. 11. Configuration of (a) isotactic PMMA (meso-dyad), (b) syndiotactic PMMA (racemic dyad).

In PMMA the two skeletal bond angles are not equal. This leads to a pronounced curvature of the polymer chain in its all-trans conformation (Fig. 13) with $R_{\text{curv}} = 12.8 \text{ \AA}$ for the C^α -atoms. Furthermore, in *s*-PMMA the racemic dyads are energetically favoured in their trans-trans conformation with regard to their gauche-trans conformation, which is much less the case for the meso-dyads in *i*-PMMA. This has as a consequence an average sequence of 9 monomer units in all-trans conformation in *s*-PMMA, in comparison with only 3 units for *i*-PMMA (Yoon and Flory, 1975). These particular features readily account for the great differences in the scattering behaviour of the two configurations of PMMA (Fig. 12).

Especially in the case of *s*-PMMA, the regularities in the conformation are clearly reflected in the oscillations of the scattering curve around the infinite rod asymptote (Eqn 46), which may be compared with the scattering functions of the persistence chains with preferred curvature of Kirste (Fig. 9a and b).

On the other hand, *i*-PMMA is much closer to the worm-like chain behaviour, reflecting its more random bending mechanism.

Although the rotational isomeric state model is the most realistic approach to the conformation of real polymer chains, the thickness of the chain has still been neglected in the calculations of the scattering functions. However, the thickness of a dissolved polymer thread not only includes all the atoms of the

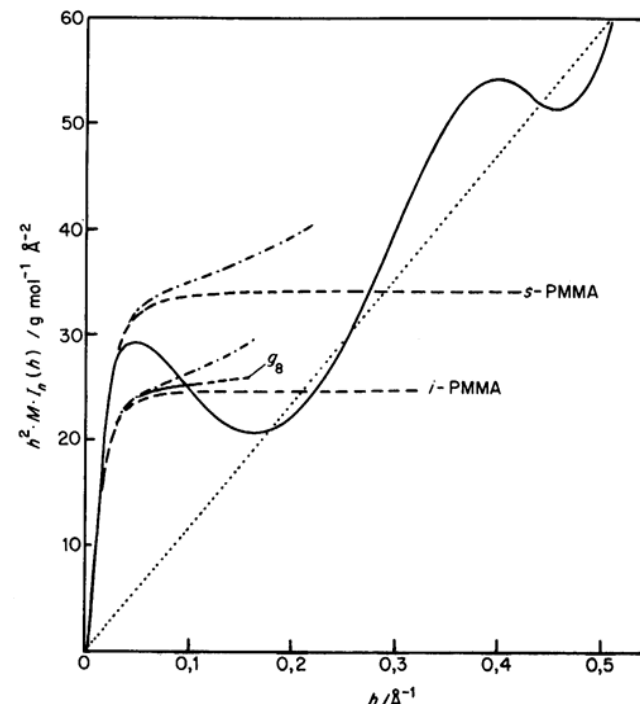


FIG. 12. Scattering functions for PMMA of $M = 1.00 \cdot 10^5 \text{ g}(\text{mol})^{-1}$ with $M_L = 37.3 \text{ g}(\text{mol} \cdot \text{\AA})^{-1}$. Dotted line and dashed curves: cf. Fig. 10. Dash-dotted curves: scattering of Kratky-Porod chains with the same statistical chain element as *i*-PMMA ($b = 18.0 \text{ \AA}$) and *s*-PMMA ($b = 13.1 \text{ \AA}$), respectively (cf. Schulz *et al.*, 1964). The drawn curve for *s*-PMMA is based on a Monte-Carlo calculation (Yoon and Flory, 1976b), the drawn curve for *i*-PMMA has been obtained by a series expansion according to Eqn (49), truncated at g_8 (Yoon and Flory, 1975). Its dashed continuation stands for the limit of reliability of this calculation.

macromolecule itself, but also the fluctuations of the solvent around the dissolved polymer chain.

If a Gaussian electron density distribution in the cross-section of an infinitely long rod is assumed, its scattering function is given by (cf. Eqn 46)

$$M \cdot I_n(h) = \frac{\pi \cdot M_L}{h} \cdot \exp \left(-\frac{R_c^2 \cdot h^2}{2} \right) \quad (53)$$

where R_c is the radius of gyration of the cross-section. A value of $R_c = 2.2 \text{ \AA}$, which is typical for substituted vinyl polymers, would already lead to an intensity drop of a calculated function of an infinitely thin chain by 10% at $h = 0.2 \text{ \AA}^{-1}$. On the other hand, as Kirste (1964) has demonstrated, the solvent fluctuations around the polymer thread, which are in the same order of

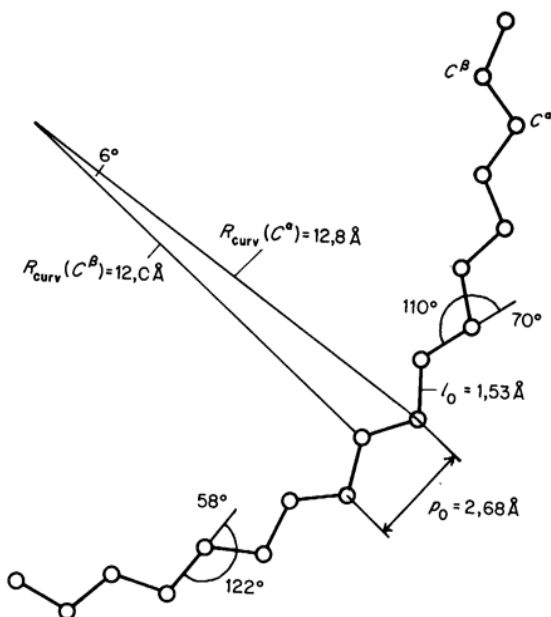


FIG. 13. Segment of the polymer backbone of PMMA in all-trans conformation (data for bond length and valence angles from Yoon and Flory, 1976b).

magnitude as the thread diameter, can easily influence the structure factor of the cross-section in the opposite way, so that interpretations of scattering curves of chain molecules beyond $h \simeq 0,2 \text{ \AA}^{-1}$ are always affected by some ambiguity.

B. Perturbed Coils

Fortunately, the perturbation of polymer coils by long range interactions usually affects only the scattering functions in that range of scattering vectors h , where under theta-conditions the Debye function (Eqn 33) is valid. So all the calculations of scattering functions of chain molecules which have been undertaken as improvements of Eqn (33) for large h are unaffected by the perturbation. Moreover, possibly a medium range of h exists, where the Debye function is valid under theta- as well as under non-theta conditions, which shifts the excluded volume effect on the scattering function to even lower values of h .

Several attempts have been undertaken to calculate the scattering curves of expanded coils. In most of them the distribution function $p(r_{ij})$ of Eqn (27) is used in connection with Eqn (24) for the mean square intersegmental distance $\langle r_{ij}^2 \rangle$ as a function of $|i - j|$, the intersegmental separation along the chain. The

approximate character of the calculations arises mainly from the fact that the form of the distance distribution is assumed not to depend on $|i - j|$ and its position in the coil. The various attempts differ in the choice of the parameters s and t in Eqn (27). The first calculations were performed by Ptitsyn (1957) and by Benoit (1957) setting $s = t = 2$, thus retaining the Gaussian distribution. They already obtained the characteristic $h^{-2/(1+\epsilon)}$ -course of the perturbed coil scattering for large h , which may be given in the general form

$$\lim_{h \rightarrow \infty} M \cdot I_n(h) = \frac{M \cdot f(\epsilon, s, t)}{\langle R^2 \cdot h^2 \rangle^{1/(1+\epsilon)}} \quad (54a)$$

$$= \frac{f(\epsilon, s, t)}{h^{2/(1+\epsilon)} \cdot K_{r,\epsilon}^{1/(1+\epsilon)}} \quad (54b)$$

It turns out that this asymptote is again independent of the molar mass of the coil like the asymptotes for Gaussian coils (Eqns 34c and 41c). Furthermore, it becomes evident that the slope of the asymptote depends only on ϵ , which allows a determination of ϵ from only one scattering curve (cf. Eqn 23). The $h^{-2/(1+\epsilon)}$ -course is independent of the choice of the parameters s and t in Eqn (27) and depends only on Eqn (24).

At small values of $\langle R^2 \cdot h^2 \rangle$, however, the function of Ptitsyn and Benoit did not agree with experiment. Subsequent work led to a better fit of the calculated scattering functions to experimental data by a suitable choice of the parameters s and t in Eqn (27), in agreement with distributions, obtained by self-avoiding walk calculations (McIntyre *et al.*, 1968; Mazur *et al.*, 1968; Utiyama *et al.*, 1970). It turned out that the scattering function of an expanded coil is not as universal as the Debye function for a theta coil. Although within a given polymer/solvent system at constant temperature the same function is valid independent of molar mass (cf. Fig. 20), a change of temperature or of solvent also affects the shape of the scattering function (Mazur and McIntyre, 1975). The respective functions are given in series expansions for large and for small values of h and may be obtained from the cited literature.

For the perturbed coil distribution function of Fig. 6 with $\epsilon = 0,2$, $s = 2,8$ and $t = 2,5$ the factor $f(\epsilon, s, t) = 1,2$ is obtained, which may be compared with $f(\epsilon, s, t) = 2$ for a Gaussian coil (Eqn 34b). A double logarithmic plot (Fig. 14) of the corresponding structure factors $I_n(h)$ versus $\langle R^2 \rangle^{1/2} \cdot h$ reveals the characteristic differences. It becomes evident that the slope of the asymptote for large h , which is equal to $-1,67$ for $\epsilon = 0,2$, is less steep than the slope of -2 for a Gaussian coil. Another important feature from Fig. 14 is that at small $\langle R^2 \rangle \cdot h^2$ the differences in the scattering behaviour of the Gaussian coil and the perturbed coil are negligible.

For the comparison between the unperturbed and the expanded coil scattering

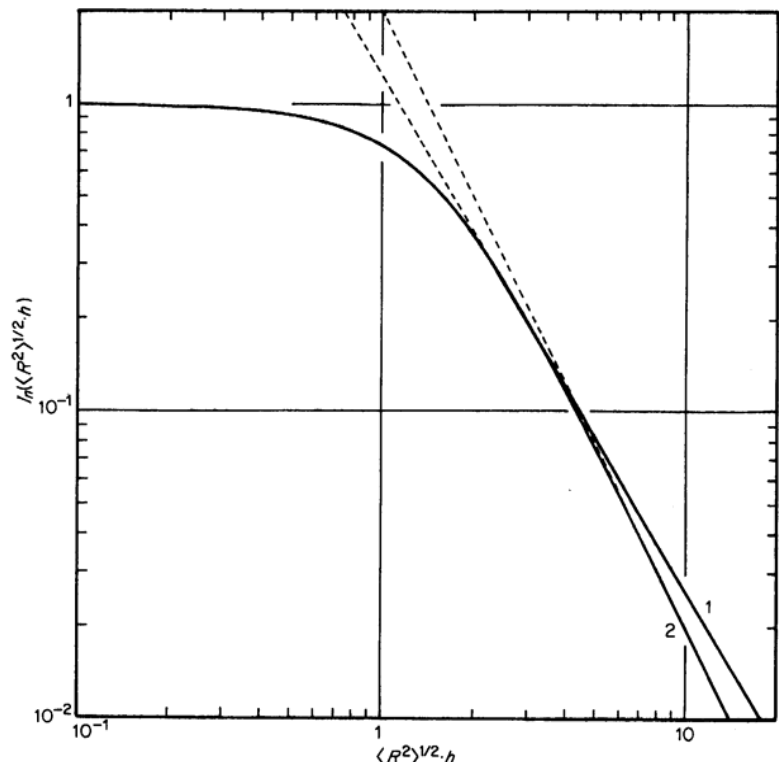


FIG. 14. Comparison of the structure factors (drawn curves) of an expanded coil (1) and a Gaussian coil (2) reduced to the same mean square radius of gyration. The dashed straight lines are the corresponding asymptotes for $h \rightarrow \infty$.

function of one and the same coil species Fig. 14 is not adequate, because with coil expansion the radius of gyration is changed. Therefore in Fig. 15 the two functions of Fig. 14 are plotted against $h \cdot b$ for an arbitrary coil expansion of $\langle R^2 \rangle_{\text{expanded}} / \langle R^2 \rangle_{\text{unperturbed}} = 1.3$ together with the rod scattering asymptote (Eqn 46) assuming that M_L and b remain constant. It is evident that the two coil scattering functions must have an intersection point, the abscissa of which depends on the strength and the range of the transversal forces (cf. Fig. 3). An increase in the transversal forces shifts the dashed curve in Fig. 15 to the left so that the intersection point with Debyes scattering function occurs at larger h . At sufficiently large h the scattering function of an expanded coil must approach the scattering of the unperturbed coil, because short segments are not expanded. Figure 16 shows the effect of coil perturbation on the same scattering curve in a Kratky-plot.

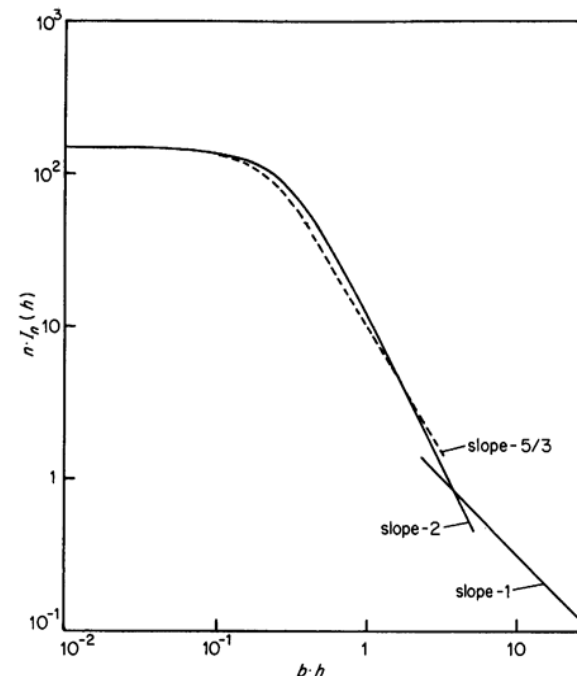


FIG. 15. Presentation of the general features of the scattering behaviour of a polymer chain with $n = L/b = 150$ in a double logarithmic plot. Drawn curve: scattering in a theta-solvent. Dashed curve: modification of the scattering after coil expansion in a good solvent. The drawn straight line with slope -1 is the scattering of an infinitely long rod (Eqn 46).

IV. Some Specific Experimental Applications

The applications of scattering methods (SAXS, SANS and LS) to the study of polymers in solution can be divided into

- investigations which only exploit the initial part of the scattering curve, the so-called Guinier region, to obtain M_w , $\langle R^2 \rangle_z$ and A_2 , and
- investigations which try to obtain information from the general course of the scattering function.

A. Molar Mass, Radius of Gyration and Second Virial Coefficient

Experiments in the Guinier region are usually designed to obtain $\langle R^2 \rangle_z$ and A_2 as a function of M_w to characterize the thermodynamic state of the dissolved

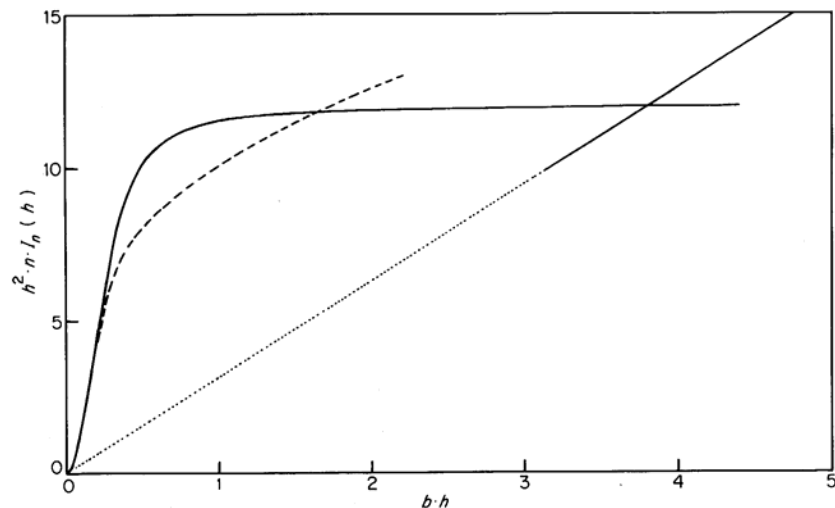


FIG. 16. Presentation of the curves of Fig. 15 in a Kratky-plot.

polymer and its size in solution. Here, SAXS can be used as a continuation of LS experiments in the range of small molecules.

Polypropyleneglycol (PPG) in acetone has been studied as an example for a short polymer chain in a thermodynamically good solvent (Meyerhoff *et al.*, 1971). Whereas the second virial coefficient could be measured by both LS and SAXS, the radius of gyration could only be obtained by SAXS. Figure 17 shows the experimental data of $\langle R^2 \rangle_z$ versus M_w in a double logarithmic plot together with the calculated relations $\langle R^2 \rangle_z = f(M_w, U)$ for unperturbed worm-like chains (Eqn 20) with Schulz-distribution (Eqn 39) (cf. Oberthür, 1978). Equation (43) cannot be applied in this case, because for a worm-like chain $\langle R^2 \rangle$ is not proportional to the molar mass M which is the basic requirement for Eqn (43).

Another example for a polymer in a good solvent is provided by PS in toluene (Rahlwes and Kirste, 1976; Kirste and Wild, 1969). Here a combined use of LS and SAXS for the determination of $\langle R^2 \rangle$ of the chain molecules in a wide range of molar mass is demonstrated (Fig. 18). For $\langle R^2 \rangle^{1/2} = 100 \text{ \AA}$ both methods can be used with similar accuracy (see Wunderlich, 1967; Serdyuk and Grenader, 1974). The example shows an increasing coil perturbation with increasing molar mass from an unperturbed coil behaviour with $\langle R^2 \rangle \propto M$ to the behaviour of an expanded coil with $\langle R^2 \rangle \propto M^{1+\epsilon}$ and $\epsilon = 0,20$.

A final example illustrates the limits of SAXS in polymer research. It describes the investigation of the shape of PS molecules in concentrated solution and in the bulk by the use of statistical copolymers of styrene with *p*-iodostyrene

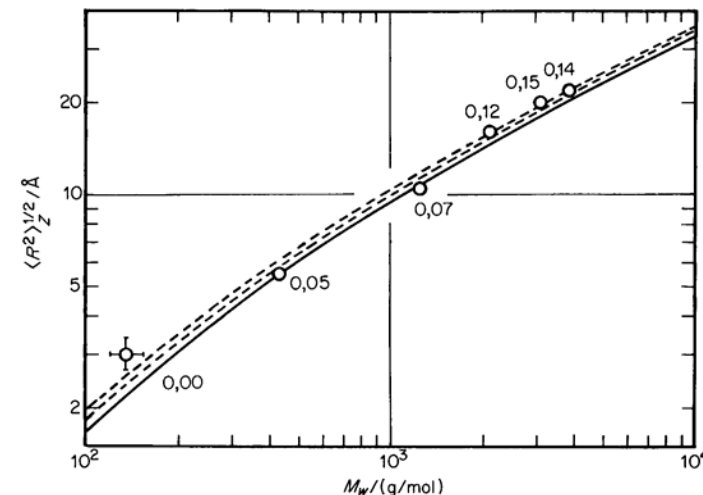


FIG. 17. Double logarithmic plot of $\langle R^2 \rangle_z^{1/2}$ as a function of M_w from SAXS of PPG in acetone at 20°C (open circles with error bars) (Meyerhoff *et al.*, 1971). The drawn curve corresponds to Eqn (20) for monodisperse Kratky-Porod chains ($M_L = 15,5 \text{ g}(\text{mol} \cdot \text{\AA})^{-1}$; $b = 10,5 \text{ \AA}$), the dashed curves are calculated for Kratky-Porod chains with Schulz-distributions (Eqn 39) of increasing polydispersity ($U = 0,1$ and $U = 0,2$) (Oberthür, 1978). The numbers beneath the experimental points denote the experimental (from GPC) non-uniformities U of the samples. The deviation for the dimer can be attributed to the fact that its diameter appreciably contributes to $\langle R^2 \rangle$.

(randomly tagged polymer) dissolved in polystyrene/toluene solutions of varying concentration (Hayashi *et al.*, 1974). To eliminate perturbations of the chain dimensions by the iodine label, the obtained radii of gyration of the labelled polymer molecules were extrapolated to zero iodine content. The resultant radius of gyration of a PS-chain ($M_w = 1,1 \cdot 10^5 \text{ g}(\text{mol})^{-1}$; $U = 0,06$) as a function of polymer concentration is plotted in Fig. 19 together with the theoretical relation (Daoud *et al.*, 1975)

$$\langle R^2 \rangle \propto M \cdot \rho_m^{-\frac{2\epsilon}{1+3\epsilon}} \quad (55)$$

which is valid in the semi-dilute concentration range. $\epsilon = 0,04$ is obtained in agreement with the ϵ -value of a tangent to the experimental function in Fig. 18 at the corresponding molar mass (Hayashi *et al.*, 1977). The gathered data reflect a gradual increase of the coil dimensions from the unperturbed coil in the bulk to the expanded coil in toluene.

Although the use of heavy atom labels may be limited to concentrated solutions and amorphous polymers, the use of isotope labels (Kirste *et al.*, 1972), which cause less perturbations in the labelled chain, combined with neutron scattering, has found an increasing field of application in polymer science (cf. Higgins and Stein, 1978).

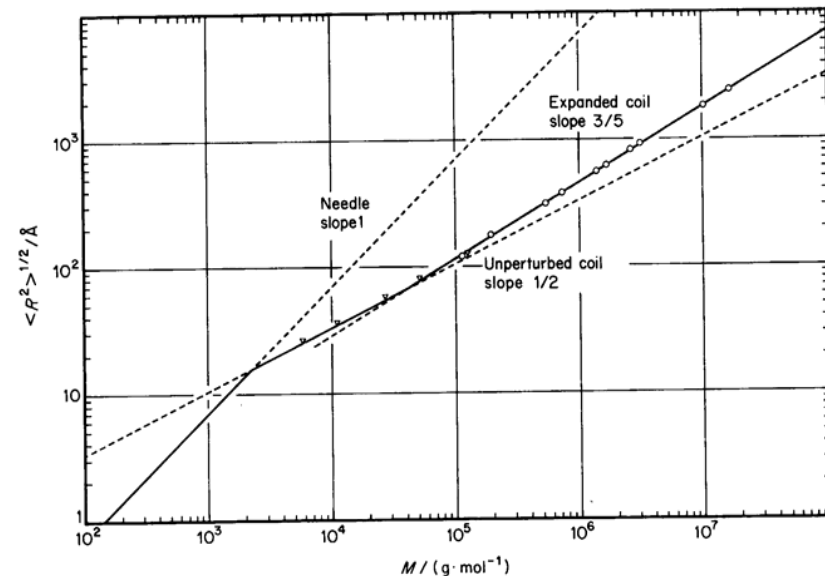


FIG. 18. Double logarithmic plot of $\langle R^2 \rangle^{1/2}$ as a function of M for PS in toluene at 25°C from LS (open circles: Rahlwes and Hack, 1976; Rahlwes and Kirste, 1977) and from SAXS (open triangles: Kirste and Wild, 1969), together with the asymptotes for a rod and an unperturbed coil (cf. Eqn (20) for $n \rightarrow 0$ and $n \rightarrow \infty$) as well as for an expanded coil (Eqn 23) of the same polymer with $M_L = 41.6 \text{ g}(\text{mol} \cdot \text{\AA})^{-1}$ and $b = 27 \text{ \AA}$.

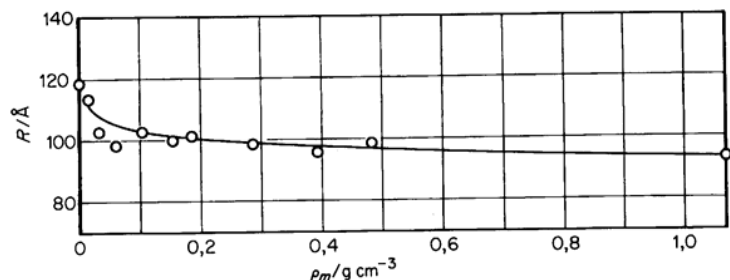


FIG. 19. $\langle R^2 \rangle^{1/2}$ of a PS-chain with $M = 1.1 \cdot 10^5 \text{ g}(\text{mol})^{-1}$ and $U < 0.06$ in a concentrated solution of PS in toluene at 25°C from SAXS of randomly tagged PS (open circles: Hayashi *et al.*, 1977), together with the calculated function according to Eqn (55).

B. Analysis of the Scattering Function

1. EXCLUDED VOLUME EFFECT

A phenomenon which has mainly been observed by LS experiments is the scattering of perturbed coils (Loucheux *et al.*, 1958; Smith and Carpenter,

1968; Mazur and McIntyre, 1975). If the scattering curves of PS in toluene collected by LS in a large range of molar mass (Rahlwes and Hack, 1976; Rahlwes and Kirste, 1977) are put together in the form $I_n(\langle R^2 \rangle \cdot h^2)$, they reduce to one general scattering function, which is valid for PS in toluene (Fig. 20). For $\langle R^2 \rangle \cdot h^2 < 10$ this function is well represented by the corresponding Debye function (Eqn 33) even slightly better than by the best fit with a perturbed coil scattering function based on Eqn (27). At higher values of the reduced momentum transfer, however, an $h^{-2/(1+\epsilon)}$ -course with $\epsilon = 0.2$, typical for the effect of an excluded volume on the scattering behaviour, is attained. This leads to a continuous increase of the intensity in a Kratky-plot in contrast to the plateau of the Debye curve as shown in Fig. 16.

Although this has been demonstrated by LS, the $h^{-2/(1+\epsilon)}$ -course of the scattering of perturbed coils can be followed up to the h -range of SAXS, which allows the determination of the excluded volume exponent ϵ from one single scattering curve. This has been demonstrated by SANS (Cotton *et al.*, 1974). Even the transition from the $h^{-2/(1+\epsilon)}$ - to the h^{-2} -course of the unperturbed coil (cf. Fig. 15) has been detected by SANS (Farnoux *et al.*, 1978), which may open up a new field for investigations by SAXS as well.

2. BRANCHED AND CIRCULAR POLYMERS

Branched polymers have also been investigated mainly by light scattering (cf. Burchard, 1977; Bywater, 1979). A typical example for a six-branched star polyisoprene of molecular weight $M = 1.70 \cdot 10^6 \text{ g}(\text{mol})^{-1}$ dissolved in cyclohexane at 35°C (Toporowski and Roovers, 1978) is shown in Fig. 20b. In this case, a combination of light scattering with X-ray small angle scattering or neutron small angle scattering should provide additional information about the asymptotic behaviour of the scattering function towards high values of h , as postulated in Eqn (36a).

In the case of comb-shaped polymers, if the length of each branch is short in comparison with the backbone length, the scattering behaviour of a worm-like chain with increased mass per unit length and cross-sectional radius of gyration may be obtained by X-ray small angle scattering, as shown by Garg and Stivala (1978). These data could be used to estimate the degree of branching of dextran hydrolysates. Finally, Higgins *et al.* (1979) have performed a comparative neutron small angle scattering study of circular and linear polydimethylsiloxane (PDMS) dissolved in deuterobenzene at room temperature in the range of molecular weight $5000 \leq M / (\text{g}(\text{mol})^{-1}) \leq 21000$. They obtain a ratio of the mean square radii $\langle R^2 \rangle_{\text{ring}} / \langle R^2 \rangle_{\text{lin}} = 0.53 \pm 0.05$, which agrees well with the theoretical value of Eqn (22).

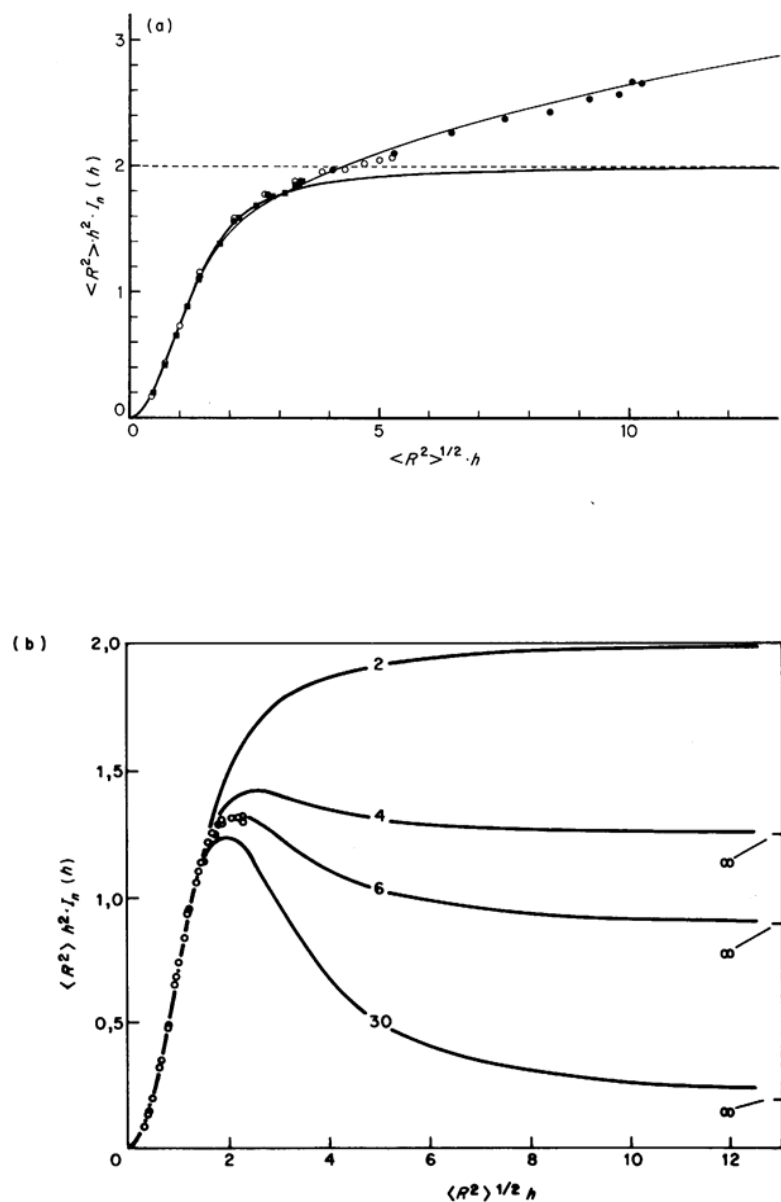


FIG. 20. (a) Kratky-plot of LS-data of PS in toluene at 25°C (○, ● Rahlwes and Hack, 1976; ■ Rahlwes and Kirste, 1977) reduced to the same radius of gyration, together with the calculated structure factors (drawn curves) for a Gaussian coil and an expanded coil with the same parameters as in Figs 6 and 14. (b) Angular scattering functions for regular star-branched polymers with $f = 2, 4, 6, 30$. Experimental points: Six-branched star polyisoprene ($M_w = 1.70 \cdot 10^6$) in cyclohexane (Toporowski and Roovers, 1978).

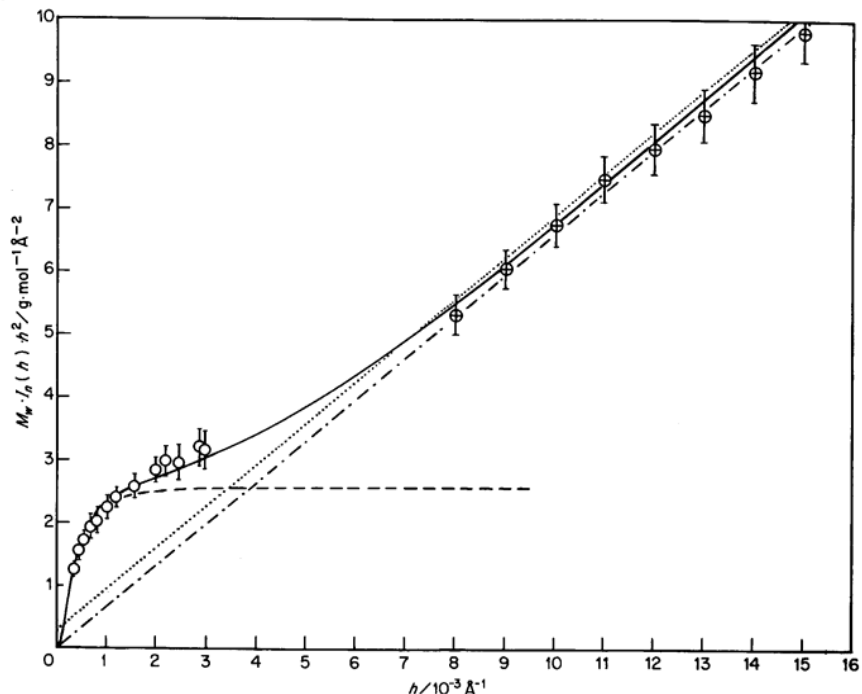


FIG. 21. Kratky-plot of the scattering curve of DNA-Na in 0.2 M NaCl/H₂O at 20°C from LS-data (open circles: Zierenberg, 1971) and SAXS-data (filled circles: Oberthür, 1974). Drawn curve: best fit to the data by the scattering of a Kratky-Porod chain ($M_w = 2.02 \cdot 10^7 \text{ g(mol)}^{-1}$; $U = 1.0$ (assumed); $M_L = 210 \text{ g(mol} \cdot \text{Å})^{-1}$; $b = 980 \text{ Å}$; root mean square relative deviation $\langle (\Delta I_{\text{exp}} / I_{\text{exp}})^2 \rangle^{1/2} = r.d. = 3.9\%$).

3. CHAIN FLEXIBILITY

The statistical chain element b has been introduced to characterize the overall chain flexibility without reference to specific bending mechanisms (equivalent chain). In principle this quantity can be determined from the transition from coil to rod scattering as defined in Eqn (47) (cf. Kratky, 1962, 1966; Zipper *et al.*, 1969; Durchschlag *et al.*, 1970a and b; Burchard and Kajiwara, 1970). In practice, however, this transition is not always as pronounced as it should be for a reliable determination of b . Therefore a least squares fit of the scattering function of a persistence coil (Eqn 48) with Schulz-distribution of molar mass (Eqn 39) $M_w \cdot I_n(M_L, b, U, h)$ has been tried for the determination of b . This procedure, applied to the combined LS- and SAXS-curves of DNA-Na in 0.2 M NaCl/H₂O (Fig. 21) yielded a statistical chain element $b = 980 \text{ Å}$. The thickness of the DNA-thread in this range of momentum transfer can still be neglected, since it is two orders of magnitude smaller than b .

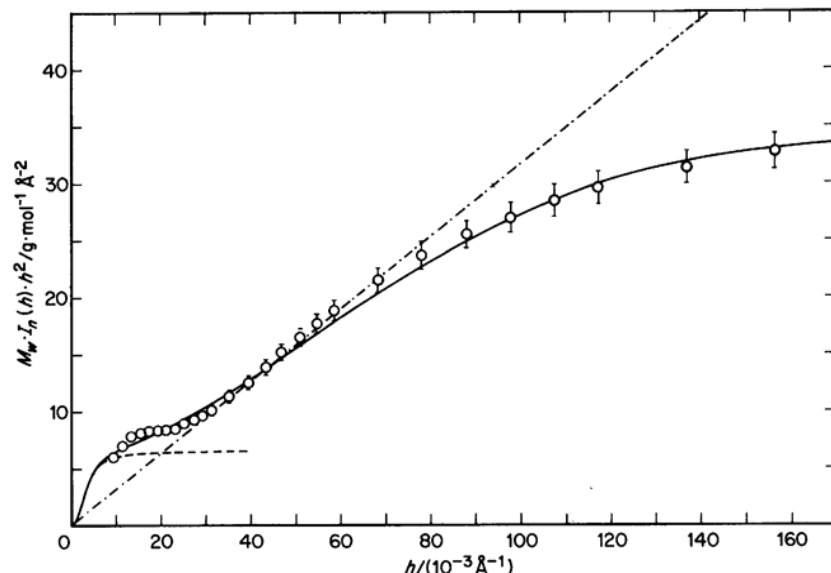


FIG. 22. Kratky-plot of the SAXS-curve of cellulose carbanilate in acetone at room temperature (open circles, originally in arbitrary units: Burchard and Kajiwara, 1970). Drawn curve: cf. Fig. 21 ($M_w = 5,0 \cdot 10^5 \text{ g(mol)}^{-1}$ (assumed); $U = 0,23$ (assumed); $M_L = 101 \text{ g(mol \cdot Å)}^{-1}$ (assumed); $b = 190 \text{ Å}$; $R_c = 6,0 \text{ Å}$; r.d. = 4,2%).

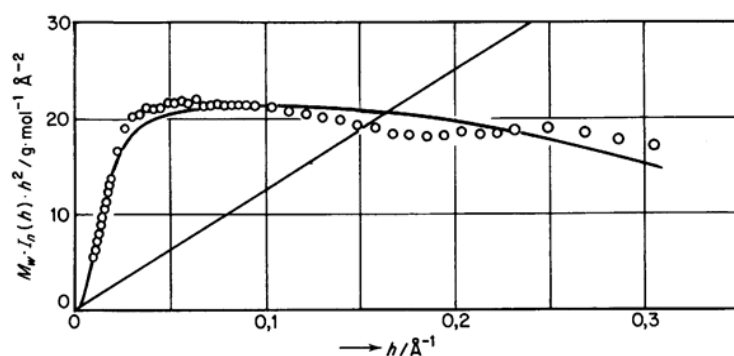


FIG. 23. Kratky-plot of the SAXS-curve of PS in cyclohexane at 40°C (open circles: Durchschlag *et al.*, 1970a). Drawn curve: cf. Fig. 21 ($M_w = 8,2 \cdot 10^4 \text{ g(mol)}^{-1}$; $U = 0,08$ (assumed); $M_L = 40 \text{ g(mol \cdot Å)}^{-1}$; $b = 22 \text{ Å}$; $R_c = 4,7 \text{ Å}$; r.d. = 6,2%).

The same procedure applied to cellulose carbanilate in acetone (Burchard and Kajiwara, 1970) resulted in $b = 190 \text{ Å}$ (Fig. 22). However, here the thickness of the thread had to be taken into account by introduction of the cross-sectional factor of Eqn (53) with $R_c = 6,0 \text{ Å}$.

A final example is given by PS in cyclohexane (Durchschlag *et al.*, 1970), where $b = 22 \text{ Å}$ and $R_c = 4,7 \text{ Å}$ is obtained (Fig. 23). Since $R_c \ll b$ is no more valid for this case, even the transition region from coil to rod scattering is influenced by the cross-section structure of the chain, which makes the determination of b rather difficult.

It should be mentioned in this connection that the possible mass per unit length has a limit, which is given by the extended chain conformation. The construction of the corresponding rod scattering asymptote (Eqn 46) can be of great help for a first guess at the value of b (cf. Kratky, 1962).

Probably DNA can be regarded as the best example for the realization of a persistence chain in nature, whereas the deviation of the PS-curve from the scattering behaviour of a persistence chain with Gaussian cross-section may already reflect some peculiarities of its molecular structure.

4. INDIVIDUAL CHAIN PROPERTIES

The finding of Kirste and Wunderlich (1964; Wunderlich and Kirste, 1964) that PMMA in the isotactic and in the syndiotactic configuration exhibits a different SAXS-pattern (Fig. 24), was the first strong experimental evidence for the hypothesis that each polymer in solution in fact forms its individually coiled chain (Kirste, 1967). Comparison with the calculated scattering functions of Fig. 12 shows a qualitative agreement, however, the corresponding maxima

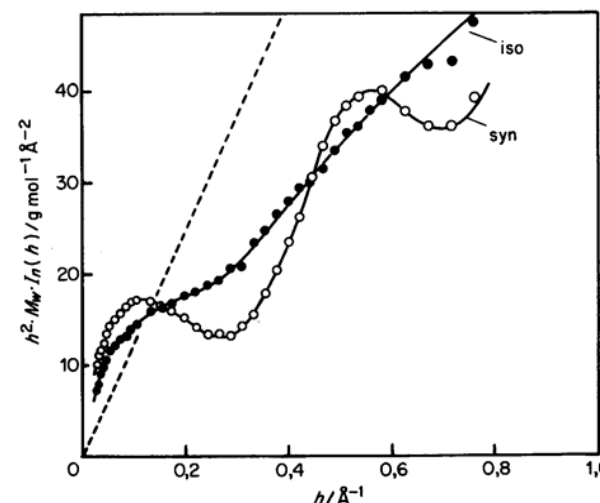


FIG. 24. Kratky-plot of the experimental SAXS-curves of *i*-PMMA (filled circles) and *s*-PMMA (open circles) in acetone at 20°C (Wunderlich and Kirste, 1964). The dashed straight line represents the rod scattering (Eqn 46) with $M_L = 39,4 \text{ g(mol \cdot Å)}^{-1}$.

and minima of the calculated curve occur at smaller values of momentum transfer than in the experimental curve. Kirste (1967a, b) tried an interpretation of the experimental data for *s*-PMMA by the persistence chain with persistence of direction and curvature (Fig. 9b) and obtained the agreement given in Fig. 25 with the parameters $b = 10.8 \text{ \AA}$ and $R_{\text{curv}} = 6.7 \text{ \AA}$. The cross-section factor was set equal to unity (cf. Kirste, 1964). These values are smaller than the theoretical results of Yoon and Flory, which may imply that the inequality of the skeletal bonds in PMMA is greater than they assumed in their calculation. Another principle difference between the two models lies in the fact that Yoon and Flory describe the *s*-PMMA thread as a sequence of kinked circular segments, whereas Kirste describes *s*-PMMA as a continuously "curled" thread without kinks (cf. Figs 12 and 5c). On the other hand, coil expansion at small angles, a cross-section structure factor at intermediate h -values and some ambiguity in the solvent subtraction (cf. Kirste, 1965; Durchschlag *et al.*, 1970b) at large angles makes a comparison of the experimental data with the calculated scattering functions of Figs 9b and 12 still somewhat uncertain.

V. Conclusion

From the scattering behaviour of dissolved polymer molecules a great number of parameters can be extracted. If the various parameters which are to be

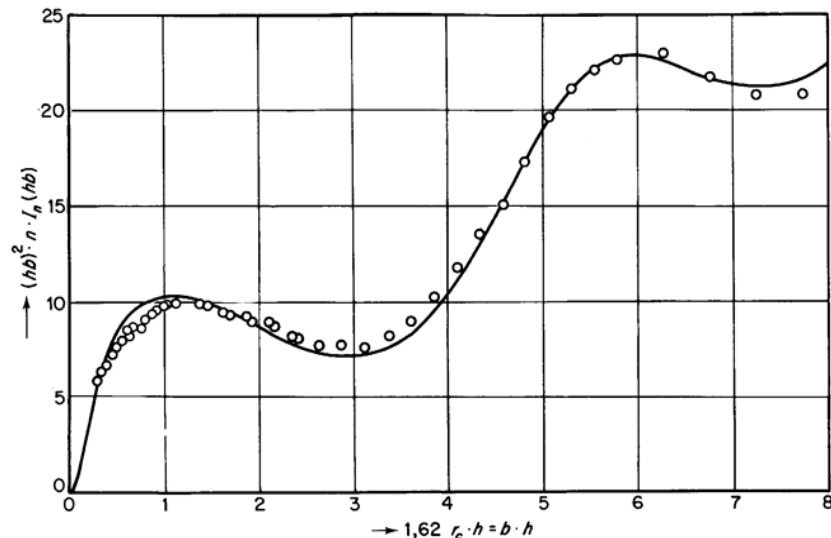


FIG. 25. Comparison of the experimental SAXS-curve of *s*-PMMA (open circles, cf. Fig. 24) with the calculated scattering curve of Fig. 9b (drawn curve) in a Kratky-plot.

determined differ greatly in their magnitude this is easy to perform (DNA). However, if they are of the same order of magnitude (PS), they may influence the scattering behaviour in the same h -range. In this case it is inevitable to consider the entire experimentally accessible scattering curve in the interpretation and to compare it as a whole with the final model.

References

- Altgelt, K. and Schulz, G. V. (1960). *Makromol. Chem.* **36**, 209–219.
- Benoit, H. (1953). *J. Polymer Sci.* **11**, 507–510.
- Benoit, H. (1957). *C.R. Acad. Sci.* **245**, 2244–2247.
- Benoit, H. and Doty, P. (1953). *J. Phys. Chem.* **57**, 958–963.
- Birshtein, T. M. and Ptitsyn, O. B. (1966). "Conformations of Macromolecules". Interscience Publishers, New York.
- Burchard, W. (1977). *Macromolecules* **10**, 919–927.
- Burchard, W. and Kajiwara, K. (1970). *Proc. Roy. Soc. London A* **316**, 185–199.
- Bywater, S. (1979). Preparation and properties of star-branched polymers. In "Advances in Polymer Science", Vol. 30. Springer-Verlag, Berlin.
- Casassa, E. F. (1965). *J. Polymer Sci. Part A3*, 605–614.
- Cloizeaux, J. des (1973). *Macromolecules* **6**, 403–407.
- Cotton, J. P., Decker, D., Benoit, H., Farnoux, B., Higgins, J. S., Jannink, G., Ober, R., Picot, C. and des Cloizeaux, J. (1974). *Macromolecules* **7**, 863–872.
- Daoud, M., Cotton, J. P., Farnoux, B., Jannink, G., Sarma, G., Benoit, H., Duplessix, R., Picot, C. and de Gennes, P. G. (1975). *Macromolecules* **8**, 804–818.
- Debye, P. (1915). *Ann. Physik* **46**, 809–823.
- Debye, P. (1947). *J. Phys. Colloid. Chem.* **51**, 18–32.
- Durchschlag, H., Kratky, O., Breitenbach, J. W. and Wolf, B. A. (1970a). *Monatsh. Chem.* **101**, 1462–1470.
- Durchschlag, H., Puchwein, G., Kratky, O., Breitenbach, J. W. and Olaj, O. F. (1970b). *J. Polymer Sci. Part C* **31**, 311–343.
- Eyring, H. (1932). *Phys. Rev.* **39**, 746–748.
- Farnoux, B., Boué, F., Cotton, J. P., Daoud, M., Jannink, G., Nierlich, M., and de Gennes, P. G. (1978). *J. Physique* **39**, 77–86.
- Fisher, M. E. (1966). *J. Chem. Phys.* **44**, 616–622.
- Flory, P. J. (1953). "Principles of Polymer Chemistry". Cornell University Press, Ithaka, N.Y.
- Flory, P. J. (1969). "Statistical Mechanics of Chain Molecules". Interscience Publishers, New York.
- Flory, P. J. and Bueche, A. M. (1958). *J. Polymer Sci.* **27**, 219–229.
- Garg, S. K. and Stivala, S. S. (1978). *J. Polym. Sci.: Polym. Phys. Ed.* **16**, 1419–1434.
- Greschner, G. Š. (1973). *Makromol. Chem.* **170**, 203–229.
- Hack, H. and Meyerhoff, G. (1978). *Makromol. Chem.* **179**, 2475–2488.
- Hayashi, H., Hamada, F. and Nakajima, A. (1974). *Macromolecules* **7**, 959–961.
- Hayashi, H., Hamada, F. and Nakajima, A. (1977). *Makromol. Chem.* **178**, 827–842.
- Heine, S., Kratky, O. and Roppert, J. (1962). *Makromol. Chem.* **56**, 150–168.

- Higgins, J. S. and Stein, R. S. (1978). *J. Appl. Cryst.* **11**, 346–375.
- Higgins, J. S., Dodgson, K. and Semlyen, J. A. (1979). *Polymer* **20**, 553–558.
- Kirste, R. G. (1964). *Z. Physik. Chem. Neue Folge* **42**, 351–357.
- Kirste, R. G. (1967a). *Makromol. Chem.* **101**, 91–103.
- Kirste, R. G. (1967b). *J. Polymer Sci. Part C* **16**, 2039–2048.
- Kirste, R. G. (1967c). In "Small Angle X-Ray Scattering" (H. Brumberger, ed.), pp. 33–61.
- Kirste, R. G. (1971). *Kolloid-Z. u. Z. Polymere* **244**, 290–292.
- Kirste, R. G. and Kratky, O. (1962). *Z. Physik. Chem. Neue Folge*, **31**, 363, 374.
- Kirste, R. G. and Wild, G. (1969). *Makromol. Chem.* **121**, 174–183.
- Kirste, R. G. and Wunderlich, W. (1964). *Makromol. Chem.* **73**, 240–243.
- Kirste, R. G. and Wunderlich, W. (1965). *Makromol. Chem.* **87**, 60–65.
- Kirste, R. G. and Wunderlich, W. (1968). *Z. Physik. Chem. Neue Folge* **58**, 133–147.
- Kirste, R. G., Kruse, W. A. and Schelten, J. (1972). *Makromol. Chem.* **162**, 299–303.
- Kratky, O. (1962). *Kolloid-Z. u. Z. Polymere* **182**, 7–24.
- Kratky, O. (1966). *Pure Appl. Chem.* **12**, 483–523.
- Kratky, O. and Porod, G. (1949). *Rec. Trav. Chim. Pays-Bas* **68**, 1106–1122.
- Kuhn, W. (1934). *Kolloid-Z.* **68**, 2–15.
- Loucheux, C., Weill, G. and Benoit, H. (1958). *J. Chem. Phys.* **55**, 540–546.
- McIntyre, D., Mazur, J. and Wims, A. M. (1968). *J. Chem. Phys.* **49**, 2887–2895.
- McKenzie, D. S. (1976). *Phys. Lett.* **C27**, 35–88.
- Mazur, J. and McIntyre, D. (1975). *Macromolecules* **8**, 464–476.
- Mazur, J., McIntyre, D. and Wims, A. M. (1968). *J. Chem. Phys.* **49**, 2896–2904.
- Meyerhoff, G., Moritz, U., Kirste, R. G. and Heitz, W. (1971). *Eur. Polymer J.* **7**, 933–941.
- Neugebauer, T. (1943). *Ann. Physik* **42**, 509–533.
- Oberthür, R. C. (1974). Dissertation, Universität Mainz.
- Oberthür, R. C. (1978). *Makromol. Chem.* **179**, 2693–2706.
- Peterlin, A. (1955). *J. Chem. Phys.* **23**, 2464–2465.
- Peterlin, A. (1960). *J. Polymer Sci.* **47**, 403–415.
- Ptitsyn, O. B. (1957). *Zh. fiz. khim.* **31**, 1091–1102.
- Rahlwes, D. (1974). Dissertation, Universität Mainz.
- Rahlwes, D. and Hack, H. (1976). Unpublished results.
- Rahlwes, D. and Kirste, R. G. (1977). *Makromol. Chem.* **178**, 1793–1810.
- Schulz, G. V. (1939). *Z. Physik. Chem.*, Abt. B. **43**, 25–46.
- Schulz, G. V. and Kirste, R. G. (1961). *Z. Physik. Chem. Neue Folge* **30**, 171–200.
- Schulz, G. V., Wunderlich, W. and Kirste, R. G. (1964). *Makromol. Chem.* **75**, 22–34.
- Serdyuk, I. N. and Grenader, A. K. (1974). *Makromol. Chem.* **175**, 1881–1892.
- Sharp, P. and Bloomfield, V. A. (1968). *Biopolymers* **6**, 1201–1211.
- Smith, T. E. and Carpenter, D. K. (1968). *Macromolecules* **1**, 204–213.
- Toporowski, P. M. and Roovers, J. E. L. (1978). *Macromolecules* **11**, 365–368.
- Utiyama, H., Tsunashima, Y. and Kurata, M. (1971). *J. Chem. Phys.* **55**, 3133–3145.
- Volkenstein, M. V. (1963). "Configurational Statistics of Polymer Chains", Interscience Publishers, New York.
- Wunderlich, W. (1967). *Makromol. Chem.* **108**, 315–317.
- Wunderlich, W. and Kirste, R. G. (1964). *Ber. Bunsenges. Physik. Chem.* **68**, 646–652.
- Yamakawa, H. (1971). "Modern Theory of Polymer Solutions". Harper & Row, New York.
- Yamakawa, H. and Fujii, M. (1974). *Macromolecules* **7**, 649–654.
- Yoon, D. Y. and Flory, P. J. (1975). *Polymer* **16**, 645–648.
- Yoon, D. Y. and Flory, P. J. (1976a). *Macromolecules* **9**, 294–299.
- Yoon, D. Y. and Flory, P. J. (1976b). *Macromolecules* **9**, 299–303.
- Zierenberg, B. E. (1971). Dissertation, Universität Mainz.
- Zimm, B. H. (1948). *J. Chem. Phys.* **16**, 1093–1116.
- Zimm, B. H. and Stockmayer, W. H. (1949). *J. Chem. Phys.* **17**, 1301–1314.
- Zipper, P., Krigbaum, W. R. and Kratky, O. (1969). *Kolloid.-Z. u. Z. Polym.* **235**, 1281–1287.

13

Synthetic Polymers in the Solid State

C. G. VONK

DSM Central Laboratory, Geleen, Holland

I. The model of the ideal polymer structure	434
II. The semi-quantitative approach	435
III. Intensity calculations, based on the ideal lamellar model	438
A. Direct calculation of the one-dimensional intensity function	438
B. Methods involving the use of the correlation function	446
IV. The application of general relations	453
A. Use of the invariant	454
B. Use of the fourth moment of the intensity distribution	455
C. Use of Porod's law	456
D. Deviations from Porod's law	457
V. Miscellaneous topics	459
A. Correction for the sample background scattering	459
B. Determination of phase transitions in polymers	459
VI. Applications of SAXS to the study of solid polymers	461
A. Studies of polymer single crystals	461
B. Studies of bulk polymers	462
C. Heterophase polymers	463
References	464

Semicrystalline polymers are ideal objects to be studied by small angle scattering. First, they show electron density variations of which the correlation length is usually well within the range covered by this technique (1–100 nm). Secondly, their structures may in many cases be adequately described by assuming the electron density variations to occur in one coordinate direction only; this allows a rigorous calculation of the diffraction pattern, even if the deviations from an ideal periodic structure are quite large. These circumstances have, on the one hand, prompted important contributions to the theory of diffraction

in general and, on the other, have led to much experimental work, giving useful information on polymer morphology. Sections I-V of this chapter will be mainly devoted to the various aspects of the diffraction theories involved and results will be shown only by way of demonstration; moreover, this survey will be restricted to the diffraction from the internal polymer structure, and studies of the preferred orientation resulting from special ways of producing or processing of the samples will not be considered. Section VI will deal with applications, primarily by referring to a number of review papers, which will be supplemented with a survey of some recent publications on the topics of this chapter.

I. The Model of the Ideal Polymer Structure

The interpretation of small angle scattering data is very much dependent on the cooperation with other techniques of submicroscopic investigation, of which electron microscopy is the most important one. These techniques have to be used to obtain such information as is necessary to compose a model which adequately describes the qualitative features of the structure. Once such a model is found, analysis of the intensity of the diffracted radiation allows us to determine the parameters of this model, such as dimensions and density variations, sometimes with remarkable accuracy.

The basis for the model that applies to semicrystalline polymers is the electron microscopic observation of single crystals which can be obtained by cooling dilute solutions of these substances. These crystals usually consist of numerous parallel lamellae, which are connected to each other by screw dislocations. That such lamellae also occur in melt-crystallized polymers is shown by many electron microscopic observations of fracture surfaces, free surfaces, ultra-thin sections and of the debris remaining after partial oxidation of polymers with nitric acid. The model thus is a pseudo-periodic layered structure, in which the electron density varies only in the direction perpendicular to the layers. The problem left to small angle scattering is to describe the density variations within the periods, as well as the deviations of the individual periods from the mean value.

Probably the most important result of small angle scattering and other studies devoted to this problem has been the recognition that, at least to a first approximation, the density distribution corresponds to a two-phase structure, in which crystalline and amorphous regions alternate. Though there are still controversies as to the actual arrangement of the chains within the crystalline layers (here, the chains may have a folded configuration), this two-phase concept seems to be generally accepted now.

In the following a model, consisting of alternating parallel crystalline and amorphous lamellae that are placed in stacks of dimensions that are large enough

not to effect the small angle scattering, will be called the ideal lamellar model. It is to be noted that in this model the deviations of the identity periods from the mean value are considered to be inherent to the polymer structure and as such are included. This model necessarily is a simplification of the real situation, as in all electron micrographs deviations from it can be seen, such as undulations of the layers, splaying layers or other irregularities. Also the lamellae are known to be organized in spherulites, in which the direction of the lamellar normals varies gradually instead of abruptly, as in the model at the stack boundaries. However, especially for polymers of relatively high crystallinity (about 50% and above), the model seems a very good approximation, yielding a satisfactory interpretation of the small angle scattering intensities. Only at lower crystallinities are deviations from the calculated intensities observed that may indicate certain shortcomings of the model; these will be discussed at the end of Section III.

II. The Semi-quantitative Approach

The interpretation of the small angle scattering from polymers with the aid of simple crystallographic tools may be extended quite far without the need to resort to the more elaborate treatments to be presented in the next section. The intensity function of a single stack of the ideal lamellar model is confined to a central line in reciprocal space, that is perpendicular to the lamellae. Most treatments start from this function, which therefore has to be derived from the observed intensity first. If the intensity is recorded with the aid of slit geometry, and the sample is isotropic, this usually involves the following three steps.

(1) Correction for the continuous background due to liquid scattering. In many cases this background can be observed as a region of almost constant intensity at angles intermediate between small and wide angle scattering; this constant value may be subtracted from the small angle scattering. More complicated procedures, that are discussed in Section V, do not fit in character with the simple treatments proposed in this section.

(2) Desmearing. As the smearing due to the use of slit collimation may cause substantial shifts in the Bragg *D*-value of broad peaks, any such value obtained from smeared curves must be considered with great reserve.

(3) Reduction of the desmeared intensity $I(s)$ to the one-dimensional intensity function $I_1(s)$ of a single stack. As the intensities of all the stacks at a certain *s*-value are distributed in reciprocal space over the surface of a sphere of radius *s*, this is achieved by setting

$$I_1(s) = 4\pi s^2 I(s)$$

The factor $4\pi s^2$ is generally indicated as the Lorentz factor. If the intensity function of a single stack is not confined to a central line but is extended in the other directions also, or if the sample is not isotropic, this factor may be of a more complicated form (Hosemann and Bagchi, 1962).

The function $I_1(s)$ obtained in this way usually is of the type shown in Fig. 3. The peak or peaks can be associated with the various orders of the Bragg reflection from the lamellae, and the average value of the period D , which is the sum of the average thicknesses of the crystalline layers C and the amorphous layers A , can be obtained from Bragg's law. For small angle scattering this can be approximated by

$$n\lambda = D \cdot 2\theta_m, \quad \text{or} \quad D = n/s_m$$

where λ is the wavelength of the X-rays, $2\theta_m$ is the scattering angle of the peak, n the order of the peak, and s_m the distance of the peak from the origin in reciprocal space.

An estimate of the volume crystallinity $\phi = C/D$ can be obtained from the ratio of the integrated intensities of the higher order peaks $I_1(n)$ to the integrated intensity of the first order peak $I_1(1)$. In the case of an ideal periodic lattice this ratio may be shown to be given by

$$\frac{\int_0^\infty I_1(n) ds}{\int_0^\infty I_1(1) ds} = \frac{\sin^2(\pi\phi n)}{\sin^2(\pi\phi) \cdot n^2}$$

A plot of this ratio against ϕ is presented in Fig. 1; it shows that in general only the second order will be of value in estimating ϕ , as the intensities of the third and higher orders usually will be too low. The higher order reflections are furthermore obscured by the fact that with increasing value of n , the width of the peaks increases rapidly, which causes them to overlap and finally merge into a common background. Actually in the patterns obtained from isotropic samples at most two orders are observed.

The symmetry of the function shown in Fig. 1 with respect to $\phi = \frac{1}{2}$ is in agreement with Babinet's principle, according to which the crystalline and amorphous areas in these two-phase structures may be exchanged without the diffraction pattern being changed. Furthermore, in the region of $\phi = \frac{1}{2}$, the second order peak is very low and consequently ϕ can not be determined with any accuracy from small angle scattering data. The size of this region depends, of course, on the quality of the intensity data, but may be assumed to run in practice from $\phi = 1/3$ to $\phi = 2/3$.

If the integrated intensities of two (or more) orders of reflection are available, one may also extract from I_1 some information about the way in which the individual identity periods x_D are distributed around the average value D . If

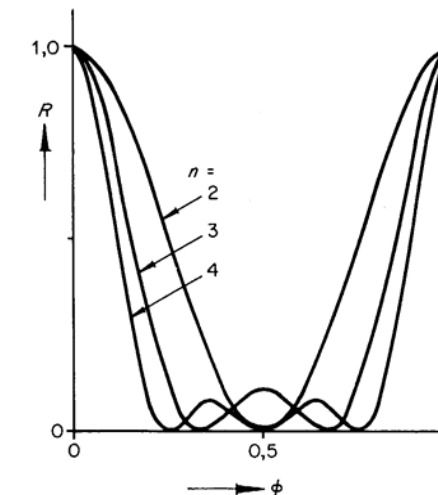


FIG. 1. Ratio of the intensity of the n th order reflection to the intensity of the first order reflection for a perfectly periodic lamellar structure of crystallinity ϕ .

this distribution is such that within each stack all x_D values are distributed in random succession, according to the overall distribution function $P_D(x_D)$ (paracrystalline order), the integral widths of the reflections increase with n^2 . If, on the other hand, the x_D values are equal within one stack, but differ between the stacks (heterogeneous distribution), the increase in the integral widths of the peaks will be proportional to n . In this case, each stack may be considered to give a very sharp Bragg peak, and one may obtain the distribution function $P_D(x_D)$ of the x_D values in the entire sample directly from the intensity distribution in the first order Bragg peak, by transformation of the s coordinate to the x_D coordinate using the relation $x_D = 1/s$. Recent results indicate that this heterogeneous distribution is more likely to occur in some samples rather than the paracrystalline one (Strobl and Müller, 1973; Meyer and Kilian, 1978).

The reliability of the conclusions obtained by the simple methods outlined above will decrease with increasing width of the distribution function P_D . Broad distributions of x_D may lead to deviations from Bragg's law, if applied to the position of peak maxima; also the curves presented in Fig. 1 will be affected by the width of these distributions. More general methods, which are not restricted by the width of P_D , are to be discussed in the next section.

III. Intensity Calculations, Based on the Ideal Lamellar Model

The first complete calculation of the intensity from a one-dimensional paracrystalline structure was presented as early as 1927 by Zernike and Prins. In an attempt to explain the diffraction by liquids, they considered a one-dimensional lattice consisting of identical regions of constant electron density – the molecules – separated by regions of zero electron density, of which the lengths showed a Poisson distribution. Hermans (1944) and Hosemann (1949) extended the treatment to include general distribution functions of the two types of regions. In the Section III.A, these approaches will be presented in a somewhat simplified form, which nevertheless shows all the important features of the original calculations.

A different approach to the interpretation of intensity data is through the direct calculation of the autoconvolution of the electron density function, which is equivalent to the Patterson function used in structure analysis and, if properly scaled, is called the correlation function in small angle scattering. The use of this function in connection with the ideal lamellar model, as advocated by Vonk and Kortleve (1967), is described in Section III.B.

Finally, in Section III.C a new method described by Ruland (1977), by which the distribution functions of the thicknesses of the crystalline and amorphous lamellae can, in principle, be obtained directly from the scattering curve is outlined.

The discussions in these sections are not meant to be exhaustive, but are given to supply the reader with the basic concepts of the various methods, that may facilitate the reading of the original literature. The reader is assumed to be familiar with the relations between Fourier transformations and convolutions, and with their application to diffraction phenomena, such as presented in various textbooks (see, for example, Vainshtein, 1966; Guinier, 1963; Hosemann and Bagchi, 1962; Int. Tables, 1959).

A. Direct Calculation of the One-dimensional Intensity Function

In this chapter the symbol η is used to indicate the deviation of the electron density ρ from some reference value, which may differ according to the requirements of the model. In this section this reference value will be the electron density of the amorphous phase. If $\eta(x)$ represents such deviations in a stack of the ideal lamellar model of infinite size, the value $\eta_L(x)$ for a stack of size L in the x direction may be presented by

$$\eta_L(x) = \eta(x) \cdot S(x),$$

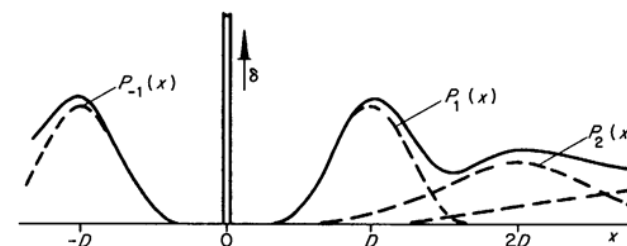


FIG. 2. Schematic representation of the distance statistics function $z(x)$, as composed of the distribution functions $P_n(x)$ and $\delta(0)$.

where $S(x)$ is a shape function, having the value 1 within, and 0 outside the stack. The autoconvolution is given by

$$p_L(x) = \overbrace{\eta_L(x)}^2 = \overbrace{\eta}^2 S^2$$

As S can only have the values 0 and 1, one may show that this is equal to

$$p_L(x) = \overbrace{\eta}^2 \cdot \overbrace{S}^2 \quad (1)$$

Assuming all the crystalline lamellae to be identical, one may consider the function $\eta(x)$ to be in turn the convolution of a function η_c , representing the electron density deviations within one crystalline layer, and a function $T(x)$, which is the sum of a number of δ -functions of which each one is located at the centre of a crystalline layer. Thus:

$$p_L(x) = \overbrace{T}^2 \overbrace{\eta_c}^2 \cdot \overbrace{S}^2 \quad (2)$$

If the stack contains N crystalline lamellae per cm, the function T will consist of N^2 δ -functions per cm. Let $z(x)dx$ be the average number of centres within an interval dx at a distance x from a specified centre; then clearly

$$\overbrace{T}^2(x) = Nz(x)$$

As presented schematically in Fig. 2, one may consider $z(x)$ as the sum of a number of normalized functions as follows:

$$\begin{aligned} z(x) &= \delta(0) + P_1(x) + P_2(x) + \dots \\ &\quad + P_{-1}(x) + P_{-2}(x) + \dots \end{aligned} \quad (3)$$

Here, $P_n(x)dx$ is the chance of finding the centre of the n th neighbour in the interval dx . This chance can be expressed in the nearest neighbour distance distribution $P_D(x)$, which in the following will be indicated by $P_D^n(x)$, by

$$P_n(x) = \overbrace{P_D(x)}^n \quad (4)$$

Furthermore, the function P_n and P_{-n} are symmetrical with respect to $x = 0$, by which

$$P_{-n}(x) = P_n(-x)$$

This leads to

$$p_L(x) = N \tilde{n}_c^2 \left\{ \delta_0 + \sum_1^\infty P_n(x) + \sum_1^\infty P_n(-x) \right\} \cdot \widetilde{S(x)}$$

The one-dimensional intensity function $I_1(s)$ is related to this by

$$I_1(s) = \mathcal{F}_1\{p_L(x)\}$$

where \mathcal{F}_1 is the operator for one-dimensional Fourier transformation.

With the aid of the above relations one obtains:

$$I_1(s) = N \cdot f_c f_c^* \cdot Z(s) \cdot \widetilde{V}(s) \quad (5)$$

Here, $f_c(s) = \mathcal{F}_1\{n_c(x)\}$, while $f_c f_c^*$, in analogy with a similar function occurring in the treatment of particle scattering, is often called the "particle factor". Furthermore, $V(s) = \mathcal{F}_1\{\widetilde{S(x)}\}$ and $Z(s) = \mathcal{F}_1\{z(x)\}$. The function $Z(s)$ is generally called the "interference function", as it represents the effect of the interference of the rays diffracted by different lamellae. From the Eqns (3) and (4) it follows that

$$Z(s) = 1 + \sum_1^\infty n (F^n + F^{*n})$$

or

$$Z(s) = 1 + \frac{F}{1-F} + \frac{F^*}{1-F^*} = \operatorname{Re} \left[\frac{1+F}{1-F} \right] \quad (6)$$

Here, $F(s) = \mathcal{F}_1\{P_D(x)\}$, while $\operatorname{Re}[G]$ indicates the real part of the complex function G . The function $P_D(x)$ can be considered to be the convolution of a δ -function at $x = D$, where D is the average of the x_D values, with a function $P_0(x)$ giving the distribution of the x_D values around the average: $P_D(x) = P_0(x) \delta(x - D)$. Accordingly,

$$F(s) = \mathcal{F}_1\{P_0\} e^{-2\pi i D s} \quad (7)$$

If the function $P_0(x)$ is symmetrical around $x = 0$, the transform $\mathcal{F}_1\{P_0\}$ will be a real function; if, however, it is an asymmetric function, this transform will be complex, and may be written as $R(s) e^{i\psi}$, where R is real, and ψ is also a function of s . F will then be given by

$$F(s) = R(s) e^{i(\psi - 2\pi D s)}$$

Using this relation one may transform Eqn (6) into

$$Z(s) = \frac{1 - R^2}{1 + R^2 - 2R \cos \chi} \quad (8)$$

where χ is the angle $\psi - 2\pi D s$.

The properties of this function are discussed at length in various textbooks and papers. In the following we will, in a number of separate points, present its most important features and indicate in what way it can be extended to the more accurate relations involving independent distributions of the thicknesses of the crystalline and amorphous layers.

1. GENERAL FEATURES

The interference function, of which some examples are shown in Fig. 3, generally shows maxima and minima, due to the variation of $\cos \chi$ in the denominator of Eqn (8) between -1 and $+1$. Furthermore, from the fact that the function $z(x)$ reaches a constant level of height $1/D$ as z goes to infinity, it follows that the Fourier transform $Z(s)$ contains a δ -function of magnitude $1/D$ in the origin (not shown in Fig. 3). If the phase angle $\psi = 0$ (symmetrical P_0 -function), the positions of the maxima in the $Z(s)$ function will be very close to $s = D^{-1}, 2D^{-1}, 3D^{-1}$, etc. As can be seen from the lower curves in Fig. 3, broad distributions of the periods x_D may give rise to small deviations from these positions; these are brought about by the variation of the function R in the interval around the s value where $\cos \chi$ equals $+1$.

Furthermore, the maxima in the function $I_1(s)$ may be displaced to smaller s values because of the variation of the factor $f_c f_c^*$ (see Fig. 3, dotted line), which occurs in the expression for $I_1(s)$ (Eqn 5). In the case of non-symmetrical distributions P_0 the deviations may be expected to be larger because of the non-zero value of the term ψ in the argument of the cos-function.

The oscillations in the $Z(s)$ function damp out to a constant level of height 1 , which corresponds to the Fourier transform of the δ -function in the origin of the function $z(x)$. A useful property of $Z(s)$ is furthermore obtained by integrating it between the positions of neighbouring minima, corresponding to $(n - \frac{1}{2})D^{-1}$ and $(n + \frac{1}{2})D^{-1}$. Taking into account that in comparison with $\cos \chi$, R is a slowly varying function of s , one may assume R to be constant within these intervals. The integral is then found to be equal to $1/D$, irrespective of the values of n and R .

2. THE USE OF GAUSSIAN DISTRIBUTIONS

These distributions have been most widely used to describe the deviations of the nearest neighbour distances x_D from the average D . If Δ is the second moment of this distribution, it is given by

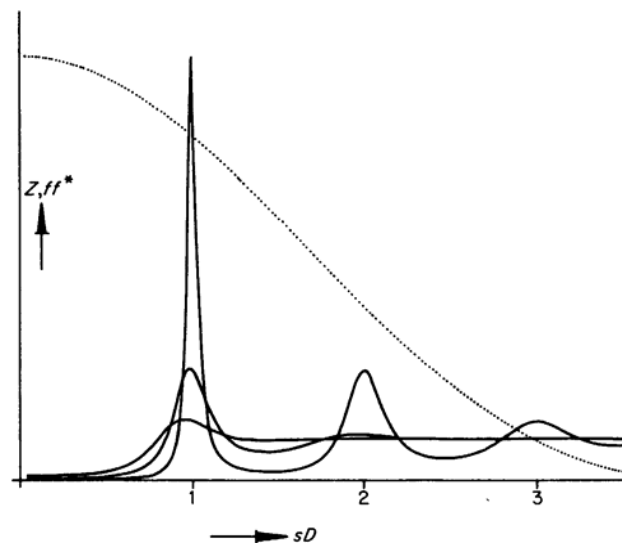


FIG. 3. Interference functions $Z(s)$ for periods x_D that are distributed according to Gaussian functions with second moments of $0,1D$, $0,2D$ and $0,3D$ respectively. The dotted line represents the particle function for a crystallinity $\phi = 0,25$ (0,75).

$$P_D(x_D) = \frac{1}{\sqrt{(2\pi\Delta^2)}} e^{-(x_D-D)^2/(2\Delta^2)}$$

Its Fourier transform, separated into factors as indicated in Eqn (7), is equal to

$$F(s) = \frac{1}{2} e^{-2\pi s^2 \Delta^2} \cos(2\pi sD)$$

This function has been used in drawing the curves of Fig. 3, in which also the particle factor for lamellae of thickness $C = \frac{1}{4}D$ is shown. This expression leads to the following values of the height of the maxima:

$$Z_{\max}(s) = D^2/(\pi n \Delta)^2$$

Of more importance in practice is the shape of the peaks above the background, in which the background may be taken equal to the average of Z in the neighbouring minima. The integral widths of the peaks defined in this way can be shown to be given by

$$B_n = D^{-1} \pi^2 n^2 (\Delta/D)^2$$

It is to be noted that this width increases with n^2 , which is a general result for paracrystalline lattices.

3. EFFECT OF THE SHAPE FUNCTION

According to Eqn (5), the finite size L of the stacks in the direction of the layer normals affects the intensity function through the convolution with the function $V(s)$. From its definition, given in connection with Eqn (5), it follows that

$$V(s) = \sin^2(\pi L s)/(\pi L s)^2$$

The second moment of this function is $1/L$. As by convolution, the squares of the second moments of the peaks in the convoluting functions are added, the peaks in $I_1(s)$ will not be greatly affected unless $1/L$ is of the order of the width of the peaks in $Z(s)$.

However, in all cases the zero-order δ -function will be broadened. In the present model, this is the most important source of broadening of the origin peak, and observation of a broadened origin peak in the $I_1(s)$ function has therefore often been attributed to finite L values. This interpretation must, however, be regarded with caution. Any particle-like inhomogeneity in the sample, such as catalyst remnants (Wendorff and Fischer, 1973a), may cause a strong zero order peak. If one wants to be sure that an observed origin peak is caused by the semi-crystalline morphology that is to be studied, one should, if possible, re-examine the sample in the molten state, where any remaining scattering near the origin must be attributed to such inhomogeneities. Furthermore, as will be discussed below, certain deviations from the ideal lamellar model may also give rise to an origin peak in the $I_1(s)$ function.

4. EFFECT OF VARIATIONS IN THE CRYSTALLINE LAMELLAR THICKNESSES

If variations in the thicknesses of the crystalline layers are assumed to occur, the previously given derivations may be maintained, if in Eqn (5) the values x_c of the thicknesses of the individual lamellae are entered. As shown by Guinier (1963) in his textbook, eqns 2-57, this leads to the following equation, which is the analogue to Eqn (5)

$$I_1(s) = N[\bar{f}_c^2 - \bar{f}_c^2 + \bar{f}_c^2 Z(s)] \widehat{V}(s) \quad (9)$$

Taking the origin of the x -axis in one of the interfaces of the lamellae, and assuming a homogeneous electron density distribution within the lamellae, one may write:

$$f_c = \eta_c \int_0^{x_c} e^{-2\pi i k x} dx$$

from which it follows that

$$|\bar{f_c^2}| = \frac{1}{2\pi^2 s^2} \{1 - \overline{\text{Re}(e^{-2\pi i x_c s})}\} = \frac{1}{2\pi^2 s^2} (1 - \text{Re } F_c)$$

Here, $F_c = \mathcal{F}_1\{P_c(x_c)\}$, and $P_c(x_c)$ is the normalized distribution function of the x_c values. As shown by Brämer (1972), this leads to the following expression:

$$I_1(s) = \frac{1}{4\pi^2 s^2} \left[1 - |F_c|^2 + (|1 - F_c|^2) \text{Re} \left(\frac{1 + F_D}{1 - F_D} \right) \right]$$

Here, the function F , defined in connection with Eqn (6), is indicated as F_D . According to Buchanan (1971), the first two terms of the expression in the square brackets may well be responsible for an origin peak.

5. EFFECT OF INDEPENDENT VARIATIONS FOR THE THICKNESSES OF THE CRYSTALLINE AND AMORPHOUS LAMELLAE

In the previous discussions, it was assumed that the distributions of the x_c - and x_D -values in the sample are independent of each other. This would imply that the probability of finding a certain value for x_c within a certain distance x_D is determined by the shape of the functions P_c and P_D only. This, however, obviously cannot hold if the chosen value of x_c is larger than the one of x_D . To remove this inconsistency one has to start the derivation of $I_1(s)$ with the functions $P_c(x_c)$ and $P_a(x_a)$, describing the distributions of the thicknesses of the crystalline and amorphous layers respectively; the shape of $P_D(x_D)$ may then be derived from

$$P_D = \widehat{P_c P_a}$$

Following Brämer (1972), we will call the model, based on the distribution P_c and P_a , the "stacking model" ("Stapelmodell"), and the model based on P_D and P_c the "lattice model". Though being somewhat more complicated, the derivation of the intensity function for the stacking model is similar to the one given in this section for the lattice model, and leads to the following expression:

$$I_1(s) = \frac{N}{4\pi^2 s^2} \text{Re} \left[\frac{(1 - F_c)(1 - F_a)}{1 - F_D} \right] \quad (10)$$

where $F_a = \mathcal{F}_1\{P_a(x_a)\}$. The difference between the two models were thoroughly discussed by Brämer (1972, 1974); as is to be expected the two models yield identical results in the case of narrow distributions of x_c and x_a , especially at crystallinities close to either 0 or 1. Brämer, furthermore, points out that in calculating diffraction curves there is no reason for preferring the less accurate lattice model over the stacking model. The reason for using the lattice model for the derivations in this chapter is that the separation into an

interference- and a particle-factor, which cannot be made if the stacking model is used, allows an easier and more revealing discussion of the various properties of the one-dimensional intensity function. As to these properties, the two models lead to conclusions that differ only in minor aspects.

6. FURTHER CONSIDERATIONS CONCERNING THE I_1 FUNCTION

In the ideal lamellar model, the assumption that the electron density within each phase is constant leads to the presence of infinitely sharp phase boundaries, which would seem to be unrealistic.

Phase boundaries with a gradual transition of the electron density were first introduced by Tsvankin (1965) and later discussed by Blundell (1970). In the latter study, the effect of the width E of the phase boundary on the intensities of the various orders of reflection was analysed; however, the results show that in general these effects are too small to be of practical use. In the next section more powerful methods for estimating the width of the phase boundary will be discussed.

In deriving Eqn (5) of the intensity from a lamellar stack of finite dimension L in the x direction, it was silently assumed that the electron density outside the stacks is equal to the reference value, which here was taken to be the value pertaining to the amorphous phase. As was remarked previously, various authors have used L as a parameter for matching observed and calculated $I_1(s)$ functions. In view of this, it is to be noted that the above assumption, which clearly is not satisfied in a sample in which the clusters are to be space filling, may have a large effect on the value of L that can be obtained in this way (see, for example, Schultz, 1976). This can be rectified by introducing a third phase, representing the environment of the clusters, of which the electron density is equal to the average value of the electron density within the clusters, as was done by Wenig and Brämer (1978). Their results show that this new assumption leads to larger values of L than the original one; however the difference becomes negligible if the clusters contain 10 or more crystalline lamellae.

In literature the use of various distribution functions P_c , P_a and P_D in calculating $I_1(s)$ for either the stacking or the lattice model is described. Surveys of this literature have been given in publications by Crist (1973) and Brämer (1973). A general conclusion that follows from inspection of their results is that the intensity function is primarily affected by the width of the distribution functions, and only in a secondary way by their shapes. A reasonable, good agreement between observed and calculated I_1 functions is therefore not a guarantee for the correctness of the distribution functions used in the calculation. If conclusions as to this matter are required, a separate study of the effect of varying these shapes must be made.

7. SPECIAL METHODS OF ANALYSIS

Tsvankin (1965) developed a short-cut method in which certain characteristic quantities of the $I_1(s)$ curve are related to structural parameters with the aid of calibration curves. In this way, in analysing an observed intensity curve, the calculation of the $I_1(s)$ curve can be avoided; however, this is of course at the expense of checking the results by comparing the observed and calculated functions. The method was later extended by Buchanan (1971), whereas Crist (1973) drew attention to some shortcomings of the method that are inherent to the use of the lattice model. Generally speaking, one may expect the method of Tsvankin to be restricted by the fact that only one peak is used in the analysis of the scattering curve, whereas, according to the discussion in the previous section, the information concerning the crystallinity is mainly contained in the second order peak.

Strobl (1972, 1973) devised a method of analysis in which use is made of the property of the interference function $Z(s)$, that its integral between the limits $(n - \frac{1}{2})/D$ and $(n + \frac{1}{2})/D$ is approximately equal to $1/D$, irrespective of the values of n and R (see point 1). Assuming the stacks to be of infinite size one may, with the aid of Eqn (5), from an observed $I_1(s)$ function, derive the value of the particle function at the midpoints of such intervals, which correspond with the positions of the Bragg reflections. In general in the diffraction curves of isotropic samples, the number of observable Bragg reflections will be too small to allow a detailed analysis of the electron density variations. However, Strobl shows that if two orders are observed, and a genuine two-phase structure is assumed, values of the electron density deviations in the two phases and of the average thicknesses of the two types of layers may be derived. It is of interest to note that the information obtained in this way is independent of the information to be obtained from the invariant (see Section IV, Eqn 17); the results may therefore be checked on their internal consistency. The method was combined with a method for desmearing which was derived earlier (Strobl, 1970); as a result the data to be used can be obtained directly from smeared curves.

B. Methods Involving the Use of the Correlation Function

In single crystal structure analysis, the auto-convolution of the electron density, or Patterson function, is widely used in determining the approximate positions of the atoms in the unit cell. It can be obtained directly from the intensity function by Fourier transformation, and contains all the information that is hidden in the diffraction pattern. The advantage of using the Patterson function is that it is in real space instead of reciprocal space, which makes it easier to interpret than the intensity function itself. In small angle scattering the Patterson

function is usually scaled to have the value 1 in the origin; it is then called the correlation function. Its general properties have been discussed by Porod (1951, 1952) and by Debye *et al.* (1957), and are reviewed in Chapter 2. It was used in a variety of problems in connection with particle scattering and with random two-phase structures. Vonk and Kortleve (1967) applied it to the scattering of the ideal lamellar model, and Ruland (1977) used it to obtain the interface distribution function for this model; these methods are described below.

1. CORRELATION FUNCTION OF THE IDEAL LAMELLAR MODEL

Like the function representing the electron density deviations, the correlation function for a single stack of the ideal lamellar model is a three-dimensional function which, however, varies in the x -direction only. It will be indicated by $\Gamma^0(x, y, z)$; its value in the x -direction by $\gamma_1(x)$. This function can be obtained from the one-dimensional intensity function by Fourier transformation:

$$\gamma_1(x) = \int_0^\infty I_1(s) \cos(2\pi xs) ds / \int_0^\infty I_1(s) ds$$

or from the isotropic three-dimensional intensity function:

$$\gamma_1(x) = \int_0^\infty I(s) s^2 \cos(2\pi xs) ds / \int_0^\infty I(s) s^2 ds \quad (11)$$

It may also be obtained from the intensity \tilde{I} of an isotropic sample recorded with the aid of slit geometry by

$$\gamma_1(x) = \int_0^\infty s\tilde{I}(s) [J_0(2\pi xs) - (2\pi xs)J_1(2\pi xs)] ds / \int_0^\infty s\tilde{I}(s) ds \quad (12)$$

where J_0 and J_1 are zero- and first-order Bessel functions. In the following the function $\gamma_1(x)$ obtained in any of these ways will be indicated as the observed one-dimensional correlation function, to distinguish it from the "calculated" correlation function that can be obtained from calculations based on a certain model. In these calculations the zero level of the electron density deviations η is taken equal to the average electron density within the stacks of the model. From its definition it follows that $\gamma_1(x)$ can be calculated from the model by

$$\gamma_1(x) = \int_0^\infty \eta(\xi)\eta(x-\xi) d\xi / \int_0^\infty \eta^2(\xi) d\xi \quad (13)$$

which may also be written as

$$\gamma_1(x) = \overline{\eta_A \eta_B} / \overline{\eta_A^2}$$

In the second formulation AB is a vector of length x normal to the layers, while

η_A and η_B indicate the electron density deviations at A and B respectively. The averaging is done over all points A within the structure. Clearly, $\gamma_1(x)$ has a maximum value of 1 at $x = 0$; at $x = \frac{1}{2}D$ the values of η_A and η_B will largely be of opposite sign, and γ_1 will show a minimum of negative value; at $x = D$ a maximum will occur, as A and B tend to be in corresponding positions in layers of the same type. If $x \gg D$ the values of η_A and η_B will no longer be correlated, and $\gamma_1(x)$ will consequently damp out to the average value of $\eta_A \eta_B$, which is 0. The general shape of γ_1 can be seen from the examples given in Fig. 4, curves (b) and (c).

In their calculations of $\gamma_1(x)$, Vonk and Kortleve (1967), started from general relations derived by Debye *et al.* (1957), and arrived at the following relation:

$$\gamma_1(x) = \frac{\phi}{1-\phi} \left\{ \frac{1}{\phi^2} \int_x^\infty (x_c - x) P_c(x_c) dx_c + P_{cac} + P_{cacac} + \dots - 1 \right\} \quad (14)$$

Here, the terms $P_{ca\dots c}$ indicate convolution products of the type $Q_c \widehat{P_a} \dots \widehat{Q_c}$, in which $Q_c(x) = 1/\phi (\int_x^\infty P_c(x_c) dx_c)$. In the above expression, the average period D has been set to 1. Though this expression is not symmetric with respect to the interchanging of the crystalline and amorphous layers, it can be rearranged to give an expression which does show this property.

In Fig. 4, some examples of calculated correlation functions are presented. As shown by curve (a), the correlation function of a strictly periodic function is itself a strictly periodic function. Between the points X and Y it reaches a constant negative value, which is equal to $-\phi/(1-\phi)$ if $\phi < \frac{1}{2}$, and to $-(1-\phi)/\phi$ if $\phi > \frac{1}{2}$. The length of XY is $(1-2\phi)$ if $\phi < \frac{1}{2}$, and $(2\phi-1)$ if $\phi > \frac{1}{2}$. The peaks at $x/D = 0, 1, 2, \dots$ correspond to the first, second, third, etc. term in the right-hand side of Eqn (14), and can be attributed to the contributions from the vectors AB , which have A and B both in the crystalline phase, and intersect a number of 0, 1, 2, etc. amorphous layers respectively.

As shown by curve (b) in Fig. 4, introduction of the distribution functions P_c and P_a of non-zero widths causes broadening of these peaks. The minimum between X and Y is filled up, but in observed correlation functions such as the one shown in Fig. 4 curve (b), part of it can often still be recognized, which allows us to determine ϕ from its depth. Clearly, this situation will be met only if the functions P_c and P_a are relatively narrow, and the interval XY relatively large, that is if ϕ differs appreciably from $\frac{1}{2}$. If an observed correlation function, like the one represented by curve (c) in Fig. 4, does not show a horizontal region, the base line at $\gamma_1 = -\phi/(1-\phi)$ or $-(1-\phi)/\phi$ is bound to be below the minimum. This allows us to determine an interval between ϕ' and $(1-\phi')$ within which the crystallinity must lie; here ϕ' is found from $\gamma_{min} = -\phi'/(1-\phi')$ or $-(1-\phi')/\phi'$, where γ_{min} is the value of γ_1 at the minimum.

Like the one-dimensional intensity function, one may expect the one-dimensional correlation function to be much more sensitive to the width of the

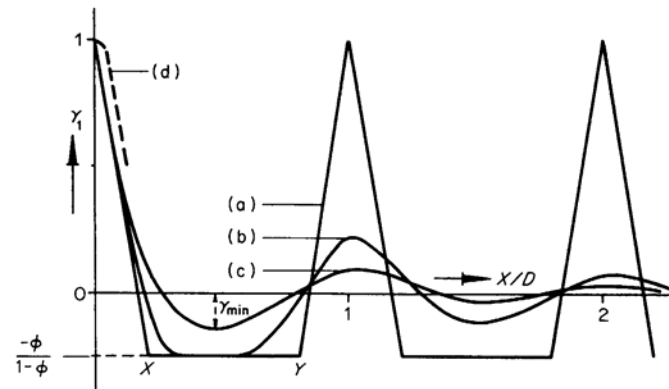


FIG. 4. One-dimensional correlation function $\gamma_1(x)$, based on the ideal lamellar model, for $\phi = 0.2$ and three different widths of the distribution functions P_c and P_a (curves a, b and c). Curve d indicates the effect of the occurrence of a transition layer between the two phases.

distribution functions P_c and P_a than to the shape of these functions. In their calculations, Kortleve and Vonk (1968) used log-normal functions, of which the relative widths B_c/C and B_a/A were taken to be equal. This was done to reduce the number of parameters to be fitted. Only if the observed correlation function shows a horizontal region of the type discussed above, may it be meaningful to assign different relative widths to P_c and P_a , as in this case the effect of the shapes of the two functions can be recognized more or less separately near the points X and Y (Fig. 4).

2. EFFECT OF DEVIATIONS FROM THE IDEAL LAMELLAR STRUCTURE

The presence of a transition layer of width E in which η changes linearly from η_a to η_c mainly affects the one-dimensional correlation function in the region near $x = 0$ (Vonk, 1973). If the width E is zero, the first derivative of γ_1 at the origin has a non-zero value of $[\phi(1-\phi)D]^{-1}$ (see curves a, b and c in Fig. 4); the presence of a transition layer causes the origin peak to have a non-zero second derivative at $x = 0$, equal to $2 [\phi(1-\phi)DE]^{-1}$. The corresponding part of a correlation function of this type is shown by curve (d) in Fig. 4. These results might be used in the determination of E , but other methods to be discussed below are to be preferred.

According to Eqn (1), introduction of a finite length L of the stacks in the x -direction may be taken into consideration by modifying Eqn (13) in the following way:

$$\gamma_1(x) = \tilde{\eta} \tilde{S} / \eta^2 \quad (15)$$

From the definition of S given in connection with Eqn (1), it follows that \tilde{S} is a linear function, decreasing from 1 at $x = 0$ to 0 at $x = \pm L$. The factor \tilde{S}^2 accounts for the vectors AB which have A inside the stacks, and B outside, where η is assumed to be zero. This assumption implies that outside the stacks the electron density has the average value, which corresponds with a structure in which the stacks are space filling.

In discussing other deviations from the ideal lamellar model we distinguish between deviations of the first and of the second kind. Deviations of the first kind are those in which the long range order is preserved, but the short range order is reduced.

An important example of such deviations occurs in structures in which there are local deviations of the interfaces from the average interfaces, the latter being flat and parallel as required by the ideal lamellar model. It can be shown (Vonk, 1978) that the correlation function of a structure containing such deviations is still essentially a one-dimensional function, except at the origin, where it falls off also in the directions perpendicular to x .

Deviations of the second kind do not affect the short range order, but reduce the long range order; an example of this is shown schematically in Fig. 5a. As was already discussed in the first section, deviations of this nature, like splaying and undulations of the layers, are bound to occur in real structures; furthermore, their presence clearly obviates the difficulties connected with the assumption of the occurrence of stacks. For these reasons it is of importance to understand, if only in a qualitative way, their effect on the small angle scattering intensity.

The discussion (Vonk, 1978) of the deviations of the second kind is based on the assumption that at all points A within the sample the lamellar structure can be recognized sufficiently well to indicate the direction x of the lamellar normal at A . Then, first a so-called locally oriented correlation function Γ is constructed by adding all contributions $\eta_A \eta_B / \eta^2$ from the points A for which these normals have a certain common direction. This function will be of rotational symmetry, with the x -axis in the chosen direction; it is presented schematically in Fig. 5b. The total three-dimensional correlation function γ_0 is then obtained by adding the functions Γ for all directions occurring in the sample.

In relating Γ to the locally oriented correlation function pertaining to the ideal lamellar model Γ^0 , the number n of the intersections that each vector AB makes with the lamellar interfaces in the ideal lamellar structure is counted, as well as the change in this number due to the distortion. The average length of the vectors for which this change is ± 1 is called the distortion length a ; clearly, it will decrease with increasing degree of distortion. Assuming that a is independent of the direction of the vectors with respect to the x direction, and that the lengths of the vectors contributing to a are distributed according to a Poisson function, one may derive

$$\Gamma = \Gamma^0 \exp(-2r/a)$$

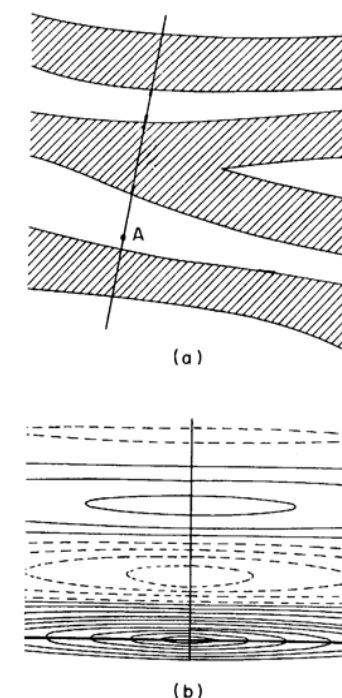


FIG. 5. (a) Schematic representation of deviations of the second kind from the ideal lamellar model. (b) Section through the corresponding locally oriented correlation function.

which, after addition of all Γ functions in an isotropic structure, leads to

$$\gamma_0(r) = \gamma_0^0(r) \exp(-2r/a).$$

Here, γ_0^0 is the isotropic correlation function pertaining to the ideal lamellar structure; it is related to $\gamma_1(x)$ by $\gamma_1(x) = [d\{r\gamma_0^0(r)\}/dr]_{r=x}$.

To apply these results to actual structures one might compare observed and calculated functions $\gamma_0(r)$. This type of function however shows little detail, and it is recommended to use the three-dimensional intensity function instead. This can be obtained from $\gamma_0(r)$ by Fourier transformation according to

$$I(s) \propto 4\pi \int_0^\infty r^2 \gamma_0(r) \frac{\sin(2\pi rs)}{2\pi rs} dr$$

Intensity functions obtained in this way, in which P_c and P_a were assumed to be either Gauss or modified Poisson functions, showed that the distortions cause a lowering of the intensity of the first order peak; however, in contrast to the effect caused by a reduction of the stack size L , or by an increase of the widths

of the distribution functions P_c and P_a , this lowering of the intensity is accompanied with a decrease of the intensity of the origin peak.

3. THE USE OF THE INTERFACE DISTRIBUTION FUNCTION

The interface distribution function is the one-dimensional analogue of the chord distribution function, which describes the distribution of the lengths of all chords that can be drawn between the interfaces in a two-phase structure; here, the contributions of the chords making an odd number m of intersections with interfaces is given the negative sign. In the one-dimensional case, the chords for which $m = 0$ can obviously be identified with the lamellar thicknesses. The use of this function, which is related to the one-dimensional correlation function by

$$g_1(x) = \gamma''_1(x)/\eta^2 \quad (16)$$

was proposed by Ruland (1977). It is presented schematically in Fig. 6, which shows that, if the first three peaks do not overlap, the distribution functions P_c and P_a as well as the crystallinity ϕ can be directly obtained from the interface distribution function, without curve fitting being needed. As is to be expected, and was actually found in practice by Stribeck and Ruland (1978), the second and third peaks will generally overlap, in which case the crystallinity and the distribution function for the type of layers with the smallest average thickness can still be read directly from the curve. If, however, the first and second peaks overlap, as will occur when ϕ is close to $\frac{1}{2}$, one may only separate P_c and P_a by making certain assumptions about their relative positions and shapes while, as in all other methods discussed before, the determination of ϕ becomes problematic. The maxima and minima occurring beyond $x = 1$ in the g_1 curve are convolutions of P_c and P_a , which increasingly overlap and merge as x increases. Their magnitudes are connected to the stack size L in a way that is similar to the one described by Eqn (15).

Instead of using Eqn (16), one may calculate $g_1(x)$ directly from $I(s)$ by taking the second derivative of Eqn (11), which leads to

$$g_1(x) = -16\pi^3 \int_0^\infty s^4 I(s) \cos(2\pi x s) ds / \eta^2$$

From the integral in this expression, which is the Fourier transform of $s^4 I(s)$, a part $\int_0^\infty \lim_{s \rightarrow \infty} (s^4 I(s)) \cos(2\pi x s) ds$ can be separated; as, according to Porod's law, $\lim_{s \rightarrow \infty} (s^4 I(s))$ is a constant, this separated part corresponds to a δ -function in the origin of $g_1(x)$, which may be ignored in the calculation of $g_1(x)$.

The remaining part can be written as

$$g_1(x) = 16\pi^3 \int_0^\infty G(s) \cos(2\pi x s) ds / \eta^2$$

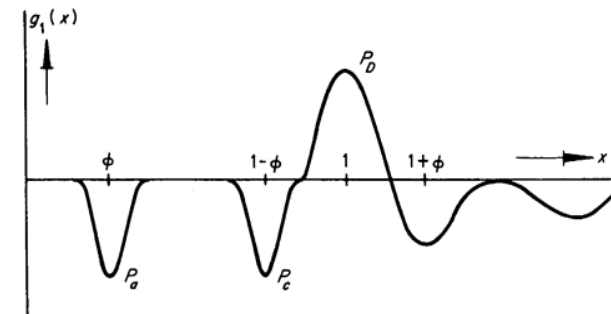


FIG. 6. Schematic representation of an interface distribution function for $D = 1$, $\phi = 0.25$.

where

$$G(s) = \lim_{s \rightarrow \infty} (s^4 I(s)) - s^4 I(s)$$

A similar relation may be derived from Eqn (12) for use with intensities recorded with the aid of slit geometry.

The determination of $c = \lim_{s \rightarrow \infty} (s^4 I(s))$ is a critical step in this procedure, which requires accurate intensity measurements over the whole range of small angle scattering, and a correct determination of the background. Also, deviations from Porod's law due to the occurrence of transition regions between the two phases must be taken into account, for which the procedures to be described in the next section may be used. If, however, such precautions are taken, good results may be obtained, as was shown by Stribeck and Ruland (1978).

IV. The Application of General Relations

The general relations of which the applications are to be discussed in this chapter are independent of the arrangement of the crystalline and amorphous regions in the polymer sample, in which only the occurrence of a two-phase structure, either with or without a transition layer at the phase boundary, is presupposed. These relations are especially powerful as they allow conclusions about the structure to be obtained without a detailed analysis of the scattering curve being necessary. It must be emphasized that the intensities have to be corrected for the background due to liquid scattering, for which the procedures to be described in the next section are to be recommended. Moreover, in a number of applications, absolute intensities are required; these are to be indicated by i or, if smeared by a slit of infinite height, by \tilde{i} . Most frequently, absolute intensities are obtained by relating the measured intensities to the intensity of a calibration sample, as described by Kratky *et al.* (1966). These authors have also set themselves the task of distributing the Lupolen platelets which serve as calibration

samples. It is however to be noted that for this purpose also, samples of known scattering power may be used, as was done by Hermans *et al.* (1959), and more recently by Shaffer and Beeman (1970).

A. Use of the Invariant

The general relation involving the invariant is:

$$Q_s = \int_0^\infty i(s) dv_s = \bar{\eta}^2$$

where η is the deviation of the electron density from the average value, and the integration is to be extended over all elements dv_s of reciprocal space. In the case of an isotropic polymer sample in which the crystalline and amorphous electron densities are ρ_c and ρ_a respectively, this can be shown to be equal to

$$4\pi \int_0^\infty i(s)s^2 ds = 2\pi \int_0^\infty \tilde{i}(s)s ds = \phi(1-\phi)(\rho_c - \rho_a)^2 \quad (17)$$

If the two phases are connected by a transition layer in which the electron density varies linearly from ρ_c to ρ_a , the right part of this equation is equal to

$$\left[\phi(1-\phi) - \frac{ES}{6V} \right] (\rho_c - \rho_a)^2$$

where S/V is the specific surface of the phase boundary. Both S/V and E may be found by the use of general relations, as is to be described below.

The invariant is often measured together with the mass density d ; this is related to the electron density ρ expressed in mole electrons per cm^3 by $d = (\Sigma M / \Sigma A)\rho$ where ΣM is the sum of the atomic weights and ΣA the sum of the atomic numbers of the atoms in the repeat unit of the polymer. The average electron density ρ is given by

$$\rho = \phi\rho_c + (1-\phi)\rho_a \quad (18)$$

It is to be noted that ϕ is the crystallinity by volume, which is related to the crystallinity by weight ψ as $\psi = \phi\rho_c/\rho$.

Equation (18) will also be valid if a transition layer between the phases occurs, provided that in calculating ϕ the phase boundary is assumed to be at the position where the electron density equals $(\rho_c + \rho_a)/2$. If one of the three parameters ϕ , ρ_c or ρ_a is known, as well the value of $ES/(6V)$, the other two parameters may be obtained by combining Eqn (17) with Eqn (18). However, often only approximate or limiting values of one of these parameters are available.

In this case a convenient way of expressing the results of the calculations is

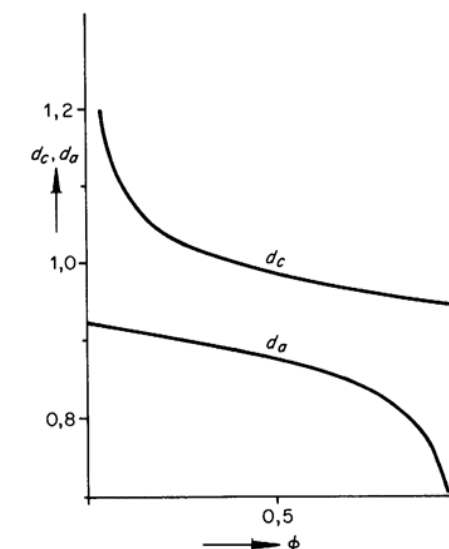


FIG. 7. Plot of the crystalline and amorphous densities d_c and d_a for a linear polyethylene sample, as obtained with the aid of the invariant, versus the crystallinity ϕ .

to plot the densities ρ_c and ρ_a as functions of ϕ ; an example of such a plot is presented in Fig. 7.

The value of ϕ to be used in the above calculations is not necessarily the same as the one to be used in calculations based on the ideal lamellar model. Of late, it has been found that crystallinities obtained by the present method, or by other methods involving wide angle scattering or calorimetry, are generally lower than those derived from the $I_1(s)$ curve based on the ideal lamellar model. The difference seems to increase with decreasing crystallinity, and may amount to as much as 30% (absolute) in samples of low crystallinity. The discrepancy has to be attributed to the presence of amorphous material outside the stacks, which would imply that in such samples the stacks are not space-filling (Stribeck and Ruland, 1978; Vonk, unpublished results).

B. Use of the Fourth Moment of the Intensity Distribution

The value of the fourth moment of the absolute intensity obtained from an isotropic sample is given by (Vonk, 1973):

$$16\pi^3 \int_0^\infty s^4 i(s) ds = 12\pi^3 \int_0^\infty s^3 \tilde{i}(s) ds = \int |\text{grad } \eta|^2 dv_r \quad (19)$$

The vertical bars indicate the absolute value of the vector $\text{grad } \eta$; the integration

on the right-hand side is to be extended over all volume elements dV_r within the irradiated part of the sample.

In the case of a genuine two-phase structure the gradient of η is infinite at the phase boundary; if, however, the electron density varies smoothly everywhere, a finite value for the integral on the right-hand side is obtained. Thus, a two-phase structure with a transition layer of the type discussed before, yields a value of the integral equal to $(\rho_c - \rho_a)^2 S/(EV)$. If the other quantities are known, this may be used to find E with the aid of Eqn (19).

If no absolute intensities are available, the ratio R of $|\text{grad } \eta|^2$ to $\overline{\eta^2}$ may be obtained by determining both the fourth and the second moment (invariant) of $I(s)$. This ratio is related to E by $ER \phi(1-\phi) = S/V$, from which the following expression may be derived:

$$E = -\frac{4}{R} \left(\frac{d\gamma_0}{dr} \right)_E$$

Here, $(d\gamma_0/dr)_E$ is the slope of the correlation function at a distance E from the origin, where γ_0 decreases linearly with r . This slope is related to the slope in the one-dimensional correlation function (see Fig. 4, curve d) by

$$\left(\frac{d\gamma_1}{dx} \right)_E = 2 \left(\frac{d\gamma_0}{dr} \right)_E$$

Unlike the method to be discussed in the next section, this method for the determination of E does not involve the use of approximations. However, because of the multiplication of I or \tilde{I} with s^4 or s^3 respectively, it requires a high accuracy of the intensities in the very tail of the diffraction curve, which implies the need for a correct determination of the background. Furthermore, the statistical errors in the intensity measurements in the tail of the curve may cause undesired deviations of the integrals involved, and smoothing was found to be necessary before the integrations are performed. This smoothing may be done with the aid of a plot of $\tilde{I}s$ against $1/s^2$, which is to be discussed in Section IV.D.

C. Use of Porod's Law

According to Porod's law (Porod, 1952; Debye *et al.*, 1957), the intensity in the tail of a diffraction curve from a two-phase structure with sharp phase boundaries is given by

$$c = \lim_{s \rightarrow \infty} (s^4 i) = \frac{2}{\pi} \lim_{s \rightarrow \infty} (s^3 \tilde{I}) = \frac{(S/V)(\rho_c - \rho_a)^2}{8\pi^3} \quad (20)$$

If absolute intensities are not available, this equation may be combined with the one giving the value of the invariant (Eqn 17); this leads to the following expression

$$\frac{\lim_{s \rightarrow \infty} s^4 I}{\int_0^\infty s^2 I(s) ds} = \frac{4}{\pi} \frac{\lim_{s \rightarrow 0} s^3 \tilde{I}}{\int_0^\infty s \tilde{I}(s) ds} = \frac{S/V}{2\pi^2 \phi(1-\phi)} \quad (21)$$

Furthermore, S/V can be shown to be related to the slope of γ_0 and γ_1 at the origin by

$$\left(\frac{d\gamma_0}{dr} \right)_{r=0} = \frac{1}{2} \left(\frac{d\gamma_1}{dx} \right)_{x=0} = \frac{S/V}{4\phi(1-\phi)} \quad (22)$$

The use of Eqn (21) or (22) requires knowledge about ϕ , but if ϕ is close to $\frac{1}{2}$, the value of S/V is not very sensitive to variations in ϕ and a high accuracy is not required.

In the case of an ideal periodic structure, the value of S/V should be equal to $2/D$, where D is the "number" average of the distribution $P(D)$. However, the value of D found from the first order peak on γ_1 or I_1 corresponds to the "weight" average of $P(D)$. As a result S/V usually exceeds $2/D$ by a factor between 1 and 2.

D. Deviations from Porod's Law

In practice, Porod's law is found to be best obeyed in polymers with a high crystallinity like linear polyethylene, polyoxymethylene, polyethylene oxide, etc. Polymers of lower crystalline often show a more rapid decrease of the intensities in the tail of the diffraction curve than predicted by Porod's law, indicating the presence of transition layers. If such layers occur, one may consider the actual electron density distribution to be the convolution of the corresponding distribution ρ^0 of the ideal two-phase structure with a smoothing function $h(x)$ (Ruland, 1971). Here, the x -direction is perpendicular to the phase boundary. This leads to the following modification of the intensity I^0 from the ideal structure:

$$I(s) = I^0(s) \mathcal{F}_1\{h\}$$

If the electron density within the phase boundary varies linearly over the distance E , the function h is a top-hat function of width E , giving

$$I(s) = I^0(s) \sin^2(\pi Es)/(\pi Es)^2 \quad (23)$$

In the region where I^0 obeys Porod's law this may be approximated by

$$I(s) = (c/s^4)(1 - \pi^2 E^2 s^2/3) \quad (24)$$

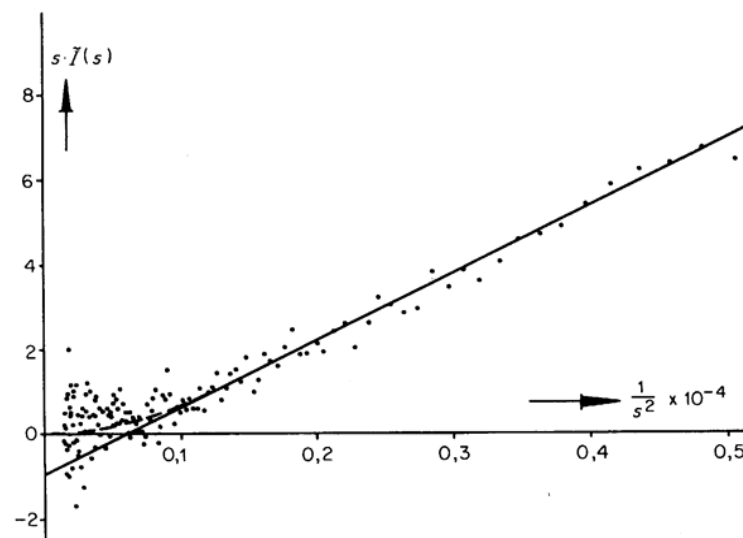


FIG. 8. Plot of $s\tilde{I}(s)$ versus $1/s^2$ for a polypropylene sample. From the slope and the position of the straight line, the constant c from Porod's law, and the width E of the transition layer may be found. Near the origin the data points are scattered around the broken line rather than around the straight line.

where c is the constant defined by Eqn (20). The equivalent relation for intensities smeared by slit collimation is

$$I(s) = (\pi c / 2s^3)(1 - 2\pi^2 E^2 s^2 / 3)$$

These relations may be used to find E by plotting the various quantities in a suitable way. As such, a plot of $s^3 I$ versus s^2 may be used (Ruland, 1971) or, alternatively, a plot of $\tilde{I}s$ versus $1/s^2$ (Vonk, 1973). An example of the latter is shown in Fig. 8; it has the advantage that the data points are most crowded in the region where the accuracy is the lowest. In Fig. 8 the effect of the approximation made in deriving Eqn (24) from Eqn (23) is evident: whereas the straight line at small values of $1/s^2$ reaches negative values, the true value of $\tilde{I}s$ must of course be positive. If the plot is to be used to smooth the intensities as described in Section B above, the straight line in this region should be replaced by a smooth curve, like the broken line in Fig. 8, drawn through the data points at the lowest values of $1/s^2$.

If E is relatively large, no part of the plot of $\tilde{I}s$ versus $1/s^2$ may show the desired linear relation; in that case the method described in Section B above has to be preferred. In general, when both methods are applicable, their results agree reasonably well (Vonk, 1973).

V. Miscellaneous Topics

A. Correction for the Sample Background Scattering

In view of the high accuracy required for the intensities in the tail of the scattering curve in applying the procedures described in the previous section, special attention must be paid to the subtraction of the background due to liquid scattering.

In Section II it was mentioned that if at intermediate angles a 2θ region of constant intensity can be observed, this intensity may be subtracted from the small angle scattering intensities at lower angles. However, at close inspection, such a region is seldom observed; usually the background intensity rises slowly with increasing 2θ , as is shown for a polyethylene sample, by curve (a) in Fig. 9 (Kortleve *et al.*, 1972). If melting of the sample is possible, the shape of the background may be obtained by recording the intensity of the sample above its melting point; the result for the sample of Fig. 9 is shown by curve (b). This shows some extraordinary scattering below 2° , which probably results from heterogeneities in the polymer. By ignoring this scattering, curve (c) is obtained. It may be assumed that the background belonging to curve (a) can be found by scaling curve (c) with a factor that is equal to the ratio of the intensities of curve (a) and (b) in the region to the right of $2\theta_{\min}$, which is the 2θ value corresponding with the minimum in curve (a). In this way curve (d) in Fig. 9 is obtained.

This rather time-consuming procedure may be avoided if one assumes that the intensity in the background can be represented by an expression of the type

$$Y(s) = c_1 + c_2(2\theta)^n$$

where c_1 and c_2 are positive constants, and n is an even number. Values of these constants and of n may be found by fitting a curve of the above equation to the data points to the right of $2\theta_{\min}$. In practice, $n = 4$ was found to apply to a number of polyethylene samples (Vonk, 1973).

B. Determination of Phase Transitions in Polymers

The small angle scattering of most semicrystalline polymers is very temperature dependent, which can be explained by examining the effect of temperature variations on the quantities occurring in the expression for the invariant, Eqn (17). As the expansion coefficient for the amorphous part of a polymer is usually much larger than the one for the crystalline part, the value of $(\rho_c - \rho_a)^2$ will increase with temperature. On the basis of literature data (Swan, 1962; Wilski, 1964), an increase in the invariant of polyethylene at room temperature of almost 1% per degree Kelvin is calculated. At temperatures close to the

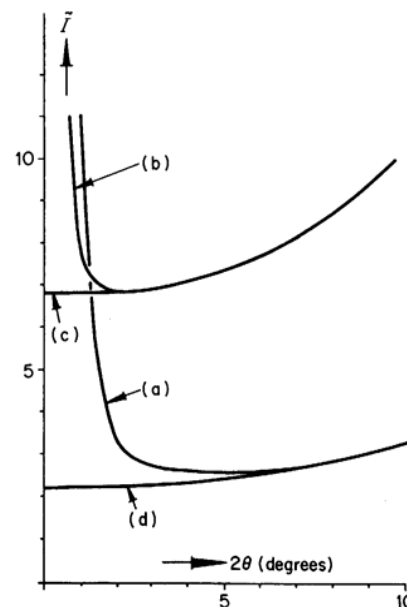


FIG. 9. X-ray scattering from a polyethylene sample at intermediate angles. (a) at room temperature, and (b) in the molten state; (c) liquid scattering of the molten polymer; (d) liquid scattering of this sample at room temperature.

melting point variation of ϕ will also affect the invariant, though this effect will not be large as long as ϕ does not differ too much from $\frac{1}{2}$. However, the invariant will become proportional to ϕ as it approaches zero. The registration of small angle scattering may be used as a sensitive method for detecting the first signs of crystallization in a cooling melt; in fact, it is reported to have been observed before crystallization could be detected by wide angle scattering (Katayama *et al.*, 1968).

Furthermore, the discontinuity in $(\rho_c - \rho_a)^2$ occurring at the glass transition temperature T_g can be used to find this temperature. To this end Fischer and Kloos (1970) used a plot of the square root of the intensity, measured at the peak of the small angle scattering of both linear and branched polyethylene, against temperature, which showed a pronounced discontinuity at T_g .

Finally, also in completely amorphous polymers, second order transitions may be observed with the aid of small angle scattering. Amorphous samples generally show a scattering curve of the type presented in curve (b) of Fig. 9. By extrapolation of this curve to $2\theta = 0$, as indicated by curve (c), the quantity $I(0)$ may be obtained. Above the glass transition temperature T_g this can be shown to be proportional to the isothermal compressibility and to the absolute temperature T . Below T_g , $I(0)$ is much less dependent on T , and a plot of $I(0)$

against T will therefore show a change of slope at T_g . These effects have been used to study the mobility of polymer molecules and the occurrence of second order transitions in both fully amorphous and semicrystalline polymers by various authors (Wendorff and Fischer, 1973b; Rathje and Ruland, 1976; Wiegand and Ruland, 1979).

VI. Applications of SAXS to the Study of Solid Polymers

A number of reviews covering the use of SAXS for the study of solid polymers has already appeared. Of the older ones those by Geil (1963) and by Kratky (1966) may be mentioned; a survey giving special attention to some experimental aspects was presented by Alexander (1969). More recent reviews are by Brown and Wetton (1978) and by Higgins and Stein (1979) of which, specially the latter, is very comprehensive. Here these papers will be used as a starting point for a brief discussion of contributions on the topics of this chapter that have appeared since up to the present date (April, 1979).

Apart from the reviews mentioned above, the recent one by Welte and Kreutz (1979), dealing with theories and applications of SAXS in connection with the study of lamellar structures in biological membranes is of interest. The subject is closely connected to the topics treated in this chapter, but as in bio-membranes it is the internal structure of the layers which is of prime importance, the theoretical approach is rather different; however, the thorough treatment of undulating layers may be especially of interest to polymer physicists as well.

A. Studies of Polymer Single Crystals

It is now generally assumed that the single crystals obtained from dilute solutions are covered by layers of amorphous material; however the details of the molecular conformation within these layers are not yet clear at all. For obtaining further information on this matter Wang and Harrison (1978) suspended single crystals of linear polyethylene in two different liquids (xylene and hexane) in order to establish the degree of penetration of these liquids into the surface layers. Their method was to determine the radius of gyration from the SAXS curves, which for infinitely extended lamellae is proportional to the lamellar thickness (see Chapter 4), and to compare this with the D -value obtained from the dried crystal mats. They concluded that crystals which have not been dried before, do not change in shape or density when the dispersing liquid is exchanged, and that in fact under the conditions of their experiments no liquid penetrates the amorphous covering layers at all.

Also related to this problem is a study of Strobl and Eckel (1977), who

compared the lamellar structure of dried crystal mats as revealed by SAXS with data obtained by Raman spectroscopy. From a calculation of the frequency of the Raman longitudinal acoustic mode (LAM), in which they used the thicknesses and densities of the layers obtained by the SAXS method of Strobl (see Section III.A7), they concluded that the Young's modulus of the amorphous layers must be between 0.4 and 1 times the one of the crystalline regions. This result, which is in agreement with the conclusions reached by Folkes *et al.* (1975), cannot fully be accounted for by the circumstance that at the frequency of the LAM the amorphous material at room temperature is in the glassy state. Accordingly, the authors suggested that the chains in the amorphous layers show a high degree of orientation in the same direction as in the crystalline material.

B. Studies of Bulk Polymers

In a study of bulk-crystallized polyethylene samples of different molecular weights, Capaccio *et al.* (1978) combined SAXS with Raman spectroscopy and nitric acid etching followed by gel permeation chromatography. The SAXS intensity curves were used to obtain D -values, from which the crystal thicknesses C were found by multiplication with the volume crystallinity. If the tilting of the chains in the crystalline regions was taken into account, fair agreement of these C -values with those obtained from the Raman LAM frequency was found in the case of slowly crystallized samples. Accordingly, in these samples little coupling between the acoustic waves in the two phases was supposed to occur, which is inconsistent with a high Young's modulus of the amorphous phase, as found by Strobl and Eckel in the work mentioned above. In quenched samples, however, the agreement was worse, and coupling was indeed assumed to occur.

The study of the lamellar morphology was continued by Blundell (1978) who evaluated the SAXS patterns of low density polyethylenes. He concluded that here the infinite stack model in its original form is not applicable, whereas the finite stack model can only be fitted to theoretical intensity- or correlation-functions if at most two crystalline layers are assumed to be present within each stack, which does not seem realistic. However, the author showed that a good fit can be obtained on the basis of the infinite stack model if the crystallinity is assumed to differ from stack to stack. Such variations, which may be brought about by local variations in the degree of short chain branching, are of course very similar and probably indistinguishable from those discussed in Section II, in which D varies from stack to stack. The paper, furthermore, contains a recommendation to use both the one-dimensional intensity function and the correlation function for comparison with calculations based on models.

The work of Schultz (1976) on the SAXS of high density polyethylene

during isothermal crystallization from the melt was continued by Schultz *et al.* (1978) using the powerful SAXS facility at Oak Ridge (Hendricks, 1978). This allowed the collection of diffraction curves with a lower limit corresponding to a Bragg distance of 150 nm in 30 s. The results were similar to those obtained by Schultz in that during crystallization, initially a zero-order maximum develops, which later decreases as a first-order maximum builds up. The zero-order maximum was interpreted to result from isolated crystalline lamallae, the thickness of which can be derived from the corresponding Guinier plot. This thickness was found to remain constant as long as the zero-order maximum could be observed; it furthermore showed the expected increase with crystallization temperature. The first-order maximum was attributed to an increase in the number of lamellae growing parallel to each other. On cooling from the crystallization temperature to room temperature, a second-order maximum was found to come into existence, which was explained by an increase in the crystallinity because of a thickening of the crystalline layers at the expense of the amorphous ones.

Using the methods described in Section V.B, Duiser and Keyzers (1978) studied the effect of plasticizers and additives on the glass transition temperature T_g of solid PVC. It is noteworthy that though this polymer is of low crystallinity, and the SAXS curves accordingly show only faint shoulders, these methods were found to work quite well. A linear decrease of T_g with increasing plasticizer concentration, and a decrease of about 10°C due to the normal additives, were observed. Similar measurements on polyethylene terephthalate showed deviations from the expected behaviour, which were attributed to time dependent volume relaxation in the amorphous phase at temperatures just above T_g . Actually this process could be followed by recording the intensity at the top of the first-order maximum as a function of time.

C. Heterophase Polymers

Segmented polyurethanes, being of great commercial importance, are the subject of continuing SAXS investigations. Bonart (1977) reviewed the work of his group on these substances, including the methods that were employed in the analysis of the SAXS curves. A systematic study of the phase separation, mainly with the aid of the methods described in Section IV of this chapter, was published by Ophir (1979) and by Ophir and Wilkes (1978, 1979). It was shown that the reduction of Young's modulus, that can be brought about by the introduction of cross links, is accompanied by a decrease of the invariant and in most cases also by an increase in the width E of the transition layer between the two phases. Furthermore, cross links were observed to decrease the rate of the phase separation occurring on cooling the materials from the state of complete miscibility to temperatures where demixing occurs. Polyurethanes

containing polyether blocks showed better phase separation than those containing polyester blocks; a tentative conclusion is that about 10% of the hard segments dissolves in the polyether phase. As to the morphology in general, the authors agree with Bonart's conclusion that the structure is most likely to consist of hard phase lamellae in a more or less parallel configuration.

The phase separation in block copolymers was studied by Todo *et al.* (1978), with the special aim of obtaining the best possible values of the width E of the transition layer. They compared the values obtained with the aid of a traditional Kratky camera with the ones obtained with a camera equipped with Soller slits. The corresponding weighting functions were used in desmearing the scattering curves from styrene-isoprene diblock copolymers. The best E -value they considered to be the one for which the density function in the transition layer is of sigmoidal shape, for which the equivalent of Eqn (23) is $I(s) = I^0(s) \exp(-\pi^2 E^2 s^2/3)$. In their case, this relation yielded the highest value for E ; the values obtained from smeared curves under the assumption of infinite slit height are definitely lower (about 30%), whereas those obtained from Eqn (24), after applying the correct desmearing procedure, were just slightly lower.

References

- Alexander, L. E. (1969). "X-Ray Diffraction Methods in Polymer-Science". Wiley-Interscience, New York.
 Blundell, D. J. (1970). *Acta Cryst. A* **26**, 472–476, 476–483.
 Blundell, D. J. (1978). *Polymer* **19**, 1258–1266.
 Bonart, R. (1977). *Angew. Makr. Chem.* **58/59**, 259–297.
 Brämer, R. (1972). *Kolloid Z.Z. Polym.* **250**, 1034–1038.
 Brämer, R. (1973). "Zur Bedeutung eindimensionaler Modelle bei der Auswertung isotroper Röntgenkleinwinkelstreukurven" (Dissertation, Ulm).
 Brämer, R. (1974). *Colloid Polymer Sci.* **252**, 504–515.
 Brown, D. S. and Wetton, R. E. (1978). "Polymer Characterisation I". Applied Science Publishers, Barking Road.
 Buchanan, D. R. (1971). *J. Polymer Sci. A2*, **9**, 645–658.
 Capaccio, G., Ward, I. M., Wilding, M. A. and Longman, G. W. (1978). *J. Macrom. Sci. B* **15**, 381–407.
 Crist, B. (1973). *J. Polymer Sci. Polymer Phys. Ed.* **11**, 635–661.
 Debye, P., Anderson, Jr. H. R. and Brumberger, H. (1957). *J. Appl. Phys.* **28**, 679–683.
 Duiser, J. A. and Keijzers, A. E. M. (1978). *Polymer* **19**, 889–894.
 Fischer, E. W. and Kloos, F. (1970). *Polymer Lett.* **8**, 685–693.
 Folkes, M. J., Keller, A., Stejny, J., Goggin, P. L., Fraser, G. V. and Hendra, P. J. (1975). *Colloid Polymer Sci.* **253**, 354–361.
 Geil, P. H. (1963). "Polymer Single Crystals". Interscience, New York.
 Guinier, A. (1963). "X-Ray Diffraction". Freeman, San Francisco.
 Hendricks, R. W. (1978). *J. Appl. Cryst.* **11**, 15–30.
 Hermans, J. J. (1944). *Rec. Trav. Chim. Pays-Bas* **63**, 211–218.

- Hermanns, P. H., Heikens, D. and Weidinger, A. (1959). *J. Polymer Sci.* **35**, 145–165.
 Higgins, J. S. and Stein, R. S. (1978). *J. Appl. Cryst.* **11**, 346–375.
 Hosemann, R. (1949). *Z. Phys.* **127**, 16.
 Hosemann, R. and Bagchi, S. N. (1962). "Direct Analysis of Diffraction by Matter". North Holland, Amsterdam.
 "International Tables for X-Ray Crystallography" II. The Kynoch Press, Birmingham.
 Katayama, K., Amano, T. and Nakamura, K. (1968). *Kolloid Z.Z. Polymer* **226**, 125–134.
 Kortleve, G. and Vonk, C. G. (1968). *Kolloid Z.Z. Polymer* **225**, 124–131.
 Kortleve, G., Tuijnman, C. A. F. and Vonk, C. G. (1972). *J. Polymer Sci. A2* **10**, 123–131.
 Kratky, O. (1966). *Pure Appl. Chem.* **12**, 483–523.
 Kratky, O., Pilz, I. and Schmitz, P. J. (1966). *J. Colloid Interface Sci.* **21**, 24–34.
 Meyer, H. and Kilian, H. G. (1978). *Progr. Colloid Polymer Sci.* **64**, 166–173.
 Ophir, Z. H. (1979). "Structure-Property Relationships in Solid Polymers". PhD Thesis, University of Princeton.
 Ophir, Z. H. and Wilkes, G. L. (1978). *ACS Polym. Preprints* **19**, 26.
 Ophir, Z. H. and Wilkes, G. L. (1979). *ACS Polym. Preprints* **20**, 503.
 Porod, G. (1951). *Kolloid Z.Z. Polymer* **124**, 83–114.
 Porod, G. (1952). *Kolloid Z.Z. Polymer* **125**, 51–57, 108–122.
 Rathje, J. and Ruland, W. (1976). *Colloid Polymer Sci.* **254**, 358–370.
 Ruland, W. (1971). *J. Appl. Cryst.* **4**, 70–73.
 Ruland, W. (1977). *Colloid Polym. Sci.* **255**, 417–427.
 Schultz, J. M. (1976). *J. Polymer Sci. Polymer Phys. Ed.* **14**, 2291–2311.
 Schultz, J. M., Lin, J. S. and Hendricks, R. W. (1978). *J. Appl. Cryst.* **11**, 551–557.
 Shaffer, L. B. and Beeman, W. W. (1970). *J. Appl. Cryst.* **3**, 379–384.
 Stribeck, N. and Ruland, W. (1978). *J. Appl. Cryst.* **11**, 535–539.
 Strobl, G. R. (1970). *Acta Cryst. A* **26**, 367–375.
 Strobl, G. R. (1972). *Kolloid Z.Z. Polymer* **250**, 1039–1046.
 Strobl, G. R. (1973). *J. Appl. Cryst.* **6**, 365–370.
 Strobl, G. R. and Eckel, R. (1977). *Progr. Colloid Polym. Sci.* **62**, 9–15.
 Strobl, G. R. and Müller, N. (1973). *J. Polymer Sci. Polymer Phys. Ed.* **11**, 1219–1233.
 Swan, P. R. (1962). *J. Polymer Sci.* **56**, 403–407.
 Todo, A., Hashimoto, T. and Kawai, H. (1978). *J. Appl. Cryst.* **11**, 558–563.
 Tsvankin, D. Ya. (1965). *Polymer Sci. USSR Eng. Transl.* **6**, 2304–2317.
 Vainshtein, B. K. (1966). "Diffraction of X-Rays by Chain Molecules". Elsevier, Amsterdam.
 Vonk, C. G. (1973). *J. Appl. Cryst.* **6**, 81–86.
 Vonk, C. G. (1978). *J. Appl. Cryst.* **11**, 540–546.
 Vonk, C. G. and Kortleve, G. (1967). *Kolloid Z.Z. Polymer* **220**, 19–24.
 Wang, J. I. and Harrison, I. R. (1978). *J. Appl. Cryst.* **11**, 525–530.
 Welte, W. and Kreutz, W. (1979). *Adv. Polymer Sci.* **30**, 161–225.
 Wendorff, J. H. and Fischer, E. W. (1973a). *Kolloid Z.Z. Polymer* **251**, 884–891.
 Wendorff, J. H. and Fischer, E. W. (1973b). *Kolloid Z.Z. Polymer* **251**, 876–883.

- Wenig, W. and Brämer, R. (1978). *Colloid Polymer Sci.* **256**, 125–132.
Wiegand, W. and Ruland, W. (1979). *Progr. Colloid Polym. Sci.* **66**, 355–366.
Wilski, H. (1964). *Kunststoffe* **54**, 10–15.
Zernike, F. and Prins, J. A. (1927). *Z. Phys.* **41**, 184.

14

Inorganic Substances

G. KOSTORZ

*Institut für Angewandte Physik, Eidgenössische Technische Hochschule, Zürich,
Switzerland*

I.	Introduction	467
II.	Fields of interest	469
	A. Tests of sample homogeneity	469
	B. Size or extent of inhomogeneity	469
	C. Size distributions	470
	D. Interparticle interference	471
	E. Particle surface or interface	472
	F. Miscibility limits from integrated intensities	473
III.	Defects in metals	475
	A. Voids in neutron-irradiated aluminium	476
	B. Radiation damage in molybdenum	478
	C. Vacancy clusters in electron-irradiated copper	481
IV.	Alloys	481
	A. Decomposition	482
	B. Reversion	486
	C. Internal oxidation	486
	D. Particle shape	487
V.	Glasses and liquids	489
	A. The vitreous state	490
	B. Phase separation in glasses	493
	C. Liquids	494
	D. Critical scattering	495
VI.	Epilogue	496
	References	497

I. Introduction

Inorganic substances comprise many of our most common materials such as alloys, glasses, ceramics etc. (we restrict ourselves to condensed matter). Often, these substances are studied using various methods in order to understand,

control and improve their properties, and in many cases these properties are strongly influenced by inhomogeneities on a scale from a few interatomic distances to several hundreds of angströms. Also, from a more fundamental point of view, there is an increasing need to obtain more reliable information on small clusters of defects or solute atoms, compositional fluctuations etc., for a critical test of theories of defects, diffusion and phase separation in inorganic systems. X-ray small angle scattering seems to be quite an appropriate tool for such studies, as the accessible range of scattering vectors yields the required spatial resolution.

More than forty years ago, Guinier (1938) used X-ray small angle scattering to study inhomogeneities in alloys and revealed some metastable decomposition products now known as Guinier-Preston zones. Unfortunately, however, X-ray small angle scattering is not as universally applicable as may be desired.

The most severe restriction comes from the fact that many materials contain rather heavy elements that strongly absorb X-rays. With CuK α radiation, the optimum thickness (i.e. 1/e-absorption) is, for example, 76 μm for pure Al, but less than 10 μm for atomic numbers 23 to 27 and above 41 (except no. 55). Using MoK α , the corresponding value for Al is 713 μm , but for most heavier materials of interest, a thickness of only 20–100 μm should be used. The irradiated volume is thus not very large and may not always be representative of the bulk material. Also, sample containment for experiments at high or low temperature, or in the liquid state, presents major difficulties because of additional undesired scattering. With the advent of more powerful X-ray sources, somewhat thicker samples may be studied, but for quantitative measurements it is not recommended to work with very high absorption.

Another difficulty arises from double Bragg scattering in polycrystalline samples and, to a lesser extent, from double scattering in liquid and amorphous substances. These scattering contributions are often stronger than the scattering due to inhomogeneities and thus obscure the effects to be studied. If a good single crystal can be made, double Bragg scattering can normally be avoided, and low-contrast problems can be investigated.

Despite these difficulties and the increasing role of neutron small angle scattering (Schmatz *et al.*, 1974; Kostorz, 1979), numerous X-ray small angle scattering experiments on inorganic substances have been performed in recent years. Higher beam intensities, use of point collimation, position-sensitive detection and creative experimental innovations are the main reasons for today's improved utility of X-ray small angle scattering.

Since Gerold's (1963) account of the basic principles of X-ray small angle scattering as applied to the field of physical metallurgy, many of the more recent results of both neutron and X-ray small angle scattering have been reviewed by Schmatz (1973) and by Gerold and Kostorz (1978). Therefore, this brief chapter is not intended to give a complete collection of available

publications. Rather, an attempt will be made to characterize the areas of research where X-ray small angle scattering can be helpful, and the methods used to extract valuable information. A few selected experiments will be discussed in more detail, covering problems of defect clustering, alloy decomposition and reversion, aggregation in liquid alloys and the structure and decomposition of glasses.

II. Fields of Interest

We assume that the reader is familiar with the contents of Chapters 2 to 7 where the small angle scattering method and the interpretation of its results have been fully described. The general laws and approximations presented there are, of course, also applicable to inorganic substance, but complications often arise because of the complexity of the systems to be studied. In the following, different fields of interest are listed where X-ray small angle scattering experiments are useful.

A. Tests of Sample Homogeneity

To check whether a sample is homogeneous or inhomogeneous on a scale accessible to X-ray small angle scattering is the least demanding experiment one may imagine. It can, nevertheless, be an important experiment that shows whether a heat treatment, a quenching procedure etc. have any influence on the microstructure of a material, and whether this influence or its absence are reproducible (see, for example, Dartyge *et al.*, 1972).

B. Size or Extent of Inhomogeneity

The presence of a small angle scattering intensity $I(\mathbf{h})$ shows – as a generalization of the basic statements made in Chapter 2 – that a sample contains regions where the electron density varies over distances of about $2\pi/|\mathbf{h}|$. In contrast to Chapter 2, Section I.C, it is generally not justified to assume that a system is statistically isotropic. Crystalline substances, when investigated in the form of single crystals, more often than not reveal "anisotropic" small angle scattering. Of course, these details are lost if the sample is polycrystalline on a scale much smaller than the beam aperture *and* has no pronounced texture. Also, the contrast

$$\eta(r) = \rho(r) - \bar{\rho} \quad (1)$$

may not be a step function of r but a continuous function (e.g. dislocation strain fields or compositional fluctuations). In general, one thus obtains an

intensity $I(\mathbf{h})$ according to Eqn (3) of Chapter 2, and further conclusions have to rely on some further – experimental or theoretical – knowledge of the system.

If it can be assumed that the small angle scattering is due to the presence of homogeneous small particles (voids, precipitates) embedded in a homogeneous matrix, the analysis follows the procedure outlined in Chapter 2, except that the intensity may depend on the direction of the scattering vector \mathbf{h} . From the experimental data, an experimental radius of gyration R_h can still be assigned to each direction of \mathbf{h} (Guinier, 1963),

$$I(\mathbf{h}) \propto \exp(-R_h^2 \mathbf{h}^2) \quad (2)$$

(note the different exponent in Eqn (22) of Chapter 2), and the “anisotropy” of R_h can be used to characterize the shape of the scattering particles. If no influence of lower symmetry (e.g. uniaxial stress) is present, the anisotropy of scattering will be related to the crystal symmetry (which influences the particle shape), and the multiplicity of planes and directions in many common structures will provide for a number of subsets of differently oriented particles that may all contribute to the intensity measured at a given \mathbf{h} .

The information contained in $I(\mathbf{h})$ thus yields size parameters of particles in the two-phase model provided that interparticle interference is unimportant or can be separated reliably. For systems exhibiting a continuous variation of $\eta(r)$, the extent and symmetry of these variations may still be determined. The use of the Guinier approximation and the concept of a radius of gyration, however, are only of limited value for these systems (see Chapter 2, Section VI.C, for a general discussion of non-particulate systems).

Precipitates in alloys strongly influence such important properties as mechanical strength, electrical conductivity, magnetic coercive force, critical currents of superconductors etc. The variation of size, as a function of some treatment, and possibly the orientation of non-spherical particles, may be determined rapidly by means of X-ray small angle scattering, and correlated property changes can be rationalized and properly interpreted. The same ideas apply to the decomposition of glasses, ceramics etc. For all substances, more data on the development of small-scale inhomogeneity at the beginning of the decomposition process are required to improve the theoretical description of the evolution of unstable and metastable solid solutions. Also, the production and behaviour of defects upon quenching or irradiation and subsequent annealing can be followed with X-ray small angle scattering. Measurements of the temperature dependence of statistical compositional fluctuations may be useful for the theory of phase transformations and critical phenomena.

C. Size Distributions

Even if homogeneous second-phase particles are at the origin of the measured small angle scattering intensity, they will normally not have a uniform size.

The problems of obtaining the size distribution from a measured small angle scattering curve are discussed in Chapter 4, Section III.E. For inorganic systems, only spherical particles have been considered, and Baur and Gerold (1964) have shown that the square of the radius of gyration, R^2 , as determined from a Guinier plot according to Eqn (22) of Chapter 2, is in fact a ratio of moments of the size distribution,

$$R^2 = 3\langle r^8 \rangle / 5\langle r^6 \rangle \quad (3a)$$

for point collimation, and

$$R^2 = 3\langle r^7 \rangle / 5\langle r^5 \rangle \quad (3b)$$

for slit collimation. Here, r refers to the radius of each particle. Harkness *et al.* (1969) have used Eqn (3b) and a different moment ratio that can be shown to hold in the Porod region (Baur and Gerold, 1964), in order to obtain the geometric mean and the variance of an assumed log-normal size distribution. The procedure works well for simple, not too concentrated systems, as shown by Harkness *et al.* (1969) for *Al*-Ag and *Al*-Zn. The parameters obtained from this evaluation may be helpful in detailed studies of ageing and associated property changes (see Harkness and Hren, 1970, for an investigation of strengthening in *Al*-Zn single crystals). For the evaluation of size distributions without any restricting assumptions, only more general numerical methods, as described in Chapter 4, remain. They require very precise data over a wide range of \mathbf{h} values.

Gerstenberg (1980) has used the fitting procedure proposed by Vonk (1976) to analyse results on polycrystalline *Al*-Mg-Zn alloys. As the grain size was relatively large, only one distribution corresponding to precipitates in the internal regions of the grains could be characterized with any reliability. Larger zones are often formed at or near grain boundaries, and for sufficiently small grains, a bimodal size distribution may be revealed. As more complex microstructures, e.g. those produced by double-ageing, are of considerably practical importance, more work on size distributions will certainly emerge.

D. Interparticle Interference

Interference effects due to a high concentration of inhomogeneities are quite common with alloys, glasses and other substances. They can reduce the intensity at low \mathbf{h} values, so that it becomes difficult or even impossible to use the Guinier approximation to estimate a particle size. Chapter 5, Section IV.A, gives a general outline of the problem of distance distributions and interparticle interference. A drastic demonstration of the variation of experimentally determined particle sizes with concentration (using the Guinier approximation) has been given by Rothwell (1968) for the case of “Ludox” (silica spheres dispersed in water). For volume fractions between 1% and 16%, the apparent diameter (of the same particles) changed from 148 Å to 210 Å. These results can be rationalized in terms of a hard-sphere model, as discussed by Guinier and

Fournet (1955), but for particles in a solid matrix, one can only try to separate a single-particle curve from the interparticle interference function (see, for example, Laslaz *et al.*, 1977, and Dauger *et al.*, 1979, for neutron small angle scattering results on *Al-Zn* and *Al-Mg* alloys evaluated in this manner). The obtained interference functions may indicate how particles are arranged in the sample but the reasons for this arrangement remain to be explored. The study of interparticle interference effects is particularly rewarding if single crystalline samples are available and if a position-sensitive detector is used. Such detailed investigations, initially performed with neutrons, have since been tried with X-rays too (see below).

E. Particle Surface or Interface

As explained in Sections III.C and VI.D of Chapter 2, the "final slope" of the small angle scattering curve is related to the total surface or interface S of the scattering system. The Porod law is valid as long as there is a well-defined interface and orientational disorder (Eqn 81 of Chapter 2). Combined with the integrated intensity, the "invariant" Q introduced in Section I.D of Chapter 2, and the specific surface, S/V (where V is the sample volume), can be determined without absolute intensity measurements. In practice, Eqns (43) and (82) of Chapter 2 cannot be applied directly as some background scattering is always present and measured in addition to the small angle scattering signal. For simplicity, this background I_b (Laue scattering, Compton scattering) is assumed to be h -independent (see Naudon and Caisso, 1974). The measured intensity in the Porod regime is then given by (apart from a calibration factor)

$$I(h) = (\Delta\rho)^2 \frac{2\pi S}{h^4} + I_b \quad (4)$$

Plotting $I(h)h^4$ against h^4 should yield a straight line for large h , and the intercept of this line with the ordinate corresponds to the "Porod constant" $C_p = 2\pi(\Delta\rho)^2 S$. The specific surface is obtained after dividing C_p by the "invariant" Q (Eqn 69 of Chapter 2, integrated after subtraction of I_b from the measured intensity)

$$S/V = \pi C_p / Q \quad (5)$$

Values of C_p (in arbitrary units) or of S/V from Eqn (5) are determined quite frequently to study changes or differences of total surface or interface area of catalysts, colloid suspensions etc. Also, precise measurements in the Porod regime (where intensities are small) and a determination of the Porod constant are necessary if one is finally interested in reliable values of Q .

F. Miscibility Limits from Integrated Intensities

Most of the procedures referred to above do not normally require an absolute intensity scale. If, however, calibrated small angle scattering results are used to obtain the "invariant" Q , it becomes possible to determine the limits of metastable and stable miscibility gaps in binary systems. The method has been outlined and used extensively by Gerold and co-workers (see Gerold, 1967; Gerold and Kostorz, 1978) and is based on the properties of the "invariant" Q that, for a two-phase system, is given by (see Eqn 69 of Chapter 2)

$$Q = 2\pi^2 V(\rho_1 - \rho_2)^2 \xi_1 \xi_2 \quad (6)$$

where ρ_1 is the electron density of phase 1, the "solvent", for solid systems normally called "matrix" if a majority phase can be defined, and ξ_1 is its volume fraction. The "solute", i.e. a precipitate or pre-precipitate phase, has the electron density ρ_2 and occupies a volume fraction $\xi_2 = 1 - \xi_1$ of the total volume V . Equation (6) can be rearranged to read

$$Q = 2\pi^2 V(\rho_2 - \bar{\rho})(\bar{\rho} - \rho_1) \quad (7)$$

and shows that ρ_1 and ρ_2 may be determined if for different $\bar{\rho}$, i.e. different initial concentrations, one obtains the same final values of ρ_1 and ρ_2 . For binary alloys decomposed at constant temperature, this is the case if for each initial concentration within a (meta-)stable miscibility gap, (meta-)stable equilibrium is reached. The discussion becomes particularly simple if atomic volume changes upon alloying and decomposition are neglected, a case not too unrealistic for metastable, coherent precipitates. (The inclusion of volume changes is not difficult and has been treated most recently by Gerold, 1977.) Then, the electron densities can be simply expressed in terms of ρ_A and ρ_B , the electron densities of the pure component A and B and the atomic fraction of component B , X_B . For example, one obtains

$$\bar{\rho} = \rho_A(1 - \bar{X}_B) + \rho_B \bar{X}_B \quad (8)$$

and corresponding expressions for phases 1 and 2 with composition X_{B1} and X_{B2} . Rewriting Eqn (7),

$$Q(\bar{X}_B) = 2\pi^2 V(\rho_A - \rho_B)^2 (X_{B2} - \bar{X}_B)(\bar{X}_B - X_{B1}) \quad (9a)$$

or

$$Q_c(\bar{X}_B) = (X_{B1} + X_{B2})\bar{X}_B - X_{B1}X_{B2} \quad (9b)$$

where

$$Q_c(\bar{X}_B) = \bar{X}_B^2 + Q(\bar{X}_B)/[2\pi^2 V(\rho_A - \rho_B)^2] \quad (9c)$$

Equation (9c) shows that $Q(\bar{X}_B)$ must be determined in the appropriate absolute units. A plot of Q_c against \bar{X}_B according to Eqn (9b) then yields $X_{B1}X_{B2}$ and $X_{B1} + X_{B2}$ and finally X_{B1} and X_{B2} . Figure 1 shows results obtained for Guinier-Preston zones formed in *Al-Zn* alloys aged at room temperature, plotted as

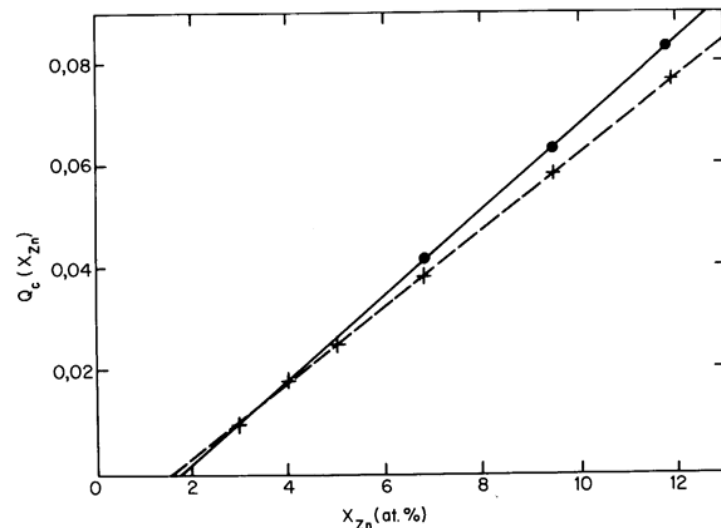


FIG. 1. The quantity $Q_c(\bar{X}_B)$ according to Eqn (9c), plotted as a function of zinc concentration X_{Zn} , for binary Al-Zn alloys (dots). Crosses refer to corrected values including an atomic volume change and a corresponding change of scale [$X'_{Zn} = X_{Zn}/(1 + \kappa_{Zn} X_{Zn})$]. (From Gerold 1977).

described (Gerold, 1977). The effects of a lattice misfit, that has to be considered in Al-Zn, can be seen too. An atomic volume change obeying Vegard's law, $v_a(X_{Zn}) = v_a(1 + \kappa_{Zn} X_{Zn})$, with $\kappa_{Zn} = -0.06$, leads to the dashed line and yields $X_{Zn1} \approx 1.8\%$ and $X_{Zn2} \approx 71\%$ rather than 1.7 and 81% without this correction (Gerold, 1977). An extension of this procedure to ternary systems is straightforward if one knows the different initial compositions that lead to the same (meta-)stable precipitate and matrix concentrations. Although it is known that these initial compositions lie on a straight line, a tie-line in an isothermal section of a ternary system, the direction of this line is usually unknown. If one uses small angle scattering alone, the problem can only be solved by investigating the same samples in two different experiments with different scattering contrast $\rho_A - \rho_B$ and $\rho_A - \rho_C$. This may be possible in some cases by working with synchrotron radiation and choosing wavelengths in the vicinity of the absorption edge of one of the components. To date, a combination of X-ray and neutron small angle scattering has been tried (Gerold, 1977; Gerold *et al.*, 1977), using nine different alloys of Al-Zn-Mg aged at room temperature. Figure 2 shows that the results for the gap limits are not too precise. Apart from the general problem of obtaining sufficiently reliable values of Q , the change of contrast, i.e. of $(\rho_A - \rho_B)/(\rho_A - \rho_C)$, between the two experiments must also be quite large in order to extract meaningful results.

The above presentation has shown that the evaluation of X-ray small angle

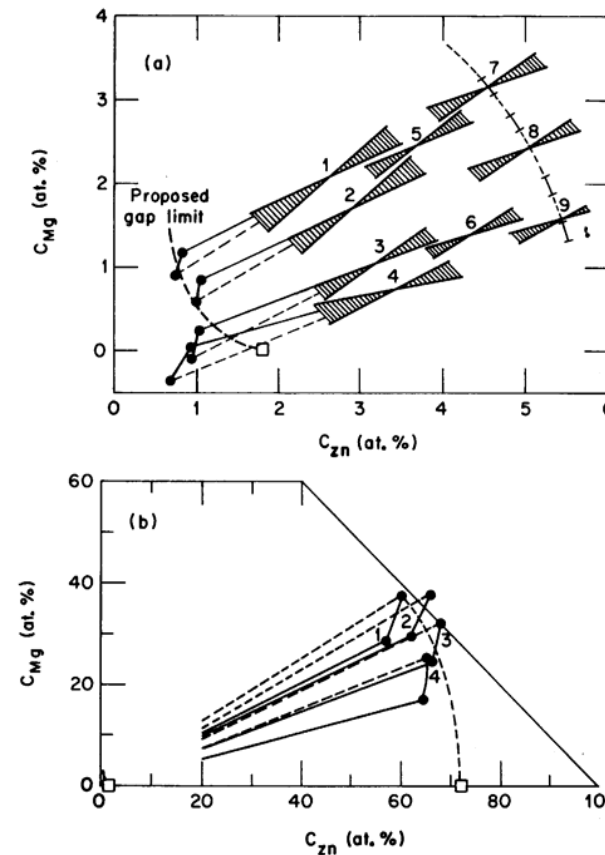


FIG. 2. Isothermal section of the Al-rich corner (a) and the Al-Zn-Mg system (b) at room temperature. (a) The nine alloys selected for the investigation, calculated ranges of tie-line slopes, and proposed lower gap limit as obtained from the integrated intensities Q of neutron and X-ray small angle scattering; (b) the upper limits of the metastable miscibility gap. (From Gerold *et al.*, 1977).

scattering results can provide useful information in different fields of research on inorganic substances. Subsequent sections are intended to give some current examples of the application of the principles described above to some actual materials.

III. Defects in Metals

Agglomerates of vacancies produced, e.g. during or after irradiation or after quenching from a higher temperature, give rise to a relatively strong small angle

scattering signal, as the contrast is given by the full value of the electron density of the material and not by the small difference often encountered with precipitates. For the same reasons, other defects, such as interstitial clusters and dislocations, show less scattering and no recent attempts to study these other defects in crystalline materials have been reported.

A. Voids in Neutron-irradiated Aluminium

An extensive study on aluminium single crystals after irradiation with fast neutrons at ambient (reactor) temperature has been reported (Epperson *et al.*, 1974; Hendricks *et al.*, 1974; Hendricks *et al.*, 1977; Lindberg *et al.*, 1977) where several methods have been combined to give a very detailed picture of the size, shape, density etc. of the voids formed during irradiation. Restricting here our view to the X-ray small angle scattering results (Epperson *et al.*, 1974; Lindberg *et al.*, 1977), Fig. 3 shows two photographic recordings of the small angle scattering pattern of an irradiated crystal, obtained with different resolution. This crystal had been irradiated to 1.5×10^{21} neutrons cm^{-2} ($> 0.18 \text{ MeV}$) at $50^\circ\text{C} \pm 5^\circ\text{C}$, and slices of different orientations were cut for small angle scattering and transmission electron microscopy (TEM). The patterns show that the small angle scattering is symmetric (isotropic in the film plane) only for $h \leq 0.04 \text{ \AA}^{-1}$. The lower-resolution pattern, Fig. 3b, contains streaks of high intensity along $\langle 111 \rangle$ directions for higher values of h . Although only qualitative, these measurements show that the voids are faceted and that some details of this sort may be overlooked if a line focus is used. Combined with TEM and neutron small angle scattering (Hendricks *et al.*, 1974), a complete description of the voids as truncated octahedra with a radius of gyration of 210–230 Å emerges (see Fig. 4), and quantitative measurements also provide data on the total void volume and surface. Further studies (Lindberg *et al.*, 1977) are concerned with the annealing of these voids at higher temperatures. X-ray small angle scattering experiments were performed using a new, powerful instrument (Hendricks, 1978), with pin-hole collimation and a two-dimensional position-sensitive detector. Figure 5 shows radius of gyration and void swelling $\Delta V/V$ from X-ray small angle scattering of specimens prepared from an Al crystal irradiated with 5×10^{21} fast neutrons cm^{-2} at $55^\circ\text{C} \pm 5^\circ\text{C}$. Isochronal one-hour anneals in 25°C steps between 150 and 275°C were followed by 20-minute anneals in steps of 6°C up to 319°C. According to Fig. 5, the voids anneal out between 306° and 319°C, and the radius of gyration increases considerably in this range. A change in the void-size distribution and/or the void shape – as indicated by the scattering at higher scattering vectors – may lead to the increase in R . The surprising stability of the voids is most probably due to the contamination of the void surfaces by Si. Although the crystals were made from high-purity Al, thermal neutrons also present during irradiation produced

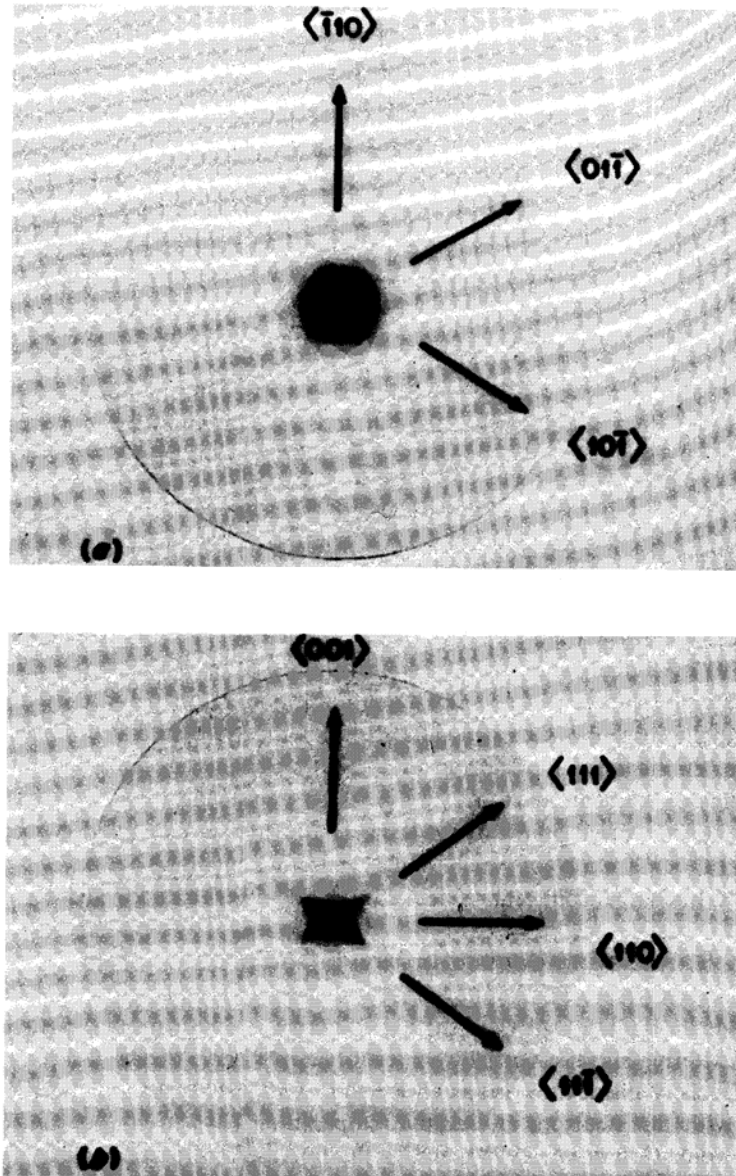


FIG. 3. Kiessig camera pin-hole small angle scattering patterns from a neutron-irradiated aluminium single crystal. (a) Separation of pin-hole collimators 500 mm, pin-hole diameter 0.3 mm, sample-to-film distance 1000 mm; (b) Separation of pin-hole collimators 200 mm, diameter 1 mm, distance 200 mm. CuK_α radiation, graphite monochromator. (From Epperson *et al.*, 1974).

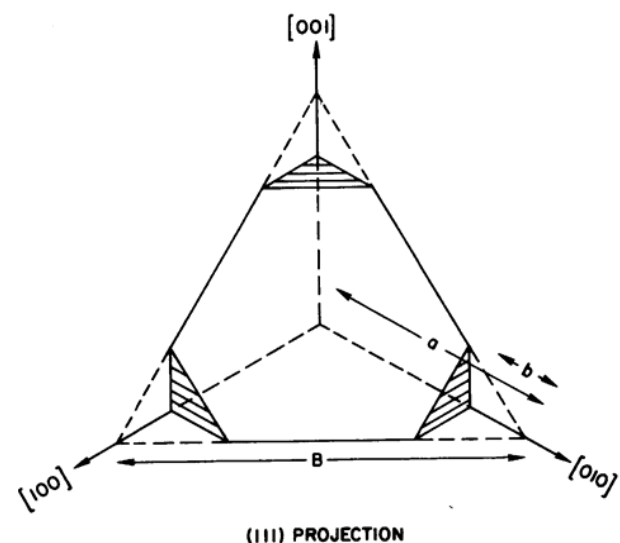


FIG. 4. One octant of a truncated octahedral void in neutron-irradiated aluminium. (From Hendricks *et al.*, 1974.)

about 0.1% ^{28}Si by transmutation of Al. Other experimental facts (Hendricks *et al.*, 1977; Lindberg *et al.*, 1977) support the view that Si precipitates contaminate the void surfaces and stabilize them until, above 306°C, both dissolve and much smaller vacancy-silicon clusters also present after irradiation (revealed by positron annihilation, Lindberg *et al.*, 1977) start growing, possibly incorporating some of the Si atoms, too.

This very involved study of voids in Al provides a very good example for the useful application of small angle scattering in combination with other methods. In comparison, other defect studies are more limited in scope.

B. Radiation Damage in Molybdenum

The voids in irradiated Al were sufficiently large and numerous to yield a small angle scattering signal essentially unperturbed by other, smaller scattering entities, especially dislocation loops (Epperson *et al.*, 1974). In molybdenum irradiated with fast neutrons at elevated temperatures ($\geq 220^\circ\text{C}$), one finds much smaller voids (Liu *et al.*, 1978), and as the forward scattering intensity (at constant volume fraction of voids) is proportional to R^3 , other scattering contributions may not be negligible. Liu *et al.* (1978) have investigated molybdenum samples after irradiation with 10^{21} fast neutrons cm^{-2} (at temperature between 220°C and 900°C) using TEM and X-ray small angle scattering (MoK_α , optimum sample thickness 60 µm). Figure 6 shows a scattering curve for an irradiated

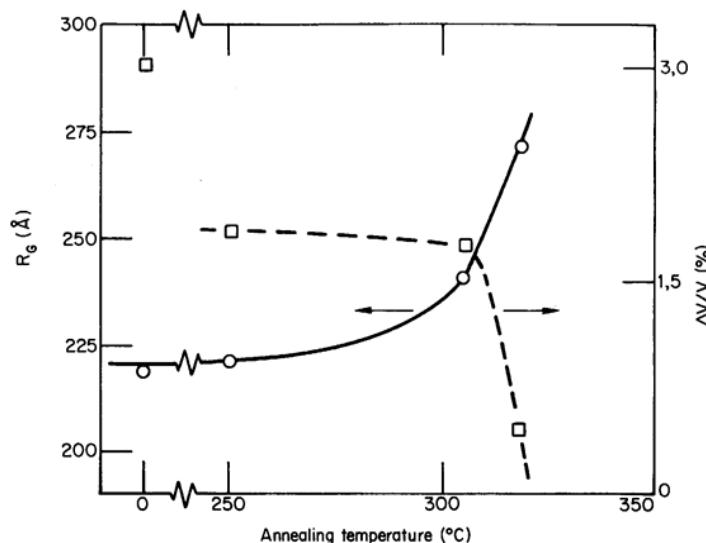


FIG. 5. Radius of gyration of voids and swelling $\Delta V/V$, determined from X-ray small angle scattering, as a function of annealing temperature for an Al single crystal irradiated with fast neutrons at 55°C. (From Lindberg *et al.*, 1977.)

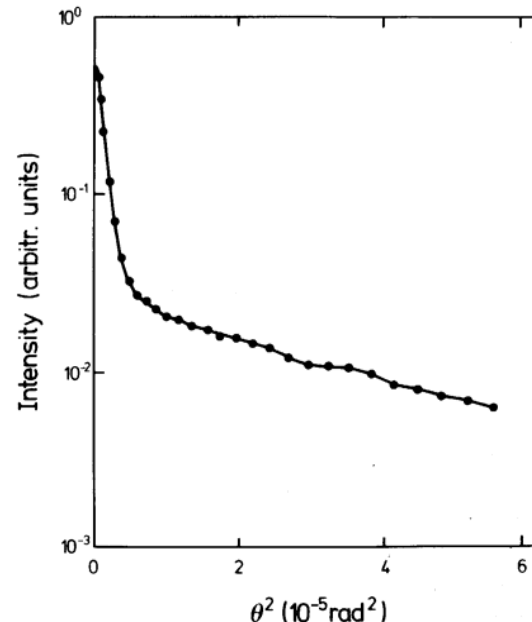


FIG. 6. Small angle scattering intensity (MoK_α) of polycrystalline commercial-grade molybdenum irradiated at 650°C, plotted as a function of θ^2 . (From Liu *et al.*, 1978.)

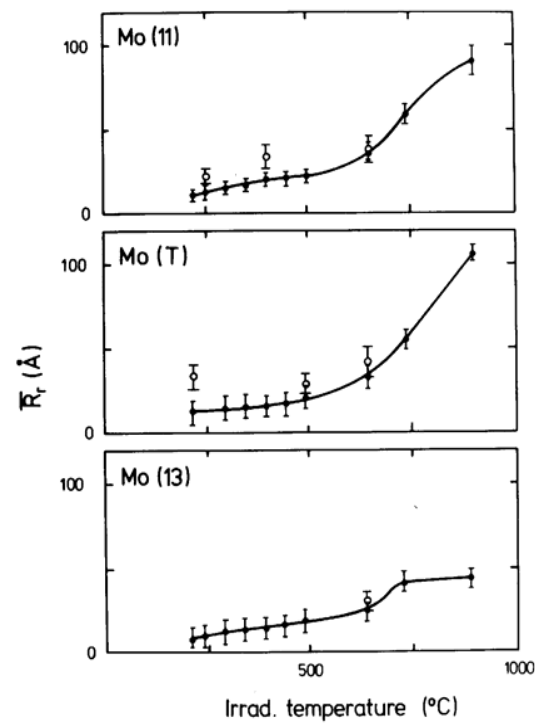


FIG. 7. Average void radii \bar{R}_r as a function of irradiation temperature for three different qualities of molybdenum, Mo(T), polycrystalline; Mo(11) and Mo(13), single crystals of different purity. Open circles are from X-ray small angle scattering, full circles from transmission electron microscopy. (From Liu *et al.*, 1978.)

polycrystalline sample. The steep increase at small angles requires a scattering entity of $R \gtrsim 100 \text{ \AA}$. However, TEM reveals voids of about half this size, and the corresponding small angle scattering manifests itself in the less steep portion at larger scattering angles. As the narrow, steep scattering also occurs in unirradiated samples and is sensitive to the exact orientation of the samples with respect to the incident beam, the authors conclude that this part of the scattering curve is related to surface imperfections. Irregular oxide layers, pores, pits and electropolishing debris may in fact lead to important small angle scattering contributions (see Parker, 1972, for X-ray, and Roth, 1977, and Kostorz, 1977, for neutrons) and render an analysis of the forward scattering region unreliable. Such artefacts are quite common, especially in practically important materials. In the present case, it was not possible to eliminate the surface scattering, but nevertheless, the average void radii could be estimated from the less perturbed regions of the scattering curves. Figure 7 shows some of the results, compared with TEM values. The agreement is good, considering that the small angle

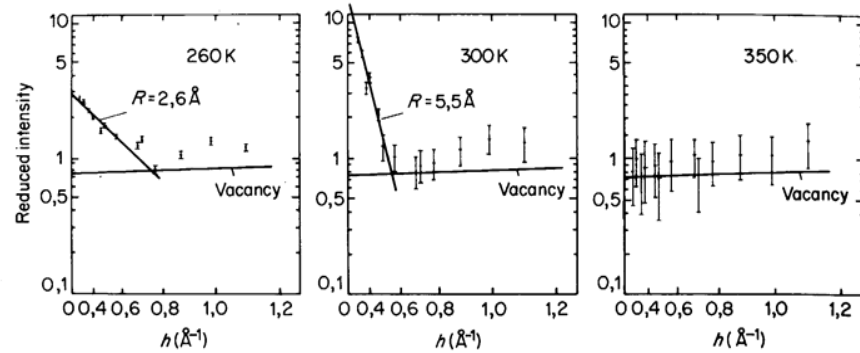


FIG. 8. Guinier plots of small angle scattering cross-sections in annealing stage III of electron-irradiated copper after isochronal anneals at the indicated temperatures. (From Haubold and Martinsen, 1978.)

scattering cannot distinguish dislocation loops from voids, and that large sizes in a size distribution are over-emphasized in an evaluation based on the Guinier approximation. Larger deviations are found for values of $\Delta V/V$, with the small angle scattering values overestimating the swelling.

C. Vacancy Clusters in Electron-irradiated Copper

In a study on the annealing behaviours of Frenkel pairs in Cu, produced at 4 K by 3 MeV electrons, some clustering phenomena were observed at the lower angles in the course of a diffuse scattering experiment (Haubold and Martinsen, 1978). Figure 8 shows Guinier plots of the results obtained after annealing at 260, 300 and 350 K. The scattering for monovacancies is indicated, and it can be seen that some agglomeration of defects occurs at 260 K, the size increases at 300 K, and probably is beyond the resolving power of the instrument at 350 K. Although radii of gyration are given, it should be noted that the Guinier approximation is not valid for more than the three points on the low angle side at 260 K. The size of clusters inferred from these plots may not, therefore, be very precise. Nevertheless, the authors present detailed arguments to conclude that these clusters occurring in annealing stage III of Cu consist of vacancies.

IV. Alloys

The study of decomposition in alloys constitutes a major field of application of X-ray small angle scattering since its early days. In particular, aluminium alloys have very frequently been investigated. The situation has recently been

reviewed in detail for X-rays and neutrons (Gerold and Kostorz, 1978; Kostorz, 1979), and only new results will be emphasized here.

A. Decomposition

As discussed previously (Gerold and Kostorz, 1978), it is not easy to decide from the shape and rate of change of small angle scattering curves upon ageing of alloys, what mechanisms or theoretical models are best suited to describe the situation. Thus, for the binary Al-Zn system, the view that the absence or presence of a small angle scattering peak at a position $h_m \neq 0$ could be taken as an indication for a change in the mode of decomposition (e.g. Junqua *et al.*, 1976) prevailed only until neutron small angle scattering showed that the peak continued to appear at progressively smaller h_m for increasing temperature of decomposition (Laslaz *et al.*, 1977; 1978). Meanwhile, Naudon *et al.* (1979) have reinvestigated the same alloy composition, Al-6.8 at.% Zn, with X-rays, extending the range of accessible values of h down to $5 \times 10^{-3} \text{ \AA}^{-1}$ at $\lambda = 1.54 \text{ \AA}$. This was possible by using a small angle scattering arrangement at a synchrotron (L.U.R.E.-D.C.I. at Orsay, France, see Tchoubar *et al.*, 1978), placing a linear position-sensitive detector with its long axis in the vertical direction, in order to take advantage of the small divergence of the X-ray beam (0.2 mrad) in this direction. With a distance of 110 cm between sample and detector, this installation reaches a resolution comparable to the one of the 10 m X-ray instrument at Oak Ridge (Hendricks, 1978), but with higher intensity. Figure 9 shows the small angle scattering patterns recorded at room temperature, and a peak at about $2.3 \times 10^{-2} \text{ \AA}^{-1}$ is clearly revealed for Al-6.8% Zn. Apparently, the highly collimated X-ray beam also leads to a reduced scattering at very low angles, possibly because of a smaller contribution of multiple scattering near the forward direction. With the neutron measurements performed at an ageing temperature of 133°C (Laslaz *et al.*, 1978), the peak at comparable ageing times was still covered by a larger background scattering intensity increasing strongly towards $h = 0$, but appeared without any background subtraction after about 10 h.

From the above, it can be concluded that small angle scattering does not yield, for this thoroughly investigated alloy of Al-6.8 at.% Zn (a composition not too far away from the lower limit of the miscibility gap), a clear transition between the mechanisms of spinodal decomposition (supposed to be operative at lower temperatures) and nucleation and growth. Theoretically, a sharp transition is neither required nor expected (Hillard, 1970) for initial alloy compositions near the (metastable) miscibility line. On the other hand, if Al-6.8 at.% Zn is allowed to decompose at 20°C (where the solubility limit is at about 1.8 at.%, see Section II.E), Carraud *et al.* (1979) have shown that the mechanical strength of the alloy can be related to the small angle scattering curves

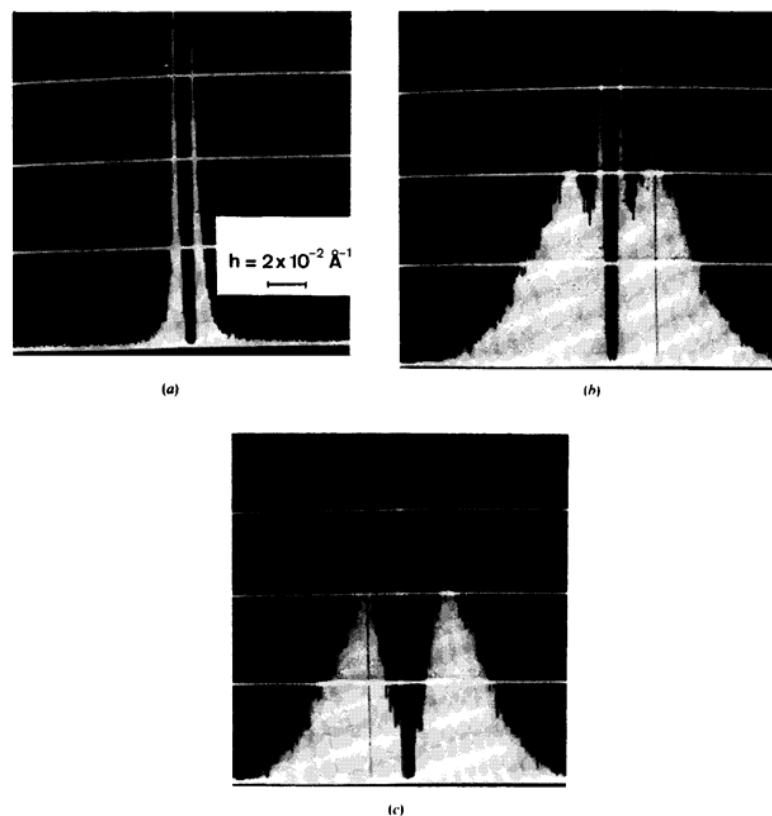


FIG. 9. Multichannel analyser display of small angle scattering patterns obtained with a linear position-sensitive detector. The centre was covered by a beam stop. (a) pure Al; (b) Al-6.8 at.% Zn, aged 7 h at 135°C; (c) difference between alloy and pure Al (long white lines in the centre are artifacts). Measuring time 100 s, intensity range (full scale) 51 200 counts. (From Naudon *et al.*, 1979.)

on the basis of Cahn's theory of spinodal hardening, assuming that the scattering intensity $I(h)$ measures the probability of finding a concentration modulation of wavelength $2\pi/h$ and that the increment of strength, $\Delta\sigma$, is obtained by integrating over all contributions of various wavelengths,

$$\Delta\sigma \propto \int \frac{I(h)}{h} dh \quad (10)$$

Figure 10 shows that this linear relationship holds well at least for the initial 85 min of ageing investigated in this study.

Most studies on Al-Zn were performed with Zn concentrations below about

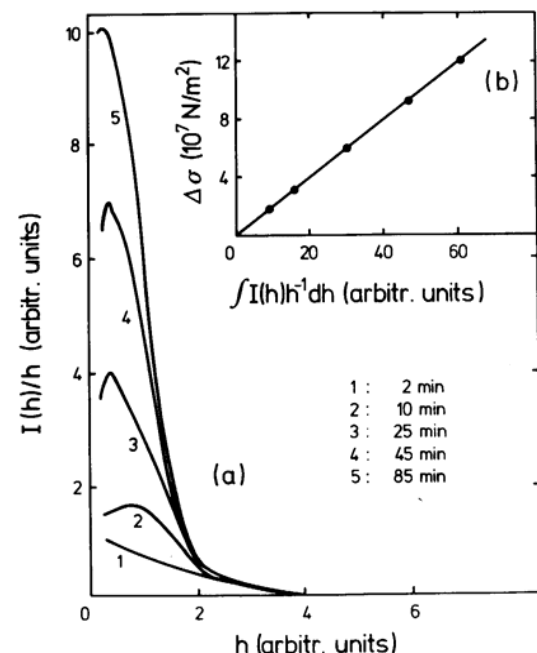


FIG. 10. (a) Small angle scattering intensity $I(h)$ divided by h plotted as a function of h for Al-6.8 at.% Zn alloys quenched from 235°C and aged at 20°C for the times (in minutes) in the diagram; (b) flow-stress increment $\Delta\sigma$ as a function of corresponding results of $\int I(h)h^{-1}dh$, confirming Eqn (10). (From Carraud *et al.*, 1979.)

15 at.%. Acuña (1980) has recently analysed the small angle scattering of Al-Zn containing about 15–22 at.% Zn and found a sharp decrease in the rate of decomposition at room temperature between 16.3 and 17.6 at.% Zn. Whereas for lower Zn concentrations, high quenched-in vacancy concentrations lead to fast decomposition at room temperature, no such effects are seen for the more concentrated alloys. The small angle scattering pattern evolves much more slowly, the maximum is broader and occurs at larger h . The apparent radii of gyration decrease with increasing Zn concentration. Figure 11 shows the “final state” of decomposition for five different alloys, illustrating this behaviour. An explanation probably has to take into account how the precipitation of transition phases, that takes place during the quench, influences the concentration and distribution of excess vacancies retained after the quench.

Ternary Al-Zn-Mg alloys have also frequently been studied by X-ray small angle scattering. Flank and Naudon (1977) have compared Al-6.8 at.% Zn and Al-6.8 at.% Zn-0.2% Mg and found that Mg slows down the decomposition process at room temperature, probably because of the formation of Zn-Mg vacancy complexes. The small addition of Mg seems to introduce a widening

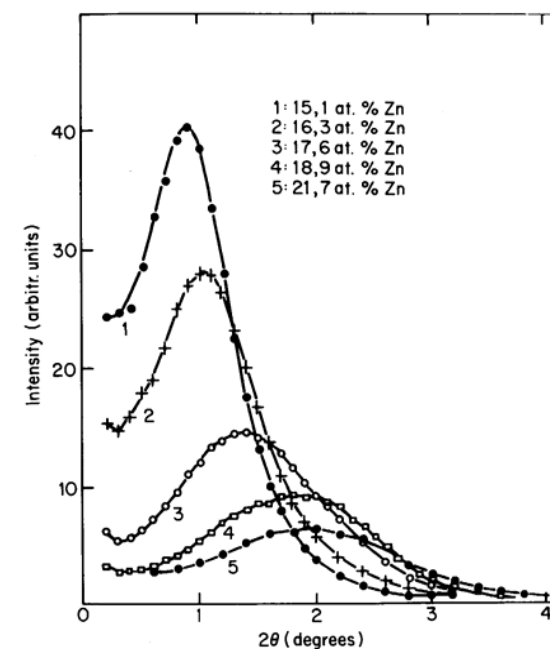


FIG. 11. Small angle scattering curves for the final state of decomposition of Al-Zn alloys containing 15.1–21.7 at.% Zn. The samples were annealed at 400°C, quenched in water at 0°C, and aged at room temperature for extended periods. (From Acuña, 1980.)

of the miscibility gap as indicated in Fig. 2: at room temperature, the integrated intensity Q for the ternary alloy is larger than for the binary alloy (note that Al and Mg are almost identical for CuK_α radiation), and the ternary alloy starts decomposing at a slightly higher temperature. In contrast to the findings at room temperature, the kinetics of decomposition is accelerated by Mg at elevated temperatures, probably because of easier nucleation and a higher thermal vacancy concentration. Recent measurements of small angle scattering from Al-Zn-Mg with higher Mg and lower Zn concentrations decomposed at room temperature (Groma *et al.*, 1979), also confirm the shape of the solubility limit at the Zn-rich side, whereas the upper gap limit is suggested to be near 40% Zn, 20% Mg for the alloys studied by these authors.

Much less small angle scattering work has been performed on alloys where Al is not a major component. Tsujimoto's (1977; Tsujimoto *et al.*, 1975) extensive study of Cu-5.2 at.% Ti also includes numerous small angle scattering results, that are too involved to be properly discussed here. By combination with high angle diffraction results on the evolution of side bands and $\beta'(\text{Cu}_4\text{Ti})$ reflections, a complex ageing sequence with four different stages is developed.

However, the small angle scattering curves are not always simple to interpret, and radii of gyration are often assigned where the Guinier approximation does not hold. Also, no indication is given on the precision of the integrated-intensity values.

B. Reversion

Small metastable precipitates (zones) formed at relatively low temperatures can redissolve when a decomposed sample is warmed up. Simultaneously, a new metastable or stable precipitate will form as long as one remains within the stable miscibility gap, but this decomposition process may often be much slower — the alloy is undergoing reversion. A study of the redissolution of small metastable, coherent precipitates seems interesting as the initial conditions — established by a controlled ageing treatment — tend to be better known than in the case of decomposition after a more or less reproducible, never perfect, quench. As reversion, once it sets in, may not take long to complete (or to be covered by newly forming precipitates), small angle scattering experiments are preferably done *in situ* and require high intensities. The feasibility of such experiments was demonstrated with neutrons and Guinier-Preston zones in an Al-11.8 at.% Zn alloy (Allen *et al.*, 1978), and Gerstenberg (1980), using X-rays from a 12 kW generator, has studied reversion in Al-2.7 at.% Zn and several Al-Zn-Mg alloys. As an example, Fig. 12 shows the evolution of the invariant during reversion at three different temperature for one of the ternary alloys aged at room temperature for several years. The increase in Q seen at 140°C and — to a lesser extent — at 120°C after an initial decrease is related to the formation of η' -precipitates at these temperatures. The position of the minimum depends not only on temperature but also on the Mg concentration (at approximately constant Zn concentration), with a tendency towards retardation of η' formation with decreasing Mg content. In binary Al-Zn, full reversion can be obtained, e.g. after less than 1000 s at 120°C. Simultaneous changes of the radius of gyration and of size distribution parameters deduced from these experiments provide detailed information on the reversion process and the precipitation sequence.

C. Internal Oxidation

The small angle scattering of finely dispersed oxide particles in Cu base alloys after internal oxidation of the initial solid solutions has been evaluated by Allain *et al.* (1979). For four solutes, Be, Ti, Al, Mg, radii of gyration, Porod constants, values of Q and of I_b (according to Eqn 4, modified for slit collimation) were determined after the oxidation treatment. From the observed values of the particle radii (e.g. around 30 Å for Cu-0.9 at.% Mg oxidized at

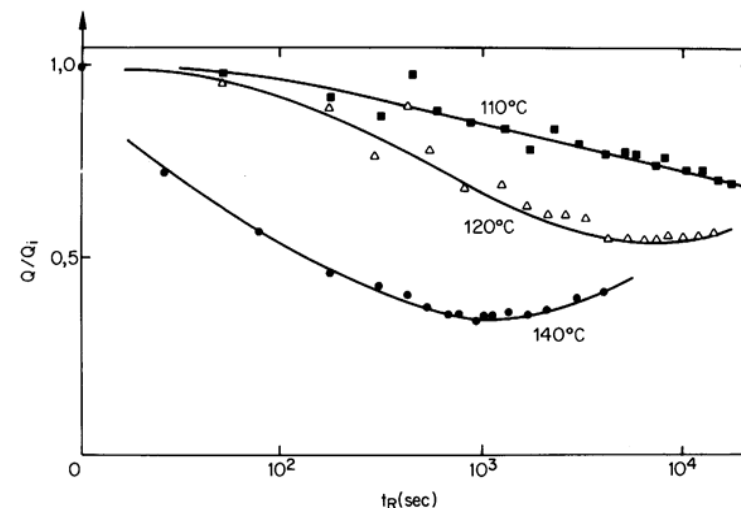


FIG. 12. The evolution of the invariant Q/Q_i (where Q_i is the value after ageing) of Al-3 at.% Zn-1.5 at.% Mg aged at room temperature, upon reversion at the indicated temperatures. (From Gerstenberg, 1980.)

600–800°C), the authors conclude that the passage of the oxidation front induces a “quasi-instantaneous” formation of relatively large oxide particles. Subsequent ageing treatments have little effect on their size. From the values of I_b , it can be concluded that a certain amount of solute remains in solid solution. Figure 13 shows how I_b is determined from a plot of the small angle scattering power j times s^3 , where $s = h/2\pi$, against s^3 , as appropriate for slit collimation. Such accurate measurements were made possible by the use of a linear position-sensitive detector. The values of I_b indicate that about 1/7 of the Be remains dissolved in the Cu matrix. This result is compatible with the fact that the experimental values of Q are lower than theoretically expected for complete oxidation. For Cu-Be, it is thus no longer necessary to postulate a mixed Cu-Be-O oxide (see Naudon and Allain, 1974). Between 900°C and 1000°C, a transition from the formation of coherent to the formation of incoherent BeO was found. In Cu-Ti, the method used for the internal oxidation treatment seems to have an effect on the type of oxide formed. In this system, particle coarsening is also more pronounced, probably because the oxide rapidly loses coherency with the matrix.

D. Particle Shape

In single crystals containing precipitates etc., the scattering pattern may reflect directly the symmetry of particle shape and possibly also preferred arrangements

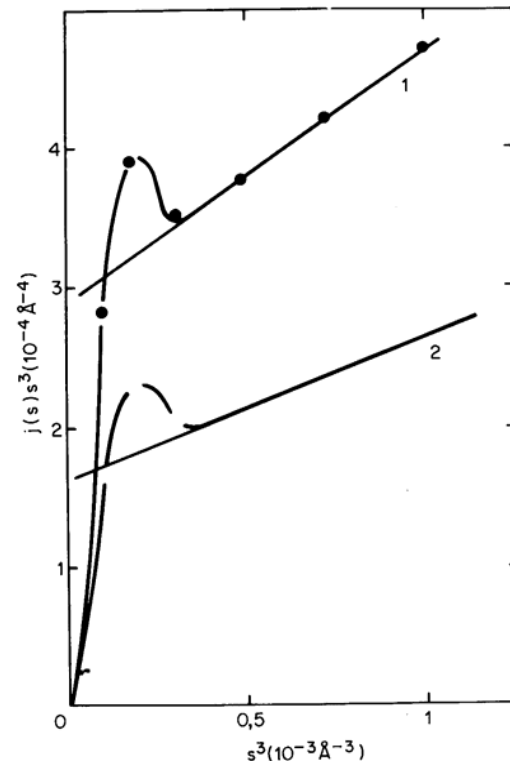


FIG. 13. Plot of $j(s)s^3$ v. s^3 ($s = h/2\pi$) to reveal the h -independent scattering I_b of internally oxidized Cu-Be alloys. (1) Cu-2 at.% Be, $I_b = 0.23 \text{ Å}^{-1}$; (2) Cu-1 at.% Be, $I_b = 0.11 \text{ Å}^{-1}$. (From Allain *et al.*, 1979.)

along certain crystallographic directions. Of course, two-dimensional position-sensitive detectors are ideally suited for such measurements, but it is also possible to use a one-dimensional detector and rotate detector or sample around the incident beam. Naudon *et al.* (1978) have used sample rotation and a fixed linear detector to look again at small Guinier-Preston zones in an Al-1.74 at.% Cu single crystal. The incident CuK_α beam was close to point collimation, and the detector window was a very narrow slit in the scattering plane. Under these conditions, a good angular resolution was obtained, even for the smallest angles. Figure 14 shows schematically that for the [001] direction along the incident beam, the scattering pattern of the sample, quenched from 540°C and aged for 14 h at 60°C , has four-fold symmetry and reveals small angle scattering maxima at $h \neq 0$, most prominently along the $\langle 100 \rangle$ directions, but also along $\langle 110 \rangle$ (at smaller angles). A simple explanation is based on the assumption that each of three sets of disc-shaped zones, corresponding to the three $\{100\}$ planes, establishes some

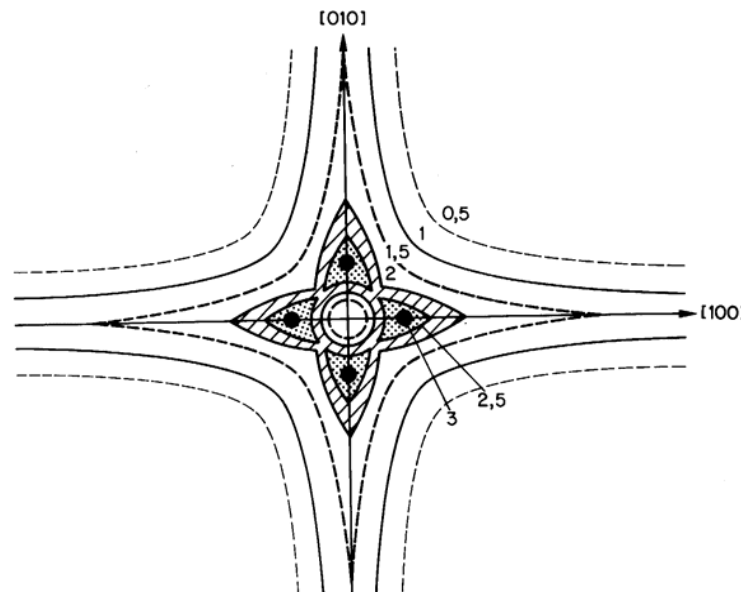


FIG. 14. Schematic small angle scattering pattern of an Al-1.74 at.% Cu single crystal quenched from 540°C and aged for 14 h at 60°C . Lines of equal intensity (in arbitrary units) are indicated. The peak in $\langle 100 \rangle$ direction corresponds to a periodicity of about 45 Å. (From Naudon *et al.*, 1978.)

periodicity along the $\langle 100 \rangle$ direction perpendicular to the disc plane. The authors conclude that correlations within one habit plane and between different sets should also be considered to explain the shape of the scattering pattern.

Even in a "simple" system like Al-Zn, where Guinier-Preston zones always appear to be spherical for radii of less than about 25 Å, a closer study on a single crystal revealed that correlations in the arrangement of zones are more pronounced along preferred directions. Figure 15, obtained with neutrons and a two-dimensional detector, shows the well known scattering "ring" of Al-Zn, but also a variation of the peak intensity with orientation (Bubeck *et al.*, 1981). Similar effects have been found for larger particles in Al-Mg (Dauger *et al.*, 1979). Although X-rays would not have been suitable for the latter system, corresponding experimental X-ray facilities could certainly provide comparably detailed results for Al-Zn and other systems.

V. Glasses and Liquids

Our discussion so far has been limited to examples where the substances studied were crystalline. Vitreous, amorphous and liquid systems can also contain

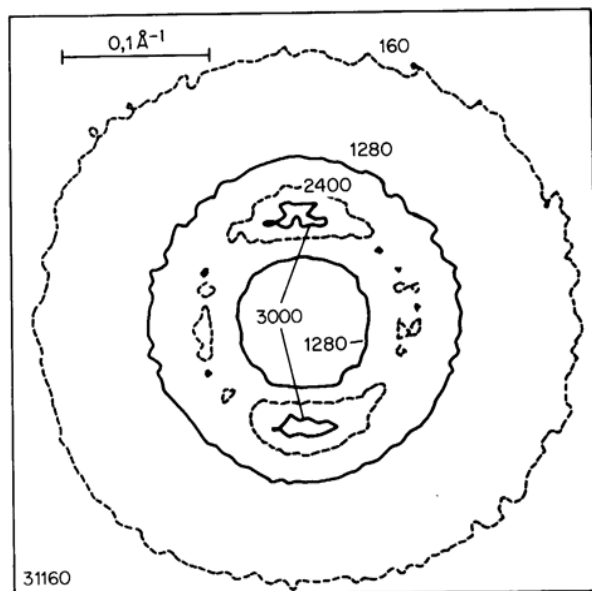


FIG. 15. Measured small angle scattering pattern of an Al-6.8 at.% Zn single crystal slowly cooled from 250°C and aged at room temperature for ~ 4 h ($R \approx 18 \text{ \AA}$). (Results obtained with neutrons of a wavelength of 5.91 Å, using the two-dimensional detector of the D11 instrument at the Institut Laue-Langevin, Grenoble. Detector artifacts and beam stop effects are omitted.) (Bubeck *et al.*, 1980, run 31160.)

inhomogeneities giving rise to small angle scattering effects, and fluctuations may also be estimated from the small angle region.

A. The Vitreous State

The role of small angle scattering in the study of non-crystalline solids has been emphasized by, for example, Porai-Koshits (1976) who distinguishes "technological" inhomogeneities (inclusions) that can be revealed in as-prepared glasses, and density fluctuations (see Chapter 2, Section IV.C). The latter can be determined in the small angle scattering region by extrapolating from intermediate h values to $h = 0$, ignoring any particle scattering, as (cf. Chapter 2)

$$I(0) = \overline{(\rho - \bar{\rho})^2} \quad (11)$$

Figure 16 illustrates the method of separation for the small angle scattering curves of initially crystalline (α)-quartz, irradiated with 9×10^{19} fast neutrons cm^{-2} and subsequently annealed as indicated (Bates *et al.*, 1974). The increasing portions of the curves at larger h values are related to the non-crystalline phase produced by the irradiation, whereas the steep parts of the curves at very small

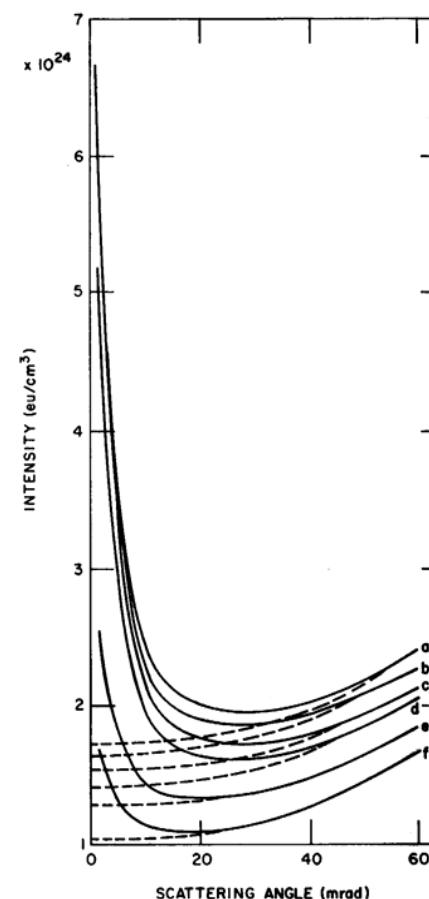


FIG. 16. Small angle scattering curves (MoK_{α}) for α -quartz, irradiated with 9×10^{19} fast neutrons cm^{-2} at ~ 55°C and annealed for 8 h at constant temperatures. (a) as irradiated; (b) 300°C; (c) 400°C; (d) 600°C; (e) 800°C; (f) 1000°C. Solid lines are measured curves, dashed lines represent contributions from the non-crystalline phase. (From Bates *et al.*, 1974.)

angles are due to the remaining microcrystallites. Figure 17 shows that after double the fast neutron dose, no crystalline material remains. The value of $I(0)$ for the as-irradiated α -quartz sample is identical with the value obtained for vitreous SiO_2 irradiated to the same fast neutron dose.

The fact that $I(0)$ of the non-crystalline phase increases with increasing neutron dose (see Fig. 17b), combined with density measurements, electron diffraction and Raman scattering, yields some insight into the structure of non-crystalline SiO_2 . Although the density increases with neutron dose, the

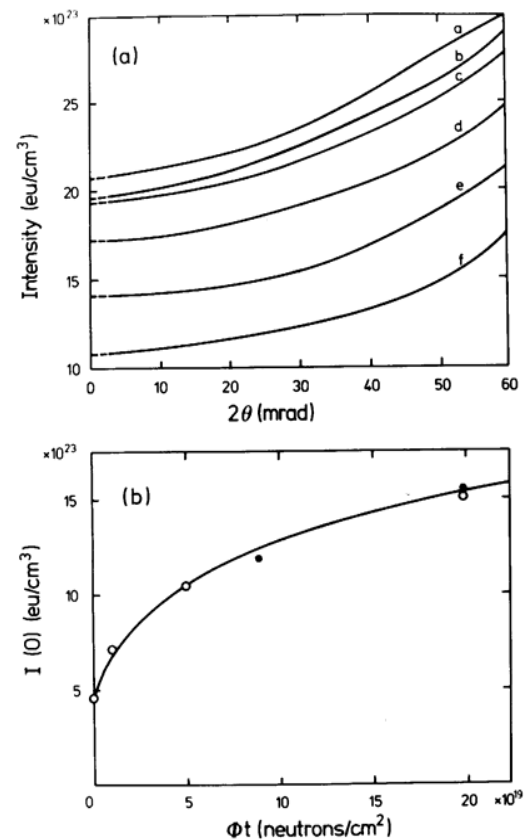


FIG. 17. (a) Small angle scattering for α -quartz irradiated with 2×10^{20} fast neutrons cm^{-2} and annealed for 8 h at constant temperatures. (a) as irradiated; (b) 300°C; (c) 400°C; (d) 600°C; (e) 800°C; (f) 1000°C. (b) $I(0)$ (corrected for multiple scattering) from irradiated vitreous SiO_2 (open circles) and α -quartz (full circles). The α -quartz point at 9×10^{19} neutrons cm^{-2} corresponds to the non-crystalline phase as indicated in Fig. 16. (From Bates *et al.*, 1974.)

density fluctuations also increase, indicating a larger disorder after irradiation. A consistent interpretation can be given based on the random network model for vitreous SiO_2 . Irradiation produces regions of higher density, but the (limited) cooperative properties of the SiO_2 network — seen in phonon-like modes in the Raman scattering data — are simultaneously destroyed, and more localized vibrational modes appear. Porai-Koshits (1976) estimates from similar results that the disorder in quartz produced by 2×10^{20} fast neutrons cm^{-2} is equivalent to thermal fluctuations at about 2400 K.

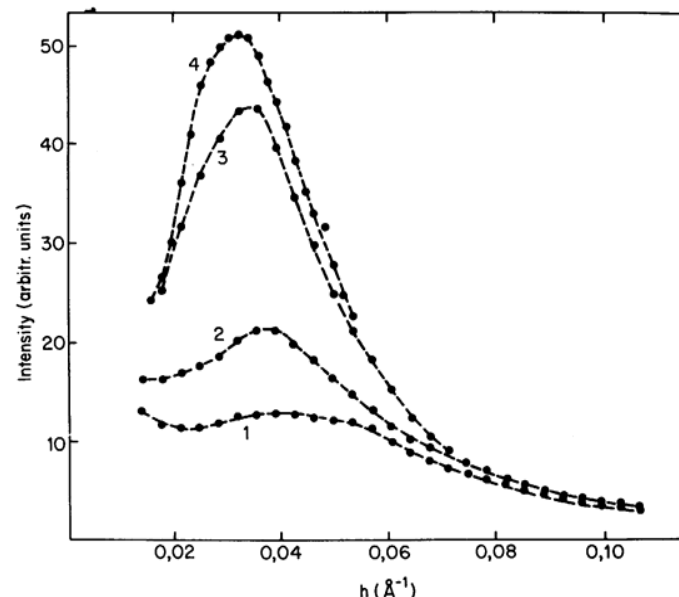


FIG. 18. Small angle scattering curves (CuK_{α}) for a set of B_2O_3 – PbO – Al_2O_3 samples splat-cooled with variable cooling rate ranging from about 2×10^3 (curve 4) to $2 \times 10^4 \text{°C s}^{-1}$ (curve 1). (From Acuña and Craievich, 1979.)

B. Phase Separation in Glasses

Phase-separation processes in multi-component glasses can be of technological importance and are receiving increasing attention, and small angle scattering techniques are also used (e.g. Kranold *et al.*, 1977; Becherer *et al.*, 1979).* The most extensive recent study with X-rays, though, is concerned with the “classical” system PbO – B_2O_3 – Al_2O_3 . As it is often impossible to quench rapidly enough from a homogeneous high-temperature state to avoid some decomposition, Acuña and Craievich (1979) have analysed the small angle scattering of 80% B_2O_3 –15% PbO –5% Al_2O_3 (weight %) splat-cooled from the liquid state to room temperature at different quench-rates. The thickness of the splat-cooled samples quenched between two spring-loaded copper blocks was taken as a measure of the cooling rate. For thicknesses between 0,1 and 0,35 mm, the cooling rates were estimated to vary between about 2×10^3 and $2 \times 10^4 \text{°C s}^{-1}$. Figure 18 shows the experimental results reduced to equivalent beam intensity and sample thickness, and corrected for collimation errors. A numerical integration of Cahn’s (1962, 1968) linear equation for spinodal decomposition, after inclusion of the fluctuation term introduced by Cook (1970), is presented

* Fink *et al.* (1979) have combined X-ray and light scattering to characterise the decomposition product in MgO – Al_2O_3 – SiO_2 glasses.

by the authors to describe the decomposition process during continuous cooling. The experiment confirms main trends of the calculation, and for the two lower small angle scattering curves, there is even good agreement. Similar experiments may be useful on other rapidly decomposing systems, too. For Al-Zn, corresponding calculations have already been announced (Acuña and Craievich, 1979).

A comparison of neutron and X-ray small angle scattering of ultra-rapidly cooled $\text{Al}_2\text{O}_3\text{-SiO}_2$ glasses aged between 200 and 850°C showed very similar intensities for the decomposed states (Jantzen *et al.*, 1981a, b). As Al and Si have only slightly different scattering amplitudes for X-rays, the presence of a strong small angle scattering signal indicates considerable density changes during decomposition.

C. Liquids

Liquid systems without clustering or phase separation may be investigated in the small angle scattering range (just like glassy systems) in order to obtain values on the statistical fluctuations that can be related to thermodynamic quantities.

For binary systems (Bhatia and Thornton, 1970), it is useful to write the intensity $I(0)$ as the sum of a concentration-concentration structure factor S_{CC} and a density fluctuation term. Whereas the latter is proportional to the isothermal compressibility, the former is given by

$$S_{CC}(0) = X_B / (\partial \ln a_A / \partial X_A)_{T,N} \quad (12)$$

where a_A is the activity of component A and N is the total number of atoms. Figure 19 shows $S_{CC}(0)$ as a function of composition for the Na-K system at 100°C (Alblas and van der Lught, 1980). The experimental points lie clearly above the curve for an ideal solution, where $S_{CC}(0) = X_B(1 - X_B)$, and confirm results obtained from activity measurements. The higher values of $S_{CC}(0)$ are compatible with a regular solution model and the Flory model (see Alblas and van der Lught, 1980, for a more detailed discussion of other systems too).

If the tendency towards clustering or phase separation becomes stronger, the variation of $S_{CC}(h)$ gives some indication of the extent of compositional fluctuations or cluster size. In the case of dynamical compositional fluctuations, the h dependence should follow an Ornstein-Zernike relationship

$$C_1/I(h) = (1 + \xi^2 h^2) \quad (13)$$

where C_1 is a constant, and ξ is the correlation length. For clusters, the Guinier approximation should be more appropriate. The experimental distinction is not

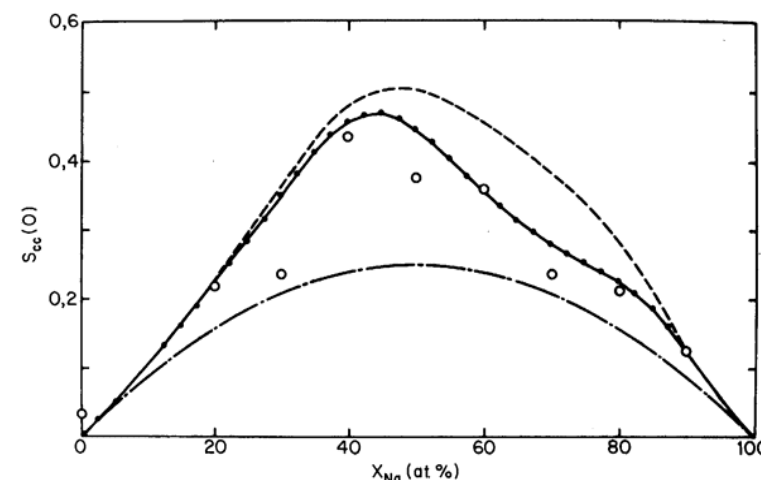


FIG. 19. $S_{CC}(0)$ for liquid Na-K alloys as a function of Na concentration at 100°C. Circles are experimental results from the small angle scattering region, the upper two curves are calculated from Eqn (12), using two sets of activity measurements, and the lower curve is expected for ideal solutions. (From Alblas and van der Lught, 1980.)

always easy (see Hoehler and Steeb, 1975), especially if the range of fluctuations remains small. Quite a few molten alloy systems have been investigated and showed small angle scattering effects corresponding to cluster diameters of a few interatomic distances (Steeb, 1978; Hezel and Steeb, 1980).

D. Critical Scattering

Equation (13) finds a very dramatic confirmation if compositional fluctuations near a second-order phase transformation are investigated, where ξ increases towards infinity. In the solid state, such studies with X-rays on Al-Zn gave misleading results (Münster and Sagel, 1958), and the correct coherent critical temperature was only recently found to be about 323°C (from neutron small angle scattering, see Schwahn and Schmatz, 1978). In liquids, studies of critical scattering are not complicated by competing metastable and stable phase formation. Figure 20 shows the X-ray scattering of liquid Li-NH₃ solutions at 210 K up to $h = 1 \text{ \AA}^{-1}$. With increasing Li concentration, the small angle scattering increases until at 4,35 MPM and 210 ± 0,5 K, pronounced critical scattering occurs. This scattering decreases rapidly with a further increase in Li concentration, and a hump at larger h develops. Knapp and Bale (1978) report similar results for Na-NH₃ and find reasonable agreement of $S_{CC}(0)$ from small angle scattering with values deduced from thermodynamic data.

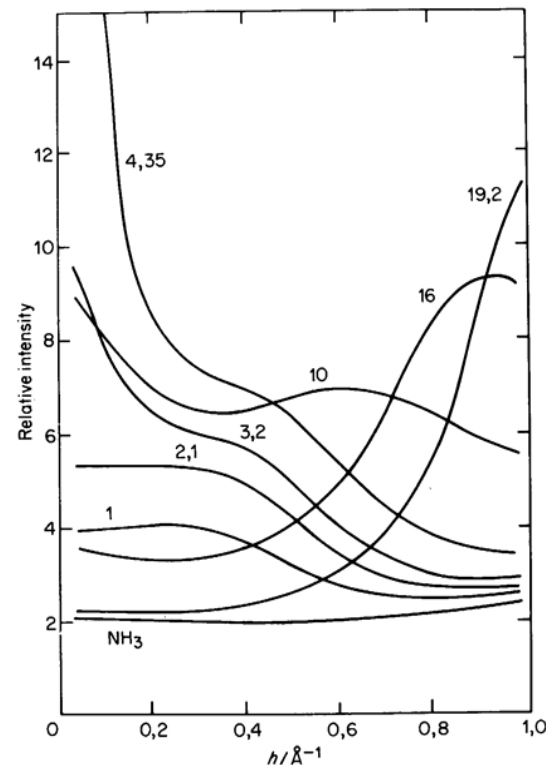


FIG. 20. Scattered X-ray intensity (MoK_α) as a function of scattering vector h for $\text{Li}-\text{NH}_3$ solutions at 210 K. Li concentrations are given in MPM. (From Knapp and Bale, 1978.)

VI. Epilogue

A brief survey of the applications of X-ray small angle scattering to inorganic substances has been given, with emphasis on general fields of interest and on a few selected, mostly recent, experiments. A more extended view of the subject, including neutron small angle scattering, can be obtained by consulting the review papers cited above.

Despite its limitations, X-ray small angle scattering will continue to be an important research method for inorganic materials. Further progress in instrumentation will make it easier to study kinetic processes, anisotropic scattering, weak scattering problems etc., and more work in these directions can be expected. Best results will probably be obtained where small angle scattering can be combined with other methods in order to reduce the number of possible explanations of non-trivial small angle scattering patterns. This is particularly

indicated for many complex multi-phase materials being studied and developed for a variety of future applications.

References

- Acuña, R. J. (1980). *J. Mat. Sci.* **15**, 20.
- Acuña, R. J. and Craievich, A. F. (1979). *J. Non-Cryst. Solids* **34**, 13.
- Alblas, B. P. and van der Lugt, W. (1980). *J. Phys. F: Metal Phys.* **10**, 531.
- Allain, J., Naudon, A. and Caisso, J. (1979). *Acta Metall.* **27**, 545.
- Allen, D., Messoloras, S., Stewart, R. J. and Kostorz, G. (1978). *J. Appl. Cryst.* **11**, 578.
- Bates, J. B., Hendricks, R. W. and Shaffer, L. B. (1974). *J. Chem. Phys.* **61**, 4163.
- Baur, R. and Gerold, V. (1964). *Acta Metall.* **12**, 1449.
- Becherer, G., Fink, H.-P. and Kranold, R. (1979). In "Conference on Applied Crystallography" (Proc. of the conference held at Kozubnik, Poland, August 1978, Z. Bojarski and T. Bołd, eds.), Vol. I, p. 298. Silesian University, Katowice.
- Bhatia, A. B. and Thornton, D. E. (1970). *Phys. Rev. B2*, 3004.
- Bubeck, E., Friedrich, C. and Kostorz, G. (1981). To be published. See also "Annexe to the Annual Report 1980", p. 303, Institut Laue-Langevin, Grenoble.
- Cahn, J. W. (1962). *Acta Metall.* **10**, 907.
- Cahn, J. W. (1968). *Trans. TMS-AIME* **242**, 166.
- Cartraud, M., Guillot, J., Mimault, J. and Grilhé, J. (1979). *Scripta Metall.* **13**, 281.
- Cook, H. E. (1970). *Acta Metall.* **18**, 297.
- Dartyge, E., Lambert, M., Leroux, G. and Levelut, A. M. (1972). *Acta Metall.* **20**, 233.
- Dauger, A., Fumeron, M., Guillot, J. P. and Roth, M. (1979). *J. Appl. Cryst.* **12**, 429.
- Epperson, J. E., Hendricks, R. W. and Farrell, K. (1974). *Philos. Mag.* **30**, 803.
- Fink, H.-P., Göcke, W., Kranold, R. and Walter, G. (1979). *Wiss. Ztschr. Friedrich-Schiller-Univ. Jena* **28**, 557-565.
- Flank, A. M. and Naudon, A. (1977). *J. Appl. Cryst.* **10**, 151.
- Gerold, V. (1967). In "Small-Angle X-Ray Scattering" (Proc. of the conference held at Syracuse Univ., June 1965, H. Brumberger, ed.), p. 277. Gordon and Breach, New York.
- Gerold, V. (1977). *J. Appl. Cryst.* **10**, 25.
- Gerold, V. and Kostorz, G. (1978). *J. Appl. Cryst.* **11**, 376.
- Gerold, V., Epperson, J. E. and Kostorz, G. (1977). *J. Appl. Cryst.* **10**, 28.
- Gerstenberg, K. W. (1980). Ph.D. Thesis, University of Stuttgart, Germany.
- Groma, G., Kovács-Csetényi, E., Kovács, I., Lendvai, J. and Ungár, T. (1979). *Philos. Mag. A40*, 653.
- Guinier, A. (1938). *Nature* **142**, 569.
- Guinier, A. (1963). In "X-Ray Diffraction" (Translation by P. Lorrain and D. Lorrain). Freeman, San Francisco.
- Guinier, A. and Fournet, G. (1955). "Small-Angle Scattering of X-Rays" (Translation by C. B. Walker). Wiley, New York, and Chapman and Hall, London.
- Harkness, S. D. and Hren, J. J. (1970). *Met. Trans.* **1**, 43.

- Harkness, S. D., Gould, R. W. and Hren, J. J. (1969). *Philos. Mag.* **19**, 115.
 Haubold, H.-G. and Martinsen, D. (1978). *J. Appl. Cryst.* **11**, 592.
 Hendricks, R. W. (1978). *J. Appl. Cryst.* **11**, 15.
 Hendricks, R. W., Schelten, J. and Schmatz, W. (1974). *Philos. Mag.* **30**, 819.
 Hendricks, R. W., Schelten, J. and Lippman, G. (1977). *Philos. Mag.* **36**, 907.
 Hezel, R. and Steeb, S. (1980). *Z. Naturforsch.* **25a**, 1085-1091.
 Hilliard, J. E. (1970). In "Phase Transformations" (ASM Seminar), p. 497.
 Chapman and Hall, London.
 Hoehler, J. and Steeb, S. (1975). *Z. Naturforsch.* **30a**, 775.
 Jantzen, C. M., Schwahn, D., Schelten, J. and Herman, H. (1981a). *Phys. Chem. Glasses* **22**, 122-137.
 Jantzen, C. M., Schwahn, D., Schelten, J. and Herman, H. (1981b). *Phys. Chem. Glasses* **22**, 138-144.
 Junqua, A., Mimault, J. and Delafond, J. (1976). *Acta Metall.* **24**, 779.
 Knapp, D. N. and Bale, H. D. (1978). *J. Appl. Cryst.* **11**, 606.
 Kranold, R., Fink, H.-P., Göcke, W. and Becherer, G. (1977). *Kristall und Technik* **12**, 1079.
 Kostorz, G. (1976). *Z. Metallkde.* **67**, 704.
 Kostorz, G. (1979). In "A Treatise on Materials Science and Technology" (H. Herman, ed.), Vol. 15, p. 227. Academic Press, New York and London.
 Laslaz, G., Kostorz, G., Roth, M., Guyot, P. and Stewart, R. J. (1977). *Phys. Stat. Sol. (a)* **41**, 577.
 Laslaz, G., Guyot, P. and Kostorz, G. (1978). *J. Phys. (Paris)* **38**, C7, 407.
 Lindberg, V. W., McGervey, J. D., Hendricks, R. W. and Triftshäuser, W. (1977). *Philos. Mag.* **36**, 117.
 Liu, S., Motteff, J., Hendricks, R. W. and Lin, J. S. (1978). *J. Appl. Cryst.* **11**, 597.
 Münster, A. and Sagel, K. (1958). *Molec. Phys.* **1**, 23.
 Naudon, A. and Allain, J. (1974). *J. Appl. Cryst.* **7**, 225.
 Naudon, A. and Caisso, J. (1974). *J. Appl. Cryst.* **7**, 25.
 Naudon, A., Delafond, J., Junqua, A. and Mimault, J. (1978). *J. Appl. Cryst.* **11**, 569.
 Naudon, A., Lemonnier, M. and Rousseaux, F. (1979). *C.R. Acad. Sci. (Paris)* **288**, 21.
 Parker, B. A. (1972). *J. Appl. Cryst.* **5**, 372.
 Porai-Koshits, E. A. (1976). *Ann. Rev. Mat. Sci.* **6**, 389.
 Roth, M. (1977). *J. Appl. Cryst.* **10**, 172.
 Rothwell, W. S. (1968). *J. Appl. Phys.* **39**, 1840.
 Schmatz, W. (1973). In "A Treatise on Materials Science and Technology" (H. Herman, ed.), Vol. 3, p. 105. Academic Press, New York and London.
 Schmatz, W., Springer, T., Schelten, J. and Ibel, K. (1974). *J. Appl. Cryst.* **7**, 96.
 Schwahn, D. and Schmatz, W. (1978). *Acta Metall.* **26**, 1571.
 Steeb, S. (1978). 4me Colloque International sur les "Méthodes Analytiques par Rayonnement X". Strasbourg 1977.
 Tschoubar, D., Rousseaux, F., Pons, Ch. and Lemonnier, M. (1978). *Nucl. Instr. Methods* **152**, 301.
 Tsujimoto, T. (1977). *Trans. Jap. Inst. Met.* **18**, 393.
 Tsujimoto, T., Saito, K. and Hashimoto, K. (1975). *Trans. Jap. Inst. Met.* **16**, 445.
 Vonk, C. G. (1976). *J. Appl. Cryst.* **9**, 433.

15

Aggregations and Micellar Structures of Small Molecules in Solution

O. KRATKY and K. MÜLLER

Institut für Röntgenfeinstrukturforschung der Österreichischen Akademie der Wissenschaften und des Forschungszentrums Graz, Graz, Austria

I. Soaps and detergents	500
II. Sodiumdodecylsulfate (SDS)	500
III. Bile salts in solution	502
IV. Mixed micellar systems	502
V. Organic dyes in solution	504
A. β -naphtholorange	505
B. Copper – phtalocyanine – tetrasulfonate	508
References	510

As well as common macromolecules, some types of aggregations of small molecules also fall into the range of resolution accessible to X-ray small angle scattering. These aggregations can be formed by all known types of side-bondings, as well as by entropic reasons, for example the hydrophobic effect (Tanford, 1973).

The latter is very interesting since the existence of numerous micelles, of technical as well as of biological importance, is based upon this phenomenon. The best known aggregates of practical significance are soap and detergent micelles, on the one hand, and biological membranes, vesicles etc. (see Chapter 10) formed by biological amphiphiles, on the other.

We will confine ourselves in this chapter to only a few selected examples, which will allow an estimate at the possibilities of modern X-ray scattering methods being used on related systems.

I. Soaps and Detergents

Measurements on an absolute scale were first carried out by Reiss *et al.* (1964, 1966): A variety of soaps and detergents has been examined over a wide range of concentrations and a concentration dependent polymorphism has been detected describing the micelles as spherical at low concentrations, whereas they appeared rod-like at high concentration.

The contrast variation method, allowing the dissection of the scattering contribution of the overall shape and the internal structure (Chapter 6), cannot be used for X-ray experiments since the additives for contrast adjustment in general lead to drastic changes or even total disruption of the micelles.

Measurements on *p*-alkylbenzenesulfonates using neutron scattering (Cabos *et al.*, 1977) on the whole confirmed the picture of detergent micelles as obtained from X-ray scattering, although small systematic differences in the total dimensions were detected.

The essential problem in these studies is the obscuring effect on the unknown dependence of particle size and shape on the concentration, on the one hand, and the dependence of the interparticle interference effect on the concentration, on the other. This prevents an unambiguous evaluation of the scattering function at small angles.

II. Sodiumdodecylsulfate (SDS)

Essential progress has been the application of the indirect Fourier transformation method that allows one to distinguish clearly between these disturbing effects mentioned above.

As described in detail in Chapter 5, the interparticle interference results in a negative trough of the $p(r)$ function in the region of the maximum diameter of the particle. The position of this trough remains constant when the sample is measured at different concentrations, provided that no change in the particle size occurs with the change of concentration. If this is the case, a simple elimination of the concentration effect can be carried out and relevant values for the molecular weight and radius of gyration can be derived. A further advantage, that becomes important especially in the case of micellar systems, is the possibility of distinguishing clearly between background scattering and the contribution of the particle scattering at large angles (Chapter 5), offered by the indirect transformation method. It was found, that even after background subtraction in this improved way, the scattering intensity at large angles remains relatively high and is part of the particle scattering function. Another advantage is that the maximum diameter is directly obtainable from $p(r)$, whereas the radius of gyration measured at only one contrast is not a valid measure of the particle size in the case of particles with inhomogeneous internal electron density distribution.

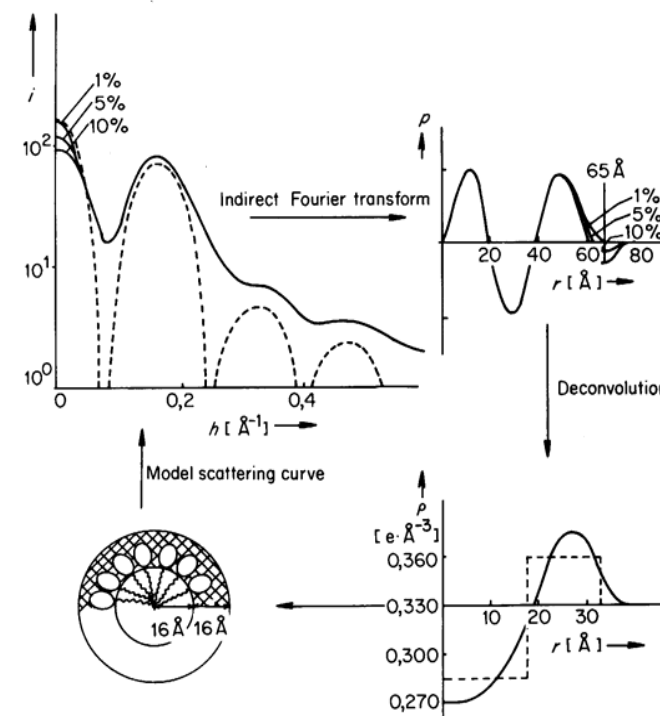


FIG. 1. Scattering data of sodiumdodecylsulfate. From the distance distribution function $p(r)$ the radial electron density distribution function was derived by direct deconvolution (Glatter, 1981). From the equivalent step function (broken line) the model was constructed from which the model scattering curve was calculated (broken line). The latter fits well to the experimental $i(h)$ -function.

In the following and in Sections III and IV, a short survey of the results obtained for some special cases of micelles in solution shall be given, using the indirect Fourier transformation method.

The experimental findings (Müller, unpublished results) on Sodiumdodecylsulfate (SDS) (see Fig. 1) show that the micelles have a constant size of 64 Å in the concentration range of 1–10% mass concentration (37°C; 0,15 m NaCl). The shape of the p -function indicates a spherical particle with two regions, one of low and one of high electron density. Deconvolution of $p(r)$ as well as Fourier transformation of the scattering amplitudes yield the radial electron density distribution with a region of $0,270 \text{ e} \cdot \text{\AA}^{-3}$ from the centre up to 16 Å and a shell of about 16 Å thickness and an electron density of $0,360 \text{ e} \cdot \text{\AA}^{-3}$. The scattering curve based upon this model fits the experimental curve very well. In connection with the apparent partial specific volume of $0,875 \text{ cm}^3 \text{ g}^{-1}$, a micellar mass of 23 000, and consequently an aggregation number of 80, was obtained.

From the comparatively low electron density in the outer region, as well as from its extended volume as compared with the volume of the headgroup alone, a high degree of water and counterion binding can be deduced. From the well resolved minima of the scattering curve one can roughly estimate that deviations from sphericity and polydispersity remain below acceptable limits.

III. Bile Salts in Solution

Bile salts are of considerable biological importance, especially because of their role as physiological detergents. Although numerous studies have been performed with different methods to clarify the structure of the micellar aqueous solutions, the data available are rather controversial. X-ray scattering studies (Eckwall and Fontell, 1956; Fontell, 1971) dealing with this substance were also not able to eliminate these inconsistencies. The reason for this is the more complex structure of the bile salt molecules with not only a polar head group but an additional polar site at the apolar sterol moiety, which led to complex models for the aggregation behaviour.

Although our measurements are not finished yet several features can already be established being in contradiction with the hitherto accepted picture of these micelles. We studied (Müller, unpublished results) different bile salts, i.e. sodium-cholate, -deoxycholate, -chenodeoxcholate and the specific conjugates with taurine and glycine, respectively, of all three bile salts. The range of concentration was varied between 1% and 10% mass concentration and the counterion concentration (NaCl) varied between 0 and 0,6 molar.

As a result we found practically no dependence of the micelle diameter either on the concentration or on the ion milieu. Only the aggregation number increased with increasing counterion concentration without significant micellar growth. All bile salt species behaved quite similarly. The dimensions of the micelles increased with decreasing number of hydroxyl groups. Trihydroxy-bile salts were found to have an aggregation number of about 8 (0,15 m NaCl) whereas for the dihydroxy compounds an average of 18 monomers were found per micelle. The diameter of the highly isometrical micelles varied from 4,0 nm (unconjugated trihydroxy bile salts) up to 6,0 nm (conjugated dihydroxy-bile salts).

IV. Mixed Micellar Systems

These aggregates are of particular interest since their structure provides information on how hydrophobic compounds are solubilized by incorporation in

these detergent micelles. Only a few systems have been examined by X-ray scattering, for example the system sodiumoctanoate-fatty alcohol (Svens and Turpeinen, 1975). The micellar system bile salt-lecithin was investigated for the first time by X-ray small angle scattering (Müller, 1981). This system is responsible for the solubilization of cholesterol and other water insoluble substances excreted with the biliary liquid. Malfunctions of this solubilizing mechanism lead to cholesterol gall stone formation. Recent physiological studies on this phenomenon suggest the conclusion that apart from oversaturation of bile with additional cholesterol, possibly structural factors also play a role in this connection. According to our findings, two different types of mixed micelles are formed in dependence of the bile salt/lecithin mixing ratio. At bile salt contents higher than 65 M%, the micelles are spherical with a centrosymmetrical arrangement of the individual lipid molecules. When the bile salt content is lowered and the lecithin comes up to more than 35 M%, disc-shaped particles are formed with an internal arrangement comparable to that of a lipid bilayer. This was suggested by the quite different behaviour of the micelles on the two sides beyond the transition point. Shifting the mixing ratio in the bile salt rich region, the shape remained constant and the micellar mass increased only slightly with increasing lecithin content. In the lecithin-rich range, any further incorporation of lecithin causes a dramatic increase in the molecular weight and the degree of anisometry, determined from the ratio between the radius of gyration and the maximum diameter. This strongly indicates a lateral growth of lecithin-rich micelles. Finally, the detailed comparison of the experimental scattering and distance distribution functions allows a clear distinction to be made between spherical and disc-like particles. The results are shown in Fig. 2. Besides the electron density profiles on an absolute scale, in the one case three-dimensional, in the other one-dimensional, the mass per unit area can be determined from the thickness factor according to the equation

$$M_t = i_t(0)^{1/2} \cdot \Delta Z^{-1}$$

whereas $i_t(0)$ can be obtained from p_t , as

$$i_t(0) = 2 \int_0^{\infty} p_t(r) \cdot dr$$

$$p_t(r) = \frac{1}{\pi} \int_0^{\infty} i_t(h) \cos hr \cdot dr$$

we obtained a mass of 19 \AA^{-2} or an average area of 66 \AA^2 per molecule. In connection with the electron density level of $0,390 e \cdot \text{\AA}^{-3}$, a high degree of hydration can be derived from this value. The physiological relevance of this transition remains to be established.

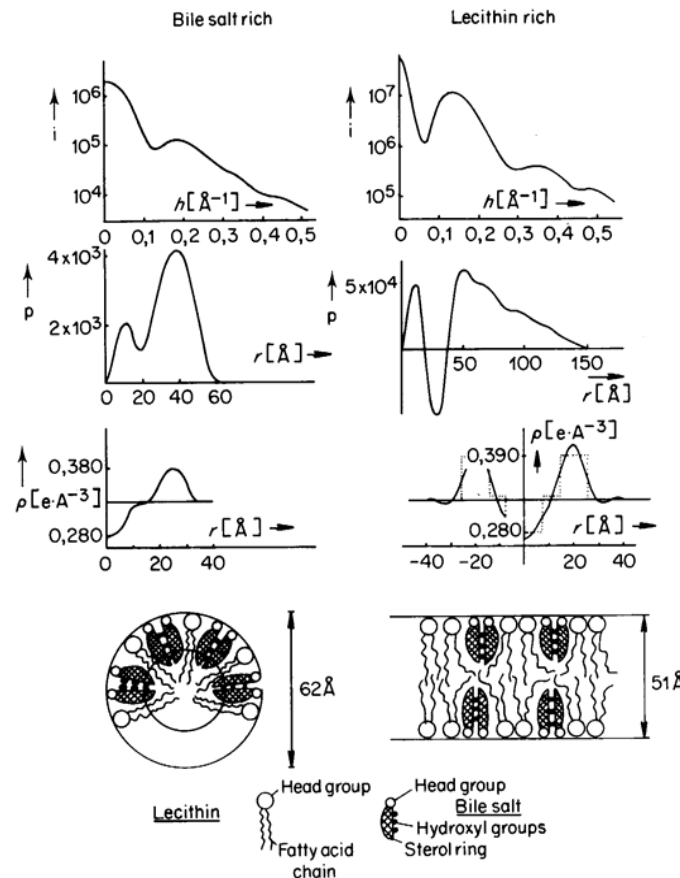


FIG. 2. Scattering functions (upper row), distance distribution functions (second row), electron density distribution functions ($\rho = \text{radial}$, $\rho_t = \text{one dimensional}$) (third row) and molecular models (bottom) of bile salt-rich and lecithin-rich mixed micelles.

V. Organic Dyes in Solution

A thorough understanding of the process of dyeing requires knowledge of the solution properties of the dye, in particular the degree and geometry of association as a function of concentration, temperature and ionic composition. The application of SAXS to such problems has until now — as far as we know — only been attempted in the author's laboratory. This restraint becomes understandable in view of the following two facts, which make such investigations extremely difficult.

In the limit of high dilution, one frequently observes dissociation to

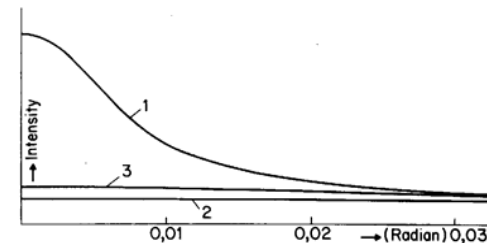


FIG. 3. Schematic presentation of the scattering curve of a 0.5% protein solution $M = 64000$ (curve 1), a 0.5% dye solution (curve 3), the solvent (curve 2).

monomeric molecules. Their molecular weight (several hundred) is around two orders of magnitude lower than the one of a small biological macromolecule. The experimental difficulties encountered in the study of particles of only several Ångströms diameter are schematically illustrated in Fig. 3, which compares the scattering curve of a protein solution with the one of a dye of equal concentration. In the latter case, the net scattering (difference between curves 3 and 2) is always much smaller than the scattering of the pure solvent. This puts high demands on the required accuracy of both curves, since otherwise large errors will result.

A second fundamental difficulty is the required extrapolation to zero concentration, in order to correct for interparticle interference effects. For most dyes the degree of association is itself concentration dependent, which makes the extrapolation strictly only valid for the limit of highest dilution. Interference effects, however, mainly affect the innermost part of the scattering curve; if the extrapolation is therefore carried out in a Guinier-plot, reasonable results can be obtained even for modest concentrations.

We shall confine the following section to two examples of organic dyes: to β -Naphtholorange, which will be discussed extensively to exemplify the course of such an investigation, and to copperphthalocyanine-tetrasulfonate, for which only a summary of the results will be given.

A. β -Naphtholorange

We have chosen this azo-dye for the discussion (Kratky *et al.*, 1967a; 1967b), as there exist studies on the degree of association using other techniques, one of whose results will be compared with the small angle results.

1. AQUEOUS SOLUTIONS

The molecular weight can be obtained from absolute intensity measurements, according to Eqn. 49 in Chapter 4. Division by the chemical molecular weight

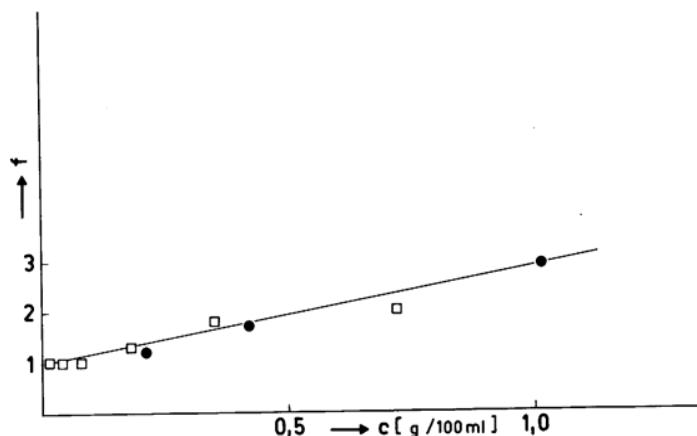


FIG. 4. β -naphtholorange: dependence of the mean degree of association f of the concentration in aqueous solution. Comparison of the results found with small angle measurement ● (Kratky *et al.*, 1967a, 1967b) and with other methods □ (Milicévic and Eigenmann, 1964).

yields the mean degree of association f . Figure 4 compares the results from SAXS with the molecular weight from the absorption of visible light (Milicévic and Eigenmann, 1964). The agreement is very satisfactory and there can be no doubt that in the limit of high dilution, the dye is dissociated to monomeric molecules.

2. POTASSIUM CHLORIDE SOLUTIONS

Figure 5 quotes the degree of association observed in 0.1 m KCl solution. Again, high dilution leads to single molecules.

It should be noted that it is not usually possible to detect such high degrees of association with the standard visible-light absorption technique, since the transparency becomes prohibitively small.

The shape determination is based on the important fact that for all concentrations, except low ones, one observes the characteristic behaviour of lamellar shaped particles with the same radius of gyration of the thickness R_t and the same mass per unit area M_t :

$$R_t = 3.9 \text{ \AA}; \quad t = R_t \sqrt{12} = 13.5 \text{ \AA}; \quad M_t = 3.86 \pm 0.3$$

Since the thickness $t = 13.5 \text{ \AA}$ is about equal to the largest linear dimension of the monomer molecule of about 14 \AA (see Fig. 6 for the chemical formula), it is reasonable to assume that the particles associate in the two directions perpendicular to the longest molecular axis. If the molecule is approximated by a parallelepiped, one can easily compute its dimensions. From the radii of

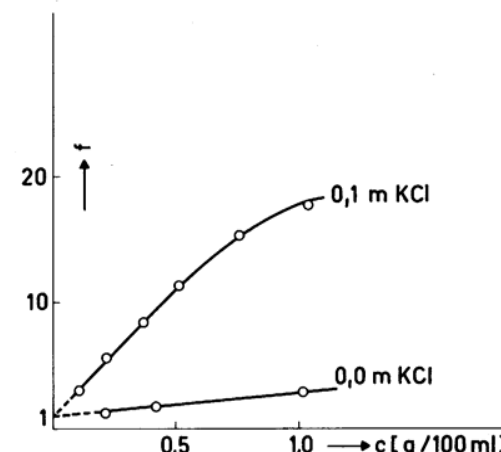


FIG. 5. β -naphtholorange: dependence of the mean degree of association f of the concentration in aqueous solution and 0.1 m KCl solution.

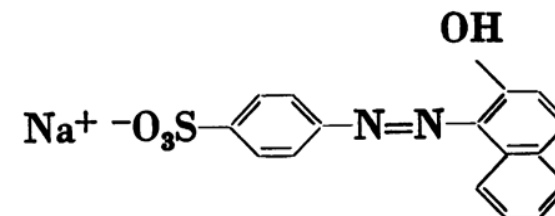


FIG. 6. Formula of β -naphtholorange.

gyration of the cross-section (R_c) and the thickness (R_t), the lamellar length l_R and width b_R are given by

$$l_R^2 = 12(R^2 - R_c^2) \quad (1a)$$

$$and \quad b_R^2 = 12(R_c^2 - R_t^2) \quad (1b)$$

Table 1 lists the experimental ratios $t:b_R:l_R$ for several measurements. A check on these results is possible by comparing the experimental scattering curves with theoretical ones for parallelepipeds of appropriate axial ratios. At the time of these investigations, however, no theoretical curves with exactly the required axial ratios were available; the comparison was therefore carried out with two theoretical curves whose axial ratios embraced the experimental values (Table 1) (only in one case, No. 9, a theoretical curve for exactly the required axial ratio was at hand). Figure 7 shows that the experimental points always lie between the corresponding theoretical curves. The suggested axial ratios can therefore be regarded as a reasonable approximation of the particles in solution. The value

TABLE 1
Ratios $(t:b_R:l_R)_{exp}$ found according to Eqns (1a) and (1b) and ratios $(t:b:l)_{theor}$ of theoretical calculated curves of rectangular prism.

No.	$(t:b_R:l_R)_{exp}$	$(t:b:l)_{theor}$
3	1:0,96:2,22	1:1:2 1:1:3
4	1:0,96:2,44	1:1:2 1:1:3
5	1:1,48:3,41	1:1,33:2,67 1:1,33:4
6	1:1,55:4,00	1:1,33:4 1:2:4
7	1:1,63:4,75	1:1,33:4 1:2:6
8	1:1,85:5,55	1:2:4 1:1,33:6,67
9	1:2,00:6,00	1:2:6

obtained for the area required by one molecule $b_R \times l_R/f \approx 95 \text{ \AA}^2$ is surprisingly large; this is apparent if we compare the volume occupied by one subunit in the aggregate of $13,5 \times 95 = 1280 \text{ \AA}^3$ with the volume obtained from the partial specific volume of the monomeric particles; with $v'_1 = 0,52$ and $M = 350$, the latter volume is 302 \AA^3 . Particles thus aggregate in a remarkably loose fashion, which can be explained in a number of ways, e.g. the hydrophobic effect (Tanford, 1973).

While it is possible to obtain information concerning the degree of association with several other methods as well, the small angle technique is certainly the most suitable one if information about particle size and shape is required.

B. Copper – Phtalocyanine – Tetrasulfonate

This dye has a molecular weight of $M = 1116$. Size and shape of its aggregates were investigated in aqueous solutions (Kratky and Oelschlaeger, 1965). The dependence of the degree of association on the concentration, ionic composition and temperature was determined. The smallest aggregates found consisted of 2 molecules, the largest of more than 200. Oblique piles of variable height were proposed for their shape, and a simple model was derived for the composition of polydisperse systems formed by the various association equilibria (Oelschlaeger, 1969). Relations between concentration, mean degree of association and mean radius of gyration were established for these model systems.

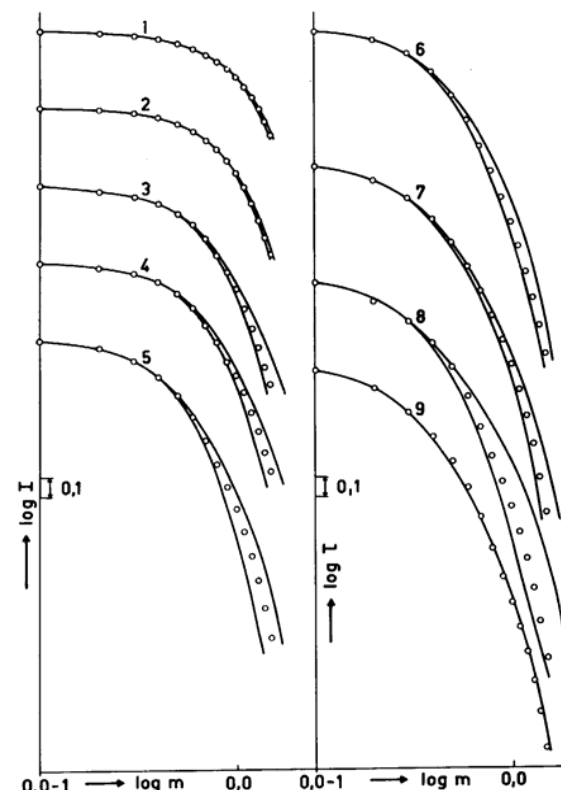


FIG. 7. β -naphtholorange: comparison of measured scattering curves (\circ) with theoretical calculated curves (full lines). Table 1 gives the corresponding ratios $t:b_R:l_R$.

The heat association can be determined by comparing the temperature dependence (measurements were carried out at 20°C , 35°C and 50°C) and the concentration dependence of the system. The energy of the intermolecular aggregation was estimated to be $10\,000 \text{ cal(mol)}^{-1}$ by application of van't Hoff's equation. This value appears rather low in view of the large number of atoms which can come into van der Waals contact in such a planar macrocyclic molecule.

The geometrically obtained volume is larger by a factor of 3 than the value from the partial specific volume, which is similar to the situation observed for β -Naphtholorange. In both cases, this discrepancy is obviously the result of a particular mode of aggregation, which would require further investigations.

For the measurement on other dye stuffs, especially on chlorantinlichtviolet 2 RLL, refer to Kratky *et al.* (1966).

References

- Cabos, P. C., Delord, P. and Rouviere, J. (1977). *J. Appl. Cryst.* **10**, 37–44.
 Ekwall, P. and Fontell, K. (1956). *Acta Chem. Scand.* **10**, 327.
 Fontell, K. (1971). *Kolloid Z.Z. Polymers* **246**, 710–718.
 Glatter, O. (1981). *J. Appl. Cryst.* (in press).
 Kratky, O. and Oelschlaeger, H. (1969). *J. Colloid Interface Sci.* **31**, 490–502.
 Kratky, O., Ledwinka, H. and Pilz, I. (1966). *Ber. Bunsenges. physik. Chem.* **70**, 904–912.
 Kratky, O., Pilz, I. and Ledwinka, H. (1967a). *Mh. Chem.* **98**, 227–230.
 Kratky, O., Ledwinka, H. and Pilz, I. (1967b). *Makrom. Chem.* **105**, 171–192.
 Milicévic, M. and Eigenmann, G. (1964). *Helv. Chim. Acta* **47**, 1039–1047.
 Müller, K. (1981). *Biochemistry* **20**, 404–414.
 Oelschlaeger, H. (1969). *J. Colloid Interface Sci.* **31**, 503–507.
 Reiss-Husson, F. and Luzzati, V. (1964). *J. Phys. Chem.* **68**, 3504–3511.
 Reiss-Husson, F. and Luzzati, V. (1966). *J. Colloid Interface Sci.* **21**, 534–546.
 Svens, B. and Turpeinen, M. (1975). *Progr. Colloid Polymer Sci.* **56**, 30–36.
 Tanford, Ch. (1973). "The Hydrophobic Effect", John Wiley, New York.

Subject Index

- A**
 Abscissa-scaling, 156
 Absolute intensity, 18, 77
 filter method, 78
 moving slit method, 78
 rotator, 78
 secondary standards, 78
 Absorption-coefficient, 55
 Aggregation, 41, 175, 499
 Amplitude, 19
 scattering, 140
 Angle
 Bragg, 90
 glancing, 90
 scattering, 19
 Anisometric particles, 23
 Anode
 material, 54
 rotating, 58
 Autocorrelation, 20
 Average
 over all orientations, 25
 spatial, 126
 weighted, 28
- B**
 Babinet principle, 42
 Background, 21, 191
 scattering, 130, 230
 subtraction, 232, 307, 335, 435, 459
 Beam
 divergence of, 70
 incident, 18
 monochromatic, 70
 scattered, 18
 Bessel function, 34, 200
 Bragg relation, 136, 436
- B-spline**, 129, 131, 144
- C**
 Camera
 block, 62
 Bonse-hart, 69
 cone, 73
 dimension of, 61
 for synchrotron radiation, 93
 glass, 72
 integrated block, 67
 mirror-monochromator, 96
 Chain
 branched, 371, 397, 423
 flexibility of, 425
 flexible segment, 364
 Kratky-Porod, 408
 linear, 392
 molecules, 179
 persistence, 396, 407
 valence angle, 394
 wormlike, 361, 396
 Channel width, 74
 Characteristic function, 26
 Chord, 27
 distribution, 27, 168, 272, 452
 Clusters, 481
 Coherence, 18
 Coil
 branched, 397
 Gaussian, 362, 397, 401
 models for, 392
 perturbed, 397, 416
 unperturbed, 392, 401
 Collimation
 point, 85
 slit, 59
 system of, 59, 120

Complex
contrast variation, 206
scattering density, 206
scattering length, 205
Composite particles, 36, 175
Concentration, 38, 41, 242
effect, 189, 225, 244, 500
Contrast variation, 169, 185, 204,
270, 313, 330, 339
complex, 206
Convolution, 143
integral, 122
square, 20, 140
square root, 140, 142, 308, 501
Corners, 31
Correlation
function, 21, 26, 44, 49, 446
length, 29, 46, 153
volume, 45, 154
Cosine-transformation, 36, 142
Cross-section, 32, 140, 153, 171
circular, 34
function, 33, 256, 362, 378, 435
Curvature, 31

D

Debye formula, 21, 37, 157, 197, 401,
402
Decomposition, 482
Defects, 475
Density measurements, 234
Densely packed systems, 30, 373
Desmearing, 128, 435
iterative, 129, 130
problem, 126
Detector, 92, 107
depth of, 123
electronics, 110
position sensitive, 93, 106, 114
proportional counter, 108
scintillation, 109
slit length, 123
slit width, 123
solid state, 108
window, 123
Deuteration, 199, 210, 280, 315
Diffraction, 18
Dimers, 175, 255
Distance distribution function, 130,
168, 212, 248, 401

of cross-section, 141
of thickness, 142, 347, 503
of models, 162
Dynamic range, 106, 113

E

Edges, 31
Electron density, 19, 198
difference, 26, 168, 201, 205, 227
fluctuation, 21
non-uniform, 48
radial, 139, 260, 501
Ellipsoids, 24, 156, 175
Equilibrium Data, 286
Error
propagated, 133
statistical, 132
systematic, 132, 149, 216
Excess electrons, 23, 201, 205
Experimental
design, 149
practice, 215

F

Film, 107, 113
X-ray, 90
Fine structure, 29
Finite elements, 157
Flat particles, 35, 151, 173, 186
Flexible-thread, 35
Fluctuation
intensity, 80
mean square, 43
statistical, 41
Focus
line, 57
square, 58
Focusing-elements, 87
condition, 91
monochromators, 87
Fourier
coefficients, 200
filtering technique, 135
ripples, 138, 146
transform, 19, 200
Fourier transformation
conventional, 130, 191, 307, 334
fast, 162
indirect, 131, 308, 337, 500

inverse, 22
Fragments, 278

G

Gaussian distribution, 441
Glancing angle, 90
Globular particles, 170, 181
Goniometer, 106
Guinier-approximation, 25, 155
plot, 248, 257, 376, 390

H

Hankel-transformation, 141, 200
H/D exchange, 205, 313
Heavy atom, 207, 210, 280
Hermite-function, 129
Heterogeneous particles, 48
Hollow particles, 181
cylinder, 184
sphere, 181
Homogeneity, 242, 469
Homogeneous particles, 168, 170

I

Incoherence, 18
Indirect Transformation Method, 131
modification of, 133
Information content, 138
Inhomogeneity
axial, 185
cross-sectional, 186
in-plane, 187
radial, 183
Inhomogeneous particles, 168, 181
Intensity, 19
absolute, 18
primary, 18, 219
at zero angle, 133, 201, 208
Interaction
long range, 392
short range, 392
Interface Distribution Function, 452
Interference
effects, 38
function, 212, 316
interparticle, 39, 189, 471, 500
of waves, 18
Interpretation, 167
Intersection length, 27
Invariant, 22, 28, 43, 454, 474
Isomorphous replacement, 210

K

K_β -filter, 74
Kuhn's model, 394

L

Label, 210, 280, 315
Lamellar-particles, 174, 261, 346
model, 438
Lamellea
amorphous, 444
crystalline, 444
Laplace transformation, 130
Length of particles, 171, 256
Light scattering, 390
Linear system of equations, 129

M

Mass
per unit area, 151, 503
per unit length, 151, 257, 296, 366,
379
Maximum distance, 131, 252
Membranes
spherical, 142
Mirrors
curved, 94
Model parameters, 192
Models
cube method, 160
distance distribution function of,
161
geometrical, 193
mathematical, 193
multibody, 157
scattered intensities of, 157
sphere method, 160
triaxial, 157
Molecular-parameters, 149, 247
weight, 150, 250, 365, 419
Monitor, 80
Monochromatization, 74
by balanced filters, 75, 77
by crystals, 76, 95
electronic, 110
numerical, 75, 77
by totally reflecting mirrors, 77, 94
Monte Carlo method, 363, 408
Mosaic spread, 76
Multiple reflections, 69
Multipole expansion, 193, 200, 274

N
 Neutron scattering, 199, 205, 310, 320, 390

Non-particulate systems, 42
 Normalization of primary beam profiles, 151
 Notation, 154

O
 Optical elements, 90
 Order
 long range, 21
 Oriented particles, 23
 Origin, 139

P
 Parallelepipedons, 24, 32, 156, 174
 Parameters
 model, 168
 molecular, 149
 structural, 153
 Parasitic scattering, 59, 62
 Particle scale, 152
 Path difference, 18
 Patterson function, 20
 Persistence length, 362
 Phase, 18
 factor, 21, 23, 34, 37
 problem, 140, 207, 307, 336
 separation, 493
 transition, 459
 Photomultiplier, 109
 Point-collimation, 85
 of inflection, 172
 Polarization factor, 18
 Polydisperse systems, 147, 285, 403
 Polymer
 bulk, 462
 heterophase, 463
 single crystals, 461

Polynomials, 129
 Porod law, 27, 29, 34, 36, 47, 49 456, 472
 Positioning, 111
 Position sensitive detector, 93, 107, 114
 Power
 per unit length, 152
 Primary-intensity, 18
 beam geometry, 218

Prism, 174
 Pulse height discriminator, 74

R
 Radial
 distribution function, 38
 inhomogeneity, 183, 501
 Radiation damage, 224, 243, 478
 Radius of gyration, 25, 133, 155, 156, 201, 209, 247, 419
 of the cross-section, 34, 155, 257, 296, 363, 415
 of the thickness, 36, 155, 261
 Reciprocal space, 20
 Reciprocity, 20
 Remote control, 93
 Resolution, 136
 Rod-like particles, 32, 150, 171, 183, 256, 316

S
 Sample, 220
 amount, 221, 241
 homogeneity, 469
 temperature, 217
 thickness, 55, 221
 Sampling
 distance, 137
 theorem, 129, 131, 137
 Scattered intensity
 desmeared, 133
 smeared, 121
 at zero angle, 133, 201
 Scattering
 angle, 19, 105
 critical, 495
 curve, 105
 density, 199
 length, 205
 neutron, 199
 Scattering function, 168
 basic, 207
 central part of, 27
 of coil molecules, 401
 final slope of, 27, 29, 34, 36, 47, 49
 shape, 207

Shape, 23, 41, 46, 252, 487
 determination, 147, 203
 function, 443
 Simulation, 133, 149

Sine-functions, 135
 Size distributions, 39, 188, 470
 particle, 147

Slit length, 58
 effect, 121
 Slit width, 58
 effect, 122
 Smoothing, 128
 procedure, 129
 Soller slit, 61
 Solution
 dilute, 22
 Solvent, 241
 Spatial average, 25, 126
 Sphere, 23, 175
 Spherical

 harmonics, 194
 structure, 202, 207, 334, 501
 symmetry, 23, 141, 304, 333
 vesicles, 183, 349
 viruses, 202, 304

Stabilization
 parameter, 132
 routine, 132
 Statistical fluctuations, 41
 Structure

 changes, 282
 determination, 167
 quaternary, 240, 274
 secondary, 240, 268, 300
 tertiary, 240, 270
 Subunits, 163, 178, 255, 277
 Surface, 30, 47, 153, 472
 internal, 30
 specific, 31, 153, 381, 472
 Surrounding function, 39
 Swelling, 376
 Symmetry, 168

 cylindrical, 141
 deviations from 144
 icosahedral, 202
 lamellar, 142
 special, 23

spherical, 23, 141, 304, 333
 Synchrotron radiation, 87, 206, 287

T
 Temperature factor, 131, 307
 Temperature variation, 343
 Termination effect, 130, 132, 307, 335
 Thickness, 153, 174
 factor, 35, 261
 lamellar, 443
 Thomson-factor, 150
 formula for, 18
 Titchmarsh-transformation, 148
 Triangulation method, 280, 315

V
 Virial coefficient, 390, 419
 Voids, 476
 Volume, 28, 153, 208, 250, 341
 excluded, 422
 hydrated, 251
 partial molecular, 49
 partial specific, 233

W
 Wave length, 20, 54
 effect of, 124, 129
 integral of, 124
 distribution of, 218
 Weighted least squares, 129, 130, 132, 143
 stabilized, 132
 Wide angle scattering, 271, 297

X
 X-ray
 film, 92, 113
 optics, 90
 tube, 57

Z
 Zimm-plot, 244, 387